THE HOST RESPONSE TO GRAPEVINE FANLEAF VIRUS AND IMPLICATIONS FOR SYMPTOMATOLOGY AND TRANSMISSION

A Dissertation

Presented to the Faculty of the Graduate School

of Cornell University

In Partial Fulfillment of the Requirements for the Degree of

Doctor of Philosophy

by

Brandon Guy Roy

May 2025

© 2025 Brandon Guy Roy

THE HOST RESPONSE TO GRAPEVINE FANLEAF VIRUS INFECTION AND IMPLICATIONS FOR SYMPTOMATOLOGY AND TRANSMISSION

Brandon Guy Roy, Ph.D.

Cornell University 2025

Grapevine fanleaf virus (GFLV) is a causative agent of fanleaf degeneration in vineyards worldwide, leading to drastic losses in a high commodity crop. GFLV infection modulates host metabolic and immune pathways to result in leaf mottling and chlorosis, as well as uneven fruit set and ripening. Symptoms of GFLV-infected vines in diseased vineyards are defined by the 'patchy' radial spread in relation to the mobility of the ectoparasitic dagger nematode vector *Xiphinema index*.

GFLV (species *Nepovirus foliumflabelli*, genus *Nepovirus, family Secoviridae*) is grouped within the order *Picornavirales* with cowpea mosaic virus and poliovirus. Like all members of *Picornavirales*, GFLV encodes a putative viral RNA-dependent RNA polymerase (protein $1E^{Pol*/Sd}$) to accomplish replication of the viral genome. Previous work elucidated that the C-terminal region of protein $1E^{Pol*/Sd}$ is a symptom determinant, where a single amino acid is necessary but not sufficient to induce symptoms in the model plant *Nicotiana benthamiana*. Given the differences in reaction of this plant host to wildtype and mutant GFLV strains, I sought out to document differences in molecular host regulation to shed light on the function of the elusive symptom determinant.

In Chapter 1 of this dissertation, I summarize current understandings of GFLV

biology and symptom development upon infection. Despite many advances, limited information is available on the host reaction to GFLV infection.

In Chapter 2, I conducted a systematic review of grapevine viruses and their study in model herbaceous plant hosts. Grapevine virology has benefitted greatly from the basic and translational research conducted in faster growing, annual plants. Herbaceous hosts have been, and will continue to be, an excellent tool to understand more about grapevine virus biology, including GFLV biology.

In Chapter 3, I summarize efforts in *in silico* predictive protein modeling of all GFLV proteins, alongside Dr. Choi, to update the current understandings of the viral proteome repertoire and to gain further insights in potential unknown protein domains.

In Chapter 4, I document the capacity of wildtype GFLV strains, as well as engineered mutants, to modulate the immune system of the model plant host *Nicotiana benthamiana* for sustaining infection. I profiled the abundance of transcripts and proteins to explore virus-host interactions by using 3'RNA-sequencing and tandem liquid chromatography mass spectrometry analyses (LC-MS/MS).

In Chapter 5, I characterize the root system architecture (RSA) traits of *N. benthamiana* infected by thirteen wildtype and mutant GFLV strains, and document for the first time, GFLV induced symptomatology in root systems. I employed 3'RNA-Seq to determine differentially abundant transcripts found in root tissue of plants infected with different GFLV strains. The differentially abundant gene categories indicated disruptions to host pathways for inositol signaling, RNA silencing, and production of reactive oxygen species upon infection with symptomatic GFLV strains.

In Chapter 6, I describe a unified mechanism of the host response to GFLV by

integrating all the ‘omics datasets previously produced. GFLV infection induced reactive oxygen species production and modified inositol-mediated signaling in root and leaf tissue, ultimately showing parallels in the infection of root and leaf tissue. Predictive protein modeling indicated a phosphatase domain in the central region of protein $1E^{Pol*/Sd}$, which was hypothesized to be involved in immune regulatory pathways.

In Chapter 7, I document varying levels of transmission in relation to GFLV strains by using a one-step or *continuous* transmission assay. The identity of the viral strain and identity of the amino acid at position 802 of the protein $1E^{Pol*/Sd}$ both contributed to the transmission rate of GFLV. This work provided new molecular insights into GFLV-host-*X. index* interactions.

Finally, the prospectives and conclusions chapter suggests future research and leading hypotheses regarding the function of GFLV protein $1E^{Pol*/Sd}$. Insights on protein structure and protein localization will be imperative to confirm hypothesized functions of the C-terminal domains in protein $1E^{Pol*/Sd}$.

Together, my findings suggest that the C-terminal domain of protein $1E^{Pol*/Sd}$ is involved in the suppression of the plant host immune response, which manifests into leaf and root symptomatic phenotypes. Moreover, I uncovered differences in transmission of symptomatic and asymptomatic GFLV strains through a novel continuous transmission assay. This work has broadened our understanding of virus-host-vector interactions in a soil-borne pathogen and has uncovered molecular pathways unique to GFLV infection that are implicated in symptomatic virus-host relationships.

BIOGRAPHICAL SKETCH

Brandon Guy Roy was born in Phoenix, Arizona and raised in Palmyra, Pennsylvania where he attended Palmyra Area High School. He began research in the lab of Dr. Michelle Rasmussen in summer 2016 as part of the Research First Program at Lebanon Valley College (LVC), where he subsequently pursued a B.S. in Biochemistry and Molecular Biology. During undergraduate work, he continued research in several labs and was also mentored by Dr. Eric Ryndock, Dr. Robert Carey, Dr. Walter Patton, and Dr. Courtney Lappas. He was the first student at LVC to be awarded the Barry Goldwater Scholarship from the United States Department of Defense, National Defense Education Program in April 2019. Brandon completed his undergraduate thesis to graduate summa cum laude and was the Anthony Neidig Award recipient, the LVC top student award, in May 2020.

Brandon joined the Plant Pathology and Plant-Microbe Biology section at Cornell University on a Cornell Graduate School Fellowship and joined the lab of Dr. Marc Fuchs upon completing rotations within his first year. He dedicated time during graduate school to mentor through the Boyce Thompson Institute and the Cornell Agritech Summer Scholars program, and contribute to the Plant Pathology Graduate Student Association and Scholars at the Geneva Experiment Station (SAGES) in various roles. He was awarded a National Science Foundation Research Traineeship in Digital Agriculture for interdisciplinary research on GFLV spanning transcriptomic, proteomic, and bioinformatic informed approaches. Brandon gained motivation and support through collaborators and lab mates who appreciated witty humor and dry sarcasm.

I dedicate this to my younger self: for the challenges faced, the resilience to overcome, and the courage to stand tall in the face of adversity.

If you are reading this, know that you are loved and valued.

ACKNOWLEDGMENTS

To my mentor, colleague, and doctoral thesis advisor Dr. Marc Fuchs. You have gone far beyond your responsibilities of mentorship during this journey. I am inspired by your dedication and commitment to helping others through extension and research. I truly feel as I have grown into a confident scientist and researcher because of the mentorship and trust I received. I was able to achieve because of your unwavering support. Thank you for putting me in the driver's seat, and for your help in navigating this journey.

To my committee members, Dr. Michelle Heck and Dr. Magdalena Julkowska. Thank you for your mentorship and thoughtful guidance. To have your expertise, passion, and advice to aid in this research was irreplaceable. This committee formed a team that kept me balanced, supported, and confident to get here.

To lab members. Anna Wunsch, Elliot McGinity-Schneider, Fu-Wah Choi, Heather McLane, Jiyeong Choi, Kyle Hegel, Larissa Osterbaan, Libby Cieniewicz, Madison Flasco, Rosemary Cox, Scottie Browning, and Victoria Hoyle. Thank you for your comradery, compassion, and encouragement.

To collaborations of the highest caliber. Thank you, Stacy DeBlasio, for your guidance and passion, you quickly became my role model in research skills.

Gérard Demangeat, thank you for your hospitality and generosity in our research together in Colmar. I am so thankful for the experience I was able to have thanks to you. I learned far beyond anything I expected. *Merci infiniment*.

To collaborators Yong Yang and Theodore Thannhauser, thank you for sharing your expertise and insights in mass spectrometry to further understand GFLV.

To the scientists at INRAE and Strasbourg University; particularly the ViVE team of

Emmanuelle Vigne, Anne Sicard, Jean-Michel Hily, Corinne Schmitt-Keichinger, Isabelle Martin, Thémis Léger, Sophie Meyer, Olivier Lemaire, and the entire vibrant community at INRAE Colmar. Thank you for your hospitality and letting me experience a small part of your world. I will never forget the coffee and conversations we shared.

To my dearest friends and colleagues I have gained at Cornell Agritech. To George Stack, Liga Astra-Kalnina, Michael Quade, Kathleen Kanaley, Fernando Romero Galvan, Jaclyn Eller, Stephanie Preisling, and many more. To see you triumph and succeed has been the greatest privilege as your friend. I am so lucky to be surrounded by such wonderful and brilliant scientists.

To the summer scholars of 2022, and to Cary Hicks and Trisha Mutisya. You brought vibrant energy and a spark back to GFLV when I truly needed it. It was deeply rewarding to watch you grow as scientists and work alongside you.

To my partner and greatest support, Robert Robb. You have facilitated one of the biggest transformations in my life and taught me how to love myself. Your unending support and encouragement have allowed me to lean on others and show me who I can become. Your selflessness and integrity are inspiring beyond words, no doubt making me a better human each day.

And to Stella Robb, whose company has been most appreciated during writing and data analysis.

To the Lesbian, Gay, Bisexual, Transgender, Queer, Questioning, Intersex, Asexual, and ally community (LGBTQia+). I have felt support and heartfelt gratitude in many ways from my community. You are loved, you are cared about, and through these many struggles you will unknowingly be able to conquer so much more in your life.

TABLE OF CONTENTS

INTRODUCTION III

BIOGRAPHICAL SKETCH VI

DEDICATION VII

ACKNOWLEDGMENTS VIII

TABLE OF CONTENTS X

LIST OF FIGURES XV

LIST OF TABLES XXV

CHAPTER 1: GRAPEVINE FANLEAF VIRUS BIOLOGY AND SYMPTOMATOLOGY ASSOCIATED WITH FANLEAF DEGENERATION 1

REFERENCES 7

CHAPTER 2: HERBACEOUS PLANT HOSTS AS SUPERMODELS FOR GRAPEVINE VIRUSES: A HISTORICAL PERSPECTIVE 12

ABSTRACT 12

INTRODUCTION 14

EARLIEST HERBACEOUS MODEL SYSTEMS FOR GRAPEVINE VIRUSES 32

HERBACEOUS HOSTS AS INDICATOR PLANTS OF GRAPEVINE VIRUSES 33

GRAPEVINE VIRUSES AND THEIR HERBACEOUS HOSTS THROUGHOUT HISTORY 38

VIRUSES AND THEIR HERBACEOUS HOSTS THAT FOSTER

RESEARCH 38

HERBACEOUS HOSTS SERVING IN HYPOTHESIS DRIVEN RESEARCH 46

DISCUSSION 56

CONCLUSIONS 59

REFERENCES 62

CHAPTER 3: PREDICTIVE MODELING OF PROTEINS ENCODED BY A PLANT VIRUS SHED A NEW LIGHT ON THEIR STRUCTURE AND INHERENT MULTIFUNCTIONALITY 115

ABSTRACT 115

INTRODUCTION 116

MATERIALS AND METHODS 122

RESULTS 127

DISCUSSION 170

REFERENCES 181

CHAPTER 4: PROFILING PLANT PROTEOME AND TRANSCRIPTOME CHANGES DURING GRAPEVINE FANLEAF VIRUS INFECTION 210

ABSTRACT 210

INTRODUCTION 212

EXPERIMENTAL SECTION 218

RESULTS 228

DISCUSSION 263

CONCLUSIONS 274

REFERENCES 275

CHAPTER 5: A SINGLE VIRAL AMINO ACID SHAPES THE ROOT SYSTEM ARCHITECTURE OF A PLANT HOST UPON VIRUS INFECTION 320

ABSTRACT 320

INTRODUCTION 322

MATERIALS AND METHODS 325

RESULTS 332

DISCUSSION 361

CONCLUSIONS 369

REFERENCES 370

CHAPTER 6: MECHANISTIC UNDERPINNINGS OF ABOVE AND BELOW-GROUND PLANT SYMPTOM DEVELOPMENT UPON INFECTION BY GRAPEVINE FANLEAF VIRUS 406

ABSTRACT 406

INTRODUCTION 408

METHODS 413

RESULTS 423

DISCUSSION 463

REFERENCES 472

CHAPTER 7: A SOIL-BORNE VIRUS MODIFIES THE ROOT SYSTEM ARCHITECTURE OF A PLANT HOST VIA A SINGLE AMINO ACID TO

INFLUENCE NEMATODE TRANSMISSION 516

ABSTRACT 516

INTRODUCTION 518

MATERIALS AND METHODS 512

RESULTS 531

DISCUSSION 548

REFERENCES 554

CHAPTER 8: CONCLUSIONS, PROSPECTIVES, AND FUTURE DIRECTIONS FOR GRAPEVINE FANLEAF VIRUS-HOST INTERACTIONS 578

REFERENCES 593

APPENDIX 1: PROCESSING AND MAINTENANCE OF *NICOTIANA BENTHAMIANA* TISSUE FOR PHENOTYPIC, HISTOLOGICAL, AND RIBONUCLEIC ACID ANALYSIS 597

ABSTRACT 597

MATERIALS 598

METHODS 600

REFERENCES 605

APPENDIX 2: EFFORTS TO PURIFY AND CHARACTERIZE THE GRAPEVINE FANLEAF VIRUS ENCODED PROTEIN $1E^{POL*/SD}$, PUTATIVE RNA-DEPENDENT RNA POLYMERASE, PREDICTED PHOSPHATASE, AND SYMPTOM DETERMINANT 606

MATERIALS AND METHODS 607

RESULTS 614

CONCLUSIONS 623

REFERENCES 624

APPENDIX 3: GRAPEVINE RED BLOTCH VIRUS IS TRANSMITTED BY THE THREE-CORNERED ALFALFA HOPPER IN A CIRCULATIVE, NONPROPAGATIVE MODE WITH UNIQUE ATTRIBUTES 626

ABSTRACT 626

INTRODUCTION 627

MATERIALS AND METHODS 631

RESULTS 641

DISCUSSION 659

REFERENCES 668

APPENDIX 4: LACK OF VERTICAL TRANSMISSION OF GRAPEVINE RED BLOTCH VIRUS BY SPISSISTILUS FESTINUS AND SEX-ASSOCIATED DIFFERENCES IN HORIZONTAL TRANSMISSION 680

ABSTRACT 680

INTRODUCTION 682

MATERIALS AND METHODS 683

RESULTS 693

DISCUSSION 708

REFERENCES 712

LIST OF FIGURES

Figure 2-1 Major herbaceous hosts of grapevine viruses that cause disease in *Vitis* species 16

Figure 2-2 Abundance of herbaceous hosts of grapevine viruses described in the literature 35

Figure 2-3 Number of viruses infected grapevine organized by family and their ability to infect herbaceous hosts 41

Figure 3-1 Structure and expression of the grapevine fanleaf virus genomic RNA1, RNA2, and satRNA 120

Figure 3-2 Description of a suite of openly available software used in a protein structure and function prediction pipeline to document the grapevine fanleaf virus (GFLV) protein structure and function 123

Figure 3-3 The performance and relative confidence for protein prediction software across the grapevine fanleaf virus (GFLV) proteins revealed trends behind protein-specific and software-specific challenges in producing confident models 136

Figure 3-4 Computational analysis and protein structure prediction of the five mature proteins encoded by grapevine fanleaf virus (GFLV) RNA1 138

Figure 3-5 Transmembrane domain predictions by Phyre2 of grapevine fanleaf virus (GFLV) proteins returned only two possible candidates, protein $1B^{Hel*/VSR}$ and protein $1E^{Pol*/Sd}$ 140

Figure 3-6 Analyses of the top predictions for proteins of grapevine fanleaf virus (GFLV) to map the putative helicase ($1B^{Hel*/VSR}$), protease ($1D^{Pro}$), and

putative RdRP active sites (1E$^{Pol*/Sd}$) 142

Figure 3-7 Predicted modeling of the structure and function(s) of proteins encoded by RNA2 of grapevine fanleaf virus (GFLV) 144

Figure 3-8 Predicted modeling of the structure and function(s) of the protein encoded by satRNA of grapevine fanleaf virus (GFLV) 146

Figure 3-S1 Grapevine fanleaf virus coat protein predictions align well with the already resolved crystalline structure (PDB:5FOJ) 207

Figure 4-1 Grapevine fanleaf virus (GFLV) genetic composition and symptom expression in *Nicotiana benthamiana* 215

Figure 4-2 Principal component analysis for unbiased observation of acquired proteomics and transcriptomics data 230

Figure 4-3 Select transcriptomics contrasts at four, seven, and twelve days post inoculation of *Nicotiana benthamiana* infected with various grapevine fanleaf virus strains 235

Figure 4-4 Select proteomics contrasts at four, seven, and twelve days post inoculation of *Nicotiana benthamiana* infected with various grapevine fanleaf virus strains 237

Figure 4-5 Gene set enrichment analysis of overrepresented genes present in the transcriptome analyses 245

Figure 4-6 Overrepresented gene ontologies for proteomic analysis 246

Figure 4-7 Differential gene set enrichment analysis network of wildtype grapevine fanleaf virus strain ‘GHu’ at seven days post inoculation of *Nicotiana benthamiana* contrasted against all other viral treatments 249

Figure 4-8 Functional categorization of weighted gene co-expression network analysis eigengene modules unique to infection of *Nicotiana benthamiana* infected by grapevine fanleaf virus wildtype strain GHu at seven days post inoculation 253

Figure 4-9 Overlapping identified genes present within differential abundance analysis at transcriptomic and proteomic levels 256

Figure 4-10 Hypothesized major networks for symptom development in *Nicotiana benthamiana* upon infection by grapevine fanleaf virus strain GHu deduced from profiling proteome and transcriptome changes 259

Figure 4-S1 Schematic representation of tissue collection, transcript and peptide acquisition, and bioinformatic analysis of data collected for the summative analysis presented 297

Figure 4-S2 Summary analysis of full proteome data retrieved from 73 samples specific to the number of proteins identified across all samples of proteins isolated from *Nicotiana benthamiana* 298

Figure 4-S3 Distribution of protein counts and missing values before and after variance stabilizing normalization 299

Figure 4-S4 Missing values pattern across entire experiment reveals many proteins are missing not at random and are specific to viral contrasts 300

Figure 4-S5 Summary statistics of protein samples 301

Figure 4-S6 Euclidian heatmaps, Pearson correlation matrices, and Gower's distance matrices of protein expression in *Nicotiana benthamiana* infected with various grapevine fanleaf virus strains 302

Figure 4-S7 Summary analysis of full transcriptome data retrieved from 75 samples specific to the number of transcripts identified across all samples of RNA isolated from Nicotiana benthamiana infected with various grapevine fanleaf virus strains and mutants 304

Figure 4-S8 Dispersion estimates of DESeq2 transcriptome analysis 305

Figure 4-S9 Hierarchal clustering via 'McQuitty' method for transcriptomic sample alignment files 307

Figure 4-S10 Principal component analysis of transcriptomics full experimental design 309

Figure 4-S11 Boxplots depicting grapevine fanleaf virus (GFLV) titer in infected *Nicotiana benthamiana* measured by RNA-Seq and LC-MS/MS 310

Figure 4-S12 Additional transcriptomics data of *Nicotiana benthamiana* leaf tissue 311

Figure 4-S13 Additional volcano plots of proteomic contrasts 313

Figure 4-S14 Eigengene modules created from the transcriptomic dataset 315

Figure 4-S15 Functional categorization of weighted gene co-expression network analysis eigengene modules unique to mutant grapevine fanleaf virus (GFLV) strain F13 mutant 1EK802G in *Nicotiana benthamiana* plants at four days post inoculation 317

Figure 4-S16 RNA expression levels of Niben101Scf01478g00014, 60S ACIDIC RIBOSOMAL PROTEIN P1 through 3'RNA-Seq normalized counts and reverse transcription quantitative polymerase chain reaction 318

Figure 5-1 Root system architecture traits for *Nicotiana benthamiana* infected with

four strains of grapevine fanleaf virus at 17 days post-inoculation 334

Figure 5-2 Root system architecture traits for *Nicotiana benthamiana* infected with four strains of grapevine fanleaf virus at 26 days post-inoculation 335

Figure 5-3 The root system architecture of *Nicotiana benthamiana* plants upon grapevine fanleaf virus infection is dependent on the identity of amino acid 802 in protein $1E^{Pol*/Sd}$ 336

Figure 5-4 Reactive oxygen species transiently produced in *Nicotiana benthamiana* primary root pericycle by four grapevine fanleaf virus strains at 7- and 11-days post-inoculation 342

Figure 5-5 Volcano plot contrasts of *Nicotiana benthamiana* plants infected with two grapevine fanleaf virus strains (i.e., wildtype GHu and mutant GHu $1E^{Pol*/Sd}_{K802G}$) reveal perturbations of the root transcriptome at three time points; 4-, 17- and 26 days post-inoculation 352

Figure 5-6 Downstream overabundance of transcript dysregulation in *Nicotiana benthamiana* roots infected with wildtype grapevine fanleaf virus strain GHu through gene set enrichment analysis and Kyoto Encyclopedia of Genes and Genomes reveals several conserved pathways of overabundance 357

Figure 5-7 The dysregulation of three major pathways in the roots of *Nicotiana benthamiana* infected by grapevine fanleaf virus revealed by ontology and enrichment analysis. a Immune receptors and innate immune pathways were disrupted at 4- and 17-days post-inoculation when comparing viral treatments to mock inoculated plants 359

Figure 5-S1 Reannotation of the *Nicotiana benthamiana* genome from data curation to enrichment analysis 391

Figure 5-S2 Representative root phenotypes of *Nicotiana benthamiana* upon differential grapevine fanleaf virus strain infections at four-, 17-, and 26-days post inoculation 392

Figure 5-S3 Correlation matrices of acquired root phenotypic data for *Nicotiana benthamiana* infected with grapevine fanleaf virus 393

Figure 5-S4 Root system architecture traits for *Nicotiana benthamiana* infected with four strains of grapevine fanleaf virus at four days post inoculation 394

Figure 5-S5 Additional root traits of *Nicotiana benthamiana* infected with grapevine fanleaf virus at various time points after inoculation 395

Figure 5-S6 Quantitative real-time polymerase chain reaction and 3'RNA-sequencing based detection of grapevine fanleaf virus from *Nicotiana benthamiana* root tissue 397

Figure 5-S7 Linear model generation for *Nicotiana benthamiana* infected with grapevine fanleaf virus strain 'GHu' at 26 days post inoculation 398

Figure 5-S8 Primary analysis of input RNA-Seq data shows presence of outlier 'mutant GFLV-GHu $1E^{Pol}{}_{K802G}$ at 17 days post inoculation 399

Figure 5-S9 Analysis of input RNA-Seq data shows grouping of viral treated individuals and acceptable input for differential abundance testing after removal of outlier sample 400

Figure 5-S10 Experiment wide gene set enrichment analysis shows small overlaps of treatment-wise comparisons through differential abundance testing 401

Figure 5-S11 Enrichment results of differentially abundant host genes through Kyoto Encylopedia of Genes and Genomes (KEGG) analysis of grapevine fanleaf virus infected *Nicotiana benthamiana* 403

Figure 6-1 Strains of grapevine fanleaf virus (GFLV) used in this study 414

Figure 6-2 Chlorophyll quantification upon infection with GFLV 423

Figure 6-3 Root system architecture analysis across 13 strains of GFLV 429

Figure 6-4 Root image cross sections of selected *Nicotiana benthamiana* plants used for X-ray tomography-based imaging 430

Figure 6-5 Impact of foliar application of myo-inositol and phytohormones on GFLV infection 437

Figure 6-6 Integration of transcriptomics and proteomics datasets 438

Figure 6-7 GFLV protein $1E^{Pol*/Sd}$ contains a structurally predicted phosphatase domain 453

Figure 6-8 Functional predictions for the predicted phosphatase domain 457

Figure 6-9 The hypothesized mechanism in which GFLV induces symptoms 461

Figure 6-S1 Reactive oxygen species detection in apical leaves upon GFLV infection of *Nicotiana benthamiana* 503

Figure 6-S2 Principal component analysis (PCA) of root systems upon differential strain GFLV infection 504

Figure 6-S3 Biplot expansion of PCA features 505

Figure 6-S4 Quantitative comparison of primary root features 506

Figure 6-S5 Stem-down view of micro-CT scans obtained of primary roots 507

Figure 6-S6 Side view of micro-CT scans obtained of primary roots 508

Figure 6-S7 Overview of omics integration for technique, tissue type, time collected, and viral treatments used 509

Figure 6-S8 Transcriptomic profiling of genes identified through co-immunoprecipitation 510

Figure 6-S9 Documented dysregulation of the inositol signaling cascade upon GFLV infection 511

Figure 6-S10 Dysregulation of metabolic pathways for lignin deposition upon GFLV infection 512

Figure 6-S11 Additional identified protein domain and motifs in GFLV protein 1E 513

Figure 6-S12 Schematic representation of possible ways GFLV could elicit symptoms and ROS production during infection 514

Figure 7-1 Experimental design of transmission assays evaluated 525

Figure 7-2 Transmission of continuous assays and viral titer in roots at the conclusion of the assay 536

Figure 7-3 Correlation analysis of root traits to transmission rate and viral titer accumulation in nematode samples 538

Figure 7-4 Spatial modeling of plant systems rejects differences in titer to influence transmission rates 539

Figure 7-5 Recovered nematodes and respective titer rejects differences in vectoring capacity to influence transmission 542

Figure 7-6 Root system architecture influences GFLV transmission 546

Figure 7-S1 Elutriation technique for the isolation of *Xiphinema index* 572

Figure 7-S2 Spatial distribution of GFLV continuous assays, donor and recipient plant placement, and replications 574

Figure 7-S3 Root system architecture traits of donor and recipient plants 575

Figure 7-S4 Inter-plate normalization metrics and evaluation of standard curves 576

Figure 8-1 Cumulative understandings on grapevine fanleaf virus-host-vector-environment interactions 581

Figure 8-2 Phylogenetic analysis of 1E protein across the *Nepovirus* genus 586

Figure A2-1 Vector diagram and multiple cloning site of pCAV4 608

Figure A2-2 Domain prediction analysis of protein 1E 615

Figure A2-3 Secondary structure prediction of protein 1E 616

Figure A2-4 Protein purification analysis of protein 1E 620

Figure A2-5 Ion exchange chromatography of protein 1E 621

Figure A3-1 Schematic representation of the transmission assays performed in this study 636

Figure A3-2 Quantitative determination of grapevine red blotch virus in *Spissistilus festinus* after exposure to infected *Vitis vinifera* 654

Figure A3-3 Quantification of grapevine red blotch virusby quantitative polymerase chain reaction after gut clearing on alfalfa 655

Figure A4-1 Schematic representation of the transovarial transmission assays performed in this study 685

Figure A4-2 Schematic representation of the *Spissistilus festinus* dispersal experiments on detached snap bean trifoliates 688

Figure A4-3 Schematic representation of transmission assays with grapevine red blotch virus-infected bean trifoliates (male vs female) 689

Figure A4-4 Transmission of grapevine red blotch virus from bean trifoliate to bean trifoliate, compared by sex 698

Figure A4-5 Cumulative distribution of *Spissistilus festinus* across 30 *Phaseolus vulgaris* trifoliates comparing morning and afternoon presence 700

Figure A4-6 Cumulative distribution of *Spissistilus festinus* across 30 *Phaseolus vulgaris* compared by experimental replicate over time 701

Figure A4-7 Locations of girdling behaviors observed by male and female *Spissistilus festinus* on detached bean trifoliates 702

Figure A4-8 GRBV quantification in *Spissistilus festinus* 705

LIST OF TABLES

Table 2-1 List of viruses identified in *Vitis* species, their genome composition, GenBank accession numbers, and infectious clones if available 17

Table 2-2 Experimental herbaceous hosts of grapevine viruses 21

Table 2-S1 Ability of grapevine viruses to infect herbaceous hosts (expanded) 103

Table 2-S2 Summary of herbaceous host status across families of grapevine viruses 109

Table 2-S3 Status of the 26 plant species most referred to herbaceous hosts for currently documented grapevine viruses 110

Table 3-1 Putative and experimentally confirmed functions and subcellular localization of GFLV proteins 128

Table 3-2 Protein prediction algorithms utilized for this study 131

Table 3-3 Predicted ontologies for GFLV strain F13 147

Table 3-4 Predicted ontologies for GFLV strain GHu 149

Table 3-S1 Accessions of grapevine fanleaf virus used in this study 198

Table 3-S2 Grapevine fanleaf virus amino acid sequences used in protein prediction tools, with respective strain and NCBI accession numbers 199

Table 3-S3 Reporting metrics for protein prediction software in the determination of protein structure 200

Table 3-S4 Curated functional annotations of grapevine fanleaf virus (GFLV) proteins 202

Table 3-S5 Predicted subcellular localization for proteins encoded by grapevine fanleaf virus strain F13 and GHu and satRNAs 203

Table 3-S6 Nucleotide binding-site prediction table based on NsitePred (Chen et al. 2012) 204

Table 3-S7 Binding site prediction encoded by grapevine fanleaf virus proteins according to prediction modeling and previously reported findings 205

Table 3-S8 Transmembrane domains/helices and/or pore-lining domains, encoded by proteins of grapevine fanleaf virus strain F13 and GHu and satRNAs 206

Table 4-1 Summary of differentially abundant transcripts between grapevine fanleaf virus treatment groups at four, seven, and twelve-days post inoculation of *Nicotiana benthamiana* 239

Table 4-2 Summary of differentially abundant proteins identified with medium or high confidence between grapevine fanleaf virus treatment groups at three time points post-inoculation of *Nicotiana benthamiana* 240

Table 4-S1 Sequence of primers used in quantitative reverse transcription polymerase chain reaction 287

Table 4-S2 Summary of proteomics mapping peptides to reference genome 288

Table 4-S3 Statistics of transcriptomics data mapping to *Nicotiana benthamiana* genomes v0.4.4, v1.0.1, and manually curated Nepo3 alignment files 289

Table 4-S4 Overlap between differentially abundant host genes identified by transcriptomics and proteomics following infection of *Nicotiana benthamiana* by grapevine fanleaf virus (GFLV) 291

Table 4-S5 Top five proteins and transcripts by fold change in the proteomics and

transcriptomics analyses, respectively, for wildtype grapevine fanleaf virus strain GHu vs mutant GHu 1E$_{K802G}$ contrast 292

Table 4-S6 Gene names of differentially abundant genes with associated statistics in contrasts across proteomics and transcriptomics data, organized by contrasts of interest 293

Table 4-S7 List of differentially abundant genes with annotated name and function found in transcriptomics and proteomics datasets at seven days post inoculation when contrasting wildtype 294

Table 4-S8 Overlapping genes from transcriptomics and proteomics differential abundance contrasts 295

Table 4-S9 Gene count matrix of defined target genes including RNA silencing components, 43S pre-initiation complex components, receptors, receptor-like proteins, and unknown proteins 296

Table 5-1 Differentially abundant transcripts as compared through DESeq2 analysis of *Nicotiana benthamiana* plant roots infected with two strains of grapevine fanleaf virus 347

Table 5-2 The top ten differentially abundant transcripts present in each viral contrast with their respective gene ID, name, Log2FoldCahnge, and p-value, ranked by p-value 348

Table 5-S1 Grapevine fanleaf virus (GFLV) RNA1 sequence analyses of DNA amplicons obtained from root tissue of *Nicotiana benthamiana* by reverse transcription and quantitative polymerase chain reaction 381

Table 5-S2 Primer sets used in polymerase chain reaction for detection of grapevine

fanleaf virus (GFLV) 382

Table 5-S3 Root system architecture traits of *Nicotiana benthamiana* plants infected with four grapevine fanleaf virus strains at three time points following mechanical inoculation of leaves 383

Table 5-S4 Relative percentage change of root system architecture traits of *Nicotiana benthamiana* plants infected with four distinct grapevine fanleaf virus trains compared with mock control at three time points following mechanical inoculation of leaves 385

Table 5-S5 Root system architecture metrics of Nicotiana benthamiana at four, seventeen, and twenty six days post inoculation with grapevine fanleaf virus (GFLV), organized by viral treatment group 387

Table 5-S6 Symptomology observations of *Nicotiana benthamiana* plants from infection of grapevine fanleaf virus strain wildtype GHu 388

Table 5-S7 Metrics corresponding to 3'RNA-Seq data acquisition, trimming, alignment and gene encoding products, and quality per sample 389

Table 5-S8 All differentially abundant genes across all contrasts generated in DESeq2 analysis 390

Table 6-1 Infection rates upon application of myo-inositol 435

Table 6-2 Infection rates upon application of phytohormones 436

Table 6-3 Symptomology persistence after application of phytohormones 436

Table 6-4 Co-immunoprecipitation resolved protein interactors of protein 1E 442

Table 6-5 Comparative analysis of root and shoot transcriptomes 446

Table 6-6 Domains prediction for protein $1E^{Pol*/Sd}$ 452

Table 6-S1 Primers used in this study 485

Table 6-S2 Experimental design and infection rates of grapevine fanleaf virus 486

Table 6-S3 Repeated SPAD readings of GFLV infected plants 487

Table 6-S4 Temporal chlorophyll quantification of apical leaves upon infection 488

Table 6-S5 Pairwise comparison analysis of temporal SPAD readings 489

Table 6-S6 Primary root trait analysis, area and circumference 491

Table 6-S7 Proteins identified in co-immunoprecipitation assays 492

Table 6-S8 Count summary of omics overlap for GFLV infection *in planta* 493

Table 6-S9 Overlapping genes between root and shoot transcriptomic data 495

Table 6-S10 Dysregulated transcripts for all datasets analyzed 496

Table 6-S11 Functional enrichment analysis of overlapping genes 497

Table 6-S12 Top protein databank matches for protein $1E^{Pol*/Sd}$ predictions 498

Table 6-S13 Detailed analysis of top protein matches 499

Table 6-S14 Enzyme classification predictions 500

Table 6-S15 Active site prediction overlap for all protein predictions 501

Table 6-S16 Predicted protein models summary 502

Table 7-1 Transmission rates of GFLV by *Xiphinema index* from various plant hosts to grapevine 531

Table 7-2 Transmission rates of GFLV by *Xiphinema index* to and from identical plant species 531

Table 7-3 Transmission rates of GFLV by *Xiphinema index* across multiple wildtype and mutant viral strains 535

Table 7-4 Aviruliferous *Xiphinema index* detected in the continuous transmission

assay 543

Table 7-S1 Primers used in this study 565

Table 7-S2 Experimental design for inter-plate standards and normalization 566

Table 7-S3 Serial dilution of stock GFLV purification standard 567

Table 7-S4 Number of *X. index* recovered from each experimental bin 568

Table 7-S5 Quantitative metadata of associated root images for the determination of root system architecture traits 569

Table 7-S6 Total root system architecture traits analyzed in this study 571

Table A2-1 Primers used in this study 607

Table A2-2 Characteristics of protein 1E domains 613

Table A3-1 Detection of grapevine red blotch virus (GRBV) in herbaceous hosts following *Agrobacterium tumefaciens*-mediated inoculation of GRBV infectious clones NY175 and NY358 643

Table A3-2 Detection of grapevine red blotch virus (GRBV) by RT-PCR in *Phaseolus vulgaris*, a pseudo-systemic host, following Agrobacterium tumefaciens-mediated inoculation of infectious clone NY175 644

Table A3-3 Transmission of grapevine red blotch virus (GRBV) on excised *Phaseolus vulgaris* and *Vitis vinifera* leaves following acquisition by *Spissistilus festinus* on infected *P. vulgaris* during various acquisition access periods 647

Table A3-4 Detection of grapevine red blotch virus (GRBV) in dissected organs (gut and head with salivary glands) of *Spissistilus festinus* following virus acquisition on infected *Phaseolus vulgaris* 648

Table A3-5 Detection of grapevine red blotch virus (GRBV) in dissected organs (guts and heads with salivary glands) and collected hemolymph of *Spissistilus festinus* after virus acquisition on naturally infected *Vitis vinifera* 651

Table A4-1 Lack of transovarial transmission of GRBV by *Spissistilus festinus* ... 693

Table A4-2 No detectable GRBV in *Phaseolus vulgaris* trifoliates following feeding by the nymphal progeny of *Spissistilus festinus* females and males exposed to GRBV-infected plants across all developmental stages ... 694

Table A4-3 Transmission of GRBV isolates NY358 (phylogenetic clade 2) and NY175 (phylogenetic clade 1) by male and female *Spissistilus festinus* 697

Table A4-4 Rate of grapevine red blotch virus transmission by *Spissistilus festinus* males and females in arenas with single or hotspot infections 704

CHAPTER 1

GRAPEVINE FANLEAF VIRUS BIOLOGY AND SYMPTOMATOLOGY ASSOCIATED WITH FANLEAF DEGENERATION

GRAPEVINE FANLEAF VIRUS

Fanleaf degeneration is the disease caused by grapevine fanleaf virus that is known globally by many different names such as arriccianmento (Italian), court-noué and dégénérescence infectieuse (French), and Reisigkrankheit (German). Some of the first mentions of this disease is in a late 19th century publication from a scientist working outside present day Vienna, Austria (Ráthay 1882; 1883). Here it was first postulated that the soil somehow linked the peculiar branching, distorted leaf shapes, and undesirable fruit in diseased vineyards. This astute observation links grapevine fanleaf virus (GFLV, species *Nepovirus foliumflabelli,* genus *Nepovirus,* family *Secoviridae*) to fanleaf degeneration that still impacts grape production at the global scale (Andret-Link et al. 2004a). Reports indicate up to 80% yield loss and reduced fruit quality, which is costly for wine production (Martelli and Taylor 1990). It was estimated that in 2015 alone, GFLV was responsible for over $1.5 billion USD in losses in France (Fuchs and Lemaire, 2017). Leaf mosaic and yellowing, semantic leaf fanning and shortened internodes, and malformed leaf sinuses are noticeable for GFLV-infected vines early in the spring. Fruit associated symptoms become visible later in the growing season with fruit set and fruit maturation. The impact of GFLV infection can vary due to differences in host genotype (*Vitis* spp.), viral genotype, vineyard site, and environmental factors.

GFLV can be disseminated through vegetative propagation and grafting (Cadman et al. 1960). This virus is also transmitted via the ectoparasitic dagger nematode vector *Xiphinema index* (family *Longidoridae*) (Hewitt et al. 1958). These distinct modes are particularly troublesome for the perennial cultivation style of *Vitis* sp. but especially considering the biology of the vector in vineyard ecosystems. *X. index* can survive multiple years (≥ 4) in the absence of host plants while retaining detectable levels of GFLV (Demangeat et al. 2005). The long retention of GFLV in *X. index* would suggest that a grower should wait five or more years to replace infected vines. This is a largely unobtainable goal in most grape-growing regions. There is no cure for GFLV and no means of control for GFLV or *X. index*. Therefore, prevention and the use of virus-tested plant material is highly recommended to reduce the risk of infection. New, innovative approaches are needed to address disease induced by GFLV infection.

Recent research in plant virology has aimed to understand the molecular basis of symptom elicitation upon infection. Symptoms of viral disease have been linked to susceptibility factors in plant hosts as well as viral proteins that are linked to replication, silencing, and host evasion (Akhter et al. 2021; García and Pallas 2015; Osterbaan et al. 2019; Pallas and García 2011). Substantial progress has been made to document the biology of GFLV, however the response of plant hosts to infection is severely lacking in understanding.

SYMPTOM ELICITATION IN PLANT HOSTS UPON VIRAL INFECTION

Our understandings of viral disease draw from both viral and host biology, where the response and counter-response of each organism results in a variety of

phenotypic displays. Upon entry, viruses hijack the cellular machinery to facilitate replication and spread in a new plant or host. As a result, cellular signatures such as viral proteins, double-stranded RNA, and changes in host gene expression can trigger several anti-viral stress responses (Osterbaan and Fuchs 2019; Jiang and Zhou 2023). Generally, dysregulation of host pathways results in reactive oxygen species accumulation to hinder and stop virus replication. The most drastic ends of this spectrum of host response are incompatible virus-host relationships (resistance) and asymptomatic infections (tolerance). In a resistant or non-susceptible host, plants prevent movement of a virus beyond the initial infection site, associated with the blocking of plasmodesmata by callose deposition (i.e. localized hypersensitive response) (Wang et al. 2021). Conversely, asymptomatic infections manipulate host defense mechanisms to avoid detection and typically accumulate at low levels. Some viral infections present symptoms briefly and then appear asymptomatic after some time, a concept referred to as recovery. In other closely related systems, recovery is also thought to be linked to viral silencing mechanisms (Ghoshal and Sanfaçon 2015), but the link between symptoms and viral silencing has not been confirmed for GFLV.

Symptom determinants have been described in other plant virus systems. Tomato yellow leaf curl China virus encodes protein ßC1 that is a viral silencing suppressor and symptom determinant that drastically modifies leaf shape and induces chlorosis (Yang et al. 2008). The coat protein of cucumber mosaic virus also is both a suppressor of viral silencing and symptom determinant (Qui et al. 2018). Many other examples have been compiled in recent literature reviews (Osterbaan and Fuchs 2019; Jiang and Zhou 2023). The mechanism of symptom elicitation is largely unknown for

many plant viruses (Rao 1999). On this premise I utilized GFLV with the model host *Nicotiana benthamiana* to determine host genes implicated in transient symptom expression in leaf and root tissue.

THE PUTATIVE RNA-DEPENDENT RNA POLYMERASE IS A GFLV SYMPTOM DETERMINANT IN A MODEL PLANT HOST

GFLV encodes protein $1E^{Pol*/Sd}$, the putative RNA-dependent RNA polymerase that is also coined a symptom determinant (Vigne et al. 2013; Osterbaan et al. 2019). The difference in genotype between two naturally occurring strains of GFLV, GFLV-F13 and GFLV-GHu (Huss et al. 1989) are noted for asymptomatic and vein-clearing phenotypes in *N. benthamiana*, respectively. This difference allowed for the iterative swapping and mutation of this protein sequence to isolate the C-terminal amino acid at position 802 to contribute to symptom elicitation (Vigne et al. 2013; Osterbaan et al. 2019). By modifying this residue at position 802 from lysine (K) to glycine (G) in GFLV-GHu, mutant GFLV-GHu $1E_{K802G}$ remained infectious but the transient vein clearing phenotype was abolished (Osterbaan et al. 2019). Conversely, modifying the native G of GFLV-F13 to K did not induce symptoms (Osterbaan et al. 2019). This work concluded that K at amino acid 802 is necessary but not sufficient to elicit vein clearing in *N. benthamiana*. This region has no assigned protein function beyond the descriptor 'symptom determinant region', defined by the phenotypic observations.

It is not known how GFLV protein $1E^{Pol*/Sd}$ interacts with host components to elicit symptoms. The C-terminus of this protein is largely non-homologous to known sequences, where only closely related viruses contain similar identity (Osterbaan et al.

2019). It is hypothesized from current understandings that GFLV protein $1E^{Pol*/Sd}$ interacts with host proteins to dampen the host immune response, at varying levels of success. It is also not understood why a soil-borne virus would elicit symptoms in leaf tissue, when evolutionary pressures suggest that GFLV would adapt strategies to manipulate the nematode vector rather than any above ground traits. Despite understandings of soil-borne virus transmission, root systems of GFLV-infected plants have not been quantitatively evaluated in the absence of nematode vector pressure.

LIMITATIONS OF RESEARCH FOR A SOIL-BORNE PATHOGEN IN *VITIS*

Roots are a largely understudied plant organ in grapevine, and even moreso when considering GFLV. Previous observations of grapevine roots have convoluted the impacts of *X. index* and GFLV, where it is uncertain if nematode feeding, viral infection, or their combined presence lead to perturbations in root system morphology (Valat et al. 2004). My research is the first to indicate that GFLV alone can modify root system architecture (RSA) traits of *N. benthamiana* and that a single amino acid of the C-terminal region of protein $1E^{Pol*/Sd}$ is necessary and sufficient to induce these symptoms. This was complemented by transmission assays with *X. index*, where the same GFLV strains and mutants were examined in a novel one-step transmission assay. This work was largely inspired by techniques used in above-ground plant virus transmission assays to reduce the amount of intervention in experimental procedures. There is a need for attention to root physiology and anatomy to further understand molecular mechanisms of viral disease symptoms, and downstream impacts on transmission.

OTHER SYMPTOM DETERMINANTS OF GFLV

GFLV homing protein $2A^{HP}$ is also recognized as a symptom determinant in the model host *Nicotiana occidentalis* (Martin et al. 2017) In this instance, GFLV strain F13 induces necrotic lesions on inoculated leaves, while strain GHu induces systemic vein clearing in uninoculated apical leaves (Martin et al. 2017). Interestingly, this has been documented as an avirulence factor, where strain F13 is suggested to contain a protein motif compatible with a host immune receptor (R gene) to result in an immune response. The presentation of necrotic lesions upon transient expression of $2A^{HP}$ supports this hypothesis (Martin et al. 2018).

Plant hosts identified for compatible interactions with GFLV (*Chenopodium*, *Nicotiana*, *Vitis*, etc.) differ largely in their response to GFLV infection. The hardships of perennial crops have impeded upon progress to identify host components involved in GFLV induced symptom development, further convoluted by the large genome and genetic diversity of grapevine. Substantial work was performed to optimize environmental conditions (humidity, light, temperature) to result in symptom development for *N. benthamiana* (Osterbaan and Fuchs 2018). Such conditions have not been explored for other plant hosts. The role of host genetics and environmental conditions undoubtedly contribute to the degree of symptom expression during GFLV infection, however these have yet to be examined. Given the many factors contributing to symptomatic GFLV infection, methodical, interdisciplinary approaches will be required to unravel the molecular mechanism(s) of symptom development.

REFERENCES

Andret-Link, P., Laporte, C., Valat, L., Ritzenthaler, C., Demangeat, G., Vigne, E., Laval, V., Pfeiffer, P., Stussi-Garaud, C., and Fuchs, M. 2004. Grapevine fanleaf virus: Still a major threat to the grapevine industry. Journal of Plant Pathology 86:183–195.

Andret-Link, P., Schmitt-Keichinger, C., Demangeat, G., Komar, V., and Fuchs, M. 2004. The specific transmission of *Grapevine fanleaf virus* by its nematode vector *Xiphinema index* is solely determined by the viral coat protein. Virology 320:12–22. https://doi.org/10.1016/j.virol.2003.11.022.

Choi, J., Browning, S., Schmitt-Keichinger, C., and Fuchs, M. 2024. Mutations in the WG and GW motifs of the three RNA silencing suppressors of grapevine fanleaf virus alter their systemic suppression ability and affect virus infectivity. Front. Microbiol. 15. https://doi.org/10.3389/fmicb.2024.1451285.

Choi, J., Pakbaz, S., Yepes, L. M., Cieniewicz, E. J., Schmitt-Keichinger, C., Labarile, R., Minutillo, S. A., Heck, M., Hua, J., and Fuchs, M. 2023. Grapevine fanleaf virus RNA1-encoded proteins 1A and 1BHel suppress RNA silencing. Mol Plant Microbe Interact. https://doi.org/10.1094/MPMI-01-23-0008-R.

Demangeat, G., Voisin, R., Minot, J.-C., Bosselut, N., Fuchs, M., and Esmenjaud, D. 2005. Survival of *Xiphinema index* in vineyard soil and retention of *Grapevine fanleaf virus* over extended time in the absence of host plants. Phytopathology 95:1151–1156. https://doi.org/10.1094/PHYTO-95-1151.

Fuchs, M., and Lemaire, O. 2017. Novel Approaches for Viral Disease Management. In *Grapevine Viruses: Molecular Biology, Diagnostics and Management*, eds.

Baozhong Meng, Giovanni P. Martelli, Deborah A. Golino, and Marc Fuchs. Cham: Springer International Publishing, pp. 599–621. https://doi.org/10.1007/978-3-319-57706-7_29.

García JA, Pallás V. Viral factors involved in plant pathogenesis. Current opinion in virology. 2015 Apr 1;11:21-30.

Ghoshal, B., and Sanfaçon, H. 2015. Symptom recovery in virus-infected plants: Revisiting the role of RNA silencing mechanisms. Virology 479–480:167–179. https://doi.org/10.1016/j.virol.2015.01.008.

Hewitt, W., Raski, D., and Goheen, A. 1958. Transmission of fanleaf virus by Xiphinema index Thorne and Allen. In AMER PHYTOPATHOLOGICAL SOC 3340 PILOT KNOB ROAD, ST PAUL, MN 55121, pp. 393–394.

Huss, B., Walter, B., and Fuchs, M. 1989. Cross-protection between arabis mosaic virus and grapevine fan leaf virus isolates in Chenopodium quinoa. Annals of Applied Biology 114:45–60.

Jiang, T., and Zhou, T. 2023. Unraveling the Mechanisms of Virus-Induced Symptom Development in Plants. Plants (Basel) 12:2830. https://doi.org/10.3390/plants12152830.

Margis, R., and Pinck, L. 1992. Effects of site-directed mutagenesis on the presumed catalytic triad and substrate-binding pocket of grapevine fanleaf nepovirus 24-kDa proteinase. Virology 190:884–888. https://doi.org/10.1016/0042-6822(92)90931-E.

Margis, R., Ritzenthaler, C., Reinbolt, J., Pinck, M., and Pinck, L. 1993. Genome organization of grapevine fanleaf nepovirus RNA2 deduced from the 122K

polyprotein P2 *in vitro* cleavage products. Journal of General Virology 74:1919–1926.

Margis, R., Viry, M., Pinck, M., Bardonnet, N., and Pinck, L. 1994. Differential proteolytic activities of precursor and mature forms of the 24K proteinase of Grapevine fanleaf nepovirus. Virology 200:79–86. https://doi.org/10.1006/viro.1994.1165.

Margis, R., Viry, M., Pinck, M., and Pinck, L. 1991. Cloning and *in vitro* characterization of the grapevine fanleaf virus proteinase cistron. Virology 185:779–787. https://doi.org/10.1016/0042-6822(91)90549-Q.

Martelli, G. P., and Taylor, C. E. 1990. Distribution of Viruses and Their Nematode Vectors. In *Advances in Disease Vector Research*, Advances in Disease Vector Research, ed. Kerry F. Harris. New York, NY: Springer New York, pp. 151–189. https://doi.org/10.1007/978-1-4612-3292-6_6.

Martin, I. R., Vigne, E., Berthold, F., Komar, V., Lemaire, O., Fuchs, M., and Schmitt-Keichinger, C. 2017. The 50 distal amino acids of the $2A^{HP}$ homing protein of *Grapevine fanleaf virus* elicit a hypersensitive reaction on *Nicotiana occidentalis*. Molecular Plant Pathology 19:731–743. https://doi.org/10.1111/mpp.12558.

Osterbaan, L. J., Choi, J., Kenney, J., Flasco, M., Vigne, E., Schmitt-Keichinger, C., Rebelo, A. R., Heck, M., and Fuchs, M. 2019. The identity of a single residue of the RNA-dependent RNA polymerase of grapevine fanleaf virus modulates vein clearing in *Nicotiana benthamiana*. Molecular Plant-Microbe Interactions 32:790–801. https://doi.org/10.1094/MPMI-12-18-0337-R.

Osterbaan, L. J., Schmitt-Keichinger, C., Vigne, E., and Fuchs, M. 2018. Optimal systemic grapevine fanleaf virus infection in *Nicotiana benthamiana* following agroinoculation. Journal of Virological Methods 257:16–21. https://doi.org/10.1016/j.jviromet.2018.04.006.

Osterbaan, L. J., and Fuchs, M. 2019. Dynamic interactions between plant viruses and their hosts for symptom development. J Plant Pathol 101:885–895. https://doi.org/10.1007/s42161-019-00323-5.

Pallas V, García JA. How do plant viruses induce disease? Interactions and interference with host components. Journal of General Virology. 2011 Dec;92(12):2691-705.

Qiu, Y., Zhang, Y., Wang, C., Lei, R., Wu, Y., Li, X., and Zhu, S. 2018. Cucumber mosaic virus coat protein induces the development of chlorotic symptoms through interacting with the chloroplast ferredoxin I protein. Sci Rep 8:1205. https://doi.org/10.1038/s41598-018-19525-5.

Rathay, E.; 1882. Die Gabler-oder Zwiewipflerreben, eine vorläufige Mittheilung. Österr. Bot. Z. 32, 316-320.

Rathay, E.; 1883. Über die in Nieder-Österreich als “Gabler“ oder “Zwiewipfler” bekannten Reben, 1-26. Verlag der k.k. önol. und pomol. Lehranstalt, Klosterneuburg.

Ritzenthaler, C., Viry, M., Pinck, M., Margis, R., Fuchs, M., and Pinck, L. 1991. Complete nucleotide sequence and genetic organization of grapevine fanleaf nepovirus RNA1. Journal of General Virology 72:2357–2365. https://doi.org/10.1099/0022-1317-72-10-2357.

Ritzenthaler, C., Laporte, C., Gaire, F., Dunoyer, P., Schmitt, C., Duval, S., Piéquet, A., Loudes, A.-M., Rohfritsch, O., Stussi-Garaud, C., and Pfeiffer, P. 2002. Grapevine fanleaf virus replication occurs on endoplasmic reticulum-derived membranes. Journal of Virology 76:8808–8819. https://doi.org/10.1128/JVI.76.17.8808-8819.2002.

Vigne, E., Gottula, J. W., Schmitt-Keichinger, C., Komar, V., Ackerer, L., Belval, L., Rakotomalala, L., Lemaire, O., Ritzenthaler, C., and Fuchs, M. 2013. A strain-specific segment of the RNA-dependent RNA polymerase of grapevine fanleaf virus determines symptoms in *Nicotiana* species. Journal of General Virology 94:2803–2813. https://doi.org/10.1099/vir.0.057646-0.

Yang, J.-Y., Iwasaki, M., Machida, C., Machida, Y., Zhou, X., and Chua, N.-H. 2008. βC1, the pathogenicity factor of TYLCCNV, interacts with AS1 to alter leaf development and suppress selective jasmonic acid responses. Genes Dev. 22:2564–2577. https://doi.org/10.1101/gad.1682208.

Wang, Y., Li, X., Fan, B., Zhu, C., and Chen, Z. 2021. Regulation and Function of Defense-Related Callose Deposition in Plants. Int J Mol Sci 22:2393. https://doi.org/10.3390/ijms22052393.

CHAPTER 2

HERBACEOUS PLANT HOSTS AS SUPERMODELS FOR GRAPEVINE VIRUSES: A HISTORICAL PERSPECTIVE[1]

ABSTRACT

Herbaceous plant hosts are essential to grapevine virus research. Such plants offer numerous advantages as experimental hosts of viruses over *Vitis* species, the natural hosts. They grow faster, have a shorter generation time, and require little maintenance in the greenhouse or growth chamber in comparison with the natural hosts for which experiments are more technically challenging and last substantially longer. Local, pseudo-local, systemic, and pseudo-systemic herbaceous plants have been identified among infected experimental hosts and used for advances in grapevine virology. The discovery pipeline made possible by alternative model hosts has had a tremendous impact on the field. Species of *Chenopodium*, *Nicotiana, Phaseolus, Cucumis, Petunia,* and *Cuscuta* have served to document mechanical or graft transmission of grapevine viruses, fulfill Koch's postulates, study pathogenesis, examine movement, determine replication, purify and observe virus particles, image virions at the atomic level, develop diagnostic assays, characterize vector-mediated transmission, assess defense and counter defense mechanisms, and engineer resistance, among many other critical milestones. Alternative hosts continue to have intrinsic value for discoveries, although many technologies, including high-throughput sequencing, have largely outperformed their use for diagnostic applications. This review focuses on

the critical role of herbaceous plant hosts in important discoveries on the biology of grapevine viruses.

---

[1]This chapter has been published: Roy, B.G., and Fuchs, M. 2024. Herbaceous plant hosts as supermodels for grapevine viruses: a historical perspective. *Journal of Plant Pathology.* 106:327-356. https://doi-org/10.1007/s42161-022-01267-z

INTRODUCTION

At the end of the 19th century, tobacco mosaic virus (TMV) was the first virus ever identified, hereby the genesis of virology as a discipline and a focal point for plant virology (Beijerinck 1898). The origins of grapevine virology coincided with the description of virus-like disease symptoms in the late 19th century (Martelli 1979). As of early 2020, 86 viruses were identified in *Vitis* spp. (Fuchs 2020) but some of these viruses were unlikely pathogens of grapevines. Since the publication of the 2020 review, several additional grapevine viruses were identified for a total of 95 at the submission of this review (Table 2-1). Positive sense single-stranded RNA (ssRNA) viruses constitute the larger proportion of currently known viruses infecting grapevine (Table 2-1), and eukaryotes at large. Other grapevine viruses have a negative sense ssRNA, double-stranded (ds)RNA, ssDNA, or dsDNA genome (Table 2-1).

Viral infections of *Vitis spp.* can lead to a diverse set of disease symptomologies, including asteroid mosaic, berry inner necrosis, degeneration, fanleaf, leaf deformation, leaf discoloration, leaf mottling, leaf roll, mosaic, red blotch, rugose wood, vein clearing, and yellow line pattern. In addition to *Vitis vinifera*, viruses are also increasingly identified in interspecific hybrids (Fall et al. 2020; Schoelz et al. 2021), and free-living vines including *Vitis sylvestris* (Reynard et al. 2020; Sabella et al. 2018), *V. californica* and its hybrids (Klaassen et al. 2011; Cieniewicz et al. 2018), *V. cinerea* (Keith 2018), *Vitis coignetiae* (Nabeshima and Abe 2021), the related *Ampelopsis cordata* (Petersen et al. 2018), and others that were not identified (Hu et al. 2021).

All grapevine viruses are transmitted through vegetative propagation and grafting, and most are mechanically transmissible (53%, 50 of 95) to herbaceous hosts

using crude extracts of infected grapevine tissue while nearly half of them (47%, 45 of 95) have yet to be transmitted to model hosts (Table 2-2). Positive sense ssRNA viruses tend to have a larger host range compared with the other viruses of different genome composition (Table 1), consistent with observations in other hosts (Moury et al. 2017, Fuchs 2020).

Insect vectors of grapevine viruses include aphids, beetles, eriophyid mites, mealybugs, dagger nematodes, planthoppers, soft scale insects, thrips, treehoppers, and whiteflies (Table 2-S1). Some of the grapevine viral diseases and insect vectors have greater economic impact than others (Martelli 2017; Fuchs 2020). Regardless of the level of economic impact from viral diseases, herbaceous hosts heavily influenced biological discoveries throughout the history of grapevine virology (Figure 2-1).

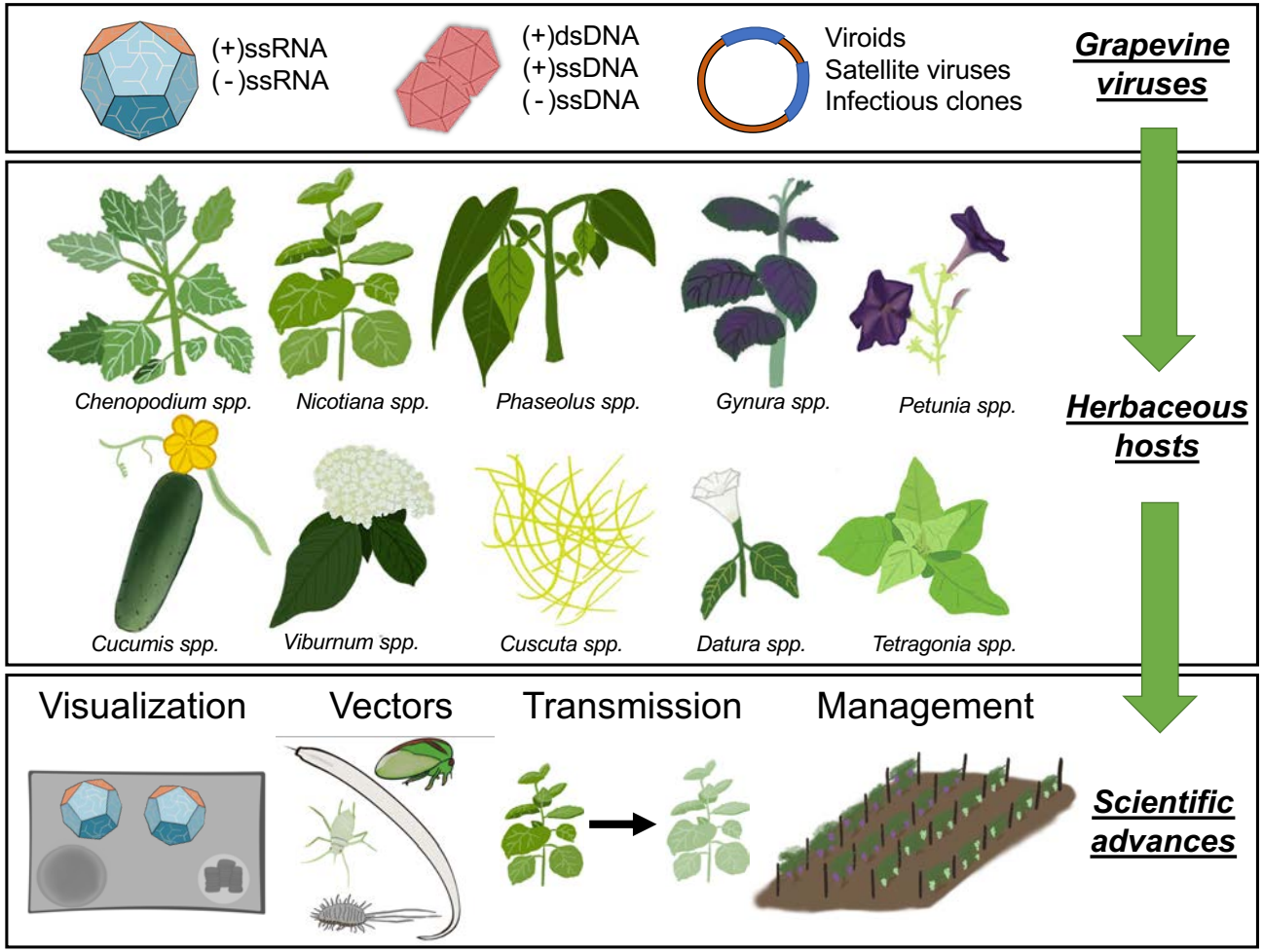

Figure 2-1. Major herbaceous hosts of grapevine viruses that cause disease in *Vitis spp.* Each depicted plant species sustains infection. Downstream discoveries are shown from using herbaceous hosts, i.e., visualization of particles, transmission characteristics, and vector biology.

Table 2-1. List of viruses identified in *Vitis* spp, their genome composition, GenBank accession numbers, and infectious clones, if available.

Table 2-1.

dsDNA viruses	GenBank accession	Infectious clone
Grapevine vein clearing virus (GVCV)	NC015784	(Zhang 2016)
Grapevine badnavirus 1 (GBV1)	MF781082	–
Grapevine Roditis leaf discoloration-associated virus (GRLDaV)	NC027131	–
Grapevine-associated caulimovirus	MN716782	–

ssDNA viruses	GenBank accession(s)	Infectious clone
Grapevine begomovirus A (GBVA)	MT075773, MT075774	–
Grapevine red blotch virus (GRBV)	NC022002	(Yepes et al. 2018)
Wild *Vitis* latent virus 1 (WvL1)	NC035480	–
Grapevine-associated nano-like virus	–	–
Grapevine geminivirus A (GGVA)	NC031340	(Sun et al. 2020)
Temperate fruit-decay-associated virus (TFDaV)	NC027632	–

Negative-sense ssRNA viruses	GenBank accession(s)	Infectious clone
Grapevine-associated ilarvirus 1 (GaIV-1)	MN520742, MN520743, MN520744	–
Grapevine-associated cogu-like virus-1 (GaVLV-1)	MN520751, MN520752, MN520753	–
Grapevine Garan dmak virus (GGDV)	MK728657, MK728658, MK728659	–
Grapevine Muscat rose virus (GMRV)	MK728654, MK728655, MK728656	–
Tomato spotted wilt virus (TSWV)	NC002052, NC002050, NC002051	(Feng et al. 2020)
Vitis varicosavirus (VVV)	LC604719, LC604720	–
Vitis emaravirus (VEV)[a]	BCS90314	–

dsRNA viruses	GenBank accession	Infectious clone
Grapevine Cabernet Sauvignon reovirus (GCSV)	GCA002375125	–

(+) ssRNA viruses	GenBank accession(s)	Infectious clone
Alfalfa mosaic virus (AMV)	NC001495, NC002024, NC002025	(Tenllado and Bol 2000)
Apple latent spherical virus (ALSV)	NC003787, NC003788	(Li et al. 2004)
Arabis mosaic virus (ArMV)	NC006057, NC006056	(Jelkmann et al. 1988)
Artichoke Italian latent virus (AILV)	NC043684, NC043685	–
Bean common mosaic virus (BCMV)	NC003397	(Naderpour and Johansen 2011)
Blackberry virus S (BlVS)	NC038328	–
Blueberry leaf mottle virus (BBLMV)	U20622, NC043076	–
Broad bean wilt virus (BBMV)	NC005289, NC005290	(Atsumi et al. 2013)
Carnation mottle virus (CarMV)	NC001265	–
Cherry leafroll virus (CLRV)	NC018383, NC018384	–
(+) ssRNA viruses	**GenBank accession(s)**	**Infectious clone**

[a]Also reported as grapevine emaravirus (GEV) (MW888853–MW888857) but should be considered as a single virus based on sequence homology and ICTV species demarcation criteria.

Table 2-1. (Continued)

(+) ssRNA viruses	GenBank accession(s)	Infectious clone
Cucumber mosaic virus (CMV)	NC00203(4/5), NC001440	(Rizzo and Palukaitis 1990)
Grapevine Ajinashika virus (GAgV)	–	–
Grapevine Algerian latent virus (GALV)	NC011535	(Lovato et al. 2014)
Grapevine Anatolian ringspot virus (GARSV)	NC018383, NC018384	–
Grapevine angular mosaic virus (GaMoV)	AY830918	–
Grapevine asteroid mosaic-associated virus (GAMaV)	NC012484	–
Grapevine Kizil Sapak virus (GKSV)	LC541735	–
Grapevine labile rod-shaped virus (GLRSV)	–	–
Grapevine leafroll-associated virus 1 (GLRaV1)	NC016509	–
Grapevine leafroll-associated virus 13 (GLRaV13)	NC029783	–
Grapevine leafroll-associated virus 2 (GLRaV2)	NC007448	–
Grapevine leafroll-associated virus 3 (GLRaV3)	NC004667	(Jarugula et al. 2010, 2018)
Grapevine leafroll-associated virus 4 (GLRaV4)	NC016416	–
Grapevine leafroll-associated virus 7 (GLRaV7)	NC016436	–
Grapevine line pattern virus (GLPV)	MT319109, MT319110, MT319111	–
Grapevine nepovirus A (GNVA)	MT507290, MT507291	–
Grapevine Pinot gris virus (GPGV)	NC015782	(Tarquini et al. 2019)
Grapevine polerovirus 1 (GPoV-1)	MT008025	–
Grapevine red globe virus (GRGV)	NC040837	–
Grapevine rupestris stem pitting-associated virus (GRSPaV)	NC001948	(Meng et al. 2013)
Grapevine rupestris vein feathering virus (GRVFV)	AY706994	–
Grapevine stunt virus (GSV)	–	–
Grapevine Syrah virus 1 (GSyV1)	NC012484	–
Grapevine Tunisian ringspot virus (GTRV)	–	–
Grapevine virus A (GVA)	NC003604	(Galiakparov et al. 1999; Saldarelli et al. 2000)
Grapevine virus B (GVB)	NC003602	(Saldarelli et al. 2000; Moskovitz et al. 2008)
Grapevine virus D (GVD)	NC038326	–
Grapevine virus E (GVE)	NC011106	–
Grapevine virus F (GVF)	NC018458	–
Grapevine virus G (GVG)	NC040616	–
Grapevine virus H (GVH)	NC040545	–
Grapevine virus I (GVI)	NC037058	–
Grapevine virus J (GVJ)	NC040564	–
(+) ssRNA viruses	**GenBank accession(s)**	**Infectious clone**

Table 2-1. (Continued)

(+) **ssRNA viruses**	**GenBank accession(s)**	**Infectious clone**
Grapevine virus L (GVL)	MT269789	–
Grapevine virus M (GVM)	MK492703	–
Grapevine virus N (GVN)	MZ682355	–
Grapevine virus O (GVO)	MZ_682356	–
Grapevine virus S (GVS)	JX_513898[a], JX_513899[a]	–
Grapevine virus satellite (GV-Sat)	NC_021480	–
Grapevine virus T (GVT)	MH_182704	–
Grapevine-associated ilarvirus	MN_520742, MN_520743, MN_520744	–
Peach rosette mosaic virus (PRSM)	NC_034214, NC_034215	–
Petunia asteroid mosaic virus (PAMV)	NC_038692[a]	–
Plum bark necrosis stem pitting-associated virus (PBNSPaV)	EF_54644	–
Potato virus X (PVX)	NC_011620	(Hemenway et al. 1990)
Potato virus Y (PVY)	NC_001616	(Fakhfakh et al. 1996)
Raspberry bushy dwarf virus (RBDV)	NC_003739, NC_003740	(Isogai et al. 2019)
Raspberry ringspot virus (RpRSV)	NC_005266, NC_005267	(Wetzel et al. unpublished)
Sowbane mosaic virus (SoMV)	NC_011187	–
Strawberry latent ringspot virus (SLRSV)	NC_006964, NC_006965	–
Tobacco mosaic virus (TMV)	NC_001367	(Turpen et al. 1993)
Tobacco necrosis virus D (TNV-D)	NC_003487	(Coutts et al. 1991)
Tobacco ringspot virus (TRSV)	NC_005097, NC_005096	–
Tomato black ring virus (TBRV)	NC_004439, NC_004440	(Zarzyńska-Nowak et al. 2017)
Tomato mosaic virus (ToMV)	NC_002692	(Weber et al. 1992)
Tomato ringspot virus (ToRSV)	NC_003840, NC_003839	(Zhao et al. 2015)
(+) ssRNA viruses	**GenBank accession(s)**	**Infectious clone**

[a]Partial sequence

Table 2-2. Experimental herbaceous hosts of grapevine viruses.

[a]Hosts are defined to have at least one viral isolate infecting at least one cultivar. Non-hosts are not able to sustain infection after inoculation. Mixed reports are instances in which the literature does not clearly define viral isolates and/or host cultivars and their impact on systemic host infection/resistance. Pseudo-hosts (local/systemic) are defined as intermediates of fully local or systemic hosts and are defined on a case-by-case basis.
[b]Only shown to be infectious in grapevine protoplasts.
[c]Difficulty in establishing infection.
[d]Considered the same species as grapevine emaravirus (GEV).

Table 2-2. Experimental herbaceous hosts of grapevine viruses.

Virus	Herbaceous hosts and non-hosts[a]	Source(s)	Importance to virus biology
Alfalfa mosaic virus (AMV)	*Arabidopsis thaliana, Capsiceae, Chenopodium album, Ch. quinoa, Cucumis sativus, Cuscuta spp., Datura stramonium, Glycine max, Medicago sativa, Melilotus officinalis, Nicotiana benthamiana, N. clevelandii, N. glutinosa, N. tabacum, Phaseolus vulgaris, Viburnum tinus, Vicia faba*	(Price 1940; Hull 1969; Bol et al. 1971; Schmelzer and Wolf 1977; Zadjaii et al. 2002; Bol 2003; Chatzivassiliou et al. 2004; Balasubramaniam et al. 2006; Matthews 1993/2019)	Extensive host range
[b]Apple latent spherical virus (ALSV)	*Arabidopsis thaliana, Beta vulgaris, Celosia cristata, Ch. Amaranticolor, Ch. Quinoa, Cucumis melo, Cucurbita pepo, Citrullus lanatus, Gomphrena globosa, Glycine max, Luffa cylindrical, Lagenaria siceraria, Lithospermum erythrorhizon, N. benthamiana, N. occidentalis, Tetragonia expansa, Vigna angularis, V. unfuiculata* **Not:** *Antirrhinum majus, Brassica rapa, Dianthus superbus, Phaseolus vulgaris* cvs. Honkinntoki and Masterpiece*, Pisum sativum, Vicia faba, Vigna sesquipedalis, Zinnia elegans* **Mixed reports:** *Cucumis sativus*, *N. glutinosa, N. tabacum, Petunia hybrida, Pisum sativum*	(Li et al. 2000; Igarashi et al. 2009; Izuishi et al. 2020)	Study of RNA silencing suppressors, particle visualization, transmission
Arabis mosaic virus (ArMV)	*Asclepias syriaca, Ch. Amaranticolor, Ch. Quinoa, Cucumis sativus, Gomphrena globosa, N. clevelandii* cv. Gray*, N. rustica, N. tabacum, Petunia hybrida, Phaseolus vulgaris*	(Harrison and Nixon 1960; Taylor and Hewitt 1964; Bertioli et al. 1991, 1992; Steinkellner et al. 1992; Spielmann et al. 2000; Wetzel et al. 2004)	Transmission studies
Artichoke Italian latent virus (AILV)	*Beta vulgaris, Ch. Album, Ch. Amaranticolor, Ch. Murale, Ch. Quinoa, Cucumis sativus, Cucurbita pepo, Gomphrena globosa, N. benthamiana, N. clevelandii, N. occidentalis, N. tabacum* (multiple cultivars with variable symptomology), *Petunia hybrida, Phaseolus vulgaris* cv. La Victoire, *Tetragnoia tetragonioides* **Not:** *N. glutinosa, Vicia faba*	(Quacquarelli and Avgelis 1975; Savino et al. 1977; Rana and Kyriakopoulou 1982; Roca et al. 1982; Kyriakopoulou 1995; Matthews 1993/2019)	Transmission studies
Bean common mosaic virus (BCMV)	*Ch. quinoa, N. benthamiana, N. clevelandii, P. vulgaris* **Not:** *Cucumis sativus, Datura stramonium, N. glutinosa, N. tabacum*	(Melinda 2013; Matthews 1993/2019)	

Virus	Herbaceous hosts and non-hosts[a]	Source(s)	Significance

Table 2-2. (Continued) Experimental herbaceous hosts of grapevine viruses.

Virus	Herbaceous hosts and non-hosts[a]	Source(s)	Significance
Blackberry virus S (BlVS)	**Not:** *Ch. amaranticolor, Ch. quinoa, Glycine max, N. tabacum* cv. Turkish, *N. benthamiana, N. rustica, N. glutinosa, Phaseolus vulgaris* cvs. Bountiful and Cherokee Wax, *Ocimum basilicum*	(Sabanadzovic 2009)	
Blueberry leaf mottle virus (BBLMV)	*Ch. amaranticolor, Ch. quinoa, N. clevelandii, N. tabacum* cv. Xanthi **Not**: *Datura stramonium, Petuina hybrida, Vigna unguiculata, Zinnia elegans*	(Uyemoto et al. 1977; Ramsdell and Stace-Smith 1980, 1981)	
Broad bean wilt virus (BBMV)	*Ch. album, Ch. amaranticolor, Ch. quinoa, Cicer spp., Cucumis melo, Cucumis sativus, Cucurbita pepo, Glycine max, Gomphrena globosa, Lathyrus annuus, L. aphaca, L. cicera, L. gorgnoi, L. marmoratus, L. ochrus, N. benthamiana, N. clevelandii, Phaseolus vulgaris* cvs. Imuna, Redlands Greenleaf (B/C), Amanda, *Pisum* spp. **Not:** *Beta vulgaris, Brassica spp., Datura stramonium, Daucus carota, Helanthus annus, Lactuca sativa, Lycopersicon esculentum, Medicago* spp*., Raphanus sativus, Solanum nigrum, Spinacia oleracea, Tetragonia expansa,* several *Phaseolus vulgaris,* several *Vicia* spp.	(Makkouk et al. 1990; Matthews 1993/2019)	Extensive host range
Carnation mottle virus (CarMV)	*Ch. amaranticolor, Ch. quinoa, Dianthus caryophyllus, Gomphrena globosa, Nicotiana clevelandii, Tetragonia expansa* **Not**: *D. stramonium, N. glutinosa, Pisum sativum, Vigna sinensis, V. sinensis* cv. Blackeye	(Rumbos and Avgelis 1989; Martelli 1993; Matthews 1993/2019)	Purification and re-inoculation
Cherry leaf roll virus (CLRV)	*Ch. amaranticolor, Ch. quinoa, Cucumis sativus, N. benthamiana, N. clevelandii, N. glutinosa, N. occidentalis, N. rustica, N. tabacum, Phaseolus vulgaris, Solanum nigrum* **Not**: *Cucurbita pepo*, *Petunia hybrida, Solanum rostratum*	(Cropley 1961; Jones 1973; Jones et al. 1981; Lebas et al. 2016; Matthews 1993/2019)	Purification, development of molecular tools
Cucumber mosaic virus (CMV)	*Ch. quinoa, D. stramonium, N. benthamiana, N. clevelandii, N. megalosiphon, P. vulgaris, Vigna unguiculata* **Not:** *Beta vulgaris*	(Doolittle and Gilbert 1919; Bos and Maat 1974; Matthews 1993/2019)	
Grapevine Ajinashika virus (GAgV)	**Not:** *Ch. amaranticolor, Ch. quinoa, Cucumis sativa, Cucurbita moshata, D. stramonium, Lactuca, sativa, Lycopersicon esculentum, N. glutinosa, N. rustica, N. tabacum, Petunia hybrida, Vigna sesquipedalis*	(Namba et al. 1979)	Not mechanically transmissible

Virus	Herbaceous hosts and non-hosts[a]	Source(s)	Significance

Table 2-2. (Continued) Experimental herbaceous hosts of grapevine viruses.

Virus	Herbaceous hosts and non-hosts[a]	Source(s)	Significance
Grapevine Algerian latent virus (GALV)	*Ch. amaranticolor, Ch. quinoa, D. stramonium, G. globosa, N. benthamiana, N. clevelandii, N. glutinosa, N. occidentalis, Petunia hybrida, P. vulgaris, Tetragonia expansa, Vicia faba* **Not:** *Cucumis sativus, Lycopersicon esculentum* **Mixed reports:** *N. tabacum*	(Ohki et al. 2006; Fujinaga et al. 2009; Kim et al. 2012, Tang et al. 2022)	Infectious cDNA clone, visualization and microscopy
Grapevine Anatolian ringspot virus (GARSV)	*Ch. amaranticolor, N. occidentalis*	(Abou Ghanem-Sabanadzovic et al. 2005)	Passage and sequencing
Grapevine angular mosaic virus (GaMoV)	*Ch. murale, Ch. quinoa, G. globosa*[c]*, N. benthamiana, N. glutinosa, N. tabacum* (cvs. Samsun & Xanthi) **Not:** *Ch. amaranticolor, Datura stramonium, N. clevelandii, N. rustica, Petunia hydrida, P. vulgaris, Vicia faba* (cv. minor), *Zea mays*	(Girgis et al. 2009)	*C. quinoa* helped fulfill Koch's postulates
Grapevine asteroid mosaic-associated virus (GAMaV)	None reported	(Hewitt 1954; Hewitt et al. 1962; Refatti 1966)	
Grapevine badnavirus 1 (GBV1)	None reported	(Vocina and Almeida 2018)	
Grapevine begomovirus A (GBVA)	None reported	(Debat et al. 2020)	
Grapevine berry inner necrosis virus (GINV)	*Ch. amaranticolor, Ch. murale, Ch. quinoa, G. globosa, N. occidentalis, P. vulgaris* **Not**: *Beta vulgaris, Cucumis sativus, Cucurbita maxima, Datura stramonium, Lycoperisicon esculentum, N. benthamiana, N. clevelandii, N. debneyi, N. glutinosa, N. rustica, N. tabacum* cvs. Samsun and Xanthi, *Raphanus sativus, Vigna unguiculata, Zea mays*	(Yoshikawa et al. 1997; German-Retana and Candresse 1999; Fan et al. 2020)	Fulfilled Koch's postulates
Grapevine Bulgarian latent virus (GBLV)	*Celosia cristata* L.*, Ch. amaranticolor, Ch. quinoa, G. globosa, N. benthamiana, N. clevelandii, N. megalosiphon, N. rustica, N. tabacum* (cvs. White Burley, Samsun, Xanthi) **Not:** *Datura stramonium, N. tabacum* cv. Havana 423, *Vigna unguiculata* **Mixed reports:** *Cucumis sativus, Phaseolus vulgaris*	(Martelli et al. 1980; Gallitelli et al. 1983; Matthews 1993/2019)	Ultrastructural studies
Grapevine Cabernet Sauvignon reovirus (GCSV)	**Not**: *Ch. amaranticolor, Ch. quinoa, Cucumis sativus, N. clevelandii*	(Al Rwahnih et al. 2015)	
Virus	**Herbaceous hosts and non-hosts[a]**	**Source(s)**	**Significance**

Table 2-2. (Continued) Experimental herbaceous hosts of grapevine viruses.

Virus	Herbaceous hosts and non-hosts[a]	Source(s)	Significance
Grapevine chrome mosaic virus (GCMV)	*Ch. quinoa, G. globosa, N. clevelandii, P. vulgaris* **Not:** *N. glutinosa, N. tabacum, Petunia hybrida*	(Martelli 1966; Doz 1982; Brault et al. 1993)	Infectious cDNA clone, certification scheme
Grapevine deformation virus (GDefV)	*Ch. amaranticolor, Ch. bushianum, Ch. foetidum, Ch. quinoa, Gomphrea globosa, N. benthamiana, N. cavicola, N. clevelandii, N. glutinosa, N. occidentalis* **Not**: *Datura stramonium, Ocymum basilicum*	(Cigsar et al. 2003; Abou Ghanem-Sabanadzovic et al. 2005)	Passage, cloning, sequencing
Grapevine enamovirus 1 (GEV1)	None reported	(Sabanadzovic 2009; Silva et al. 2017)	
Grapevine fabavirus (GFabV)	None reported	(Rwahnih et al. 2016)	
Grapevine fanleaf virus (GFLV)	*Ch. album, Ch. amaranticolor, Ch. murale, Ch. quinoa, Cucumis sativus, Cynodon dactylon, G. globosa, N. attenuata, N. benthamiana, N. clevelandii, N. rustica, N. tabacum, Phaseolus aureus, P. vulgaris, Polygonum aviculare* **Not:** *N. glutinosa* **Mixed reports:** *Datura stramonium, Petunia hybrida*	(Vuittenez 1960; Taylor and Hewitt 1964; Savino et al. 1985; Izadpanah et al. 2003)	Diagnostics, Koch's postulates, resistance engineering, etc.
Grapevine fleck virus (GFkV)	*Cuscuta campestris* **Not**: *Ch. amaranticolor, Ch. quinoa, Cucumis sativus, N. clevelandii, N. glutinosa*	(Woodham and Krake 1983b; Boulila et al. 1990; Al Rwahnih et al. 2015)	Dodder-mediated transmission
Grapevine fovevirus A (GFVA)	None reported	(Hily et al. 2018a)	
Grapevine Garan dmak virus (GGDV)	None reported	(Diaz-Lara et al. 2019)	
Grapevine geminivirus A (GGVA)	*Nicotiana benthamiana* **Not**: *Ch. amaranticolor, Ch. quinoa, Cucumis sativus, N. clevelandii*	(Al Rwahnih et al. 2016; Sun et al. 2020)	Infectious clone generation
Grapevine Kizil Sapak virus (GKSV)	None reported	(Rwahnih et al. 2019)	
Grapevine labile rod-shaped virus (GLRSV)	**Not:** *Ch. amaranticolor, Ch. quinoa, Cucurbita pepo, Datura stramonium, Gomphrena globosa, N. benthamiana, N. clevelandii, N. glutinosa, N. tabacum, Ocimum basilicum, Petunia hybrida, Pisum sativum, Vicia faba*	(Faggioli et al. 1992)	
Grapevine leafroll-associated virus 1 (GLRaV1)	*N. benthamiana*[c] **Not:** *N. clevelandii, N. glutinosa*, *N. tabacum, Cuscuta campestris*	(Woodham and Krake 1983b)	
Grapevine leafroll-associated virus 2 (GLRaV2)	*N. benthamiana*[c] **Not**: *Ch. amaranticolor, Ch. quinoa, Cucumis sativus, N. clevelandii*	(Goszczynski et al. 1996a, 1996b; Abou-Ghanem et al. 1998; Castellano et al. 2000; Ling et al. 2008; Kurth et al. 2012)	VIGS/RNAi, resistance, sequencing, and ultrastructural studies
Virus	**Herbaceous hosts and non-hosts[a]**	**Source(s)**	**Significance**

Table 2-2. (Continued) Experimental herbaceous hosts of grapevine viruses.

Virus	Herbaceous hosts and non-hosts[a]	Source(s)	Significance
Grapevine leafroll-associated virus 3 (GLRaV3)	*N. benthamiana*[c] **Not:** *Ch. amaranticolor*, *Ch. quinoa*, *Cucumis sativus*, *Nicotiana clevelandii*	(Orecchia et al. 2008; Jarugula et al. 2010; Prator et al. 2017; Jarugula et al. 2018)	Infectious clone, antibody expression in *N. benthamiana*
Grapevine leafroll-associated virus 4 (GLRaV4)	None reported		
Grapevine leafroll-associated virus 7 (GLRaV7)	*Cuscuta campestris, C. europea, C. reflexa, N. occidentalis, Tetragonia expansa* **Not**: *Ch. amaranticolor, Ch. quinoa, Cucumis sativus, Gomphrena globosa, N. glutinosa, N. tabacum, Petunia hybrida*	(Tanne et al. 1974; Woodham and Krake 1983b; Mikona and Jelkmann 2010)	
Grapevine leafroll-associated virus 13 (GLRaV13)	None reported		
Grapevine line pattern virus (GLPV)	*Ch. amaranticolor, C. quinoa, N. glutinosa*	(Martelli 1993; Martelli et al. 2017)	
Grapevine Muscat rose virus (GMRV)	None reported	(Diaz-Lara et al. 2019)	
Grapevine nepovirus A	*Ch. amaranticolor, Ch. quinoa*	(Al Rwahnih et al. 2021)	
Grapevine Pinot gris virus (GPGV)	*Ch. album, N. benthamiana, Silene latifolia* subsp. Alba (Mill.)	(Gualandri et al. 2017; Tarquini et al. 2018)	
Grapevine polerovirus 1 (GPaV-1)	None reported	(Candresse et al. 2020)	
Grapevine red blotch virus (GRBV)	*Phaseolus vulgaris* (pseudo-systemic) Local hosts: *Nicotiana benthamiana, Solanum lycopersicum* **Not**: *Medicago sativa*	(Flasco et al. 2021)	Transmission
Grapevine redglobe virus (GRGV)	None reported	(Blouin 2018)	
Grapevine Roditis leaf discoloration-associated virus (GRLDaV)	*Ch. quinoa, Gomphrena globosa, N. benthamiana, N. rustica, N. tabacum, Physalis floridana* **Not**: *Cucumis sativus, Phaseolus vulgaris*	(Rumbos and Avgelis 1989; Maliogka et al. 2015b)	
Grapevine rupestris stem pitting-associated virus (GRSPaV)	*N. benthamiana , N. clevelandii, N. occidentalis* **Not**: *Ch. amaranticolor, Ch. quinoa, Cucumis sativus*	(Rowhani 2000; Lima et al. 2006; Meng and Gonsalves 2007; Meng et al. 2013, 2017; Meng and Rowhani 2017; Basso et al. 2017b)	
Grapevine stunt virus (GSV)	None reported	(Namba et al. 1986; Martelli 1993)	
Grapevine Syrah virus 1 (GSyV1)	None reported	(Al Rwahnih et al. 2009)	

| Virus | Herbaceous hosts and non-hosts[a] | Source(s) | Significance |

Table 2-2. (Continued)

Virus	Herbaceous hosts and non-hosts[a]	Source(s)	Significance
Grapevine Tunisian ringspot virus (GTRV)	*Ch. amaranticolor, Ch. quinoa, Cucumis sativus, Cucurbita pepo, G. globosa, N. benthamiana, N. cavicola, N. clevelandii, N. megalosiphon, N. occidentalis, N. rotundifolia, N. rustica, Petunia hybrida* **Not:** *N. glutinosa, N. tabacum* cvs. White Burley and Samsun, *Ocymum basilicum, P. aureus, P. vulgaris*	(Ouertani et al. 1992)	Purification and microscopy
Grapevine vein clearing virus (GVCV)	*Nicotiana benthamiana*	(Guo et al. 2014; Petersen et al. 2018)	
Grapevine virga-like virus (GVLV)	None reported	(Chiapello et al. 2020)	
Grapevine virus A (GVA)	*Datura stramonium, Gomphrena globosa, N. benthamiana, N. occidentalis* **Not**: *Ch. amaranticolor, Ch. giganteum, Ch. quinoa, Cucumis sativus,* **Mixed reports**: *N. clevelandii*	(Conti et al. 1980; Monette and James 1990; Martelli et al. 1994; La Notte et al. 1997; Minafra et al. 1998)	Transmission
Grapevine virus B (GVB)	*N. benthamiana, N. cavicola, N. occidentalis, N. rotundifolia* **Not:** *Ch. amaranticolor, Ch. quinoa, Cucumis sativus, Cucurbita pepo, Datura stramonium, Gomphrena globosa, N. clevelandii, N. glutinosa, N. megalosiphon, N. rustica, N. tabacum, Ocymum basilicum, Petunia hybrida, Phaseolus vulgaris*	(Boscia et al. 1994; Minafra et al. 1998)	Transmission
Grapevine virus D (GVD)	*N. benthamiana, N. clevelandii, N. occidentalis* **Not:** *Ch. amaranticolor, Ch. foetidum, C. sativus, Cucurbita pepo, D. stramonium, G. globosa, Ocymum basilicum, N. amplexicaulis, N. glutinosa, N. langsdorfii, N. megalosiphon, N. nudicaulis, N. rustica, N. tabacum, N. undulata, P. hybrida, Phaseolus aureus, P. vulgaris* **Latent:** *C. quinoa*	(Boscia et al. 1992; Abou-Ghanem et al. 1997; Boscia et al. 2001)	Transmission
Grapevine virus E (GVE)	**Not**: *N. benthamiana, N. clevelandii, N. glutinosa, N. occidentalis*	(Nakaune et al. 2008)	
Grapevine virus F (GVF)	None reported	(Al Rwahnih et al. 2012)	
Grapevine virus G (GVG)	None reported	(Blouin et al. 2018)	
Grapevine virus H (GVH)	**Not**: *Ch. murale, N. benthamiana*	(Candresse et al. 2018; Jaguni´c et al. 2021)	
Grapevine virus I (GVI)	None reported	(Blouin et al. 2018)	
Grapevine virus J (GVJ)	None reported	(Diaz-Lara et al. 2018)	
Grapevine virus K (GVK)	None reported	(Jo et al. 2017)	
Grapevine virus L (GVL)	None reported	(Debat et al. 2019)	
Grapevine virus M (GVM)	None reported	(Alabi et al. 2019)	
Grapevine virus N (GVN)	None reported	(Read et al. 2022)	

| Virus | Herbaceous hosts and non-hosts[a] | Source(s) | Significance |

Table 2-2. (Continued)

Virus	Herbaceous hosts and non-hosts[a]	Source(s)	Significance
Grapevine virus O (GVO)	None reported	(Read et al. 2022)	
Grapevine virus S (GVS)	None reported	(Rott et al. *unpublished*)	
Grapevine satellite virus (GV-Sat)	None reported	(Al Rwahnih et al. 2013; Bragard et al. 2019)	
Grapevine virus T (GVT)	**Not**: *Ch. quinoa, N. benthamiana*	(Hily et al. 2018b)	
Grapevine-associated caulimovirus	None reported	(Hu et al. 2021)	
Grapevine-associated cogu-like virus (GaCLV1)	**Not**: *Ch. quinoa, N. benthamiana*	(Bertazzon et al. 2020)	
Grapevine-associated ilarvirus 1 (GaIV-1)	None reported	(Chiapello et al. 2020)	
Grapevine-associated nano-like virus	None reported	(Hu et al. 2021)	
Grapevine-associated poty-like virus 1	**Not:** *Ch. quinoa, N. benthamiana*	(Bertazzon et al. 2020)	
Peach rosette mosaic virus (PRMV)	*Ch. amaranticolor, Ch. quinoa, N. tabacum,* [number of weeds; *T. officinale, S. carolinense, R. crispus*]	(Dias and Cation 1976; Ramsdell and Myers 1978)	
Petunia asteroid mosaic virus (PAMV)	*Datura stramonium, Nicotiana benthamiana, Petunia hybrida* **Not**: *Cucumis sativus, Cucurbita pepo, Lactuca sativa, Phaseolus radiata*	(Quacquarelli and Avgelis 1975; Campbell et al. 1975)	Virus purification
Plum bark necrosis stem pitting-associated virus	None reported	(Marais et al. 2014)	
Potato virus X (PVX)	*Arabidopsis thaliana*[c], *D. stramonium*, *Gomphrena globosa*[c], *N. glutinosa*, *N. tabacum*	(Rochow and Ross 1955; Vance 1991)	
Potato virus Y (PVY)	*Ch. album, Ch. amaranticolor, Ch. quinoa, Nicotiana tabacum* var. Samsun, *Nicotiana glutinosa, Lactuca serriola, Capsella bursapastoris, Erodium cicutarium, Geranium pusillum, Lamium purpureum, Solanum nigrum* **Not**: *Amaranthus retroflexus, Achillea millefolium, Artemisia vulgaris, Cichorium intybus, Conyza canadensis*[c], *Galinsoga parviflora, Solidago canadensis, Taraxacum officinale*[c], *Tripleurospermum indorum, Capsella bursapastoris*[c], *Meladrium album, Plantago laceolata*[c], *Plantago major, Galium aparine, Solanum dulcamara*[c]	(Vance 1991; Kazinczi et al. 2002; Kaliciak and Syller 2009)	Disagreements amongst references but new bioassays in Kaliciak and Syller 2009.

Virus	Herbaceous hosts and non-hosts[a]	Source(s)	Significance

Table 2-2. (Continued)

Virus	Herbaceous hosts and non-hosts[a]	Source(s)	Significance
Raspberry bushy dwarf virus (RBDV)	Symptomatic (bold is only local infection): *Atriplex hortensis, Celosia argentea, Ch. album, Ch. amaranticolor, Ch. botyrs,* ***Ch. murale****, Ch. quinoa, Cucumis melo, C. sativus, N. benthamiana, Phaselous mungo,* ***P. vulgaris****,* ***Vigna clyindrica, V. sinensis****, Petunia hybrida* Infected with no symptoms: *Amaranthus caudatus, Anethum graveolens, Anthriscus cerefolium, Aphanes arvensis, Apium graveolens,* ***Beta vulgaris,*** *Browallia speciosa,* ***Ch. ambrosioides*** **(nom. illeg.),** ***Ch. bonus-henricus****, Ch. capitatum, Ch. ficicolium, Ch. foetidum, Ch. foliosum, Coriandrum sativus, Cucurbita pepo,* ***Datura stramonium****, Daucus carota,* ***Dolichos lablab****,* ***Dysphania ambrosiodes*** **(syn.** ***Ch. ambrosioides*****),** *Fragaria vesca, Gomphrena globosa, Lacuca sativa,* ***Lagenaria siceraria****, Nicandra physalodes, Nicotiana clevelandii, N. glutinosa, N. megalosiphon,* ***N. rustica****,* ***N. tabacum*** **cvs. 'Kawala', 'White Burley', 'Xanthi-nc'**, ***Spinacia oleracea,*** *Tetragonia expansa, Vinca rosea* **Not:** *N. debneyi, N. sylvestris, N. tabacum* cv. Samsun*, Pisum sativum, Vigna sinesis, Vigna sesquipedalis, Zinnia elegans*	(Barnett and Murant, 1970; Kubelcova and Spak, 1998)	Vertical transmission
Raspberry ringspot virus (RpRSV)	*Ch. amaranticolor, Ch. quinoa, N. benthamiana, N. clevelandii, N. tabacum, Petunia hybrida, Phaseolus vulgaris*	(Harrison and Nixon 1960; Harrison et al. 1974; Bruckbauer 1982; Brunt 1986)	
Sowbane mosaic virus (SoMV)	*Ch. amaranticolor, Ch. murale, Ch. quinoa* **Not**: *Cucumis sativus, Cucurbita maxima, Datura stramonium, N. benthamiana, N. glutinosa, N. megalosiphon, N. tabacum, P. vulgaris, Vigna sinensis*	(Quacquarelli and Avgelis 1975; Matthews 1993/2019)	
Strawberry latent ringspot virus (SLRSV)	*Ch. ambrosioides* (nom. illeg.), *Ch. amaranticolor, Ch. bybridum, Ch. murale, Ch. opifolium, Ch. polyspermum, Ch. quinoa, Ch. rubrum, Ch. schraderanum, Ch. strictum, Ch. urbicum, Cucumis sativus, Dysphania ambrosiodes* (syn*. Ch. ambrosioides*)*, N. clevelandii, N. glutinosa, N. megalosiphon, N. occidentalis, N. glutinosa x N. tabacum, Tetragonia expansa, Tetragonia tetragonioides* **Mixed reports:** *N. tabacum* **Not**: *Cucumis melo, Datura stramonium, Gomphrena globosa, Lycopersicon esculentum, Phaseolus vulgaris, Pisum sativum*	(Hanson and Campbell 1979; Belli et al. 1979, 1981; Babini and Bertaccini 1982; Hicks 1985; Brown 1985)	Transmis-sion studies
Temperate fruit-decay-associated virus (TFDaV)	**Not:** *N. benthamiana*	(Basso et al. 2015)	Transmission study

Virus	Herbaceous hosts and non-hosts[a]	Source(s)	Significance

Table 2-2. (Continued)

Virus	Herbaceous hosts and non-hosts[a]	Source(s)	Significance
Tobacco mosaic virus (TMV)	*Asclepias syriaca, Ch. amaranticolor, N. benthamiana, N. glutinosa, N. tabacum, N. sylvestris* **Not**: *Pisum satvium, Trifolium* spp.	(Quacquarelli and Avgelis 1975; Schmelzer and Wolf 1977; Matthews 1993/2019)	Visualization
Tobacco necrosis virus D (TNV-D)	*N. benthamiana, P. vulgaris*	(Quacquarelli and Avgelis 1975)	
Tobacco ringspot virus (TRSV)	*Ch. amaranticolor, Ch. quinoa, Cucumis sativis, Datura stramonium, N. clevelandii, N. glutinosa, N. sylvestris, N. rustica, N. tabacum, Petunia hybrida*	(Price 1940; Gilmer et al. 1970)	
Tomato black ring virus (TBRV)	*Ch. amaranticolor, Ch. quinoa, N. tabacum, Petunia hybrida* **Not:** *Medicago sativa*	(Harrison and Nixon 1960; Stellmach 1970)	
Tomato mosaic virus (ToMV)	*Capsicum* spp*., Ch. murale, Cucumis sativus, Datura stramonium, N. rustica, N. sylvestris, N. tabacum, Petunia hybrida, P. nyctagyniflora, Phaseolus vulgaris, Physalis ixocarpa, Solanum giganteum* **Not:** *Vigna sinensis* cv. Blackeye	(Brunt 1986)	
Tomato ringspot virus (ToRSV)	*Cucumis sativus, P. vulgaris, N. benthamiana and many others*	(Sanfacon et al. 2006)	
Tomato spotted wilt virus (TSWV)	*Ch. album, Ch. amaranticolor, Ch. murale, Ch. quinoa, Cucumis melo, C. sativus, Cucurbita pepo, Cynodon dactylon, Datura stramonium, Dianthus chinensis, Glycine max, Gomphrena globosa, Gynura aurantiaca, Lactuca sativa, N. benthamiana, N. clevelandii, N. glutinosa, N. occidentalis, N. rustica, N. sylvestris, N. tabacum, Petunia hybrida, Phaseolus vulgaris, Pisum sativum, Silene sp., Spinacia oleracea, Tetragonia expansa, Tropaeolum majus, Vicia faba, Zinnia elegans*	(Parrella et al. 2003)	
Vitis cryptic virus (VCV)	**Not:** *N. benthamiana, S. lycopersicum*	(Nabeshima and Abe 2021)	
Vitis emaravirus (VEV) Grape emaravirus (GEV)[d]	**Not:** *N. benthamiana, S. lycopersicum*	(Nabeshima and Abe 2021)	
Vitis varicosavirus (VVV)	**Not:** *N. benthamiana, S. lycopersicum*	(Nabeshima and Abe 2021)	
Wild *Vitis* latent virus (WVlV)	None reported	(Perry et al. 2018)	

| Virus | Herbaceous hosts and non-hosts[a] | Source(s) | Significance |

Table 2-2. (Continued) Experimental herbaceous hosts of grapevine viruses.

[a]Hosts are defined to have at least one viral isolate infecting at least one cultivar. Non-hosts are not able to sustain infection after inoculation. Mixed reports are instances in which the literature does not clearly define viral isolates and/or host cultivars and their impact on systemic host infection/resistance. Pseudo-hosts (local/systemic) are defined as intermediates of fully local or systemic hosts and are defined on a case-by-case basis.
[b]Only shown to be infectious in grapevine protoplasts.
[c]Difficulty in establishing infection.
[d]Considered the same species as grapevine emaravirus (GEV).

Earliest herbaceous model systems for grapevine viruses

Early work focused on the experimental host range of a given viral agent. One of the earliest documented studies to observe experimental host range was performed in 1927 (Wingard 1928). This paper showed the first advance to studying symptomology of hosts other than the natural host, including model host species that are still used nearly a century later. In that late 1920's study, many of the reported plant species did not display symptoms but could maintain infection for passage to an indicator plant on which symptoms were displayed. Although Wingard (1928) characterized tobacco ringspot virus (TRSV) in tobacco rather than in grapevines, it was the first report of the use of an indicator plant species for diagnostics. In the next couple of decades, herbaceous plants were commonly used as indicators in bioassays for grapevine viruses.

Early on, *Petunia hybrida* plants were used as model hosts for several viruses for a variety of crops, including grapevines, and were often the first choice in bioassays although other herbaceous hosts were used too (Harrison and Nixon 1960). For example, the purification of three plant viruses, their visualization in microscopy, and the description of virus specific host species provided insight into groundbreaking methods: *Chenopodium amaranticolor* was used as an indicator for tomato black ring virus (TBRV) and raspberry ringspot virus (RpRSV) while *Phaseolus vulgaris* was used as an indicator for Arabis mosaic virus (ArMV) (Harrison and Nixon 1960). Thereafter, herbaceous plants were extensively used to study virions, movement, and replication, and many other important features of grapevine viruses. To contextualize these advances, visual proof of viruses was deemed crucial in the 1960s as evidence of disease, eventually leading to establishment of the entire discipline of plant virology.

Studying viruses in alternative herbaceous hosts allows for a multi-dimensional systems approach *in planta*, given a quick turnover of growth material, reliable viral inoculum, and easier to process tissue for more efficient lab work. Remarkably, the model plant of biology, *Arabidopsis thaliana,* currently holds no position in grapevine virology other than one study on differences in immune response by grapevine leafroll-associated virus 3 (GLRaV-3) and TMV with regards to senescence in *Vitis* and *Arabidopsis,* respectively (Espinoza et al. 2007). Grapevine has been elusive in plant virology since mechanical inoculation has low success, the physiology behind viral movement is poorly defined, and the intricate perennial growth cycle with regards to varying viral titer creates technical challenges (Dolja et al. 2017). Numerous efforts to understand the evolutionary history behind these important steps of a virus infectious cycle have been discussed although major conclusions have not been articulated (Dolja et al. 2017). Slower growth and generation time of *Vitis* spp. makes acquiring enough tissue for experimentation difficult, thus studies are lengthier than on model hosts (Zherdev et al. 2018). The utility of herbaceous models is apparent on many fronts when attempting to unravel the biology behind viral infection in a difficult-to-study host.

Herbaceous hosts as indicator plants of grapevine viruses

Herbaceous hosts are used in biological indexing for diagnostics. This is typically achieved by preparing a crude sap from an infected *Vitis spp.* that is then mechanically inoculated, most often onto one of the following plant species: *Ch. amaranticolor, Ch. quinoa, Cucumis sativus, Nicotiana benthamiana, N. occidentalis,* and *N. tabacum* (Rowhani et al. 2005: Zherdev et al. 2018). Many of the economically relevant viruses of grapevines, particularly nepoviruses, can systemically infect most of

these herbaceous hosts and display symptoms. Other viruses may locally or systemically infect, while causing a variety of symptoms, or be asymptomatic in herbaceous hosts.

The following plant genera have proved particularly useful for grapevine virus diagnosis: *Amaranthus*, *Capsicum*, *Chenopodium*, *Cucumis*, *Cucurbita*, *Datura*, *Gomphrena*, *Lycium*, *Nicotiana* (specifically *N. clevelandii*, *N. glutinosa*, *N. benthamiana*), *Phaseolus*, *Pisum*, *Physalis*, *Solanum*, *Tetragonia*, and *Vigna* (Figure 2-2A). Early resources and conference notes were valuable resources for the completion of this review (Martelli 1993; Martelli 1979; Martelli 2017; Matthews 1993/2019; Meng et al. 2017).

Among the herbaceous plant hosts of grapevine viruses, *Ch. quinoa* sustains the multiplication of 33 different viruses (Figure 2-2A). *Ch. amaranticolor*, *N. benthamiana* and *N. clevelandii* sustain the multiplication of more than 20 different viruses each (Figure 2-2A). *N. tabacum*, *G. globosa*, *N. glutinosa*, *N. rustica*, *N. occidentalis*, *P. vulgaris*, *C. sativus* and *D. stramonium* host 10 or more different grapevine viruses each. Finally, 12 other herbaceous species sustain the multiplication of at least one grapevine virus (Figure 2-2A), amongst others mentioned less frequently on a case-by-case basis (Table 2-2). Among grapevine viruses, tomato spotted wilt virus (TSWV), cucumber mosaic virus (CMV), alfalfa mosaic virus (AMV) and GFLV have the most herbaceous hosts followed by grapevine Algerian latent virus (GALV), grapevine Tunisian ringspot virus (GTRV), TRSV, raspberry bushy dwarf virus (RBDV), and ArMV (Figure 2-2B).

Figure 2-2. Abundance of herbaceous hosts of grapevine viruses described in the literature. **(a)** Each species of herbaceous host with the relative number of grapevine viruses is represented by size, and **(b)** viruses and the relative number of herbaceous hosts they can be passaged onto. The size of each slice/box is proportional to the number of herbaceous hosts. Additional information is available in Table 2-S3.

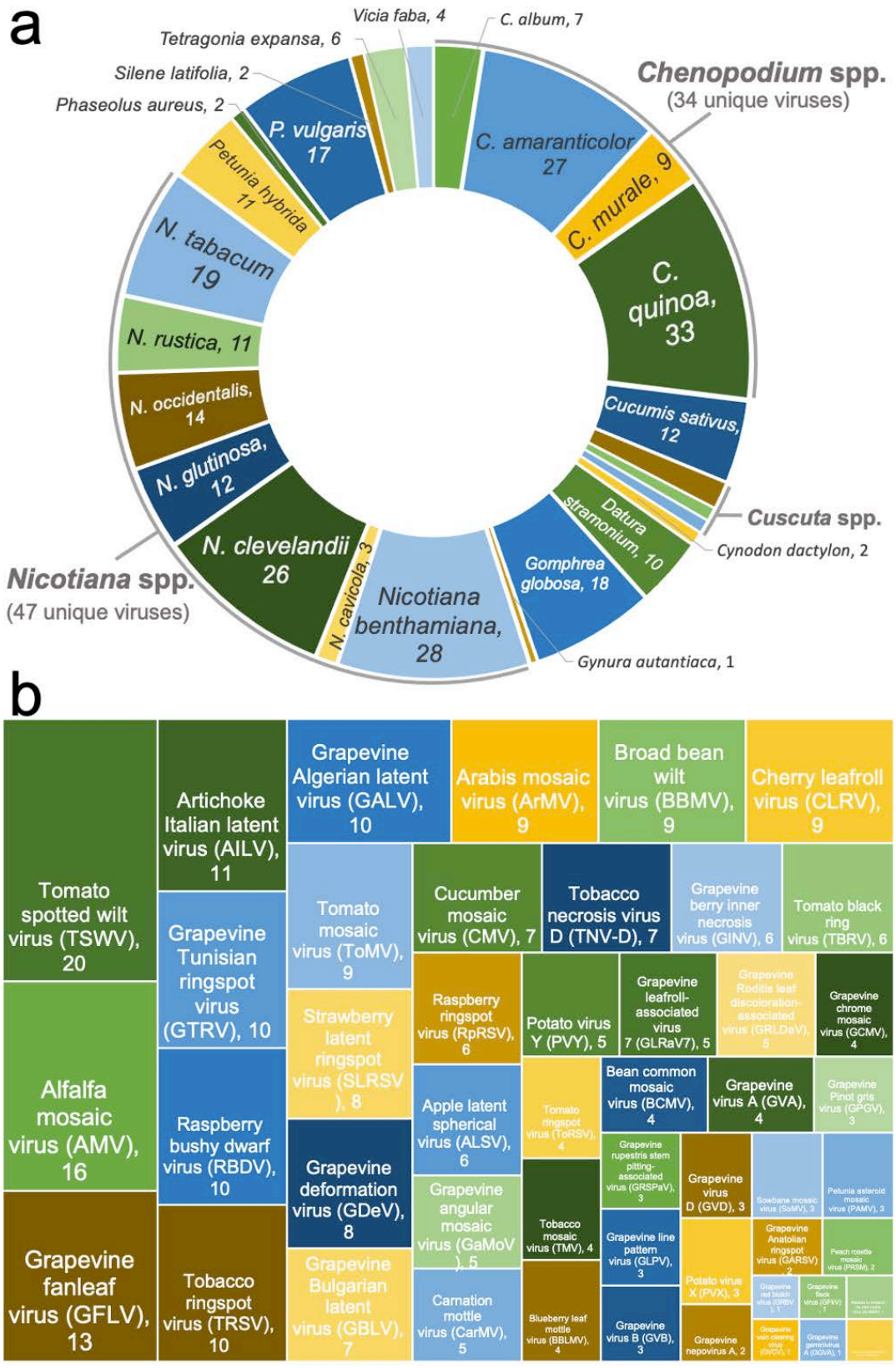
a
Vicia faba, 4
C. album, 7
Tetragonia expansa, 6
Silene latifolia, 2
Phaseolus aureus, 2
Chenopodium spp.
(34 unique viruses)
P. vulgaris 17
C. amaranticolor 27
Petunia hybrida 11
C. murale, 9
N. tabacum 19
C. quinoa, 33
N. rustica, 11
N. occidentalis, 14
Cucumis sativus, 12
N. glutinosa, 12
Cuscuta spp.
Datura stramonium, 10
Cynodon dactylon, 2
N. clevelandii 26
Gomphrea globosa, 18
Nicotiana spp.
(47 unique viruses)
N. cavicola, 3
Nicotiana benthamiana, 28
Gynura autantiaca, 1
b
Tomato spotted wilt virus (TSWV), 20
Artichoke Italian latent virus (AILV), 11
Grapevine Algerian latent virus (GALV), 10
Arabis mosaic virus (ArMV), 9
Broad bean wilt virus (BBMV), 9
Cherry leafroll virus (CLRV), 9
Grapevine Tunisian ringspot virus (GTRV), 10
Tomato mosaic virus (ToMV), 9
Cucumber mosaic virus (CMV), 7
Tobacco necrosis virus D (TNV-D), 7
Grapevine berry inner necrosis virus (GINV), 6
Tomato black ring virus (TBRV), 6
Alfalfa mosaic virus (AMV), 16
Strawberry latent ringspot virus (SLRSV), 8
Raspberry ringspot virus (RpRSV), 6
Potato virus Y (PVY), 5
Grapevine leafroll-associated virus 7 (GLRaV7), 5
Grapevine Roditis leaf discoloration-associated virus (GRLDaV), 5
Grapevine chrome mosaic virus (GCMV), 4
Raspberry bushy dwarf virus (RBDV), 10
Grapevine deformation virus (GDeV), 8
Apple latent spherical virus (ALSV), 6
Tomato ringspot virus (ToRSV), 4
Bean common mosaic virus (BCMV), 4
Grapevine virus A (GVA), 4
Grapevine Pinot gris virus (GPGV), 3
Grapevine fanleaf virus (GFLV), 13
Tobacco ringspot virus (TRSV), 10
Grapevine Bulgarian latent virus (GBLV), 7
Grapevine angular mosaic virus (GaMoV), 5
Tobacco mosaic virus (TMV), 4
Grapevine rupestris stem pitting-associated virus (GRSPaV), 3
Grapevine virus D (GVD), 3
Solanum mosaic virus (SoMV), 3
Petunia asteroid mosaic virus (PAMV), 3
Grapevine line pattern virus (GLPV), 3
Grapevine Anatolian ringspot virus (GARSV), 2
Peach rosette mosaic virus (PRSM), 2
Carnation mottle virus (CarMV), 5
Blueberry leaf mottle virus (BBLMV), 4
Potato virus X (PVX), 3
Grapevine red blotch virus (GRBV), 1
Grapevine fleck virus (GFkV), 1
Grapevine B (GVB), 3
Grapevine nepovirus A, 2
Grapevine vein clearing virus (GVCV), 1
Grapevine yellow speckle A (GYSVA), 1

After inoculation, virions or viral genetic material are found in different organs and tissues of the plant depending on compatibility between host and virus. Herbaceous plant hosts of grapevine viruses can be classified into local, pseudo-local, systemic, and pseudo-systemic hosts, while all (except ALSV) are assumed to be systemic in *Vitis* spp. (Table 2-2). Local hosts only sustain viral replication close to the initial infection point and a few millimeters away, while pseudo-local hosts sustain the replication and movement of the virus a few centimeters away from the initial infection point. Systemic hosts are defined by an infection that can be detected in any plant tissue type away from the initial inoculation point. Pseudo-systemic hosts sustain some level of virus movement beyond the initial inoculation sites, but the virus does not reach all tissues of the plant. All types of virus-host relationships can result in symptomology at the local, systemic, or pseudo- level together or exclusively. For example, *Ch. quinoa* is a systemic host and *G. globosa* is a pseudo-local host of grapevine fanleaf virus (GFLV) (Dias 1963); *N. glutinosa* and *Ch. amaranticolor* are local hosts of RpRSV (Harrison and Nixon 1960, Bruckbauer 1982); and *P. vulgaris* is an asymptomatic pseudo-systemic host of grapevine red blotch virus (GRBV) (Flasco et al. 2021). Additionally, non-hosts are defined by the incompatibility to sustain viral replication and movement *in planta*.

There are some disagreements among reports on viral infection in herbaceous hosts that would need clarification, at the very least to recognize the role of isolate specificity or inoculation technique (Table 2-S2, gray boxes). Differences in genetic components in respect to both viral strain as well as host genotype make understanding these phenomena complex and elusive. Aside from genotype, plant health and

environmental conditions such as temperature and relative humidity should be optimal for viral infection *in planta*. Optimization of these factors may be undertaken in environmentally controlled growth chambers to observe virus symptomology more reliably, but consistency is difficult to achieve when considering numerous variables for each pathosystem. This is because what works for one research group in each environment and location may be different for another group. Below we discuss selected examples of disease-causing viruses of grapevines or selected viruses associated with major grapevine diseases, and the herbaceous hosts (or lack thereof) used to study them.

Grapevine viruses and their herbaceous hosts throughout history

Nearly half (47%, 45 of 95) of the grapevine viruses have *Vitis* sp. as the only known natural plant host. Many of the other 53% of grapevine viruses tend to have a very narrow herbaceous host range. Other grapevine viruses such as tomato ringspot virus (ToRSV) have a wider host range, infecting for example fruit crops other than *Vitis* sp., vegetables, and field crops. Host range is continually explored for each virus system, but the most economically relevant viruses have received the most attention. Described below are a few examples of grapevine viruses for which herbaceous hosts have been essential to advance our understanding of their biology (Table 2-2).

2. *VIRUSES AND THEIR HERBACEOUS HOSTS THAT FOSTER RESEARCH*

2.1. Grapevine fanleaf virus (**genus *Nepovirus*, family *Secoviridae***). *Chenopodium amaranticolor, G. globosa,* and *N. clevelandii* were established early on as herbaceous hosts for GFLV and used for particle visualization with electron microscopy (Cadman et al. 1960). More recently *Cynodon dactylon* (Bermuda grass) was identified as an

alternative host in the vineyard (Izadpanah et al. 2003). Using GFLV-infected *C. quinoa,* electron micrographs of virions were obtained in tubule-like structures formed by the GFLV RNA2-encoded movement protein $2B^{MP}$ (Ritzenthaler et al. 1995). In addition, the *N. tabacum* cell line BY-2 was used to characterize replication events on the endoplasmic reticulum. This cell line is of great importance for live cell imaging (Brandizzi et al. 2003). Advances in GFLV research due to the use of *Chenopodium* and *Nicotiana* species resulted in the identification of RNA1- and RNA2-encoded determinants of symptoms by reverse genetics (Martin et al. 2018; Osterbaan et al. 2019). This work is the culmination of previous efforts to optimize infection conditions using RNA1 and RNA2 cDNA clones via *Agrobacterium tumefaciens*-mediated delivery (Vigne et al. 2013; Osterbaan et al. 2018). It will be interesting for future studies to determine if GFLV symptom determinants identified on herbaceous hosts will act similarly in grapevines.

2.2. Artichoke Italian latent virus (**AILV, genus *Nepovirus*, family *Secoviridae***). AILV is another causative agent behind grapevine degeneration. It has a large host range and model hosts were used to investigate transmission (Savino et al. 1977; Roca et al. 1982; Kyriakopoulou 1995). Almost all (94.7%, 18 of 19) closely related viruses of the family *Secoviridae* infecting grapevine have been successfully transferred to and propagated in herbaceous hosts (Figure 2-3). The only exception is grapevine fabavirus (GFabV).

2.3. Grapevine Roditis leaf discoloration-associated virus (GRLDaV, genus *Badnavirus*, family *Caulimoviridae*). The existence of GRLDaV was first postulated

in Greece for having distinct symptomology on grapevine (Rumbos and Avgelis 1989), and the virus was characterized later (Maliogka et al. 2015). Three indicator plants were identified using sap-mediated inoculation experiments: *Ch. quinoa, G. globosa,* and *N. benthamiana*. Other common bioassay plants, *C. sativus* and *P. vulgaris*, did not test positive for the virus following inoculation.

2.4. Grapevine angular mosaic virus (GaMoV, genus *Ilarvirus,* family *Bromoviridae*). Hosts of GaMoV include *Ch. quinoa, Ch. murale, N. benthamiana, N. glutinosa*, two *N. tabacum* cultivars, and *G. globosa* while eight non-host plants were identified (Girgis et al. 2009). Extracts of infected *Ch. quinoa* were used to fulfill Koch's postulates by passaging the virus through the herbaceous host, infecting grapevines with *Ch. quinoa* homogenates, and observing disease symptomology after infection (Girgis et al. 2009).

2.5. Grapevine berry inner necrosis virus (GINV, genus *Trichovirus*, family *Betaflexiviridae*). This virus causes a severe disease of grapevines in Japan and China. Infection of GINV was established in *N. occidentalis* using infectious cDNA clones yet was unsuccessful in *N. benthamiana* (Fan et al. 2020). The establishment of cDNA clones not only provided a platform for further studies on GINV, but also proved disease causality by fulfilling Koch's postulates directly in grapevine. In addition, electron microscopy images from infected plant tissue allowed further characterization of GINV virions.

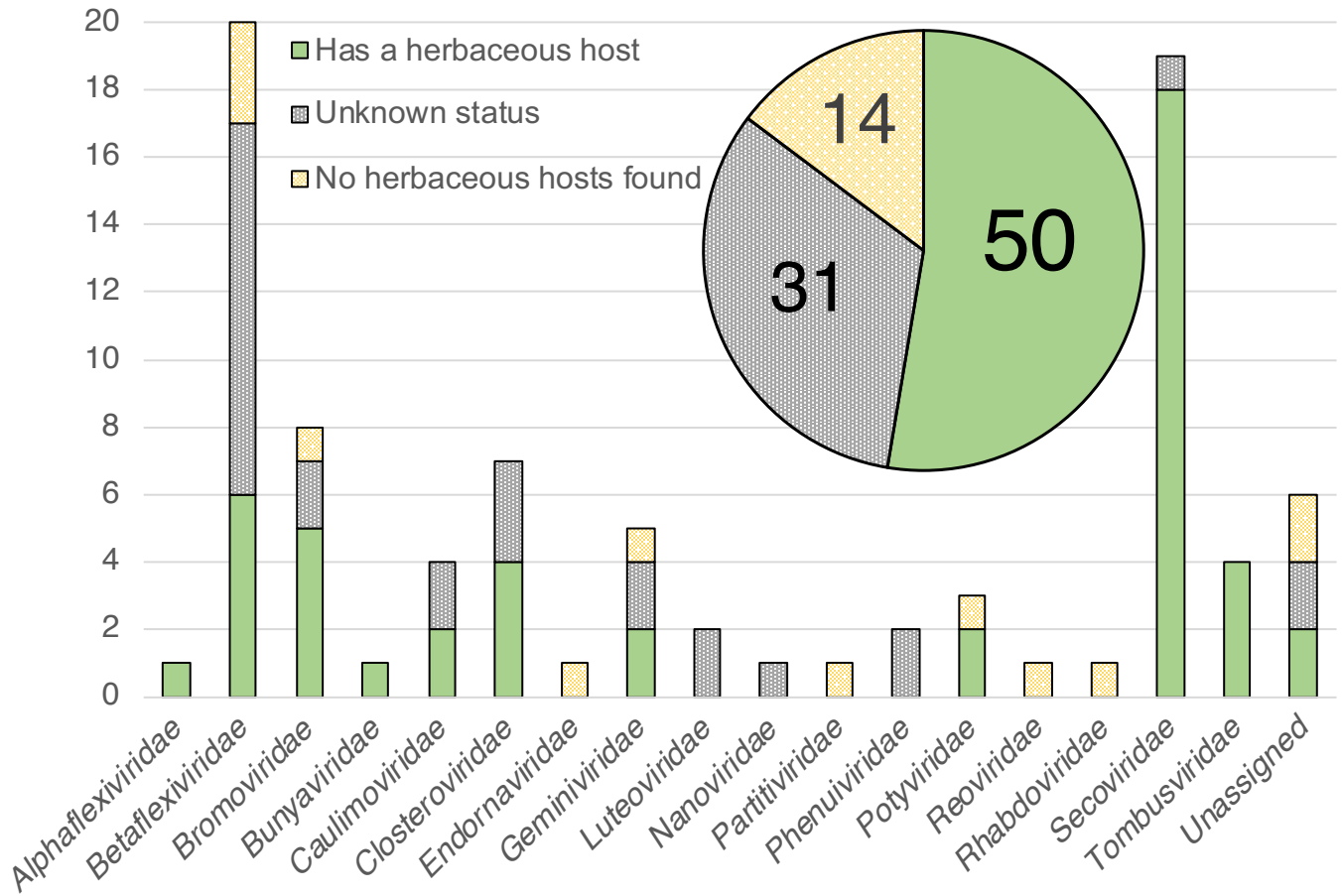

Figure 2-3. Number of viruses infecting grapevine organized by family and their ability to infect herbaceous hosts. While over half of the viruses infecting grapevine (53%, 50 of 95) infect herbaceous hosts, 15% (14 of 95) have not been successfully passaged to herbaceous hosts after inoculation attempts, and 33% (31 of 95) have yet to be reported on their ability to infect herbaceous hosts to any extent.

2.6. Grapevine Pinot gris virus (GPGV, genus *Trichovirus*, family *Betaflexiviridae*). GPGV is a rather recently described agent that has been shown to infect two herbaceous hosts: *Ch. album* and *Silene latifolia* (Gualandri et al. 2017). These two plant species were located on the perimeter of a diseased vineyard and considered to be potential reservoirs for the virus to propagate and spread, providing further relevance to the biological nature and transmission of this virus.

2.7. Alfalfa mosaic virus (**AMV, genus *Alfamovirus,* family *Bromoviridae***). AMV is found in over 600 species in 70 different plant families (Schmelzer and Wolf 1977; Schmelzer et al. 1973). *N. benthamiana* was used to study the viral replication cycle (Bol 2003). AMV can be transmitted through an aphid vector to cause yellow mosaic symptoms on grapevine, albeit a minor threat to grapevine in comparison with other diseases (Castillo and Orlob 1966; Novák and Lanzová 1976).

2.8. Raspberry bushy dwarf virus (RBDV, genus *Idaeovirus*, family *Mayoviridae*) is another virus that has a large host range. It is primarily studied in *Chenopodium* and *Nicotiana* species (Barnett and Murant 1970). RBDV isolates constitute two major host specific clades for (i) raspberry, and (ii) grapevine. The host range for this virus remains convoluted based on reports prior to this differentiation (Valasevich et al. 2011).

2.9. Leafroll disease-associated viruses (**GLRaV, family *Closteroviridae***). Viruses associated with grapevine leafroll disease (GLD) belong to the genera *Ampelovirus,* C*losterovirus,* and *Velaravirus* in the family *Closteroviridae*.

2.9.1 Grapevine leafroll-associated virus 1 (**GLRaV-1, genus *Ampelovirus***) has been shown to passage through *Cuscuta campestris* to a grapevine woody indicator (Woodham and Krake 1983a). The RNA silencing suppressor p24 of GLRaV-1 was recently shown to elicit a hypersensitive response in *N. benthamiana* (Zhang et al. 2020).

2.9.2 Grapevine leafroll-associated virus 2 (**GLRaV-2**, **genus *Closterovirus***) can be transmitted into *Nicotiana* species, although with difficulty, and remains unsuccessful in transmission efforts for several other species (Goszczynski et al. 1996a).

2.9.3 Grapevine leafroll-associated virus 3 (GLRaV-3, genus *Ampelovirus*) has shown variable results for infection of *N. benthamiana* (Prator et al. 2017; Jarugula et al. 2018) but virions were visualized and purified from infected *N. benthamiana* tissue (Prator et al. 2017). However, due to the low success of inoculation, virus-host interactions remain largely unknown for GLRaV-3 (Perrone et al. 2017).

2.9.4 Grapevine leafroll-associated virus 7 (**GLRaV-7, genus *Velarivirus***). A large host range was found for GLRaV-7 from the genus *Velarivirus* in the family *Closteroviridae*, including, *N. occidentalis*, *Tetragonia expansa*, and *Cuscuta* spp. (Mikona and Jelkmann 2010) but the association of GLRaV-7 with leafroll disease remains uncertain.

2.10. Grapevine red blotch virus (GRBV, genus *Grablovirus*, family *Geminiviridae*). GRBV is a recently identified virus that poses a major threat to grape production in North America (Cieniewicz et al. 2017). Recent efforts to understand transmission of

GRBV by *Spissistilus festinus*, the three-cornered alfalfa hopper, have placed some emphasis on herbaceous hosts. In addition to grapevines, transmission was successful from infected to healthy plants using *P. vulgaris* as a pseudo-systemic herbaceous host of GRBV, and a feeding and reproductive host of *S. festinus* (Flasco et al. 2021). In addition, *Medicago sativa* was observed to be a non-host of GRBV and was utilized for a gut-clearing period of insect vectors during transmission experiments (Flasco et al. 2021, Hoyle et al. 2022). Knowing hosts and non-hosts of GRBV was valuable to better understand transmission biology (Flasco et al. 2021).

2.11. Rugose wood disease complex-associated viruses. Several viruses are associated with the grapevine rugose wood disease complex, although wine grape cultivars remain asymptomatic.

2.11.1 Grapevine Rupestris stem pitting-associated virus (GRSPaV, genus *Foveavirus*, family *Betaflexiviridae*) remains without fulfilling Koch's postulates due to several technical difficulties (Meng et al. 1998) and the inability to reliably establish infection in *N. benthamiana* (Basso et al. 2017; Meng and Rowhani 2017) using infectious GRSPaV clones following *Agrobacterium tumefaciens*-mediated delivery (Meng et al. 2013).

2.11.2 Grapevine virus A (GVA, genus *Vitivirus*, family *Betaflexiviridae*) is mechanically transmitted to *N. clevelandii* and *N. benthamiana* (Conti et al. 1980; Minafra et al. 1998; Monette and James 1990), as well as *Ch. amaranticolor*, *Ch. quinoa*, and *G. globosa* with a longer latency for infection in *D. stramonium* (Martelli et al. 1994). Work in *Nicotiana* spp. furthered the understanding of transmission biology

for GVA, as well as early imaging efforts for virions (Rosciglione and Castellano 1985; Rosciglione et al. 1983).

2.11.3 Grapevine virus B (**GVB, genus *Vitivirus*, family *Betaflexiviridae***) infects *N. benthamiana, N. occidentalis, N. cavicola,* and *N. rotundifolia*. In addition, the following plants were not infected: *N. clevelandii, N. glutinosa, N. megalosiphon, N. undulata, N. rustica, N. tabacum* cvs. 'Samsun' and 'White Burley'*, P. hybrida, D. stramonium, P. vulgaris, G. globosa, Ch. quinoa, Ch. amaranticolor, C. sativus, C. pepo,* and *Ocimum basilicum* (Boscia et al. 1994).

2.11.4 Grapevine virus D (GVD, genus *Vitivirus*, family *Betaflexiviridae*) shares similar herbaceous host ranges with GVA and GVB within *Chenopodium* spp. and *Nicotiana* spp. (du Preez et al. 2011). Grapevine virus E (GVE) and many of the more recently described vitiviruses have no known herbaceous hosts (Nakaune et al. 2008). For example, attempts at transmitting grapevine virus H were unsuccessful on *Ch. murale* and *N. benthamiana* (Jagunic et al. 2021) (Table 2-2 for additional references).

2.12. Other grapevine viruses.

2.12.1 Grapevine asteroid mosaic-associated virus (GAMaV, genus *Marafivirus*, family *Tymoviridae*) is associated with asteroid mosaic or vein feathering symptomologies. There have been no reports of herbaceous hosts.

2.12.2 Grapevine fleck virus (GFkV, genus *Maculavirus,* family *Tymoviridae*) causes fleck symptomology. Dodder transmission to woody indicator plants had been successful but not to herbaceous hosts (Woodham and Krake 1983; Boulila et al. 1990).

3. *HERBACEOUS HOSTS SERVING IN HYPOTHESIS DRIVEN RESEARCH*

A discovery pipeline was born during the 1950's when plant viruses were rapidly transferred to alternative hosts by mechanical inoculation of sap from infected plant tissue (Hollings 1956). This was the first intentional use of indicator plants for diagnostics. Most of the previous decade focused on the identification of vector candidates, general biology, and management tactics as virology was becoming more established as a discipline (Broadbent and Martini 1959). In contrast, soil-borne transmission of viruses was poorly understood and was speculated to be either mediated by an aerial insect vector or through passive diffusion of virus particles/vesicles in soil (Lister 1959). It is also in the 1950's and early 1960's that knowledge linking grapevine diseases to viruses was pioneered (Hewitt 1954; Cadman et al. 1960; Vuittenez 1960; Dias 1963). Over the next several decades, key trends in plant virology research became apparent.

3.1. Favored herbaceous model plants. Two model systems have continually driven grapevine virology research: *Chenopodium* and *Nicotiana* species (Figure 2-2A). These hosts display symptomology varying from local lesions, necrosis, mosaic, mottling, and chlorosis when infected with certain grapevine viruses, and other times are asymptomatic following infection. The ability to maintain systemic infection, re-inoculate, and transmit viruses make these herbaceous hosts even more useful when probing molecular functions. Transmission through mechanical inoculation or delivery of virus infectious clones via *Agrobacterium tumefaciens* can occur over the course of a few days to a few weeks from inoculation to symptom development – much quicker

than graft transmission in grapevines or sap inoculation of grapevine seedlings, which can take weeks, months, or even years. Further, reliance on insect vector-mediated transmission of grapevine viruses to establish infection is cumbersome, and for several viruses, the transmission efficiency is very low from grapevine to grapevine while higher transmission rates can be obtained with herbaceous hosts, as documented for GRBV (Flasco et al. 2021), GFLV (Belval et al. 2019 and references therein), GVA (La Notte et al. 1997), and others.

Co-infections by multiple viruses are very frequent in a vineyard setting, hampering studies on virus biology for which single virus infections are ideal. Heterografting is an elegant technique to achieve single virus infections with agents that are mechanically transmissible to *Ch. quinoa*. Indeed, *Ch. quinoa* has also been used in heterografting experiments to transfer a given virus or a virus isolate to a healthy grapevine rootstock (Bass and Vuittenez 1979). This technique was successfully applied to produce a population of infected grapevines used in comparative phenotypic, transcriptomic and metabolomic studies of distinct GFLV strains on different *V. vinifera* cultivars (Martin et al. 2021). Producing this experimental plant population using infected herbaceous hosts was more efficient and faster than graft-inoculations of woody indicators or nematode-mediated transmissions.

3.2. Why *Nicotiana benthamiana*? Part of the Solanaceae family, *N. benthamiana* is distant in terms of evolutionary constraints from *Vitis* spp. These two plant species first diverged at the clade level from the classification of eudicots into asterids and rosids, respectively. Both have 19 pairs of chromosomes (38 total), with grapevine being diploid and *N. benthamiana* being tetraploid. One might consider *N. benthamiana* as an

essential player in grapevine virology research simply because many viruses infect this host but cannot infect *Arabidopsis thaliana,* a major model in plant pathology and physiology. It is important to note that this phenomenon is only due to the limited repertoire of immune genes for *N. benthamiana* compared with other plant species (Chakravarthy et al. 2010). The genetic basis of the apparent virus susceptibility of *N. benthamiana* may be related to a 72-nucleotide insertion mutation that introduced tandem stop codons in the RNA-dependent RNA polymerase I (*Nb-RDR1*) involved in small interfering RNA synthesis and virus resistance (Yang et al. 2004). The influence of *N. benthamiana* is undeniably large for research efforts in plant virology (Goodin et al. 2008), particularly grapevine virology, yet many mysteries surround the origins of this widely adopted laboratory species (Wylie and Li 2022).

N. benthamiana is extensively used for transient expression of transgenes through agroinfiltration, where *Agrobacterium tumefaciens* harboring a T-DNA plasmid is introduced locally into a leaf. Transient local over-expression of plant genes from T-DNA enables studies of gene or protein expression and regulation via virus-induced gene silencing (VIGS) without the need to express transgenes stably in a whole plant. VIGS was first reported and optimized for use in *N. benthamiana* (Kumagai et al. 1995). This technology can be readily employed for studying the effects of depleting certain genes *in planta* without risking developmental obstacles as seen in CRISPR-Cas9 studies. VIGS becomes a powerful tool when probing immune system pathways and viral-related defenses. Studies can start in the herbaceous model host and then be optimized and translated in the natural host, as seen in a study of GVA (Muruganantham et al. 2009). Using an expression vector of a naturally occurring virus promoter and

machinery leaves less optimization work and can be used as a tool for many downstream molecular assays. Recently the Sol Genomics Network at the Boyce Thompson Institute, Cornell University, has generated an online tool for designing VIGS constructs in addition to other resources for *N. benthamiana* research (Fernandez-Pozo et al. 2015). The rapid generation of these constructs allows for strides in our understanding of molecular virus-host interactions in *Nicotiana* and other related plants.

3.3. Fulfilling Koch's postulates. The development of virus infectious clones is valuable to research efforts as viruses are obligate biotrophs. A cDNA copy of the viral genome is cloned into the T-DNA backbone of *A. tumefaciens* and can be utilized to establish infection and advance virus biology through reverse genetics. From numerous accounts of generating infectious clones, herbaceous hosts have served to produce additional inoculum or as another lens to study the virus infection cycle. In addition, *A. tumefaciens*-mediated delivery of infectious clones has provided another inoculation technique to obtain infected plants.

Infectious clones are available for at least 28 of the 95 (29%) grapevine viruses identified so far (Table 1). Historically, this is one of the first steps in molecular characterization of a virus. From here, Koch's postulates can be examined for existing or new viruses in association with disease, or other studies in herbaceous hosts (mentioned in Table 2 for select viruses). With new technologies like high-throughput sequencing (HTS), viruses are being described at a faster rate than infectious clones can be generated for biological characterization. It is noteworthy that many ssRNA viruses of grapevine can be mechanically transmitted in herbaceous hosts and can bypass the need to engineer an infectious clone.

One virus that is not mechanically transmissible to herbaceous hosts and relies heavily upon an infectious clone for hypothesis-driven research is GRBV. Characterization of this virus began in the mid-2000's (Calvi 2011) and was initially referred to as GRBaV until Koch's postulates were fulfilled with infectious virus clones and then was named GRBV (Yepes et al. 2018). Infectious clones of GRBV were next successfully used in transmission experiments with *S. festinus* in the pseudo-systemic host *P. vulgaris* (Flasco et al. 2021).

In a similar way, Koch's postulates were fulfilled for GINV using an infectious virus clone in *N. occidentalis* (Fan et al. 2020). Infected herbaceous plants displayed chlorotic mottling at nine days post inoculation and GINV virions were observed through transmission electron microscopy. The infectious clone of GINV was then introduced to grapevine and identical results were obtained in the natural host.

3.4. Transmission assays with insect vectors. Hemipteran and nematode vectors have been identified for numerous viruses in grapevine (34%, 32 of 95), although vectors for most viruses (66%, 63 of 95) remain undetermined (Table 2-S1). Some of this work was propelled with the use of herbaceous hosts. Many of the herbaceous plants described here have been utilized in transmission assays of ArMV (Jha and Posnette 1961), CLRV (Jones et al. 1981), GRBV (Flasco et al. 2021), GVA (Rosciglione and Castellano 1985), GFLV (Andret-Link et al. 2004), GLRaV-3 (McGreal et al. 2021) and more. In the case of GRBV, *P. vulgaris* was used as a feeding and a reproductive host to rear *S. festinus* (Flasco et al. 2021). While this may not be feasible for mealybugs and other insect vectors, it should be considered when herbaceous hosts are the most easily managed plants for a laboratory. Further, hosts of insect vectors that do not host the viral agent of

interest can be of great use in transmission assays, as recently demonstrated (Flasco et al. 2021). These are some of the multifaceted values of herbaceous hosts for viral transmission assays.

3.5. Vertical transmission. Several studies have shown that grapevine viruses can be transmitted in a vertical fashion through pollen or seeds of previously infected hosts (Hanada and Harrison 1976; Tobias 1995). For example, GFLV is transmitted through both pollen and seed in grapevine, albeit at a low frequency (Katsirdakis et al. 1989; Lazar et al. 1990). Vertical transmission is uncommon for grapevine viruses and is considered a limited threat for breeding programs of grape (Gasparro et al. 2016) or in vineyard settings (Martelli 1978). Gasparro and colleagues (2016) further elaborated that seed transmission of GFLV is more successful in herbaceous hosts such as *Ch. amaranticolor, Ch. quinoa,* and soybean than grapevines. Genetic differences between herbaceous hosts and grapevine limit the transfer of knowledge for vertical transmission, albeit this field depends on model plants for basic mechanistic understandings.

3.6. Cytopathological observations. Some of the first reports of plant virus visualization contained some of the most inspiring details. Particles documented for TBRV, RpRSV and ArMV had great propulsion for the field while heavily relying on herbaceous hosts (Harrison and Nixon 1960). The next two decades displayed leaps for grapevine virus visualization in which *Ch. quinoa*, *Ch. amaranticolor, N. clevelandii, and P. hybrida* were noticed as efficient hosts with organized arrangements of particles (Russo 1985). ArMV was observed in parenchyma and in phloem tissue. GFLV

particles within these hosts were in patterned pockets (known today as viral replication complexes), which were more abundant and organized than observed in the natural host (Gerola et al. 1969). In systemically infected herbaceous hosts, such as *Ch. quinoa*, *Ch. amaranticolor*, *N. clevelandii*, and *P. hybrida*, virus particles were observed in more abundant patterns, arrayed in long parallel rows or in viral inclusion bodies (Gerola et al., 1969; Peña-Iglesias and Rubio-Huertos, 1971; Šarič and Wrischer, 1975).

3.7. Electron microscopy visualization of virus particles. A technique for investigating virus biology used to commonly involve the visualization of virions *in planta* by electron micro*s*copy. This approach has been used as a detection tool as well as a characterization method for many plant viruses. Light microscopy largely dominated studies until the 1970's (Martelli and Russo 1977) with a central focus on investigating the viral infection cycle. Only after the shift in focus to structural characteristics of virions were major aspects of transmission, replication, and movement of many viral groups better understood. Several reviews have extensively discussed the value of this technique (Baker et al. 1985; Pina et al. 2021). Virions have been visualized or mentioned in herbaceous hosts for potato virus Y (PVY) and TMV (Derrick 1973), GINV (Yoshikawa et al. 1997), GVA (Galiakparov et al. 1999), and many more.

To highlight a recent study, grapevine nepovirus A (GNVA) was initially described with HTS techniques although the infected grapevine from which the virus was identified did not exhibit symptoms. The virus was successfully transmitted through mechanical inoculation to two herbaceous hosts, visualized with transmission electron microscopy, and characterized based on genomic structure and particle shape (Al Rwahnih et al. 2021). These sequential steps were essential for the molecular

characterization and acceptance of GNVA as a viral agent, regardless of causing visual symptoms on the natural host. Proving infectivity was a rigorous process that was helped with the use of herbaceous hosts (Al Rwahnih et al. 2021).

In addition, herbaceous hosts can facilitate the purification of viral particles and subsequent visualization in cryo-electron microscopy. This technique often provides enhanced resolution down to 3-4 Å quality. Such studies are limited for grapevine viruses, but these have shown promise with GFLV-nanobody (Nb) interactions (Orlov et al. 2020). GFLV's closely related ArMV has also been probed using this technique for capsid structure determination (Lai-Kee-Him et al. 2013). We anticipate more resolved virus structures will become available as this technology becomes more accessible.

3.8. Purification of virions and production of antibodies. Herbaceous hosts have played a salient role in the purification of grapevine viruses and production of antibodies. Antibodies are important in grapevine virology to create diagnostic serological assays such as enzyme-linked immunosorbent assay (ELISA). This field has led to the generation of specific immunoglobulins, monoclonal antibodies and Nbs. Development of an ELISA against GFLV was a historical diagnostic tool that is still currently used in many laboratories today (Shanmuganathan and Fletcher 1982). Infected and healthy *Ch. quinoa* were essential to validate serological assays and aid the generation of reagents using rabbit immunoglobulins (Jankulova et al. 1982). Recent efforts to generate antibodies have moved to an expression vector in *Escherichia coli.* This approach was applied, for example, for the simultaneous detection or differential testing between GFLV and ArMV (Koolivand et al. 2016; Shibaei et al. 2018). A similar

history is seen with GVA, in which monoclonal antibodies were generated in mouse myeloma cells using virus particles purified from *N. benthamiana* (Boscia et al. 1992). Antibodies were produced and resulted in a reliable diagnostic assay. Similarly, antibodies were produced in mouse myeloma cells using GVD particles purified from *N. occidentalis* (Boscia *et al.* 2001). This allowed for the differentiation between closely related viral species.

A review on grapevine virus detection with double antibody sandwich (DAS)-ELISA techniques is found within Blouin *et al.* (2017). Further detection methods have also been reviewed in detail in Rowhani *et al.* (2017a). Early stages of these techniques benefited greatly from virus isolation in herbaceous hosts.

3.9. Engineered resistance against grapevine viruses. Transgenic expression of viral coat protein (CP) genes has been well established in numerous crops that have shown durable resistance (Fitchen and Beachy 1993; Xu *et al.* 1998, 1999; Jayasena *et al.* 2001; Bastet *et al*. 2018). For example, transgenic tobacco expressing the CP gene of GFLV conferred resistance to mechanical inoculation of the cognate virus (Bardonnet *et al.* 1994). Alternatively, antibody production in transgenic *N. benthamiana* conferred resistance against GFLV and ArMV (Nölke *et al.* 2009). This research area is still in development as viral resistance loci in grapevines are characterized (Djennane *et al.* 2021). Taking steps to first characterize these loci is challenging and efficiency in breeding for these loci is demanding. The limitations and challenges of transgenic grapevines are reviewed in Campos *et al.* (2021).

MicroRNA (miRNA) and more recently, Nb have been introduced as defense tools against some grapevine viruses (Kurth *et al.* 2012; Hemmer *et al.* 2018; Avital *et*

al. 2021). For example, Nb against the CP of GFLV have been expressed in *N. benthamiana* and *Vitis* rootstock (Hemmer *et al.* 2018). For the characterization of the interaction between the GFLV CP and Nb, transgenic expression in *N. benthamiana* was used to characterize Nb recognition sites (Orlov *et al.* 2020). Nb-mediated resistance was ultimately overcome through viral mutation of the recognition site between CP and Nb, suggesting the need for a more robust, stacking technology to confer resistance to GFLV. A review of all technology in engineering resistance can be found within Zhao *et al.* (2020) and Fuchs (2021).

The study of RNAi and miRNA defense is well characterized in model plants such as *N. benthamiana* (Jovel *et al.* 2007; Ling *et al*. 2008; Muruganantham *et al.* 2009). This process involves the activation of several pathways upon pathogen infection including the construction of the RISC-complex (Pratt and MacRae 2009), expression of argonaute proteins (Tolia and Joshua-Tor 2007), dicer, RNA-binding proteins, and more (Csorba *et al.* 2015). RNAi was first discovered in the model worm *Caenorhabditis elegans* and has been successfully characterized in many other organisms (Lee *et al.* 1993; Campbell and Choy 2005). This pathway is one of the most effective active defense strategies against viruses in plants. RNA viruses go through a dsRNA phase during replication which is perceivable by RNA-induced silencing complex (RISC), and degradation of viral genetic material occurs. Viruses can overcome this antiviral pathway by encoding silencing suppressors of RISC complex components, or upstream/downstream players of the signaling cascade (Csorba *et al.* 2015). This molecular interplay can be further manipulated *in planta* with VIGS of the host targets or site-directed mutagenesis of the viral genome to determine gene function

of both hosts and viruses. This work is completed at a much faster rate in herbaceous hosts than in *Vitis* spp. and will likely continue in this direction until more efficient gene-editing and gene-delivery technologies come to fruition for grapevine.

DISCUSSION

Previous literature reviews have brought into perspective the use of herbaceous hosts to understand virus biology and the transfer of this knowledge to grapevine, but only to the effect of fundamental viral properties (Russo 1985). While this information is extremely valuable, further efforts need to focus on connecting scientific discoveries to end-user information. Some of the end goals of grapevine virology research are to better inform growers to avoid disease and best manage diseased vineyards (Maliogka *et al.* 2015a; Fuchs 2020). Understanding biological traits of viruses such as infectivity, host range, and attributes of vector-mediated transmission reveal imperative information essential to provide disease management strategies for growers. The most successful forms of virus management options in vineyards have been in early detection and elimination of infected planting material. Diagnostics based on ELISA and PCR assays have made great strides thanks to virus propagation and studies in herbaceous hosts (Rowhani et al. 2017b). We expect that as new technologies emerge, herbaceous hosts will continue playing large roles in the development of robust diagnostic tools and serve as a proof-of-concept before research is done directly on grapevine.

This review compiled data from the field of grapevine virology, showing the salient role of herbaceous hosts for hypothesis driven research. We depict the field as utilizing herbaceous hosts to benefit vector-mediated transmission assays, particle

visualization, fulfillment of Koch's postulates, and systems biology studies, ultimately informing management strategies common to all viral agents such as utilizing clean planting material, reducing virus inoculum, and limiting vector spread (Figure 1). Unfortunately, many grapevine viruses are still not established in any herbaceous systems, primarily because they are not mechanically transmissible. Most of these agents are documented using HTS technologies (Saldarelli et al. 2017). In addition, there are technical obstacles when attempting to passage a virus into herbaceous hosts (Rowhani *et al.* 2017a). Optimization steps are crucial, as crude sap inoculations often show low efficacy. This can involve the use of differing buffer inoculation solutions, creation of infectious clones, or using different entry techniques with infiltration or mechanical damage of plant tissue via the application of carborundum, sonication or pricking (Rowhani et al. 2017a). Genetic modifications to recessive host determinants are another way, albeit more intensive, to facilitate introduction of viral agents to typical non-hosts (Martinez-Turino et al. 2021).

HTS has recently allowed for a more holistic approach to viral diagnostics by examining the virome of grapevine (Mehetre et al. 2021). With these techniques, all nucleic acids are collected from a sample, characterized, and compared to sequence information available in data repositories. If sequence reads are unique and loosely similar to previously described virus sequences, a new report on a putative novel virus may be generated. The discovery pipeline of HTS is described in great detail by Massart et al. (2018). Recently, the addition of 13 putative viruses in *Vitis* spp. have been announced through publications, conferences, and announcements via sequencing-based discovery (Table 2). While HTS is an unbiased and reliable approach to detecting

viruses, it does not provide information regarding their biology. With a wealth of information on plant viruses being generated with the latest sequencing technologies, there is a need to return to asking applied biological questions (Hou et al. 2020).

Nicotiana and *Chenopodium* species are best suited for diagnostic assays, however, they do not identify all grapevine viruses or all virus strains and lose value when considering the dynamics of multiple viral strains and species. *Ch. amaranticolor, Ch. quinoa, C. sativus,* and *N. clevelandii* were used in a bioassay comparison against HTS and PCR-based diagnostic assays for 15 grapevine accessions (Al Rwahnih et al. 2015). The methods used in this research relied on the recommended hosts for biological indexing for *Vitis* and *Prunus* viruses, as per California regulations (Rowhani et al. 2005). This panel of four herbaceous plant species can predictably host a majority of documented mechanically transmissible and economically relevant grapevine viruses, according to our survey of the literature. Thus, our findings agree with the four herbaceous hosts selected in this study (Al Rwahnih et al. 2015). However, it seems that *C. sativus* is a less relied upon herbaceous host for indexing and could have ultimately been replaced with an additional *Nicotiana* species to capture nearly half of the documented grapevine viruses (Figure 2A). We recognize that this was not an objective of the study that elegantly revealed how HTS outperforms biological indexing and the other diagnostic assays, but the use of an additional *Nicotiana* species may have provided a broader biological context to some of the minor viruses identified (Al Rwahnih et al. 2015).

CONCLUSIONS

Herbaceous hosts serve as models for grapevine viruses in nearly every facet of viral biology. All viral types (RNA or DNA), but not all viral species of grapevine-infecting viruses have been transferred to and passaged in herbaceous plants of varying species, resulting in particle visualization, vector identification, replication characteristics, viral protein localization in plant cells, pathogenicity determination, and systems biology. Landmark studies documented host ranges through transmission by mechanical methods or a vector, identified viral protein function, or validated development of detection assays for grapevine viruses. Knowledge behind these characteristics of viral biology are critical to inform recommendations for viral disease control in the vineyard (Fuchs 2020). We found that the large body of literature has converged on a few ideal herbaceous species for hypothesis-driven research studies, mainly *N. benthamiana* and *Ch. quinoa*. Further, *Nicotiana* and *Chenopodium* species combined represented a majority of the herbaceous hosts for grapevine viruses identified in the literature (Figure 2A and Table 2).

Viruses relating to devastating diseases have been well characterized in many regards by research on herbaceous hosts (Figure 3) but could benefit from additional research efforts in terms of imagining more efficient management strategies. Nineteen of 20 members of the family *Secoviridae*, often linked to fanleaf degeneration disease, have been successfully passaged in herbaceous hosts, with only GFabV remaining undocumented in herbaceous hosts. Investment of time and resources into this viral family has resulted in a large body of knowledge on vector biology and transmission

characteristics. Other viruses depicted have seen less attention, in part because of limited, if any known economic impact (Supplementary Table 2).

The growing list of grapevine viruses has now reached 95 species. All the viruses added in the last few years have been identified as a result of HTS approaches and, in most cases, have not been linked to disease symptoms. Additionally, knowledge of their biology is scarce. With the advent of HTS technologies, it is necessary to revisit herbaceous indexing as a method for biological discovery with new and emerging viruses. It is undeniable that HTS outperforms the use of herbaceous hosts for diagnostic applications and is a great way for identifying viral genetic material (Soltani et al. 2021). However, HTS lacks biological relevance when considering disease and symptomology outside nucleotide sequences. Therefore, HTS should be paired with the use of herbaceous hosts to ascertain some level of biological relevance. We anticipate our list of alternative hosts to at least be of interest for colleagues working on new and emerging viruses of *Vitis* spp.

While bioinformatic methods are extremely powerful tools to explore biological systems, there is an abundance of work to be done with many grapevine viruses in biological settings. As such, we cannot stress enough the salient role of herbaceous hosts to advance the characterization of viruses beyond the identification of their genetic composition and diversity. As technology continues to advance, the roots of grapevine virology will continually push the field forward through reliance upon alternative plant host models for experimentation. Hypothesis driven research will ultimately provide answers for more efficiently combating viral diseases in the natural hosts and lead to imperative and actionable information for grape growers and vineyard managers.

ACKNOWLEDGEMENTS

We pay special attribution to the work of previous pioneers in this field, especially the late Giovanni Paolo Martelli. This review would not be possible without the foundational knowledge summarized during conferences and meetings, or without the transparency of scientific reports. We acknowledge that all reports could not be included due to space constraints.

REFERENCES

Abou Ghanem-Sabanadzovic, N., Sabanadzovic, S., Digiaro, M., and Martelli, G. P. 2005. Complete nucleotide sequence of the RNA-2 of Grapevine deformation and Grapevine Anatolian ringspot viruses. Virus Genes. 30:335–340.

Abou-Ghanem, N., Sabanadzovic, S., Minafra, A., Saldarelli, P., and Martelli, G. P. 1998. Some properties of Grapevine leafroll-associated virus 2 and molecular organization of the 3' region of the viral genome. Journal of Plant Pathology. 80:37–46. http://www.jstor.org/stable/41997899

Abou-Ghanem, N., Saldarelli, P., Minafra, A., Buzkan, N., Castellano, M. A., and Martelli, G. P. 1997. Properties of grapevine virus d, a novel putative Trichovirus. Journal of Plant Pathology. 79:15–25 http://www.jstor.org/stable/41997863

Al Rwahnih, M., Alabi, O. J., Hwang, M. S., Tian, T., Mollov, D., and Golino, D. 2021. Characterization of a new Nepovirus infecting grapevine. Plant Disease. 105:1432–1439. https://doi.org/10.1094/PDIS-08-20-1831-RE

Al Rwahnih, M., Alabi, O. J., Westrick, N. M., Golino, D., and Rowhani, A. 2016. Description of a novel monopartite Geminivirus and its defective subviral genome in grapevine. Phytopathology®. 107:240–251. https://doi.org/10.1094/PHYTO-07-16-0282-R

Al Rwahnih, M., Daubert, S., Golino, D., Islas, C., and Rowhani, A. 2015. Comparison of next-generation sequencing versus biological indexing for the optimal detection of viral pathogens in grapevine. Phytopathology®. 105:758–763. https://doi.org/10.1094/PHYTO-06-14-0165-R

Al Rwahnih, M., Daubert, S., Golino, D., and Rowhani, A. 2009. Deep sequencing analysis of RNAs from a grapevine showing Syrah decline symptoms reveals a multiple virus infection that includes a novel virus. Virology. 387:395–401. https://doi.org/10.1016/j.virol.2009.02.028

Al Rwahnih, M., Daubert, S., Sudarshana, M. R., and Rowhani, A. 2013. Gene from a novel plant virus satellite from grapevine identifies a viral satellite lineage. Virus Genes. 47:114–118. https://doi.org/10.1007/s11262-013-0921-3

Al Rwahnih, M., Sudarshana, M. R., Uyemoto, J. K., and Rowhani, A. 2012. Complete genome sequence of a novel vitivirus isolated from grapevine. Journal of Virology. 86:9545. https://doi.org/10.1128/JVI.01444-12

Alabi, O. J., McBride, S., Appel, D. N., Al Rwahnih, M., and Pontasch, F. M. 2019. Grapevine virus M, a novel vitivirus discovered in the American hybrid bunch grape cultivar Blanc du Bois in Texas. Archives of Virology. 164:1739–1741. https://doi.org/10.1007/s00705-019-04252-7

Andret-Link, P., Schmitt-Keichinger, C., Demangeat, G., Komar, V., and Fuchs, M. 2004. The specific transmission of *Grapevine fanleaf virus* by its nematode vector *Xiphinema index* is solely determined by the viral coat protein. Virology. 320:12–22. https://doi.org/10.1016/j.virol.2003.11.022

Atsumi, G., Tomita, R., Kobayashi, K., and Sekine, K.-T. 2013. Establishment of an agroinoculation system for broad bean wilt virus 2. Archives of Virology. 158:1549–1554. https://doi.org/10.1007/s00705-013-1625-7

Avital, A., Muzika, N. S., Persky, Z., Bar, G., Michaeli, Y., Fridman, Y., Karny, A., Shklover, J., Shainsky, J., Savaldi-Goldstein, S., Weissman, H., Shoseyov,

O., Schroeder, A. 2021. Foliar delivery of siRNA particles for treating viral infections in agricultural grapevines. Adv. Funct. Mater. 2101003. https://doi.org/10.1002/adfm.202101003

Babini, A. R., and Bertaccini, A. 1982. Viral Aggregates Induced by a Distinctive Strain of Strawberry latent ringspot virus from grapevine. Journal of Phytopathology. 104:304–308. https://doi.org/10.1111/j.1439-0434.1982.tb00013.x

Baker, K. K., Ramsdell, D. C., and Gillett, J. 1985. Electron microscopy: Current applications to plant virology. Plant disease. 69:85–91. https://doi.org/10.1094/PD-69-85

Balasubramaniam, M., Ibrahim, A., Kim, B.-S., and Loesch-Fries, L. S. 2006. *Arabidopsis thaliana* is an asymptomatic host of Alfalfa mosaic virus. Virus Research. 121:215–219. https://doi.org/10.1016/j.virusres.2006.04.005

Bardonnet, N., Hans, F., Serghini, M. A., and Pinck, L. 1994. Protection against virus infection in tobacco plants expressing the coat protein of grapevine fanleaf nepovirus. Plant Cell Reports. 13:357–360. https://doi.org/10.1007/BF00232637

Barnett, O. W. and Murant, A. F. 1970. Host range, properties and purification of raspberry bushy dwarf virus. Ann Applied Biology. 65:435–449. https://doi.org/10.1111/j.1744-7348.1970.tb05512.x

Bass, P. and Vuittenez, A. 1979. Méthode d'inoculation virale par "hétérogreffage" entre plantes hôtes herbacées et ligneuses en culture aseptique in vitro. Application à la transmission de souches définies de népovirus de *Chenopodium quinoa* à la vigne *Vitis* sp.. Annales de Phytopathologie, INRA, 1979, 11:565-566.

Basso, M. F., Fajardo, T. V. M., and Saldarelli, P. 2017. Grapevine virus diseases: economic impact and current advances in viral prospection and management. Rev. Bras. Frutic. 39. https://doi.org/10.1590/0100-29452017411

Basso, M. F., da Silva, J. C. F., Fajardo, T. V. M., Fontes, E. P. B., and Zerbini, F. M. 2015. A novel, highly divergent ssDNA virus identified in Brazil infecting apple, pear and grapevine. Virus Research. 210:27–33. https://doi.org/10.1016/j.virusres.2015.07.005

Bastet, A., Lederer, B., Giovinazzo, N., Arnoux, X., German-Retana, S., Reinbold, C., Brault, V., Garcia, D., Djennane, S., Gersch, S., Lemaire, O., Robaglia, C., and Gallois, J. L. 2018. Trans-species synthetic gene design allows resistance pyramiding and broad-spectrum engineering of virus resistance in plants. Plant biotechnology journal, 16(9), 1569–1581. https://doi.org/10.1111/pbi.12896

Beijerinck, M. W. 1898. On a *Contagium vivum fluidum* causing the Spot disease of the Tobacco leaves. Koninklijke Nederlandse Akademie van Wetenschappen Proceedings Series B Physical Sciences. 1:170–176.

Belli, G., Fortusini, A., and Vegetti, G. 1979. Properties of a strain of strawberry latent ringspot virus, associated with a rosetting disease of peach in Northern Italy. In XI International Symposium on Fruit Tree Virus Diseases 94:113–118. https://doi.org/10.17660/ActaHortic.1981.94.13

Belval, L.; Marmonier, A.; Schmitt-Keichinger, C.; Gersch, S.; Andret-Link, P.; Komar, V.; Vigne, E.; Lemaire, O.; Ritzenthaler, C.; Demangeat, G. From a Movement-Deficient Grapevine Fanleaf Virus to the Identification of a New Viral Determinant

of Nematode Transmission. Viruses. 2019, 11, 1146. https://doi.org/10.3390/v11121146

Bertazzon, N., Chitarra, W., Angelini, E., and Nerva, L. 2020. Two new putative plant viruses from wood metagenomics analysis of an esca diseased vineyard. Plants (Basel). 9:835. DOI: 10.3390/plants9070835

Bertioli, D. J., Cooper, J. I., Edwards, M. L., and Hawes, W. S. 1992. Arabis mosaic nepovirus coat protein in transgenic tobacco lessens disease severity and virus replication. Annals of Applied Biology. 120:47–54. https://doi.org/10.1111/j.1744-7348.1992.tb03402.x

Bertioli, D. J., Harris, R., Edwards, M., Cooper, J., and Hawes, W. 1991. Transgenic plants and insect cells expressing the coat protein of Arabis mosaic virus produce empty virus-like particles. Journal of General Virology. 72:1801–1809. https://doi.org/10.1099/0022-1317-72-8-1801

Blouin, A. 2018. Virus diversity in New Zealand grapevines: Sequence, history and impact. Univ. of Auckland.

Blouin A.G., Chooi K.M., Cohen D., MacDiarmid R.M. 2017. Serological methods for the detection of major grapevine viruses. In: Meng B, Martelli GP, Golino DA, Fuchs M (eds) Grapevine viruses: molecular biology, diagnostics and management. Springer Verlag, Cham, Switzerland, 409–430. https://doi.org/10.1007/978-3-319-57706-7_21

Blouin, A. G., Chooi, K. M., Warren, B., Napier, K. R., Barrero, R. A., and MacDiarmid, R. M. 2018. Grapevine virus I, a putative new vitivirus detected in co-

infection with grapevine virus G in New Zealand. Archives of Virology. 163:1371–1374. https://doi.org/10.1007/s00705-018-3738-5

Bol, J. F. 2003. Alfalfa mosaic virus: coat protein-dependent initiation of infection. Molecular Plant Pathology. 4:1–8. https://doi.org/10.1046/j.1364-3703.2003.00146.x

Bol, J. F., Van Vloten-Doting, L., and Jaspars, E. M. J. 1971. A functional equivalence of top component a rna and coat protein in the initiation of infection by Alfalfa mosaic virus. Virology. 46:73–85. https://doi.org/10.1016/0042-6822(71)90007-9

Bos, L., and Maat, D. Z. 1974. A strain of cucumber mosaic virus, seed-transmitted in beans. Netherlands Journal of Plant Pathology. 80:113–123.

Boscia, D., Abou-Ghanem, N., Saldarelli, P., Minafra, A., Castellano, M. A., Garau, R., et al. 1994. A comparative study of Grapevine virus B isolates. Rivista di Patologia Vegetale. 4:11–24 http://www.jstor.org/stable/42555743

Boscia, D., Aslouj, E., Elicio, V., Savino, V., Castellano, M. A., and Martelli, G. P. 1992. Production, characterization, and use of monoclonal antibodies to grapevine virus A. Arch Virol. 127:185–194. https://doi.org/10.1007/BF01309583

Boscia, D., Digiaro, M., Safi, M., Garau, R., Zhou, Z., Minafra, A., et al. 2001. Production of monoclonal antibodies to Grapevine virus D and contribution to the study of its aetiological role in grapevine diseases. Vitis. 40:69–74. https://doi.org/10.5073/vitis.2001.40.69-74

Boulila, M., Boscia, D., Terlizzi, B. D., Castellano, M. A., Minafra, A., Savino, V., et al. 1990. Some properties of a phloem-limited non mechanically-transmissible

grapevine virus. Journal of Phytopathology. 129:151–158. https://doi.org/10.1111/j.1439-0434.1990.tb04298.x

Bouyahia, H., Boscia, D., Savino, V., Notte, P. L., Pirolo, C., Castellano, M. A., et al. 2005. *Grapevine rupestris stem pitting-associated virus* is linked with grapevine vein necrosis. VITIS - Journal of Grapevine Research. 44:133–133. https://doi.org/10.5073/VITIS.2005.44.133-137

Bragard, C., Dehnen-Schmutz, K., Gonthier, P., Jacques, M.-A., Miret, J. A. J., Justesen, A. F., et al. 2019. Pest categorisation of non-EU viruses and viroids of Vitis L. EFSA Journal. 17:e05669. https://doi.org/10.2903/j.efsa.2019.5669

Brandizzi, F., Irons, S., Kearns, A., and Hawes, C. 2003. BY-2 cells: culture and transformation for live cell imaging. Current Protocols in Cell Biology. 19. https://doi.org/10.1002/0471143030.cb0107s19

Brault, V., Candresse, T., le Gall, O., Pierre Delbos, R., Lanneau, M., and Dunez, J. 1993. Genetically engineered resistance against grapevine chrome mosaic nepovirus. Plant Mol Biol. 21:89–97. https://doi.org/10.1007/BF00039620

Broadbent, L., and Martini, B. 1959. The spread of plant viruses. Advances in Virus Research. 6:93–135. https://doi.org/10.1016/S0065-3527(08)60489-3

Brown, D. J. F. 1985. the transmission of two strains of Strawberry latent ringspot virus by populations of *Xiphinema diversicaudatum* (Nematoda: Dorylaimoidea). Nematologia mediterranea.

Bruckbauer, H. 1982. Mogliche Beziehungen zwischen Virus und Symptomauspragung bei der Rebe. Wein-Wissenschaft.

Brunt, A. A. 1986. Tomato mosaic virus. In *The plant viruses*, Springer, p. 181–204.

Burger, J. T., and Maree, H. J. 2015. Metagenomic next-generation sequencing of viruses infecting grapevines. In Plant Pathology, Springer, p. 315–330. https://doi.org/10.1007/978-1-4939-2620-6_23

Cadman, C. H., Dias, H. F., and Harrison, B. D. 1960. Sap-transmissible viruses associated with diseases of grape vines in Europe and North America. Nature. 187:577–579. https://doi.org/10.1038/187577a0

Calvi, B.L. 2011. Effects of red-leaf disease on Cabernet Suavignon at the Oakville experimental vineyard and mitigation by harvest delay and crop adjustment. M.S. thesis, University of California, Davis.

Campbell, R. N., Lovisolo, O., and Lisa, V. 1975. Soil transmission of Petunia asteroid mosaic strain of Tomato bushy stunt virus. Phytopathologia Mediterranea. 14:82–86 http://www.jstor.org/stable/42684265

Campbell, T. N., and Choy, F. Y. M. 2005. RNA interference: Past, present and future. Curr Issues Mol Biol. 7:1–6. https://doi.org/10.21775/cimb.007.001

Campos, G., Chialva, C., Miras, S., and Lijavetzky, D. 2021. New technologies and strategies for grapevine breeding through genetic transformation. Front. Plant Sci. 12:767522. https://doi.org/10.3389/fpls.2021.767522

Candresse, T., Marais, A., Faure, C., Lefebvre, M., Lacombe, T., and Boursiquot, J. M. 2020. Complete genome sequence of a novel grapevine-infecting member of the genus *Polerovirus*, grapevine polerovirus 1. Arch Virol. 165:1683–1685. https://doi.org/10.1007/s00705-020-04640-4

Candresse, T., Theil, S., Faure, C., and Marais, A. 2018. Determination of the complete genomic sequence of grapevine virus H, a novel vitivirus infecting grapevine. Arch Virol. 163:277–280. https://doi.org/10.1007/s00705-017-3587-7

Castellano, M. A., Abou-Ghanem, N., Choueiri, E., and Martelli, G. P. 2000. Ultrastructure of grapevine leafroll-associated virus 2 and 7 infections. Journal of Plant Pathology. 82:9–15.

Castillo, M. B., and Orlob, G. B. 1966. Transmission of 2 strains of cucumber and alfalfa mosaic viruses by single aphids of *Myzus persicae*. Phytopathology. 56:1028.

Chakravarthy, S., Velásquez, A. C., Ekengren, S. K., Collmer, A., and Martin, G. B. 2010. Identification of *Nicotiana benthamiana* Genes Involved in Pathogen-Associated Molecular Pattern-Triggered Immunity. Mol Plant Microbe Interact. 23:715–726. https://doi.org/10.1094/MPMI-23-6-0715

Chatzivassiliou, E. K., Efthimiou, K., Drossos, E., Papadopoulou, A., Poimenidis, G., and Katis, N. I. 2004. A survey of tobacco viruses in tobacco crops and native flora in Greece. European Journal of Plant Pathology. 110:1011–1023. https://doi.org/10.1007/s10658-004-1598-1

Chiapello, M., Rodríguez-Romero, J., Nerva, L., Forgia, M., Chitarra, W., Ayllón, M. A., et al. 2020. Putative new plant viruses associated with *Plasmopara viticola*-infected grapevine samples. Annals of Applied Biology. 176:180–191.

Cieniewicz, E., Perry, K., and Fuchs, M. 2017. Grapevine red blotch: molecular biology of the virus and management of the disease. In Grapevine Viruses: Molecular Biology, Diagnostics and Management, eds. Baozhong Meng, Giovanni P. Martelli,

Deborah A. Golino, and Marc Fuchs. Cham: Springer International Publishing, p. 303–314. https://doi.org/10.1007/978-3-319-57706-7_14

Cieniewicz, E., Thompson, J. R., McLane, H., Perry, K. L., Dangl, G. S., Corbett, Q., et al. 2018. Prevalence and genetic diversity of Grabloviruses in free-living *Vitis* spp. Plant Disease. 102:2308–2316. https://doi.org/10.1094/PDIS-03-18-0496-RE

Cigsar, I., Digiaro, M., Gokalp, K., Ghanem-Sabanadzovic, N. A., Stradis, A. D., Boscia, D., et al. 2003. Grapevine deformation virus, a novel nepovirus from turkey. Journal of Plant Pathology. 85:183–191. https://doi.org/10.4454/jpp.v85i3.1029

Conti, M., Milne, R. G., Luisoni, E., and Boccardo, G. 1980. A closterovirus from a stem-pitting-diseased grapevine. Phytopathology. 70:394–399.

Coutts, R. H., Rigden, J. E., Slabas, A. R., Lomonossoff, G. P., and Wise, P. J. 1991. The complete nucleotide sequence of tobacco necrosis virus strain D. Journal of General Virology. 72:1521–1529. https://doi.org/10.1099/0022-1317-72-7-1521

Cropley, R. 1961. Cherry leaf-roll virus. Annals of Applied Biology. 49:524–529. https://doi.org/10.1111/j.1744-7348.1961.tb03645.x

Csorba, T., Kontra, L., Burgyan, J. 2015. Viral silencing suppressors: Tools forged to fine-tine host-pathogen coexistence. Virology. 479-480:85-103. https://doi.org/10.1016/j.virol.2015.02.028

Debat, H., Zavallo, D., Brisbane, R. S., Vončina, D., Almeida, R. P., Blouin, A. G., et al. 2019. Grapevine virus L: a novel vitivirus in grapevine. European Journal of Plant Pathology. 155:319–328. https://doi.org/1045477.s10658-019-01727

Debat, H., Zavallo, D., Moyano, S., Luna, F., Asurmendi, S., and Gomez-Talquenca, S. 2020. A new world begomovirus infecting Grapevine. bioRxiv. https://doi.org/10.1101/2020.02.20.957548v1

Derrick, K. S. 1973. Quantitative assay for plant viruses using serologically specific electron microscopy. Virology. 56:652–653. https://doi.org/10.1016/0042-6822(73)90068-8

Dias, H. F. 1963. Host range and properties of grapevine fanleaf and grapevine yellow mosaic viruses. Ann Applied Biology. 51:85–95. https://doi.org/10.1111/j.1744-7348.1963.tb03677.x

Dias, H. F., and Cation, D. 1976. The characterization of a virus responsible for peach rosette mosaic and grape decline in Michigan. Canadian Journal of Botany. 54:1228–1239. https://doi.org/10.1139/b76-133

Diaz-Lara, A., Golino, D., and Al Rwahnih, M. 2018. Genomic characterization of grapevine virus J, a novel virus identified in grapevine. Arch Virol. 163:1965–1967. https://doi.org/10.1007/s00705-018-3793-y

Diaz-Lara, A., Navarro, B., Di Serio, F., Stevens, K., Hwang, M. S., Kohl, J., et al. 2019. Two novel negative-sense RNA viruses infecting grapevine are members of a newly proposed genus within the family Phenuiviridae. Viruses. 11(8):685. https://doi.org/10.3390/v11080685

Djennane, S., Prado, E., Dumas, V. et al. 2021. A single resistance factor to solve vineyard degeneration due to grapevine fanleaf virus. Commun Biol. 4:637. https://doi.org/10.1038/s42003-021-02164-4

Dolja, V. V., Meng, B., and Martelli, G. P. 2017. Evolutionary aspects of grapevine virology. In Grapevine Viruses: Molecular Biology, Diagnostics and Management, eds. Baozhong Meng, Giovanni P. Martelli, Deborah A. Golino, and Marc Fuchs. Cham: Springer International Publishing, p. 659–688. https://doi.org/10.1007/978-3-319-57706-7_32

Doolittle, S. P., and Gilbert, W. W. 1919. Seed transmission of cucurbit mosaic by the wild cucumber. Phytopathology. 9:326–327.

Doz, B. 1982. Premunition: une compétition entre souches faibles et souches sévères pour une voie commune d'expression des symptômes. INRA. Vol 11.

Eichmeier, A., Komínková, M., Komínek, P., and Baránek, M. 2016. Comprehensive virus detection using next generation sequencing in grapevine vascular tissues of plants obtained from the wine regions of Bohemia and Moravia (Czech Republic). PLoS One. 11:e0167966.

Espinoza, C., Medina, C., Somerville, S., and Arce-Johnson, P. 2007. Senescence-associated genes induced during compatible viral interactions with grapevine and *Arabidopsis*. Journal of Experimental Botany. 58:3197–3212. https://doi.org/10.1093/jxb/erm165

Faggioli, F., Riccioni, L., Mazzei, M., and Barba, M. 1992. Purification and characterization of a new virus found in grapevine. Phytopathologia Mediterranea. 31:37–40. http://www.jstor.org/stable/42685805

Fajardo, T. V. M., Silva, F. N., Eiras, M., and Nickel, O. 2017. High-throughput sequencing applied for the identification of viruses infecting grapevines in Brazil

and genetic variability analysis. Trop. plant pathol. 42:250–260. https://doi.org/10.1007/s40858-017-0142-8

Fakhfakh, H., Vilaine, F., Makni, M., and Robaglia, C. 1996. Cell-free cloning and biolistic inoculation of an infectious cDNA of potato virus Y. Journal of General Virology. 77:519–523. https://doi.org/10.1099/0022-1317-77-3-519

Fan, X., Zhang, Z., Ren, F., Hu, G., Li, C., Zhang, B., et al. 2020. Development of a full-length infectious cDNA clone of the grapevine berry inner necrosis virus. Plants (Basel). 9(10):1340. https://doi.org/10.3390/plants9101340

Feng, M., Cheng, R., Chen, M., Guo, R., Li, L., Feng, Z., et al. 2020. Rescue of tomato spotted wilt virus entirely from complementary DNA clones. PNAS. 117:1181–1190. DOI: 10.1073/pnas.1910787117

Fernandez-Pozo, N., Menda, N., Edwards, J. D., Saha, S., Tecle, I. Y., Strickler, S. R., et al. 2015. The Sol Genomics Network (SGN)—from genotype to phenotype to breeding. Nucleic Acids Research. 43:D1036–D1041. https://doi.org/10.1093/nar/gku1195

Flasco, M., Hoyle, V., Cieniewicz, E., Roy, B., McLane, H., Perry, K. L., et al. 2021. Grapevine red blotch virus is transmitted by the three-cornered alfalfa hopper in a circulative, non-propagative mode with unique attributes. Phytopathology. https://doi.org/10.1094/PHYTO-02-21-0061-R

Fuchs, M. 2020. Grapevine viruses: a multitude of diverse species with simple but overall poorly adopted management solutions in the vineyard. J Plant Pathol. 102:643–653. https://doi.org/10.1007/s42161-020-00579-2

Fuchs, M. 2021. Plant resistance to viruses: engineered resistance. In: Bamford, G.H. and Zuckerman, M. (eds.) Encyclopedia of Virology, 4th Edition. 3:52-59. https://doi.org/10.1016/B978-0-12-809633-8.21310-1

Fujinaga, M., Ogiso, H., Wakabayashi, H., Morikawa, T., and Natsuaki, T. 2009. First report of a Grapevine Algerian latent virus disease on statice plants *Limonium sinuatum* in Japan. J Gen Plant Pathol. 75:157–159 https://doi.org/10.1007/s10327-009-0144-6

Galiakparov, N., Tanne, E., Sela, I., and Gafny, R. 1999. Infectious RNA transcripts from grapevine virus A cDNA clone. Virus Genes. 19:235–242. https://doi.org/10.1023/A:1008192831883

Gallitelli, D., Savino, V., and De Sequeira, O. A. 1983. Properties of a distinctive strain of Grapevine Bulgarian latent virus. Phytopathologia Mediterranea. 22:27–32.

Gasparro, M., Caputo, A. R., Forleo, L. R., Perniola, R., Alba, V., Milella, R. A., et al. 2016. Study of main grapevine viruses transmission in breeding programs ed. Jean-Marie Aurand. BIO Web Conf. 7:01039. https://doi.org/10.1051/bioconf/20160701039

German-Retana, S., and Candresse, T. 1999. Trichoviruses. In Encyclopedia of Virology (Second Edition), eds. Allan Granoff and Robert G. Webster. Oxford: Elsevier, p. 1837–1842. https://doi.org/10.1006/rwvi.1999.0293

Gerola, F., Bassi, M., and Belli, G. 1969. An electron microscope study of different plants infected with grapevine fanleaf virus. Plant Biosystem. 103:271–290. https://doi.org/10.1080/11263506909426506

Gilmer, R. M., Uyemoto, J. K., and Kelts, L. J. 1970. A new grapevine disease induced by tobacco ringspot virus. Phytopathology. 60:619–27. https://doi.org/10.1094/Phyto-60-619

Girgis, S. M., Bem, F. P., Dovas, C. I., Sclavounos, A., Avgelis, A. D., Tsagris, M., et al. 2009. Characterisation of a novel ilarvirus causing grapevine angular mosaic disease. Eur J Plant Pathol. 125:203–211. https://doi.org/10.1007/s10658-009-9472-9

Goodin, M. M., Zaitlin, D., Naidu, R. A., and Lommel, S. A. 2008. Nicotiana benthamiana: its history and future as a model for plant-pathogen interactions. Mol. Plant Microbe Interact. 21:1015-1026. https://doi.org/10.1094/MPMI-218-1015

Goszczynski, D. E., Kasdorf, G. G. F., Pietersen, G., and Tonder, H. van. 1996a. Grapevine leafroll-associated virus 2 (GLRaV-2)- mechanical transmission, purification, production and properties of antisera, detection by ELISA. South African Journal of Enology and Viticulture. 17:15–26.

Goszczynski, D., Kasdorf, G., Pietersen, G., and Van Tonder, H. 1996b. Detection of two strains of grapevine leafroll-associated virus 2. Vitis-Geilweilerhof. 35:133–136.

Gualandri, V., Asquini, E., Bianchedi, P., Covelli, L., Brilli, M., Malossini, U., et al. 2017. Identification of herbaceous hosts of the Grapevine Pinot gris virus (GPGV). Eur J Plant Pathol. 147:21–25. https://doi.org/10.1007/s10658-016-0989-4

Guo, Q., Honesty, S., Xu, M. L., Zhang, Y., Schoelz, J., and Qiu, W. 2014. Genetic diversity and tissue and host specificity of *Grapevine vein clearing virus*. Phytopathology®. 104:539–547. https://doi.org/10.1094/PHYTO-03-13-0075-R

Hanada, K. and Harrison, B.D. 1977. Effects of virus genotype and temperature on seed transmission of nepoviruses. Ann. Appl. Biol. 85:79-92. DOI: 10.1111/j.1744-7348.1977.tb00632.x

Hanson, C. M., and Campbell, R. N. 1979. Strawberry latent ringspot virus from 'Plain' parsley in California. Plant Dis. Rep. 63:142–146.

Harrison, B. D., and Nixon, H. L. 1960. Purification and electron microscopy of three soil-borne plant viruses. Virology. 12:104–117. https://doi.org/10.1016/0042-6822(60)90152-5

Harrison, B., Murant, A., Mayo, M., and Roberts, I. 1974. Distribution of determinants for symptom production, host range and nematode transmissibility between the two RNA components of Raspberry ringspot virus. Journal of General Virology. 22:233–247. https://doi.org/10.1099/0022-1317-22-2-233

Hemenway, C., Weiss, J., O'Connell, K., and Tumer, N. E. 1990. Characterization of infectious transcripts from a potato virus X cDNA clone. Virology. 175:365–371. https://doi.org/10.1016/0042-6822(90)90421-m

Hemmer, C., Djennane, S., Ackerer, L., Hleibieh, K., Marmonier, A., Gersch, S., et al. 2018. Nanobody-mediated resistance to Grapevine fanleaf virus in plants. Plant Biotechnology Journal. 16:660–671. https://doi.org/10.1111/pbi.12819

Hewitt, W. B. 1954. Some virus and virus-like diseases of grapevines. Bulletin Department of Agriculture, California. 43:47–64.

Hewitt, W. B., Goheen, A. C., Easki, D. J., and Gooding, G. V. 1962. Studies on virus diseases of the grapevine in California. Vitis. 3.

Hicks, R. G. T. 1985. An electron microscope study of tubules in homogenates of *Chenopodium quinoa* infected with strawberry latent ringspot virus. Journal of Phytopathology. 112:359–362. https://doi.org/10.1111/j.1439-0434.1985.tb00814.x

Hily, J.-M., Beuve, M., Vigne, E., Demangeat, G., Candresse, T., and Lemaire, O. 2018a. A genome-wide diversity study of grapevine rupestris stem pitting-associated virus. Arch Virol. 163:3105–3111. https://doi.org/0.1007/s00705-018-3945-0

Hily, J.-M., Candresse, T., Garcia, S., Vigne, E., Tannière, M., Komar, V., et al. 2018b. High-throughput sequencing and the viromic study of grapevine leaves: from the detection of grapevine-infecting viruses to the description of a new environmental *Tymovirales* member. Front Microbiol. 9:1782. https://doi.org/10.3389/fmicb.2018.01782

Hollings, M. 1956. *Chenopodium amaranticolor* as a test plant for plant viruses. Plant Pathology. 5:57–60. https://doi.org/10.1111/j.1365-3059.1956.tb00085.x

Hoyle, V., Flasco, M. T., Choi, J., Cieniewicz, E. J., McLane, H., Perry, K., Dangl, G., Rwahnih, M. A., Heck, M., Loeb, G., and Fuchs, M. F. 2022. Transmission of grapevine red blotch virus by *Spissistilus festinus* [Say, 1830] (Hemiptera: *Membracidae*) between free-living vines and *Vitis vinifera* 'Cabernet Franc.' *Viruses. 14* (6), 1156. https://doi.org/10.3390/v14061156.

Hou, W., Li, S., and Massart, S. 2020. Is There a "Biological Desert" With the Discovery of New Plant Viruses? A Retrospective Analysis for New Fruit Tree Viruses. Front. Microbiol. 11:592816. https://doi.org/10.3389/fmicb.2020.592816

Hu, R., Dias, N. P., Soltani, N., Vargas-Asencio, J., Hensley, D. D., Perry, Keith. L., et al. 2021. Cultivated and wild grapevines in Tennessee possess overlapping but distinct virus populations. Plant Disease. 105:2785–2791. https://doi.org/10.1094/PDIS-11-20-2483-SC

Hull, R. 1969. Alfalfa Mosaic Virus. Advances in Virus Research. 15:365–433. https://doi.org/10.1016/S0065-3527(08)60880-5

Igarashi, A., Yamagata, K., Sugai, T., Takahashi, Y., Sugawara, E., Tamura, A., et al. 2009. Apple latent spherical virus vectors for reliable and effective virus-induced gene silencing among a broad range of plants including tobacco, tomato, *Arabidopsis thaliana*, cucurbits, and legumes. Virology. 386:407–416. https://doi.org/10.1016/S0065-3527(08)60880-5

Isogai, M., Matsudaira, T., Ito, M., and Yoshikawa, N. 2019. The 1b gene of raspberry bushy dwarf virus is a virulence component that facilitates systemic virus infection in plants. Virology. 526:222–230. https://doi.org/10.1016/j.virol.2018.10.025

Izadpanah, K., Zaki-Aghl, M., Zhang, Y. P., Daubert, S. D., and Rowhani, A. 2003. Bermuda grass as a potential reservoir host for Grapevine fanleaf virus. Plant Disease. 87:1179–1182. https://doi.org/10.1094/PDIS.2003.87.10.1179

Izuishi, Y., Isaka, N., Li, H., Nakanishi, K., Kageyama, J., Ishikawa, K., et al. 2020. Apple latent spherical virus (ALSV)-induced gene silencing in a medicinal plant, *Lithospermum erythrorhizon*. Scientific Reports. 10:13555. https://doi.org/10.1038/s41598-020-70469-1

Jankulova, M., Eskenazy, M., Bakardzhieva, N., and Georgieva, P. 1982. ELISA for the quantitative determination of grapevine fanleaf virus / Quantitative bestimmung des

Fanleaf-Virus der weinrebe mit dem ELISA-test. Zeitschrift für Pflanzenkrankheiten und Pflanzenschutz / Journal of Plant Diseases and Protection. 89:18–29.

Jarugula, S., Gowda, S., Dawson, W. O., and Naidu, R. A. 2018. Development of infectious cDNA clones of grapevine leafroll-associated virus 3 and analyses of the 5′ non-translated region for replication and virion formation. Virology. 523:89–99. https://doi.org/10.1016/j.virol.2018.07.023

Jelkmann, W., Maiss, E., Breyel, E., and Casper, R. 1988. Production and use of cDNA clones from Arabis mosaic virus. Annals of Applied Biology. 113:483–491. DOI: 10.1111/j.1744-7348.1988.tb03326.x

Jha, A., and Posnette, A. F. 1961. Transmission of Arabis mosaic virus by the nematode *Xiphinema diversicaudatum* (Micol.). Virology. 13:119–123. https://doi.org/10.1016/0042-6822(61)90038-1

Jo, Y., Song, M.-K., Choi, H., Park, J.-S., Lee, J.-W., Lian, S., et al. 2017. Genome sequence of Grapevine Virus K, a novel Vitivirus infecting grapevine. Genome Announc. 5. https://doi.org/10.1128/genomeA.00994-17

Jones, A. T. 1973. A comparison of some properties of four strains of cherry leaf roll virus. Annals of Applied Biology. 74:211–217. https://doi.org/10.1111/j.1744-7348.1973.tb07740.x

Jones, A. T., McElroy, F. D., and Brown, D. J. F. 1981. Tests for transmission of Cherry leaf roll virus using *Longidorus, Paralongidorus* and *Xiphinema* nematodes. Annals of Applied Biology. 99:143–150. https://doi.org/10.1111/j.1744-7348.1981.tb05141.x

Jovel, J., Walker, M., and Sanfaçon, H. 2007. Recovery of *Nicotiana benthamiana* plants from a necrotic response induced by a nepovirus is associated with RNA silencing but not with reduced virus titer. Journal of Virology. https://doi.org/10.1128/JVI.01192-07

Kaliciak, A., and Syller, J. 2009. New hosts of Potato virus Y (PVY) among common wild plants in Europe. Eur J Plant Pathol. 124:707–713. https://doi.org/10.1007/s10658-009-9452-0

Katsirdakis, K. X., Potter-Damoulakis, U. J., Katis, N. I., and Roubelakis-Angelakis, K. A. 1989. Comparison of pollen grains from grapevine-fanleaf-infected and non-infected grapevines. Phytoparasitica. 17:65–66.

Kazinczi, G., Horváth, J., and Lesemann, D. E. 2002. Perennial plants as new natural hosts of three viruses / Perennierende Pflanzen als neue natürliche Wirte für drei Viren. Zeitschrift für Pflanzenkrankheiten und Pflanzenschutz / Journal of Plant Diseases and Protection. 109:301–310.

Keith, C. V. 2018. Grapevine vein clearing virus: epidemiological patterns and construction of a clone. MSU Graduate Theses. 3300:129.

Kim, S., Cho, W. K., Lee, H.G., Park, S.H., Sohn, S.H., and Kim, K.H. 2012. The p19 protein of grapevine Algerian latent virus is a determinant of systemic infection of *Chenopodium quinoa*. Virus Research. 165:81–89. https://doi.org/10.1016/j.virusres.2012.01.013

Klaassen, V.A., Sim, S.T., Dangl, G.S., Osman, F., Al Rwahbih, M., Rowhani, A., and Golino, D.A. 2011. *Vitis californica* x *Vitis vinifera hybrids* are hosts for *Grapevine*

leafroll-associated virus-2 and *3* and *Grapevine virus A* and *B.* Plant Disease 95:657-665. https://doi.org/10.1094/PDIS-09-10-0621

Koolivand, D., Bashir, N. S., Behjatnia, S. A., and Joozani, R. J. 2016. Production of Polyclonal Antibody against Grapevine fanleaf virus Movement Protein Expressed in Escherichia coli. Plant Pathol J. 32:452–459. https://doi.org/10.5423/PPJ.OA.01.2016.0031

Kubelková D, Spak J. Transmission of raspberry bushy dwarf virus by seed of *Chenopodium quinoa*. Acta Virol. 1998 Jun;42(3):195-6. PMID: 9842450.

Kumagai, M. H., Donson, J., Della-Cioppa, G., Harvey, D., Hanley, K., and Grill, L. 1995. Cytoplasmic inhibition of carotenoid biosynthesis with virus-derived RNA. Proceedings of the National Academy of Sciences. 92:1679–1683. https://doi.org/10.1073/pnas.92.5.1679

Kurth, E. G., Peremyslov, V. V., Prokhnevsky, A. I., Kasschau, K. D., Miller, M., Carrington, J. C., et al. 2012. Virus-derived gene expression and RNA interference vector for grapevine. J Virol. 86:6002–6009. https://doi.org/10.1128/JVI.00436-12

Kyriakopoulou, P. E. 1995. Artichoke Italian latent virus causes artichoke patchy chlorotic stunting disease. Ann Applied Biology. 127:489–497. https://doi.org/10.1111/j.1744-7348.1995.tb07607.x

La Notte, P., Buzkan, N., Choueiri, E., Minafra, A., and Martelli, G. P. 1997. Acquisition and transmission of Grapevine virus a by the mealybug *Pseudococcus longispinus*. Journal of Plant Pathology. 79:79–85. http://www.jstor.org/stable/41997870

Lai-Kee-Him, J., Schellenberger, P., Dumas, C., Richard, E., Trapani, S., Komar, V., et al. 2013. The backbone model of the Arabis mosaic virus reveals new insights into functional domains of Nepovirus capsid. Journal of Structural Biology. 182:1–9. https://doi.org/10.1016/j.jsb.2013.01.007

Lazar, J., Kölber, M., and Lehoczky, J. 1990. Detection of some nepoviruses (GFV, GFV-YM, GCMV, ArMV) in the seeds and seedlings of grapevines by ELISA. Kertgazdasag. 22:58–72.

Le Gall, O., Candresse, T., Brault, V., Bretout, C., Hibrand, L., and Dunez, J. 1988. Cloning full-length cDNA of grapevine chrome mosaic nepovirus. Gene. 73:67–75.

Lebas, B. S. M., Veerakone, S., Liefting, L. W., Tang, J., Perez-Egusquiza, Z., von Bargen, S., et al. 2016. Comparison of diagnostic techniques for the detection and differentiation of Cherry leaf roll virus strains for quarantine purposes. Journal of Virological Methods. 234:142–151. https://doi.org/10.1016/j.jviromet.2016.04.015

Lee, R. C., Feinbaum, R. L., and Ambros, V. 1993. The *C. elegans* heterochronic gene lin-4 encodes small RNAs with antisense complementarity to lin-14. Cell. 75:843–854. https://doi.org/10.1016/0092-8674(93)90529-y

Li, C., Sasaki, N., Isogai, M., and Yoshikawa, N. 2004. Stable expression of foreign proteins in herbaceous and apple plants using Apple latent spherical virus RNA2 vectors. Archives of Virology. 149:1541–1558. https://doi.org/10.1007/s00705-004-0310-2

Li, C., Yoshikawa, N., Takahashi, T., Kouji, Y., and Koganezawa, H. 2000. Nucleotide sequence and genome organization of Apple latent spherical virus: a new virus

classified into the family. Journal of General Virology. 81:541–547. https://doi.org/10.1099/0022-1317-81-2-541.

Lima, M. F., Rosa, C., Golino, D. A., and Rowhani, A. 2006. Detection of Rupestris stem pitting associated virus in seedlings of virus-infected maternal grapevine plants. In Embrapa Semiárido-Artigo em anais de congresso (ALICE), In: Meeting of the international council for the study of virus and virus…

Ling, K.-S., Zhu, H.-Y., and Gonsalves, D. 2008. Resistance to Grapevine leafroll associated virus-2 is conferred by post-transcriptional gene silencing in transgenic *Nicotiana benthamiana*. Transgenic Res. 17:733–740. https://doi.org/10.1007/s11248-007-9147-2

Lister, R.M. 1959. Soil-borne virus diseases. Scientific Horticulture. 14:90-96.

Lovato, A., Faoro, F., Gambino, G., Maffi, D., Bracale, M., Polverari, A., et al. 2014. Construction of a synthetic infectious cDNA clone of Grapevine Algerian latent virus (GALV-Nf) and its biological activity in Nicotiana benthamiana and grapevine plants. Virology Journal. 11:186. https://doi.org/10.1186/1743-422X-11-186

Makkouk, K. M., Kumari, S. G., and Bos, L. 1990. Broad bean wilt virus: Host range, purification, serology, transmission characteristics, and occurrence in faba bean in West Asia and North Africa. Netherlands Journal of Plant Pathology. 96:291–300. https://doi.org/10.1007/BF02000170

Maliogka, V.I., Martelli, G.P., Fuchs, M., Katis, N.I. 2015. Chapter six: control of viruses infecting grapevine. Advances in Virus Research. 91:175-227. https://doi.org/10.1016/bs.aivir.2014.11.002

Maliogka, V.I., Olmos, A., Pappi, P. G., Lotos, L., Efthimiou, K., Grammatikaki, G., et al. 2015. A novel grapevine badnavirus is associated with the Roditis leaf discoloration disease. Virus Research. 203:47–55. https://doi.org/10.1016/j.virusres.2015.03.003

Marais, A., Fuare, C., Couture, C., Bergey, B., Gentit, P., Candresse, T. Characterization by Deep Sequencing of Divergent Plum bark necrosis stem pitting-associated virus (PBNSPaV Isolates and Development of a Broad-Spectrum PBNSPaV Detection Assay. Phytopathology 2014, 104, 660-666.

Martelli, G. 1993. Graft-transmissible diseases of grapevines: handbook for detection and diagnosis. Food & Agriculture Org.

Martelli, G. 1978. Nematode-borne viruses of grapevine, their epidemiology and control.

Martelli, G. 1966. Preliminary report on purification and serology of a virus associated with Hungarian grapevines showing macroscopic symptoms of fanleaf and yellow mosaic. In Davis 1965: University of California, Division of Agricultural Sciences, p. 402–410.

Martelli, G., Di Franco, A., Russo, M., and Savino, V. 1980. The ultrastructure of Grapevine Bulgarian latent virus infections in natural and artificial hosts. Proc. 7th Meeting Intern. Counc. for the Study of Viruses and Virus-Like Diseases of the Grapevine, p. 251.

Martelli, G. P. 1979. ldentification of virus diseases of grapevine and production of disease-free plants. Vitis. 18:127–136.

Martelli, G. P., Candresse, T., and Namba, S. 1994. Trichovirus, a new genus of plant viruses. Archives of Virology. 134:451–455. https://doi.org/10.1007/BF01310583

Martelli, G. P., Golino, D. A., and Katis, N. I. 2017. Other Grapevine Viruses of Lesser Economic Importance. In Grapevine Viruses: Molecular Biology, Diagnostics and Management, eds. Baozhong Meng, Giovanni P. Martelli, Deborah A. Golino, and Marc Fuchs. Cham: Springer International Publishing, p. 365–371. https://doi.org/10.1007/978-3-319-57706-7_18

Martelli, Giovanni P., and William B. Hewitt. Comparative studies on some Italian and Californian virus diseases of grapevine. Phytopathologia Mediterranea, vol. 2, no. 4, Firenze University Press, 1963, pp. 275–84, http://www.jstor.org/stable/42683897.

Martelli, G. P., and Russo, M. 1977. Plant Virus Inclusion Bodies. In Advances in Virus Research, eds. Max A. Lauffer, Frederik B. Bang, Karl Maramorosch, and Kenneth M. Smith. Academic Press, p. 175–266. https://doi.org/10.1016/S0065-3527(08)60763-0

Martin IR, Vigne E, Velt A, Hily JM, Garcia S, Baltenweck R, Komar V, Rustenholz C, Hugueney P, Lemaire O, Schmitt-Keichinger C. 2021. Severe stunting symptoms upon Nepovirus infection are reminiscent of a chronic hypersensitive-like response in a perennial woody fruit crop. Viruses. 13, 11:2138.

Massart, S., Candresse, T., Gil, J., Lacomme, C., Predajna, L., Ravnikar, M., et al. 2017. A framework for the evaluation of biosecurity, commercial, regulatory, and ccientific impacts of plant viruses and viroids identified by NGS technologies. Frontiers in Microbiology. 8:45. https://doi.org/10.3389/fmicb.2017.00045

Matthews, R. E. F. 1993/2019. Diagnosis of Plant Virus Diseases. CRC Press. 392. eBook.

McGreal, B., Sandanayaka, M., Gough, R., Rohra, R., Davis, V., Marshall, C. W., et al. 2021. Retention and Transmission of Grapevine Leafroll-Associated Virus 3 by Pseudococcus calceolariae. Front. Microbiol. 12. https://doi.org/10.3389/fmicb.2021.663948

Mehetre, G. T., Leo, V. V., Singh, G., Sorokan, A., Maksimov, I., Yadav, M. K., et al. 2021. Current Developments and Challenges in Plant Viral Diagnostics: A Systematic Review. Viruses. 13. https://doi.org/10.3390/v13030412

Melinda. 2013. Diversity, Host Range and Transmission Efficiency of Bean common mosaic virus by Aphids on Yard Long Beans. *Thesis.* Institut Pertanian Bogor.

Meng, B., and Gonsalves, D. 2007. Grapevine rupestris stem pitting-associated virus: a decade of research and future perspectives. Plant Viruses. 1:52–62.

Meng, B., Martelli, G. P., Golino, D. A., and Fuchs, M. 2017. Grapevine viruses: molecular biology, diagnostics and management. Springer.

Meng, B., Pang, S. Z., Forsline, P. L., McFerson, J. R., and Gonsalves, D. 1998. Nucleotide sequence and genome structure of grapevine rupestris stem pitting associated virus-1 reveal similarities to apple stem pitting virus. Journal of General Virology. 79:2059–2069. https://doi.org/10.1099/0022-1317-79-8-2059.

Meng, B., and Rowhani, A. 2017. Grapevine rupestris stem pitting-associated virus. In Grapevine Viruses: Molecular Biology, Diagnostics and Management, eds. Baozhong Meng, Giovanni P. Martelli, Deborah A. Golino, and Marc Fuchs. Cham:

Springer International Publishing, p. 257–287. https://doi.org/10.1007/978-3-319-57706-7_12

Meng, B., Venkataraman, S., Li, C., Wang, W., Dayan-Glick, C., and Mawassi, M. 2013. Construction and biological activities of the first infectious cDNA clones of the genus Foveavirus. Virology. 435:453–462. https://doi.org/10.1016/j.virol.2012.09.045

Mikona, C., and Jelkmann, W. 2010. Replication of *Grapevine leafroll-associated virus*-7 (GLRaV-7) by *Cuscuta* species and its transmission to herbaceous plants. Plant Disease. 94:471–476. https://doi.org/10.1094/PDIS-94-4-0471

Minafra, A., Gölles, R., da Camara Machado, A., Saldarelli, P., Buzkan, N., Savino, V., et al. 1998. Expression of the coat protein genes of Grapevine virus A And B in *Nicotiana* species and evaluation of the resistance conferred on transgenic plants. Journal of Plant Pathology. 80:197–202.

Monette, P. L., and James, D. 1990. Use of in vitro cultures of *Nicotiana benthamiana* for the purification of grapevine virus A. Plant Cell Tiss Organ Cult. 23:131–134. https://doi.org/10.1007/BF00035833

Moskovitz, Y., Goszczynski, D. E., Bir, L., Fingstein, A., Czosnek, H., and Mawassi, M. 2008. Sequencing and assembly of a full-length infectious clone of grapevine virus B and its infectivity on herbaceous plants. Archives of Virology. 153:323–328. https://doi.org/10.1007/s00705-007-1075-1

Moury, B. B., Fabre, F., Hébrard, E., and Froissart, R. 2017. Determinants of host species range in plant viruses. Journal of General Virology. 98:862–873. https://doi.org/10.1099/jgv.0.000742

Muruganantham, M., Moskovitz, Y., Haviv, S., Horesh, T., Fenigstein, A., Preez, J. du, et al. 2009. *Grapevine virus* A-mediated gene silencing in *Nicotiana benthamiana* and *Vitis vinifera*. J Virol Methods. 155:167–174. https://doi.org/10.1016/j.jviromet.2008.10.010

Nabeshima, T., and Abe, J. 2021. High-throughput sequencing indicates novel *Varicosavirus, Emaravirus*, and *Deltapartitivirus* infections in *Vitis coignetiae*. Viruses. 13:827. https://doi.org/10.3390/v13050827

Naderpour, M., and Johansen, I. E. 2011. Visualization of resistance responses in *Phaseolus vulgaris* using reporter tagged clones of *Bean common mosaic virus*. Virus Res. 159:1–8. https://doi.org/10.1016/j.virusres.2011.04.004

Nakaune, R., Toda, S., Mochizuki, M., and Nakano, M. 2008. Identification and characterization of a new vitivirus from grapevine. Arch Virol. 153:1827. https://doi.org/10.1007/s00705-008-0188-5

Namba, S., Iwanami, T., Yamashita, S., and Hatamoto, M. 1986. Three phloem-limited viruses of grapevine: direct fluorescence detection. Plant virus diseases of horticultural crops in the tropics and subtropics.

Namba, S., Yamashita, S., Doi, Y., and Yora, K. 1979. A Small Spherical Virus Associated with the Ajinashika Disease of Koshu Grapevine. Jpn. J. Phytopathol. 45:70–73. https://doi.org/10.3186/jjphytopath.45.70

Nölke, G., Cobanov, P., Uhde-Holzem, K., Reustle, G., Fischer, R., and Schillberg, S. 2009. *Grapevine fanleaf virus* (GFLV)-specific antibodies confer GFLV and *Arabis mosaic virus* (ArMV) resistance in *Nicotiana benthamiana*. Molecular Plant Pathology. 10:41–49. https://doi.org/10.1111/j.1364-3703.2008.00510.x

Novák, J. B., and Lanzová, J. 1976. Identification of alfalfa mosaic virus and tomato bushy stunt virus in hop (*Humulus lupulus* L.) and grapevine (*Vitis vinifera* subsp. sativa (DC/HEGI)) plants in Czechoslovakia. Biologia plantarum. 18:152–154.

Ohki, T., Uematsu, S., Nakayama, Y., Lesemann, D.-E., Honda, Y., Tsuda, S., et al. 2006. Characterization of *Grapevine Algerian latent virus* isolated from nipplefruit (*Solanum mammosum*) in Japan. J Gen Plant Pathol. 72:119–122. https://doi.org/10.1007/s10327-005-0257-5

Orecchia, M., Nölke, G., Saldarelli, P., Dell'Orco, M., Uhde-Holzem, K., Sack, M., et al. 2008. Generation and characterization of a recombinant antibody fragment that binds to the coat protein of grapevine leafroll-associated virus 3. Archives of Virology. 153:1075–1084.

Orlov, I., Hemmer, C., Ackerer, L., Lorber, B., Ghannam, A., Poignavent, V., et al. 2020. Structural basis of nanobody recognition of grapevine fanleaf virus and of virus resistance loss. PNAS. 117:10848–10855.

Osterbaan, L. J., Choi, J., Kenney, J., Flasco, M., Vigne, E., Schmitt-Keichinger, C., et al. 2019. The identity of a single residue of the RNA-Dependent RNA Polymerase of grapevine fanleaf virus modulates vein clearing in *Nicotiana benthamiana*. MPMI. 32:790–801.

Osterbaan, L. J., Schmitt-Keichinger, C., Vigne, E., and Fuchs, M. 2018. Optimal systemic grapevine fanleaf virus infection in *Nicotiana benthamiana* following agroinoculation. Journal of Virological Methods. 257:16–21.

Ouertani, R., Savino, V., Minafra, A., Boscia, D., Castellano, M. A., Martelli, G. P., et al. 1992. Properties of a previously undescribed grapevine nepovirus from Tunisia. Archives of Virology. 126:107–117.

Parrella, G., Gognalons, P., Gebre-Selassiè, K., Vovlas, C., and Marchoux, G. 2003. an update of the host range of *tomato spotted wilt virus*. Journal of Plant Pathology. 85:227–264. Available at: http://www.jstor.org/stable/41998156

Perrone, I., Chitarra, W., Boccacci, P., and Gambino, G. 2017. Grapevine–virus–environment interactions: an intriguing puzzle to solve. New Phytologist. 213:983–987. https://doi.org/10.1111/nph.14271

Perry, K. L., McLane, H., Thompson, J. R., and Fuchs, M. 2018. A novel grablovirus from non-cultivated grapevine (*Vitis* sp.) in North America. Archives of Virology. 163:259–262. https://doi.org/10.1007/s00705-017-3567-y

Petersen, S. M., Keith, C., Austin, K., Howard, S., Su, L., and Qiu, W. 2018. A natural reservoir and transmission vector of grapevine vein clearing virus. Plant Disease. 103:571–577. https://doi.org/10.1094/PDIS-06-18-1073-RE

Pina, M. A. S., Gómez-Aix, C., Méndez-López, E., Bernal, B. G., and Aranda, M. A. 2021. Imaging techniques to study plant virus replication and vertical transmission. Viruses. 13:358. https://doi.org/10.3390/v13030358

Prator, C. A., Kashiwagi, C. M., Vončina, D., and Almeida, R. P. P. 2017. Infection and colonization of *Nicotiana benthamiana* by *Grapevine leafroll-associated virus* 3. Virology. 510:60–66. https://doi.org/10.1016/j.virol.2017.07.003

Pratt, A. J., and MacRae, I. J. 2009. The RNA-induced silencing complex: a versatile gene-silencing machine. The Journal of Biological Chemistry, *284*(27), 17897–17901. https://doi.org/10.1074/jbc.R900012200

du Preez, J., Stephan, D., Mawassi, M., and Burger, J. T. 2011. The grapevine-infecting vitiviruses, with particular reference to grapevine virus A. Arch Virol. 156:1495. https://doi.org/10.1007/s00705-011-1071-3

Price, W. C. 1940. Comparative Host Ranges of Six Plant Viruses. American Journal of Botany. 27:530–541. Available at: http://www.jstor.org/stable/2437088

Quacquarelli, A., and Avgelis, A. 1975. *Nicotiana benthamiana* Domin, as host for plant viruses / *Nicotiana benthamiana* Domin, quale ospite di virus vegetali. Phytopathologia Mediterranea. 14:36–39. Available at: http://www.jstor.org/stable/42684252

Ramsdell, D. C., and Myers, R. L. 1978. The rate of spread of peach Rosette mosaic virus in a *Vitis labrusca* L." Concord" vineyard; some weed hosts and the seed and pollen-borne nature of the virus [grapes]. Monografias INIA (Spain).

Ramsdell, D. C., and Stace-Smith, R. 1980. Blueberry leaf mottle, a new disease of highbush blueberry. Acta Hortic. :37–48. https://doi.org/10.17660/ActaHortic.1980.95.4

Ramsdell, D. C., and Stace-Smith, R. 1981. Physical and chemical properties of the particles and ribonucleic acid of blueberry leaf mottle virus. Phytopathology. 71:468. https://doi.org/10.1094/Phyto-71-468

Rana, G. L., and Kyriakopoulou, P. E. 1982. Artichoke Italian latent and Artichoke mottled crinkle viruses in artichoke in Greece / Il virus latente italiano del Carciofo

ed il virus dell'arricciamento maculato del Carciofo rinvenuti in Grecia. Phytopathologia Mediterranea. 21:101–104. Available at: http://www.jstor.org/stable/42684605

Read, D.A., Thompson, G.D., Cordeur, N.L., et al. Genomic characterization of grapevine viruses N and O: novel vitiviruses from South Africa. Arch Virol (2022). https://doi.org/10.1007/s00705-02105333-2.

Refatti, E. 1966. Su una possibile correlazione fra il virus del complesso dell'arricciamento e la malattia delle enazioni nella vite. Rivista di Patologia Vegetale. 2:207–217. Available at: http://www.jstor.org/stable/42555998

Reynard, J.-S., Brodard, J., Remoliff, E., Lefebvre, M., Schumpp, O., and Candresse, T. 2020. A novel foveavirus identified in wild grapevine (*Vitis vinifera* subsp. sylvestris). Arch Virol. 165:2999–3002. https://doi.org/10.1007/s00705-020-04817-x

Ritzenthaler, C., Pinck, M., and Pinck, L. 1995. Grapevine fanleaf nepovirus P38 putative movement protein is not transiently expressed and is a stable final maturation product *in vivo*. Journal of General Virology. 76:907–915. https://doi.org/10.1099/0022-1317-76-4-907

Rizzo, T. M., and Palukaitis, P. 1990. Construction of full-length cDNA clones of cucumber mosaic virus RNAs 1, 2 and 3: Generation of infectious RNA transcripts. Mol Gen Genet. 222:249–256. https://doi.org/10.1007/BF00633825

Roca, F., Rana, G. L., and Kyriakopoulou, P. E. 1982. *Longidorus fasciatus* vector of a serologically distinct strain of artichoke Italian latent virus Greece. Nematologia Mediterranea. 10(1):65-69.

Rochow, W. F., and Ross, F. 1955. Virus multiplication in plants doubly infected by potato viruses X and Y. Virology. 1:10–27. https://doi.org/10.1016/0042-6822(55)90003-9

Rosciglione, B., and Castellano, M. A. 1985. Further evidence that mealybugs can transmit Grapevine virus A (GVA) to herbaceous hosts. Phytopathologia Mediterranea. 24:186–188.

Rosciglione, B., Martelli, G. P., Savino, V., and Cannizzaro, G. 1983. Mealybug transmission of grapevine virus A. Vitis. 22:17.

Rowhani, A. 2000. Grapevine rupestris stem pitting-associated virus: population diversity, titer in the host and possible transmission vector. In Extended abstracts of the 13th meeting of ICVG, Adelaide, 12-17.

Rowhani, A., La Notte P., Uyemoto J.K., Daubert S.D., Savino V. 2017. Biological assays. In: Meng B., Martelli G., Golino D., Fuchs M. (eds) Grapevine Viruses: Molecular Biology, Diagnostics and Management. Springer, Cham. https://doi.org/10.1007/978-3-319-57706-7_20

Rowhani A, Osman F, Daubert SD, Al Rwahnih M, Saldarelli P. 2017. Polymerase chain reaction methods for the detection of grapevine viruses and viroids. In: Meng B, Martelli GP, Golino DA, Fuchs M (eds) Grapevine viruses: molecular biology, diagnostics and management. Springer Verlag, Cham, 432–452. https://doi.org/10.1007/978-3-319-57706-7_22

Rowhani, A., Uyemoto, J. K., Golino, D. A., and Martelli, G. P. 2005. Pathogen testing and certification of *Vitis* and *Prunus* species. Annu. Rev. Phytopathol. 43:261–278. https://doi.org/10.1146/annurev.phyto.43.040204.135919

Rumbos, I. C., and Avgelis, A. D. 1989. Roditis leaf discoloration - a new virus disease of grapevine: symptomatology and transmission to indicator plants. J Phytopathol. 125:274–278. https://doi.org/10.1111/j.1439-0434.1989.tb01070.x

Russo, M. 1985. Electron microscopy of grapevine virus infections. Phytopathologia Mediterranea. 24:144–147.

Rwahnih, M. A., Alabi, O. J., Hwang, M. S., Stevens, K., and Golino, D. 2019. Identification and genomic characterization of grapevine Kizil Sapak virus, a novel grapevine-infecting member of the family *Betaflexiviridae*. Arch Virol. 164:3145–3149. https://doi.org/10.1007/s00705-019-04434-3

Rwahnih, M. A., Alabi, O. J., Westrick, N. M., Golino, D., and Rowhani, A. 2016. Near-complete genome sequence of grapevine fabavirus, a novel putative member of the genus *Fabavirus*. Genome Announc. 4. https://doi.org/10.1128/genomeA.00703-16

S.A. Wingard. 1928. Hosts and symptoms of ring spot, a virus disease of plants. Journal of Ag Res. 37:127–154.

Sabanadzovic, S. 2009. Viruses of native *Vitis* germplasm in the southeastern United States. In Extended Abstracts 16th Meeting of ICVG, Dijon, France. p. 32–35.

Sabella, E., Pierro, R., Luvisi, A., Panattoni, A., D'Onofrio, C., Scalabrelli, G., et al. 2018. Phylogenetic analysis of viruses in Tuscan *Vitis vinifera sylvestris* (Gmeli) Hegi. PLOS ONE. 13:e0200875.

Saldarelli, P., Dell'Orco, M., and Minafra, A. 2000. Infectious cDNA clones of two grapevine viruses. Archives of Virology. 145(2):397-405. https://doi.org/10.1007/s007050050031

Saldarelli, P., Giampetruzzi, A., Maree, H. J., & Rwahnih, M. A. 2017. High-throughput sequencing: advantages beyond virus identification. In Grapevine viruses: molecular biology, diagnostics and management. 625-642. Springer, Cham.

Sanfacon, H., Zhang, G., Chisholm, J., Jafarpour, B., and Jovel, J. 2006. Molecular biology of Tomato ringspot nepovirus, a pathogen of ornamentals, small fruits and fruit trees. Floriculture, ornamental and plant biotechnology. 540–547.

Savino, V., Cherif, C., and Martelli, G. P. 1985. A natural serological variant of grapevine fanleaf virus. Phytopathologia Mediterranea. 24:29–34.

Savino, V., Gallitelli, D., Jankulova, M., and Rana, G. L. 1977. A comparison of four isolates of Artichoke Italian latent virus (AILV). Phytopathologia Mediterranea. 16:41–50. Available at: http://www.jstor.org/stable/42684344

Schmelzer, K., Schmidt, H., and Beczner, L. 1973. Spontane wirtspflanzen des luzernemosaik-virus. Biologisches Zentralblatt.

Schmelzer, K., and Wolf, P. 1977. Wirtspflanzen und ihre viren, virosen und mykoplasmosen. pflanzliche virologie. Registerband Verzeichnisse und Übersichten zu den Virosen in Europa. Akademie Verlag, Berlin. 1977:53–189.

Shanmuganathan, N. and Fletcher, G. 1982. Enzyme-linked immunosorbent assay to detect fanleaf virus in grapevines grown in containers. Plant Dis. 66:704-707.

Shibaei, N., Majidi, J., Bashir, N. S., Karkhaneh, A., and Razavi, K. 2018. Production and partial purification of the *Grapevine fanleaf virus* coat protein 42 polyclonal antibody against inclusion body expressed in *Escherichia coli*. Iran J Biotechnol. 16. https://doi.org/10.21859/ijb.1525

Schoelz, J., Volenberg, D., Adhab, M., Fang, Z., Klassen, V., Spinka, C., Al Rwahnih, M. 2021. Am J Enol Vitic. 72:73-84. https://doi.org/10.5344/ajev.2020.20043

Silva, J. M. F., Al Rwahnih, M., Blawid, R., Nagata, T., and Fajardo, T. V. M. 2017. Discovery and molecular characterization of a novel enamovirus, Grapevine enamovirus-1. Virus Genes. 53:667–671. https://doi.org/10.1007/s11262-017-1470-y

Soltani, N., Stevens, K. A., Klaassen, V., Hwang, M.-S., Golino, D. A., and Al Rwahnih, M. 2021. Quality Assessment and Validation of High-Throughput Sequencing for Grapevine Virus Diagnostics. Viruses. 13:1130. https://doi.org/10.3390/v13061130

Spielmann, A., Krastanova, S., Douet-Orhant V., and Gugerli V.P. 2000. Analysis of transgenic grapevine (*Vitis rupestris*) and *Nicotiana benthamiana* plants expressing an Arabis mosaic virus coat protein gene. Plant Sci. 156:235–244. https://doi.org/10.1016/s0168-9452(00)00259-4

Steinkellner, H., Himmler, G., Sagl, R., Mattanovich, D., and Katinger, H. 1992. Amino-acid sequence comparison of nepovirus coat proteins. Virus genes. 6:197–202. https://doi.org/10.1007/bf01703068

Stellmach, G. 1970. Tomato black ring in *Vitis*. Virus diseases of small fruits and grapevines.

Sun, S., Hu, Y., Jiang, G., Tian, Y., Ding, M., Yu, C., et al. 2020. Molecular characterization and genomic function of Grapevine Geminivirus A. Frontiers in microbiology. 11:2121. https://doi.org/10.3389/fmicb.2020.555194

Tang, J., Lilly, S., Veerakone, S., Kanchiraopally, D., Kelly, M., Delmiglio, C., and Thompson, J.R. 2022. First report of Grapevine Algerian latent virus in carnation in

New Zealand. First Look. Plant Dis. https://doi.org/10.1094/PDIS-03-22-0597-PDN

Tanne, E., Sela, I., and Harpaz, I. 1974. Transmission of grapevine leafroll virus to herbaceous plants. Journal of Phytopathology. 80:176–180.

Tarquini, G., Ermacora, P., Bianchi, G. L., De Amicis, F., Pagliari, L., Martini, M., et al. 2018. Localization and subcellular association of Grapevine Pinot Gris Virus in grapevine leaf tissues. Protoplasma. 255:923–935. https://doi.org/10.1007/s00709-017-1198-5

Tarquini, G., Zaina, G., Ermacora, P., De Amicis, F., Franco-Orozco, B., Loi, N., et al. 2019. Agroinoculation of *Grapevine Pinot Gris Virus* in tobacco and grapevine provides insights on viral pathogenesis. PLoS One. 14:e0214010.

Taylor, R., and Hewitt, W. 1964. Properties and serological relationships of Australian and Californian soil-borne viruses of the grapevine and arabis mosaic virus. Aust. J. Agric. Res. 15:571. https://doi.org/10.1071/AR9640571

Tenllado, F., and Bol, J. F. 2000. Genetic dissection of the multiple functions of alfalfa mosaic virus coat protein in viral RNA replication, encapsidation, and movement. Virology. 268:29–40. https://doi.org/10.1006/viro.1999.0170

Tolia NH, Joshua-Tor L. 2007. Slicer and the argonautes. Nat Chem Biol. 3(1):36-43. https://doi.org/10.1038/nchembio848.

Tóbiás, I. 1995. Characterization of different cherry leaf roll nepovirus (CLRV) isolates. Hortic. Sci. Kertészerti Tudomány 27**:**69-73.

Turpen, T. H., Turpen, A. M., Weinzettl, N., Kumagai, M. H., and Dawson, W. O. 1993. Transfection of whole plants from wounds inoculated with Agrobacterium

tumefaciens containing cDNA of tobacco mosaic virus. Journal of virological methods. 42:227–239. https://doi.org/10.1016/0166-0934(93)90035-p

Uyemoto, J. K., Taschenberg, E. F., and Hummer, D. K. 1977. Isolation and identification of a strain of grapevine Bulgarian latent virus in Concord grapevine in New York state. Plant Disease Reporter. 61:949–953.

Valasevich, N., Kukharchyk, N. & Kvarnheden, A. 2011. Molecular characterisation of *Raspberry bushy dwarf virus* isolates from Sweden and Belarus. *Arch Virol.* 156**,** 369–374. https://doi.org/10.1007/s00705-010-0912-9

Vance, V. 1991. Replication of potato virus X RNA is altered in coinfections with potato virus Y. Virology. 182:486–494. https://doi.org/10.1016/0042-6822(91)90589-4

Vigne, E., Gottula, J. W., Schmitt-Keichinger, C., Komar, V., Ackerer, L., Belval, L., et al. 2013. A strain-specific segment of the RNA-dependent RNA polymerase of grapevine fanleaf virus determines symptoms in *Nicotiana* species. Journal of General Virology. 94:2803–2813. https://doi.org/10.1099/vir.0.057646-0

Viry, M., Serghini, M. A., Hans, F., Ritzenthaler, C., Pinck, M., and Pinck, L. 1993. Biologically active transcripts from cloned cDNA of genomic grapevine fanleaf nepovirus RNAs. Journal of General Virology. 74:169–174. https://doi.org/10.1099/0022-1317-74-2-169

Voncina D, Almeida RP, 2018. Screening of some Croatian autochthonous grapevine varieties reveals a multitude of viruses, including novel ones. Archives of Virology, (in Press) https://doi.org/10.1007/s00705-018-3850-6

Vuittenez, A. 1960. Mise en evidence chez les vignes atteintes de degenerescence infectieuse, d'un virus transmissible mecaniquement aux *Chenopodes*

(*Chenopodium amaranticolor* et *C. quinoa*). In C.R. Academy of Science, Paris, p. 783–785.

Weber, H., Haeckel, P., and Pfitzner, A. J. 1992. A cDNA clone of tomato mosaic virus is infectious in plants. Journal of Virology. 66:3909–3912. https://doi.org/10.1128/jvi.66.6.3909-3912.1992

Wetzel, T., Beck, A., Wegener, U., and Krczal, G. 2004. Complete nucleotide sequence of the RNA1 of a grapevine isolate of Arabis mosaic virus. Archives of Virology. 149:989–995. https://doi.org/10.1007/s00705-003-0277-4

Wilcox, W. F., Jiang, Z.-Y., and Gonsalves, D. 1998. Leafroll virus is common in cultivated American grapevines in Western New York. Plant Dis. 82:1062. https://doi.org/10.1094/PDIS.1998.82.9.1062C

Wilkinson, C. A., Jones, J. J., Reed, T. D., and Tolin, S. A. 2006. Seed transmission of tobacco mosaic virus in tobacco. In Paris: Cooperation Centre for Scientific Research Relative to Tobacco. *Abstract*.

Wingard, S.A. 1928. Hosts and symptoms of ring spot, a virus disease of plants. Journal of Agirculture Research. 37:127-153.

Woodham, R. C., and Krake, I. R. 1983a. Investigations on transmission of grapevine leafroll, yellow speckle and fleck diseases by dodder. Journal of Phytopathology. 106:193–198. https://doi.org/10.1111/j.1439-0434.1983.tb00043.x

Wylie, S. and Li, H. 2022. Historical and scientific evidence for the origin and cultural importance to Australia's first-nations peoples of the laboratory accession of *Nicotiana benthamiana*, a model for plant virology. Viruses. 14:771. https://doi.org/10.3390/v14040771

Yang, S.-J., Carter, S. A., Cole, A. B., Cheng, N.-H., and Nelson, R. S. 2004. A natural variant of a host RNA-dependent RNA polymerase is associated with increased susceptibility to viruses by *Nicotiana benthamiana*. PNAS. 101:6297–6302. https://doi.org/10.1073/pnas.0304346101

Yepes, L. M., Cieniewicz, E., Krenz, B., McLane, H., Thompson, J. R., Perry, K. L., et al. 2018. Causative role of grapevine red blotch virus in red blotch disease. Phytopathology. 108:902–909. https://doi.org/10.1094/PHYTO-12-17-0419-R

Yoshikawa, N., Iida, H., Goto, S., Magome, H., Takahashi, T., and Terai, Y. 1997. Grapevine berry inner necrosis, a new trichovirus: comparative studies with several known trichoviruses. Arch. Virol. 142:1351–1363. https://doi.org/10.1007/s007050050165

Zadjaii, A. D., Matrooshi, A. R., and Moghal, S. M. 2002. Occurrence, distribution and properties of alfalfa mosaic virus. Jour. Agri. & Mar. Scie. 7:47–51.

Zarzyńska-Nowak, A., Ferriol, I., Falk, B. W., Borodynko-Filas, N., and Hasiów-Jaroszewska, B. 2017. Construction of *Agrobacterium tumefaciens*-mediated tomato black ring virus infectious cDNA clones. Virus Research. 230:59–62. https://doi.org/10.1016/j.virusres.2017.01.014

Zhang, C.-W., Liu, Q., Zeng, Q., Huang, W.-T., Wang, Q., and Cheng, Y.-Q. 2020. p24G1 Encoded by Grapevine leafroll-associated virus 1 suppresses RNA silencing and elicits hypersensitive response-like necrosis in *Nicotiana* species. Viruses. 12:1111. https://doi.org/10.3390/v12101111

Zhang, Y. 2016. Characterization of grapevine vein clearing virus expression strategy and development of caulimovirus infectious clones. Thesis. Univ. of Miss. https://doi.org/10.32469/10355/59794

Zhao, F., Hwang, U. S., Lim, S., Yoo, R. H., Igori, D., Lee, S.-H., et al. 2015. Complete genome sequence and construction of infectious full-length cDNA clones of tobacco ringspot *Nepovirus*, a viral pathogen causing bud blight in soybean. Virus Genes. 51:163–166. https://doi.org/10.1007/s11262-015-1221-x

Zhao, Y., Yang, X., Zhou, G., Zhang, T. 2020. Engineering plant virus resistance: from RNA silencing to genome editing strategies. Plant Biotechnology Journal. 18:328-336.

Zherdev, A., Vinogradova, S., Byzova, N., Porotikova, E., Kamionskaya, A., and Dzantiev, B. 2018. Methods for the diagnosis of grapevine viral infections: A review. Agriculture. 8:195. https://doi.org/10.3390/agriculture8120195

Table 2-S1. Ability of grapevine viruses to infect herbaceous hosts. All 95 viruses infecting grapevines are distinguished upon the taxonomical classification of their family. The ability of each virus to infect or not a herbaceous host was distinguished. The number of instances for which no herbaceous hosts were tested is also shown. References for each instance are found within Table 2-2 (Adapted and updated from Fuchs 2020) [Further adapted from Roy and Fuchs 2022 for formatting].

Table 2-S1. Ability of grapevine viruses to infect herbaceous hosts.

Family	Genus	Species	Genome	Vector	Disease	Herbaceous host status
Alphaflexiviridae	*Potexvirus*	Potato virus X (PVX)	(+)ssRNA	None	Unknown	Yes
Betaflexiviridae	*Fivirus*	Grapevine Kizil Sapak virus (GKSV)	(+)ssRNA	Unknown	Unknown	Unknown
	Foveavirus	Grapevine rupestris stem pitting-associated virus (GRSPaV)	(+)ssRNA	Unknown	Rugose wood	Yes
		Grapevine fovevirus A (GFVA)	(+)ssRNA	Unknown		Unknown
		Grapevine virus T (GVT)	(+)ssRNA	Unknown		No
	Trichovirus	Grapevine berry inner necrosis virus (GINV)	(+)ssRNA	Eriophyid mite	Berry inner necrosis	Yes
		Grapevine Pinot gris virus (GPGV)	(+)ssRNA	Eriophyid mite	Leaf mottling/ deformation	Yes
	Vitivirus	Grapevine virus A (GVA)	(+)ssRNA	Mealybug	Rugose wood	Yes
		Grapevine virus B (GVB)	(+)ssRNA	Mealybug		Yes
		Grapevine virus D (GVD)	(+)ssRNA	Unknown		Yes
		Grapevine virus E (GVE)	(+)ssRNA	Mealybug		No
		Grapevine virus F (GVF)	(+)ssRNA	Unknown		Unknown
		Grapevine virus G (GVG)	(+)ssRNA	Unknown		Unknown
		Grapevine virus H (GVH)	(+)ssRNA	Mealybug		No
		Grapevine virus I (GVI)	(+)ssRNA	Unknown		Unknown
		Grapevine virus J (GVJ)	(+)ssRNA	Unknown		Unknown
		Grapevine virus K (GVK)	(+)ssRNA	Unknown		Unknown
		Grapevine virus L (GVL)	(+)ssRNA	Unknown		Unknown
		Grapevine virus M (GVM)	(+)ssRNA	Unknown		Unknown
		Grapevine virus N (GVN)	(+)ssRNA	Unknown		Unknown
		Grapevine virus O (GVO)	(+)ssRNA	Unknown		Unknown

Table 2-S1. Ability of grapevine viruses to infect herbaceous hosts. (Continued)

Family	Genus	Species	Genome	Vector	Disease	Herbaceous host status
Bromoviridae	*Alfamovirus*	Alfalfa mosaic virus (AMV)	(+)ssRNA	Aphid	Yellow mosaic	Yes
	Anulavirus	Related to Amazon lily mild mottle virus (ALiMMV)	(+)ssRNA	None	Unknown	Yes
	Cucumovirus	Cucumber mosaic virus (CMV)	(+)ssRNA	Aphid	Unknown	Yes
	Ilarvirus	Grapevine angular mosaic virus (GaMoV)	(+)ssRNA	None	Angular mosaic	Yes
		Grapevine-associated ilarvirus 1 (GaIV-1)	(+)ssRNA	Unknown		Unknown
		Grapevine line pattern virus (GLPV)	(+)ssRNA	Unknown	Line pattern	Yes
		Grapevine virus S (GVS)	(+)ssRNA	Unknown	Unknown	Unknown
	Unassigned	Grapevine-associated cogu-like virus (GaCLV1)	(+)ssRNA	Unknown		No
Bunyaviridae	*Tospovirus*	Tomato spotted wilt virus (TSWV)	(-)ssRNA	Thrip		Yes
Caulimoviridae	*Badnavirus*	Grapevine vein clearing virus (GVCV)	dsDNA	Aphid	Vein clearing	Yes
		Grapevine badnavirus 1 (GBV1)	dsDNA	Unknown	Unknown	Unknown
		Grapevine Roditis leaf discoloration-associated virus (GRLDaV)	dsDNA	Unknown	Roditis discoloration	Yes
		Grapevine-assocated caulimovirus	dsDNA	Unknown		Unknown
Closteroviridae	*Closterovirus*	Grapevine leafroll-associated virus 2 (GLRaV2)	(+)ssRNA	Unknown	Leafroll/ Incompatibility	Yes
	Ampelovirus	Grapevine leafroll-associated virus 1 (GLRaV1)	(+)ssRNA	Mealybug	Leafroll	Yes
		Grapevine leafroll-associated virus 3 (GLRaV3)	(+)ssRNA	Mealybug		Yes
		Grapevine leafroll-associated virus 4 (GLRaV4)	(+)ssRNA	Mealybug		Unknown
		Plum bark necrosis stem pitting-associated virus	(+)ssRNA	Mealybug		Unknown
		Grapevine leafroll-associated virus 13 (GLRaV13)	(+)ssRNA	Unknown	Leafroll	Unknown

Table 2-S1. Ability of grapevine viruses to infect herbaceous hosts. (Continued)

Family	Genus	Species	Genome	Vector	Disease	Herbaceous host status
Closteroviridae	*Velarivirus*	Grapevine leafroll-associated virus 7 (GLRaV7)	(+)ssRNA	Unknown	Unknown	Yes
Endornaviridae	*Emaravirus*	Vitis emaravirus (VEV)		Unknown	–	No
Geminiviridae	*Begomovirus*	Grapevine begomovirus A (GBVA)	ssDNA	Whitefly	Unknown	Unknown
	Grablovirus	Grapevine red blotch virus (GRBV)	ssDNA	Treehopper	Red blotch	Yes
		Wild Vitis latent virus 1 (WVV1)	ssDNA	Unknown	Unknown	Unknown
	Unassigned	Grapevine geminivirus A (GGVA)	ssDNA	Unknown	Unknown	Yes
		Temperate fruit-decay-associated virus (TFDaV)	ssDNA	Unknown	–	No
Luteoviridae	*Enamovirus*	Grapevine enamovirus 1 (GEV1)	(+)ssRNA	Aphid	Unknown	Unknown
	Polerovirus	Grapevine polerovirus 1 (GPaV-1)	(+)ssRNA	Unknown	–	Unknown
Nanoviridae	Unassigned	Grapevine-associated nano-like virus		Unknown	–	Unknown
Partitiviridae	*Deltapartitivirus*	Vitis cryptis virus (VCV)		Unknown	–	No
Phenuiviridae	*Rubodvirus*	Grapevine Garan dmak virus (GGDV)	(−)ssRNA	Unknown	Unknown	Unknown
		Grapevine Muscat rose virus (GMRV)	(−)ssRNA	Unknown	Unknown	Unknown
Potyviridae	*Potyvirus*	Bean common mosaic virus (BCMV)	(+)ssRNA	Aphid	Unknown	Yes
		Potato virus Y (PVY)	(+)ssRNA	Aphid		Yes
	Unassigned	Grapevine-associated poty-like virus 1	(+)ssRNA	Unknown		No
Reoviridae	*Unassigned*	Grapevine Cabernet Sauvignon reovirus (GCSV)	dsRNA	Plant/Leafhopper	Unknown	No
Rhabdoviridae	*Varicosavirus*	Vitis varicosavirus (VVV)	(-)ssRNA	Unknown		No
Secoviridae	*Cheravirus*	Apple latent spherical virus (ALSV)e	(+)ssRNA	Unknown	Unknown	Yes
	Fabavirus	Broad bean wilt virus (BBMV)	(+)ssRNA	Aphid	Unknown	Yes
		Grapevine fabavirus (GFabV)	(+)ssRNA	Unknown		Unknown

Table 2-S1. Ability of grapevine viruses to infect herbaceous hosts. (Continued)

Family	Genus	Species	Genome	Vector	Disease	Herbaceous host status
Secoviridae	*Nepovirus*	Artichoke Italian latent virus (AILV)	(+)ssRNA	Unknown	Degeneration	Yes
		Arabis mosaic virus (ArMV)	(+)ssRNA	Dagger nematode		Yes
		Blueberry leaf mottle virus (BBLMV)	(+)ssRNA	Unknown		Yes
		Cherry leafroll virus (CLRV)	(+)ssRNA	Unknown		Yes
		Grapevine Anatolian ringspot virus (GARSV)	(+)ssRNA	Unknown		Yes
		Grapevine Bulgarian latent virus (GBLV)	(+)ssRNA	Unknown		Yes
		Grapevine chrome mosaic virus (GCMV)	(+)ssRNA	Unknown		Yes
		Grapevine fanleaf virus (GFLV)	(+)ssRNA	Dagger nematode		Yes
		Grapevine nepovirus A	(+)ssRNA	Unknown		Yes
		Grapevine Tunisian ringspot virus (GTRV)	(+)ssRNA	Unknown		Yes
		Peach rosette mosaic virus (PRSM)	(+)ssRNA	Dagger nematode		Yes
		Raspberry ringspot virus (RpRSV)	(+)ssRNA	Dagger nematode		Yes
		Tobacco ringspot virus (TRSV)	(+)ssRNA	Dagger nematode		Yes
		Tomato ringspot virus (ToRSV)	(+)ssRNA	Dagger nematode		Yes
		Tomato black ring virus (TBRV)	(+)ssRNA	Dagger nematode		Yes
	Unassigned	Strawberry latent ringspot virus (SLRSV)	(+)ssRNA	Dagger nematode		Yes
Tombusviridae	*Carmovirus*	Carnation mottle virus (CarMV)	(+)ssRNA	None	Unknown	Yes
	Necrovirus	Tobacco necrosis virus D (TNV-D)	(+)ssRNA	None	Unknown	Yes
	Tombusvirus	Grapevine Algerian latent virus (GALV)	(+)ssRNA	None	Unknown	Yes
		Petunia asteroid mosaic virus (PAMV)	(+)ssRNA	None		Yes
Tymoviridae	*Marafivirus*	Blackberry virus S (BlVS)	(+)ssRNA	Leafhopper	Unknown	No

Table 2-S1. Ability of grapevine viruses to infect herbaceous hosts. (Continued)

Family	Genus	Species	Genome	Vector	Disease	Herbaceous host status
Tymoviridae	*Maculavirus*	Grapevine asteroid mosaic-associated virus (GAMaV)	(+)ssRNA	Unknown	Asteroid mosaic	No
		Grapevine Syrah virus 1 (GSyV1)	(+)ssRNA	Unknown	Unknown	Unknown
		Grapevine fleck virus (GFkV)	(+)ssRNA	Unknown	Fleck	Yes
		Grapevine redglobe virus (GRGV)	(+)ssRNA	Unknown	Unknown	Unknown
Virgaviridae	*Tobamovirus*	Grapevine virga-like virus (GVLV)	(+)ssRNA	None	Unknown	Unknown
		Tobacco mosaic virus (TMV)	(+)ssRNA	None		Yes
		Tomato mosaic virus (ToMV)	(+)ssRNA	None		Yes
Unassigned	*Idaeovirus*	Raspberry bushy dwarf virus (RBDV)	(+)ssRNA	None	Yellow line pattern	Yes
	Sobemovirus	Sowbane mosaic virus (SoMV)	(+)ssRNA	None	Unknown	Yes
	Virtovirus	Grapevine virus satellite (GV-Sat)	(+)ssRNA	Beetle	Unknown	Unknown
	Unassigned	Grapevine Ajinashika virus (GAgV)	(+)ssRNA	Unknown	Unknown	No
		Grapevine labile rod-shaped virus (GLRSV)	Unknown	Unknown	Unknown	No
		Grapevine stunt virus (GSV)	Unknown	Leafhopper	Unknown	Unknown

Table 2-S2. Summary of herbaceous host status across virus family for grapevine infecting viruses.

Viral family	Total family members	Herbaceous hosts	Not tested	No herbaceous hosts found
Alphaflexiviridae	1	1	0	0
Betaflexiviridae	20	6	11	3
Bromoviridae	8	5	2	1
Bunyaviridae	1	1	0	0
Caulimoviridae	4	2	2	0
Closteroviridae	7	4	3	0
Endornaviridae	1	0	0	1
Geminiviridae	5	2	2	1
Luteoviridae	2	0	2	0
Nanoviridae	1	0	1	0
Partitiviridae	1	0	0	1
Phenuiviridae	2	0	2	0
Potyviridae	3	2	0	1
Reoviridae	1	0	0	1
Rhabdoviridae	1	0	0	1
Secoviridae	19	18	1	0
Tombusviridae	4	4	0	0
Tymoviridae	5	1	2	2
Virgaviridae	3	2	1	0
Unassigned	6	2	2	2
Cumulative:	**95**	**50**	**31**	**14**
	Total family members	**Herbaceous hosts**	**Not tested**	**No herbaceous hosts found**

Table 2-S3. **Status of the 26 most commonly referred to herbaceous hosts for the study of 65/95 grapevine infecting viruses.** Data from the literature is referenced in Table 2 and is depicted here by boxes in white (no reports), black (confirmed host of virus), yellow (non-host), purple (pseudo-host), red (difficult to inoculate), or gray (mixed reports).

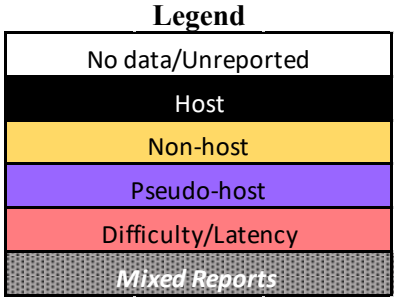

Table 2-S3. (Continued)

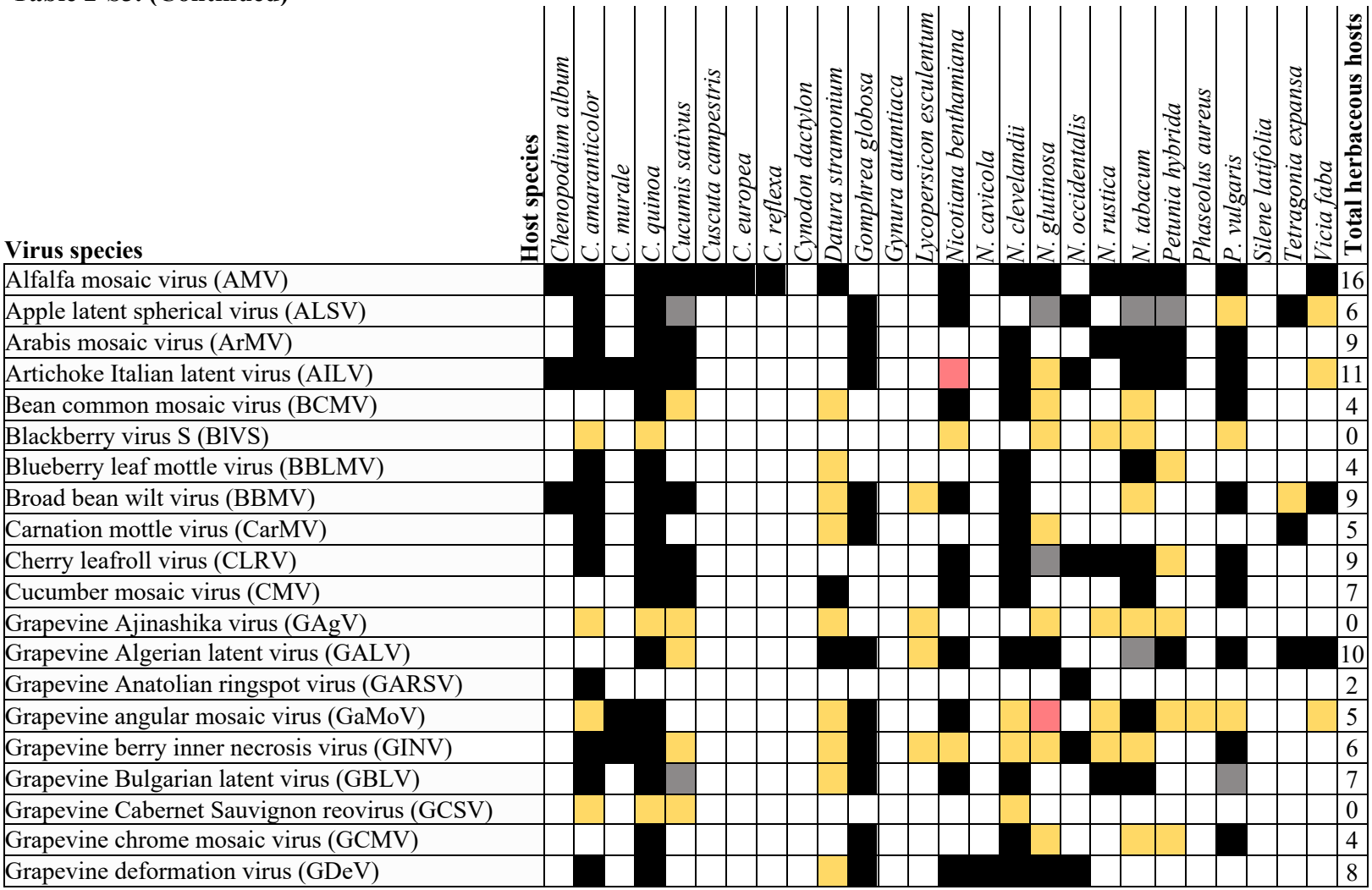

Virus species	Host species	*Chenopodium album*	*C. amaranticolor*	*C. murale*	*C. quinoa*	*Cucumis sativus*	*Cuscuta campestris*	*C. europea*	*C. reflexa*	*Cynodon dactylon*	*Datura stramonium*	*Gomphrea globosa*	*Gynura autantiaca*	*Lycopersicon esculentum*	*Nicotiana benthamiana*	*N. cavicola*	*N. clevelandii*	*N. glutinosa*	*N. occidentalis*	*N. rustica*	*N. tabacum*	*Petunia hybrida*	*Phaseolus aureus*	*P. vulgaris*	*Silene latifolia*	*Tetragonia expansa*	*Vicia faba*	**Total herbaceous hosts**
Alfalfa mosaic virus (AMV)																												16
Apple latent spherical virus (ALSV)																												6
Arabis mosaic virus (ArMV)																												9
Artichoke Italian latent virus (AILV)																												11
Bean common mosaic virus (BCMV)																												4
Blackberry virus S (BlVS)																												0
Blueberry leaf mottle virus (BBLMV)																												4
Broad bean wilt virus (BBMV)																												9
Carnation mottle virus (CarMV)																												5
Cherry leafroll virus (CLRV)																												9
Cucumber mosaic virus (CMV)																												7
Grapevine Ajinashika virus (GAgV)																												0
Grapevine Algerian latent virus (GALV)																												10
Grapevine Anatolian ringspot virus (GARSV)																												2
Grapevine angular mosaic virus (GaMoV)																												5
Grapevine berry inner necrosis virus (GINV)																												6
Grapevine Bulgarian latent virus (GBLV)																												7
Grapevine Cabernet Sauvignon reovirus (GCSV)																												0
Grapevine chrome mosaic virus (GCMV)																												4
Grapevine deformation virus (GDeV)																												8

Table 2-S3. (Continued)

Virus species	Host species	*C. album*	*C. amaranticolor*	*C. murale*	*C. quinoa*	*Cucumis sativus*	*Cuscuta campestris*	*C. europea*	*C. reflexa*	*Cynodon dactylon*	*D. stramonium*	*Gomphrea globosa*	*Gynura autantiaca*	*L. esculentum*	*N. benthamiana*	*N. cavicola*	*N. clevelandii*	*N. glutinosa*	*N. occidentalis*	*N. rustica*	*N. tabacum*	*Petunia hybrida*	*Phaseolus aureus*	*P. vulgaris*	*Silene latifolia*	*T. expansa*	*Vicia faba*	**Total identified**
Grapevine fanleaf virus (GFLV)																												13
Grapevine fleck virus (GFkV)																												1
Grapevine fovevirus A (GFVA)																												0
Grapevine geminivirus A (GGVA)																												1
Grapevine labile rod-shaped virus (GLRSV)																												0
Grapevine leafroll-associated virus 1 (GLRaV1)																												1
Grapevine leafroll-associated virus 2 (GLRaV2)																												0
Grapevine leafroll-associated virus 3 (GLRaV3)																												0
Grapevine leafroll-associated virus 7 (GLRaV7)																												5
Grapevine leafroll-associated virus 13 (GLRaV13)																												0
Grapevine line pattern virus (GLPV)																												3
Grapevine nepovirus A																												2
Grapevine Pinot gris virus (GPGV)																												3
Grapevine red blotch virus (GRBV)																												1
Grapevine Roditis leaf discoloration-associated virus (GRLDaV)																												5
Grapevine rupestris stem pitting-associated virus (GRSPaV)																												3
Grapevine Tunisian ringspot virus (GTRV)																												10
Grapevine vein clearing virus (GVCV)																												1
Grapevine virus A (GVA)																												4
Grapevine virus B (GVB)																												3
Grapevine virus D (GVD)																												3
Grapevine virus E (GVE)																												0

Table 2-S3. (Continued)

Virus species / Host species	*C. album*	*C. amaranticolor*	*C. murale*	*C. quinoa*	*Cucumis sativus*	*Cuscuta campestris*	*C. europea*	*C. reflexa*	*Cynodon dactylon*	*D. stramonium*	*Gomphrea globosa*	*Gynura autantiaca*	*L. esculentum*	*N. benthamiana*	*N. cavicola*	*N. clevelandii*	*N. glutinosa*	*N. occidentalis*	*N. rustica*	*N. tabacum*	*Petunia hybrida*	*Phaseolus aureus*	*P. vulgaris*	*Silene latifolia*	*T. expansa*	*Vicia faba*	**Total identified**
Grapevine virus H (GVH)																											0
Grapevine virus T (GVT)																											0
Grapevine-associated poty-like virus 1																											0
Grapevine-associated tymo-like virus (GaTLV)																											0
Peach rosette mosaic virus (PRSM)																											2
Petunia asteroid mosaic virus (PAMV)																											3
Potato virus X (PVX)																											3
Potato virus Y (PVY)																											5
Raspberry bushy dwarf virus (RBDV)																											10
Raspberry ringspot virus (RpRSV)																											6
Related to Amazon lily mild mottle virus (ALiMMV)																											1
Sowbane mosaic virus (SoMV)																											3
Strawberry latent ringspot virus (SLRSV)																											8
Tobacco mosaic virus (TMV)																											4
Tobacco necrosis virus D (TNV-D)																											7
Tobacco ringspot virus (TRSV)																											10
Tomato black ring virus (TBRV)																											6
Tomato mosaic virus (ToMV)																											9
Tomato ringspot virus (ToRSV)																											4
Tomato spotted wilt virus (TSWV)																											20
Vitis cryptic virus (VCV)																											0
Vitis emaravirus																											0
Vitis varicosavirus (VVV)																											0
Total Number of Grapevine Viruses Hosted	7	27	9	33	12	4	2	2	2	10	18	1	0	28	3	26	12	14	11	19	11	2	17	2	6	4	

CHAPTER 3

PREDICTIVE MODELING OF PROTEINS ENCODED BY A PLANT VIRUS SHED A NEW LIGHT ON THEIR STRUCTURE AND INHERENT MULTIFUNCTIONALITY[3]

ABSTRACT

Plant virus genomes encode proteins that are involved in replication, encapsidation, cell-to-cell, and long-distance movement, avoidance of host detection, counter-defense, and transmission from host to host, among other functions. Even though the multifunctionality of plant viral proteins is well documented, contemporary functional repertoires of individual proteins are incomplete. However, these can be enhanced by modeling tools. Here, predictive modeling of proteins encoded by the two genomic RNAs, i.e., RNA1 and RNA2, of grapevine fanleaf virus (GFLV) and their satellite RNAs by a suite of protein prediction software confirmed not only previously validated functions (suppressor of RNA silencing [VSR], viral genome-linked protein [VPg], protease [Pro], symptom determinant [Sd], homing protein [HP], movement protein [MP], coat protein [CP], and transmission determinant [Td]) and previously identified putative functions (helicase [Hel] and RNA-dependent RNA polymerase [Pol]), but also predicted novel functions with varying levels of confidence. These include a T3/T7-like RNA polymerase domain for protein $1A^{VSR}$, a short-chain reductase for protein $1B^{Hel/VSR}$, a parathyroid hormone family domain for protein $1E^{Pol/Sd}$, overlapping domains of unknown function and an ABC transporter domain for protein $2B^{MP}$, and DNA topoisomerase domains, transcription factor FBXO25 domain,

or DNA Pol subunit cdc27 domain for the satellite RNA protein. Structural predictions for proteins $2A^{HP/Sd}$, $2B^{MP}$, and $3A^{?}$ had low confidence, while predictions for proteins $1A^{VSR}$, $1B^{Hel*/VSR}$, $1C^{VPg}$, $1D^{Pro}$, $1E^{Pol*/Sd}$, and $2C^{CP/Td}$ retained higher confidence in at least one prediction. This research provided new insights into the structure and functions of GFLV proteins and their satellite protein. Future work is needed to validate these findings.

---

[3]This chapter has been published: Roy, B. G., Choi, J., and Fuchs, M. F. 2024. Predictive modeling of proteins encoded by a plant virus sheds a new light on their structure and inherent multifunctionality. Biomolecules. 14:62.

INTRODUCTION

Predictive modeling is increasingly relevant in virus-host interaction research with regard to functional predictions of virus proteins and their interactions with host proteins (Ghosh et al. 2022; Gutnik et al. 2023; Liu et al. 2023; Zhou et al. 2018). The information gained from prediction models can be used to better understand the nature of virus-virus, virus-host, and host-host protein interactions during viral infection. For example, powerful computational methods can predict protein structure and protein functions from viral amino acid sequences (Ghosh et al. 2022; Gutnik et al. 2023; Liu et al. 2023). In cases where the structure of a similar protein to a candidate viral protein is experimentally determined, algorithms based on modeling can provide accurate predictions of the protein structure. When no sequences of similar proteins to the candidate viral protein are available, AlphaFold, a deep learning system, is widely utilized to predict the three-dimensional protein structure by "free modeling" (Gutnik et al. 2023).

Grapevine fanleaf virus (GFLV) causes fanleaf degeneration, one of the most devastating viral diseases of grapevine (*Vitis* spp.) in most vineyards worldwide (Andret-Link et al. 2004; Digiaro et al. 2017; Martelli 2019). This disease was first described in the late 1800′s (Cazalis-Allut et al. 1865), but it was not until the early 1960′s that GFLV was identified as a causative agent (Cadman et al. 1960). GFLV is transmitted by the ectoparasitic dagger nematode, *Xiphinema index*, in a semi-persistent manner (Hewitt et al. 1958; Taylor and Brown 1997). Infections of GFLV can reduce crop yield by up to 80% and elicit a progressive decline of vines that limits the productive lifespan of a vineyard (Andret-Link et al. 2004).

GFLV is a member of the species *Nepovirus foliumflabelli* of the family *Secoviridae* (Fuchs et al. 2022). The genome of GFLV is bipartite and consists of two positive-sense, single-stranded RNAs: RNA1 and RNA2 (Figure 3-1) (Fuchs et al. 2022; Stothard 2000). GFLV RNA1 can replicate solely in single plant cells, but both genomic RNAs are required for systemic plant host infection (Viry et al. 1993). The GFLV genome is encapsidated into icosahedral particles with a pseudo $T = 3$ symmetry and a diameter of approximately 28 nm (Fuchs et al. 2017; Schmitt-Keichinger et al. 2017). The 5′ end of the genomic RNAs is attached to a viral genome-linked protein (VPg, $1C^{VPg}$), and the 3′ end is polyadenylated and mono-uridylated (Joly et al. 2023; Schmitt-Keichinger et al. 2017). GFLV RNA1 (7342 nts) and RNA2 (3806 nts) encode polyprotein P1 (253 kDa) and polyprotein P2 (123 kDa), respectively (Andret-Link et al. 2004; Fuchs et al. 2017; Schmitt-Keichinger et al. 2017).

GFLV P1 and P2 are proteolytically cleaved by the RNA1-encoded 3C-like protease (Pro; $1D^{Pro}$) upon monocistronic translation (Gorbalenya and Snijder 1996). GFLV P1 is processed in *cis*, resulting in five individual, mature proteins: protein $1A^{VSR}$ (45 kDa), a viral silencing suppressor (VSR); protein $1B^{Hel*/VSR}$ (88 kDa), a putative helicase (Hel*) and a VSR; protein $1C^{VPg}$ (3 kDa), a VPg; protein $1D^{Pro}$ (25 kDa), a proteinase; and protein $1E^{Pol*/Sd}$ (92 kDa), a putative RNA-dependent RNA polymerase (RdRP*) and a symptom determinant in the model herbaceous host *Nicotiana benthamiana* (Figure 2-1) (Andret-Link et al. 2004; Choi et al. 2023; Morris-Krsinich et al. 1983; Osterbaan et al. 2019; Schmitt-Keichinger et al. 2017; Vigne et al. 2013). GFLV P2 is processed in *trans*, resulting in three mature proteins: protein $2A^{HP/Sd}$ (29 kDa), a homing protein (HP) that directs RNA2 to the virus replication sites (Gaire et

al. 1999) and elicits a hypersensitive reaction on *N. occidentalis* (Martin et al. 2018); protein $2B^{MP}$ (38 kDa), a movement protein (MP) that facilitates cell-to-cell movement of virions via plasmodesmata in a tubule-guided manner (Andret-Link et al. 2004; Belin et al. 1999; Ritzenthaler et al. 1995); and protein $2C^{CP/Td}$ (56 kDa), the structural coat protein (CP) that composes virions and determines nematode transmission specificity (Figure 2-1) (Andret-Link et al. 2004; Schellenberger et al. 2010; Schellenberger et al. 2011; Schmitt-Keichinger et al. 2017; Serghini et al. 1990). The crystal structure of protein $2C^{CP/Td}$ was determined at a 2.7 Å resolution (Andret-Link et al. 2004; Schellenberger et al. 2010; Schellenberger et al. 2011; Serghini et al. 1990). The function(s) of GFLV-encoded proteins were predicted based on conserved, canonical amino acid sequences or confirmed through biological validation assays.

Some GFLV isolates contain an extraneous RNA molecule referred to as a satellite (sat) RNA or RNA3 (Figure 2-1) (Čepin et al. 2016; Fuchs et al. 1989; Pinck et al. 1988). The size of the nongenomic GFLV satRNA varies from 1,104 to 1,140 nts and encodes a single nonstructural protein $3A^{?}$ (37 kDa), which is also referred to as protein P3 (Čepin et al. 2016; Fuchs et al. 1989; Pinck et al. 1988; Saldarelli et al. 1993). GFLV satRNA molecules belong to two phylogenetic clades based on their nucleotide or amino acid sequence variability (Čepin et al. 2016). GFLV satRNA replication and encapsidation depend on its helper virus. The GFLV satRNA does not affect virus accumulation or symptom expression either in the natural host, grapevine (Saldarelli et al. 1993), or in the experimental model herbaceous host, *Chenopodium quinoa* (Gottula et al. 2013). The function(s) of protein $3A^{?}$ has yet to be elucidated.

Despite substantial advances in GFLV biology, many aspects of GFLV-encoded protein structure and function, as well as their potential roles in molecular and cellular processes that govern virus-host interactions, have not been elucidated. We hypothesized that publicly available, open source bioinformatic tools and computational modeling software would not only confirm previous findings regarding GFLV protein function and structure but also provide new insights into viral protein domain function beyond a simple analysis of primary sequence composition. The combination of previously performed functional assays and localization studies, the availability of a protein $2C^{CP/Td}$ crystal structure, and the identification of many putative functions make this plant virus a great case study for leveraging functional protein predictive modeling. Here, we present our findings on the predictive modeling of GFLV proteins, analyze our data considering current understandings in the literature, and suggest future biological studies.

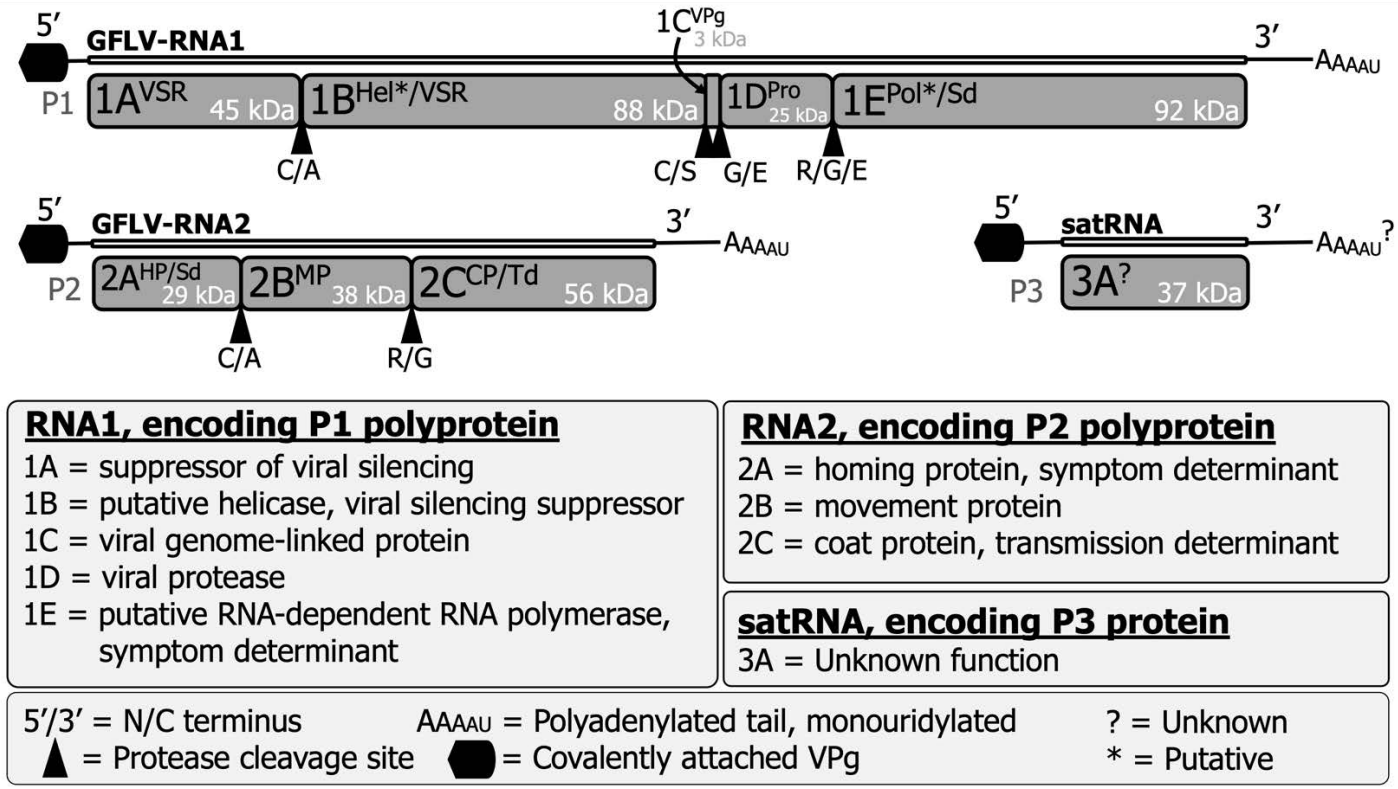

Figure 3-1. Structure and expression of the grapevine fanleaf virus genomic RNA1, RNA2, and satRNA. These molecules encode five, three, and one mature protein(s), respectively. Associated and biologically validated functions are shown in the legend, along with putative functions denoted by asterisks (*) and unknown functions or unknown sequences are denoted by question marks (?). Proteolytic cleavage sites are indicated by solid triangles. The molecular weight for each protein (kDa) was updated using current bioinformatic predictions via The Sequence Manipulation Suite (Stothard 1993).

MATERIALS AND METHODS

Grapevine fanleaf virus (GFLV) sequence retrieval and curation

GFLV strains F13 and GHu were selected for this study for their extensive biological characterization and genetic distance (Eichmeier et al. 2011; Fuchs et al. 1989; Pompe-Novak et al. 2007; Ritzenthaler et al. 1991; Serghini et al. 1990). Amino acid sequences of GFLV proteins encoded by RNA1, RNA2, and satRNA were retrieved from NCBI entries (Supplementary Table A3-1). Sequences of GFLV RNA1, RNA2, and satRNA were manually parsed for the nine encoding regions in Jalview [v.2.11.2.6] (Supplementary Tables 3-1 and 3-2) (Waterhouse et al 2009).

Disorder and Secondary Structure Prediction

Secondary structure prediction was determined intrinsically in 3D pipelines (Figure A2-2) or was produced by PyMOL v2.5.1 (Schrodinger, LLC, New York, NY, USA) upon visualization.

In Silico *Protein Modeling*

The amino acid sequences of GFLV proteins were subjected to several 3D protein modeling servers for in silico predictions. Most GFLV proteins are non-homologous to known structures apart from protein 2CCP/Td, for which the structure was determined at a 2.7 Å resolution (Andret-Link et al. 2004; Orlov et al. 2020; Schellenberger et al. 2010; Schellenberger et al. 2011; Serghini et al. 1990). Therefore, all varieties of protein structure prediction tools, ranging from ab initio to homology-guided software, were selected and utilized (Figure 3-2). First, GFLV protein amino acid sequences were submitted to AlphaFold2, specifically ColabFold v1.5.2, with

default parameters to construct simple 3D models (Jumper et al. 2021; Mirdita et al. 2022; Varadi et al. 2022). Then, GFLV protein amino acid sequences were submitted to the Deep-learning based Iterative Threading ASSEmbly Refinement (D-I-TASSER) server (Roy et al. 2010; Yang et al. 2015; Zhang 2008; Zheng et al. 2023) to reconstruct AlphaFold2 predictions and produce structure-based protein function annotations via BioLiP (Yang et al. 2013). Any single protein sequence that is too large for D-I-TASSER was alternatively analyzed by Extended I-TASSER for multidomain protein structure and function predictions (I-TASSER-MTD) (Zhou et al. 2019; Zhou et al. 2022). Any protein sequence that retained a TM-score of less than 0.50 by both algorithms was then subject to Contact-guided Iterative Threading ASSEmbly Refinement (C-I-TASSER), an expansion of I-TASSER that uses inter-residue contact maps and neural net prediction capabilities (Zheng et al. 2021). For further 3D motif detection, the highest-ranking pdb file generated for each protein was submitted to DALI for structural analysis (Holm 2020; Holm 2022). The highest TM-scoring prediction of the I-TASSER suite was used for the main functional prediction to retain consistency through COFACTOR (Roy et al. 2012; Zhang et al. 2017).

Sequences were also submitted to ESMFold (Lin et al. 2023), RGN2 (Chowdhury et al. 2022), and ProtGPT2 (Ferruz et al. 2022), which are designed as single-sequence or non-homologous protein prediction language models. *De novo* structure prediction was performed by trRosetta (Du et al. 2021; Yang et al. 2020). *Ab initio* structure prediction was performed with Contact-assisted QUARK (C-QUARK) (Mortuza et al. 2021). A combined *ab initio* and comparative folding pipeline called Robetta (https://robetta.bakerlab.org/, accessed 6 September 2023) (Baek et al. 2021;

Raman et al. 2009; Song et al. 2013) which combines ROSETTA use of protein folding with HHSEARCH (Gabler et al. 2020; Zimmermann et al. 2018), SPARKS-X (Yang et al. 2011), and RaptorX (Källberg et al. 2012) programs were utilized. Default parameters were used for sequences submitted to the Robetta server and recorded according to top model predictions for each protein submitted.

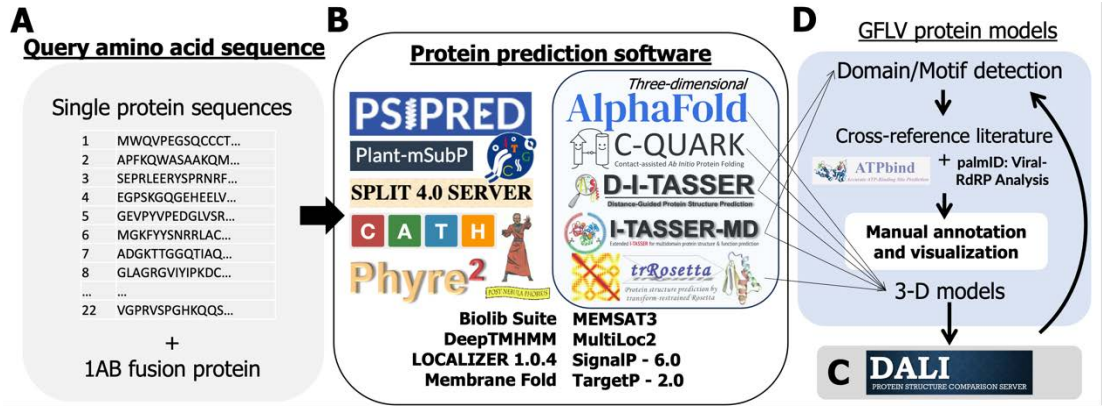

FIGURE 3-2. Description of a suite of openly available software used in a protein structure and function prediction pipeline to document the grapevine fanleaf virus (GFLV) protein structure and function. (**A**) A total of 22 GFLV sequences were submitted for analysis in a suite of protein motif and three-dimensional prediction software. (**B**) Some modeling software integrated both folding algorithms with follow-up functional analysis, (**C**) Other software performed one task, (**D**) and All programs were compared and curated to generate a consensus prediction of function(s). Programs are under CC BY 4.0 License with the ability to share with proper citation, as in the methods.

Domain, motif, and structural site predictive modeling

The GFLV protein sequences and 3D models were utilized in predictive modeling software to identify putative functions. As previously described, BioLiP is integrated into the D-I-TASSER pipeline to generate gene ontology (GO) predictions based on molecular function, biological process, and cellular compartment (Yang et al. 2015). Additional motif detection was performed against the five proteins encoded by GFLV RNA1 ($1A^{VSR}$, $1B^{Hel*/VSR}$, $1C^{VPg}$, $1D^{Pro}$, $1E^{Pol*/Sd}$) and three proteins encoded by GFLV RNA2 ($2A^{HP/Sd}$, $2B^{MP}$, and $2C^{CP/Td}$) using MOTIF Search (GenomeNet, Kyoto University Bioinformatics Center, Kyoto, Japan) against publicly available PROSITE, NCBI-CDD, and Pfam databases with E-value parameter relaxed to 5.0 (Marchler and Bryant 2004; Mistry et al. 2021; Sigrist et al. 2010; Wang et al. 2023). Five programs were used to predict the cellular localization of GFLV proteins. LOCALIZER (v1.0.4) prediction of subcellular localization was utilized on all protein sequences (Sperschneider et al. 2017). Plant mSubP (Sahu et al. 2020), MultiLoc2 (Blum et al. 2009), and TargetP (Armenteros et al. 2019) were used as additional algorithms to predict the subcellular localization of GFLV proteins. SignalP was used to detect signal peptide encoding regions on GFLV proteins (Almagro Armenteros et al. 2019). The ScanProsite tool (www.prosite.expasy.org/scanprosite/, accessed 21 June 2023) was used against all proteins with the following modifications to default settings: deselection of the exclusion of motifs with a high probability of occurrence from the scan and selection 'Run the scan at high sensitivity' (SIB—Swiss Institute of Bioinformatics) (De Castro et al. 2006). Certain prediction servers had additional limitations that were not

conducive to the prediction of larger proteins of GFLV and were, therefore, excluded from the analysis and methodology.

Analysis of GFLV protein sequences was also performed with the Protein Homology/Analogy Recognition Engine (Phyre2) V2.0 server (Kelley et al. 2015). The palmID: Viral-RdRP Analysis server (https://www.serratus.io/palmid, accessed 22 June 2023) was used for protein 1EPol*/Sd analysis (Edgar et al. 2022). Functional family annotation was performed using the Cath/Gene3D v4.3 server by submitting GFLV RNA1 and RNA2 amino acid sequences (Lewis et al. 2018; Sillitoe et al. 2021). Advanced curation of ATP binding and all nucleotide binding was determined through 3D and 2D methods using ATPbind (Hu et al. 2018) and NsitePred (Chen et al. 2012), respectively. The predicted nucleotide binding sites were determined based on the overlap between NsitePred and ATPbind results. Transmembrane domain and membrane helix predictions were analyzed using MembraneFold (Gutierrez et al. 2022), DeepTMHMM (Hallgren et al. 2022), Split 4.0 (Juretić et al. 2002), Phobius (Käll et al. 2004), MEMSAT3 with PSIPRED (Nugent and Jones 2009), and Phyre2 (Kelley et al. 2015). The predicted transmembrane domains/helices were determined based on the overlap from a minimum of two programs listed.

Statistical considerations, graphic generation, and visualization

All metrics provided by each software were extracted, as previously described (Mariani et al. 2013; Studer et al. 2020). PDB files were visualized in PyMOL v2.5.1 with manual annotation and color schemes. Further, the PyMOL native 'align' function was used to assess the predictions of $2C^{CP/Td}$, whose crystallography structure was previously reported (PDB:5FOJ) (Schellenberger et al. 2011). The output of RMSD was

extracted and compiled for future analyses of protein structure. Images of protein models and graphics were annotated in Microsoft® PowerPoint (©Microsoft 2023) and Adobe Illustrator® (Adobe Inc., San Jose, CA, USA). Consensus motifs, domains, and functional properties were calculated to scale per sequence in 2D and 3D space unless otherwise indicated. Any proteins without pLDDT metrics were submitted to QMEANDisCo to obtain a confidence metric (Studer et al. 2020; Zhang and Skolnick 2024).

RESULTS

Current documented features of GFLV proteins

Putative and experimentally validated functions and cellular localization are known for the eight proteins encoded by GFLV RNA1 and RNA2, and the satRNA (Table 3-1). Putative functions have been assigned to GFLV proteins $1B^{Hel*/VSR}$ and $1E^{Pol*/Sd}$ based on conserved amino acid sequence motifs or similarity, yet experimental confirmation is lacking.

Among the proteins of GFLV P1, proteins $1A^{VSR}$ and $1B^{Hel*/VSR}$ are experimentally confirmed as viral silencing suppressors (VSRs) with the ability to reverse systemic RNA silencing individually or as a fused form ($1A^{VSR}B^{Hel*/VSR}$), a predicted intermediary product of proteolytic processing (Choi et al. 2023). Protein $1C^{VPg}$ has been characterized via sequencing (Pinck et al. 1991), and protein $1D^{Pro}$ cleaves P1 in *cis* and P2 in *trans* through a triad proteolytic pocket (Margis et al. 1991; Margis and Pinck 1992; Margis et al. 1993; Margis et al. 1994). Protein $1E^{Pol*/Sd}$ is a symptom determinant in *N. benthamiana* with vein-clearing symptomology depending

on the identity of a single amino residue at amino acid (aa) position 802 (Laporte et al. 2003; Osterbaan et al. 2019; Osterbaan et al. 2021; Vigne et al. 2013). Protein $1B^{Hel*/VSR}$ localizes in the endoplasmic reticulum (Joly et al. 2023; Käll et al. 2004) and is predicted as a putative helicase based on helicase domain homology with picornaviruses (Eichmeier et al. 2011; Ritzenthaler et al. 1991), and protein $1E^{Pol*/Sd}$ is predicted as a putative RdRP based on conserved sequence homology of RdRP domains in other nepoviruses and picornaviruses (Eichmeier et al. 2011; Ritzenthaler et al. 1991; Viry et al. 1993). However, the helicase activity of protein $1B^{Hel*/VSR}$ and the polymerase function of protein $1E^{Pol*/Sd}$ are yet to be confirmed experimentally (Figure 3-1 and Table 3-1).

TABLE 3-1. List of putative and experimentally confirmed functions and cellular localizations of grapevine fanleaf virus (GFLV) encoded proteins and satRNA protein.

GFLV RNA	Protein[a]	Experimentally Validated Function[b]	Putative Function[c]	Confirmed Localization	Reference(s)
RNA1	1A^{VSR}	Viral silencing suppressor	-	-	(Choi et al. 2023)
	1B$^{Hel*/VSR}$	Viral silencing suppressor	Helicase	-	(Choi et al. 2023; Eichmeier et al. 2011; Schmitt-Keichinger et al. 2017; Viry et al. 1993)
	1C^{VPg}	Viral genome-linked protein	-	Endoplasmic reticulum	(Pinck et al. 1991; Ritzenthaler et al. 1991; Ritzenthaler et al. 2002; Viry et al. 1993)
	1D^{Pro}	Viral protease	-	-	(Margis et al. 1991; Margis and Pinck 1992; Margis et al. 1993; Margis et al. 1994; Morris- Krsinich et al. 1983)
	1E$^{Pol*/Sd}$	Symptom determinant	RNA-dependent RNA polymerase	-	(Eichmeier et al. 2011; Osterbaan et al. 2019; Osterbaan et al. 2021; Ritzenthaler et al. 1991; Roy et al. 2023; Vigne et al. 2013)
RNA2	2A$^{HP/Sd}$	Homing protein, Symptom determinant	-	-	(Gaire et al. 1999; Martin et al. 2018; Laporte et al. 2003)
	2B^{MP}	Movement protein	-	Perinuclear space	(Amari et al. 2010; Belin et al. 1999; Laporte et al. 2003; Ritzenthaler et al. 1995)
	2C$^{CP/Td}$	Coat protein, Transmission determinant	-	Plasmodesmata	(Andret-Link et al. 2004; Serghini et al. 1990; Margis et al. 1993; Quacquarelli et al. 1976; Schellenberger et al. 2010; Schellenberger et al. 2011)
RNA3	3A$^{?}$	-	-	-	(Čepin et al. 2016; Fuchs et al. 1989; Gottula et al. 2013; Pinck et al. 1988; Saldarelli et al. 1993)

[a]GFLV proteins with asterisks (*) represent putative functions.
[b]Function(s) of GFLV proteins experimentally confirmed.
[c]Putative functions of GFLV proteins predicted based on sequence homology.

Amongst the proteins of GFLV P2, protein $2A^{HP/Sd}$ is required for RNA2 replication and guides RNA2 to the replication site (Gaire et al. 1999; Laporte et al. 2003). Protein $2A^{HP/Sd}$ is found in aggregated forms in the juxtanuclear space, where it colocalizes with proteins $1C^{VPg}$ and $1D^{Pro}$ in protoplasts (Gaire et al. 1999). Protein $2A^{HP/Sd}$ is also a symptom determinant that triggers a hypersensitive reaction in *N. occidentalis* (Martin et al. 2018). Protein $2B^{MP}$ is responsible for tubule-mediated cell-to-cell movement of the virus through plasmodesmata (Amari et al. 2010; Belin et al. 1999; Laporte et al. 2003; Ritzenthaler et al. 1995). Protein $2B^{MP}$ interacts with plasmodesmata located proteins for tubule formation in a myosin-dependent manner (Amari et al. 2010; Laporte et al. 2003). Protein $2C^{CP/Td}$ is composed of three jelly- roll ß-barrel domains called A, B, and C and forms virions (Schellenberger et al. 2011; Serghini et al. 1990; Quacquarelli et al. 1976). Protein $2C^{CP/Td}$ determines the transmission specificity of GFLV by the ectoparasitic dagger nematode *X. index* (Andret-Link et al. 2004; Schellenberger et al. 2010; Schellenberger et al. 2011; Serghini et al. 1990) (Figure 3-1 and Table 3-1). It seems that the surface charge of the B domain pocket or ligand-binding pocket dictates nematode vector specificity (Schellenberger et al. 2010; Schellenberger et al. 2011).

The function of the satRNA-encoded protein P3 is unknown (Čepin et al. 2016; Fuchs et al. 1989; Gottula et al. 2013; Pinck et al. 1988; Saldarelli et al. 1993). No functional predictions have been made on P3 due to its low sequence homology with well-characterized proteins for which sequence information is available in databases (Figure 3-1 and Table 3-1).

Predictions of Functions and Structures for GFLV Proteins

Since studies on the functions of GFLV proteins were primarily centered on GFLV strains F13 or GHu, both viral strains were included in our study. Manually curated amino acid sequences for GFLV RNA1 and RNA2 proteins (strains F13 and GHu) and satRNA protein (strains F13, CO2, LR4/29, Py17, SACH44, and SWT6) were analyzed for motif detection and tertiary protein modeling (Table 3-S2 and File 3-S1), and the relative confidence of each modeling output was assessed (Figure 3-3 and Table 3-S3). These sequences were subject to analyses with the aforementioned 28 bioinformatic programs to probe their structural and functional characteristics (Table 3-2). The total predicted functions for GFLV strains F13 and GHu are summarized (Table 3-4,) while those with predictions with C-scores of ≥0.30 for GFLV strain F13 (Table 3-3) and GFLV strain GHu (Table 3-4) were compiled and tabulated.

Table 3-2. List of protein prediction algorithms utilized to investigate the grapevine fanleaf virus (GFLV) protein repertoire.

	Program	Algorithm	Modeling method	Output	Confidence metric	Confidence range	Reference(s)
1	AlphaFold2 (ColabFold)	Neural network	Template based	Tertiary protein model	eTM and pLDDT	0.00–1.00 and 0.00–100	(Jumper et al. 2021; Mirdita et al. 2022; Varadi et al. 2022)
2	C-Quark	Contact-assisted *ab initio*	Free modeling	Tertiary protein model	eTM	0.00–1.00	(Mortuza et al. 2021)
3	C-I-TASSER	Neural network	Free modeling	Tertiary protein model	pTM/TM-align	0.00–1.00	(Yang et al. 2013; Zheng et al. 2021; Zhou et al. 2019; Zhou et al. 2022)
4	D-I-TASSER	Neural network	Template based	Tertiary protein model	pTM/TM-align	0.00–1.00	(Roy et al. 2010; Yang et al. 2013; Yang et al. 2015; Zhang 2008; Zheng et al. 2023)
5	D-I-TASSER MTD	Neural network	Template based	Tertiary protein model	pTM/TM-align	0.00–1.00	(Yang et al. 2013; Zhou et al. 2019; Zhou et al. 2022)
6	ESMFold	Neural network	Single input sequence	Tertiary protein model	pTM/pLDDT	0.00–1.00 and 0.00–100	(Lin et al. 2023)
7	Robetta	Extension of RoseTTAFold and trRosetta	Free modeling	Tertiary protein model	GDT	0.00–1.00	(Baek et al. 2021; Raman et al. 2009; Song et al. 2013)
8	trRosetta	Neural network	Free modeling	Tertiary protein model	eTM/pLDDT	0.00–1.00 and 0.00–100	(Du et al. 2021; Yang et al. 2020)
9	BioLiP	Semi-manually curated database	Guided	Functional predictions	C-Score	0.00–1.00	(Yang et al. 2013)
10	RGN2	Neural network	Free modeling	Tertiary protein model	GDT	0.00–1.00	(Chowdhury et al. 2022)
11	ProtGPT2	Neural network	Free modeling	Tertiary protein model	pLDDT	0.00–100	(Ferruz et al. 2022)
12	QMEANDisCo	Distance based model quality estimation	NA	Confidence metric	QMEANDisCo	0.00–100	(Zhang and Skolnick 2004)
13	Phyre2	Multiple sequence alignment	Multiple sequence alignment	Secondary/tertiary protein model	Coverage and Identity	0.00–100	(Kelley et al. 2015)
14	palmID	Sequence conservation	NA	Confidence for RdRP	RdRP score	0.00–100	(Edgar et al. 2022)
15	MOTIF Search	Sequence conservation	Multiple sequence alignment	Primary sequence domain detection	E-value or *p*-value	Lower *p*-value is better	(Marchler-Bauer and Bryant 2004; Mistry et al. 2021; Sigrist et al. 2010; Wang et al. 2023)

Table 3-2. List of protein prediction algorithms utilized to investigate the GFLV protein repertoire (Continued).

	Program	Algorithm	Modeling method	Output	Confidence metric	Confidence range	Reference (s)
16	CATH/Gene3D	Semi-manually curated database	Multiple sequence alignment	Primary sequence domain detection	Extensive metrics	Multiple	(Lewis et al. 2018; Sillitoe et al. 2021)
17	LOCALIZER	Machine learning	Feature detection based on known sequences	Primary sequence domain detection	Ranking	Priority ranking	(Sperschneider et al. 2017)
18	Plant mSubP	Machine learning	Feature detection based on known sequences	Primary sequence domain detection	Percentage probability	Percentage	(Sahu et al. 2020)
19	MultiLoc2	Machine learning	Feature detection based on known sequences	Primary sequence domain detection	Percentage probability	Percentage	(Blum et al. 2009)
20	TargetP[a]	Neural network	Feature detection based on known sequences	Primary sequence domain detection	Ranking	Percentage	(Armenteros et al. 2019)
21	SignalP[a]	Neural network	Feature detection based on known sequences	Primary sequence domain detection	Ranking	Percentage	(Almagro Armenteros et al. 2019)
22	MembraneFold[a]	AlphaFold/OmegaFold based	Feature detection based on known sequences	Primary sequence domain detection	pLDDT for membrane proteins	0.00–100	(Chen et al. 2012)
23	DeepTMHMM[a]	Neural network	Feature detection based on known sequences	Primary sequence domain detection	Probability	0.00–1.00	(Hallgren et al. 2022)
24	Split 4.0	Consensus hidden Markov model	Feature detection based on known sequences	Primary sequence domain detection	Binary	Threshold	(Juretić et al. 2002)
25	Phobius	Hidden Markov model (HMM)	Feature detection based on known sequences	Primary sequence domain detection	Probability	Threshold	(Käll et al. 2004)
26	MEMESAT3 (PSIPRED)	HMM and model recognition	Feature detection based on known sequences	Primary sequence domain detection	Log likelihood ratio	Threshold	(Nugent and Jones 2009)
27	ATPbind	Machine learning	Feature detection based on structural configuration	Tertiary sequence domain detection	Identity of residues	Threshold	(Hu et al. 2018)
28	NsitePred	Machine learning	Feature detection based on known sequences	Primary sequence domain detection	Probability	0.00–1.00	(Chen et al. 2012)

[a]None or irrelevant predictions were obtained with these programs for GFLV proteins.

Results revealed that primary sequence alignment software outperformed tertiary protein model predictions in all instances (Figure 3-3). However, alignment coverage and known sequences may bias this result, which is further confounded by the disparity of known crystallized proteins available for comparison to the predictions. The differences in these types of programs suggested that we separate our analyses into two groupings when attempting to compare protein prediction software, one for motif and specific domain descriptions and the other for overall structural or functional characteristics (Supplementary File 3-S1). Output of tertiary protein structure amongst available programs can vary in their confidence metric and the intrinsic calculation; however, most are highly correlated (Olechnovič et al. 2019). Calculations of eTM/pTM/TM-scores or GDT scores are ranked from 0 to 1, with 1 being of highest confidence (Table 3-2). Global error scores such as pLDDT or QMEANDisCo are calculated per residue and then averaged on a scale of 0 to 100 or 0 to 1, respectively (Table 3-2). Most of these metrics consider root mean square deviation (RMSD) error at some stage or are derived directly as RMSD with minor adjustments for length bias or torsion angles. Examination and comparison were conducted with caution for each program against others, on a per protein basis, because not all algorithms provide the same output in the same metrics (Table 3-2).

In terms of 3-D protein prediction, software performance to confidently predict structure from the primary sequence was highly variable across proteins but was relatively similar across all software. Similar to the performance of

AlphaFold2, we found the C-I-TASSER, D-I-TASSER, and D-I-TASSER MTD to be the most beneficial and confident software based on TM-score and comprehensive analysis despite using each in a different instance, (Figure 3-3 and Table 3-S3). The highest TM-score for proteins solely submitted to the D-I-TASSER server was indeed achieved by the D-I-TASSER server, while the Robetta GDT was of similar confidence (Figure 3-3 and Table 3-S3). Per the protein 3A[?] sequences, C-I-TASSER performed just above D-I-TASSER with TM-align scores of 0.426 and 0.424, respectively (Table 3-S3). Pearson's correlation of all metrics generated from 3D models showed positive, significant associations between protein models (Figure 3-3D). Variability was observed with the best program on a protein-by-protein basis. Mainly, homology-guided protein prediction models were of similar confidence even if calculated in different ways. Incomplete predictions from D-I-TASSER MTD, mainly where predictions did not need to be performed, left 'NA' in the plot (Figure 3-3D). As with other studies (Holm 2022; Mariani et al. 2013; Studer et al. 2020; Zhang and Skolnick 2004), we found significant correlations of model metrics per algorithm. Interestingly, these metrics were not all statistically correlated across algorithms, leaving additional difficulty when discerning the true best model created by each algorithm.

Indeed, AlphaFold2 was able to produce models with minimized conflicting atomic structure (Figure 3-S3E) when compared to D-I-TASSER models. However, pTM/eTM scores indicate that D-I-TASSER was more suitable for protein prediction. It is increasingly obvious that, for ESMFold and

trRosetta, the homology-guided AlphaFold2 outperformed every protein of GFLV in terms of pLDDT and predicted TM-scores (Figure 3-S3F). Nonetheless, with this small subset of proteins, it is difficult to discern the 'best' prediction method, as positive RNA viruses retain little crystallized entries in the PDB. A unified metric that all programs must provide would be an excellent addition for efficient comparison- making.

Nevertheless, based on the predicted accuracy of each protein encoded by RNA1 ($1A^{VSR}$, $1B^{Hel*/VSR}$, $1C^{VPg}$, $1D^{Pro}$, and $1E^{Pol*/Sd}$) and two proteins of RNA2 ($2A^{HP/Sd}$ and $2B^{MP}$), the top model, using the derived TM-score, was deposited into ModelArchive (SIB, Swiss Institute of Bioinformatics, modelarchive.org, accessed on 12 November 2023) under the following identifiers: ma-nqabp, ma-gzevc, ma- 3h6c, ma-wg6ry, ma-pufyr, ma-gs2nn, and ma-yhs0u, respectively. We did not deposit any predictive models for protein $2C^{CP/Td}$ as they were redundant for the already crystallized structure of this protein (PDB 5FOJ) (Schellenberger et al. 2010; Schellenberger et al. 2011).

Results of predictive secondary and tertiary protein structure modeling are presented for each of the eight GFLV encoded proteins, i.e., five proteins in RNA1 and three proteins in RNA2, plus one satRNA protein, as well as the fusion protein $1A^{VSR}B^{Hel*/VSR}$, an intermediary product of polyprotein P1 processing (Figures 3-4 to 3-8, and File 3-S1). Image depictions of any generated tertiary structure were the most confident prediction based mostly on TM-score, the most widely accepted metric of protein folding by CASP unless otherwise indicated.

Figure 3-3. The performance and relative confidence for protein prediction software across the grapevine fanleaf virus (GFLV) proteins revealed trends behind protein-specific and software-specific challenges in producing confident models. (**A**) All protein predictions are shown per program as individual bar graphs separated for GFLV strain F13, GFLV strain GHu, and all $3A^{?}$ satRNA proteins. The Y-axis shows the confidence metric, while the X-axis shows individual GFLV proteins. (**B**) The average and standard error of protein structure predictions for each individual protein of the GFLV genome and satRNA. (**C**) Average confidence and standard error per software used in the generation of three-dimensional structure prediction for GFLV proteins. Numbers within bars indicate the number of times each software was able to produce the highest confidence prediction per protein. (**D**) Pearson's correlation matrix shows significant, positive agreement amongst most protein prediction algorithm confidence metrics (*p*-value; * = <0.05, ** = <0.01, *** = <0.001). Linear models of confidence metrics for multiple programs show minor differences on a protein-by-protein basis. (**E**) AlphaFold2 and D-I-TASSER report similar estimated TM-score and global QMEANDisCo scores for each protein prediction. (**F**) In contrast, AlphaFold2 outperforms ab initio programs ESMFold or trRosetta for nearly all GFLV proteins for both estimated TM-scores and pLDDT metrics.

(AlphaFold2 = pTM [yellow/brown]; C-I-TASSER = TM-aligned [lime green]; D-I-TASSER-MTD = TM-aligned [dark green]; D-I-TASSER = TM-aligned [light blue]; ESMFold = pTM [blue]; Robetta = predicted GDT [dark blue]; trRosetta = eTM [black]).

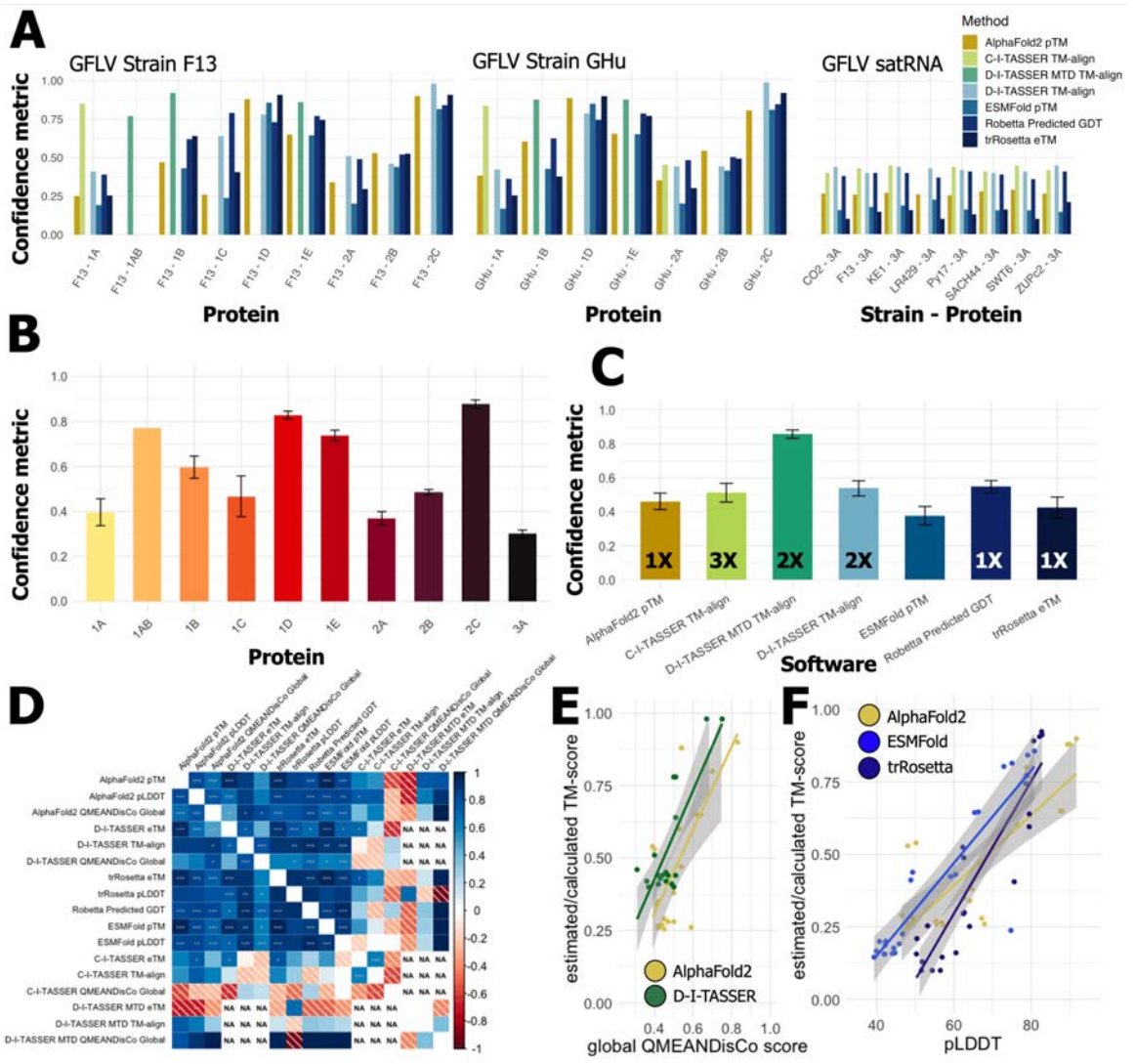
A
GFLV Strain F13
GFLV Strain GHu
GFLV satRNA
Method
AlphaFold2 pTM
C-I-TASSER TM-align
D-I-TASSER MTD TM-align
D-I-TASSER TM-align
ESMFold pTM
Robetta Predicted GDT
trRosetta eTM
Confidence metric
Protein
Protein
Strain - Protein
B
Confidence metric
Protein
C
Confidence metric
1X
3X
2X
2X
1X
1X
Software
D
E
estimated/calculated TM-score
global QMEANDisCo score
AlphaFold2
D-I-TASSER
F
AlphaFold2
ESMFold
trRosetta
estimated/calculated TM-score
pLDDT

Figure 3-4. Computational analysis and protein structure prediction of the five mature proteins encoded by grapevine fanleaf virus (GFLV) RNA1. Domain detection returned eight confident predictions of T3/T7-like RNA polymerase domain (protein $1A^{VSR}$, purple), S3 helicase domain (protein $1B^{\mathbf{Hel*/VSR}}$, orange), short-chain reductase domain (protein $1B^{\mathbf{Hel*/VSR}}$, green), protease domain (protein $1D^{Pro}$, blue), three RNA-dependent RNA polymerase profiles (protein $1E^{Pol*/Sd}$, red, light blue, and gold), and parathyroid hormone family domain (protein $1E^{Pol*/Sd}$, dark blue). The sequence alignment in AlphaFold2 varied from ~30 alignments to over 500 alignments with varying confidence levels based on similarity and coverage against GFLV encoding proteins. Similarly aligned and confidence protein sequences returned confident pLDDT upon tertiary protein model generation through five iterations in AlphaFold2. Several programs were utilized to provide the most confident structure which used D-I-TASSER, Robetta, and trRosetta with predictions ranging in TM-align scores from 0.79 to 0.91. Ribbon diagrams display the predicted motifs and domains in the same color as above, while gray areas are not defined.

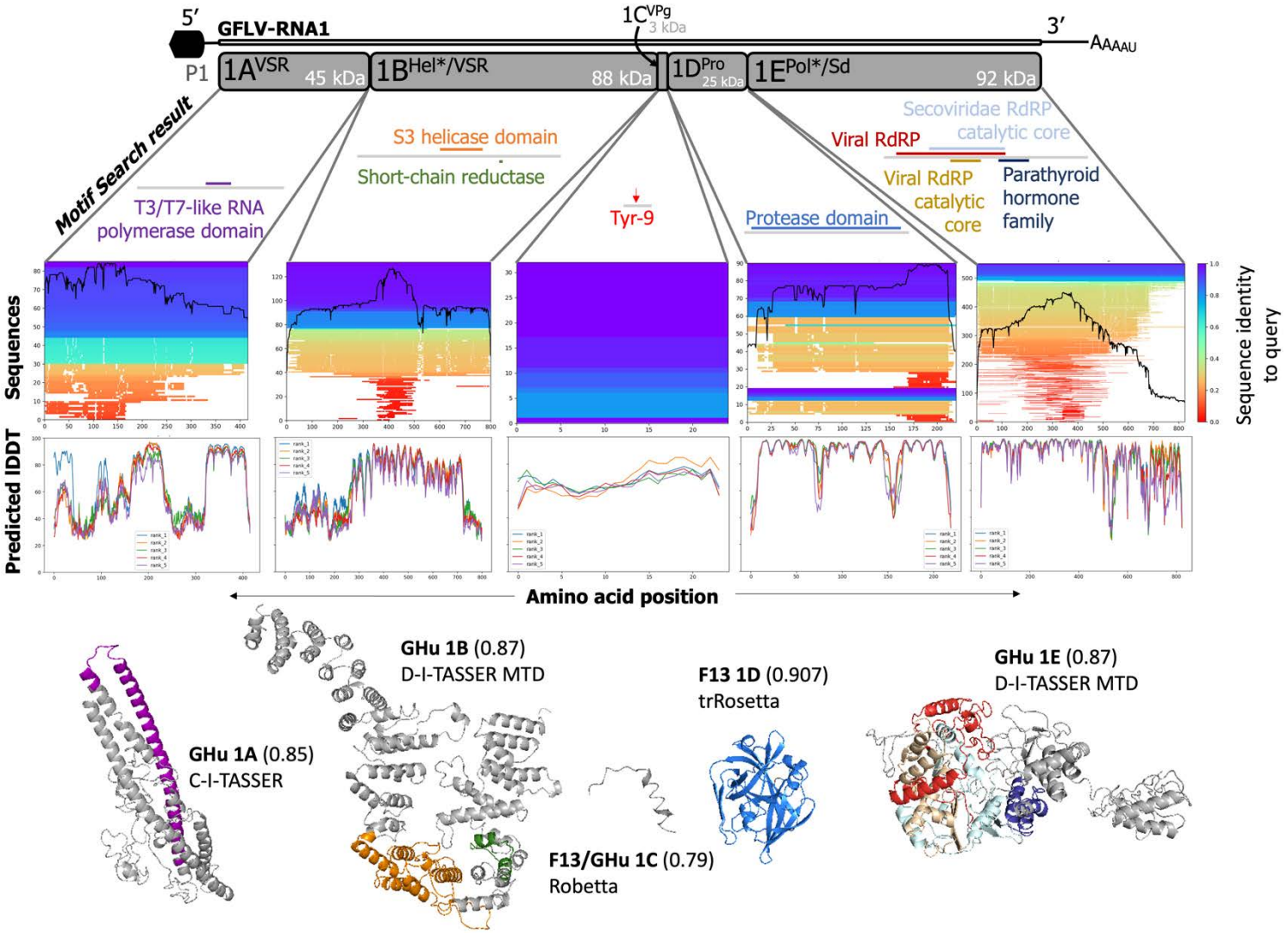
5′
GFLV-RNA1
1C^VPg 3 kDa
3′
AAAAU
P1
1A^VSR 45 kDa
1B^Hel*/VSR 88 kDa
1D^Pro 25 kDa
1E^Pol*/Sd 92 kDa
Motif Search result
T3/T7-like RNA polymerase domain
S3 helicase domain
Short-chain reductase
Tyr-9
Protease domain
Secoviridae RdRP catalytic core
Viral RdRP
Viral RdRP catalytic core
Parathyroid hormone family
Sequences
Predicted lDDT
Sequence identity to query
Amino acid position
GHu 1A (0.85)
C-I-TASSER
GHu 1B (0.87)
D-I-TASSER MTD
F13/GHu 1C (0.79)
Robetta
F13 1D (0.907)
trRosetta
GHu 1E (0.87)
D-I-TASSER MTD

Figure 3-5. Transmembrane domain predictions by Phyre2 of grapevine fanleaf virus proteins returned only two possible candidates, protein 1B$^{Hel*/VSR}$ and protein 1E$^{Pol*/Sd}$. (A) Protein 1B$^{Hel*/VSR}$ was predicted to contain up to five transmembrane domains (purple, transmembrane helices spanning from the extracellular space to the cytoplasm), while **(B)** Protein 1E$^{Pol*/Sd}$ was predicted to contain two transmembrane domains (green). The sequence of amino acids was then projected onto AlphaFold2 generated protein models for visualization. **(C)** The overlap with the sequence of transmembrane domains (purple helices S1-S5) and the predicted protein structure seems likely for protein 1B$^{Hel*/VSR}$ (helicase domain highlighted in orange, reductase in green), but **(D)** additional context is needed on the poorly understood virus replication complex, membrane association predictions (green helices, S1-S2) and behavior of protein 1E$^{Pol*/Sd}$ *in planta*.

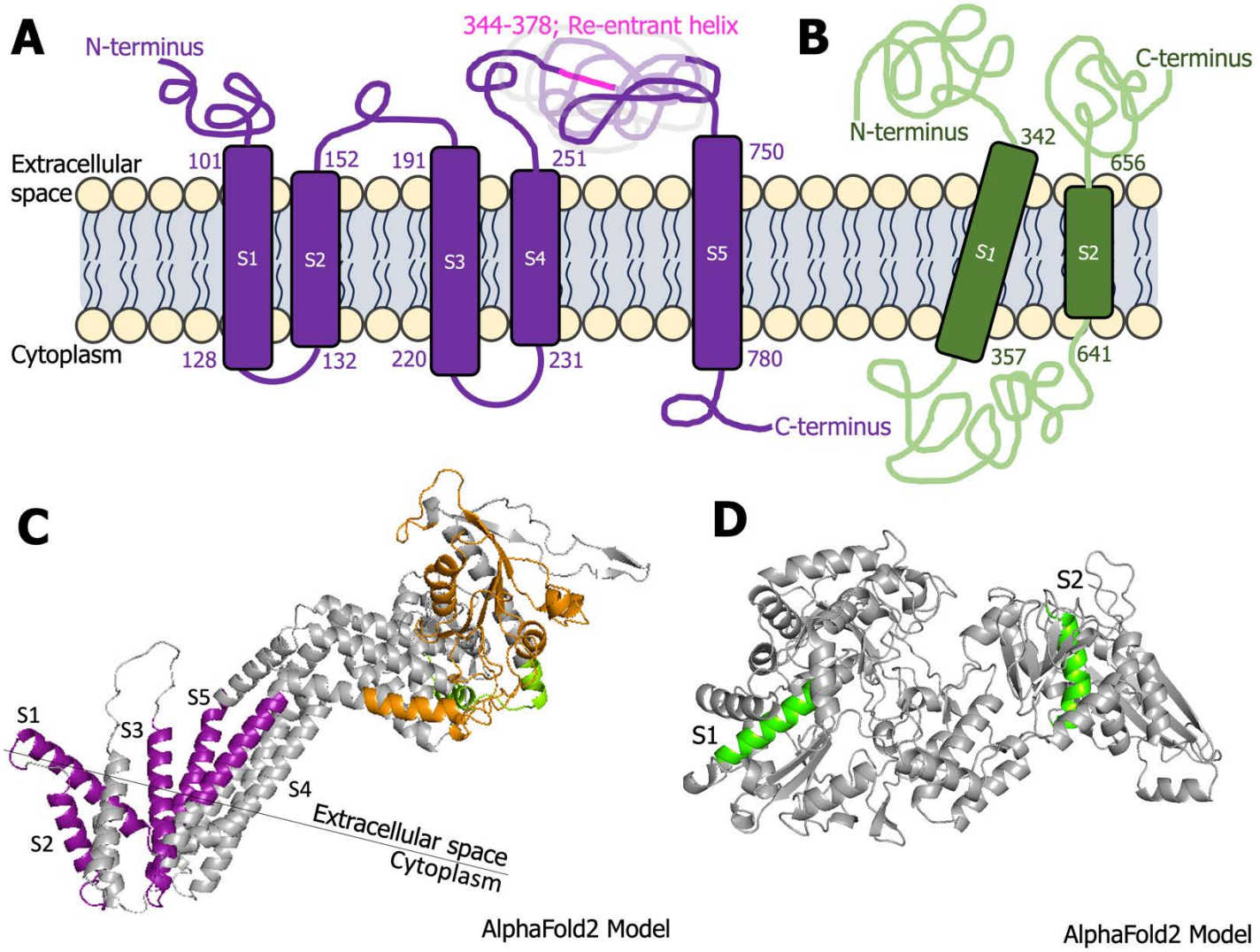
A
N-terminus
344-378; Re-entrant helix
Extracellular space
Cytoplasm
101
128
152
132
191
220
251
231
750
780
S1
S2
S3
S4
S5
C-terminus
B
N-terminus
C-terminus
342
357
656
641
S1
S2
C
S1
S2
S3
S4
S5
Extracellular space
Cytoplasm
AlphaFold2 Model
D
S1
S2
AlphaFold2 Model

Figure 3-6. Analyses of the top predictions for proteins of grapevine fanleaf virus (GFLV) to map the putative helicase ($1B^{Hel*/VSR}$), protease ($1D^{Pro}$), and putative RdRP active sites ($1E^{Pol*/Sd}$). **(A)** The AlphaFold2 model of protein $1B^{Hel*/VSR}$ shows a tertiary structure site for ATP/ADP binding which aligns with ATPbind and NSitePred predictions at residues 368-373 (in red) and 415-417 (in orange). **(B)** The His-Glu-Leu pocket of protein $1D^{Pro}$ of GFLV-F13 is highlighted in blue with a putative central proteolysis site indicated by a single yellow sphere (trRosetta model). **(C)** The prediction of protein $1E^{Pol*/Sd}$ of GFLV-GHu displays consistent structure with other picornaviruses to contain the RdRP palm, fingers, thumb (green), VPg binding site (orange), catalytic pocket, and nucleotide entry site. Residues past 496 of protein $1E^{Pol*/Sd}$ are colored white as they are not considered part of the polymerase core domain, but rather the C-terminal domain that contains in position 802, the symptom determinant in the herbaceous host *Nicotiana benthamiana*. This image was created with PyMol v2.5.1 (Schrodinger, LLC).

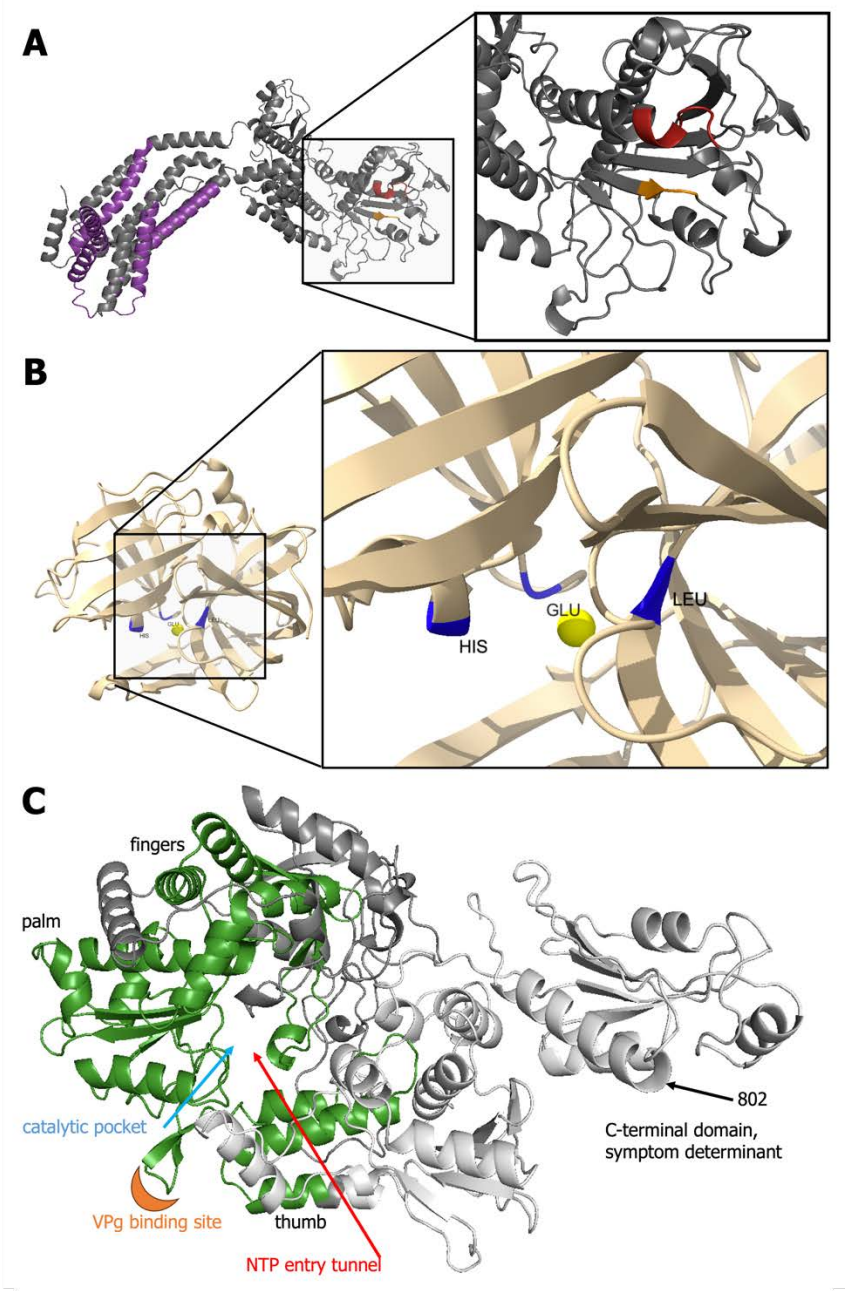
A
B
HIS
GLU
LEU
C
fingers
palm
catalytic pocket
VPg binding site
thumb
NTP entry tunnel
802
C-terminal domain,
symptom determinant

Figure 3-7. Predicted modeling of the structure and function(s) of proteins encoded by RNA2 of grapevine fanleaf virus (GFLV). The GFLV RNA2 proteins provided confident predictions against the already resolved coat protein structure but less confident and consistent predictions against proteins $2A^{HP/Sd}$ and protein $2B^{MP}$. For protein $2A^{HP/Sd}$, only one motif was detected as nepovirus A polyprotein (orange). This model returned higher for GFLV-F13 using D-I-TASSER with TM-align to result a TM-score of 0.51. Protein $2B^{MP}$ returned two consistent motifs of "Domain of unknown function" and "ABC transporter" in green and yellow, respectively. Sequence coverage and identity did not differ greatly from protein $2A^{HP/Sd}$, and therefore resulted in a similar low confidence model from AlphaFold2 with a pTM-score of 0.54. Protein $2C^{CP/Td}$ with a crystal structure maintains high sequence similarity to viral coat proteins of nepoviruses. The highest confidence model returned from D-I-TASSER with a TM-score of 0.98. The three coat protein domains A, B and C are displayed in blue, lavender, and navy on both models.

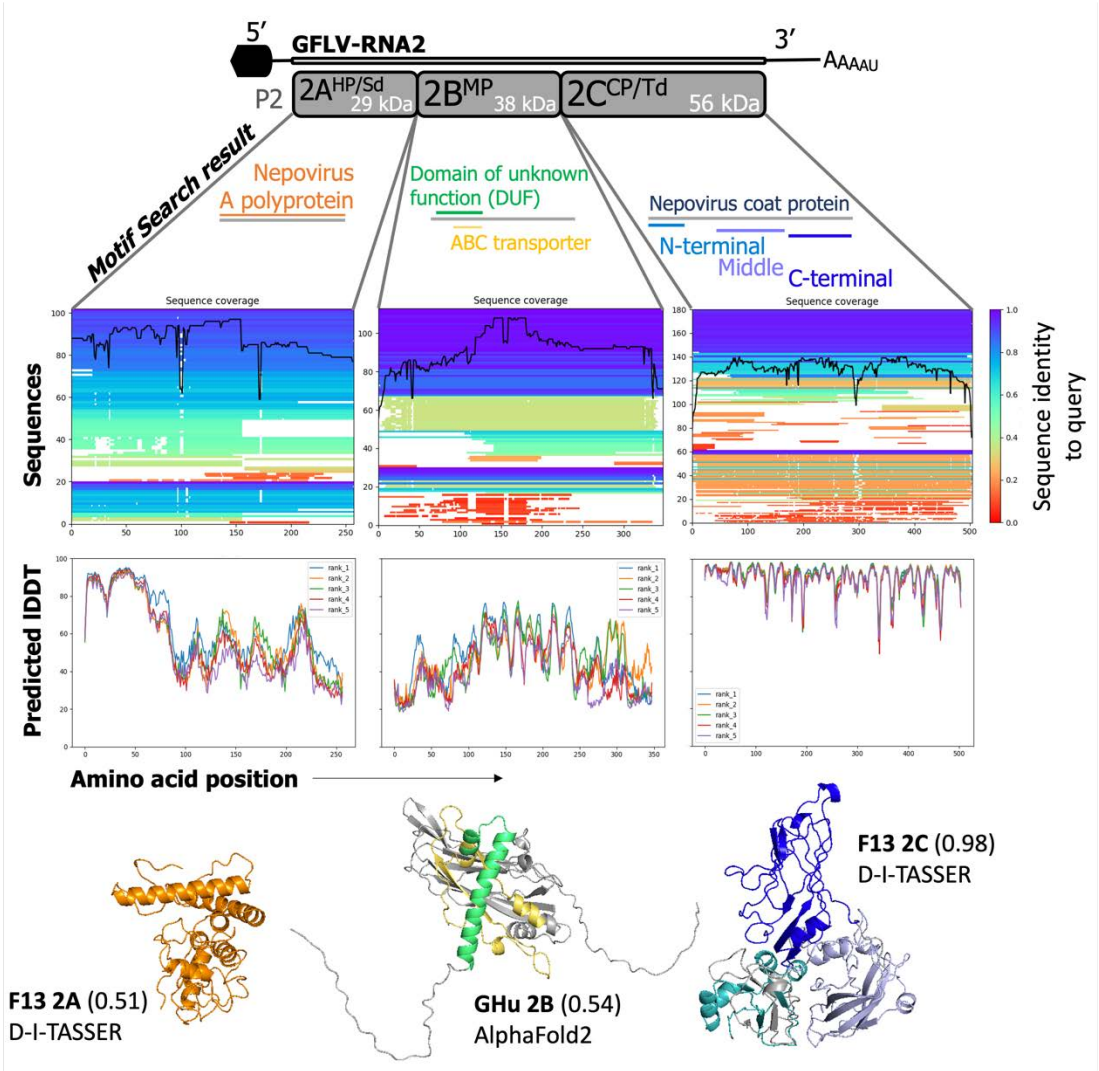
5′
GFLV-RNA2
3′
AAAAAU
P2
2A HP/Sd 29 kDa
2B MP 38 kDa
2C CP/Td 56 kDa
Motif Search result
Nepovirus A polyprotein
Domain of unknown function (DUF)
ABC transporter
Nepovirus coat protein
N-terminal
Middle
C-terminal
Sequence coverage
Sequences
Sequence identity to query
Predicted lDDT
Amino acid position
F13 2A (0.51)
D-I-TASSER
GHu 2B (0.54)
AlphaFold2
F13 2C (0.98)
D-I-TASSER

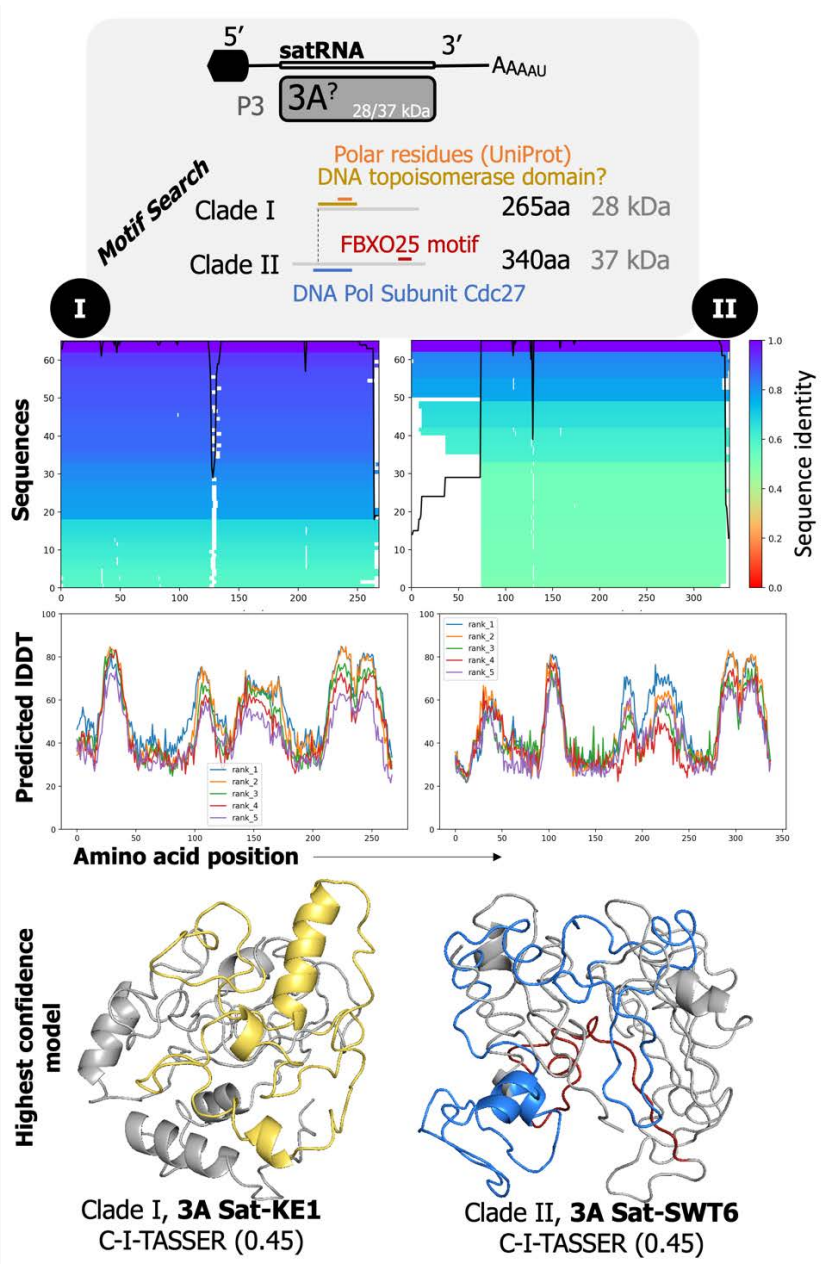

Figure 3-8. Predicted modeling of the structure and function(s) of the protein encoded by satRNA of grapevine fanleaf virus (GFLV). Protein 3A$^{?}$ of phylogenetic clade I satRNAs (left) has a shorter sequence of approximately 265 residues for which GFLV-KE1 returned the highest prediction through C-I-TASSER with a TM-Score through TM-align of 0.45. Protein 3A$^{?}$ of phylogenetic clade II satRNAs (right) have a longer sequence of approximately 340 amino acids, mostly extended on the N-terminal end when comparing the two sequences, and likewise had poor model generation. Protein 3A$^{?}$ of GFLV-SWT6 returned a TM-score of 0.45 through C-I-TASSER model generation and TM-score alignment. While some functions were assigned through Motif Search, their confidence or similarity were low and should be considered with caution.

Table 3-3. Output ontologies of proteins encoded by grapevine fanleaf virus (GFLV) strain F13.

GFLV protein	Molecular function (MF)			Biological process (BP)			Cellular component (CC)		
	GO	C-score[a]	Name	GO	C-score	Name	GO	C-score	Name
1A^{VSR}	0015462	0.92	protein-transmembrane transporting ATPase activity	0050658	0.57	RNA transport	0005737	0.94	cytoplasm
	0005524	0.92	ATP binding	0045184	0.57	establishment of protein localization	0043227	0.57	membrane-bounded organelle
	-	-	-	-	-	-	0005634	0.50	nucleus
1B$^{Hel*/VSR}$	0003723	0.50	RNA binding	0039503	0.97	suppression by virus of host innate immune response	0019028	0.85	viral capsid
	0015075	0.49	ion transmembrane transporter activity	0009968	0.96	negative regulation of signal transduction	0033655	0.76	host cell cytoplasm part
	0004386	0.37	helicase activity	0039537	0.95	suppression by virus of host viral-induced cytoplasmic pattern recognition receptor signaling pathway	0033648	0.72	host intracellular membrane-bounded organelle
1C^{VPg}	0016798	0.59	hydrolase activity, acting on glycosyl bonds	0044238	0.51	primary metabolic process	0044444	0.67	cytoplasmic part
							0009507	0.33	chloroplast
							0005576	0.33	extracellular region
1D^{Pro}	0003824	0.97	catalytic activity	0044003	0.94	modification by symbiont of host morphology or physiology	0016020	0.86	membrane
	0004197	0.78	cysteine-type endopeptidase activity	0039520	0.89	induction by virus of host autophagy	-	-	-
	0003723	0.71	RNA binding	0039544	0.84	suppression by virus of host RIG-I activity by RIG-I proteolysis			
1E$^{Pol*/Sd}$	0034062	0.68	RNA polymerase activity	0039507	0.97	suppression by virus of host molecular function	0019028	0.85	viral capsid

Table 3-3. Output ontologies of proteins encoded by grapevine fanleaf virus (GFLV) strain F13 (continued).

GFLV protein	Molecular function (MF)			Biological process (BP)			Cellular component (CP)		
	GO	C-score[a]	Name	GO	C-score	Name	GO	C-score	Name
1E$^{Pol*/Sd}$	0003676	0.63	nucleic acid binding	0039503	0.97	suppression by virus of host innate immune response	0033655	0.76	host cell cytoplasm part
	0035639	0.54	purine ribonucleoside triphosphate binding	0039694	0.77	viral RNA genome replication	0016020	0.63	membrane
2A$^{HP/Sd}$	0046872	0.47	metal ion binding	0044710	0.47	single-organism metabolic process	0016020	0.93	membrane
	0052933	0.37	alcohol dehydrogenase (cytochrome c(L)) activity				0042597	0.64	periplasmic space
				-	-	-	0030288	0.57	outer membrane-bounded periplasmic space
				-	-	-			
2B^{MP}	0046914	0.36	transition metal ion binding	0044710	0.36	single-organism metabolic process	0005576	0.75	extracellular region
							0044464	0.50	cell part
	-	-	-	-	-	-	0031988	0.50	membrane-bounded vesicle
	-	-	-	-	-	-			
2C$^{CP/Td}$	0005198	0.72	structural molecule activity	0046740	0.65	transport of virus in host, cell to cell	0043231	0.38	intracellular membrane-bounded organelle
	-	-	-	-	-	-	0009341	0.38	beta-galactosidase complex
	-	-	-	-	-	-	0019028	0.31	viral capsid
3A$^{?}$	0046914	0.36	transition metal ion binding	0098662	0.36	inorganic cation transmembrane transport	0016020	0.94	membrane
	0016676	0.36	oxidoreductase activity, acting on a heme group of donors, oxygen as acceptor	0045333	0.36	cellular respiration	0044464	0.89	cell part
	0015078	0.36	hydrogen ion transmembrane transporter activity	0015992	0.36	proton transport	0005886	0.78	plasma membrane

Table 3-4. Output ontologies of proteins encoded by grapevine fanleaf virus (GFLV) strain GHu.

GFLV protein	Molecular function (MF)			Biological process (BP)			Cellular component (CC)		
	GO	C-score[a]	Name	GO	C-score	Name	GO	C-score	Name
1A^{VSR}	0097493	0.92	structural molecule activity conferring elasticity	0044763	0.94	single-organism cellular process	0044444	0.97	cytoplasmic part
	005101	0.92	actin filament binding	0045944	0.34	positive regulation of transcription from RNA polymerase II promoter	0044446	0.97	intracellular organelle part
	0005524	0.41	ATP binding	0043123	0.34	positive regulation of I-kappaB kinase/NF-kappaB signaling	0004323 4	0.94	protein complex
1B$^{Hel*/VSR}$	0003824	0.49	catalytic activity	0080134	0.93	regulation of response to stress	0043231	0.85	intracellular membrane-bounded organelle
	0070182	0.36	DNA polymerase binding	0019054	0.93	modulation by virus of host process	0005634	0.81	nucleus
	-	-	-	0039537	0.92	suppression by virus of host viral-induced cytoplasmic pattern recognition receptor signaling pathway	0044444	0.41	cytoplasmic part
1C^{VPg}	0016798	0.59	hydrolase activity, acting on glycosyl bonds	0044238	0.51	primary metabolic process	0044444	0.67	cytoplasmic part
	-	-	-	-	-	-	0009507	0.33	chloroplast
	-	-	-	-	-	-	0005576	0.33	extracellular region
1D^{Pro}	0003824	0.98	catalytic activity	0044003	0.94	modification by symbiont of host morphology or physiology	0019028	0.97	viral capsid
	0004197	0.81	cysteine-type endopeptidase activity	0039520	0.89	induction by virus of host autophagy	0016020	0.80	membrane
	0005524	0.74	ATP binding	0039544	0.85	suppression by virus of host RIG-I activity by RIG-I proteolysis	-	-	-

Table 3-4. Output ontologies of proteins encoded by grapevine fanleaf virus (GFLV) strain GHu (continued).

GFLV protein	Molecular function (MF)			Biological process (BP)			Cellular component (CC)		
	GO	C-score[a]	Name	GO	C-score	Name	GO	C-score	Name
$1E^{Pol*/Sd}$	0003968	0.63	RNA-directed RNA polymerase activity	0019054	0.99	modulation by virus of host process	0019028	0.87	viral capsid
	0003723	0.52	RNA binding	0039503	0.97	suppression by virus of host innate immune response	0030430	0.76	host cell cytoplasm
	0022838	0.43	substrate-specific channel activity	0039694	0.78	viral RNA genome replication	0033648	0.75	host intracellular membrane-bounded organelle
$2A^{HP/Sd}$	0005088	0.46	Ras guanyl-nucleotide exchange factor activity	0051345	0.56	positive regulation of hydrolase activity	0044424	0.75	intracellular part
				0043087	0.56	regulation of GTPase activity	0016020	0.75	membrane
				0035556	0.56	intracellular signal transduction	0005829	0.62	cytosol
$2B^{MP}$	-	-	-	-	-	-	0005576	0.78	extracellular region
	-	-	-	-	-	-	0043227	0.72	membrane-bounded organelle
	-	-	-	-	-	-	0043234	0.50	protein complex
$2C^{CP/Td}$	0005198	0.72	structural molecule activity	0046740	0.64	transport of virus in host, cell to cell	0043231	0.38	intracellular membrane-bounded organelle
	-	-	-	-	-	-	0009341	0.38	beta-galactosidase complex
	-	-	-	-	-	-	0019028	0.31	viral capsid

GFLV RNA1 proteins

Native to the AlphaFold2 Colaboratory resource (https://colab.research.google.com/github/sokrypton/ColabFold/blob/v1.2.0/AlphaFold2.ipynb), MMseqs2 multiple sequence alignments were generated against query sequences of protein encoding regions of GFLV RNA1 for strains F13 and GHu. $1A^{VSR}$, 85/96 sequences; $1B^{Hel*/VSR}$, 132/200 sequences; $1C^{VPg}$, 32/52 sequences; $1D^{Pro}$, 90/129 sequences; and $1E^{Pol*/Sd}$, 550/567 sequences were found at the species/sub-species level (Figure 3-4). Further, the relative coverage of each of these sequences against the query protein varied for each protein with general trends of linking higher pLDDT of predictions with the most conserved and homologous regions of each protein (Figure 3-4). All reported molecular function, biological process, and cellular component localization predictions are given by protein and are denoted by a C-score of confidence from 0 (lowest) to 1 (highest) with a gene ontology (GO) identifier (Table 3-3, Table 3-4, and Table 3-S4). For additional predictions of the cellular localization of GFLV proteins, predictions from LOCALIZER and those that exhibited confidence level of < 0.70 from four other localization prediction programs were selected in this study (Table 3-S5). The predicted nucleotide bindings sites that overlapped between two programs NsitePred (Table 3-S6) and ATPbind (Table 3-S7) were selected to be presented in this study. Lastly, transmembrane domains/helices that were predicted from a minimum of two out of seven programs were presented (Table 3-S8).

GFLV 1A^{VSR}

The functions of protein 1A^{VSR} (416 aa) are unresolved and have low confidence from the absence of similar sequences in protein repositories. Regardless, Motif Search predicted three motifs within the GFLV-F13 sequence, a T3/T7-like RNA polymerase, a STIM1 Orai1-activating region, and a protein of unknown function at aa 195-269, 196-242, 386-403, respectively (Figure 3-4 and Table 3-S4). The molecular function prediction for protein 1A^{VSR} of GFLV-F13 returned two results of protein-transmembrane transporting ATPase (GO:0015462) and ATP binding (GO:0005524), both with C-scores of 0.92 (Table 3-3). Interestingly, protein 1A^{VSR} of GFLV-GHu was predicted to have molecular functions such as structural molecule activity conferring elasticity (GO:0097493) and actin filament binding (GO:0051015) with a C-score of 0.92 in addition to ATP binding (GO:0005524) with a C-score of 0.41 (Table 3-4 and Table 3-S4). The biological process predictions were RNA transport (GO:0050658) and establishment of protein localization (GO:0045184) for protein 1A^{VSR} of GFLV-F13, both a with C-score of 0.57 (Table 3-3 and Table 3-S4), as well as single-organism cellular process (GO:0044763, C-score = 0.94), positive regulation of transcription from RNA polymerase II promoter (GO:0045944, C-score = 0.34), positive regulation of I-kappaB kinase/NF-kappaB signaling (GO:0043123, C-score = 0.34) for protein 1A^{VSR} of GFLV-GHu (Table 3-4 and Table 3-S4). No biological process or molecular function was predicted to directly relate to the described VSR function of 1A^{VSR} (Choi et al. 2023) (Table 3-3, Table 3-4, and Table 3-S4)**.** Predictions of cellular localization for protein 1A^{VSR} included cytoplasm (F13, GO:0005737, C-score = 0.94) or cytoplasmic part (GFLV-GHu, GO:0044444, C-score

= 0.97), membrane-bounded organelle (F13, GO:0043227, C-score = 0.57), intracellular organelle part (GFLV-GHu, GO:0044446, C-score = 0.97), nucleus (GFLV-F13 and -GHu, GO:0005634, C-score = 0.50), and protein complex (GFLV-GHu, GO:0043234, C-score = 0.94) C (Table 3-3, Table 3-4, and Table 3-S4) according to C-I-TASSER, D-I-TASSER, and D-I-TASSER-MTD pipelines, while it was predicted to be localized in the nucleus according to LOCALIZER program (Table 3-S5).

Some of the nucleotide binding sites based on binding potential to five ligands (ATP, ADP, AMP, GTP, and GDP) were predicted for protein $1A^{VSR}$ but at low probability < 0.30 and with inconsistent numbers of binding sites between GFLV strains F13 (17 sites) and GHu (seven sites) (Table 3-S6 and Table 3-S7). Transmembrane domains or helices were not observed across a minimum of two out of the seven programs that we used (Table 3-S8).

GFLV 1B$^{Hel*/VSR}$

GFLV protein $1B^{Hel*/VSR}$ (801 aa) had predicted sequences of known and previously undescribed functions. Phyre2 aligned 32% of the amino acid sequence with prediction confidence of 99.8% (Figure 3-3 and Table 3-S3). Tertiary *de novo* modeling returned TM aligned scores of up to 0.87 against known structures through D-I-TASSER-MTD (Figure 3-3, Figure 3-4, and Table 3-S3). The model with the highest confidence contained many alpha helices stacking throughout a 'U' shape, where the two predicted functional motifs lie (Figure 3-4).

Helicase activity is a previously described putative function of protein

1B$^{Hel*/VSR}$ (Ritzenthaler et al. 1991; Viry et al. 1993), which aligned with Motif Search to be located between residues 361-465 for the "superfamily 3 helicase of positive ssRNA viruses" domain profile (Figure 4 and Table S4). An additional motif was predicted as a short-chain dehydrogenases/reductases family signature at residues 564-592 (Figure 3-4 and Table 3-S4). Molecular functions were predicted as RNA binding activity (GFLV-F13, GO:0003723), ion transmembrane transporter activity (GFLV-F13, GO:0015075), helicase activity (GFLV-F13, GO:0004386), catalytic activity (GFLV-GHu, GO:0003824), and DNA polymerase binding (GFLV-GHu, GO:0070182) with a C-score of 0.5, 0.49, 0.37, 0.49, and 0.36, respectively (Table 3-3, Table 3-4, and Table 3-S4).

A total of 25 biological processes were predicted for protein 1B$^{Hel*/VSR}$ of GFLV-F13 and 30 biological processes for that of GFLV-GHu in which 14 of 25, and 13 of 30, respectively, had C-scores above 0.90 (Table 3-S4). Several predicted processes are involved in cellular metabolism including, but not limited to: organic substance metabolic process (GFLV-GHu, GO:0071704, C-score = 0.97), primary metabolic process (GFLV-F13 and -GHu, GO:0044238, C-score = 0.98 and 0.97, respectively), macromolecule metabolic process (GFLV-F13 and -GHu, GO:0043170, C-score = 0.98 and 0.96, respectively), multi-organism metabolic process (GFLV-F13 and -GHu, GO:0044033, C-score = 0.97 and 0.93, respectively) (Table 3-S4). Other predictions were related to involvement in host immunity, stress response, or signaling pathways: suppression by virus of host innate immune response (GFLV-F13, GO:0039503, C-score = 0.97), negative regulation of signal transduction (GFLV-F13, GO:0009968, C-score = 0.96), suppression of host viral-induced cytoplasmic pattern

recognition receptor signaling pathway (GFLV-F13 and –GHu, GO:0039537, C-score = 0.95 and 0.92, respectively), regulation of response to stress (GFLV-GHu, GO:0080134, C-score = 0.93), and modulation of host process (GFLV-GHu, GO:0019054, C-score = 0.93) (Table 3-3, Table 3-4, and Table 3-S4). From the tertiary predictions of D-I-TASSER-MTD, the protein was predicted to be found or associated within the viral capsid (GFLV-F13, GO:0019028, C-score = 0.85), host cell cytoplasm part (GFLV-F13, GO:0033655, C-score = 0.76), or cytoplasmic part (GFLV-GHu, GO:0044444, C-score = 0.41), and host intracellular membrane-bounded organelle (GFLV-F13 and -GHu, GO:0033648, C-score = 0.72 and 0.85, respectively) (Table 3-3, Table 3-4, and Table 3-S4). No specific subcellular localization with prediction confidence > 0.60 was observed for protein $1B^{Hel*/VSR}$ from five localization predicting programs used in this study (Table 3-S5).

Protein $1B^{Hel*/VSR}$ contained the majority of the predicted nucleotide binding sites with high probability (> 0.8) among the GFLV-encoded proteins: S367, Q368, S369, K371, T372 (GFLV-GHu only), and T373 (GFLV-F13 only) or I373 (GFLV-GHu only) (Table 3-S6 and Table 3-S7). Residues S367, Q368, and S369 specifically showed high probability (approximately 1.0) at binding to GDP, while Q368 showed high probability (≥ 0.8) at binding to GTP (both GFLV-F13 and -GHu) or GTP and ADP (GFLV-GHu only) (Table 3-S6). Those three residues were also predicted to bind to ATP (Table 3-S7). Phyre2 predicted five intermembrane domains (S1; aa 101-128, S2; aa 132-152, S3; aa 191-220, S4; aa 231-251, and S5; aa 750-780) within protein $1B^{Hel/VSR}$ of GFLV-F13 (Figure 3-5A and Figure 3-5C). Several transmembrane domains/helices were predicted among four of the seven programs with three common

overlapping domains at positions 102-119, 132-151 and 754-779 for GFLV-F13 and 96-116, 131-151, and 753-776 for GFLV-GHu (Table 3-S8).

Fusion protein GFLV-1A^{VSR}B$^{Hel*/VSR}$

GFLV protein 1A^{VSR}B$^{Hel*/VSR}$ is a suppressor of RNA silencing **[19].** Results obtained with I-TASSER-MTD showed a TM-score of 0.77 in the determination of gene ontology properties using the MetaGO program, against PDB structure 6BFI, a viniculin homolog in a sponge organism (Miller et al. 2018). Molecular functions of VIN1 include cytoskeletal protein binding, actin binding, protein binding (Miller et al. 2018). Biological processes included cell adhesion and cellular process and cellular component annotations of VIN1 were ubiquitous across the cell (Miller et al. 2018).

Similar annotations for protein 1A^{VSR}B$^{Hel*/VSR}$ through the MetaGO server yielded molecular functions of cytoskeletal protein binding, actin binding, protein complex binding, cell adhesion molecule binding, RNA binding, and eukaryotic initiation factor 4E binding (Table 3-S4 and File 3-S1). Biological processes were more expansive to include broadly cellular process, biological regulation, regulation of cellular process (both positive and negative), regulation of multicellular organismal process, response to stimulus, negative regulation of signal transduction, and single-organism cellular process (Table 3-S4 and File 3-S1).

A TM-score of 0.77 was produced by the MetaGO program in the determination of structural homologues, to include the top candidate, PDB entry, 82AQ (Table 3-S3). This protein is a DNA binding protein from the Fanconi anemia group D2, or FANCD2, under the same umbrella of over 22 FANC proteins. This protein is crucial in DNA

damage repair mechanisms and carries out several functions of signal transduction, DNA damage response, damage-sensing, and DNA repair **[106]**.

GFLV 1C^{VPg}

Given its small size, GFLV protein 1C^{VPg} (24 aa) is not optimal for tertiary prediction programs that rely on iterative overlapping sequences to construct alpha helices and beta sheets for confident scoring structures. The penalties associated with attempts to use the 24 aa long-protein resulted in errors for most programs, and Phyre2 is unable to accept such short sequences. Regardless, a tertiary structure was completed by D-I-TASSER with a TM-score of 0.64 with two small alpha helices that minimize folding energy (Figure 3-3 and Table 3-S3). Robetta created an *ab initio* form with a GDT of 0.79 (Figure 3-3, Figure 3-4, and Table 3-S3). The final form of the protein may look different in the predicted 5'-RNA complex or in complex with other proteins. Additionally, this protein is identical in amino acid sequence between GFLV strains F13 and GHu (Table 3-S2).

With low confidence (C-score < 0.60), molecular function of GFLV 1C^{VPg} for both strains F13 and GHu was predicted to be hydrolase activity, acting on glycosyl bonds (GO:0016798) and biological process was predicted to be primary metabolic process (GO:0044238) (Table 3-3, Table 3-4, and Table 3-S4). Scores below 0.60 are not confident and may relate to the restrictions behind iterative homology-guided protein prediction. The cellular component was predicted to be within the cytoplasmic part (GO:0044444, C-score = 0.67) but had other low confidence predictions (C-score < 0.40) in the chloroplast (GO:0009507) and extracellular region (GO:0005576) (Table 3-3, Table 3-3-4, and Table 3-S4). Similar to cellular component results (Table 3-3 and

Table 3-4), MultiLoc2 predicted cytoplasmic localization for protein $1C^{VPg}$ with confidence at 0.66 (Table 3-S5).

Nucleotide binding sites could not be predicted for $1C^{VPg}$ due to its small size (Table 3-S6 and Table 3-S7). No transmembrane domains and subcellular localization with high probability (> 0.8) were predicted for this protein (Table 3-S8).

GFLV 1D^{Pro}

GFLV protein $1D^{Pro}$ (219 aa) is a highly conserved protease with several closely related proteins with crystal structures. Phyre2 was able to cover 95% of the sequence with 99.5% confidence. Similarly, high levels of confidence were returned with trRosetta *de novo* modeling with a TM-Score of 0.907 (Figure 3-3, Figure 3-4, and Table 3-S3). D-I-TASSER returned a TM-Score 0.78 (Figure 3-3 and Table 3-S3). These were extremely high confidence models compared with those obtained for other GFLV proteins. Many models including the trRosetta output contained a single globular domain with beta strands and alpha helices for a tight organization. The proteolytic pocket projected onto the trRosetta prediction indicated the close spatial proximity of residues 43 (His), 87 (Glu), and 197 (Leu) (Figure 3-6), as previously suggested (Osterbaan et al. 2021).

With high coverage and alignment, Motif Search predicted the picornaviruses 3C/3C-like protease domain profile (Figure 3-4 and Table 3-S4), as previously reported (Schmitt-Keichinger et al. 2017), to stretch near the entirety of the protein. Additionally, at its N-terminus, the active site was described as coronavirus 6B/7B protein, which is currently undescribed (Figure 3-4). Eight molecular functions were assigned for this

protein for both GFLV strains F13 and GHu, in which the three foremost functions were catalytic activity (GO:0003824, C-score 0.97 and 0.98, respectively), cysteine-type endopeptidase activity (GO:0004197, C-score = 0.78 and 0.81, respectively), and ATP binding (GO:0005524, C-score = 0.71 and 0.74, respectively) (Table 3-3, Table 3-4, and Table 3-S4). Eighteen biological processes were assigned, eight of which had C-scores above 0.80: modification by symbiont of host morphology or physiology (GO:0044003), viral process (GO:0016032), primary metabolic process (GO:0044238), protein metabolic process (GO:0019538), induction by the virus of host autophagy (GO:0039520), and suppression by virus of host RIG-I activity by RIG-I proteolysis (GO:0039544) for both GFLV-F13 and –GHu protein $1D^{Pro}$ (Table 3-3, Table 3-4, and Table 3-S4). The cellular localization of the tertiary structure was predicted as membrane bound (GFLV-F13 and –GHu, GO:0016020, C-score = 0.86 and 0.80, respectively) (Table 3-3 and Table 3-4) or viral capsid (GFLV-GHu, GO:0019028, C-score = 0.97) (Table 3-4). In contrast, MultiLoc2 predicted it to be localized in the cytoplasm with a high probability (≥ 0.87) (Table 3-S5).

No nucleotide binding sites with high probability (> 0.8) were predicted in our study for protein $1D^{Pro}$, but it has protein binding sites for its proteolytic cleavage processing (Hallgren et al. 2022) (Table 3-S6 and Table 3-S7). Despite membrane localization prediction for protein $1D^{Pro}$ (Table 3-3 and Table 3-4), no common transmembrane domains from at least two prediction programs were observed (Table 3-S8).

GFLV 1E$^{Pol*/Sd}$

GFLV protein 1E$^{Pol*/Sd}$ (824 aa) is the largest protein encoded by GFLV. Homology by sequence alignment was highly confident at the N-terminal RdRP domain, in which Phyre2 was able to cover up to 62% of the sequence with 100% confidence (Figure 3-3 and Table 3-S3). With the overrepresentation of plant virus RdRP sequences in databases, few alignments were made to the C-terminal 328 amino acids that were defined here as the middle and C-terminal domains (Figure 3-5). Tertiary structure prediction with D-I-TASSER-MTD produced the best TM-score of 0.87, which is very high considering the lack of homologous templates at the C-terminus (Figure 3-3, Figure 3-4, and Table 3-S3). A closer look at homologous templates revealed a heavy indication towards coverage towards the N-terminal RdRP and not with the entire length of the protein. A globular structure was mainly found for the polymerase domain, however, the C-terminal end of the protein with little sequence homology contained two smaller domains with increased amounts of disorder (Figure 3-4 and Figure 3-6). Domain prediction via Motif Search identified the family *Secoviridae* catalytic core domain of the RdRP (cd23196) (Figure 3-4 and Table 3-S4).

Molecular function was guided to RdRP activity (GFLV-F13 and -GHu, GO:0034062, C-score = 0.68 and 0.63, respectively), as expected, nucleic acid binding (GFLV-F13, GO:0003676, C-score = 0.63), or RNA binding (GFLV-GHu, GO:0003723, C-score = 0.52), purine ribonucleoside triphosphate binding (GFLV-F13, GO:0035639, C-score = 0.54), and substrate-specific channel activity (GFLV-GHu, GO:0022838, C-score = 0.43) (Table 3-3, Table 3-4, and Table 3-S4). For both GFLV strains F13 and GHu, biological processes of suppression of host molecular function

(GO:0039507) and host innate immune response (GO:0039503), modulation of host process (GO:0019054) with high confidence were predicted (C-score ≥ 0.97) in addition to viral RNA genome replication (GFLV-F13 and -GHu, GO:0039694, C-score = 0.77 and 0.78, respectively), and suppression by virus of host translation (GFLV-F13 and GHu, GO:0039604, C-score = 0.69 for both) (Table 3-3, Table 3-4, and Table 3-S4). Those functions might be related to the symptom determinant function of $1E^{Pol*/Sd}$. For protein $1E^{Pol*/Sd}$ of GFLV strains F13 and GHu, the cellular localization predictions varied from host cytoplasm (Table 3-3, Table 3-4, and Table 3-S5) and membrane parts (GO:0033655 and GO:0016020, respectively) to viral capsid (GO:0019028), all of which with C-score above 0.60 (Table 3-3, Table 3-4, and Table 3-S4). MuliLoc2 predicted protein $1E^{Pol*/Sd}$ for both strains GFLV-F13 and GFLV-GHu to localize in cytoplasmic component with high confidence (≥ 0.83) (Table 3-S5).

Protein $1E^{Pol*/Sd}$ had the most nucleotide binding sites among the GFLV proteins with confidence below 0.80 (Table 3-S6) and a majority (17 to 21 sites) having the binding potential to GDP (17 to 21 sites) and ATP (13 to 15 sites) within positions 197-214 and 276-279, respectively (Table 3-S6 and Table 3-S7). Phyre2 predicted two intermembrane domains spanning from the extracellular space into the cytoplasm back into the extracellular space (S1; aa 342-357, S2; aa 641-656) for protein $1E^{Pol/Sd}$ of GFLV strain GHu (Figure 3-5B). Interestingly, transmembrane domains in protein $1E^{Pol*/Sd}$ were observed in both MEMSTAT3 and Phyre2 for GFLV-GHu ,while observed only in MEMSTAT3 for GFLV-F13 (Table 3-S8). Nonetheless, protein $1E^{Pol*/Sd}$ for GFLV-GHu was predicted to contain transmembrane domain/helix at positions 342-356 (Table 3-S8).

GFLV RNA2 proteins

Native to the AlphaFold2 Colaboratory resource (https://colab.research.google.com/github/sokrypton/ColabFold/blob/v1.2.0/AlphaFold2.ipynb), MMseqs2 multiple sequence alignments were generated against query sequences of protein encoding regions of RNA2 for GFLV strains F13 and GHu. $2A^{HP/Sd}$, 102/114 sequences; $2B^{MP}$, 113/122 sequences; and $2C^{CP}$, 180/154 sequences were found at the species/sub-species level (Figure 3-7). Again, the relative coverage of each of these sequences against the query protein varied for each protein with general trends of linking the pLDDT of predictions against the most conserved and similar regions of each protein (Figure 3-7). All reported molecular function, biological process, and cellular component localization predictions, as well as nucleotide binding sites and transmembrane domains/helices for GFLV RNA2-encoded proteins are similarly organized as done for GFLV RNA1-encoded proteins (Table 3-3, Table 3-4, Table 3-S4, Table 3-S5, Table 3-S6, Table 3-S7, and Table 3-S8).

GFLV 2A$^{HP/Sd}$

GFLV protein $2A^{HP/Sd}$ (258 aa) is a homing protein and is associated with symptom determination in the model host species *N. occidentalis* (Martin et al. 2018). A smaller portion (31%) of the query sequence was covered with high confidence (72%) when GFLV strain GHu was subjected to Phyre2 analysis (Figure 3-3 and Table 3-S3). Three-dimensional models did not have similar levels of confidence as intracellular proteins are often less abundantly solved for their tertiary structure (Figure

3-3, Figure 3-7, and Table 3-S3). Regardless, the ribbon model generated by D-I-TASSER mainly returned with a single globular shape with alpha helices and unordered strands (TM-aligned score of 0.51) (Figure 3-7).

Domain prediction resulted in the specific annotation towards viral family protein as nepovirus subgroup A polyprotein (PFAM12312) (Figure 3-7 and Table 3-S4). Specific functional characteristics were described as protein SRG1 (PLN02216) at residues 36-106, which interestingly corresponds to oxidoreductase activity in *Arabidopsis thaliana* and is related to the biological function of leaf senescence (GO:0010150) (Figure 4 and Table S4). Overlapping the report of the 50-distal amino acids of protein $2A^{HP/Sd}$ involved in symptomatology (Martin et al. 2018) was the weak prediction of electron transfer flavoprotein subunit alpha (PRK11916, E-value = 2.70). Protein $2A^{HP/Sd}$ was predicted to have molecular functions of Ras guanyl-nucleotide exchange factor activity (GFLV-GHu, GO:0005088, C-score = 0.46), metal ion binding (GFLV-F13, GO:0046872, C-score = 0.47), alcohol dehydrogenase activity (GFLV-F13, GO:0052933, C-score = 0.37) (Table 3-3, Table 3-4, and Table 3-S4). Biological processes related to positive regulation of hydrolase activity (GFLV-GHu, GO:0043087, C-score = 0.56), regulation of GTPase activity (GFLV-GHu, GO:0043087, C-score = 0.56), intracellular signal transduction (GFLV-GHu, GO:0035556, C-score = 0.56), and single-organism metabolic process (GFLV-F13, GO:0044710, C-score = 0.47) were predicted (Table 3-3, Table 3-4, and Table 3-S4). The D-I-TASSER models of protein $2A^{HP/Sd}$ predicted its localization to several parts of the cell including membrane (GFLV-F13 and GFLV-GHu, GO:0016020, C-score = 0.93 and 0.75, respectively) and periplasmic space (GFLV-F13, GO:0042597, C-score

= 0.64) or outer membrane-bounded periplasmic space (GFLV-F13, GO:0030288, C-score = 0.57) (Table 3-3 and Table 3-4), intracellular part (GFLV-GHu, GO:0044424, C-score = 0.75), membrane (GFLV-GHu, GO:0016020, C-score = 0.75), and cytosol (GFLV-GHu, GO:0005829, C-score = 0.62) (Table 3-4) or mitochondria at a high probability (0.76-0.80) (Table 3-S5).

No nucleotide binding sites with high probability (> 0.80) were predicted in our study for protein $2A^{HP/Sd}$ (Table 3-S6) although several ATP binding sites (11 sites for $2A^{HP/Sd}$ of GFLV-F13 and two sites for $2A^{HP/Sd}$ of GFLV-GHu) were detected using the ATPbind program (Table 3-S7). No common transmembrane domains/helices for protein $2A^{HP/Sd}$ were detected from at least two of the seven programs used (Table 3-S8).

GFLV 2B^{MP}

GFLV protein $2B^{MP}$ (348 aa) performed the lowest overall among GFLV proteins in attempts to predict structure and function. Phyre2 was able to cover 40% of the query sequence with up to 7.5% confidence, most of unreliable quality (Figure 3-3 and Table 3-S3). The estimated internal eTM-Score of D-I-TASSER was better at 0.66, but with TM-aligned validation only reached 0.51 (Figure 3-3 and Table 3-S3). The AlphaFold2 model performed best at 0.54 to contain beta sheets and alpha helices between two arms of disordered random coils (Figure 3-7).

Domain prediction using Motif Search resolved a motif at residues 66-135 for a periplasmic-binding component of ABC transport systems specific for xylo-oligosaccharides (cd14749), as well as a protein of unknown function motif (DUF448)

at residues 25-51 (Figure 3-7 and Table 3-S4). Molecular function and biological processes returned predictions of low confidence (C-score < 0.30) (Table S4). For protein $2B^{MP}$ of GFLV-F13, C-score of 0.36 for transition metal ion binding (GO:0046914) of molecular process and single-organism metabolic process (GO:0044710) of biological process were predicted, however, these low scores should be taken lightly (Table 3-3). Protein $2B^{MP}$ of GFLV-GHu returned low confidence predictions (C-score < 0.30) for molecular and biological processes (Table 3-S4). Cellular component predictions for protein $2B^{MP}$ of GFLV-F13 were concentrated to extracellular regions (GO:0005576, C-score = 0.75), membrane-bound vesicle (GO:0031988, C-score: = 0.50), and cell part (GO:0044464, C-score = 0.50) (Tables 3-3 and 3-S4). Protein $2B^{MP}$ of GFLV-GHu retained similar localization predictions, except with the addition of protein complex (GO:0043234, C-score = 0.50) (Table 3-4). Protein $2B^{MP}$ was predicted to localize in the cytoplasm (Table 3-S5), consistent with its localization in the plasmodesmata (Table 3-1) (Schmitt-Keichinger et al. 2017; Quacquarelli et al. 1976; Roy et al. 2023).

Eight to 17 ATP-binding sites were detected for protein $2B^{MP}$, in which the numbers of sites varied depending on the program and GFLV strain used (Table 3-S6 and Table 3-S7). As observed for protein $2A^{HP/Sd}$, no consistent transmembrane domain was observed in this study for protein $2B^{MP}$ (Table 3-S8).

GFLV $2C^{CP/Td}$

The GFLV protein $2C^{CP/Td}$ (504 aa) is the only protein of GFLV that has a resolved structure (Shellenberger et al. 2010; 2011). The alignment and tertiary

predictions of this molecule retained high confidence at 99% alignment with 100% confidence in Phyre2, and 0.98 TM-align scores through D-I-TASSER (Figure 3-3 and Table 3-S3). This structure matched very closely the PDB submitted structure, PDB:5FOJ (Shellenberger et al. 2010; 2011).

Domain prediction by Motif Search restated the nepovirus CP by displaying the pfam signature nepovirus CP N-terminal, central, and C-terminal domains in the following aa regions: 2-91, 166-335, and 344-500, respectively (Figure 3-7). The alignment of the tertiary shape with true crystal structure was highly accurate regardless of program, and descriptions of function related to already accepted details behind CP subunits (Figure 3-7). For both GFLV strains F13 and GHu, only one biological process, transport of virus in host cell-to-cell (GO:0046740, C-score $\geq$ 0.64), was predicted for protein $2C^{CP/Td}$, along with one molecular function, structural molecule activity (GO:0005198, C-score = 0.72) (Table 3-3, Table 3-4, and Table 3-S4). For protein $2C^{CP/Td}$ of GFLV-F13 and -GHu, the cellular component prediction of D-I-TASSER was split among intracellular membrane-bounded organelle (GO:0043231, C-score = 0.38), beta-galactosidase complex (GO:0009341, C-score = 0.38), and viral capsid (GO:0019028, C-score = 0.31) (Table 3-3, Table 3-4, and Table 3-S4). In contrast, no predicted subcellular localization with high confidence level (> 0.8) was detected using LOCALIZER, TargetP, SignalP, Plant mSubP, and MultiLoc2 subcellular localization prediction programs (Table 3-S5).

Several nucleotide binding sites were predicted for protein $2C^{CP/Td}$ with the majority identified to be ATP or ADP binding sites (five to 10 for ATP and eight to nine for ADP) (Table 3-S6 and Table 3-S7). One transmembrane domain was

identified for protein $2C^{CP/Td}$ at positions 239-254 for GFLV-F13 and 238-251 for GFLV-GHu (Table 3-S8).

The alignment of PDB:5FOJ crystalline structure of protein $2C^{CP/Td}$ across predicted structures returned with various amounts of confidence (Figure 3-S1), as anticipated. AlphaFold2 predictions of the F13 and GHu strains returned RMSD values of 1.81 and 3.72, respectively. Robetta returned RMSD values over 3.0 and ESMFold returned RMSD values over 1.80. D-I-TASSER had the lowest RMSD values at 1.64 for strain F13 and 1.43 for strain GHu (Figure 3-S1). Prediction algorithms that integrate known homologous structures and multiple sequence alignments, such as D-I-TASSER and AlpahFold2, returned lower error values than *ab initio*-based algorithms.

GFLV satRNA protein 3A$^{?}$

GFLV satRNA protein 3A$^{?}$ sequences contain a segment of polar residues towards the N-terminus. MotifFinder consistently predicted an F-box domain (F-box domain found in F-box only protein 25 FBXO25) in five protein 3A$^{?}$ sequences, towards the C-terminus (Figure 3-8). Protein 3A$^{?}$ of phylogenetic clade I satRNAs (Čepin et al. 2016) contained a DNA topoisomerase domain at aa 3-100, and that of phylogenetic clade II satRNAs (Čepin et al. 2016) contained two domains, a DNA-polymerase cdc27 subunit at positions aa 46-156 and a F-box domain at positions aa 286-315 (Figure 3-8). SatRNA protein 3A$^{?}$ of GFLV strain Py17 returned glutareoxin-like domain with high confidence (E-value = 0.052) (Table 3-S4).

Additionally, protein 3A$^{?}$ of GFLV strains F13, CO2, and SWT6 returned a

DNA polymerase subunit cdc27 domain at the N-terminal half (Figure 3-8 and Table 3-S4). Molecular function, biological process, and cellular component prediction by D-I-TASSER or C-I-TASSER were unreliable, as expected, to span all parts of the cell with no tangential experimental evidence available in the literature. With great amounts of random coils and loops, models were unreliable for protein 3A$^{?}$ (Table 3-S4). Trends began to appear after analyzing all 3A$^{?}$ strain predictions to focus heavily on metal ion binding and catalysis. However, no functional characteristics have been described biologically for satRNA (Pinck et al. 1988; Saldarelli et al. 1993; Gottula et al. 2013).

Protein 3A$^{?}$ of GFLV satRNA strain F13 was predicted to have several molecular and biological processes at low confidence (C-score < 0.40) which include transition metal ion binding (GO:0046914, C-score = 0.36), oxidoreductase activity (GO:0016676, C-score = 0.36), and hydrogen ion transmembrane transporter activity (GO:0015078, C-score = 0.36), as well as biological processes such as inorganic cation transmembrane transport (GO:0098662, C-score = 0.36), cellular respiration (GO:0045333, C-score = 0.36), and protein transport (GO:0015992, C-score = 0.36) (Table 3-3 and Table 3-S4). For the cellular localization prediction, protein F13-3A$^{?}$ was predicted to be localized in the membrane (GO:0016020, C-score = 0.94), cell part (GO:0044464, C-score = 0.89), and plasma membrane (GO:0005886, C-score = 0.78) (Table 3-3 and Table 3-S4) in addition to nucleus or plastid (Table 3-S5).

Nine to 20 nucleotide binding sites were predicted for protein 3A$^{?}$ across different satRNA proteins, yet the probability scores for such predictions were low (< 0.50) (Table 3-S6). ATPbind model was not conducted for 3A$^{?}$ due to low confidence

in its protein structure modeling as mentioned above. Common transmembrane domain from at least two programs was not detected for protein $3A^{?}$ (Table 3-S8).

DISCUSSION

Protein structure prediction has blossomed into a beneficial field for guiding new hypotheses, generating short and long-chain three-dimensional structures of protein monomers or multimers (Al-Lazikani et al. 2001; Kuhlman and Bradley 2019). The benchmarks of ab initio protein prediction software have highlighted I-TASSER as one of the best current prediction software available (Al-Lazikani et al. 2001). This program and AlphaFold2 were comparable in terms of confident protein structure prediction. However, TASSER programs were increasingly useful for studying biological functions and molecular processes associated with the structure (Zheng et al. 2021). Initially, we hypothesized that GFLV proteins would contain advanced functions and structures that would deviate from initial training and algorithms of highly rated protein structure and function prediction programs. Our findings revealed that GFLV is still bound to central tenants of protein biology with confident predictions obtained using recent software.

We confirmed previously demonstrated functions for GFLV proteins (Table 3-1), verified two putative reported functions (Fuchs et al. 2017; Ritzenthaler et al. 1991; Schmitt-Keichinger et al. 2017; Viry et al. 1993) (Table 3-1), and documented the predictions of at least seven additional functions through current protein prediction software (Figures 3-4, 3-7, and 3-8; Table 3-S4). The unresolved crystal structure for seven GFLV proteins, excluding the $2C^{CP/Td}$ (Andret-Link et al. 2004; Schellenberger

et al. 2010; Schellenberger et al. 20111; Serghini et al. 1990), severely limits our understanding of biological functions. We employed the most up-to- date predictive protein modeling tools to gain a new understanding of putative functions and confirm current understandings of functions reported in the literature (Figure 3- 2). The newly predicted functional components were determined to include protein $1A^{VSR}$ with a T3/T7-like RNA polymerase domain, protein $1B^{Hel*/VSR}$ with a short-chain reductase, protein $1E^{Pol*/Sd}$ with a parathyroid hormone family domain, protein $2B^{MP}$ with overlapping domains of unknown function and an ABC transporter, and protein $3A^{?}$ to include either DNA topoisomerase domains, the transcription factor FBXO25 domain, or DNA Pol subunit cdc27 domain (Figures 3-4, 3-7 and 3-8; Table 3-S4). No novel functions were predicted for $1C^{VPg}$ due to the nature of prediction algorithms and its short aa sequence. The structure and function of $2C^{CP/Td}$ have been described (Andret-Link et al. 2004; Margis et al. 1993; Quacquarelli et al. 1976; Schellenberger et al. 2010; Schellenberger et al. 2011; Serghini et al. 1990), and most algorithms were able to predict its structure with ease to include D-I-TASSER, trRosetta, and ESMFold having average RMSD values below 2.0 (Supplementary Figure 3-1). AlphaFold2 was not far behind in predicting the structure, with average RMSD values just below 3.0. However, Robetta predictions returned larger RMSD values over 3.0. This instance shows considerable advantages for including template structures in prediction tools when predicting conserved proteins. Overall, our results highlight the importance of incorporating multiple structure prediction algorithms when studying the structure of the protein of interest *in silico* as the prediction power and error may vary depending on the algorithm (Supplementary Figure 3-1). This has been documented in recent reports

by CASP (Zheng et al. 2021).

Analyses of GFLV proteins have alluded to the following new predictions (Tables 3-3 and 3-4; Figures 3-4, 3-7, and 3-8; Table 3-S4) based on structural characteristics. For GFLV RNA1-encoded proteins, protein $1A^{VSR}$ is involved in transporting activity, cellular reorganization, and regulation of cellular process and signaling; protein $1B^{Hel*/VSR}$ performs as a helicase, as expected, some form of catalysis, perhaps as a polymerase cofactor (Chen et al. 2020), while suppressing host immune response and signaling pathways; protein $1C^{VPg}$ composes hydrolase activity and metabolic process function; protein $1D^{Pro}$ could interfere with host immune responses through proteolytic activity and/or modify host autophagy events; and protein $1E^{Pol*/Sd}$ is a suppressor of host immunity, molecular function, and host translation (Tables 3- 3, 3-4, 3-S4). These predicted functions for proteins $1A^{VSR}$, $1B^{Hel*/VSR}$, and $1E^{Pol*/Sd}$ might be related to their experimentally confirmed functions as VSRs (Choi et al. 2023) and symptom determinants (Osterbaan et al. 2019; Vigne et al. 2013) (Tables 3-1, 3-3, and 3-4). GFLV RNA2-encoded proteins provided much less confident predictions for which only the biological processes provided new insights; protein $2A^{HP/Sd}$ was predicted to be involved with the regulation of GTPase activity, intracellular signal transduction, and the positive regulation of hydrolase activity for GFLV strain GHu (Tables 3-3 and 3-4; Figure 3-7; Supplementary Table 3-4). Predictions for protein $2B^{MP}$ were suggestive of transition metal ion binding and involvement with metabolic processes; however, across both strains, there were levels of incompleteness or uncertainty (Tables 3-3 and 3-4). Finally, satRNA encoding $3A^{?}$ provided some new predicted functions, such as metal ion binding or metabolite binding (Table 3-3; Figure 3-8;

Supplementary Table 3-4), which may be involved in the host molecular process (Chaturvedi and Shrivastava 2005).

The above predictions of seemingly unrelated protein functions for an RNA virus are intriguing. Indeed, the T3/T7-like RNA polymerase domain has not been described in related systems. However, it is possible that a conserved structural or sequence pattern has alternative functions or purposes. Likewise, no function, motif, or domain has been described for the elusive satRNA encoding protein. Simply because we do not understand these biological networks does not mean that we should discount the possibilities of their utility to promote virus-host compatibility.

GFLV protein $1D^{Pro}$ is a 3C-like protease that cleaves in *cis* and *trans* the polyproteins encoded by RNA1 and RNA2, respectively (Andret-Link et al. 2004; Fuchs et al. 2022; Gorbalenya and Snijder 1996; Margis et al. 1991; Margis et al. 1992; Margis et al. 1993; Margis et al. 1994; Morris-Krsinich et al. 1983; Schmitt-Keichinger et al. 2017). Site-directed mutagenesis, by analogy to other known proteases, revealed the crucial three residue active sites required for proteolytic activity, His-Glu-Leu (Käll et al. 2004). We considered these residues via *in silico* predictions and demonstrated additional confidence behind the functional and structural aspects of protein $1D^{Pro}$ (Figure 3-5). The 3C-like proteinase of GFLV has been eloquently examined against other nepovirus proteinases through AlphaFold *in silico* predictions, highlighting the evolutionary constraints on active site configuration (Sanfaçon and Skern 2023). While sequence alignment helps bolster these claims (Sanfaçon 2022), the tertiary models provide additional context to enzymatic activity and relate more to protein function (Sanfaçon and Skern 2023).

Additionally, we considered the model for GFLV $1E^{Pol*/Sd}$ to analyze both functions of putative RdRP and documented symptom determinants. While mutagenesis of lysine to glycine at aa residue 802 in GFLV strain GHu abolishes symptoms in *N. benthamiana*, there are still unknowns behind the mechanism of symptom expression by this residue (Osterbaan et al. 2019; Osterbaan et al. 2021). The model generated in this study is consistent with interactions of protein $1E^{Pol*/Sd}$ with host protein components, given that residue 802 of $1E^{Pol*/Sd}$ is exposed on the exterior of the protein at the apex of an alpha helix and not buried in a hydrophobic pocket (Figure 3-6, arrow). No novel functions were detected at this residue, perhaps due to a lack of homologous templates or folds. Additional experimental work is needed to understand the functional and biological aspects of GFLV protein $1E^{Pol*/Sd}$.

One of the most elusive GFLV proteins is the satRNA encoding protein $3A^{?}$ (Čepin et al. 2016; Fuchs et al. 1989; Gottula et al. 2013; Pinck et al. 1988; Saldarelli et al. 1993). At least two new predicted functions were revealed through the comparison of multiple protein prediction programs, but with low confidence, especially for tertiary structure-based programs (Figure 3-8; Table 3-S4). GFLV satRNA molecules are divided into two phylogenetic clades, which have been related to geographical differences and evolutionary divergence (Gottula et al. 2013). Protein $3A^{?}$ of these two clades gave rise to two different structural and functional predictions. Clade I satRNAs contained only one consistent domain of a DNA topoisomerase at the N- terminal end, while clade II satRNAs contained a DNA Pol Subunit cdc27 motif at the same area as the DNA topoisomerase of clade I isolate, in addition to a FBXO25 motif at the C-terminal end (Figure 3-8; Supplementary Table 3-4). Most structures returned low

confidence with simple alpha helices in a globular form, with TM-scores consistently below 0.50 (Figure 3-8). In addition, template-guided or ab initio modeling consistently returned TM scores below 0.50 (Figure 3-8; Table 3-S3; File 3-S1), a common threshold for revealing a high amount of randomness in prediction. While ATPbind and BioLIP in D-I-TASSER predicted nucleotide binding and ion binding motifs for GFLV protein $3A^{?}$, these results must be taken lightly (Tables 3-S6 and 3-S7; File 3-S1). C-I-TASSER, again, did not differ in confidence against homology-guided algorithms when comparing against the available structures in the PDB. The projected accuracy of these TM scores could, in fact, reflect that satellite RNA molecules associated with RNA viruses remain elusive in terms of function and structure.

Our study revealed multiple predicted nucleotide binding sites (Tables 3-S6 and 3-S7), transmembrane domains/helices or pore-lining domains (Table 3-S8), and subcellular localization of GFLV proteins and satRNA protein (Tables 3-3 and 3-4; Tables 3-S4 and 3-S5). While NsitePred (Chen et al. 2012) (Table 3-S6) relies on sequence-based detection of nucleotide binding sites, ATPbind (Hu et al. 2018) (Supplementary Table 3-S7) relies on structure-based detection. This may explain the outcome of varying numbers and residues of nucleotide binding sites detected between these two programs (Tables 3-S6 and 3-S7). GFLV protein $1B^{Hel*/VSR}$ contained the nucleotide binding sites with the highest probabilities (0.80–1.0), which were observed in both programs (Tables 3-S6 and 3-S7). Numerous differences in predicted ATP binding site counts for proteins $1A^{VSR}$ (difference of 10 sites) and $2A^{HP/Sd}$ (difference of 9 sites) were observed between GFLV strains F13 and GHu (Table 3-S7). These

findings highlight the importance of incorporating sequence and structure homology into the prediction models when characterizing proteins *in silico*. Unlike nucleotide binding site prediction, a total of nine transmembrane domains/helices (only considering those that were detected from at least two out of the seven prediction programs) were present in three GFLV proteins (three in $1B^{Hel*/VSR}$ of GFLV strains F13 and GHu; one in $1E^{Pol*/Sd}$ of GFLV strain GHu; one in $2C^{CP/Td}$ of GFLV strains F13 and GHu) (Table 3-S8). Phyre2 predicted the transmembrane domain in protein $1E^{Pol*/Sd}$ of GFLV strain GHu but not strain F13. Knowing the composition of the transmembrane domain provides information regarding possible subcellular localization, as well as putative functions, which include but are not limited to membrane transporting, cell-to-cell signaling, and energy transfer (Borkakoti and Thornton 2023; Cuthbertson et al. 2005). For the subcellular localization prediction, most of the GFLV proteins were predicted to be localized in the nucleus ($1A^{VSR}$), cytoplasm ($1D^{Pro}$, $1E^{Pol*/Sd}$, and $2B^{MP}$), or mitochondrion ($2A^{HP/Sd}$), while most satRNA-encoded proteins were estimated to be localized in either the plastid or nucleus (Tables 3-3 and 3-4; Table 3-S5). Protein $1B^{Hel*/VSR}$ was predicted to be localized in host intracellular membrane- bounded organelle such as endoplasmic reticulum, confirming previous findings (Ritzenthaler et al. 2002) (Tables 3-1, 3-3, and 3-4; Table 3-S5). Some of these predictions also confirmed previous findings of protein $2B^{MP}$ localizing in the plasmodesmata (Amari et al. 2010; Laporte et al. 2003) (Tables 3-1, 3-3, and 3-4). Subcellular localization experiments via microscopy would be useful to confirm those predictions and better understand interactions among GFLV proteins and host proteins.

Viral proteins utilize various capacities to perform multiple functions, often linked to binding pockets for a suitable substrate. With the release of AlphaFold2, there has been a resurgence in investigating molecular inhibitors of proteins related to disease and undesirable phenotypes (Borkakoti and Thornton 2023; Ren et al. 2023). Furthermore, cryptic pockets are unexposed and difficult to study, but further structural understandings can unravel additional mechanisms of enzyme or functional inhibition (Meller et al. 2023). The more data collected and experimentally resolved, the better we can understand the molecular mechanisms of virus-specific protein functions. By focusing on these binding pockets, one may identify potential ways to inhibit protein function through the discovery of allosteric sites or altered protein structures that depend on the opening or closing of the pockets (Sen Gupta et al. 2023). Predictions on binding pockets and protein interactions were made for at least every D-I-TASSER prediction. For example, the proteolysis His-Glu-Leu pocket of GFLV protein $1D^{Pro}$ and the different core RdRP motifs of GFLV protein $1E^{Pol/Sd}$ were modeled with high confidence (Figure 3-6).

Other studies have leveraged AlphaFold2 predictions to focus on resolving structural components via crystallography (Hu et al. 2022; van Breugel et al. 2022). We incurred an overabundance of computational software to analyze proteins encoded by GFLV and sought to define the best models. Using 28 independent programs (Table 3-2; Figure 3-2), we were able to construct structure models of every GFLV protein, predict functional characteristics, and compare these against functions reported in the literature (Tables 3-1, 3-3, and 3-4). While we confirmed some functional characteristics of GFLV proteins, we also uncovered potential undescribed functions.

Homology-guided and ab initio protein prediction programs are difficult to compare when GFLV proteins have varied levels of understanding. Nevertheless, we utilized standards of the field to effectively compare the output of each program's prediction and weigh each accordingly. Each program used for predictive modeling brought individual strengths and weaknesses toward our goal of annotating the GFLV proteome (Figure 3-2). MotifFinder (GenomeNet) and Phyre2 (Kelley et al. 2015) relied heavily on sequence alignment and secondary structure to construct a piece-wise understanding of protein products. These programs were fast and provided easy manipulation of search parameters (reducing stringencies of similarity or providing short sequences that were more similar) (Table 3-S3). Programs used to generate three- dimensional protein structures ab initio (AlphaFold2, D-I-TASSER, and MTD- TASSER) were more computationally intensive and took more time to yield outputs if using open-source servers (Jumper et al. 2021; Mirdita et al. 2022; Roy et al. 2010; Varadi et al. 2022; Yang et al. 2015; Zhang 2008; Zheng et al. 2023; Zhou et al. 2019; Zhou et al. 2022). These programs require more RAM and storage on local systems, which can prevent high throughput analysis. The use of D-I-TASSER (Zheng et al. 2023) often provided the most confident results (Figure 3-3; Table 3-S3). Six GFLV protein sequences returned with the highest TM scores through the I- TASSER suite and averaged 0.57 (Table 3-S3). Although conducting 3D structure-based functional annotation using extended parameters of the D-I- TASSER suite is more time-consuming compared to structural predictions only, it provided the most biologically relevant information about how a protein behaves *in vitro* in our study.

In silico predictions of protein structures and functions are constrained by the

availability and knowledge of the related solved protein structures (Gomes et al. 2022). Unique sequences or sequences with little similarity to solved structures, like GFLV proteins, are often most challenging for *in silico* predictions; however, this is intrinsic to the scoring algorithm using known sequences to adjust the probability of certain folds due to protein folding patterns. This topic has been raised in several recent publications (Azzaz et al. 2022; Lee et al. 2023; Yin et al. 2022). Our *in silico* modeling approach showed that prediction algorithms were consistent with previously reported findings of the GFLV protein functions and localizations (Amari et al. 2010; Choi et al. 2023; Fuchs et al. 2017; Gorbalenya and Snijder 1996; Laporte et al. 2003; Ritzenthaler et al. 1991; Ritzenthaler et al. 2002; Schmitt-Keichinger et al. 2017; Viry et al. 1993). The GFLV proteins with known homologous structures crystalized, such as the protease, RdRP, and CP, and returned high confidence values *in silico* prediction (Figure 3-3; Table 3-S3). As expected, proteins with little to no homology, unique functions, or lacking within the PDB returned low confidence values with homology-based programs (Figure 3-3; Table 3-S3). GFLV proteins such as the VSRs, putative helicase $1B^{Hel*/VSR}$, $1C^{VPg}$, homing protein $2A^{HP/Sd}$, and movement protein $2B^{MP}$ all benefitted from some level of refinement or ab initio programs, performing even higher than homology-guided algorithms (Figure 3-3; Table 3-S3).

In conclusion, we leveraged the value and power of *in silico* prediction and characterization of virus proteins to better understand the multifunctionality and structure of GFLV proteins and gain new insights into their potential roles in virus pathogenicity. The use of a diverse pool of predictive models and programs to study GFLV proteins enabled us to evaluate the advantages, limitations, and performance of

each program. GFLV strain-specific predictions and predictions common to GFLV strains F13 and GHu were generated using amino acid sequences of the two virus strains. After such *in silico* analyses, we retain that a central and uniformly controlled calculation for model confidence should be employed by protein prediction algorithms for accurate comparisons. Validating the models through, for instance, biological assays or X-ray crystallography following protein purification and crystal production will be essential in ensuring their accuracy and reliability.

ACKNOWLEDGMENTS

We thank Victoria Hoyle, Anna Wunsch, and Madison Flasco for their continued encouragement.

REFERENCES

Al-Lazikani, B., Jung, J., Xiang, Z., and Honig, B. 2001. Protein structure prediction. Curr. Opin. Chem. Biol. 5:51-56.

Almagro Armenteros, J. J., Tsirigos, K. D., Sønderby, C. K., Petersen, T. N., Winther, O., Brunak, S., von Heijne, G., and Nielsen, H. 2019. SignalP 5.0 improves signal peptide predictions using deep neural networks. Nat. Biotechnol. 37:420-423.

Amari, K., Boutant, E., Hofmann, C., Schmitt-Keichinger, C., Fernandez-Calvino, L., Didier, P., Lerich, A., Mutterer, J., Thomas, C. L., Heinlein, M., and Maule, A. J. 2010. A family of plasmodesmal proteins with receptor-like properties for plant viral movement proteins. PLoS Pathog. 6.

Andret-Link, P., Laporte, C., Valat, L., Ritzenthaler, C., Demangeat, G., Vigne, E., Laval, V., Pfeiffer, P., Stussi-Garaud, C., and Fuchs, M. 2004. Grapevine fanleaf virus: still a major threat to the grapevine industry. J. Plant Pathol. 86:183-195.

Andret-Link, P., Schmitt-Keichinger, C., Demangeat, G., Komar, V., and Fuchs, M. 2004. The specific transmission of grapevine fanleaf virus by its nematode vector *Xiphinema index* is solely determined by the viral coat protein. Virology 320:12-22. Armenteros, J. J. A., Salvatore, M., Emanuelsson, O., Winther, O., von Heijne, G.,

Elofsson, A., and Nielsen, H. 2019. Detecting sequence signals in targeting peptides using deep learning. Life Sci. Alliance 2.

Azzaz, F., Yahi, N., Chahinian, H., and Fantini, J. 2022. The epigenetic dimension of

protein structure is an intrinsic weakness of the AlphaFold program. Biomolecules 12:1527.

Baek, M., DiMaio, F., Anishchenko, I., Dauparas, J., Ovchinnikov, S., Lee, G. R., Wang, J., Cong, Q., Kinch, L. N., Schaeffer, R. D., Millán, C., Park, H., Adams, C., and Baker, D. 2021. Accurate prediction of protein structures and interactions using a three-track neural network. Science 373:871-876.

Belin, C., Schmitt, C., Gaire, F., Walter, B., Demangeat, G., and Pinck, L. 1999. The nine C-terminal residues of the grapevine fanleaf nepovirus movement protein are critical for systemic virus spread. J. Gen. Virol. 80:1347-1356.

Blum, T., Briesemeister, S., and Kohlbacher, O. 2009. MultiLoc2: integrating phylogeny and gene ontology terms improves subcellular protein localization prediction. BMC Bioinform. 10:274.

Borkakoti, N., and Thornton, J. M. 2023. AlphaFold2 protein structure prediction: implications for drug discovery. Curr. Opin. Struct. Biol. 78:102526.

Cadman, C. H., Dias, H. F., and Harrison, B. D. 1960. Sap-transmissible viruses associated with diseases of grape vines in Europe and North America. Nature 187:577-579.

Cazalis-Allut, L. 1865. Œuvres agricoles. Victor Masson et fils, Paris, France. De La Dégénération Des Vignes, pp. 57-61.

Čepin, U., Gutiérrez-Aguirre, I., Ravnikar, M., and Pompe-Novak, M. 2016. Frequency of occurrence and genetic variability of grapevine fanleaf virus satellite RNA. Plant Pathol. 65:510-520.

Chaturvedi, U. C., and Shrivastava, R. 2005. Interaction of viral proteins with metal

ions: role in maintaining the structure and functions of viruses. FEMS Microbiol. Immunol. 43:105-114.

Chen, J., Malone, B., Llewellyn, E., Grasso, M., Shelton, P. M. M., Olinares, P. D. B., Maruthi, K., Eng, E. T., Vatandaslar, H., Chait, B. T., Kapoor, T. M., and Darst, S. A. 2020. Structural basis for helicase-polymerase coupling in the SARS-CoV-2 replication-transcription complex. Cell 182:1560-1573.e13.

Chen, K., Mizianty, M. J., and Kurgan, L. 2012. Prediction and analysis of nucleotide-binding residues using sequence and sequence-derived structural descriptors. Bioinformatics 28:331-341.

Choi, J., Pakbaz, S., Yepes, L. M., Cieniewicz, E. J., Schmitt-Keichinger, C., Labarile, R., Minutillo, S. A., Heck, M., Hua, J., and Fuchs, M. 2023. Grapevine fanleaf virus RNA1-encoded proteins 1A and $1B^{Hel}$ suppress RNA silencing. Mol. Plant-Microbe Interact. 36:558-571.

Chowdhury, R., Bouatta, N., Biswas, S., Floristean, C., Kharkar, A., Roy, K., Rochereau, C., Ahdritz, G., Zhang, J., Church, G. M., Sorger, P. K., Bengio, Y., and LeCun, Y. 2022. Single-sequence protein structure prediction using a language model and deep learning. Nat. Biotechnol. 40:1617-1623.

Cuthbertson, J. M., Doyle, D. A., and Sansom, M. S. P. 2005. Transmembrane helix prediction: a comparative evaluation and analysis. Protein Eng. Des. Sel. 18:295- 308.

De Castro, E., Sigrist, C. J. A., Gattiker, A., Bulliard, V., Langendijk-Genevaux, P. S., Gasteiger, E., Bairoch, A., and Hulo, N. 2006. ScanProsite: detection of PROSITE signature matches and ProRule-associated functional and structural

residues in proteins. Nucleic Acids Res. 34.

Digiaro, M., Elbeaino, T., and Martelli, G. P. 2017. Grapevine fanleaf virus and other old world nepoviruses. Pages 47-82 in: Grapevine viruses: molecular biology, diagnostics and management. B. Meng, G. P. Martelli, D. A. Golino, and M. Fuchs, eds. Springer International Publishing, Cham, Switzerland.

Du, Z., Su, H., Wang, W., Ye, L., Wei, H., Peng, Z., Anishchenko, I., Baker, D., and Yang, J. 2021. The trRosetta server for fast and accurate protein structure prediction. Nat. Protoc. 16:5634-5651.

Edgar, R. C., Taylor, J., Lin, V., Altman, T., Barbera, P., Meleshko, D., Lohr, D., Novakovsky, G., Buchfink, B., Al-Shayeb, B., Banfield, J. F., and Thomas, B. C. 2022. Petabase-scale sequence alignment catalyses viral discovery. Nature 602:142- 147.

Eichmeier, A., Baránek, M., and Pidra, M. 2011. Genetic variability of grapevine fanleaf virus isolates within genes $1B^{Hel}$ and $1E^{Pol}$. J. Plant Pathol. 93:511-515.

Ferruz, N., Schmidt, S., and Höcker, B. 2022. ProtGPT2 is a deep unsupervised language model for protein design. Nat. Commun. 13:4348.

Fuchs, M., Hily, J. M., Petrzik, K., Sanfaçon, H., Thompson, J. R., van der Vlugt, R., Wetzel, T., and ICTV Report Consortium. 2022. ICTV virus taxonomy profile: *Secoviridae* 2022. J. Gen. Virol. 103:001807.

Fuchs, M., Pinck, M., Serghini, M. A., Ravelonandro, M., Walter, B., and Pinck, L. 1989. The nucleotide sequence of satellite RNA in grapevine fanleaf virus, strain F13. J. Gen. Virol. 70:955-962.

Fuchs, M., Schmitt-Keichinger, C., and Sanfaçon, H. 2017. A renaissance in nepovirus

research provides new insights into their molecular interface with hosts and vectors. Pages 61-105 in: Advances in virus research. M. Kielian, T. C. Mettenleiter, and M.

J. Roossinck, eds. Academic Press, Cambridge, MA, USA.

Gaire, F., Schmitt, C., Stussi-Garaud, C., Pinck, L., and Ritzenthaler, C. 1999. Protein 2A of grapevine fanleaf nepovirus is implicated in RNA2 replication and colocalizes to the replication site. Virology 264:25-36.

Gabler, F., Nam, S. Z., Till, S., Mirdita, M., Steinegger, M., Söding, J., Lupas, A. N., and Alva, V. 2020. Protein sequence analysis using the MPI bioinformatics toolkit. Curr. Protoc. Bioinform. 1.

Ghosh, D., Chakraborty, S., Kodamana, H., and Chakraborty, S. 2022. Application of machine learning in understanding plant virus pathogenesis: trends and perspectives on emergence, diagnosis, host-virus interplay and management. Virol. J. 19:42.

Gomes, P. S. F. C., Gomes, D. E. B., and Bernardi, R. C. 2022. Protein structure prediction in the era of AI: challenges and limitations when applying to *in silico* force spectroscopy. Front. Bioinform. 2:983306.

Gorbalenya, A. E., and Snijder, E. J. 1996. Viral cysteine proteinases. Perspect. Drug Discov. Des. 6:64-86.

Gottula, J., Lapato, D., Cantilina, K., Saito, S., Bartlett, B., and Fuchs, M. 2013. Genetic variability, evolution, and biological effects of grapevine fanleaf virus satellite RNAs. Phytopathology 103:1180-1187.

Gutierrez, S., Tyczynski, W. G., Boomsma, W., Teufel, F., and Winther, O. 2022.

MembraneFold: visualising transmembrane protein structure and topology. bioRxiv.

Gutnik, D., Evseev, P., Miroshnikov, K., and Shneider, M. 2023. Using AlphaFold predictions in viral research. Curr. Issues Mol. Biol. 45:3705-3732.

Hallgren, J., Tsirigos, K. D., Pedersen, M. D., Armenteros, J. J. A., Marcatili, P., Nielsen, H., Krogh, A., and Winther, O. 2022. DeepTMHMM predicts alpha and beta transmembrane proteins using deep neural networks. bioRxiv.

Hewitt, W. B., Raski, D. J., and Goheen, A. C. 1958. Nematode vector of soil-borne fanleaf virus of grapevines. Phytopathology 48:586-595.

Holm, L. 2020. DALI and the persistence of protein shape. Protein Sci. 29:128-140. Holm, L. 2022. Dali server: structural unification of protein families. Nucleic Acids Res. 50.

Hu, J., Li, Y., Zhang, Y., and Yu, D. J. 2018. ATPbind: accurate protein–ATP binding site prediction by combining sequence-profiling and structure-based comparisons. J. Chem. Inf. Model. 58:501-510.

Hu, L., Salmen, W., Sankaran, B., Lasanajak, Y., Smith, D. F., Crawford, S. E., Estes, M. K., and Prasad, B. V. V. 2022. Novel fold of rotavirus glycan-binding domain predicted by AlphaFold2 and determined by X-ray crystallography. Commun. Biol. 5:419.

Jumper, J., Evans, R., Pritzel, A., Green, T., Figurnov, M., Ronneberger, O., Tunyasuvunakool, K., Bates, R., Žídek, A., Potapenko, A., Bridgland, A., Meyer, C., Kohl, S. A. A., Ballard, A. J., Cowie, A., Romera-Paredes, B., Nikolov, S., Jain, R., Adler, J., Back, T., Petersen, S., Reiman, D., Clancy, E.,

Zielinski, M., Steinegger, M., Pacholska, M., Berghammer, T., Bodenstein, S., Silver, D., Vinyals, O., Senior, A. W., Kavukcuoglu, K., Kohli, P., and Hassabis, D. 2021. Highly accurate protein structure prediction with AlphaFold. Nature 596:583-589.

Joly, A. C., Garcia, S., Hily, J. M., Koechler, S., Demangeat, G., Garcia, D., Vigne, E., Lemaire, O., Zuber, H., and Gagliardi, D. 2023. An extensive survey of phytoviral RNA 3' uridylation identifies extreme variations and virus-specific patterns. Plant Physiol. 193:271-290.

Juretić, D., Zoranić, L., and Zucić, D. 2002. Basic charge clusters and predictions of membrane protein topology. J. Chem. Inf. Comput. Sci. 42:620-632.

Käll, L., Krogh, A., and Sonnhammer, E. L. L. 2004. A combined transmembrane topology and signal peptide prediction method. J. Mol. Biol. 338:1027-1036.

Källberg, M., Wang, H., Wang, S., Peng, J., Wang, Z., Lu, H., and Xu, J. 2012. Template-based protein structure modeling using the RaptorX web server. Nat. Protoc. 7:1511-1522.

Kelley, L. A., Mezulis, S., Yates, C. M., Wass, M. N., and Sternberg, M. J. E. 2015. The Phyre2 web portal for protein modeling, prediction and analysis. Nat. Protoc. 10:845-858.

Kuhlman, B., and Bradley, P. 2019. Advances in protein structure prediction and design. Nat. Rev. Mol. Cell Biol. 20:681-697.

Laporte, C., Vetter, G., Loudes, A. M., Robinson, D. G., Hillmer, S., Stussi-Garaud, C., and Ritzenthaler, C. 2003. Involvement of the secretory pathway and the cytoskeleton in intracellular targeting and tubule assembly of grapevine fanleaf

virus movement protein in tobacco BY-2 cells. Plant Cell 15:2058-2075.

Lee, S., Kim, S., Lee, G. R., Kwon, S., Woo, H., Seok, C., and Park, H. 2023. Evaluating GPCR modeling and docking strategies in the era of deep learning-based protein structure prediction. Comput. Struct. Biotechnol. J. 21:158-167.

Lewis, T. E., Sillitoe, I., Dawson, N., Lam, S. D., Clarke, T., Lee, D., Orengo, C., and Lees, J. 2018. Gene3D: extensive prediction of globular domains in proteins. Nucleic Acids Res. 46.

Lin, Z., Akin, H., Rao, R., Hie, B., Zhu, Z., Lu, W., Smetanin, N., Verkuil, R., Kabeli, O., Shmueli, Y., dos Santos Costa, A., Fazel-Zarandi, M., Sercu, T., Candido, S., and Fuchsberger, C. 2023. Evolutionary-scale prediction of atomic-level protein structure with a language model. Science 379:1123-1130.

Liu, D., Young, F., Robertson, D. L., and Yuan, K. 2023. Prediction of virus-host association using protein language models and multiple instance learning. bioRxiv.

Marchler-Bauer, A., and Bryant, S. H. 2004. CD-Search: protein domain annotations on the fly. Nucleic Acids Res. 32.

Margis, R., Pinck, L., Viry, M., Pinck, M., and Bardonnet, N. 1994. Differential proteolytic activities of precursor and mature forms of the 24K proteinase of grapevine fanleaf nepovirus. Virology 200:79-86.

Margis, R., Pinck, L. 1992. Effects of site-directed mutagenesis on the presumed catalytic triad and substrate-binding pocket of grapevine fanleaf nepovirus 24-kDa proteinase. Virology 190:884-888.

Margis, R., Ritzenthaler, C., Reinbolt, J., Pinck, M., and Pinck, L. 1993. Genome

organization of grapevine fanleaf nepovirus RNA2 deduced from the 122K polyprotein P2 *in vitro* cleavage products. J. Gen. Virol. 74:1919-1926.

Margis, R., Viry, M., Pinck, M., and Pinck, L. 1991. Cloning and *in vitro* characterization of the grapevine fanleaf virus proteinase cistron. Virology 185:779- 787.

Mariani, V., Biasini, M., Barbato, A., and Schwede, T. 2013. lDDT: a local superposition-free score for comparing protein structures and models using distance difference tests. Bioinformatics 29:2722-2728.

Martin, I. R., Vigne, E., Berthold, F., Komar, V., Lemaire, O., Fuchs, M., and Schmitt-Keichinger, C. 2018. The 50 distal amino acids of the $2A^{HP}$ homing protein of grapevine fanleaf virus elicit a hypersensitive reaction on *Nicotiana occidentalis*. Mol. Plant Pathol. 19:731-743.

Martelli, G. P. 2019. Virus diseases of grapevine. Pages 1-13 in: Encyclopedia of life sciences. John Wiley & Sons, Ltd., Hoboken, NJ, USA.

Meller, A., Bhakat, S., Solieva, S., and Bowman, G. R. 2023. Accelerating cryptic pocket discovery using AlphaFold. J. Chem. Theory Comput. 19:4355-4363.

Miller, P. W., Pokutta, S., Mitchell, J. M., Chodaparambil, J. V., Clarke, D. N., Nelson, W. J., Weis, W. I., and Nichols, S. A. 2018. Analysis of a vinculin homolog in a sponge (phylum Porifera) reveals that vertebrate-like cell adhesions emerged early in animal evolution. J. Biol. Chem. 293:11674-11686.

Mirdita, M., Schütze, K., Moriwaki, Y., Heo, L., Ovchinnikov, S., and Steinegger, M. 2022. ColabFold: making protein folding accessible to all. Nat. Methods 19:679- 682.

Mistry, J., Chuguransky, S., Williams, L., Qureshi, M., Salazar, G. A., Sonnhammer, E. L. L., Tosatto, S. C. E., Paladin, L., Raj, S., Richardson, L. J., Finn, R. D., and Bateman, A. 2021. Pfam: the protein families database in 2021. Nucleic Acids Res. 49.

Morris-Krsinich, B. A. M., Forster, R. L. S., and Mossop, D. W. 1983. The synthesis and processing of the nepovirus grapevine fanleaf virus proteins in rabbit reticulocyte lysate. Virology 130:523-526.

Mortuza, S. M., Zheng, W., Zhang, C., Li, Y., Pearce, R., and Zhang, Y. 2021. Improving fragment-based ab initio protein structure assembly using low-accuracy contact-map predictions. Nat. Commun. 12:5011.

Nepal, M., Che, R., Ma, C., Zhang, J., and Fei, P. 2017. FANCD2 and DNA damage. Int. J. Mol. Sci. 8:1804.

Nugent, T., and Jones, D. T. 2009. Transmembrane protein topology prediction using support vector machines. BMC Bioinform. 10:159.

Olechnovič, K., Monastyrskyy, B., Kryshtafovych, A., and Venclovas, Č. 2019. Comparative analysis of methods for evaluation of protein models against native structures. Bioinformatics 6:937-944.

Orlov, I., Hemmer, C., Ackerer, L., Lorber, B., Ghannam, A., Poignavent, V., Hleibieh, K., Sauter, C., Schmitt-Keichinger, C., Belval, L., Demangeat, G., and Ritzenthaler, C. 2020. Structural basis of nanobody recognition of grapevine fanleaf virus and of virus resistance loss. Proc. Natl. Acad. Sci. USA 117:10848-10855.

Osterbaan, L. J., Choi, J., Kenney, J., Flasco, M., Vigne, E., Schmitt-Keichinger, C.,

Rebelo, A. R., Heck, M., and Fuchs, M. 2019. The identity of a single residue of the RNA-dependent RNA polymerase of grapevine fanleaf virus modulates vein clearing in *Nicotiana benthamiana*. Mol. Plant-Microbe Interact. 32:790-801.

Osterbaan, L. J., Hoyle, V., Curtis, M., DeBlasio, S., Rivera, K. D., Heck, M., and Fuchs, M. 2021. Identification of protein interactions of grapevine fanleaf virus RNA-dependent RNA polymerase during infection of *Nicotiana benthamiana* by affinity purification and tandem mass spectrometry. J. Gen. Virol. 102:001607.

Pinck, L., Fuchs, M., Pinck, M., Ravelonandro, M., and Walter, B. 1988. A satellite RNA in grapevine fanleaf virus strain F13. J. Gen. Virol. 69:233-239.

Pinck, M., Reinbolt, J., Loudes, A. M., Le Ret, M., and Pinck, L. 1991. Primary structure and location of the genome-linked protein (VPg) of grapevine fanleaf nepovirus. FEBS Lett. 284:117-119.

Pompe-Novak, M., Gutiérrez-Aguirre, I., Vojvoda, J., Blas, M., Tomažič, I., Vigne, E., Fuchs, M., Ravnikar, M., and Petrovič, N. 2007. Genetic variability within RNA2 of grapevine fanleaf virus. Eur. J. Plant Pathol. 117:307-312.

Quacquarelli, A., Gallitelli, D., Savino, V., and Martelli, G. P. 1976. Properties of grapevine fanleaf virus. J. Gen. Virol. 32:349-360.

Ramasarma, T. 1996. Transmembrane domains participate in functions of integral membrane proteins. Indian J. Biochem. Biophys. 33:20-29.

Raman, S., Vernon, R., Thompson, J., Tyka, M., Sadreyev, R., Pei, J., Kim, D., Kellogg, E., DiMaio, F., Lane, T., et al. 2009. Structure prediction for CASP8 with all-atom refinement using Rosetta. Proteins Struct. Funct. Bioinform. 77:89-99.

Ren, F., Ding, X., Zheng, M., Korzinkin, M., Cai, X., Zhu, W., Mantsyzov, A., Aliper, A., Aladinskiy, V., Cao, Z., Mamoshina, P., Vedmedenko, V., Pankratov, V., Vanhaelen, Q., Aliev, R., and Zhavoronkov, A. 2023. AlphaFold accelerates artificial intelligence powered drug discovery: efficient discovery of a novel CDK20 small molecule inhibitor. Chem. Sci. 14:1443-1452.

Ritzenthaler, C., Laporte, C., Gaire, F., Dunoyer, P., Schmitt, C., Duval, S., Piéquet, A., Loudes, A. M., Rohfritsch, O., Stussi-Garaud, C., and Fuchs, M. 2002. Grapevine fanleaf virus replication occurs on endoplasmic reticulum-derived membranes. J. Virol. 76:8808-8819.

Ritzenthaler, C., Pinck, M., and Pinck, L. 1995. Grapevine fanleaf nepovirus P38 putative movement protein is not transiently expressed and is a stable final maturation product *in vivo*. J. Gen. Virol. 76:907-915.

Ritzenthaler, C., Viry, M., Pinck, M., Margis, R., Fuchs, M., and Pinck, L. 1991. Complete nucleotide sequence and genetic organization of grapevine fanleaf nepovirus RNA1. J. Gen. Virol. 72:2357-2365.

Roy, A., Kucukural, A., and Zhang, Y. 2010. I-TASSER: a unified platform for automated protein structure and function prediction. Nat. Protoc. 5:725-738.

Roy, A., Yang, J., and Zhang, Y. 2012. COFACTOR: an accurate comparative algorithm for structure-based protein function annotation. Nucleic Acids Res. 40.

Roy, B. G., DeBlasio, S., Yang, Y., Thannhauser, T., Heck, M., and Fuchs, M. 2023. Profiling plant proteome and transcriptome changes during grapevine fanleaf virus infection. J. Proteome Res. 22:1997-2017.

Sahu, S. S., Loaiza, C. D., and Kaundal, R. 2020. Plant-mSubP: a computational framework for the prediction of single- and multi-target protein subcellular localization using integrated machine-learning approaches. AoB Plants 12.

Saldarelli, P., Minafra, A., and Walter, B. 1993. A survey of grapevine fanleaf nepovirus isolates for the presence of satellite RNA. Vitis 32:99-102.

Sanfaçon, H. 2022. Re-examination of nepovirus polyprotein cleavage sites highlights the diverse specificities and evolutionary relationships of nepovirus 3C-like proteases. Arch. Virol. 167:2529-2543.

Sanfaçon, H., and Skern, T. 2023. AlphaFold modeling of nepovirus 3C-like proteinases provides new insights into their diverse substrate specificities. Virology 590:109956. Sen Gupta, P.S.; Panda, S.K.; Nayak, A.K.; Rana, M.K. Identification and investigation of a cryptic binding pocket of the p37 envelope protein of monkeypox virus by molecular dynamics simulations. *J. Phys. Chem. Lett.* **2023**, *14*, 3230–3235.

Schellenberger, P., Andret-Link, P., Schmitt-Keichinger, C., Bergdoll, M., Marmonier, A., Vigne, E., Lemaire, O., Fuchs, M., Demangeat, G., and Ritzenthaler, C. 2010. A stretch of 11 amino acids in the βB- βC loop of the coat protein of grapevine fanleaf virus is essential for transmission by the nematode *Xiphinema index*. J. Virol. 84:7924-7933.

Schellenberger, P., Sauter, C., Lorber, B., Bron, P., Trapani, S., Bergdoll, M., Marmonier, A., Schmitt-Keichinger, C., Lemaire, O., Demangeat, G., et al. 2011. Structural insights into viral determinants of nematode mediated grapevine fanleaf virus transmission. PLoS Pathog. 7.

Schmitt-Keichinger, C., Hemmer, C., Berthold, F., and Ritzenthaler, C. 2017. Molecular, cellular, and structural biology of grapevine fanleaf virus. Pages 83-107 in: Grapevine viruses: molecular biology, diagnostics and management. B. Meng, G. P. Martelli, D. A. Golino, and M. Fuchs, eds. Springer International Publishing, Cham, Switzerland.

Serghini, M. A., Fuchs, M., Pinck, M., Reinbolt, J., Walter, B., and Pinck, L. 1990. RNA2 of grapevine fanleaf virus: Sequence analysis and coat protein cistron location. J. Gen. Virol. 71:1433-1441.

Sigrist, C. J. A., Cerutti, L., de Castro, E., Langendijk-Genevaux, P. S., Bulliard, V., Bairoch, A., and Hulo, N. 2010. PROSITE, a protein domain database for functional characterization and annotation. Nucleic Acids Res. 38.

Sillitoe, I., Bordin, N., Dawson, N., Waman, V. P., Ashford, P., Scholes, H. M., Pang, C. S. M., Woodridge, L., Rauer, C., Sen, N., Abbasian, M., Le Cornu, S., Lam, S. D., Berka, K., Varekova, R. S., Svobodova, R., Lees, J. G., and Orengo, C. A. 2021. CATH: increased structural coverage of functional space. Nucleic Acids Res. 49.

Song, Y., DiMaio, F., Wang, R. Y. R., Kim, D., Miles, C., Brunette, T. J., Thompson, J., and Baker, D. 2013. High resolution comparative modeling with RosettaCM. Structure 10:1735-1742.

Sperschneider, J., Catanzariti, A. M., DeBoer, K., Petre, B., Gardiner, D. M., Singh, K. B., Dodds, P. N., and Taylor, J. M. 2017. LOCALIZER: subcellular localization prediction of both plant and effector proteins in the plant cell. Sci. Rep. 7:44598.

Stothard, P. 2000. The sequence manipulation suite: JavaScript programs for analyzing and formatting protein and DNA sequences. Biotechniques 28:1102-1104.

Studer, G., Rempfer, C., Waterhouse, A. M., Gumienny, R., Haas, J., and Schwede, T. 2020. QMEANDisCo-distance constraints applied on model quality estimation. Bioinformatics 36:1765-1771.

Taylor, C. E., and Brown, D. J. F. 1997. Nematode vectors of plant viruses. CAB International, Wallingford, UK.

van Breugel, M., Rosa e Silva, I., and Andreeva, A. 2022. Structural validation and assessment of AlphaFold2 predictions for centrosomal and centriolar proteins and their complexes. Commun. Biol. 5:312.

Varadi, M., Anyango, S., Deshpande, M., Nair, S., Natassia, C., Yordanova, G., Yuan, D., Stroe, O., Wood, G., Laydon, A., Zídek, A., Green, T., Tunyasuvunakool, K., Petersen, S., Jumper, J., Clancy, E., Green, R., Vora, A., Lutfi, M., Figurnov, M., Cowie, A., Hobbs, N., Kohli, P., Kleywegt, G., Birney, E., Hassabis, D., and Velankar, S. 2022. AlphaFold protein structure database: massively expanding the structural coverage of protein-sequence space with high-accuracy models. Nucleic Acids Res. 50.

Vigne, E., Gottula, J. W., Schmitt-Keichinger, C., Komar, V., Ackerer, L., Belval, L., Rakotomalala, L., Lemaire, O., Ritzenthaler, C., and Fuchs, M. 2013. A strain-specific segment of the RNA-dependent RNA polymerase of grapevine fanleaf virus determines symptoms in *Nicotiana* species. J. Gen. Virol. 94:2803-2813.

Viry, M., Serghini, M. A., Hans, F., Ritzenthaler, C., Pinck, M., and Pinck, L. 1993. Biologically active transcripts from cloned cDNA of genomic grapevine

fanleaf nepovirus RNAs. J. Gen. Virol. 74:169-174.

Wang, J., Chitsaz, F., Derbyshire, M. K., Gonzales, N. R., Gwadz, M., Lu, S., Marchler, G. H., Song, J. S., Thanki, N., Yamashita, R. A., Zheng, C., Lanczycki, C. J., Anderson, J. B., Liebscher, S. P., Geer, R. C., Geer, L. Y., and Bryant, S. H. 2023. The conserved domain database in 2023. Nucleic Acids Res. 51: D384-D388.

Waterhouse, A. M., Procter, J. B., Martin, D. M. A., Clamp, M., and Barton, G. J. 2009. Jalview version 2—a multiple sequence alignment editor and analysis workbench. Bioinformatics 25:1189-1191.

Yang, J., Anishchenko, I., Park, H., Peng, Z., Ovchinnikov, S., and Baker, D. 2020. Improved protein structure prediction using predicted interresidue orientations. Proc. Natl. Acad. Sci. USA 3:1496-1503.

Yang, J., Roy, A., and Zhang, Y. 2013. BioLiP: a semi-manually curated database for biologically relevant ligand–protein interactions. Nucleic Acids Res. 41.

Yang, Y., Faraggi, E., Zhao, H., and Zhou, Y. 2011. Improving protein fold recognition and template-based modeling by employing probabilistic-based matching between predicted one-dimensional structural properties of the query and corresponding native properties of templates. Bioinformatics 27:2076-2082.

Yang, J., Yan, R., Roy, A., Xu, D., Poisson, J., and Zhang, Y. 2015. The I-TASSER suite: Protein structure and function prediction. Nat. Methods 12:7-8.

Yin, R., Feng, B. Y., Varshney, A., and Pierce, B. G. 2022. Benchmarking AlphaFold for protein complex modeling reveals accuracy determinants. Protein Sci. 31

Zhang, C., Freddolino, P. L., and Zhang, Y. 2017. COFACTOR: improved protein

function prediction by combining structure, sequence and protein-protein interaction information. Nucleic Acids Res. 45.

Zhang, Y. 2008. I-TASSER server for protein 3D structure prediction. BMC Bioinform. 9:40.

Zhang, Y., and Skolnick, J. 2004. Scoring function for automated assessment of protein structure template quality. Proteins Struct. Funct. Bioinform. 57:702-710.

Zheng, W., Li, Y., Zhang, C., Zhou, X., Pearce, R., Bell, E. W., Huang, X., and Zhang,Y. 2021. Protein structure prediction using deep learning distance and hydrogen-bonding restraints in CASP14. Proteins Struct. Funct. Bioinform. 89:1734-1751.

Zheng, W., Wuyun, Q., Freddolino, P. L., and Zhang, Y. 2023. Integrating deep learning, threading alignments, and a multi-MSA strategy for high-quality protein monomer and complex structure prediction in CASP15. Proteins Struct. Funct. Bioinform. 12:1684-1703.

Zheng, W., Zhang, C., Li, Y., Pearce, R., Bell, E. W., and Zhang, Y. 2021. Folding non-homologous proteins by coupling deep-learning contact maps with I-TASSER assembly simulations. Cell Rep. Methods 3:100014.

Zhou, X., Hu, J., Zhang, C., Zhang, G., and Zhang, Y. 2019. Assembling multidomain protein structures through analogous global structural alignments. Natl. Acad. Sci. Lett. 116:15930-15938.

Zhou, X., Park, B., Choi, D., and Han, K. 2018. A generalized approach to predicting protein-protein interactions between virus and host. BMC Genom. 19:568.

Zhou, X., Zheng, W., Li, Y., Pearce, R., Zhang, C., Bell, E. W., Zhang, G., and Zhang, Y. 2022. I-TASSER-MTD: a deep-learning-based platform for multi-domain

protein structure and function prediction. Nat. Protoc. 17:2326-2353.

Zimmermann, L., Stephens, A., Nam, S. Z., Rau, D., Kübler, J., Lozajic, M., Gabler, F., Söding, J., Lupas, A. N., and Alva, V. 2018. Completely reimplemented MPI bioinformatics toolkit with a new HHpred server at its core. J. Mol. Biol. 15:2237- 2243.

Table 3-S1. Public accession numbers of grapevine fanleaf virus (GFLV) strains used in this study.

GFLV RNA molecule	Strain	NCBI Accession
RNA1	F13	NP_619689.1
RNA1	GHu	AFM91094.1
RNA2	F13	NC_003623.1
RNA2	GHu	ABR09917.1
RNA3	CO2	MH383244.1
RNA3	F13	NC_003203.1
RNA3	LR 4/29	ALA99080.1
RNA3	Py17	UZF66112.1
RNA3	REF KE1	ALA99135.1
RNA3	SACH44	AGT42202.1
RNA3	SWT6	KX034963.1
RNA3	ZUP 1/4 c2	ALA99154.1

Table 3-S2. *The respective amino acid sequences for proteins of grapevine fanleaf virus (GFLV) RNA molecules used in this study.

Strain	Amino acid length	GFLV Protein	Amino acid sequence*
F13	416	1A	…
F13	801	1B	…
F13	24	1C	…
F13	219	1D	…
F13	825	1E	…
F13	257	2A	…
F13	348	2B	…
F13	504	2C	…
GHu	416	1A	…
GHu	801	1B	…
GHu	24	1C	…
GHu	219	1D	…
GHu	825	1E	…
GHu	258	2A	…
GHu	348	2B	…
GHu	504	2C	…
CO2	338	3A	…
F13	341	3A	…
LR 4/29	265	3A	…
Py17	301	3A	…
REF KE1	265	3A	…
SACH44	338	3A	…
SWT6	339	3A	…
ZUP 1/4 c2	268	3A	…

*This is a condensed version of this table. The full version and all supplementary data is available online at: https://www.mdpi.com/2218-273X/14/1/62 and https://www.mdpi.com/article/10.3390/biom14010062/s1 .

Table 3-S3. §**Reporting metrics for protein prediction software in the determination of protein structure.** Programs include AlphaFold2, D-I-TASSER, trRosetta, Robetta, ESMFold, as well as the sequence specific Phyre2 server. Associated metrics of predicted/estimated template modeling (TM) score (pTM/eTM), TM-align scores to known PDB structures, predicted global distance test (GDT), predicted local distance difference test (pLDDT), alignment coverage, and percent confidence were extracted from such predictions for comparative analysis.

		AlphaFold2			D-I-TASSER			trRosetta		Robetta	ESMFold		Phyre2		C-I-TASSER*/ **D-I-TASSER MTD***		
Strain	Protein	pTM	pLDDT	QMEANDisCo Global	eTM	TM-align	QMEANDisCo Global	eTM	pLDDT	Predicted GDT	pTM	pLDDT	Alignment Coverage	Confidence (%)	eTM	TM-align	QMEANDisCo Global
F13	1A	0.28	67.2	0.47	0.37	0.41	0.49	0.254	53.19	0.39	0.192	45.853	0.23	0.076	0.28	0.85	0.28
F13	1B	0.47	66.5	0.54	-	-	-	0.64	79.49	0.62	0.431	60.409	0.26	0.998	**0.66**	**0.85**	**0.31**
F13	1C	0.26	67.9	0.59	0.27	0.64	0.51	0.406	75.59	0.79	0.238	74.744	-	-	-	-	-
F13	1D	0.88	89.41	0.54	0.85	0.78	0.51	0.907	82.15	0.73	0.857	80.824	0.95	0.995	-	-	-
F13	1E	0.65	88.01	0.62	-	-	-	0.745	78.62	0.77	0.645	65.364	0.61	1	**0.26**	**0.86**	**0.43**
F13	2A	0.34	64.13	0.41	0.39	0.51	0.4	0.296	62.44	0.49	0.201	42.331	0.36	0.567	-	-	-
F13	2B	0.53	48.05	0.4	0.62	0.46	0.31	0.525	62.31	0.52	0.439	49.304	0.23	0.067	-	-	-
F13	2C	0.9	91.68	0.83	0.7	0.98	0.67	0.924	82.69	0.84	0.815	75.044	0.99	1	-	-	-
GHu	1A	0.38	64.74	0.5	0.4	0.42	0.36	0.252	64.04	0.36	0.167	39.92	0.24	0.231	0.28	0.83	0.29
GHu	1B	0.6	76.66	0.53	-	-	-	0.596	79.47	0.62	0.424	59.176	0.26	0.998	**0.48**	**0.87**	**0.31**
GHu	1D	0.88	90	0.54	0.88	0.78	0.5	0.892	80.67	0.74	0.843	79.075	0.94	0.997	-	-	-
GHu	1E	0.65	87.55	0.64	-	-	-	0.773	78.85	0.78	0.647	66.355	0.62	1	**0.566**	**0.87**	**0.46**
GHu	2A	0.35	62.74	0.42	0.43	0.44	0.47	0.3	62.69	0.48	0.2	40.747	0.31	0.72	0.28	0.45	0.31

Table 3-S3. §Reporting metrics for protein prediction software in the determination of protein structure. (Continued)

		AlphaFold2			D-I-TASSER			trRosetta		Robetta	ESMFold		Phyre2		C-I-TASSER*/ **D-I-TASSER MTD***		
Strain	Protein	pTM	pLDDT	QMEANDisCo Global	eTM	TM-align	QMEANDisCo Global	eTM	pLDDT	Predicted GDT	pTM	pLDDT	QMEANDisCo Global	eTM	TM-align	QMEANDisCo Global	eTM
GHu	2B	0.54	50.16	0.39	0.66	0.44	0.44	0.489	62.54	0.5	0.412	48.839	0.4	0.075	-	-	-
GHu	2C	0.8	78.78	0.7	0.78	0.98	0.75	0.913	82.79	0.84	0.804	72.926	0.99	1	-	-	-
CO2 (338)	3A	0.266	49.35	0.42	0.3	0.44	0.51	0.1	51.59	0.38	0.158	44.06	0.24	0.084	0.22	0.4	0.36
F13 (341)	3A	0.259	48.32	0.42	0.35	0.4	0.37	0.146	56.94	0.4	0.177	44.415	0.23	0.266	0.25	0.43	0.37
KE1 (265)	3A	0.27	55.43	0.44	0.38	0.44	0.42	0.157	50.3	0.4	0.188	42.227	0.29	0.326	0.27	0.45	0.37
LR 4/29 (265)	3A	0.26	55.51	0.42	0.41	0.43	0.43	0.1	54.38	0.37	0.226	46.652	0.29	0.276	0.26	0.41	0.33
Py17 (301)	3A	0.255	57.33	0.45	0.31	0.42	0.46	0.13	51.81	0.41	0.161	44.758	0.27	0.063	0.24	0.44	0.41
SACH44 (338)	3A	0.28	49.34	0.5	0.4	0.4	0.5	0.161	60.53	0.39	0.156	42.14	0.089	0.2	0.26	0.41	0.37
SWT6 (339)	3A	0.29	46.44	0.45	0.41	0.41	0.42	0.1	56.49	0.36	0.156	41.894	0.19	0.121	0.24	0.45	0.26
ZUP c2 (268)	3A	0.265	56.91	0.43	0.34	0.45	0.46	0.21	50.4	0.41	0.146	39.312	0.29	0.098	0.25	0.42	0.4

*Programs employed only if unfit for standard protein prediction tools. †Yellow highlighted cells represent the highest confidence prediction.

§This is a condensed version of this table. The full version and all supplementary data is available online at: https://www.mdpi.com/2218-273X/14/1/62 and https://www.mdpi.com/article/10.3390/biom14010062/s1 .

Table 3-S4. *Curated functional annotations of grapevine fanleaf virus (GFLV) proteins through D-I-TASSER predictions of protein structure displayed alongside sequence dependent prediction software Motif Search (https://www.genome.jp/tools/motif/) **and ScanProsite** (Expassy, Swiss Insititute of Bioinformatics). Any annotation included by previous literature is included for convenient comparisons. Predicted molecular function (MF), biological functions (BF), and cellular compartment (CC) from COFACTOR (Zhang et al. 2017), a native protein function prediction tool to the D-I-TASSER server.

---

*This table and all supplementary data is available online at:
https://www.mdpi.com/2218-273X/14/1/62 and
https://www.mdpi.com/article/10.3390/biom14010062/s1 .

Table 3-S5. Prediction table of subcellular localization of proteins encoded by grapevine fanleaf virus strain F13 and GHu and satRNAs. Five programs (LOCALIZER 1.0.4, TargetP, SignalP, Plant mSubP, and MultiLoc2) were used for this prediction. Those that had no prediction are shown as "-". Those that had prediction probability of ≥ 0.7 are highlighted in orange while those with probability of ≥ 0.8 are highlighted in yellow. §TargetP and SignalP are reported in the same column.

Strain	Protein	LOCALIZER	Target P§	Plant mSubP		MultiLoc2		
				First	Second	First	Second	Third
F13	1A^{VSR}	Nucleus	-	Cytoplasm (29%)	Plastid (26%)	Nuclear (48%)	Cytoplasmic (38%)	Mitochondrial (7%)
	1B$^{Hel*/VSR}$	-	-	Cytoplasm (27%)	Cell membrane (24%)	Cytoplasmic (51%)	Nuclear (38%)	Mitochondrial (5%)
	1C^{VPg}	80 (Other) / 20 (Signal Peptide)		-		Cytoplasmic (66%)	Peroxisomal (11%)	Plasma membrane (5%)
	1D^{Pro}	-	-	Cytoplasm (28%)	Cell membrane (20%)	Cytoplasmic (89%)	Peroxisomal (6%)	Nuclear (4%)
	1E$^{Pol*/Sd}$	-	-	Cell membrane (26%)	Plastid (19%)	Cytoplasmic (84%)	Nuclear (13%)	Peroxisomal (2%)
	2A$^{HP/Sd}$	-	-	Golgi (36%)	Nucleus (23%)	Mitochondrial (80%)	Cytoplasmic (12%)	Peroxisomal (4%)
	2B^{MP}	-	-	Plastid (73%)	Nucleus (12%)	Cytoplasmic (78%)	Peroxisomal (10%)	Nuclear (7%)
	2C$^{CP/Td}$	-	-	Plastid (32%)	Extracellular (18%)	Nuclear (53%)	Cytoplasmic (26%)	Mitochondrial (10%)
GHu	1A^{VSR}	Nucleus	-	Cytoplasm (33%)	Plastid (32%)	Nuclear (48%)	Cytoplasmic (41%)	Mitochondrial (5%)
	1B$^{Hel*/VSR}$	-	-	Cytoplasm (19%)	Cell membrane (16.2%)	Cytoplasmic (43%)	Nuclear (32%)	Mitochondrial (17%)
	1C^{VPg}	80 (Other) / 20 (Signal Peptide)		-		Cytoplasmic (66%)	Peroxisomal (11%)	Plasma membrane (5%)
	1D^{Pro}	-	-	Cytoplasm (21%)	Plastid (17%)	Cytoplasmic (87%)	Peroxisomal (6%)	Nuclear (4%)
	1E$^{Pol*/Sd}$	-	-	Nucleus (26%)	Peroxisome (14%)	Cytoplasmic (83%)	Nuclear (14%)	Peroxisomal (2%)
	2A$^{HP/Sd}$	-	-	Plastid (28%)	Nucleus (26%)	Mitochondrial (76%)	Cytoplasmic (15%)	Peroxisomal (4%)
	2B^{MP}	-	-	Plastid (69%)	Nucleus (17%)	Cytoplasmic (60%)	Mitochondrial (10%)	Nuclear (10%)
	2C$^{CP/Td}$	-	-	Extracellular (22%)	Cell membrane (20%)	Nuclear (57%)	Cytoplasmic (23%)	Mitochondrial (5%)
SACH44	3A$^{?}$	-	-	Plastid (70%)	Nucleus (17%)	Mitochondrial (32%)	Nuclear (25%)	Chloroplast (24%)
CO2.A17d	3A$^{?}$	-	-	Plastid (86%)	Nucleus (7%)	Chloropast (49%)	Nuclear (24%)	Cytoplasmic (14%)
Py17	3A$^{?}$	-	-	Plastid (43%)	Nucleus (28%)	Mitochondrial (52%)	Nuclear (18%)	Cytoplasmic (17%)
SWT6	3A$^{?}$	-	-	Plastid (76%)	Nucleus (9.4%)	Cytoplasmic (39%)	Nuclear (34%)	Chloroplast (10%)
F13	3A$^{?}$	-	-	Nucleus (63%)	Plastid (18%)	Cytoplasmic (37%)	Chlorplast (27%)	Nuclear (14%)
LR 4/29	3A$^{?}$	-	-	Nucleus (65%)	Plastid (8%)	Chloropast (35%)	Cytoplasmic (24%)	Nuclear (20%)
Zup 1/4-c2	3A$^{?}$	-	-	Nucleus (30%)	Plastid (12%)	Cytoplasmic (51%)	Nuclear (32%)	Chloroplast (7%)
REF KE1 10/2	3A$^{?}$	-	-	Nucleus (40%)	Plastid (20%)	Cytoplasmic (55%)	Nuclear (31%)	Mitochondrial (6%)

Table 3-S6. Nucleotide binding-site prediction table based on NsitePred (Chen et al. 2012).§

Protein	ATP	ADP	AMP	GTP	GDP
F13 1A^{VSR}	4	0	0	4	5
GHu 1A^{VSR}	4	1	0	3	5
F13 1B$^{Hel*/VSR}$	12	14	3	9	9
GHu 1B$^{Hel*/VSR}$	12	13	5	8	9
F13 1D^{Pro}	4	3	3	3	0
GHu 1D^{Pro}	7	3	2	2	0
F13 1E$^{Pol*/Sd}$	14	11	7	21	11
GHu 1E$^{Pol*/Sd}$	15	12	6	17	11
F13 2A$^{HP/Sd}$	4	0	0	2	2
GHu 2A$^{HP/Sd}$	2	1	0	1	1
F13 2B^{MP}	15	2	2	9	6
GHu 2B^{MP}	11	1	2	8	6
F13 2C^{CP}	8	9	2	4	4
GHu 2C^{CP}	10	8	2	5	5
CO2_A17d 3A$^{?}$	6	1	7	3	3
F13 3A$^{?}$	4	0	0	4	5
LR4/29 3A$^{?}$	4	3	3	0	0
Py17 3A$^{?}$	7	1	5	0	2
REFKE1 3A$^{?}$	4	1	4	0	0
SACH44 3A$^{?}$	3	0	7	2	0
SWT6 3A$^{?}$	6	0	8	2	0
Zup 3A$^{?}$	4	2	5	0	0

§This is a condensed version of this table. The full version and all supplementary data is available online at: https://www.mdpi.com/2218-273X/14/1/62 and https://www.mdpi.com/article/10.3390/biom14010062/s1 .

Table 3-S7. Binding site prediction encoded by grapevine fanleaf virus proteins according to prediction modeling and previously reported findings. Model that gave the highest confidence score for protein structure prediction was chosen for each protein.

Strain (model used/reference)	Protein name	Binding target	Binding sites	Total
F13 (C-I-TASSER)	$1A^{VSR}$	ATP (a)	C12, T13, G14, K15, F17, Q93, E96, V98, V99, Q100, P103, P104, A105, D106, I107, S122, K269	17
GHu (C-I-TASSER)	$1A^{VSR}$	ATP (a)	Q100, Y101, G102, P103, P104, A105, D106	7
F13 (D-I-TASSER MTD)	$1B^{Hel*/VSR}$	ATP (a)	S367, Q368, S369, G370, K371, T372, I373	7
GHu (D-I-TASSER MTD)	$1B^{Hel*/VSR}$	ATP (a)	Q368, S369, K371, T372, T373	5
F13 (Margis and Pinck 1992)	$1D^{Pro}$	Protein (b)	H43, E87, L197	3
F13 (D-I-TASSER MTD)	$1E^{Pol*/Sd}$	ATP (a)	K197, L201, K205, R212, L213, F214, Y275, K276, A277, F278, D279, S334, D378	13
GHu (D-I-TASSER MTD)	$1E^{Pol*/Sd}$	ATP (a)	K197, L201, K205, R212, L213, F214, Y275, K276, A277, F278, D279, S334, N343, G377, D378	15
F13 (D-I-TASSER TM)	$2A^{HP/Sd}$	ATP (a)	F4, Y5, Y6, Y9, Q41, S61, W62, K63, V64, G65, S66	11
GHu (Robetta)	$2A^{HP/Sd}$	ATP (a)	R51, R184	2
F13 (AlphaFold2)	$2B^{MP}$	ATP (a)	R37, Y170, G171, H172, A233, I234, S235, V236, G237, T238, P278, E279, G280	13
GHu (AlphaFold2)	$2B^{MP}$	ATP (a)	Q48, P83, L85, R86, D107, I150, R194, A233, I234, S235, V236, T238, R249, T250, V251, A252, S253	17
F13 (D-I-TASSER MTD)	$2C^{CP/Td}$	ATP (a)	E38, V223, R293, E411, F412, P490, R491, F494	8
GHu (D-I-TASSER MTD)	$2C^{CP/Td}$	ATP (a)	D27, L202, A387, E411, E412	5

Table 3-S8. Prediction table of transmembrane domains/helices and/or pore-lining domains, encoded by proteins of grapevine fanleaf virus strain F13 and GHu and satRNAs. Six programs (MembraneFold, DeepTMHMM, Splot 4.0, Phobius, MEMSTAT3, and Phyre2) were used to predict amino acid residues that are part of the transmembrane domains/helices. Those that show no transmembrane domains/helices and/or pore-lining domains are indicated by "-". The predicted transmembrane domains/helices amino acid residues that overlapped from two or more programs are shown under "Overlap" column.

Strain	Protein	Split 4.0	Phobius	MEMSAT3	Phyre2	Overlap
F13	$1A^{VSR}$	-	-	360-375	-	-
F13	$1B^{Hel*/VSR}$	26-43 102-123 127-154 750 -779 785-801	102-121 127-151 752-769 775-794	55-70, 94-119, 123-152, 156-171, 220-250, 754-783	101-128 132-152 191-220 231-251 750-780	102-119 132-151 754-779
F13	$1C^{VPg}$	-	-	-	-	-
F13	$1D^{Pro}$	179-200	-	16-31	-	-
F13	$1E^{Pol*/Sd}$	-	-	213-236, 311-329, 333-356, 640-655	-	-
F13	$2A^{HP/Sd}$	-	-	236-251	-	-
F13	$2B^{MP}$	-	-	184-199	-	-
F13	$2C^{CP/Td}$	239-255	-	51-70, 222-251	-	239-254
GHu	$1A^{VSR}$	-	-	360-375	-	-
GHu	$1B^{Hel*/VSR}$	25-44 92-116 121-151 159-173 750-776	98-118 130-151 752-772	97-127 131-161 220-250 753-782	96-118, 122-152, 160-175, 192-220, 227-251, 752-782	96-116 131-151 753-776
GHu	$1C^{VPg}$	-	-	-	-	-
GHu	$1D^{Pro}$	179-200	-	16-31	-	-
GHu	$1E^{Pol*/Sd}$	-	-	213-236, 311-329, 336-356, 655-640	342-357 641-656	342-356
GHu	$2A^{HP/Sd}$	-	-	237-252	-	-
GHu	$2B^{MP}$	-	-	184-199	-	-
GHu	$2C^{CP/Td}$	238- 254	-	51-70, 222-251	-	238-251
CO2.A17d	$3A^{?}$	-	-	18-33	-	-
F13	$3A^{?}$	-	-	18-33	-	-
LR 4/29	$3A^{?}$	-	-	215-230	-	-
Py17	$3A^{?}$	-	-	248-263	-	-
REF KE1 10/2	$3A^{?}$	-	-	215-230	-	-
SACH44	$3A^{?}$	-	-	18-33	-	-
SWT6	$3A^{?}$	-	-	18-33	-	-
Zup 1/4-c2	$3A^{?}$	-	-	215-230	-	-

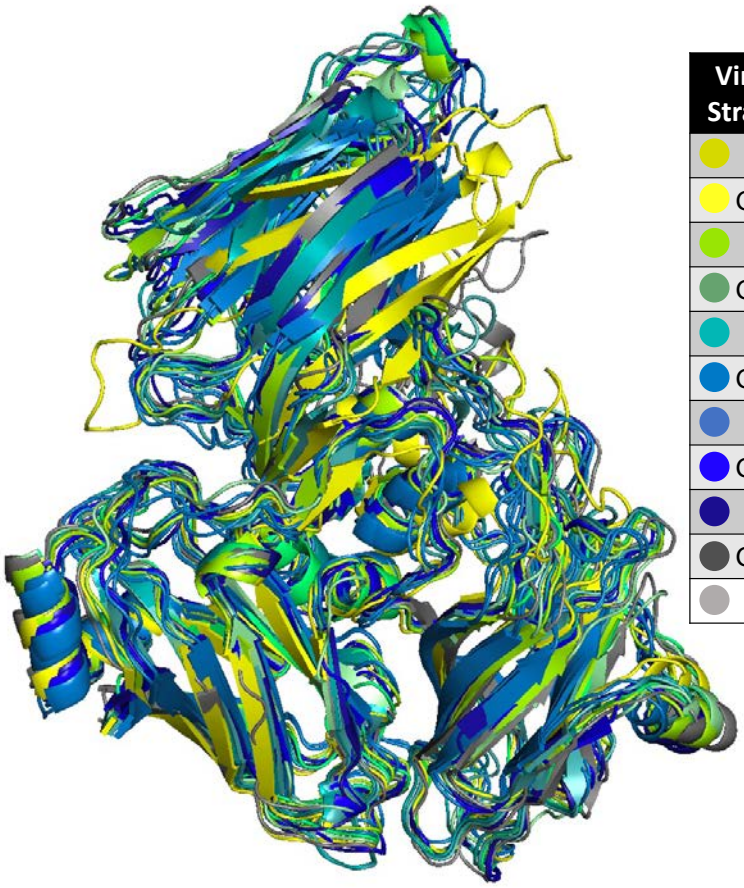

Viral Strain	Prediction Software	RMSD
F13	AlphaFold2	1.810
GHu	AlphaFold2	3.718
F13	D-I-TASSER	1.641
GHu	D-I-TASSER	1.432
F13	ESM	1.825
GHu	ESM	1.862
F13	Robetta	19.773
GHu	Robetta	14.505
F13	trRosetta	1.610
GHu	trRosetta	1.553
	PDB:5FOJ	

Figure 3-S1. Grapevine fanleaf virus coat protein predictions align well with already resolved crystalline structure PDB:5FOJ (Orlov et al. 2020).

File 3-S1. Protein data bank (.pdb) formatted files for grapevine fanleaf virus proteins generated with AlphaFold2, C-I-TASSER, D-I-TASSER (MTD), ESMFold, Robetta, and trRosetta. Associated metadata and accompanying data is presented in the same form as received from each program.

This file is available online at: https://www.mdpi.com/2218-273X/14/1/62 and https://www.mdpi.com/article/10.3390/biom14010062/s1.

CHAPTER 4

PROFILING PLANT PROTEOME AND TRANSCRIPTOME CHANGES DURING GRAPEVINE FANLEAF VIRUS INFECTION[4]

ABSTRACT

Viruses can elicit varying types and severities of symptoms during plant host infection. We investigated changes in the proteome and transcriptome of *Nicotiana benthamiana* plants infected by grapevine fanleaf virus (GFLV) with an emphasis on vein clearing symptom development. Comparative, time-course liquid chromatography tandem mass spectrometry and 3' ribonucleic acid sequencing analyses of plants infected by two wildtype GFLV strains, one symptomatic and one asymptomatic, and their asymptomatic mutant strains carrying a single amino acid change in the RNA-dependent RNA polymerase (RdRP) were conducted to identify host biochemical pathways involved in viral symptom development. During peak vein clearing symptom display at 7 days post-inoculation (dpi), protein and gene ontologies related to immune response, gene regulation, and secondary metabolite production were overrepresented when contrasting wildtype GFLV strain GHu and mutant GHu-1E$_{K802G}^{Pol}$. Prior to the onset of symptom development at 4 dpi and when symptoms faded away at 12 dpi, protein and gene ontologies related to chitinase activity, hypersensitive response, and transcriptional regulation were identified. This systems biology approach highlighted how a single amino acid of a plant viral RdRP mediates changes to the host proteome

(~1%) and transcriptome (~8.5%) related to transient vein clearing symptoms and the network of pathways involved in the virus-host arms race.

[4]This chapter has been published: Roy, B. G., DeBlasio, S., Yang, Y., Thannhauser, T., Heck, M., and Fuchs, M. 2023. Profiling plant proteome and transcriptome changes during grapevine fanleaf virus infection. J. Proteome Res. 22:1997-2017.

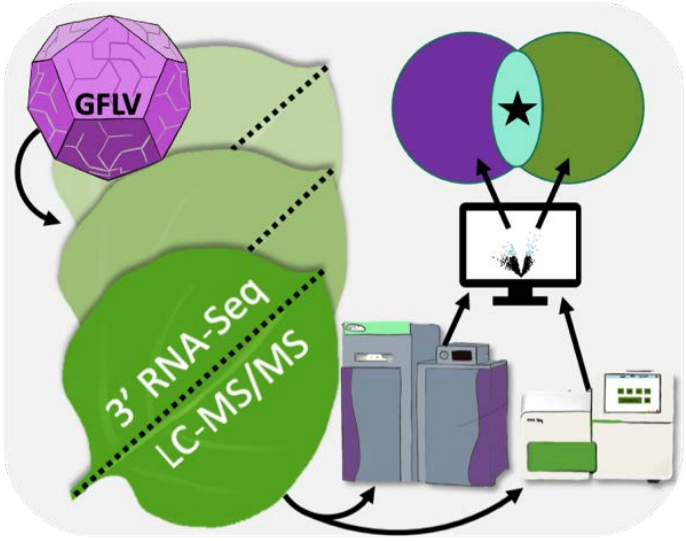

TOC Figure 4-0. Leaf tissue of *Nicotiana benthamiana* was used in comparative transcriptomic and proteomic analyses after infection with two wildtype and two mutant grapevine fanleaf virus strains that differ in disease development patterns. Differentially abundant transcripts and proteins were contrasted for biological relevance, providing a list of targets potentially involved in vein-clearing symptomatology.

INTRODUCTION

Viruses induce targeted changes to host cells to facilitate replication, movement, and propagation. Plant viruses elicit host responses that primarily occur through protein–protein (i.e., pattern-recognition receptors and pathogen-associated molecular pattern), RNA-protein (i.e., host RNA binding proteins and viral silencing pathways), or protein-lipid interactions (i.e., membrane-anchored receptors and cross-membrane signaling) [Xu *et al.* 2010, Di Carli *et al*. 2012, Osterbaan *et al*. 2019, Zanardo *et al*. 2019]. Selection has favored the evolution of a network of pathways for viral detection and suppression, typically starting with immune receptors and co-receptors (Calil and Fontes 2017, Gouveia *et al*. 2017). Likewise, selection has favored the evolution of viral proteins to combat these defense mechanisms by interfering at the host RNA or protein level to diminish plant responses (Bivalkar-Mehla et al. 2011). Common host targets by viruses are regulators of transcription and translation, small molecule/hormone pathways, and the antiviral pathways of RNA silencing. Host changes induced by viruses can be quantified at various levels, with most studies examining the differential abundance of transcripts or proteins within biological samples.

Multi-layered systems biology approaches have been performed to decipher virus–host interactions at the levels of genome, transcriptome, proteome, and the metabolome. For example, coupled proteomic–transcriptomic analyses have been used to study the infection of human and zoonotic viruses such as influenza A virus (H1N1) and severe acute respiratory syndrome coronavirus-2 (Zhang et al. 2009, Davidson et al. 2020). Similarly, comparative proteomics and transcriptomics have been used to advance our understanding of virus infections in plant hosts such as mungbean yellow

mosaic India virus (MYMIV) in soybean (Pavan Kumar et al. 2017), potato virus Y (PVY) in potato (Stare et al. 2017), sugarcane mosaic virus (SCMV) in sugarcane (Akbar et al. 2021), and turnip mosaic virus (TuMV) in cabbage (Lyu et al. 2020). For MYMIV, host genes related to stress response, metabolism, and resistance were found to be critical for symptomatic infection (Pavan Kumar et al. 2017). For PVY, photosynthesis-related genes were most impacted at both protein and transcript levels (Stare et al. 2017). Viruses have elegant mechanisms to reprogram their host for replication, and under certain conditions, these changes result in disease symptom development. The genome of a virus is significantly smaller than that of their host (approximately 500–5000 times over), indicating that multi-functional virus proteins are efficiently encoded for optimal infection and survival (Chavez et al. 2012). Furthermore, viruses encode proteins to combat host defense pathways aimed to clear viral infection. Despite tremendous progress, our understanding of viral–host interactive pathways and downstream effects in plants is still limited.

Using two or more omics techniques rather than a single omics approach has higher confirmatory value for the identification of host factors involved in functional virus–host interactions. Respectively, mass spectrometry (MS) and ribonucleic acid sequencing (RNA-Seq) are quantitative methodologies for providing insights into the changes that occur within the plant host proteome and transcriptome in response to infection. Perturbations in the relative abundance of proteins and transcripts can allude to specific host pathways and networks behind biological processes that are involved, ultimately deepening our understandings of viral infections (Hasin et al. 2017). Of note are key steps of viral pathogenesis and gene regulatory networks that contribute to

disease symptom development negatively affecting plant health. For example, many pathways utilized by viruses for replication are well-documented to contribute to symptomology, but the exact mechanisms that perturb plant cellular functions remain unresolved (Alexander and Cilia 2016). Using multiple omics techniques to quantify differentially abundant genes/proteins is a powerful approach to determine how these changes are critical for permissive host–pathogen interactions and disease development. If a mechanism is defined, efforts can then be tailored to disrupt the molecular interactions, thereby avoiding disease symptoms and curbing the negative impacts of viruses and other pathogens. In addition, tools such as genome assemblies, reverse genetics, more advanced sequencing technologies, and computational power have been integral to explore large datasets across multi-omics approaches for informing viral infections (Tang et al. 2022).

Grapevine fanleaf virus (GFLV) is the most devastating virus of grapevine (Andret-Link et al. 2004, Maliogka et al. 2015). This virus causes severe yield losses (up to 80%) and substantially reduces the productive lifespan of vineyards. GFLV is a representative member of the species *Nepovirus GFLV* in the genus *Nepovirus* of the family *Secoviridae* (Fuchs et al. 2022). Its genome consists of two RNA molecules, each encoding a polyprotein that is proteolytically cleaved by the RNA1-encoded proteinase $1D^{Pro}$ into eight mature proteins (Figure 4-1A) [Morris-Krsinich et al. 1983]. GFLV can be mechanically transferred to herbaceous hosts such as *Nicotiana benthamiana* on which distinct symptoms can develop (Roy and Fuchs 2022). Host responses and cellular reprogramming that are induced during GFLV infection, particularly for symptom development, remain largely unknown. Current hypotheses attribute symptom

eliciting responses to the GFLV RNA1-encoded RNA-dependent RNA polymerase (RdRP, protein $1E^{Pol)}$ interacting with host components via protein–protein interactions (Osterbaan et al. 2021). Previous attempts at identifying host proteins associated with GFLV $1E^{Pol}$ were performed by affinity-purification MS using infectious clones carrying a V5 epitope-tagged $1E^{Pol}$ (Osterbaan et al. 2021). Several host protein candidates were found to complex with GFLV $1E^{Pol}$; however, a large gap remains for understanding how GFLV mechanistically elicits symptoms in infected plant hosts (Osterbaan et al. 2021).

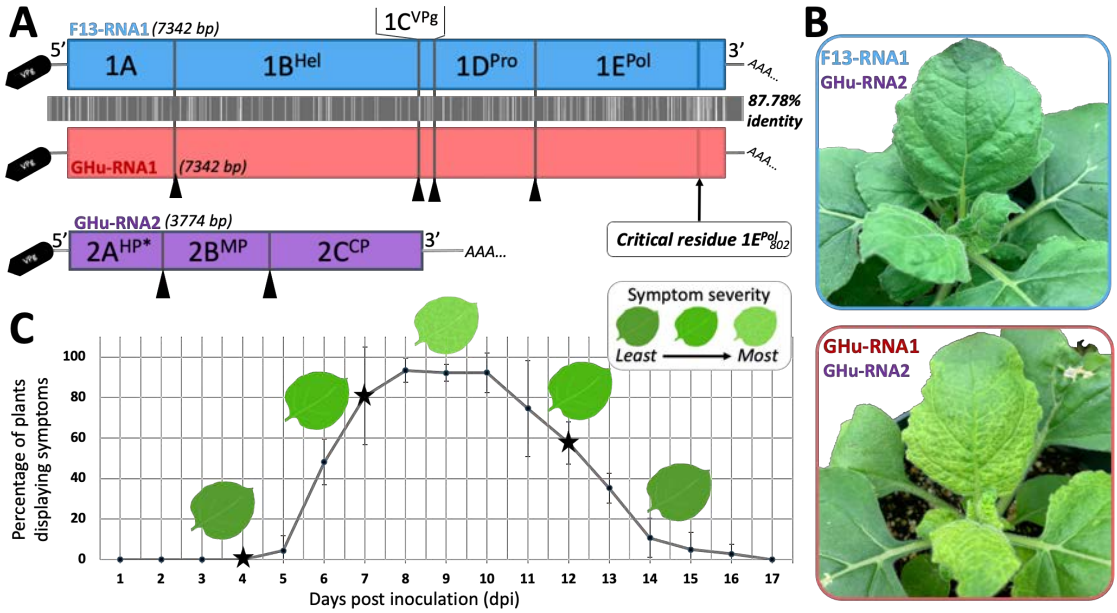

Figure 4-1. Grapevine fanleaf virus (GFLV) genetic composition and symptom expression in *Nicotiana benthamiana*. (A) Simplified schematic of the structure and expression of RNA1 of wildtype GFLV strains F13 (blue) and GHu (red), and RNA2 of wildtype GFLV strain GHu (purple). The viral genome-linked protein VPg is shown at the 5' end of the RNA molecules and the polyadenylated tail at the 3'end, respectively. Untranslated 5' and 3' regions are shown as horizontal gray bars. Vertical gray lines represent proteolytic cleavage sites as processed by RNA1-encoded proteinase $1D^{Pro}$. The nucleotide identity of 87.78% between the two GFLV RNA1s is depicted by the projection in gray created using Jalview v2.11.2.2. Critical amino acid residue $1E^{Pol}_{802}$ for vein clearing symptoms is highlighted by an arrow and colored vertical line on RNA1 molecules. **(B)** GFLV-infected *Nicotiana benthamiana* plants at seven days post inoculation (dpi) with asymptomatic wildtype strain F13 (top) and symptomatic wildtype strain GHu (bottom) causing a stark vein clearing phenotype. Plants infected with mutant GFLV-GHu $1E^{Pol}_{K802G}$ appear identical to asymptomatic plants infected with GFLV-F13. (Image editing: individual plants are shown after removal of the growth chamber background and other plants nearby). **(C)** Symptom expression of wildtype GFLV strain GHu in infected *Nicotiana benthamiana* over time. Apical leaves observed across three cohorts of plants (n_1=23, n_2=48, n_3=15) for vein clearing symptoms were rated on a binary scale (1=symptomatic, 0=asymptomatic). GFLV symptoms emerged in a few inoculated plants as early as 4-6 days-post-inoculation (dpi), most plants expressed symptoms at 7-10 dpi, and all plants fully recovered by 17 dpi. The average percent of symptomatic plants in three trials is shown with standard deviations as error bars. Severity of symptoms is diagramed as representative leaf drawings above the plotted line, while the legend shows from darker to lighter the progression of vein-clearing. The three time points used for tissue collection for transcriptomics and proteomics work are indicated with a star.

Powerful biological tools are available to study how GFLV elicits symptoms in plants using ‘omics approaches. First, *N. benthamiana* sustains systemic GFLV infection with different virus strains and mutants that vary in their ability to elicit symptoms (Vigne et al. 2013, Osterbaan et al. 2019). For example, GFLV strain GHu induces vein clearing symptoms on apical leaves of *N. benthamiana*, while strain F13 remains asymptomatic (Figure 4-1B) [Vigne et al. 2013]. A single amino acid in position 802 of GFLV-GHu $1E^{Pol}$ is critical for manifestation of vein clearing symptoms, which are transient and accompanied by a progressive host recovery within 2 weeks or less without clearing viral infection (Vigne et al. 2013). Second, the genome of *N. benthamiana* is sequenced and well-annotated (Bombarely *et al.* 2012); thus, this model herbaceous plant is ideal for conducting transcriptomics and proteomics studies to identify host factors involved in virus infection (Bombarely et al. 2012). We hypothesized that contrasting transcript/protein expression profiles between wildtype GFLV strain GHu and its single amino acid mutant GHu $1E_{K802G}^{Pol}$ in the RdRP coding region (Osterbaan et al. 2019) would allow us to pinpoint key cellular pathways putatively involved in vein clearing symptom development. In this study, we leveraged the unique features of GFLV *in planta* to test this hypothesis using parallel tandem liquid chromatography MS (LC–MS/MS) and 3′RNA-Seq analyses for profiling changes in the proteome and transcriptome of infected *N. benthamiana* over time. Our analyses revealed a short list of gene candidates that were cross-validated through both proteomics and transcriptomics, showing unique interactions of GFLV strain GHu with host components to elicit vein clearing symptoms, different from gene-for-gene or phytohormone-activated pathways most identified in plant–pathogen interactions.

Furthermore, these data showed that the change in regulatory networks was most prevalent at peak symptom development, not before nor after.

EXPERIMENTAL SECTION

Plant Material

Seeds of *N. benthamiana* were sown in "Cornell" LM-2 potting mix and transplanted 16 days after sowing into individual 3″ diameter pots. Plants were maintained in a controlled growth chamber at 25 °C and a 16:8 light/dark cycle at 70% *relative humidity.*

GFLV Strains

Four GFLV strains were used in this study: wildtype strains GHu and F13 and mutant strains GHu-1E$_{K802G}^{Pol}$ and F13-1E$_{G802K}^{Pol}$ (Vigne et al. 2013, Osterbaan et al. 2019). The bipartite genomic RNAs of wildtype strains GHu and F13 are sequenced. They share 87.78% nucleotide identity (Figure 4-1A). The mutant strains used in this study, GHu-1E$_{K802G}^{Pol}$ and F13-1E$_{G802K}^{Pol}$, differ from their wildtype strains at a single amino acid of the RdRP in position 802 with a K to G mutation for mutant GHu and a G to K mutation for mutant F13 (Figure 4-1A, arrow) [Osterbaan et al. 2019]. Infectious cDNA clones of these four GFLV strains in binary plasmid pCLEAN-G181 for *Agrobacterium tumefaciens*-mediated delivery *in planta* were used as previously described (Osterbaan et al. 2019).

Mechanical Inoculation of N. benthamiana *with GFLV*

For mechanical inoculation, leaf tissue of *N. benthamiana* plants infected with one of the four GFLV strains was macerated in inoculation buffer (0.15 M KH_2PO_4, 0.35 M Na_2HPO_4, pH 7.0) with carborundum powder by mortar and pestle. The crude sap inoculum was rubbed onto the two primary leaves of the plants at the six-leaf developmental stage (4 weeks post-germination), and carborundum was immediately rinsed off with ddH_2O.

A cohort of 75 *N. benthamiana* plants was divided into 5 groups of 15 plants each and inoculated with one of the following viral treatments: wildtype GFLV strain GHu, wildtype GFLV strain F13, GFLV mutant GHu $1E_{K802G}^{Pol}$, GFLV-F13 mutant $1E_{G802K}^{Pol}$, and inoculation buffer supplemented with carborundum as the mock control. Mock control plants were used to account for induced wounding response of the host following mechanical inoculation. These plant groups served as the five treatment categories for the proteomics and transcriptomics analysis.

GFLV-GHu Symptomology Observations

Three cohorts of *N. benthamiana* plants (n_1 = 23, n_2 = 48, and n_3 = 15) were inoculated with wildtype GFLV strain GHu, group n_3 belonging to the transcriptomics and proteomics experiments. Vein clearing symptoms (Figure 4-1B, bottom) were observed daily in the apical leaves over a 16-day period until plants fully recovered. Symptoms were rated on a binary scale (0 = asymptomatic, 1 = symptomatic). All inoculated plants were tested in duplicate 17 days post-inoculation (dpi) via double-antibody sandwich enzyme-linked immunosorbent assay (DAS-ELISA) with specific

GFLV antibodies following the manufacturer's recommendations (Bioreba, Reinach, Switzerland). Samples were tested with the positive control, buffer control, and GFLV-free samples in duplicate per 96-well microtiter plate. Only plants that tested positive for GFLV in DAS-ELISA were considered for symptomology recordings.

Leaf Tissue Collection for Proteomics and Transcriptomics Analyses

Preliminary pilot studies documented detectable GFLV in apical tissue at the protein and transcript levels using LC–MS/MS of protein tissue extracts and reverse transcription (RT) polymerase chain reaction (PCR) with specific primers (Osterbaan et al. 2019), respectively, by the fourth dpi (data not shown). Based on these results, apical tissue of *N. benthamiana* was collected at three time points following inoculation (4, 7, and 12 dpi). One leaf was removed per plant at each collection, and five 1.0 cm hole punches were taken per leaf from three leaves of the same treatment and time point. The resulting 15 leaf discs were pooled into a 2.0 mL Eppendorf tube. This was repeated five times for each treatment, resulting in five biological replicates per treatment for each time point. This was mirrored for the two 'omics techniques, as leaf discs were taken from the left or right side of leaves and placed into a microfuge tube for protein or RNA extraction, respectively. This resulted in 150 leaf tissue collections in total, including 75 for RNA isolation and 75 for protein isolation (Figure 4-S1). All tissue was flash-frozen in liquid nitrogen and kept at −80 °C until further processing.

Total RNA Purification and 3'-RNA Sequencing

Total RNA was purified from *N. benthamiana* leaf tissue using an adapted protocol from the Omega E.Z.N.A Plant RNA Mini Kit (cat no. R6827), treated with

DNAse I and filtered using RNA Clean & Concentrator (Zymo Research, cat no. R1013). An elution volume of 90 µL provided RNA concentrations above 200 ng/µL. RNA quantity and integrity were analyzed using an Agilent 2100 Bioanalyzer with RNA Nano Kits (part no. 5067-1511). Library sequencing was performed at the Cornell Institute of Biotechnology (Ithaca, NY, USA) using Illumina NextSeq500 technology (Illumina, CA, USA) with single end, 1 × 86 bp reads.

Transcriptomics Data Processing

Following Illumina sequencing, adapter sequences were trimmed using Trimmomatic (v0.39) [Bolger et al. 2014] and the quality of reads was analyzed using FastQC (v0.11.9) [Andrews 2010]. Sequence alignments were performed by creating a reference library using HiSat2 (Kim et al. 2019) and the *N. benthamiana* (v1.0.1) draft genome assembly (Bombarely et al. 2012) from Sol Genomics at the Boyce Thompson Institute (Ithaca, NY). Annotated sequences that contained the descriptor "gene" were extracted using FeatureCounts (v0.11.9) [Liao et al. 2014] from Subread (v2.0.1) [Liao et al. 2013]. Sequence alignments were also performed against a curated genome collection of GFLV isolates and manually entered mutations for strains that were used in this study to capture polyadenylated viral RNA. Mapped sequence reads were then extracted and exported as a data matrix.

The following data processing steps were performed in RStudio (v4.1.3). Count files were parsed and merged into a single count matrix, and a corresponding metadata file was created to perform differential sequence analyses with the package DESeq2 (v1.32.0) [Love et al. 2014]. DESeq2 model construction followed the methodical and classical approach of using the treatment and time point as explanatory factors.

However, this attempt resulted in poor explanation of variance. Therefore, a new factor for the model that considers treatment, time, and their interaction was created and named "group". This new model served for full-scale experiment-wide comparisons. Treatment comparisons were thereafter generated using only models per time point and never included samples from other time points. A matrix containing the counts per gene before normalization can be found on the GitHub page. Raw data files can be accessed through the NCBI database, Bioproject: PRJNA838211.

Total Protein Isolation and Liquid Chromatography Tandem MS Analysis

Total protein extractions were performed on mirrored *N. benthamiana* leaf samples to RNA extractions (Figure 4-S1). This protocol was adapted from original methods previously described (Cilia et al. 2009, Ramsey et al. 2020) with the following two modifications: First, *N. benthamiana* tissue was macerated with steel BBs in 2 mL centrifuge tubes following flash freezing in liquid nitrogen. Second, addition of 1 mL of working solution (10% trichloroacetic acid—TCA, 2% β-mercaptoethanol in acetone) to each sample was followed by probe sonication for cell lysis and membrane disruption. Samples were then incubated in an ethanol dry ice bath for at least 1 h and centrifuged to isolate insoluble proteins. The supernatant was removed and discarded, and the pellet was washed with 500 µL of pure acetone three times followed by centrifugation. The pellets were dried completely for 30 min and then were stored at −80 °C for further processing.

The protein-containing pellets were resuspended in 150 µL of 7 M urea/100 mM ammonium bicarbonate and kept on ice. Micromagnetic stir bars (Fisherbrand, Cat. no. 14-513-57) were added, and pellets were left to stir overnight at 4 °C. Resuspended

proteins were subject to a Bradford assay using bovine serum albumin (CAS: 9048-46-8) to obtain a standard curve. Equal protein concentrations were utilized to standardize protein loading amounts for sodium dodecyl sulfate-polyacrylamide gel electrophoresis (SDS-PAGE) on gradient (4–20%) Mini-PROTEAN© TGX (BIO-RAD, no. 4561096) precast protein gels for visualization of protein integrity and concentration uniformity.

Based on calculated concentrations from the Bradford analysis and gel electrophoresis, 100 µg of protein per sample was used for further processing. Reduction and cysteine blocking of proteins were performed with tris(2-carboxyethyl)phosphine and methyl methanethiosulfonate, for 1 h at 30 °C and 1 h at room temperature, respectively. Proteins were digested using ≥99.9% sequencing-grade modified trypsin (Promega, no. V5117) for 16 h at 30 °C while being agitated at 450 rpm. Peptides were subject to reverse-phase silica Sep-Pak column clean up (Waters, SKU: 186004618) and then dried via VacuFuge (Labconco Centrivap, Cat. no. 78100-00-C) evaporation. One sample was lost during the digestion step due to a handling error (wildtype GFLV-F13 at 12 dpi, biological replicate no. 1).

The nano-LC–MS/MS analysis was carried out using a Q Exactive (Thermo Fisher Scientific, San Jose, CA) mass spectrometer equipped with a nanospray ion source and coupled with the EASY-nLC (Thermo Fisher Scientific, San Jose, CA). Each peptide sample was reconstituted in 100 µL of 0.1% formic acid. A total of 4 µL for each reconstituted sample was injected onto a NanoViper C-18 RP trap column (3 µm, 75 µm × 20 mm, Thermo Fisher) at a 12 µL/min flow rate for on-line desalting and separated on a NanoViper C-18 RP trap column (2 µm, 0.075 mm × 250 mm, Thermo Fisher). The peptides were eluted in a 90 min gradient of 5–42% of 80% acetonitrile in

0.1% formic acid (elution B) at 300 nL/min, followed by a 2 min ramping to 100% elution B and then being held for 18 min. The Q Exactive is operated in the positive ion mode with nano-spray voltage set at 2.9 kV and source temperature at 250°C. The top 10 precursor ions with >2 changes were selected for the MS2 scan. MS survey scans were taken at a resolving power of 70,000 with a mass range of *m*/*z* 350–1550, AGC = 5×10^5, and Max IT = 50 ms and MS^2 scans at 17,500 resolution with AGC = 1×10^5, Max IT = 110 ms, and with isolation window 2.0 *m*/*z*. All data were acquired under Xcalibur (v4.2.47) operation software and Q Exactive Tune (v2.11 QF1 Build 3006) (Thermo Fisher Scientific). A blank was run between each sample to prevent any carry-over of peptide. One sample did not return any peptide reads (mock inoculated control at 4 dpi, biological replicate no. 3), ultimately providing a total of 73 output files. Each sample was analyzed twice as analytical replicates (A and B) culminating in 146 runs and output files.

Proteomics Data Processing

Raw files obtained from LC–MS/MS (73 samples/146 files total) were converted to .dat files with MSConvert from ProteoWizard (Adusumilli and Mallick 2017). Peptide identification was then performed via Mascot Daemon (v2.5.1) [Perkins et al. 1999] against the previously defined "NibenNepo" database (Osterbaan et al. 2021) with *N. benthamiana*, GFLV, related nepoviruses, potential contaminants, and decoys to return protein abundance for analysis, as performed previously (Osterbaan et al. 2021). Spectral counts were extracted by uploading search results of the 146 outputs into Scaffold Q+ Quantification software (v4.11.1) [Searle 2010] through MudPIT experiments that combined the two technical replicates of each sample into single

biological samples to ease computational constraints. A count matrix was constructed containing gene names, descriptions, and counts for each peptide match to that respective gene per biological replicate for a total of 73 samples (Table 4-S2, File 4-S2). A false discovery rate of 1.0% at both protein and peptide levels, a minimum of two peptides per protein, and standard protein cluster analysis were utilized across all samples. Given that the same amount of trypsin was added to each protein digest, all samples were normalized to the trypsin enzyme spectral counts through the E chain peptide hits [36.3% coefficient of variation (CV)] as in the NibenNepo database (GenBank identifier: 3318722). This matrix was then utilized for differential expression analysis through the "DEP: differential enrichment analysis of proteomics data" pipeline (v1.16.0) [Zhang et al. 2018, Smits and Huber 2022] in RStudio. After normalization and imputation, data was subject to *k*-means clustering and principal component analysis (PCA) to understand the interrelatedness of samples between time points and treatment groups. The designed summarized experiment object was broken into three smaller summarized experiments for differential protein abundance analysis and downstream analysis per time point, as done with the transcriptomics data. The MS proteomics data (reference FASTA, .raw, .dat, MudPIT combined technical mzIdent, and results) have been deposited to the ProteomeXchange Consortium via the PRIDE partner repository with the dataset identifier PCD037185 and 10.6019/PXD037185.

Statistical Analyses of Transcriptomics and Proteomics Data

Transcripts were defined as differentially abundant through the DeSeq2 default Wald Test, where only transcripts meeting adjusted p-value <0.05 and $|\log_2(\text{fold-change})| \geq 1$ were considered. Proteins were considered differentially abundant after

processing with the DEP pipeline using protein-wise linear models and empirical Bayes statistics, meeting the qualifications for highly differentially abundant proteins (DEPs) [p-value <0.05, $|\log_2(\text{fold-change})| \geq 1$] and medium DEPs [$p$-value <0.05, $|\log_2(\text{fold-change})| \geq 0.5$].

Statistical analysis of the viral titer in transcriptomics data was performed using a Kruskal–Wallis ANOVA with a post-hoc Dunnet's test. The viral titer analysis of MS-acquired reads used a Student's *t*-test with a Bonferroni multiple correction (Bonferroni 1936) after normalization to trypsin chain E.

Gene set enrichment analysis (GSEA) was performed on transcripts and proteins passing thresholds of p_{adj}/p_{value} <0.05 and $|\log_2(\text{fold-change})| \geq 1$ and 0.5, respectively. Briefly, a reference was created in gprofiler2 (v0.2.1) [Raudvere et al. 2019, Kolberg et al. 2020] with the entire annotated *N. benthamiana* genome .gff file and gene list comparisons being analyzed for enrichment. The comparison between transcripts for wildtype GFLV strain GHu at 7 dpi and transcripts of all other groups was executed in GSEA (v4.1.0) [Subramanian et al. 2005, Mootha et al. 2003] and network analysis in Cytoscape (v3.8.2) [Shannon et al. 2003]. This analysis was performed to identify transcript gene ontologies (GOs) unique to only plants infected with wildtype GFLV-GHu during symptom expression. Further GSEA contrasts were executed considering time and treatment contrasts of interest, namely, wildtype GFLV-GHu to other treatments at 7 dpi and the two GFLV-F13 strains to other treatments at 4 dpi.

Weighted gene co-expression network analysis (WGCNA) was performed using the WGCNA package (v1.71) [Langfelder and Horvath 2008, Zhang and Horvath 2005] to observe gene clusters with similar expression patterns over time between treatments.

Parameters outside default were maxBlockSize = 10,000; mergeCutHeight = 0.25; minKMEtoStay = 0.3; minModuleSize = 200; and power = 7. The 28 modules created were then assigned to colors and were referred to as ME′color′. Select modules were then exported and analyzed for GO overrepresentation. Specifically, gprofiler2 was used to group and report significant ontology overrepresentation per WGCNA module, representing a unique expression profile over time between treatments. All scripts and required files can be found in the provided GitHub page and can be clarified upon request.

Quantitative Real-Time Polymerase Chain Reaction

To confirm the expression of a gene detected by RNA-Seq but not LC–MS/MS, total RNA samples used for transcriptome analysis were partially thawed on ice and used in the Luna Universal One-Step RT-qPCR Kit (New England Biolabs Inc., no. E3005) with two primer pairs (Nb01478-FWD/REV and FBOX-F/R, Table S1). Samples were loaded in triplicate and analyzed using a BIO-RAD CFX96 Real-Time System/C1000 Touch Thermocycler qPCR with the following cycles: 55 °C for 10 min; 95 °C for 1 min; 40 cycles of 95 °C for 10 s and 60 °C for 30 s; plate read; melt curve from 65–95 °C in increments of 0.5 °C for 5 s at each level; and end incubation at 8 °C. SYBR green fluorescence was measured and compared to that of the housekeeping gene FBOX (Table S1) [Liu et al. 2012]. Target gene expression was normalized through the standard ΔΔCt method from collected Ct data and plotted for each sample using RStudio. Script and data files are available on the GitHub page.

RESULTS

GFLV Infection for Symptom Observation in N. benthamiana *and Tissue Collection*

Apical leaves of all *N. benthamiana* plants (100%, 60 of 60) that were selected for transcriptomics and proteomics analyses tested positive for GFLV in DAS-ELISA using specific antibodies when mechanically inoculated with one of the four virus strains used in this study (Figure 4-S1(1)), revealing systemic infection. None (0%, 0 of 15) of the mock control plants tested positive for GFLV in DAS-ELISA, as expected. Vein clearing symptoms (Figure 4-1B) emerged in apical leaves of plants infected with wildtype GFLV strain GHu at 5–6 dpi (average 44 and 48% of plants, respectively). Symptoms were apparent, showing strong contrast of vein clearing (Figure 4-1B, bottom) in nearly all of the plants (94%) by 7–10 dpi with full plant recovery occurring thereafter (Figure 4-1C). The percentage of plants displaying symptoms from 7 to 10 dpi was on average 81 and 93%, respectively (Figure 4-1C). Consistent with previous reports, vein clearing symptoms never appeared in new foliage after recovery, and none of the other GFLV strains elicited disease symptoms (Vigne et al. 2013, Osterbaan et al. 2019, Osterbaan et al. 2021). To capture the events leading up to vein clearing, peak symptomology, and the start of recovery, three time points of interest were selected at 4, 7, and 12 dpi (Figure 4-1C). Preliminary LC–MS/MS data (not shown here) suggested that GFLV does not replicate to detectable levels in apical tissue until at least 4 dpi and therefore was the earliest time point for consideration.

Proteomic Analysis of N. benthamiana *Leaf Tissue*

Total proteins from the mock control and GFLV-infected *N. benthamiana* leaves were isolated at 4, 7, and 12 dpi and analyzed by LC–MS/MS (Figure 4-S1). A total

report output from Scaffold Q+ was generated to display spectral counts across the entire experiment (Table 4-S2A,B). A summary of the proteome dataset obtained with 73 samples showed an average of 2176 spectral counts per sample (Figure 4-S2A). An average of 1928 spectral counts per sample were obtained after low-count filtering for values missing completely at random. The CV of raw data prior to filtering or normalization was 5.14 and 5.41% after low-count filtering. Most proteins were detected in all samples across the entire experiment, with less proteins unique per sample and a left-handed distribution of intensities (Figure 4-S2B–D). Finally, after imputation and normalization, the CV was 0.78% across all samples.

Low-count filtering removed proteins with low abundance (Figure 4-S2A,B) and reduced near-zero distribution (Figure 4-S3C). Variance-stabilized normalization (vsn) was performed as suggested by the DEP pipeline. This resulted in the dataset shifting from a left-centered distribution to a normalized curve (Figure 4-S3E,F). A large proportion of missing protein identifications was present toward the lower end of spectral counts, indicating that the instrument's detection limit was preventing total coverage of the dataset. This is generally considered to be missing values with a combination of these missing at random (MAR) and missing not at random (MNAR) (Figure 4-S3C,D). Several instances of MNAR appeared when observing the missing values (Figure 4-S4). For this reason, we tested a mixed imputation method after vsn to correct for both MNAR and MAR. We considered the most efficient and comprehensive imputation methods reported in the recent literature (Välikangas et al. 2016, Jin et al. 2021), including the biplot for principal component analysis (bpca) method for MAR and the zero method for MNAR (Figure 4-S5). These methods did not drastically

outperform simple bpca MNAR imputations in terms of hierarchal clustering and Pearson correlation. Therefore, we considered only bpca MNAR to simplify the data processing scheme. The missing values of protein identification were extracted for subsequent analyses. The simplified imputation technique resulted in an average of 2165 protein gene IDs per sample. Results showed the proteomic samples grouping by treatment and time point in hierarchal clustering. Pearson's correlation matrices and relation by Gower's matrices (Figure 4-S6) were nuanced due to the relative similarity of treatment groups besides wildtype GFLV strain GHu at 7 dpi. The overlap and mixed clustering observed at each time point for the other groups was expected from previous observations and the absence of vein clearing outside of wildtype GFLV strain GHu at the middle time point. The datasets of plants infected by wildtype GFLV strain GHu at 7 dpi (symptomatic) and 12 dpi (asymptomatic) were more distinct than those at 4 dpi (asymptomatic). Viral treatments, regardless of the GFLV strain, were distinct from mock controls by PCA loadings during late infection (12 dpi). PCA revealed lower principal components (i.e., PC2, PC3, and PC5) more likely to be discriminated by the treatment group rather than PC1 (Figure 4-2A–E). PCA also showed wildtype GFLV strain GHu at 7 dpi being distinct from all other treatments and groupings. The proteome of plants infected with wildtype GFLV strain GHu at 7 dpi segregated from all other time points and treatments by PC5 and PC2 (Figure 4-2B,D). Small differences in tissue maturity and offset of the infection state could explain the observed discrepancies of proteome profiles, as revealed by correlation matrices (Figure 4-S6) and in PCA (Figure 4-2).

FIGURE 4-2. PCA for unbiased observation of acquired proteomics and transcriptomics data. Proteomics data utilizes top 100 proteins after vsn and bpca imputation. Transcriptomics data utilizes top 500 varying genes after vsn and low-count filtering. **(A)** Key for biological replicates displaying colors for treatments and shape used for three time points (4, 7, and 12 dpi as circles, triangles, and squares, respectively) of *N. benthamiana* inoculated with various GFLV strains and controls for **(B)** proteomics analysis of 73* samples for which grouping of samples is minorly apparent, especially for the wildtype GFLV strain GHu treatment (red triangles) in the upper-right quadrant. **(C)** Breakdown of samples at 4 dpi, **(D)** 7 dpi with large separation of wildtype GFLV strain GHu symptomatic plants in red**,** and **(E)** 12 dpi with cluster effects, suggesting subtle variations of the proteome upon these treatment groups. **(F)** Key displaying colors for treatments and shape used for the three time points (4, 7, and 12 dpi) following inoculation of *N. benthamiana* with various GFLV strains for **(G)** all 75 samples from DESeq2 analysis, normalization, and transformation plotted in PCA where PC2 separates out wildtype GHu 7 dpi, **(H)** 4 dpi with minor grouping of treatment groups, **(I)** 7 dpi with a large separation PC1 for symptomatic wildtype GFLV strain GHu, and **(J)** 12 dpi with minor grouping of treatment groups, although PC2 separates control from viral treatment groups.

*Two samples were lost during sample processing resulting in 73 samples rather than the designed 75 sample experiment. This did not impact the ability of contrasts with a larger sample size taken and no more than one sample lost in a treatment group or time point.

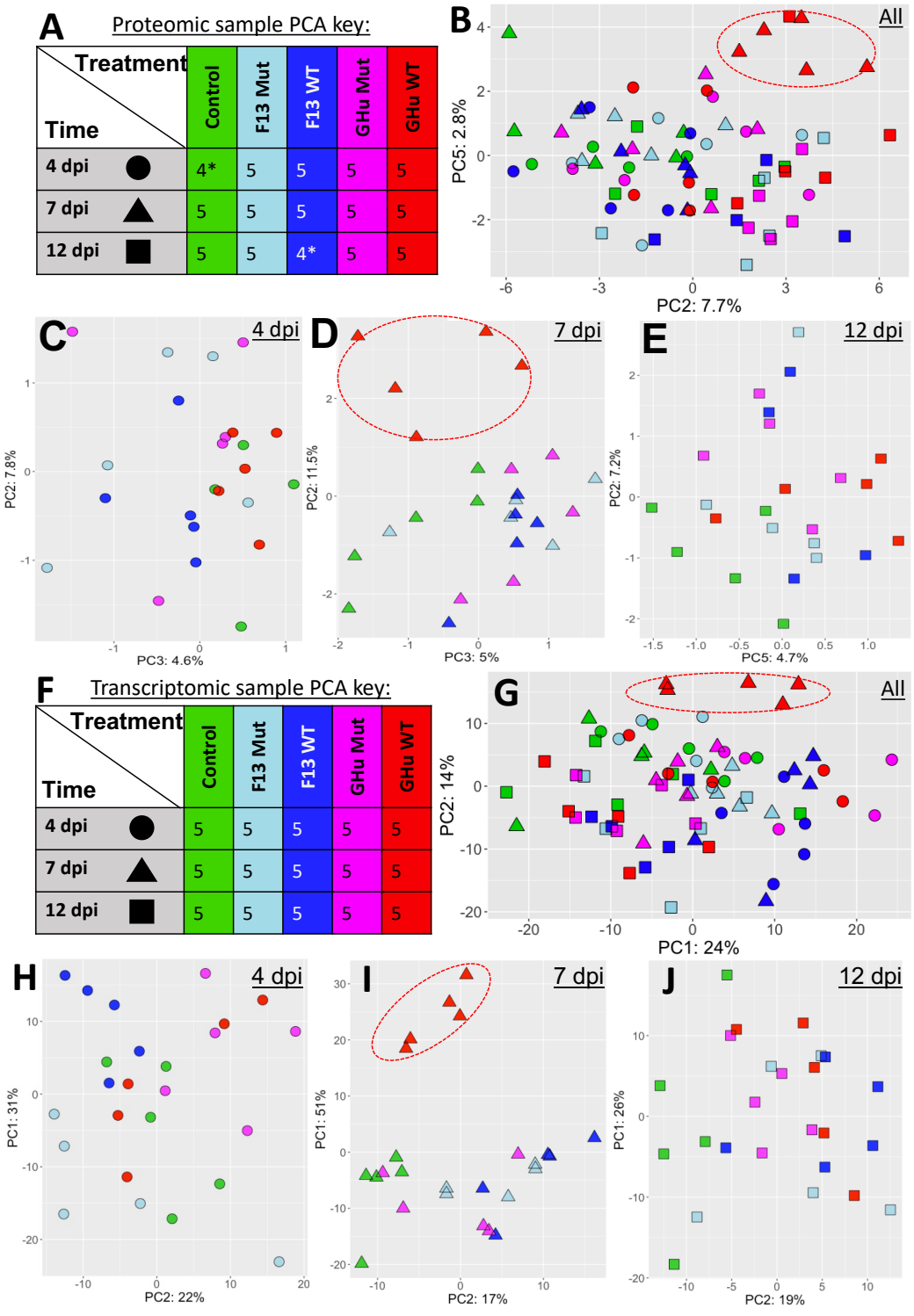
A
Proteomic sample PCA key:
Treatment
Time
Control
F13 Mut
F13 WT
GHu Mut
GHu WT
4 dpi
4*
5
5
5
5
7 dpi
5
5
5
5
5
12 dpi
5
5
4*
5
5
B
All
PC5: 2.8%
PC2: 7.7%
C
4 dpi
PC2: 7.8%
PC3: 4.6%
D
7 dpi
PC2: 11.5%
PC3: 5%
E
12 dpi
PC2: 7.2%
PC5: 4.7%
F
Transcriptomic sample PCA key:
Treatment
Time
Control
F13 Mut
F13 WT
GHu Mut
GHu WT
4 dpi
5
5
5
5
5
7 dpi
5
5
5
5
5
12 dpi
5
5
5
5
5
G
All
PC2: 14%
PC1: 24%
H
4 dpi
PC1: 31%
PC2: 22%
I
7 dpi
PC1: 51%
PC2: 17%
J
12 dpi
PC1: 26%
PC2: 19%

Transcriptomic Analysis of **N. benthamiana** *Leaf Tissue*

Total RNA from the mock control and GFLV-infected *N. benthamiana* plants was isolated and analyzed by 3′RNA-Seq (Figure 4-S1). All files passed quality control metrics (mean Phred score ~33) and were deemed acceptable for downstream analysis. On average, 79.8% of reads mapped to the host reference genome with 2,148,843 reads per sample (Table 4-S3 and Figure 4-S7A). After normalization and low-count thresholds were placed, an average of 136,809 reads were attributed per sample (Figure 4-S7B). No distinct trends were associated with any treatment or time point for count data indicating little to no technical bias from tissue processing steps, purification efforts, and sequencing. Analysis through HiSat2 returned 59,814 gene identities matching the assembly across all samples. Only 31,394 of these genes contained ≥2 counts per entry, which was used as a low-count filter threshold. A range of 10,000 to over 400,000 viral RNA2 reads were acquired in GFLV-infected plant samples, corresponding to polyadenylated ssRNA captured in 3′RNA-Seq. GFLV RNA1 reads were acquired with a range from 61 to over 60,000 reads but less consistently for the two F13 strains. The difference in abundance between GFLV RNA2 and GFLV RNA1 was 10–100-fold.

Model construction and variance stabilization normalization steps supported further analyses, as shown by dispersion estimate graphs with typical profiles (Figure 4-S8), which showed dispersion estimates centered around the fitted gene estimate line. A hierarchal clustering using the pair-wise McQuitty method (McQuitty and Clark 1968) revealed grouping of treatments within time points with minimal mixing (Figure 4-S9). PCAs on the 75 samples and groupings by time points (Figure 4-2F–J) revealed

distinct separation for wildtype GFLV strain GHu at 7 dpi by both PC1 and PC2. Overall, the host transcriptome remained unresolved by other GFLV treatments and time points, with a maximum of 10.2% variance explained by the top 500 genes (Figure 4-S10A). Both PCA and hierarchal clustering showed a distinct transcriptome profile for wildtype GFLV-GHu at 7 dpi from all the other datasets, with the major source of variation explained by the developmental or infection stage rather than from viral treatment groups (Figures 4-2B and 4-S10B,C). The individual PCA plots per time point revealed more resolution among samples than the treatment group across the entire experiment (Figure 4-2H–J). The time-based groupings were then used for further analysis to avoid possible temporal bias in the transcriptome.

Detection of GFLV RNA and Protein Abundance across Treatments and Time Is Independent of Symptom Development

Across the four GFLV strains used in this study, the RNA-Seq data suggested little viral presence in apical leaf tissue at 4 dpi with an increase at 7 dpi coinciding with vein clearing and a reduced average number of reads at 12 dpi, as measured by GFLV RNA2 mapping transcripts normalized to the total read number per million or simply transcripts per million (Figure 4-S11A). No significant difference in the virus titer among GFLV treatments was observed at any time point through paired Student's *t*-test and post-hoc Levene's test ($P > 0.05$). Wildtype GFLV strain GHu and mutant GFLV-F13 $1E_{G802K}^{Pol}$ contained elevated levels of RNA2 in comparison with wildtype GFLV-F13 and mutant GFLV-GHu $1E_{K802G}^{Pol}$, but differences were not statistically significant ($P > 0.05$). This result is consistent with the viral titer not determining symptom development, as previously reported (Osterbaan et al. 2019).

Peptides from GFLV RNA1- ($1E^{Pol}$) and RNA2-encoded ($2B^{MP}$ and $2C^{CP}$) proteins were consistently detected within the proteomics dataset (Figure 4-S11B–D). Only samples within the mutant GFLV-F13 $1E_{G802K}{}^{Pol}$ treatment group showed spectra typically at 4 dpi (Figure 4-S11C,D). This is consistent with a slightly faster replication or systemic infection rate for this GFLV strain compared to that for the other strains, which is also consistent with the RNA-Seq data (Figure 4-S11A) in addition to the trend of elevated levels (and variability) of protein $2B^{MP}$ for GFLV-F13 $1E_{G802K}{}^{Pol}$ at 7 dpi. Mock controls returned no spectra matching to viral peptides at any time point, as expected. Peptide spectra matching to GFLV protein $2B^{MP}$ were detected in the highest relative abundance as compared to other viral proteins across all treatments with our extraction protocol and showed a similar trend to strain specific abundance, as with the RNA-Seq data corresponding to RNA2 reads. Treatments with wildtype GFLV-GHu and mutant GFLV-F13-$1E_{G802K}{}^{Pol}$ returned the most reads at 7 dpi, while wildtype GFLV-F13 and mutant GFLV-GHu $1E_{K802G}{}^{Pol}$ returned lower counts; however, these were not statistically different from each other ($P > 0.05$).

GFLV-GHu Symptom Development Is Associated with Changes in the Plant Host Transcriptome and Proteome

We set out to identify genes/proteins whose change could be correlated to vein clearing symptom development by wildtype GFLV-GHu. Changes in abundance of transcripts (Figure 4-3) and proteins (Figure 4-4) were plotted using viral treatment contrasts, and the total number of differentially abundant transcripts (DEGs) (Table 4-1) and proteins (DEPs) (Table 4-2) was calculated.

FIGURE 4-3. Select transcriptomics contrasts at 4, 7, and 12 days post inoculation (dpi) of *Nicotiana benthamiana* infected with various GFLV strains. Thresholds of |log2FoldChange| > 1 and *p*-adjusted value > 0.05 were used to identify DEGs. Data points meeting both requirements (green), significant reads but insufficient expression differences (blue), expression differences but not statistical significance (gray), and neither requirement (black) are shown. Contrasts between wildtype GFLV strain GHu and mutant GFLV-GHu $1E_{K802G}^{Pol}$ at **(A)** 4 dpi with little difference in transcript expression, **(B)** 7 dpi with many DEGs, and **(C)** 12 dpi with few DEGs. Contrasts between wildtype GFLV strains GHu and F13 show a similar pattern at **(D)** 4 dpi with little difference in DEGs, **(E)** 7 dpi with many DEGs, and **(F)** 12 dpi with a reduced number of DEGs. Contrasts between wildtype GFLV strain F13 and mutant GFLV-F13 $1E_{K802G}^{Pol}$ show a different pattern at **(G)** 4 dpi with more DEGs than at **(H)** 7 dpi and **(I)** 12 dpi. **(B)** and **(E)** share 62.5% identity of significant DEGs, showing that most changes in the transcriptome are the result of a single amino acid and not the background of all other genomic differences between wildtype GFLV strains.

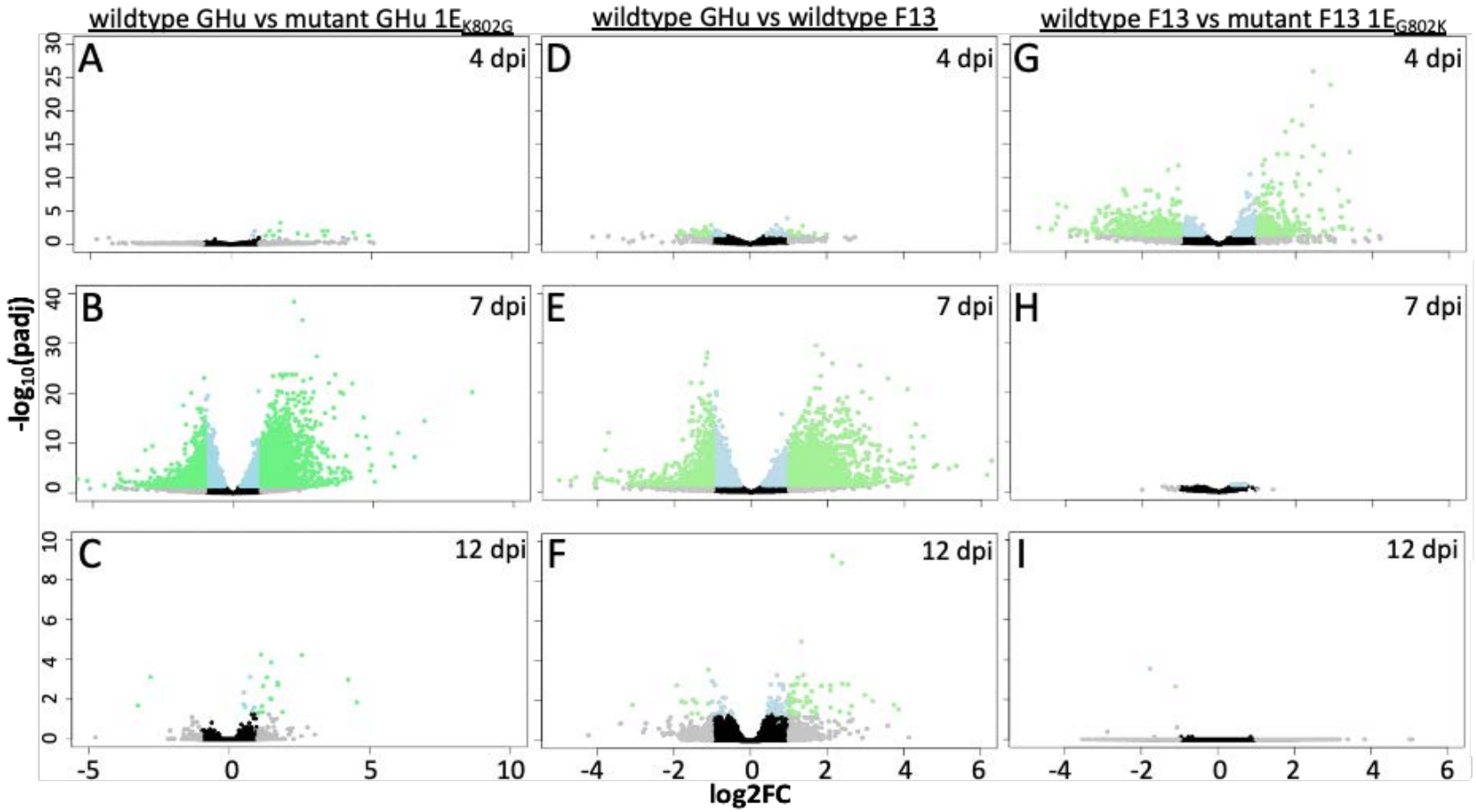
wildtype GHu vs mutant GHu 1E$_{K802G}$
wildtype GHu vs wildtype F13
wildtype F13 vs mutant F13 1E$_{G802K}$
A
4 dpi
D
4 dpi
G
4 dpi
B
7 dpi
E
7 dpi
H
7 dpi
C
12 dpi
F
12 dpi
I
12 dpi
-log$_{10}$(padj)
log2FC

Figure 4-4. Select proteomics contrasts at 4, 7, and 12 days post inoculation (dpi) of *Nicotiana benthamiana* with various GFLV strains. Thresholds of |log2FoldChange| > 1 (high confidence), |log2FoldChange| > 0.5 (medium confidence), and *p*-value <0.05 were used to identify DEPs. Data points meeting requirements for high confidence (purple), medium confidence (pink), significant reads but insufficient expression differences (blue), and neither requirement (black) are shown. Contrasts between wildtype GFLV strain GHu and mutant GFLV-GHu $1E_{K802G}^{Pol}$ at **(A)** 4 dpi with very limited DEPs, **(B)** 7 dpi with several DEPs identified with medium and high confidence, and **(C)** 12 dpi with limited DEPs. Contrasts between wildtype GFLV-GHu and F13 show a similar pattern at **(D)** 4 dpi with limited DEPs, **(E)** 7 dpi with larger differences in protein expression, and **(F)** 12 dpi with limited DEPs. Contrasts between wildtype GFLV-F13 and mutant GFLV-F13 $1E_{K802G}^{Pol}$ with few DEPs at **(G)** 4 dpi, **(H)** 7 dpi, and **(I)** 12 dpi. The illustration of these time-resolved volcano plots demonstrates that the proteome is mainly disrupted at 7 dpi only for the wildtype GFLV-GHu treatment, corresponding to vein clearing symptom expression.

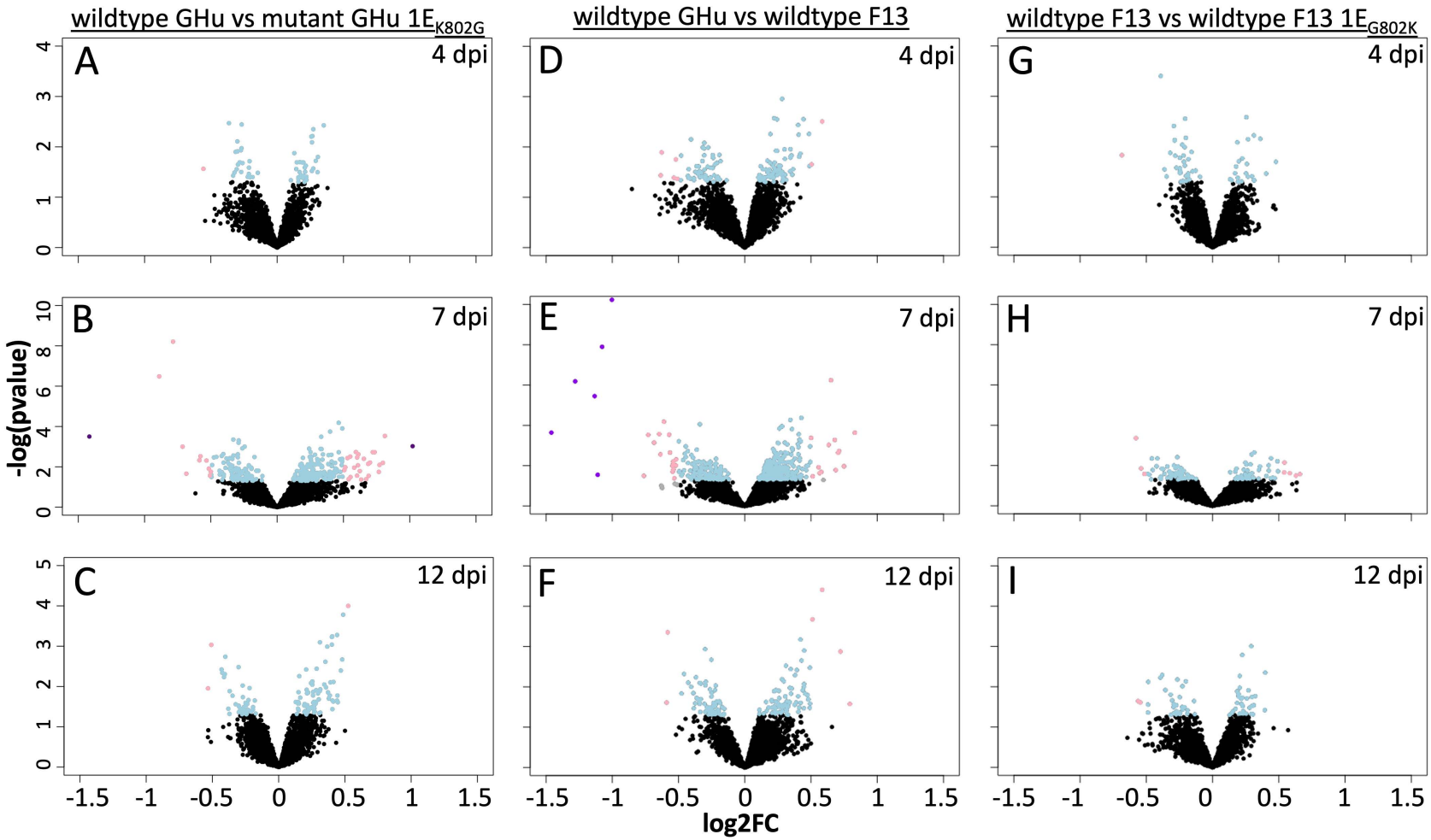
wildtype GHu vs mutant GHu 1E$_{K802G}$
wildtype GHu vs wildtype F13
wildtype F13 vs wildtype F13 1E$_{G802K}$
A
4 dpi
B
7 dpi
C
12 dpi
D
4 dpi
E
7 dpi
F
12 dpi
G
4 dpi
H
7 dpi
I
12 dpi
-log(pvalue)
log2FC

Table 4-1. Summary of differential abundant transcripts (DEGs) between grapevine fanleaf virus (GFLV) treatment groups at 4, 7, and 12 days post-inoculation (dpi) of *Nicotiana benthamiana*[a].

Contrasts[a]	Wildtype GHu vs mutant GHu[b]		Wildtype GHu vs wildtype F13		Wildtype F13 vs mutant F13		Wildtype F13 vs mutant GHu		Wildtype GHu vs mutant F13	
Time	UP	DOWN	UP	DOWN	UP	DOWN	UP	DOWN	UP	DOWN
4 dpi	12	0	9	33	227	450	229	27	347	587
7 dpi	1838	869	1944	679	0	0	2	1	1579	688
12 dpi	16	2	51	11	0	2	1	1	85	66

[a]Contrasts are shown at 4-, 7-, and 12-days post-inoculation (dpi) of *N. benthamiana* with wildtype GFLV strains GHu and F13, and mutant GFLV strains GHu $1E^{Pol}_{K802G}$ and F13 $1E^{Pol}_{G802K}$.
[b]Upregulated (UP) and downregulated (DOWN) transcripts based on abundance are indicated.

Table 4-2. Summary of differentially abundant proteins (DEPs) identified with medium or high confidence between grapevine fanleaf virus (GFLV) treatment groups at three time points post-inoculation of *Nicotiana benthamiana*[a].

Contrasts[a]	Wildtype GHu vs mutant GHu[b]		Wildtype GHu vs wildtype F13		Wildtype F13 vs mutant F13		Wildtype F13 vs mutant GHu		Wildtype GHu vs mutant F13	
	UP	DOWN	UP	DOWN	UP		UP	DOWN	UP	DOWN
4 dpi[c]	0 (0)	1 (0)	1 (0)	3 (0)	0 (0)	4 dpi[c]	0 (0)	1 (0)	1 (0)	3 (0)
7 dpi[c]	21 (0)	7 (1)	12 (0)	18 (5)	3 (0)	7 dpi[c]	21 (0)	7 (1)	12 (0)	18 (5)
12 dpi[c]	0 (0)	0 (0)	3 (0)	2 (0)	0 (0)	12 dpi[c]	0 (0)	0 (0)	3 (0)	2 (0)

[a]Contrasts are shown at 4-, 7- and 12-days post-inoculation (dpi) of *N. benthamiana* with wildtype GFLV strains GHu and F13, and mutant GFLV strains GHu $1E^{Pol}_{K802G}$, and F13 $1E^{Pol}_{G802K}$.

[b]Upregulated (UP) and downregulated (DOWN) proteins based on relative abundance are indicated for each contrast.

[c]Protein identifications with moderate and high (in parentheses) dysregulation are indicated for each contrast per time point. Thresholds of |log2FoldChange|>1 (high dysregulation), |log2FoldChange|>0.5 (medium dysregulation), and *p-value* < 0.05 (confidence value for both) were used to identify DEPs.

The symptomatic wildtype GFLV-GHu provided the largest amount of contrast to other viral treatments during symptom expression at 7 dpi (Figures 4-3 and 4-S12). Of interest were over 1800 upregulated and over 800 downregulated host transcripts for the wildtype and mutant GFLV-GHu comparison (Table 4-1) and 22 upregulated and 7 downregulated proteins at 7 dpi (Table 4-2).

Wildtype GFLV-GHu provided by far the most drastic difference in transcript expression levels when compared with any other treatments, suggesting that protein $1E^{Pol}$ residue 802 has a disproportionate impact on host response relative to the overall genetic composition of the viral genome. The difference of one amino acid between the two GFLV-F13 strains did not have a similar impact on the transcript expression levels at 7 dpi, as expected from phenotypic observations.

Contrast of the transcriptomic profiles of host plants infected with wildtype strain compared to mutant GFLV-GHu, over time, indicated that host gene expression was majorly affected at 7 dpi by the wildtype strain, but no substantial differences were observed at 4 and 12 dpi between the two (Figure 4-3A–C). This is reflected once more when contrasting wildtype GFLV-GHu with the mock control (Figure 4-S12). A total of 2707 of 31,934 (8.48%) transcripts were classified as differentially abundant at 7 dpi between the two GFLV-GHu strains that differ in a single amino acid in protein $1E^{Pol}$ (Figure 4-3B). A vast difference in significant genes with both large fold changes and adjusted *P*-values was observed at 7 dpi (Figure 4-3B,E). This pattern was also obtained when contrasting wildtype GFLV-F13 and GHu (Figure 4-3D–F) with 2623 genes identified as differentially abundant at 7 dpi. It was notable that 62.5% of the classified DEGs from 7 dpi when comparing wildtype and mutant GFLV-GHu $1E_{K802G}^{Pol}$ to

wildtype strains GHu and F13 were identical (Figure 4-3B,E), suggesting that residue 802 of protein $1E^{Pol}$ is primarily responsible for underlying changes in the transcriptome. This means that a total of 1692 detected host genes could potentially be dysregulated due to a lysine in position 802 of the RdRP upon infection by wildtype GFLV-GHu. Remarkably, a disruption of transcript abundance between wildtype and mutant GFLV-F13 $1E_{G802K}{}^{Pol}$ was observed at 4 dpi (1042 genes) but not at later time points (Figure 4-3G–I). This may indicate initial response of the host to the presence of GFLV-F13, as previously mentioned for viral titer analyses, but these differences were reverted thereafter in the 7 dpi and 12 dpi contrasts. The wildtype and mutant GFLV-F13 had a larger host response at earlier and later time points than wildtype GFLV-GHu, all compared against mock-inoculated control plants (Figure 4-S12).

Beyond these transcriptomic contrasts, treatment differences revealed dysregulation of genes from 0 (0.00%) to 2267 genes (7.10%) of the detected transcriptome (Table 4-1). Contrasting wildtype and mutant GFLV-F13 resulted in 677, 0, and 2 differentially abundant transcripts (DEGs) at 4, 7, and 12 dpi, respectively. Contrasting wildtype GFLV-F13 and mutant GFLV-GHu $1E_{K802G}{}^{Pol}$ resulted in 256, 3, and 2 DEGs at 4, 7, and 12 dpi, respectively. Additionally, contrasting wildtype GFLV-GHu and mutant GFLV-F13 $1E_{G802K}{}^{Pol}$ resulted in 934, 2267, and 151 DEGs at 4, 7 dpi, and 12 dpi, respectively.

Analyses of the proteome revealed DEPs identified with high or moderate dysregulation (Figures 4-4 and 4-S13). The number of proteins in each of these categories per treatment contrast and time point was determined out of over 2000 proteins per time point (Table 4-2). Additionally, spectral counts for each time point

were documented as averages across samples to be 10,612 at 4 dpi, 11,028 at 7 dpi, and 10,661 at 12 dpi. For wildtype GFLV-GHu and mutant GFLV-GHu $1E_{K802G}^{Pol}$ at 7 dpi, 28 (1.3%) DEPs were detected. Of these, 27 (1.3%) were moderately dysregulated proteins ($P < 0.05$ and |log2FoldChange| > 0.5), and 1 (<0.1%) was a highly dysregulated protein ($P < 0.05$ and |log2FoldChange| > 1). Similar trends of wildtype GFLV-GHu at 7 dpi reached the most pronounced contrast against other treatment groups with 30 DEPs against wildtype GFLV-F13 and 31 against mutant GFLV-F13 $1E_{G802K}^{Pol}$ both at 7 dpi (Table 4-2).

A single DEP was found at 4 dpi and none at 12 dpi when contrasting wildtype and mutant GFLV-GHu strains (Table 4-2). Nuances associated with GFLV F13 strains from transcriptomics data were not reflected in the proteomics contrasts (Figure S13). Additional proteomics contrasts revealed 0, 5, and 2 DEPs between wild and mutant GFLV-F13 at 4, 7, and 12 dpi, respectively (Table 4-2 and Figures 4-4 and 4-S13). Contrasting wildtype GFLV-F13 with mutant GFLV-GHu $1E_{K802G}^{Pol}$ found 0, 9, and 2 proteins of differential abundance at 4, 7, and 12 dpi, respectively. The consistent dysregulation of proteins between wildtype GFLV-GHu and other treatments at peak vein clearing and less DEPs at the early and late time points provide additional confidence in these findings.

GO Analyses of the Transcriptome and Proteome Indicative of Disrupted Host Pathways

GO analysis revealed GFLV- and GFLV strain-specific patterns of functional gene expression changes during infection. Contrasts for transcriptomics DEGs resulted in enriched gene functions for the wildtype GFLV-GHu against mutant GHu at 7 dpi:

nucleic acid binding (GO:0000496), nucleotide binding (GO:0000166), RNA binding (GO:0003723), structural constituent of the ribosome (GO:0003735), photosynthesis (GO:0015979), inositol-3-phosphate synthase activity (GO:0004512), mitochondrial outer membrane (GO:0005741), mitochondrial outer membrane translocase complex (GO:0005742), translation elongation factor activity (GO:0003746), and ssDNA binding (GO:0003698) (Figure 4-5). Contrasting wildtype GFLV-GHu with the mock control at 7 dpi resulted in a similar output with seven identical ontologies, two new GO terms (translation initiation factor activity (GO:0003743) and glycerol ether metabolic process (GO:0006662), and two absent GO terms (translation elongation factor activity (GO:0003746) and nucleic acid binding (GO:0000496)) (Figure 4-5). Contrasting wildtype GFLV strains GHu and F13 at 7 dpi showed additional trends with differences of the GHu strain contrast being of three additional GO terms [rRNA processing (GO:0006365), ribonucleoprotein complex (GO:0030529), and nucleus (GO:0005634)] and three GO terms removed [ssDNA binding (GO:0003698), mitochondrial outer membrane translocase complex (GO:0005742), and mitochondrial outer membrane (GO:0005741)] (Figure 4-5).

Other transcriptome contrasts are not reported here due to low numbers of DEGs, which did not return any significant GO terms ($P < 0.05$), mainly at early and late time points outside of symptom expression. Contrasts for the proteome of plants infected with wildtype GFLV-GHu showed similar trends but only resulted in three major ontologies with significance across the entire experiment: nucleotide binding (GO:0000166), isopentenyl diphosphate biosynthetic process (GO:0009240), and thiamine biosynthetic process (GO:0009228) (Figure 4-6A)

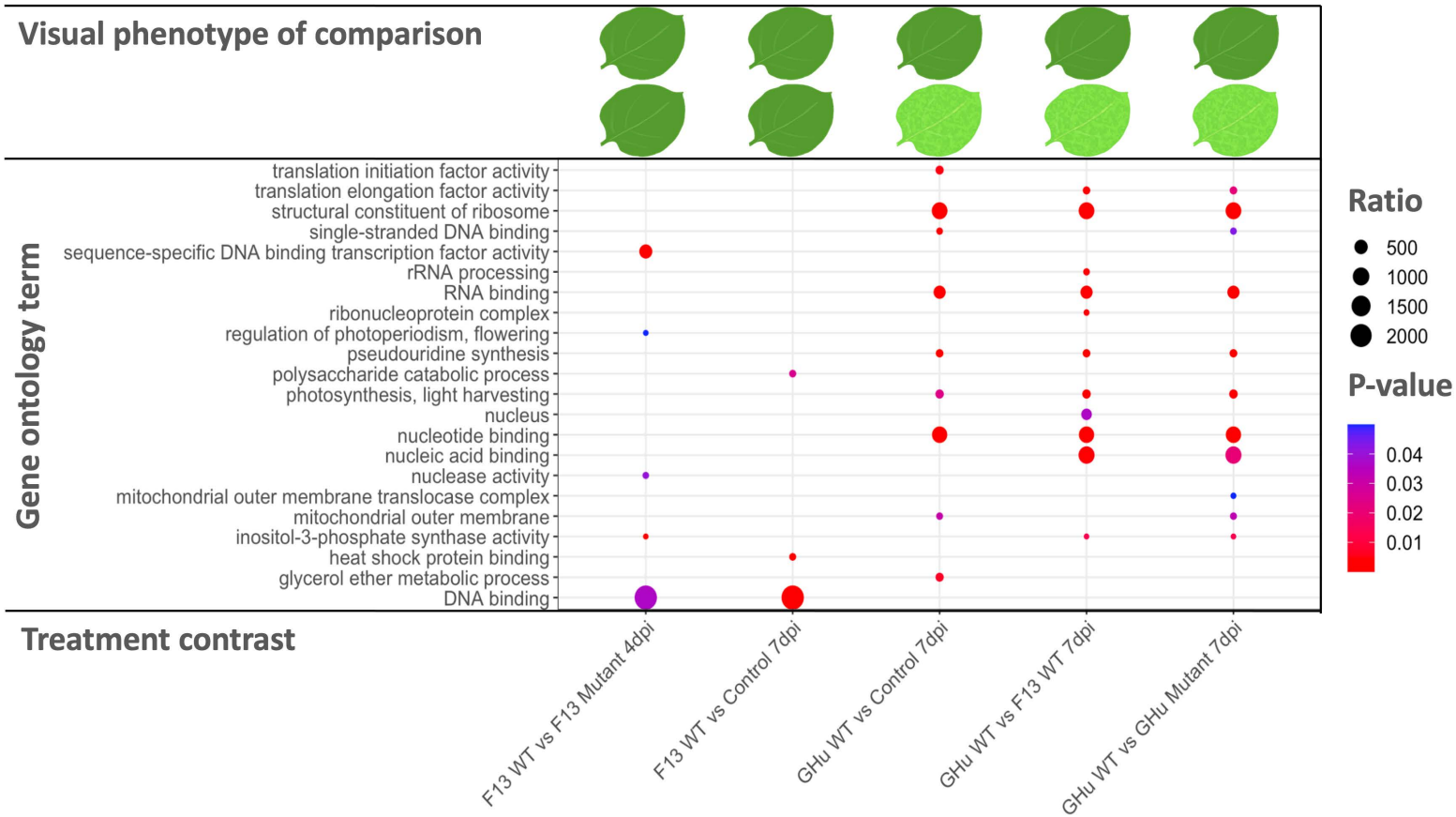

FIGURE 4-5. Gene set enrichment analysis of overrepresented genes present in the transcriptome analyses. GeneIDs were extracted from individual genes in contrasts with an |Log2FoldChange| > 1 and p-value < 0.05. GeneID was inserted into 'gprofiler2' package v0.2.1 for matching identity of functional annotation of *Nicotiana benthamiana* genes. Size of dot represents relative abundance and color from blue to red signifies increasing significance (p-value range of 0.05 to <0.01). The upper panel show phenotypes obtained following inoculation of *Nicotiana benthamiana* by various grapevine fanleaf virus strains above each contrast for ease of comparing visual phenotype to transcriptome profile

FIGURE 4-6. Overrep**resented gene ontologies (GOs) for proteomic analysis. (A) GeneIDs were extracted from individual genes in multiple treatment-wise contrasts with an |Log2FoldChange| > 0.5 and p-value < 0.05 (medium confidence)**. GeneID was inserted into 'gprofiler2' package v0.2.1 for matching identity of functional annotation of *Nicotiana benthamiana* genes and returned GO terms overrepresented in the dysregulated proteome across the entire experiment. Contrasts were included from all time points of the experiment and from the following treatment contrasts: wildtype grapevine fanleaf virus (GFLV) strain GHu vs mutant GHu $1E^{Pol}_{K802G}$, wildtype GFLV strain F13 vs mutant F13 $1E^{Pol}_{K802G}$, wildtype GFLV-GHu vs wildtype GFLV-F13, and wildtype GFLV-F13 vs mutant GHu $1E^{Pol}_{K802G}$. The relative ratio of is shown by the x-axis scale and adjusted p-value (padj) is shown by color of red to blue for most to least significant. Adjusted p-values indicated as significant by * = padj < 0.1, ** = padj <0.05, and *** = padj<0.01. (B) GOs extracted from missing not at random (MNAR) proteins across the entire 73 protein samples. Only significant ontologies are shown with adjusted p-value shown increasing from blue to red (0.025 to <0.005).

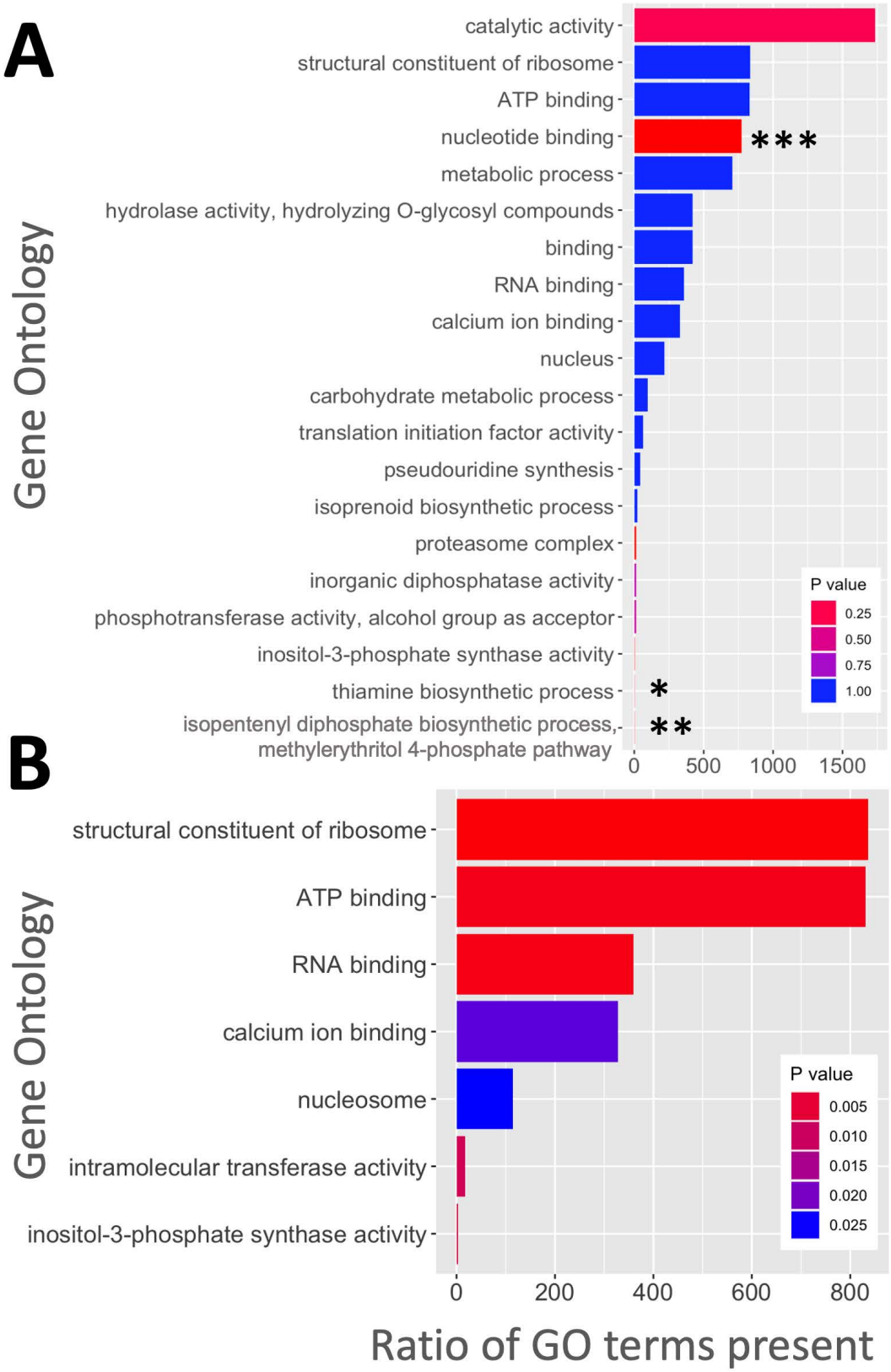
A
Gene Ontology
catalytic activity
structural constituent of ribosome
ATP binding
nucleotide binding
metabolic process
hydrolase activity, hydrolyzing O-glycosyl compounds
binding
RNA binding
calcium ion binding
nucleus
carbohydrate metabolic process
translation initiation factor activity
pseudouridine synthesis
isoprenoid biosynthetic process
proteasome complex
inorganic diphosphatase activity
phosphotransferase activity, alcohol group as acceptor
inositol-3-phosphate synthase activity
thiamine biosynthetic process
isopentenyl diphosphate biosynthetic process, methylerythritol 4-phosphate pathway
***
*
**
P value
0.25
0.50
0.75
1.00
0
500
1000
1500
B
Gene Ontology
structural constituent of ribosome
ATP binding
RNA binding
calcium ion binding
nucleosome
intramolecular transferase activity
inositol-3-phosphate synthase activity
P value
0.005
0.010
0.015
0.020
0.025
0
200
400
600
800
Ratio of GO terms present

GSEA and network analysis were performed from the significant transcriptomic DEGs for the wildtype GFLV-GHu treatment at 7 dpi versus all other treatments, providing a network of overrepresented, characteristic ontologies. The produced gene network displays three over-arching gene functions of immune response, metabolism, and gene regulation, most being up-regulated (Figure 4-7). For immune response-related genes, three main GO terms were apparent: response to oxidative stress (GO:0006979), endopeptidase activity (GO:0004175), and protein peptidyl–prolyl isomerization (GO:0000413). Additional annotated genes related to host gene regulation and host immune response included gene silencing by RNA (GO:0031047) which can act for both host and viral RNAs. Furthermore, RNA binding (GO:0003723), nucleus (GO:0005634), nuclear pore (GO:0005643), transcription/DNA-templated (GO:0006351), transcription coregulator activity (GO:0001104), translation initiation factor activity (GO:0003743), translation elongation factor activity (GO:0003746), and NAD^+ ADP-ribosyltransferase activity (GO:0003950) all were upregulated and overrepresented terms for wildtype GFLV-GHu at 7 dpi compared with all other treatments (Figure 4-7).

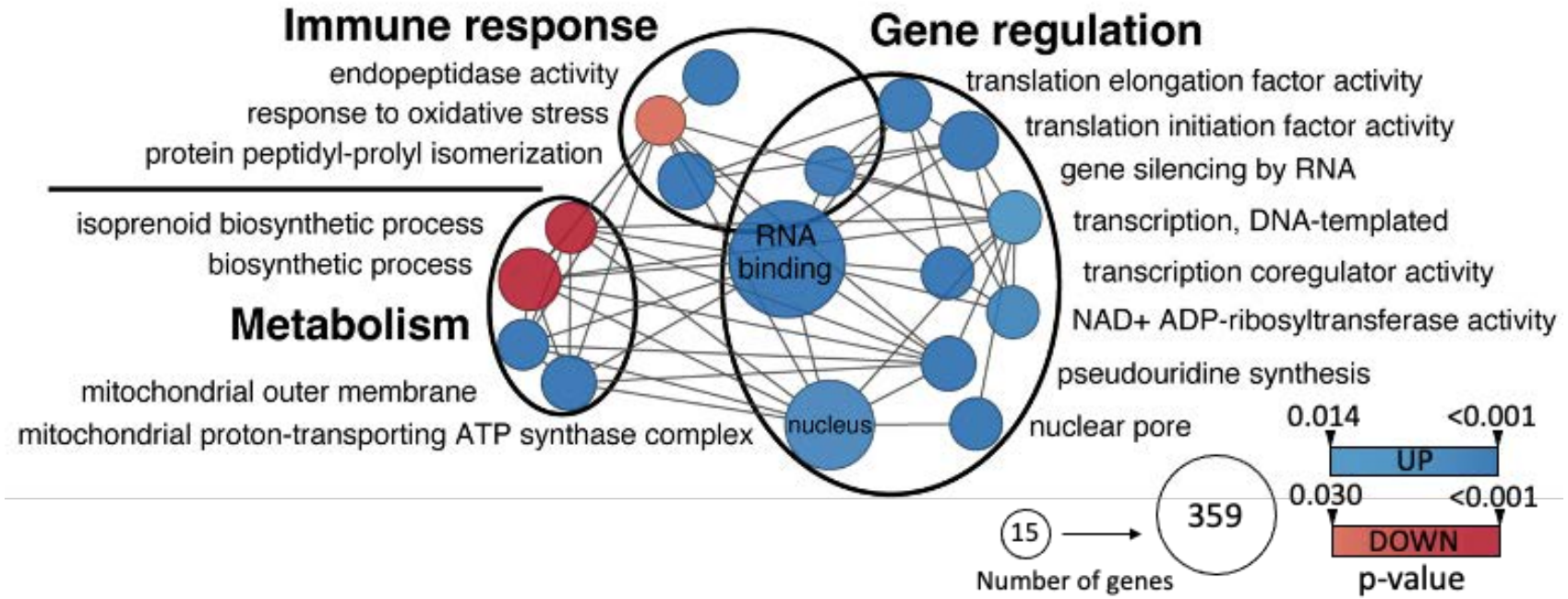

FIGURE 4-7. Differential gene set enrichment analysis network of wildtype grapevine fanleaf virus (GFLV) strain GHu at 7 days post-inoculation of *Nicotiana benthamiana* contrasted against all other treatments (wildtype GFLV-GHu at 7 dpi was contrasted against the profile of all other treatments in GSEA with parameters of |Log2FoldChange|>1 and adjusted p-value < 0.05). Gene clusters upregulated (blue circle) and downregulated (red circle) are shown and are colored by saturation according to their respective calculated p-values. The size of a circle represents the relative number of genes present within a cluster ranging from 15 to 359. Lines represent potential interactant connection network between gene ontology terms. Black lined circles encompassing several clusters represent a general classification that was manually annotated; this analysis confirmed three main categories relating metabolism, immunity, and gene regulatory processes in the event of vein-clearing symptom development.

Extrapolating the proteomics dataset revealed several proteins to be MNAR (Figure 4-S4, red brackets), for which the bulk might be relevant to treatment-specific phenotypes and representative of GFLV symptoms (i.e., downregulated beyond detection capacities through LC–MS/MS). A list containing these gene IDs was extracted from the DEP pipeline and was subject to GSEA. The resultant significant GOs were consistent with observations in the transcriptome to be structural constituent of the ribosome (GO:0003735), ATP binding (GO:0005524), RNA binding (GO:0003723), calcium ion binding (GO:0005509), nucleosome (GO:0000786), intramolecular transferase activity (GO:0016866), and inositol-3-phosphate synthase activity (GO:0004512) (Figure 4-6B). This result suggested that MNAR proteins in this dataset are associated with the vein clearing phenotype, signifying that their abundance is too low for detection in treatment-specific samples through our protocol. This difference in protein presence or absence was observed between GFLV-GHu strains against GFLV-F13 strains and mock controls. This finding was reinforced by the fact that the transcriptome shows similar dysregulated GOs.

The largest change in the host transcriptome and proteome was observed with plants infected with wildtype GFLV-GHu. The top five proteins/genes based on fold change were for (1) proteomics; NUCLEOLAR PROTEIN 56, RNA-BINDING PROTEIN-LIKE, 4-HYDROXY-3-METHYLBUT-2-ENYL DIPHOSPHATE REDUCTASE [twice], and INOSITOL-3-PHOSPHATE SYNTHASE and (2) transcriptomics; 60S ACIDIC RIBOSOMAL PROTEIN P1 [twice], GLUTATHIONE S-TRANSFERASE U9, 30S RIBOSOMAL PROTEIN S19, and TETRATRICOPEPTIDE REPEAT (TPR)-LIKE SUPERFAMILY PROTEIN (Table

4-S5). These genes represent top candidates for future investigation into their function during GFLV infection and symptom development.

Weighted Gene Co-Expression Network Analysis Further Demonstrates Time- and GFLV Strain-Specific Events

Gene clusters were constructed using WGCNA, resulting in 28 eigengene modules constructed from the transcriptomics dataset (Figure 4-S14). Four expression modules contained 6985 downregulated genes only for wildtype GFLV-GHu at 7 dpi (MEbrown, MEyellow, MEblack, and MEpurple), while MEblue contained 3582 upregulated genes only for wildtype GFLV-GHu at 7 dpi (Figure 4-8A). All other treatments had relatively constant expression profiles in comparison to wildtype GFLV-GHu. A gene list extracted from all five of these modules and subject to GSEA revealed the same GOs as those displayed in the GSEA contrast of wildtype and mutant GFLV-GHu at 7 dpi, including nucleic acid binding, structural constituent of the ribosome, GTPase activity (GO:0061745), protein folding (GO:0006457), and translation initiation factor activity (Figure 4-8B). Similarly, a separate analysis of eigengene module MEblue showed many similar GOs with nucleic acid binding (GO:0000496), nucleotide binding (GO:0000166), RNA binding (GO: 0003723), structural constituent of the ribosome (GO:0003735), and GTPase activity (GO:0003924) being the top five GOs (Figure 4-8C). The same analysis was performed on MEmagenta, MEwhite, and MEgreenyellow for genes down- or up-regulated by mutant GFLV-F13 $1E_{G802K}^{Pol}$ at 4 dpi (Figure 4-S15A), revealing GOs related to metabolic processes (GO: 0008152), nuclease activity (GO: 0004518), and cytoskeleton organization (GO: 0007010) (Figure 4-S15B). Since wildtype GFLV-F13 does not manifest symptoms, these regulated genes

are most likely unrelated to the vein clearing phenotype but may relate to virus–plant interactions early in the infection cycle of *N. benthamiana*. Other WGCNA modules were grouped based on their relative changes in expression for other treatments (i.e., mutant GFLV-F13 $1E_{G802K}^{Pol}$ at 12 dpi with MEorange and MEdarkorange), but no significant resulting GOs were found (data not shown). This was most likely due to the robust selective nature of our model and the low number of genes fitting into each module (<400 genes). All other unique gene profile expression modules were unsuccessful in fulfilling the minimum requirements and *P*-value thresholds to construct GSEA after extraction.

FIGURE 4-8. Functional categorization of WGCNA eigengene modules unique to infection of *Nicotiana benthamiana* by grapevine fanleaf virus (GFLV) wildtype strain GHu at 7 days post-inoculation (dpi). (A) Selected modules with unique expression patterns. Four of five modules (MEbrown, MEyellow, MEblack and MEpurple) display downregulation of genes, while MEblue module shows upregulation of genes. Consensus eigengene-based connectivity (kME) value was set to 0.3 and mergeCutHeight to 0.25 for selecting closely related gene expression profiles. (B) Gene ontologies overrepresented in all five modules subjected to GSEA. Gene ontologies unique to downregulated pathways are indicated by gray down arrows. Bars are colored by p-value as indicated by the in-plot legend. (C) Gene ontologies overrepresented in MEblue subjected to GSEA.

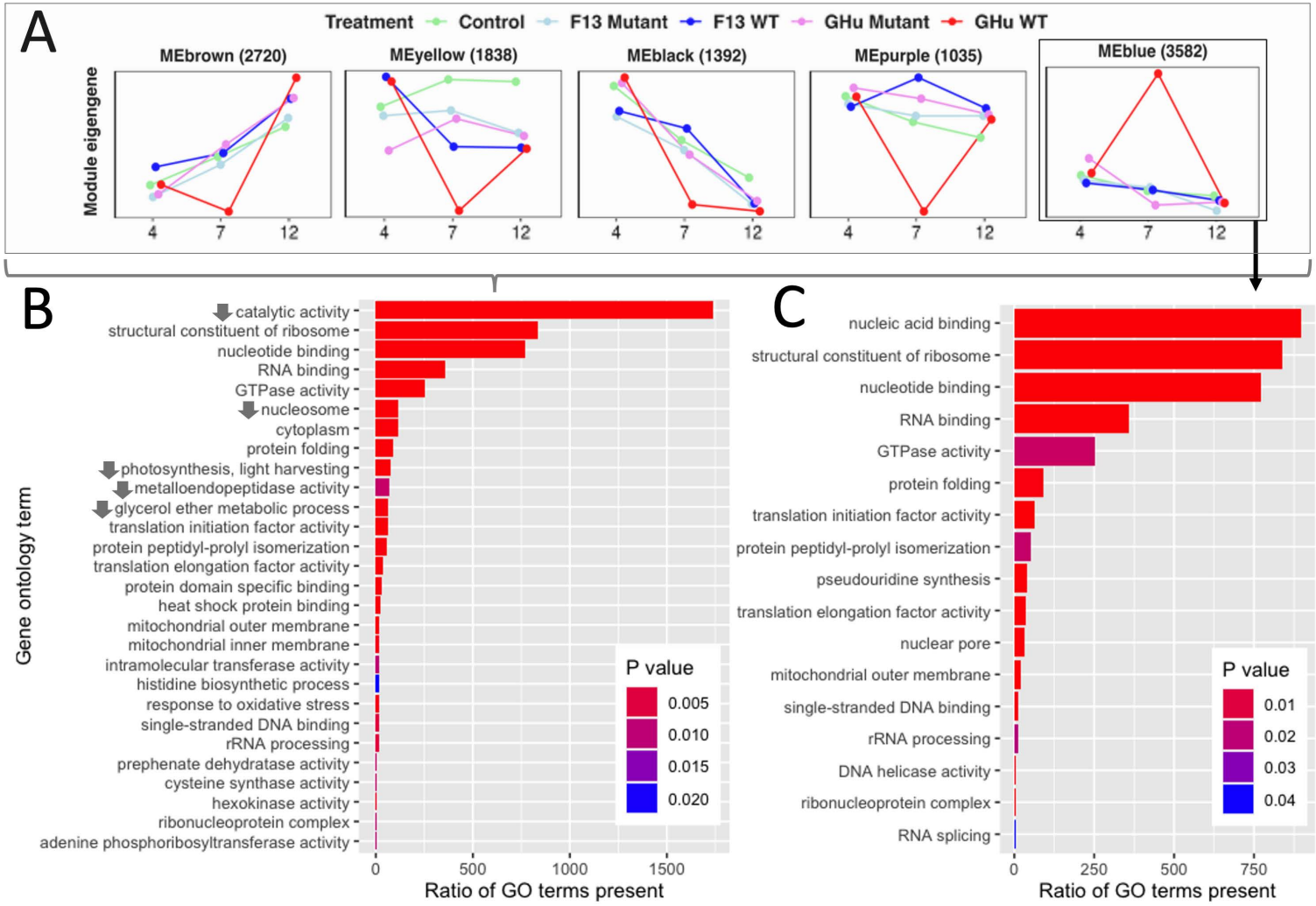
A
Treatment
Control
F13 Mutant
F13 WT
GHu Mutant
GHu WT
MEbrown (2720)
MEyellow (1838)
MEblack (1392)
MEpurple (1035)
MEblue (3582)
Module eigengene
4
7
12
B
Gene ontology term
catalytic activity
structural constituent of ribosome
nucleotide binding
RNA binding
GTPase activity
nucleosome
cytoplasm
protein folding
photosynthesis, light harvesting
metalloendopeptidase activity
glycerol ether metabolic process
translation initiation factor activity
protein peptidyl-prolyl isomerization
translation elongation factor activity
protein domain specific binding
heat shock protein binding
mitochondrial outer membrane
mitochondrial inner membrane
intramolecular transferase activity
histidine biosynthetic process
response to oxidative stress
single-stranded DNA binding
rRNA processing
prephenate dehydratase activity
cysteine synthase activity
hexokinase activity
ribonucleoprotein complex
adenine phosphoribosyltransferase activity
P value
0.005
0.010
0.015
0.020
0
500
1000
1500
Ratio of GO terms present
C
nucleic acid binding
structural constituent of ribosome
nucleotide binding
RNA binding
GTPase activity
protein folding
translation initiation factor activity
protein peptidyl-prolyl isomerization
pseudouridine synthesis
translation elongation factor activity
nuclear pore
mitochondrial outer membrane
single-stranded DNA binding
rRNA processing
DNA helicase activity
ribonucleoprotein complex
RNA splicing
P value
0.01
0.02
0.03
0.04
0
250
500
750
Ratio of GO terms present

Cross-Examination of Transcriptomics and Proteomics Datasets Shows Substantial Overlap

Overlap of differentially abundant genes from the transcriptomics and proteomics datasets was assessed by extracting gene IDs from each analysis and finding duplicates, after loosening our initial fold-change parameters of transcriptomics to cover a similar range for the proteomic values (Figure 4-9A).

The range of differently abundant genes/proteins between the two techniques was large with 30 proteins compared to over 2500 transcripts during a single contrast but showed some overlap. Contrasting wildtype GFLV-GHu vs mutant GFLV-GHu $1E_{K802G}$ revealed that most proteins classified as differentially abundant (82%, 23 of 28) were found within the transcriptomics data at 7 dpi (Figure 4-9A). Five proteins did not appear as DEGs within this contrast at 7 dpi, further stressing the need for a multi-omics approach where gene/protein candidates of interest could have been missed by one technique alone. Little overlap was found at the early and late time points, which was not surprising given the small number of DEPs in these contrasts. Additionally, the major GOs that overlapped between the two methods included biosynthetic processes, catalytic activity, GTPase activity, inositol-3 phosphate synthase, isoprenoid biosynthesis, nucleotide binding, and RNA binding. These genes followed identical trends for differential abundance with, for instance, a downregulation of INOSITOL-3 PHOSPHATE SYNTHASE in the transcriptome and proteome analyses for wildtype GFLV-GHu at 7 dpi (Figure 4-9B). Other contrasts with respective time points displayed similar trends (Table 4-S4).

FIGURE 4-9. (A) Contrast of differentially abundant gene candidates identified by LC-MS/MS (purple) and 3'RNA-Seq (green) between wildtype grapevine fanleaf virus (GFLV) strain GHu and mutant GFLV-GHu 1E$^{Pol}_{K802G}$. From left to right, Venn diagrams show the number of differentially abundant genes identified by proteomics (|Log2FoldChange|>0.5 and p-value<0.05), transcriptomics (adjusted p-value<0.05) and both (overlap) at 4-, 7-, and 12 days post-inoculation (dpi), respectively. The overlap between the two techniques shows 82% of the differentially abundant proteins also being identified within the transcriptomics pipeline for this contrast at 7 dpi. No overlap was seen at 4 dpi and 12 dpi, perhaps indicative of differences in data acquired or biological timing differences in the transcriptome and proteome upon viral infection. **(B)** Comparative bar plots for Log2FoldChange values in proteomics (purple) and transcriptomics (green) data when contrasting wildtype GFLV-GHu and mutant GFLV-GHu 1E$^{Pol}_{K802G}$. The 23 genes were pulled from the overlapping gene ID's seen in the center Venn diagram from panel A. All expression levels are in the same absolute direction between LC-MS/MS and 3'RNA-Seq acquired data.

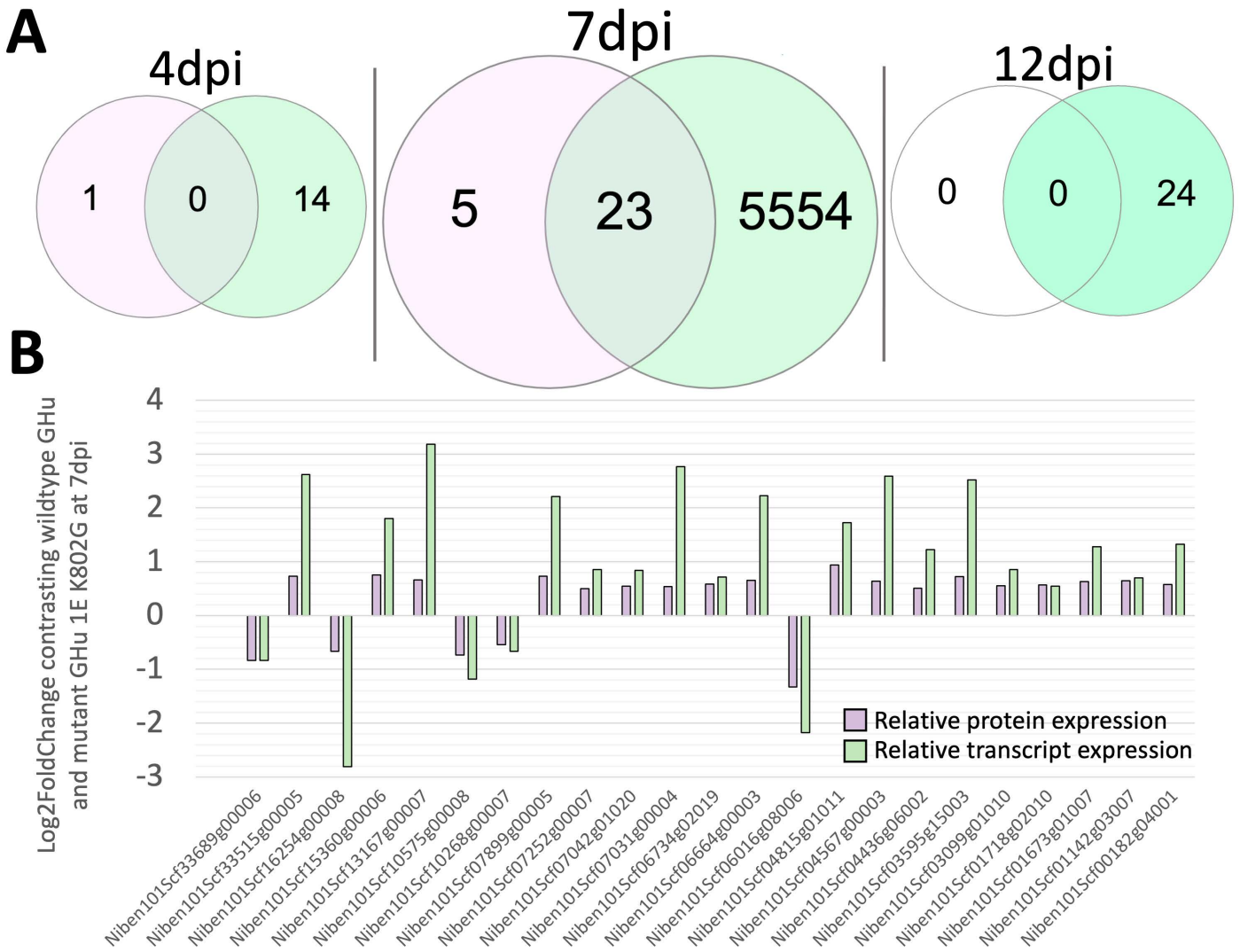
A
4dpi
1
0
14
7dpi
5
23
5554
12dpi
0
0
24
B
Log2FoldChange contrasting wildtype GHu and mutant GHu 1E K802G at 7dpi
4
3
2
1
0
-1
-2
-3
Relative protein expression
Relative transcript expression
Niben101Scf33689g00006
Niben101Scf33515g00005
Niben101Scf16254g00008
Niben101Scf15360g00006
Niben101Scf13167g00007
Niben101Scf10575g00008
Niben101Scf10268g00007
Niben101Scf07899g00005
Niben101Scf07252g00007
Niben101Scf07042g01020
Niben101Scf07031g00004
Niben101Scf06734g02019
Niben101Scf06664g00003
Niben101Scf06016g08006
Niben101Scf04815g01011
Niben101Scf04567g00003
Niben101Scf04436g06002
Niben101Scf03595g15003
Niben101Scf03099g01010
Niben101Scf01718g02010
Niben101Scf01673g01007
Niben101Scf01142g03007
Niben101Scf00182g04001

Identification of Networks of Host Pathways for GFLV Symptom Development

Previous virus–plant studies provided a springboard for profiling the host transcriptome and proteome and biological pathway in GFLV–*N. benthamiana* interactions (Pavan Kumar et al. 2017, Stare et al. 2017, Akbar et al. 2021, Lyu et al. 2020, Osterbaan et al. 2019, Osterbaan et al. 2021, Vigne et al. 2013). Then, information from closely related plant viruses with similar phenotypes was considered to provide the following list of cellular pathways to probe: viral silencing (Wang et al. 2012), viral receptors (Calil and Fontes 2017, Gouveia et al. 2017, Teixeira et al. 2019), kinase cascades (He et al. 2020), plant hormone synthesis (Pavan Kumar et al. 2017, Alazem 2014), integrated stress response (Schoof et al. 2021, Wu et al. 2022), ribosomal complexes (Park et al. 2001, Hashimoto et al. 2016), and photosynthesis-related genes (Akbar et al. 2021, Qiu et al. 2018). Searching relative terms to these seven pathways in the annotated *N. benthamiana* genome generated three pathways of interest for wildtype GFLV-GHu: (1) host defense, (2) ribosome filter hypothesis, and (3) post-transcriptional gene silencing (Figure 4-10).

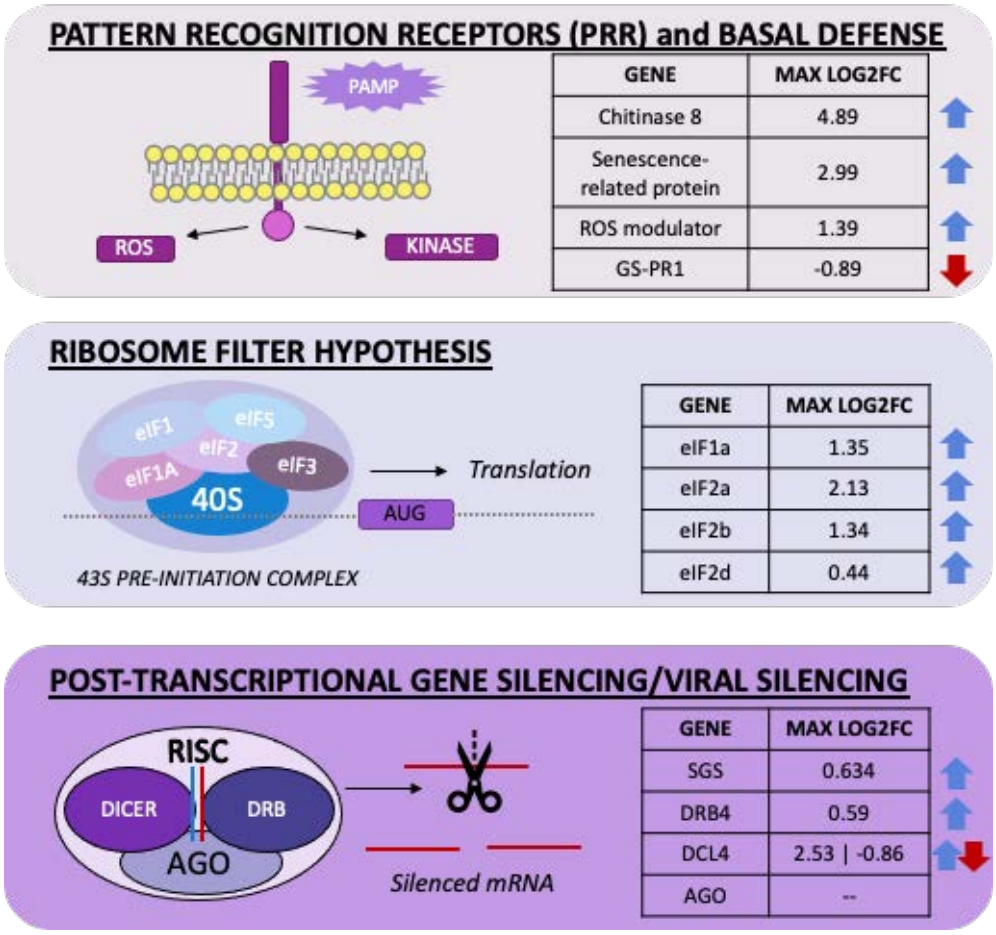

FIGURE 4-10. Hypothesized major networks for symptom development in *N. benthamiana* upon infection by grapevine fanleaf virus strain GHu deduced from profiling proteome and transcriptome changes. Highly represented at 4 days post-inoculation (dpi) and during peak symptom expression at 7 dpi were genes related to basal host defense responses including chitinases, ROS modulators, and a senescence-related protein, which were all upregulated. Other basal defense systems suppressed the expression of glutamine synthase pathogen related-1. Additionally, ribosomal subunits were upregulated at 7 dpi, relating to changes of major translational networks for protein production. An increased abundance of certain ribosomal subunits could modify translational products and reprogram cellular structure to be more conducive for the expression of the viral genome. Silencing mechanisms of miRNA- and RNAi-mediated defense involved the upregulation of SUPPRESSOR OF GENE SILENCING and DOUBLE-STRANDED RNA BINDING PROTEIN transcripts at 7dpi. Other genes of the RNA silencing pathways such as DICER-LIKE 4, returned results with conflicting expression levels or very low counts (ARGONAUTE), and therefore, may contribute in minor but non-critical capacities to the vein clearing phenotype. ROS=Reactive oxygen species, GS-PR1=glutamine synthase pathogenesis related-1, eIF=eukaryotic translation initiation factor, SGS=suppressor of gene silencing, DRB=double-stranded RNA binding protein, DCL=dicer-like protein, AGO=argonaute protein.

The normalized RNA-Seq counts of the genes involved in these three cellular pathways were calculated (Table 4-S5 and File 4-S1). Several genes had increased abundance in plants infected with wildtype GFLV-GHu at 7 dpi, such as SCENESCENCE-RELATED PROTEIN, ROS modulators (CHITINASE 8/9, ROS MODULATOR 1), viral silencing components (RNA-DEPENDENT RNA POLYMERASE 2, DICER-LIKE PROTEIN 4, SUPPRESSOR OF GENE SILENCING, and SERRATE EFFECTOR PROTEIN), and ribosomal components (60S RIBOSOMAL PROTEIN L13A-1, L13A-4) (Figure 4-10). Several other virus-related pathways that were downregulated in plants infected with wildtype GFLV-GHu included GLUTAMINE SYNTHASE and many photosynthetic components (PHOTOSYSTEM REACTION CENTER SUBUNITS PSAK1/2, PHOTOSYSTEM II 10 kDa POLYPEPTIDE, CARBONIC ANHYDRASE, and RUBISCO 1/2). Differences in isoprenoid production pathways were observed for which wildtype-GHu increased the expression of isoprenoid synthesis-related genes, while the other three GFLV strains and mock control had lower levels of these respective genes. It remains unclear how these pathways are triggered for modification in response to GFLV-GHu $1E_{802K}^{Pol}$.

Additional Transcriptomic Treatment Contrasts Reveal Host Regulatory Genes during Early GFLV Infection

Both GFLV-F13 strains modified the transcriptome at a faster rate than that of wildtype GFLV-GHu (Figure 4-S12D, G, J) The effect of the relative transcript abundance for wildtype GFLV-F13 at 4 dpi against the mock treatment was apparent with 132 genes upregulated and 259 genes downregulated (Figure 4-S12G). Comparing

mutant GFLV-F13 $1E_{G802K}^{Pol}$ and mock control treatments resulted in 605 upregulated and 481 downregulated genes (Figure 4-S12J). In contrast, when comparing wildtype GFLV-GHu and mock control at 4 dpi, only two genes were upregulated, and three genes were downregulated, while a tremendous difference in gene expression was observed at 7 dpi (Figure 4-S12D,E). Other GFLV treatments varied more drastically to the control than between viral treatments at 4, 7, and 12 dpi (Figure 4-S12A–L). For treatment groups other than wildtype GFLV-GHu, differences were more drastic at 4 and 12 dpi (Figure 4-S12D–L). Since no virus symptoms are observed for the other treatment groups, observing changes in the transcriptome at early and/or late time points is perplexing and warrants follow-up work.

Both proteome and transcriptome techniques showed that nucleotide binding is the most overrepresented GO for wildtype GFLV-GHu at 7 dpi and that several other metabolic functions could be resolved (Figures 4-5 and 4-6). Unique to wildtype and mutant GFLV-F13 were the overrepresented gene functions of DNA binding (Figure 4-5) and perturbations in metabolic processes, nuclease activity, and cytoskeleton organization (Figure 4-S15).

Confirmation of the DEG Niben101Scf01478g00014

We examined the DEG encoding 60S ACIDIC RIBOSOMAL PROTEIN P1, as it (Niben101Scf01478g00014) had a Log2FoldChange of 8.53 and an adjusted *P*-value of 6.09×10^{-21} between wildtype GFLV-GHu and mutant GFLV-GHu $1E_{K802G}^{Pol}$ at 7 dpi (Table 4-S5). The 3′RNA-Seq results only found this transcript in high abundance in plants infected with wildtype GFLV-GHu at 7 dpi (average normalized counts ∼550) as compared to basal levels in all other treatments and time points (average normalized

counts ~10) (Figure 4-S16). The corresponding protein was not present in the proteomics data likely because its expression was below the detection threshold for LC–MS/MS. The expression of Niben101Scf01478g00014 was confirmed in plants infected with GFLV-GHu by RT-qPCR at 7 dpi with a significantly higher relative expression ($2^{-\Delta\Delta CT}$) in plants infected with the wildtype strain ($p < 0.01$) when normalized to housekeeping gene FBOX but not in plants infected by mutant GFLV-GHu $1E_{K802G}^{Pol}$ and mock inoculated control plants (Figure 4-S16). This analysis validated the specific expression level of a host transcript for which the corresponding protein was undetectable through LC–MS/MS.

DISCUSSION

We characterized the proteome and transcriptome of *N. benthamiana* upon GFLV infection with four distinct virus strains, one strain (GHu) eliciting transient vein clearing symptoms and three others (GHu-$1E_{K802G}^{Pol}$, F13, and F13-$1E_{G802K}^{Pol}$) causing asymptomatic infections. A time course experiment analyzed through 3′RNA-Seq and LC–MS/MS revealed distinct host responses to GFLV infection and strain- and single amino acid-specific perturbations to the host transcript and protein expression. Changes in the transcriptome and proteome of *N. benthamiana* were prominent at peak vein clearing symptom expression (~7 dpi, Figure 4-1C) compared with earlier (4 dpi) or later (12 dpi) time points for wildtype GFLV-GHu (Figures 4-3 and 4-4). Additionally, comparative analyses of transcriptome and proteome datasets obtained with wildtype GFLV-GHu and mutant GFLV-GHu $1E_{K802G}^{Pol}$ revealed residue 802 of the RdRP highly influencing host gene and protein expression profiles (Figures 4-3A–C and 4-4B). This

work yielded a short list of five host protein and gene candidates correlated and unique to symptom expression when contrasted with other GFLV-infected plants (Table 4-S5). In total, 23 gene candidates will be selected for future validation of function in addition to leveraging the proteomics and transcriptomics datasets to examine host pathways influenced by GFLV infection (Table 4-S4).

A rigorous quality control determined that the samples after proteome and transcriptome acquisition were acceptable for the rest of the bioinformatic pipeline. LC–MS/MS resolved over 1500 proteins, while transcriptomics identified over 30,000 transcripts matching to the host genome per sample. Despite a differential resolution and range of these methodologies, both aligned with our hypotheses for wildtype GFLV-GHu related to immune response, metabolism, and host reprogramming genes for symptom development with considerable overlap at peak vein clearing expression (Figures 4-5–7). The proteome showed only a handful of proteins that were differentially abundant in the contrasts; however, additional information was gained by looking at proteins MNAR, which we suspected to be mainly identifying phenotype-specific functions (Table 4-2, Figure 4-6B). The most drastic changes in the transcriptome and proteome were observed at 7 dpi between wildtype GFLV strains GHu and F13 (Figures 4-3 and 4-4, Tables 4-1 and 4-2). This result was expected given the difference in genetic makeup between the two GFLV strains and their phenotypic differences on *N. benthamiana*. Furthermore, the wildtype and mutant GFLV-GHu contrast shared many DEGs in comparison with the wildtype GFLV strains GHu and F13 contrast (62.5%, 1692 of 2707 genes) (Table 4-1, Figure 4-3B,E). This finding suggested that the lysine (K) to glycine (G) mutation in the RdRP of GFLV-GHu has

more impact on the transcriptome and proteome of *N. benthamiana* for symptom development than the other >10% genetic differences at the nucleotide level between wildtype GFLV strains GHu and F13. Previous and current phenotypic observations remain consistent with this observation (Vigne et al. 2013, Osterbaan et al. 2019).

From the proteome analyses, plant host protein candidates potentially critical for symptom expression were identified. These included proteins involved in nucleotide binding, inositol-3-phosphate synthase activity, isopentenyl diphosphate biosynthesis, and thiamine biosynthesis (Figure 4-6A). This list was consistent with the results of transcriptomic GSEA, as analysis of the full transcriptome through DEG identification and subsequent over-enriched gene analysis showed nucleic acid binding, ribosomal component, and biosynthesis-related genes characteristic of the vein clearing phenotype (Figure 4-5). This was also confirmed through WGCNA, a gene grouping analysis across multiple treatments and time points, where these same GOs were overrepresented at 7 dpi for wildtype GFLV-GHu, and distinct from all other treatments and time points (Figure 4-8). Five gene clusters represented the unique gene expression profiles related to vein clearing symptom expression including hypersensitive response and defense-related genes being dysregulated only at 7 dpi for wildtype GFLV-GHu (Figure 4-8A). Other similar GOs were overrepresented as with previous gene set enrichment analysis (Figure 4-8B,C). These combined findings provided confidence that gene functions related to immune response (RNA binding, response to oxidative stress, and gene silencing), translation regulation (structural constituent of the ribosome, RNA binding, and translation elongation factor activity), and metabolism (inositol-3-phosphate synthase activity, pseudouridine synthesis, and thiamine biosynthetic process) are

unique to vein clearing symptom expression at 7 dpi, as they were not observed prior to (4 dpi) or after (12 dpi) symptom development. In addition, examining the GOs for MNAR proteins was equally informative to the phenotype.

A network analysis following GSEA for wildtype GFLV-GHu at 7 dpi against all other treatment groups provided the most condensed and comprehensive form of which GO is associated with vein clearing symptom expression (Figure 4-7). By adding manual group annotations to the network analysis, three key gene categories were most associated with this phenotype: gene regulation, immune response, and metabolism (Figure 4-7). These major gene functions were found again when temporal analysis through WGCNA isolated gene expression profiles specific to wildtype GFLV-GHu at 7 dpi (Figure 4-8). Together, these gene categories suggested that a hypersensitive response is induced when GFLV first enters apical tissue (4–7 dpi), and this signal is not sustained later into infection (12 dpi), yet the exact mechanism remains unclear. Nevertheless, the overlap of GSEA and WGCNA in identifying differentially abundant genes was confirmatory to other network analyses.

At peak observation of the vein clearing phenotype at 7 dpi, the list of differentially abundant host genes obtained by contrasting the proteomic and transcriptomic datasets between the wildtype GFLV-GHu and its single-amino acid mutant was consistent (Figure 4-9A). These two techniques complemented each other to provide a list of 23 protein and gene candidates associated with virus-induced symptom development, although the proteome complexity of plant tissues and stochasticity of LC–MS/MS acquisition may have prevented lower-abundance proteins from being identified (Table 4-S6). These 23 candidates once again belonged to 3 main

gene host functions: translational regulation, nucleotide binding, and metabolism. All 23 candidates showed the same absolute expression values with correlated fold change values (Figure 4-9B and Table 4-S8). Even in the instance of a gene product not being present in the proteomics dataset, confidence in our analysis was obtained by performing RT-qPCR on the top gene candidate from 3′RNA-Seq, a 60S ACIDIC RIBOSOMAL PROTEIN P1 (Niben101Scf01478g00014). A large abundance of this transcript was documented in plant samples infected only by wildtype GFLV-GHu at 7 dpi with basal levels detected in any other sample infected by one of the other three GFLV strains or the control (Figure 4-S16). We were surprised to observe only cases of overlap where the absolute value of expression (positive change in abundance or negative) was the same across both techniques with no discrepancies. This may only be reflective of thresholds we placed to obtain the 23 genes of overlap between GFLV GHu strains at 7 dpi, but we interpreted that active mRNA transcripts captured through 3′RNA-Seq are complementary to shotgun proteomics approaches such as LC–MS/MS. The complementary nature of these two techniques we found to be as, if not more satisfactory, as RT-qPCR validation of candidate genes.

The overlap of proteomics and transcriptomics revealed tRNA ligase activity to be upregulated, suggesting a fine tuning of translational regulation and amino acid availability for transcript selection (Peschek and Walter 2019). Plant tRNA ligases are non-homologous to other RNA ligases and able to perform three different catalytic functions; polynucleotide kinase activity, cyclic phosphodiesterase activity, and adenylyltransferase/ligase activity (Englert and Beier 2005). Lysine, proline, and threonine tRNA ligases were upregulated in both the proteomics and transcriptomics

data (Table 4-S7). Changing the expression pattern of these enzymes was correlated with the disruption of many genes in GFLV–*N. benthamiana* symptomatic interactions, as expected from such global regulators of host gene expression.

Secondary metabolites play major roles in plant defense against pathogens and abiotic stress (Wink 2003, Akula and Ravishankar 2011). Regulating enzymes that control secondary metabolite pathways helps maintain plant growth patterns in response to biotic and abiotic factors. Not only did two wildtype GFLV strains show drastically different host responses with GOs related to biosynthetic pathways, but mutant GFLV strain GHu-1E$_{K802G}^{Pol}$ showed a significant dysregulation of isoprenoid related enzymes. In addition, gene enrichment analysis between two treatments and network analysis showed that wildtype GFLV-GHu increased the expression of genes and proteins involved in secondary metabolite production. In fact, isoprenoids and similar biosynthetic components play major roles in viral defense in all eukaryotic organisms (Okada 2011, Fraga 2005). It is possible that this metabolite pathway identified in *N. benthamiana* is unique to wildtype GFLV-GHu, as a direct metabolite profile was documented in infected grapevines (Martin et al. 2021). Genes related to oxidative burst were also differentially expressed in symptomatic plants, suggesting that host immune response could be involved in the development of vein clearing symptoms caused by wildtype GFLV-GHu. Future work focusing on collecting quantitative data to measure oxidative stress metabolites in infected plants (i.e., peroxide, O_3^-) would be more informative to this end.

DEGs identified in this study showed parallels and juxtaposition to other virus–host plant interaction studies. MYMV, an ssDNA begomovirus, causes differential

expression of proteasome subunits, carbonic anhydrase, glutathione S transferase, and photosynthetic components (Pavan Kumar et al. 2017); many of these appeared in contrasts of symptomatic and asymptomatic GFLV strains. In the case of PVY, an ssRNA potyvirus, symptomology and response from infection were shown to be heavily regulated and initiated by salicylic acid (Stare et al. 2017). Photosynthetic components in addition to ribosomal proteins were also majorly dysregulated in PVY (Stare et al. 2017). Our study on GFLV–*N. benthamiana* interactions revealed little to no involvement of plant hormone pathways but shared similarity in the downregulation of photosynthesis genes. For SCMV, an ssRNA potyvirus, infection led to major dysregulation in photosynthetic pathway components (Akbar et al. 2021) but to a broader and deeper degree than that observed in our system. A discrepancy between SCMV and GFLV with regard to the magnitude of dysregulated photosynthesis relates perhaps to distinct symptom types resulting from infection with a transient vein clearing for GFLV and a strong and stable mosaic for SCMV.

Many reports associate recovery of virus symptoms with RNA silencing components, often when virus–host interactions induce post-transcriptional gene silencing (PTGS) and shuttle viral small interfering RNAs through vasculature tissue ahead of virus movement (Ghosal and Sanfaçon 2015). With the recent report of two viral silencing suppressors identified in the GFLV genome, proteins 1A and $1B^{Hel}$, and the previously noted interaction of protein $1E^{Pol}$ with $1B^{Hel}$, we sought out genes related to PTGS (Osterbaan et al. 2021; Choi et al. 2023). We documented dysregulation of RNA silencing pathways regardless of the GFLV strains, suggesting little, if any, involvement of RNA silencing components in GFLV-GHu vein clearing symptom

induction in *N. benthamiana* (Table 4-S9 and File 4-S1). Slightly elevated expression levels were observed for DICER-LIKE PROTEIN 4 and SUPPRESSOR OF GENE SILENCING; to the same extent, the virus titer was detected in samples, suggesting that RNA silencing components are active during infection but diminish after symptoms subside. However, the counts on many of these genes were relatively low for robust analyses and definite conclusions.

Based on our results and consistent with the literature (Osterbaan et al. 2019; 2021), the display of vein clearing symptoms was not correlated with the GFLV titer. Both the abundance of GFLV RNA2 in the transcriptomics data and three viral proteins ($1E^{Pol}$, $2B^{MP}$, and $2C^{CP}$) in the proteomics data support a statistically similar GFLV titer in infected *N. benthamiana* plants, regardless of the virus strain (Figure 4-S11). Therefore, we suspect that the overall burden of viral replication and abundance has little to no impact on symptom development in this instance. Overall lower reads were acquired for RNA1 compared with those for RNA2 for all GFLV strains in the transcriptomics data, and no reads were identified for GFLV RNA1 for the two strains F13, perhaps due to a limitation of 3′RNA-Seq or a specific feature in this strain's replication. The reason behind a lower RNA1 titer relative to RNA2 remains unresolved but is consistent with the proteomics work for which RNA2-encoded proteins were more abundant than RNA1-encoded proteins (Pinck et a. 1988). The disparate ratio of GFLV RNA molecules and departure of the viral titer related to symptomology were previously documented for *Vitis vinifera* cv. "Chardonnay" in a vineyard setting (Kubina et al. 2022). This RNA ratio was also recently documented for tobacco ringspot virus and

tomato ringspot virus (ToRSV), two nepoviruses related to GFLV, in pawpaw, another fruit crop (Choi et al. 2022).

Some parallels can be made between our findings on GFLV and other nepoviruses such as ToRSV (Jovel et al. 2011; Bitterlin and Gonsalves 1988) and artichoke Italian latent virus (AILV). A previous study used microarray analysis to identify DEGs in *N. benthamiana* infected with ToRSV, along with two other fruit crop viruses (Dardick 2007). This study examined plant host gene expression levels after plant recovery from symptoms. Many GOs similar to those identified in this study were reported including induced or upregulated genes related to stress/pathogenesis, protein synthesis components, gene regulators, proteolysis, and developmental regulators. Additionally, repressed genes related to photosynthesis, protein synthesis, and unknown components were documented for ToRSV at a greater magnitude than for the other two viruses (Dardick 2007). These same gene functions were found dysregulated in our study using 3′-RNA-Seq and LC–MS/MS, especially with an improved annotation of the *N. benthamiana* genome and a more extensive read volume for genes. Another study revealed recovery of *N. benthamiana* from ToRSV in association with reduced RNA2 translation and decreased AGO1 levels (Ghoshal and Sanfaçon 2014). Similar recovery aspects with decreased RNA2 levels were reported for AILV (Santovito et al. 2014). No major correlations with AGO proteins or GFLV RNA2 levels were found in our study when contrasting the proteome and transcriptome of symptomatic and asymptomatic GFLV infection (Figures 4-10 and 4-S11). Differences in virus–host interactions among nepoviruses add to the diversity of this plant virus genus (Sanfaçon 2022) and brings

additional merit to the uniqueness of GFLV and its protein $1E^{Pol}$ for symptom expression in *N. benthamiana*.

Our findings related to metabolic pathways in addition to immune response and translational regulation suggest an entanglement of the metabolome, transcriptome, and proteome contributing to the observed phenotype in *N. benthamiana*. By initial perception of GFLV-GHu, the host response likely triggers an oxidative burst and an overall disruption of metabolic pathways as an incomplete hypersensitive reaction to infection. The way other GFLV strains avoid this pattern is unclear because the expression of very few genes was altered by the reverse mutant GFLV F13-$1E_{G802K}^{Pol}$ treatment compared with the control when considered against the symptomatic wildtype GFLV-GHu carrying the same amino acid residue in position 802 of protein $1E^{Pol}$. Additional approaches will need to be considered to delve into not only plant–virus interactions but also virus–virus interactions and host–host interactions upon GFLV infection to address additional questions for mechanistic understandings of GFLV symptom development *in planta*. Perhaps pull-downs of tagged proteins beyond previous studies with protein $1E^{Pol}$ could be implemented to more precisely determine cell components involved in vein clearing symptoms. To focus on the tissue type, a more optimized protein elution or a longer run time on LC–MS/MS could bring further resolution to virus–host protein complexes that give rise to symptom development.

Upon systemic infection, it appears that wildtype GFLV-GHu has a delayed reaction in establishing full infection and largely avoids detection by the host, indicated by low changes in the host transcriptome and proteome at 4 dpi (Figure 4-S12D,G,J) and lower virus presence at 4 dpi (Figure 4-S11). These data suggested that *N.*

benthamiana recognizes the invasion of wildtype GFLV-GHu later than other GFLV strains and induces a hypersensitive response as an attempt to clear out or restrict the virus. The differential expression of pathogen- and immune-response-related genes at 4 dpi is unique in this instance. Host genes activated during the initial stages of viral replication might initiate signaling cascades for a robust yet short-lived oxidative burst. Some aspect of protein interactions through the GFLV $1E^{Pol}$ C-terminal end could be responsible for these major differences. Furthermore, unique gene networks of ribosomal filtering and host modification were induced by the virus. Both translation efficiency induced by viral replication and host defense were altered, as shown by translation initiation factors, translation elongation factors, tRNA ligases, and ribosomal proteins being in differential abundance analyses. Finally, vein clearing symptoms were shown to be correlated with metabolism and photosynthetic components of *N. benthamiana*. Biosynthetic and photosynthetic pathway-related genes were consistently dysregulated in plants infected with wildtype GFLV-GHu and to a much higher degree than the other GFLV strains. The transcriptome and proteome analyses were mostly consistent with this network of pathogen detection and overcoming disease symptomology. A subcellular resolution of GFLV protein $1E^{Pol}$ *in planta* or future targeted co-immunoprecipitation studies could further explore these mechanisms, particularly those triggering the cascade of events by tracking specific host interactants of protein $1E^{Pol}$.

CONCLUSIONS

Our study provided insights into host proteome and transcriptome changes and distinct GOs and pathways related to GFLV infection with an emphasis on vein clearing symptom development in *N. benthamiana*. Several differentially abundant gene candidates were identified in the proteome and transcriptome of *N. benthamiana* via bioinformatic and computational analyses for symptom development following GFLV-GHu infection. Contrasting two different omics techniques validated changes in the transcriptome and proteome with 3′RNA-Seq providing additional candidates that were in lower abundance compared with LC–MS/MS. In the arms race between GFLV and its plant host, many layers of transcriptional and translational regulation were hypothesized and subsequently identified within each dataset generated. These two techniques generated consistent results that were valuable in examining GFLV–*N. benthamiana* interactions. Ultimately, our findings suggested gene expression patterns unique to the GFLV-GHu symptom determinant residue 802 of protein $1E^{Pol}$. A functional analysis of the DEG candidates may yield exciting new information on the molecular mechanisms of symptom development during plant virus infection.

REFERENCES

Adusumilli, R., & Mallick, P. (2017). Data Conversion with ProteoWizard msConvert. In L. Comai, J. E. Katz, & P. Mallick (Eds.), Proteomics (Vol. 1550, pp. 339–368). Springer New York. https://doi.org/10.1007/978-1-4939-6747-6_23

Akbar, S., Yao, W., Yu, K., Qin, L., Ruan, M., Powell, C. A., Chen, B., & Zhang, M. (2021). Photosynthetic characterization and expression profiles of sugarcane infected by Sugarcane mosaic virus (SCMV). Photosynthesis Research, 150(1), 279–294. https://doi.org/10.1007/s11120-019-00706-w

Akula, R., & Ravishankar, G. A. (2011). Influence of abiotic stress signals on secondary metabolites in plants. Plant Signaling & Behavior, 6(11), 1720–1731. https://doi.org/10.4161/psb.6.11.17613

Alazem, M., & Lin, N. (2014). Roles of plant hormones in the regulation of host–virus interactions. Molecular Plant Pathology, 16(5), 529–540. https://doi.org/10.1111/mpp.12204

Alexander, M. M., & Cilia, M. (2016). A molecular tug-of-war: Global plant proteome changes during viral infection. Current Plant Biology, 5, 13–24. https://doi.org/10.1016/j.cpb.2015.10.003

Andret-Link, P., Laporte, C., Valat, L., Ritzenthaler, C., Demangeat, G., Vigne, E., Laval, V., Pfeiffer, P., Stussi-Garaud, C., & Fuchs, M. (2004). Grapevine fanleaf virus: Still a major threat to the grapevine industry. Journal of Plant Pathology, 86(3), 183–195.

Andrews, S. (2010). FastQC: a quality control tool for high throughput sequence data [Computer software]. http://www.bioinformatics.babraham.ac.uk/projects/fastqc/

Bitterlin, M., & Gonsalves, D. (1988). Serological grouping of tomato ringspot virus isolates: Implications for diagnosis and cross-protection. Phytopathology, 78(3), 278–285.

Bivalkar-Mehla, S., Vakharia, J., Mehla, R., Abreha, M., Kanwar, J. R., Tikoo, A., & Chauhan, A. (2011). Viral RNA silencing suppressors (RSS): Novel strategy of viruses to ablate the host RNA interference (RNAi) defense system. Virus Research, 155(1), 1–9. https://doi.org/10.1016/j.virusres.2010.10.003

Bolger, A. M., Lohse, M., & Usadel, B. (2014). Trimmomatic: A flexible trimmer for Illumina sequence data. Bioinformatics, 30(15), 2114–2120. https://doi.org/10.1093/bioinformatics/btu170

Bombarely, A., Rosli, H. G., Vrebalov, J., Moffett, P., Mueller, L. A., & Martin, G. B. (2012). A draft genome sequence of Nicotiana benthamiana to enhance molecular plant-microbe biology research. Molecular Plant-Microbe Interactions®, 25(12), 1523–1530. https://doi.org/10.1094/MPMI-06-12-0148-TA

Bonferroni, C. E. (1936). Teoria statistica delle classi e calcolo delle probabilita.

Calil, I. P., & Fontes, E. P. B. (2017). Plant immunity against viruses: Antiviral immune receptors in focus. Annals of Botany, 119(5), 711–723. https://doi.org/10.1093/aob/mcw200

Chavez, J. D., Cilia, M., Weisbrod, C. R., Ju, H.-J., Eng, J. K., Gray, S. M., & Bruce, J. E. (2012). Cross-linking Measurements of the Potato leafroll virus Reveal Protein Interaction Topologies Required for Virion Stability, Aphid Transmission, and Virus–Plant Interactions. Journal of Proteome Research, 11(5), 2968–2981. https://doi.org/10.1021/pr300041t

Choi, J., Osatuke, A. C., Erich, G., Stevens, K., Hwang, M. S., Al Rwahnih, M., & Fuchs, M. (2022). High-Throughput Sequencing Reveals Tobacco and Tomato Ringspot Viruses in Pawpaw. Plants, 11(24), Article 24. https://doi.org/10.3390/plants11243565

Cilia, M., Fish, T., Yang, X., McLaughlin, M., Thannhauser, T. W., & Gray, S. (2009). A comparison of protein extraction methods suitable for gel-based proteomic studies of aphid proteins. Journal of Biomolecular Techniques: JBT, 20(4), 201–215.

Dardick, C. (2007). Comparative Expression Profiling of Nicotiana benthamiana Leaves Systemically Infected with Three Fruit Tree Viruses. Molecular Plant-Microbe Interactions®, 20(8), 1004–1017. https://doi.org/10.1094/MPMI-20-8-1004

Davidson, A. D., Williamson, M. K., Lewis, S., Shoemark, D., Carroll, M. W., Heesom, K. J., Zambon, M., Ellis, J., Lewis, P. A., Hiscox, J. A., & Matthews, D. A. (2020). Characterisation of the transcriptome and proteome of SARS-CoV-2 reveals a cell passage induced in-frame deletion of the furin-like cleavage site from the spike glycoprotein. Genome Medicine, 12(1), 68. https://doi.org/10.1186/s13073-020-00763-0

Di Carli, M., Benvenuto, E., & Donini, M. (2012). Recent Insights into Plant–Virus Interactions through Proteomic Analysis. Journal of Proteome Research, 11(10), 4765–4780. https://doi.org/10.1021/pr300494e

Englert, M., & Beier, H. (2005). Plant tRNA ligases are multifunctional enzymes that have diverged in sequence and substrate specificity from RNA ligases of other phylogenetic origins. Nucleic Acids Research, 33(1), 388–399. https://doi.org/10.1093/nar/gki174

Fuchs, M., Hily, J.-M., Petrzik, K., Sanfaçon, H., Thompson, J. R., van der Vlugt, R., Wetzel, T., & ICTV Report ConsortiumYR 2022. (n.d.). ICTV Virus Taxonomy Profile: Secoviridae 2022. Journal of General Virology, 103(12), 001807. https://doi.org/10.1099/jgv.0.001807

Ghoshal, B., & Sanfaçon, H. (2014). Temperature-dependent symptom recovery in Nicotiana benthamiana plants infected with tomato ringspot virus is associated with reduced translation of viral RNA2 and requires ARGONAUTE 1. Virology, 456–457, 188–197. https://doi.org/10.1016/j.virol.2014.03.026

Ghoshal, B., & Sanfaçon, H. (2015). Symptom recovery in virus-infected plants: Revisiting the role of RNA silencing mechanisms. Virology, 479–480, 167–179. https://doi.org/10.1016/j.virol.2015.01.008

Gouveia, B. C., Calil, I. P., Machado, J. P. B., Santos, A. A., & Fontes, E. P. B. (2017). Immune Receptors and Co-receptors in Antiviral Innate Immunity in Plants. Frontiers in Microbiology, 7. https://www.frontiersin.org/articles/10.3389/fmicb.2016.02139

Hashimoto, M., Neriya, Y., Yamaji, Y., & Namba, S. (2016). Recessive Resistance to Plant Viruses: Potential Resistance Genes Beyond Translation Initiation Factors. Frontiers in Microbiology, 7. https://www.frontiersin.org/articles/10.3389/fmicb.2016.01695

Hasin, Y., Seldin, M., & Lusis, A. (2017). Multi-omics approaches to disease. Genome Biology, 18(1), 83. https://doi.org/10.1186/s13059-017-1215-1

He, X., Wang, C., Wang, H., Li, L., & Wang, C. (2020). The Function of MAPK Cascades in Response to Various Stresses in Horticultural Plants. Frontiers in Plant Science, 11, 952. https://doi.org/10.3389/fpls.2020.00952

Jin, L., Bi, Y., Hu, C., Qu, J., Shen, S., Wang, X., & Tian, Y. (2021). A comparative study of evaluating missing value imputation methods in label-free proteomics. Scientific Reports, 11(1), Article 1. https://doi.org/10.1038/s41598-021-81279-4

Jovel, J., Walker, M., & Sanfaçon, H. (2011). Salicylic Acid-Dependent Restriction of Tomato ringspot virus Spread in Tobacco Is Accompanied by a Hypersensitive Response, Local RNA Silencing, and Moderate Systemic Resistance. Molecular Plant-Microbe Interactions®, 24(6), 706–718. https://doi.org/10.1094/MPMI-09-10-0224

Kim, D., Paggi, J. M., Park, C., Bennett, C., & Salzberg, S. L. (2019). Graph-based genome alignment and genotyping with HISAT2 and HISAT-genotype. Nature Biotechnology, 37(8), 907–915. https://doi.org/10.1038/s41587-019-0201-4

Kolberg, L., Raudvere, U., Kuzmin, I., Vilo, J., & Peterson, H. (2020). gprofiler2—An R package for gene list functional enrichment analysis and namespace

conversion toolset g:Profiler. F1000Research, 9, ELIXIR-709. https://doi.org/10.12688/f1000research.24956.2

Kubina, J., Hily, J.-M., Mustin, P., Komar, V., Garcia, S., Martin, I. R., Poulicard, N., Velt, A., Bonnet, V., Mercier, L., Lemaire, O., & Vigne, E. (2022). Characterization of Grapevine Fanleaf Virus Isolates in 'Chardonnay' Vines Exhibiting Severe and Mild Symptoms in Two Vineyards. Viruses, 14(10), Article 10. https://doi.org/10.3390/v14102303

Langfelder, P., & Horvath, S. (2008). WGCNA: An R package for weighted correlation network analysis. BMC Bioinformatics, 9(1), 559. https://doi.org/10.1186/1471-2105-9-559

Liao, Y., Smyth, G. K., & Shi, W. (2013). The Subread aligner: Fast, accurate and scalable read mapping by seed-and-vote. Nucleic Acids Research, 41(10), e108–e108. https://doi.org/10.1093/nar/gkt214

Liao, Y., Smyth, G. K., & Shi, W. (2014). featureCounts: An efficient general purpose program for assigning sequence reads to genomic features. Bioinformatics, 30(7), 923–930. https://doi.org/10.1093/bioinformatics/btt656

Liu, D., Shi, L., Han, C., Yu, J., Li, D., & Zhang, Y. (2012). Validation of reference genes for gene expression studies in virus-infected *Nicotiana benthamiana* using quantitative real-time PCR. PloS One, 7(9), e46451. https://doi.org/10.1371/journal.pone.0046451

Love, M. I., Huber, W., & Anders, S. (2014). Moderated estimation of fold change and dispersion for RNA-seq data with DESeq2. Genome Biology, 15(12), 550. https://doi.org/10.1186/s13059-014-0550-8

Lyu, S., Gao, L., Zhang, R., Zhang, C., & Hou, X. (2020). Correlation Analysis of Expression Profile and Quantitative iTRAQ-LC-MS/MS Proteomics Reveals Resistance Mechanism Against TuMV in Chinese Cabbage (Brassica rapa ssp. Pekinensis). Frontiers in Genetics, 11. https://www.frontiersin.org/articles/10.3389/fgene.2020.00963

Maliogka, V. I., Martelli, G. P., Fuchs, M., & Katis, N. I. (2015). Chapter Six—Control of Viruses Infecting Grapevine. In G. Loebenstein & N. I. Katis (Eds.), Advances in Virus Research (Vol. 91, pp. 175–227). Academic Press. https://doi.org/10.1016/bs.aivir.2014.11.002

Martin, I. R., Vigne, E., Velt, A., Hily, J.-M., Garcia, S., Baltenweck, R., Komar, V., Rustenholz, C., Hugueney, P., Lemaire, O., & Schmitt-Keichinger, C. (2021). Severe Stunting Symptoms upon Nepovirus Infection Are Reminiscent of a Chronic Hypersensitive-like Response in a Perennial Woody Fruit Crop. Viruses, 13(11), Article 11. https://doi.org/10.3390/v13112138

McQuitty, L. L., & Clark, J. A. (1968). Clusters from Iterative, Intercolumnar Correlational Analysis. Educational and Psychological Measurement, 28(2), 211–238. https://doi.org/10.1177/001316446802800201

M. Fraga, B. (2005). Natural sesquiterpenoids. Natural Product Reports, 22(4), 465–486. https://doi.org/10.1039/B501837B

Mootha, V. K., Lindgren, C. M., Eriksson, K.-F., Subramanian, A., Sihag, S., Lehar, J., Puigserver, P., Carlsson, E., Ridderstråle, M., Laurila, E., Houstis, N., Daly, M. J., Patterson, N., Mesirov, J. P., Golub, T. R., Tamayo, P., Spiegelman, B., Lander, E. S., Hirschhorn, J. N., … Groop, L. C. (2003). PGC-1α-responsive

genes involved in oxidative phosphorylation are coordinately downregulated in human diabetes. Nature Genetics, 34(3), 267–273. https://doi.org/10.1038/ng1180

Morris-Krsinich, B. A. M., Forster, R. L. S., & Mossop, D. W. (1983). The synthesis and processing of the nepovirus grapevine fanleaf virus proteins in rabbit reticulocyte lysate. Virology, 130(2), 523–526. https://doi.org/10.1016/0042-6822(83)90105-8

Okada, K. (2011). The Biosynthesis of Isoprenoids and the Mechanisms Regulating It in Plants. Bioscience, Biotechnology, and Biochemistry, 75(7), 1219–1225. https://doi.org/10.1271/bbb.110228

Osterbaan, L. J., Choi, J., Kenney, J., Flasco, M., Vigne, E., Schmitt-Keichinger, C., Rebelo, A. R., Heck, M., & Fuchs, M. (2019). The identity of a single residue of the RNA-dependent RNA polymerase of grapevine fanleaf virus modulates vein clearing in *Nicotiana benthamiana*. Molecular Plant-Microbe Interactions, 32(7), 790–801. https://doi.org/10.1094/MPMI-12-18-0337-R

Osterbaan, L. J., & Fuchs, M. (2019). Dynamic interactions between plant viruses and their hosts for symptom development. Journal of Plant Pathology, 101(4), 885–895. https://doi.org/10.1007/s42161-019-00323-5

Osterbaan, L. J., Hoyle, V., Curtis, M., DeBlasio, S., Rivera, K. D., Heck, M., & Fuchs, M. (2021). Identification of protein interactions of grapevine fanleaf virus RNA-dependent RNA polymerase during infection of *Nicotiana benthamiana* by affinity purification and tandem mass spectrometry. Journal of General Virology, 102(5). https://doi.org/10.1099/jgv.0.001607

Park, H.-S., Himmelbach, A., Browning, K. S., Hohn, T., & Ryabova, L. A. (2001). A Plant Viral "Reinitiation" Factor Interacts with the Host Translational Machinery. Cell, 106(6), 723–733. https://doi.org/10.1016/S0092-8674(01)00487-1

Pavan Kumar, B. K., Kanakala, S., Malathi, V. G., Gopal, P., & Usha, R. (2017). Transcriptomic and proteomic analysis of yellow mosaic diseased soybean. Journal of Plant Biochemistry and Biotechnology, 26(2), 224–234. https://doi.org/10.1007/s13562-016-0385-3

Perkins, D. N., Pappin, D. J. C., Creasy, D. M., & Cottrell, J. S. (1999). Probability-based protein identification by searching sequence databases using mass spectrometry data. Electrophoresis, 20(18), 3551–3567. https://doi.org/10.1002/(SICI)1522-2683(19991201)20:18<3551::AID-ELPS3551>3.0.CO;2-2

Peschek, J., & Walter, P. (2019). tRNA ligase structure reveals kinetic competition between non-conventional mRNA splicing and mRNA decay. eLife, 8, e44199. https://doi.org/10.7554/eLife.44199

Pinck, L., Fuchs, M., Pinck, M., RAVELONANDROI, M., & WALTER, B. (1988). A satellite RNA in Grapevine Fanleaf Virus strain F13. Journal of General Virology - J GEN VIROL, 69, 233–239. https://doi.org/10.1099/0022-1317-69-1-233

Qiu, Y., Zhang, Y., Wang, C., Lei, R., Wu, Y., Li, X., & Zhu, S. (2018). Cucumber mosaic virus coat protein induces the development of chlorotic symptoms

through interacting with the chloroplast ferredoxin I protein. Scientific Reports, 8, 1205. https://doi.org/10.1038/s41598-018-19525-5

Ramsey, J. S., Chin, E. L., Chavez, J. D., Saha, S., Mischuk, D., Mahoney, J., Mohr, J., Robison, F. M., Mitrovic, E., Xu, Y., Strickler, S. R., Fernandez, N., Zhong, X., Polek, M., Godfrey, K. E., Giovannoni, J. J., Mueller, L. A., Slupsky, C. M., Bruce, J. E., & Heck, M. (2020). Longitudinal Transcriptomic, Proteomic, and Metabolomic Analysis of Citrus limon Response to Graft Inoculation by Candidatus *Liberibacter asiaticus*. Journal of Proteome Research, 19(6), 2247–2263. https://doi.org/10.1021/acs.jproteome.9b00802

Raudvere, U., Kolberg, L., Kuzmin, I., Arak, T., Adler, P., Peterson, H., & Vilo, J. (2019). g:Profiler: A web server for functional enrichment analysis and conversions of gene lists (2019 update). Nucleic Acids Research, 47(W1), W191–W198. https://doi.org/10.1093/nar/gkz369

Roy, B. G., & Fuchs, M. (2022). Herbaceous plant hosts as supermodels for grapevine viruses: A historical perspective. Journal of Plant Pathology, 1–30. https://doi.org/10.1007/s42161-022-01267-z

Sanfaçon, H. (2022). Re-examination of nepovirus polyprotein cleavage sites highlights the diverse specificities and evolutionary relationships of nepovirus 3C-like proteases. Archives of Virology, 167(12), 2529–2543. https://doi.org/10.1007/s00705-022-05564-x

Santovito, E., Mascia, T., Siddiqui, S. A., Minutillo, S. A., Valkonen, J. P. T., & Gallitelli, D. (2014). Infection Cycle of Artichoke Italian Latent Virus in

Tobacco Plants: Meristem Invasion and Recovery from Disease Symptoms. PLoS ONE, 9(6), e99446. https://doi.org/10.1371/journal.pone.0099446

Schoof, M., Wang, L., Cogan, J. Z., Lawrence, R. E., Boone, M., Wuerth, J. D., Frost, A., & Walter, P. (2021). Viral evasion of the integrated stress response through antagonism of eIF2-P binding to eIF2B. Nature Communications, 12(1), 7103. https://doi.org/10.1038/s41467-021-26164-4

Searle, B. C. (2010). Scaffold: A bioinformatic tool for validating MS/MS-based proteomic studies. PROTEOMICS, 10(6), 1265–1269. https://doi.org/10.1002/pmic.200900437

Shannon, P., Markiel, A., Ozier, O., Baliga, N. S., Wang, J. T., Ramage, D., Amin, N., Schwikowski, B., & Ideker, T. (2003). Cytoscape: A Software Environment for Integrated Models of Biomolecular Interaction Networks. Genome Research, 13(11), 2498–2504. https://doi.org/10.1101/gr.1239303

Smits, A., & Huber, W. (2022). DEP: Differential Enrichment analysis of Proteomics data (Version 1.16.0) [Computer software]. Bioconductor version: Release (3.14). https://doi.org/10.18129/B9.bioc.DEP

Stare, T., Stare, K., Weckwerth, W., Wienkoop, S., & Gruden, K. (2017). Comparison between Proteome and Transcriptome Response in Potato (Solanum tuberosum L.) Leaves Following Potato Virus Y (PVY) Infection. Proteomes, 5(3), 14. https://doi.org/10.3390/proteomes5030014

Subramanian, A., Tamayo, P., Mootha, V. K., Mukherjee, S., Ebert, B. L., Gillette, M. A., Paulovich, A., Pomeroy, S. L., Golub, T. R., Lander, E. S., & Mesirov, J. P. (2005). Gene set enrichment analysis: A knowledge-based approach for

interpreting genome-wide expression profiles. Proceedings of the National Academy of Sciences, 102(43), 15545–15550. https://doi.org/10.1073/pnas.0506580102

Tang, Z., Fan, W., Li, Q., Wang, D., Wen, M., Wang, J., Li, X., & Zhou, Y. (2022). MVIP: Multi-omics portal of viral infection. Nucleic Acids Research, 50(D1), D817–D827. https://doi.org/10.1093/nar/gkab958

Teixeira, R. M., Ferreira, M. A., Raimundo, G. A. S., Loriato, V. A. P., Reis, P. A. B., & Fontes, E. P. B. (2019). Virus perception at the cell surface: Revisiting the roles of receptor-like kinases as viral pattern recognition receptors. Molecular Plant Pathology, 20(9), 1196–1202. https://doi.org/10.1111/mpp.12816

Välikangas, T., Suomi, T., & Elo, L. L. (2016). A systematic evaluation of normalization methods in quantitative label-free proteomics. Briefings in Bioinformatics, 19(1), 1–11. https://doi.org/10.1093/bib/bbw095

Vigne, E., Gottula, J. W., Schmitt-Keichinger, C., Komar, V., Ackerer, L., Belval, L., Rakotomalala, L., Lemaire, O., Ritzenthaler, C., & Fuchs, M. (2013). A strain-specific segment of the RNA-dependent RNA polymerase of grapevine fanleaf virus determines symptoms in *Nicotiana* species. Journal of General Virology, 94(Pt_12), 2803–2813. https://doi.org/10.1099/vir.0.057646-0

Wang, M.-B., Masuta, C., Smith, N. A., & Shimura, H. (2012). RNA Silencing and Plant Viral Diseases. Molecular Plant-Microbe Interactions®, 25(10), 1275–1285. https://doi.org/10.1094/MPMI-04-12-0093-CR

Wink, M. (2003). Evolution of secondary metabolites from an ecological and molecular phylogenetic perspective. Phytochemistry, 64(1), 3–19. https://doi.org/10.1016/S0031-9422(03)00300-5

Wu, Y., Zhang, Z., Li, Y., & Li, Y. (2022). The Regulation of Integrated Stress Response Signaling Pathway on Viral Infection and Viral Antagonism. Frontiers in Microbiology, 12. https://www.frontiersin.org/articles/10.3389/fmicb.2021.814635

Xu, K., & Nagy, P. D. (2010). Dissecting virus-plant interactions through proteomics approaches. Current Proteomics, 7(4), 316. https://doi.org/10.2174/157016410793611792

Zanardo, L. G., de Souza, G. B., & Alves, M. S. (2019). Transcriptomics of plant–virus interactions: A review. Theoretical and Experimental Plant Physiology, 31(1), 103–125. https://doi.org/10.1007/s40626-019-00143-z

Zhang, B., & Horvath, S. (2005). A General Framework for Weighted Gene Co-Expression Network Analysis. Statistical Applications in Genetics and Molecular Biology, 4(1). https://doi.org/10.2202/1544-6115.1128

Zhang, L., Zhang, X., Ma, Q., Ma, F., & Zhou, H. (2010). Transcriptomics and Proteomics in the Study of H1N1 2009. Genomics, Proteomics & Bioinformatics, 8(3), 139–144. https://doi.org/10.1016/S1672-0229(10)60016-2

Zhang, X., Smits, A. H., van Tilburg, G. B., Ovaa, H., Huber, W., & Vermeulen, M. (2018). Proteome-wide identification of ubiquitin interactions using UbIA-MS. Nature Protocols, 13(3), Article 3. https://doi.org/10.1038/nprot.2017.147

Table 4-S1. Sequence of primers used in quantitative reverse transcription polymerase chain reaction.

Primer Name	Target	Sequence (5'-3')	Source
Nb01478-FWD	Niben101Scf01478g00014	gtaaggcccgtctacatattacc	This study
Nb01478-REV	Niben101Scf01478g00014	cgttgattgcattccctcataaa	This study
Fbox-F	*N. benthamiana* Fbox gene	ggcactcacaaacgtctatttc	Liu et al. 2012
Fbox-R	*N. benthamiana* Fbox gene	acctgggaggcatcctgcttat	Liu et al. 2012

Table 4-S2. Summary of proteomics mapping peptides to reference genome (.xlsx). File is split into two tabs containing (A) samples of treatments wildtype grapevine fanleaf virus (GFLV) strain GHu and mutant GFLV-GHu $1E^{Pol}_{K802G}$ and (B) samples of treatments mock control, wildtype GLFV-F13, and mutant GFLV-F13 $1E^{Pol}_{G802K}$.

This table is available at the following link:

https://pubs.acs.org/doi/suppl/10.1021/acs.jproteome.3c00069/suppl_file/pr3c00069_si_002.zip

---

Table 4-S3. Statistics of transcriptomics data mapping to *Nicotiana benthamiana* genomes v0.4.4, v1.0.1, and manually curated Nepo3 database containing nepovirus genome sequences with wildtype and mutant grapevine fanleaf virus strains. Each sample is representative of three individual leaf discs which were pooled into one tube for RNA processing. An average of 79.89% of reads mapped to the host genome across all samples.

Sample name	Treatment	Time (dpi)	Rep	Percent(%) alignment to reference		
				Niben v0.4.4	Niben v1.0.1	Nepo 3
4mock1	Control	4	1	79.05	79.86	0.02
4mock2	Control	4	2	82.43	83.73	0.02
4mock3	Control	4	3	83.21	84.54	0.03
4mock4	Control	4	4	82.15	83.29	0.01
4mock5	Control	4	5	82.75	83.39	0.09
4f13mut1	mutant GFLV-F13	4	1	64.98	66.08	0.03
4f13mut2	mutant GFLV-F13	4	2	79.43	80.84	0.07
4f13mut3	mutant GFLV-F13	4	3	80.88	82.2	0.58
4f13mut4	mutant GFLV-F13	4	4	79.59	81.22	0.92
4f13mut5	mutant GFLV-F13	4	5	77.83	79.14	2.44
4f13wt1	wildtype GFLV-F13	4	1	83.81	84.89	2.42
4f13wt2	wildtype GFLV-F13	4	2	81.86	83.42	0.02
4f13wt3	wildtype GFLV-F13	4	3	80.89	82.42	0.03
4f13wt4	wildtype GFLV-F13	4	4	82.51	83.96	0.01
4f13wt5	wildtype GFLV-F13	4	5	81.42	82.78	0.52
4ghumut1	mutant GFLV-GHu	4	1	83.76	85.1	0.61
4ghumut2	mutant GFLV-GHu	4	2	85.82	87.46	0.42
4ghumut3	mutant GFLV-GHu	4	3	85.8	87.34	0.02
4ghumut4	mutant GFLV-GHu	4	4	68.77	69.91	0.94
4ghumut5	mutant GFLV-GHu	4	5	83.87	84.95	0.5
4ghuwt1	wildtype GFLV-GHu	4	1	81.79	82.51	0.07
4ghuwt2	wildtype GFLV-GHu	4	2	84.5	85.88	0.05
4ghuwt3	wildtype GFLV-GHu	4	3	82.56	83.58	0.02
4ghuwt4	wildtype GFLV-GHu	4	4	85.07	86.57	0.16
4ghuwt5	wildtype GFLV-GHu	4	5	85.03	86.14	0.01
7mock1	Control	7	1	80.96	82.05	0.03
7mock2	Control	7	2	80.43	81.93	0.04
7mock3	Control	7	3	81.56	82.02	0.04
7mock4	Control	7	4	83.29	84.62	0.02
7mock5	Control	7	5	82.57	84.25	0.06
7f13mut1	mutant GFLV-F13	7	1	73.8	75	9.11
7f13mut2	mutant GFLV-F13	7	2	76.3	77.46	5.75
7f13mut3	mutant GFLV-F13	7	3	72.25	73.22	6.86
7f13mut4	mutant GFLV-F13	7	4	74.77	75.23	9
7f13mut5	mutant GFLV-F13	7	5	76.98	78.02	6.01
7f13wt1	wildtype GFLV-F13	7	1	76.44	77.73	6.48

Table 4-S3. (Continued)

Sample name	Treatment	Time (dpi)	Rep	Percent(%) alignment to reference		
				Niben v0.4.4	Niben v1.0.1	Nepo 3
7f13wt2	wildtype GFLV-F13	7	2	71.11	72.47	7.74
7f13wt3	wildtype GFLV-F13	7	3	66.41	67.62	5.35
7f13wt4	wildtype GFLV-F13	7	4	78.89	80.15	4.15
7f13wt5	wildtype GFLV-F13	7	5	78.11	79.44	2.97
7ghumut1	mutant GFLV-GHu	7	1	71.41	72.5	7.4
7ghumut2	mutant GFLV-GHu	7	2	69.79	70.96	7.6
7ghumut3	mutant GFLV-GHu	7	3	78.21	79.42	4.79
7ghumut4	mutant GFLV-GHu	7	4	77.14	77.88	4.52
7ghumut5	mutant GFLV-GHu	7	5	76.83	78.06	1.79
7ghuwt1	wildtype GFLV-GHu	7	1	75.53	76.53	7.36
7ghuwt2	wildtype GFLV-GHu	7	2	74.5	75.56	7.18
7ghuwt3	wildtype GFLV-GHu	7	3	75.85	76.8	6.54
7ghuwt4	wildtype GFLV-GHu	7	4	74.42	75.33	6.99
7ghuwt5	wildtype GFLV-GHu	7	5	74.07	75.12	7.62
12mock1	Control	12	1	81.87	82.55	0.1
12mock2	Control	12	2	83.19	83.94	0.04
12mock3	Control	12	3	81.7	82.69	0.02
12mock4	Control	12	4	81.71	82.47	0.07
12mock5	Control	12	5	83.41	84.86	0.03
12f13mut1	mutant GFLV-F13	12	1	76.67	77.46	4.35
12f13mut2	mutant GFLV-F13	12	2	76.24	77.61	4.51
12f13mut3	mutant GFLV-F13	12	3	77.59	78.86	4.03
12f13mut4	mutant GFLV-F13	12	4	79.6	80.66	3.28
12f13mut5	mutant GFLV-F1	12	5	78.17	78.81	2.34
12f13wt1	wildtype GFLV-F13	12	1	76.61	77.7	2.56
12f13wt2	wildtype GFLV-F13	12	2	76.1	76.92	2.76
12f13wt3	wildtype GFLV-F13	12	3	78.46	79.36	2.66
12f13wt4	wildtype GFLV-F13	12	4	77.49	78.6	3.22
12f13wt5	wildtype GFLV-F13	12	5	78.1	78.83	5.1
12ghumut1	mutant GFLV-GHu	12	1	81.29	82.33	1.39
12ghumut2	mutant GFLV-GHu	12	2	80.45	81.42	1.7
12ghumut3	mutant GFLV-GHu	12	3	77.26	78.37	3.76
12ghumut4	mutant GFLV-GHu	12	4	78.4	79.44	3.8
12ghumut5	mutant GFLV-GHu	12	5	74.93	75.67	2.3
12ghuwt1	wildtype GFLV-GHu	12	1	78.41	79.14	1.75
12ghuwt2	wildtype GFLV-GHu	12	2	77.28	77.74	5.99
12ghuwt3	wildtype GFLV-GHu	12	3	76.93	77.94	3.79
12ghuwt4	wildtype GFLV-GHu	12	4	80.32	81.2	3.57
12ghuwt5	wildtype GFLV-GHu	12	5	77.56	78.53	2.78

Table 4-S4. Overlap between differentially abundant host genes identified by transcriptomics and proteomics following infection of *Nicotiana benthamiana* by grapevine fanleaf virus (GFLV). Data from different GFLV contracts are shown. Genes were defined as differentially abundant for proteomics (p-value < 0.05 and |Log2FoldChange| > 1) and for transcriptomics (adjusted p-value < 0.05) data.

Contrast[a]	**Wildtype GHu vs mutant GHu**			**Wildtype GHu vs wildtype F13**			**Wildtype F13 vs mutant F13**		
Technique[b]	**LC-MS/MS**	**Both**	**3'RNA-Seq**	**LC-MS/MS**	**Both**	**3'RNA-Seq**	**LC-MS/MS**	**Both**	**3'RNA-Seq**
4 dpi	1	0	14	4	0	89	0	0	1068
7 dpi	5	23	5554	13	17	5419	5	0	24
12 dpi	0	0	24	0	0	119	2	0	2

[a]Treatment contrasts used to generate differentially abundant genes.
[b]LC-MS/MS was used to define differential abundant proteins while 3'RNA-Seq was utilized to obtain differentially abundant transcripts in the *N. benthamiana* genome. Overlap between the two datasets are indicated (both).

Table 4-S5. Top five proteins and genes by fold change in the proteomics and transcriptomics analyses, respectively, for the wildtype grapevine fanleaf virus strain GHu vs mutant GHu $1E^{Pol}{}_{K802G}$ contrast. The common name is provided to supplement the identified gene ID, provided alongside the Log2FC and respective p-value measurement in each analysis.

Proteomics

Common Name	Gene ID	Log2FC	*p*-value
Nucleolar protein 56	Niben101Scf04815g01011.1	0.876	5.29E-04
RNA-binding protein like	Niben101Scf15360g00006.1	0.705	1.75E-04
4-hydroxy-3-methylbut-2-enyl diphosphate reductase	Niben101Scf10575g00008.1	-0.692	2.07E-08
4-hydroxy-3-methylbut-2-enyl diphosphate reductase	Niben101Scf33689g00006.1	-0.787	3.36E-07
Inositol-3-phosphate synthase	Niben101Scf06016g08006.1	-1.25	2.08E-04

Transcriptomics

Common Name	Gene ID	Log2FC	Adjusted *p*-value
60S acidic ribosomal protein P1	Niben101Scf01478g00014.1	8.53	6.09E-21
60S acidic ribosomal protein P1	Niben101Scf03595g10007.1	6.82	3.52E-15
Glutathione S-transferase U9	Niben101Scf10254g01014.1	6.47	5.95E-08
30S ribosomal protein S19	Niben101Scf10431g00014.1	5.88	8.71E-13
Tetratricopeptide repeat (TPR)-like superfamily protein	Niben101Scf04206g00007.1	-5.92	3.00E-02

Table 4-S6. Gene names of differentially abundant genes with associated statistics in contrasts across proteomics and transcriptomics data, organized by contrasts of interest per individual tab (.xlsx).

This table is available at the following link:

https://pubs.acs.org/doi/suppl/10.1021/acs.jproteome.3c00069/suppl_file/pr3c00069_si_002.zip

---

Table 4-S7. List of differentially expressed genes with annotated name and function found in the transcriptomics and proteomics datasets at 7 days post inoculation when contrasting wildtype grapevine fanleaf virus strain GHu and mutant GFLV-GHu $1E_{K802G}$.

Relative gene function	Gene ID	Gene Name
Translational regulation	Niben101Scf01718g02010	26S proteasome non-ATPase regulatory subunit 3 homolog B
	Niben101Scf00182g04001	Lysine--tRNA ligase
	Niben101Scf01673g01007	Lysine--tRNA ligase
	Niben101Scf01142g03007	Proline--tRNA ligase
	Niben101Scf03099g01010	Threonine--tRNA ligase
	Niben101Scf06734g02019	Threonine--tRNA ligase
	Niben101Scf13167g00007	tRNA pseudouridine synthase B
	Niben101Scf07031g00004	50S ribosomal protein L7Ae
	Niben101Scf04436g06002	60S ribosomal protein L10
	Niben101Scf07252g00007	Eukaryotic translation initiation factor 3 subunit E
Nucleotide binding	Niben101Scf04815g01011*	Nucleolar protein 56
	Niben101Scf07899g00005	Nucleolar protein 56
	Niben101Scf06664g00003	Nucleolar protein 58
	Niben101Scf33515g00005	Nucleolar protein 58
	Niben101Scf07042g01020	Nucleosome assembly protein 1
	Niben101Scf15360g00006*	RNA-binding protein like
	Niben101Scf03595g15003	Polyadenylate-binding protein 1-B
	Niben101Scf04567g00003	Polyadenylate-binding protein 1-B
Metabolism	Niben101Scf10575g00008*	4-hydroxy-3-methylbut-2-enyl diphosphate reductase
	Niben101Scf33689g00006*	4-hydroxy-3-methylbut-2-enyl diphosphate reductase
	Niben101Scf16254g00008	Inositol-3-phosphate synthase
	Niben101Scf06016g08006*	Inositol-3-phosphate synthase
	Niben101Scf10268g00007	NADH:ubiquinone oxidoreductase complex I intermediate-associated protein 30

*Top five proteins of differential abundance

Table 4-S8. Overlapping genes from transcriptomics and proteomics differential abundance contrasts of wildtype grapevine fanleaf virus strain GHu and mutant GFLV-GHu 1E$^{Pol}_{K802G}$. All genes overlapping between the two analyses agreed in the directionality (up- or downregulation) consistently, and confidence. The adjusted *p*-value is shown for transcriptomics (<0.05) and the *p*-value is shown for proteomics (<0.05) with the respective Log2FoldChange (Log2FC) for each gene.

	Transcriptomics		***Proteomics***	
Gene ID	**Log2FC**	**adjusted *p*-value**	**Log2FC**	***p*-value**
Niben101Scf00182g04001	1.32611024	1.6952E-02	0.5745246	2.0687E-03
Niben101Scf01142g03007	0.697645026	4.4899E-05	0.6484607	1.9248E-03
Niben101Scf01673g01007	1.276625057	2.8030E-06	0.631372	6.3537E-03
Niben101Scf01718g02010	0.547146822	1.3899E-02	0.5698451	4.0142E-02
Niben101Scf03099g01010	0.856501207	1.6406E-04	0.5556167	1.5047E-02
Niben101Scf03595g15003	2.52434266	9.8520E-20	0.7256995	6.8764E-03
Niben101Scf04436g06002	1.222529254	3.2256E-06	0.5042212	3.2756E-03
Niben101Scf04567g00003	2.590943037	1.5529E-15	0.63763	3.6055E-02
Niben101Scf04815g01011	1.725619502	3.9372E-10	0.9387453	6.5937E-04
Niben101Scf06016g08006	-2.175128111	3.7235E-05	-1.3249295	2.2593E-04
Niben101Scf06664g00003	2.226479161	2.3442E-09	0.6555047	2.3276E-02
Niben101Scf06734g02019	0.714139424	1.2893E-02	0.5855391	3.1901E-03
Niben101Scf07031g00004	2.767154824	1.1020E-23	0.5359586	1.8960E-03
Niben101Scf07042g01020	0.842586728	1.0984E-08	0.5450014	3.3568E-03
Niben101Scf07252g00007	0.854866536	8.9788E-04	0.5010226	3.7499E-02
Niben101Scf07899g00005	2.208569145	4.7348E-12	0.7304937	5.3598E-03
Niben101Scf10268g00007	-0.663184823	1.7242E-05	-0.5379491	2.8689E-03
Niben101Scf10575g00008	-1.185297606	4.0608E-09	-0.7355387	1.4008E-08
Niben101Scf13167g00007	3.184677692	1.1897E-09	0.6593237	1.5958E-03
Niben101Scf15360g00006	1.805355418	1.5998E-12	0.7551984	1.9733E-04
Niben101Scf16254g00008	-2.806521969	7.3312E-05	-0.6670557	1.6047E-02
Niben101Scf33515g00005	2.622276097	5.3326E-11	0.7308831	1.4576E-02
Niben101Scf33689g00006	-0.838730155	1.3787E-08	-0.8337528	3.2917E-07

Table 4-S9. **Gene count matrix of defined target genes including RNA silencing components, 43S pre-initiation complex components, receptors, receptor-like proteins, and unknown proteins**.

This table is available at the following link:

https://pubs.acs.org/doi/suppl/10.1021/acs.jproteome.3c00069/suppl_file/pr3c00069_si_002.zip

---

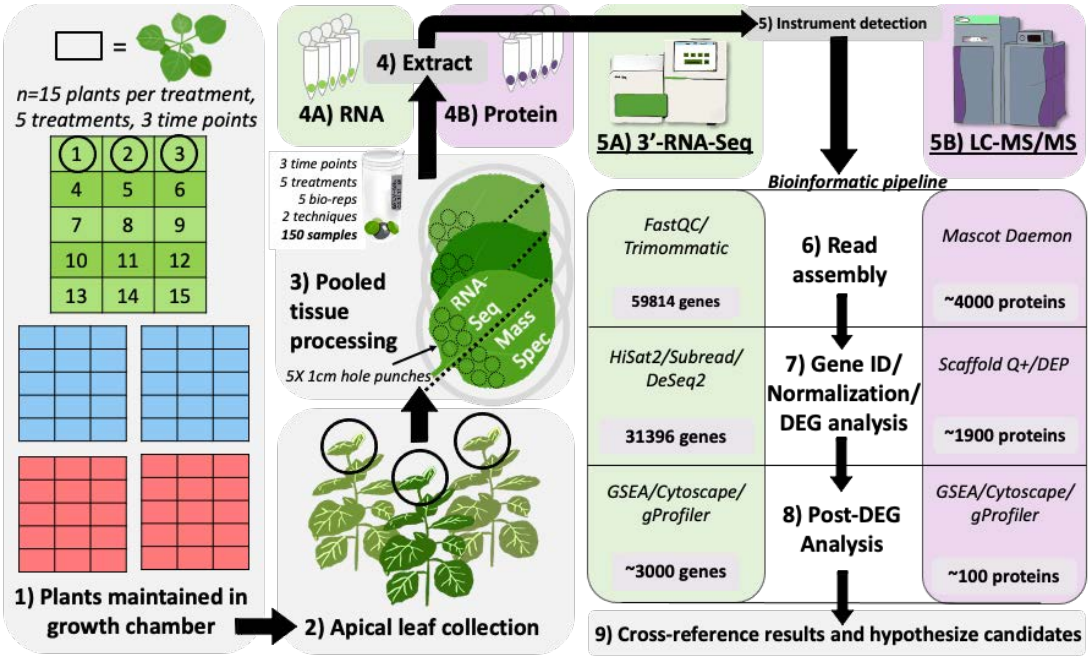

Figure 4-S1. **Schematic representation of tissue collection, transcript, and peptide acquisition, and bioinformatic analysis of data collected for the summative analysis presented. After mechanical inoculation of *Nicotiana benthamiana* with grapevine fanleaf virus (GFLV), (1)** plants were maintained in a growth chamber and inoculated with five treatments [mock inoculated control, wildtype GFLV-GHu, wildtype GFLV-F13, mutant GFLV-GHu $1E^{Pol}{}_{K802G}$, and mutant GFLV-F13 $1E^{Pol}{}_{G802K}$], **(2)** apical leaf tissue was collected at 4-, 7-, and 12 days post inoculation with **(3)** a sterile hole borer to divide five leaf discs from three individual leaves into a tube, considered a biological replicate. Five biological replicates per treatment per time point were collected and processed for each transcriptomic and proteomic analysis [75 samples per technique] by extraction of **(4A)** RNA and **(4B)** protein. Samples were then subject to **(5A)** 3'RNA-sequencing for RNA and **(5B)** tandem liquid chromatography mass spectrometry for proteins. A bioinformatic analysis followed to include **(6)** read assembly, **(7)** gene identification and normalization, and **(8)** post-differential gene abundance analysis for both transcriptome and proteome pipelines, narrowing down genes of interest to 3,000 transcripts and ~100 proteins. **(9)** Analysis of results between the two techniques was then conducted to identify gene candidates of interest.

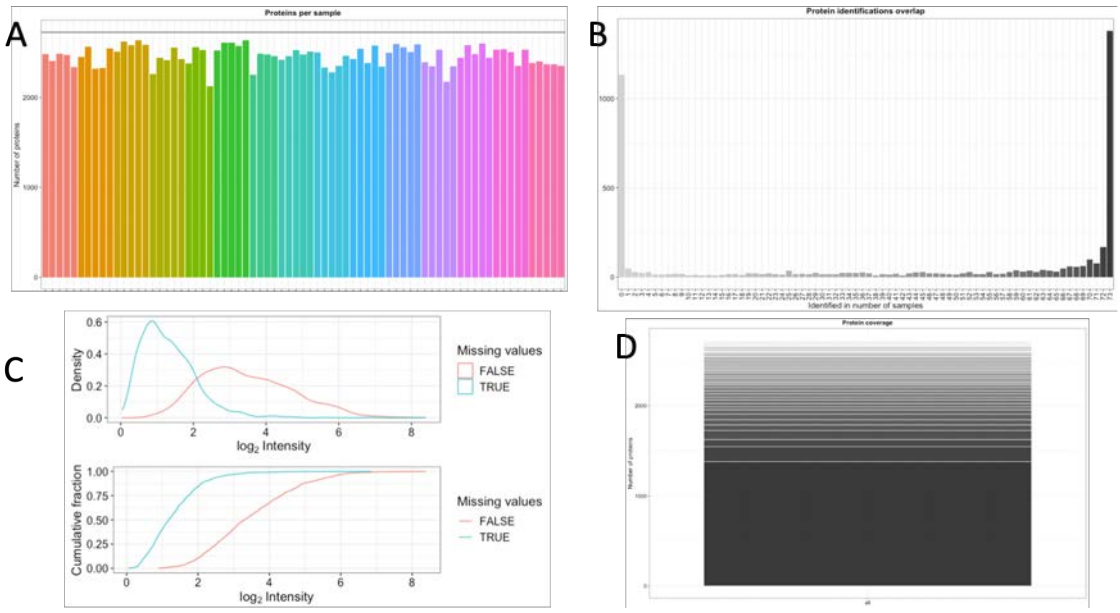

Figure 4-S2. Summary analysis of full proteome data retrieved from 73 samples specific to the number of proteins identified across all samples of proteins isolated from *Nicotiana benthamiana* infected with wildtype grapevine fanleaf virus strains GHu and F13, and mutant GHu 1E$^{Pol}_{K802G}$, and F13 1E$^{Pol}_{K802G}$ or mock inoculated. (A) Number of protein hits per sample across the entire dataset for (from left to right) control (red to yellow), mutant F13 1E$^{Pol}_{K802G}$ (greens), wildtype F13 (green blue to sky blue), mutant GHu 1E$^{Pol}_{K802G}$ (blue to light purple), and wildtype GHu (purple to pink) samples. Time points (4-, 7- and 12-days post inoculation) for each treatment (from left to right), and for bioreplicates 1-5 (from left to right) are shown. An average of ~2,200 proteins were identified per sample. (B) Number of proteins found in all samples. A large number of proteins were found in all samples, and another large proportion of proteins was found in 0-1 samples. (C) (Top) Relative density across experiment for missing peptides/proteins mapping to the Niben_nepo search base (left-shifted curve in blue). (Bottom) Cumulative fraction of missing or present values across the entire experiment. (D) Proportion of proteins found per sample with roughly 1,400 proteins detected in all samples at least once. The darkest box at the bottom represents all 73 samples, with the black gradient decreasing vertically by one each box (ex: 72 samples contained the next highest proportion of proteins detected).

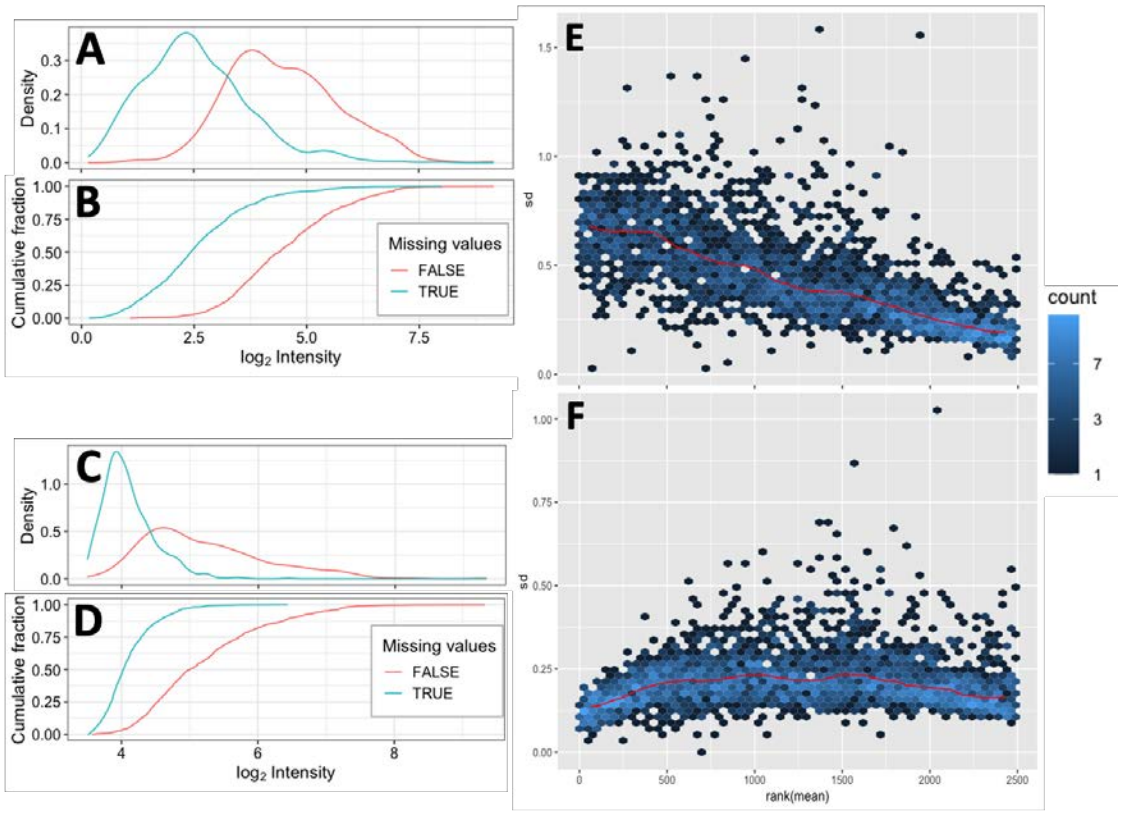

Figure 4-S3. Distribution of protein counts and missing values before and after vsn normalization. (A) Density plot of missing protein values against the log intensity value of spectral counts before normalization and (B) Cumulative fraction of all proteins as a function of the density plotted with blue showing the missing values and red showing values present. (C) Density plot after vsn normalization showing a shift left in missing values and a more normalized peak and (D) Respective cumulative fraction of this data. The standard deviation plots are shown (E) before normalization and (F) after where the variance is stabilized and corrected from a left-handed to standard distribution. Dark blue hexagons represent lower counts while light blue represent high counts as indicated by the legend.

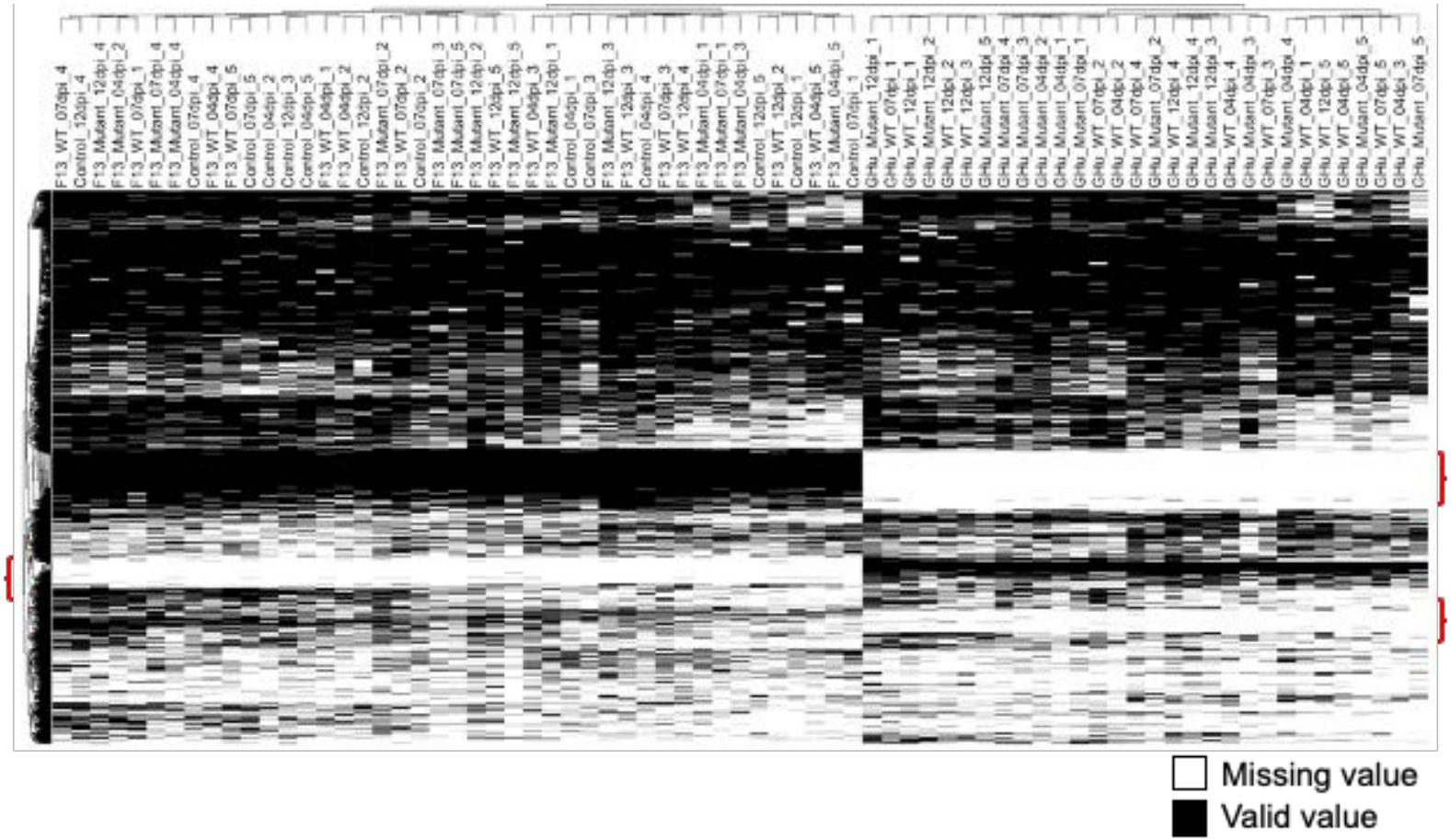

Figure 4-S4. Missing values pattern across entire experiment reveals many proteins are missing not at random (MNAR) and are specific when considering the two grapevine fanleaf virus (GFLV) strains GHu wildtype and GHu mutant 1E$^{Pol}_{K802G}$. A tree based on correlated samples is shown at the top and groups GHu strains to the right. Black bars represent proteins that are valid and present within the data while white shows missing values within the sample. Red brackets indicate large clusters of dissimilarity between treatment groups, where values are MNAR.

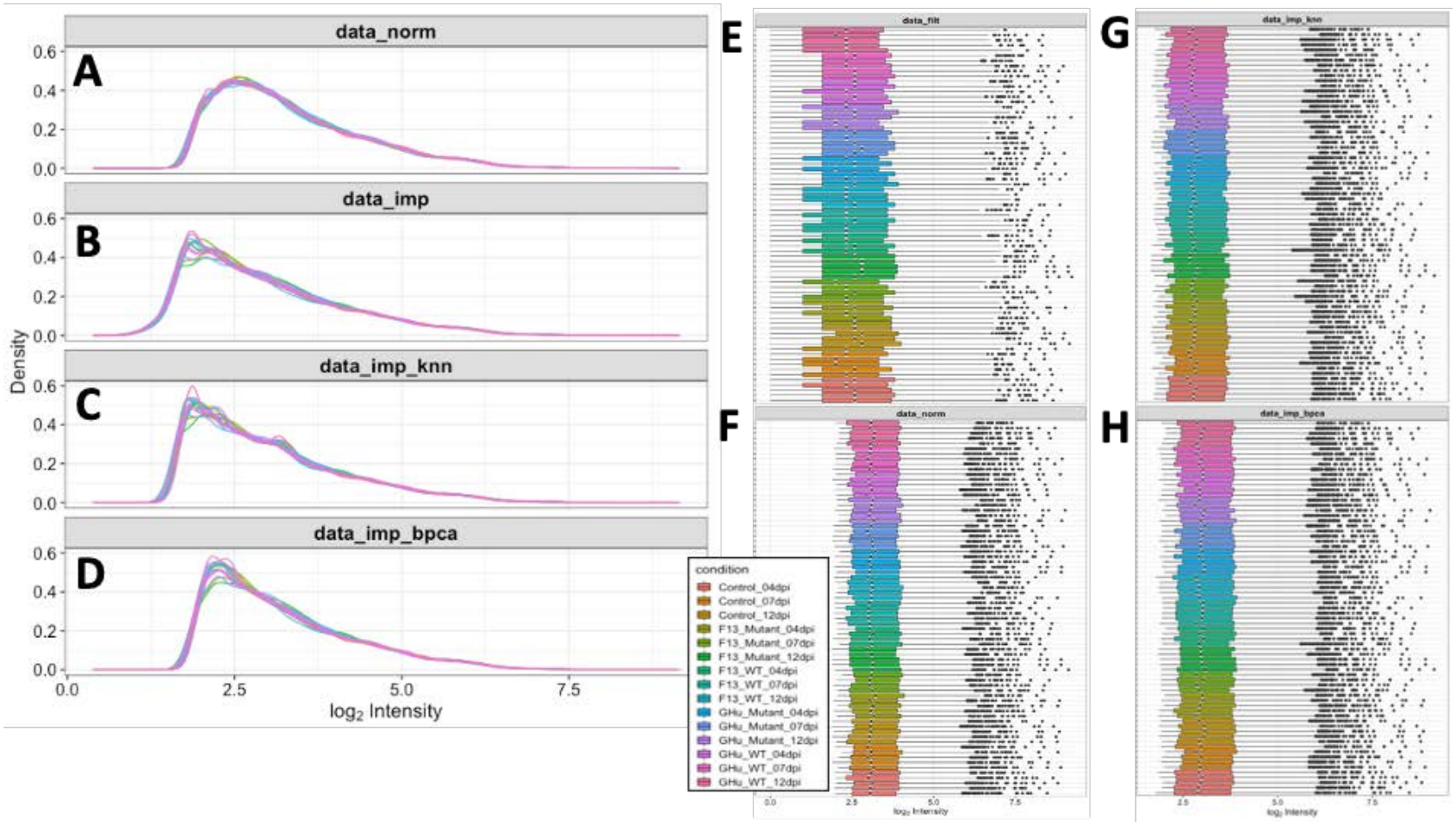

Figure 4-S5. Summary statistics of protein samples. (A) Relative density after normalization imputation algorithms, **(B)** Standard left-censored gaussian, **(C)** k-nearest neighbors, and **(D)** Bayesian principal component analysis. **(E)** Log intensity for all samples after filtering low counts, **(F)** after variance stabilization normalization **(G)** after k-nearest neighbors' imputation, and **(H)** after bpca imputation.

Figure 4-S6. Euclidian heatmaps, Pearson correlation matrices, and Gower's distance matrices of protein expression in *Nicotiana benthamiana* infected with wildtype grapevine fanleaf virus (GFLV) strains GHu and F13, and mutants GHu $1E^{Pol}_{K802G}$, and F13 $1E^{Pol}_{K802G}$, or mock inoculated at three time points (4-, 7-, and 12-days post inoculation, dpi). Euclidian heatmaps across the experiment used k-means clustering and are labeled with color for each treatment group as in the legend (right). (A) At 4 dpi, minor clustering of samples is observed, (B) At 7 dpi, samples are separated with larger similarity between wildtype GFLV strain symptomatic plants, and (C) At 12 dpi, samples are clearly separated by treatment, with wildtype GFLV strain GHu being largely different than mock controls and asymptomatic GFLV strains clustering together. A similar pattern of trends is apparent in Pearson correlation where darker purple represents an increased similarity in protein expression (D), (E), and (F), and Gower's distance matrices (G), (H), and (I) at the respective 4-, 7-, and 12 dpi. The discrimination of treatment groups across these clustering techniques suggest that the biological replicates are substantially different for wildtype GHu at most points of infection and other treatments occasionally separate out at respective time points with minimal mixing.

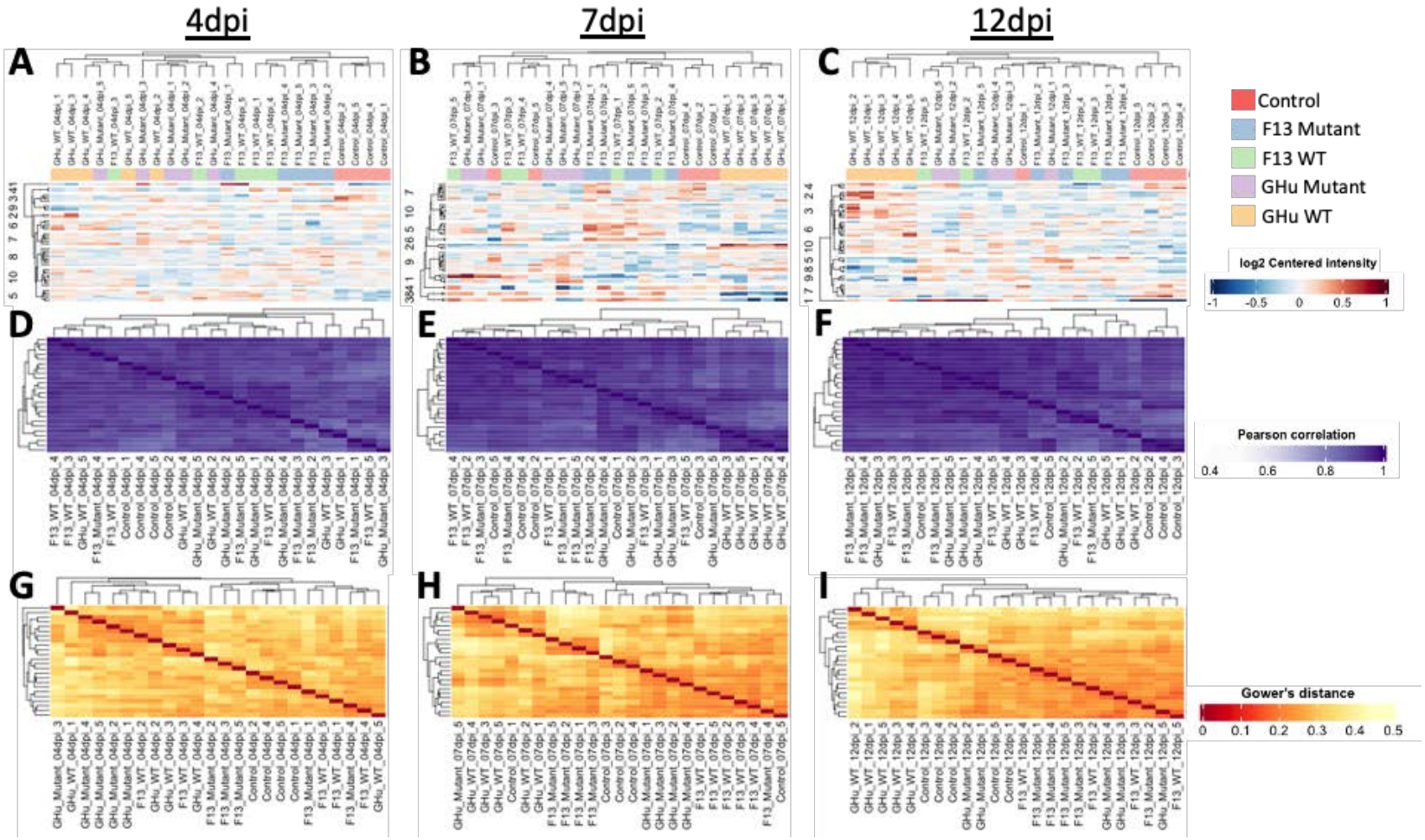
4dpi
7dpi
12dpi
A
B
C
D
E
F
G
H
I
Control
F13 Mutant
F13 WT
GHu Mutant
GHu WT
log2 Centered intensity
-1
-0.5
0
0.5
1
Pearson correlation
0.4
0.6
0.8
1
Gower's distance
0
0.1
0.2
0.3
0.4
0.5

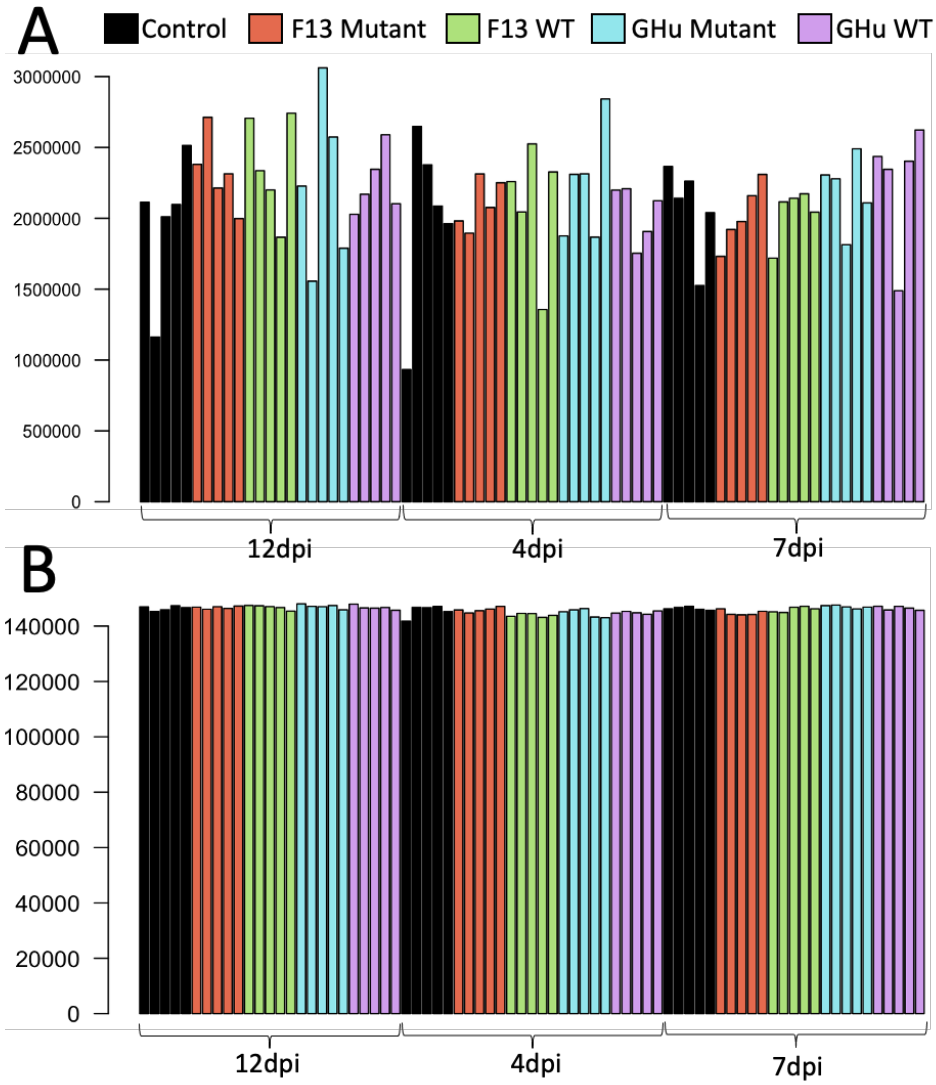

Figure 4-S7. Summary analysis of full transcriptome data retrieved from 75 samples specific to the number of transcripts identified across all samples of RNA isolated from *Nicotiana benthamiana* infected with wildtype grapevine fanleaf virus (GFLV) strain GHu (GHu WT), mutant GHu $1E^{Pol}{}_{K802G}$ (GHu mutant), wildtype strain F13 (F13 WT), and mutant F13 $1E^{Pol}{}_{K802G}$ (F13 mutant) or mock inoculated (control). (**A)** Number of transcript hits per sample across the entire dataset at 12, 4 and 7 days post inoculation (dpi), and for (from left to right) bioreplicates 1-5. An average of 4,709,000 transcripts were identified per sample. **(B)** Number of counts after variance stabilized normalization and low count filtering (≥150 counts per gene) across the entire dataset at 12-, 4-, and 7 dpi, and for (from left to right) bioreplicates 1-5. An average of 150,000 normalized transcript counts are represented per sample.

Figure 4-S8. Dispersion estimates of DESeq2 transcriptome analysis for (a) all 75 samples by group, (b) the 25 samples from 4 days post inoculation (dpi), (c) the 25 samples from 7 dpi, and (d) the 25 samples collected at 12 dpi. The mean of normalized counts along the x-axis is plotted against the dispersion on the y-axis, in which a red fitted line displays the average abundance of genes following the trend of gene-estimates (black) and final estimates after normalization (blue). The split experimental design of 4-, 7-, and 12 dpi in panels B, C, and D reflect that normality of A and were considered appropriate for further analysis individually.

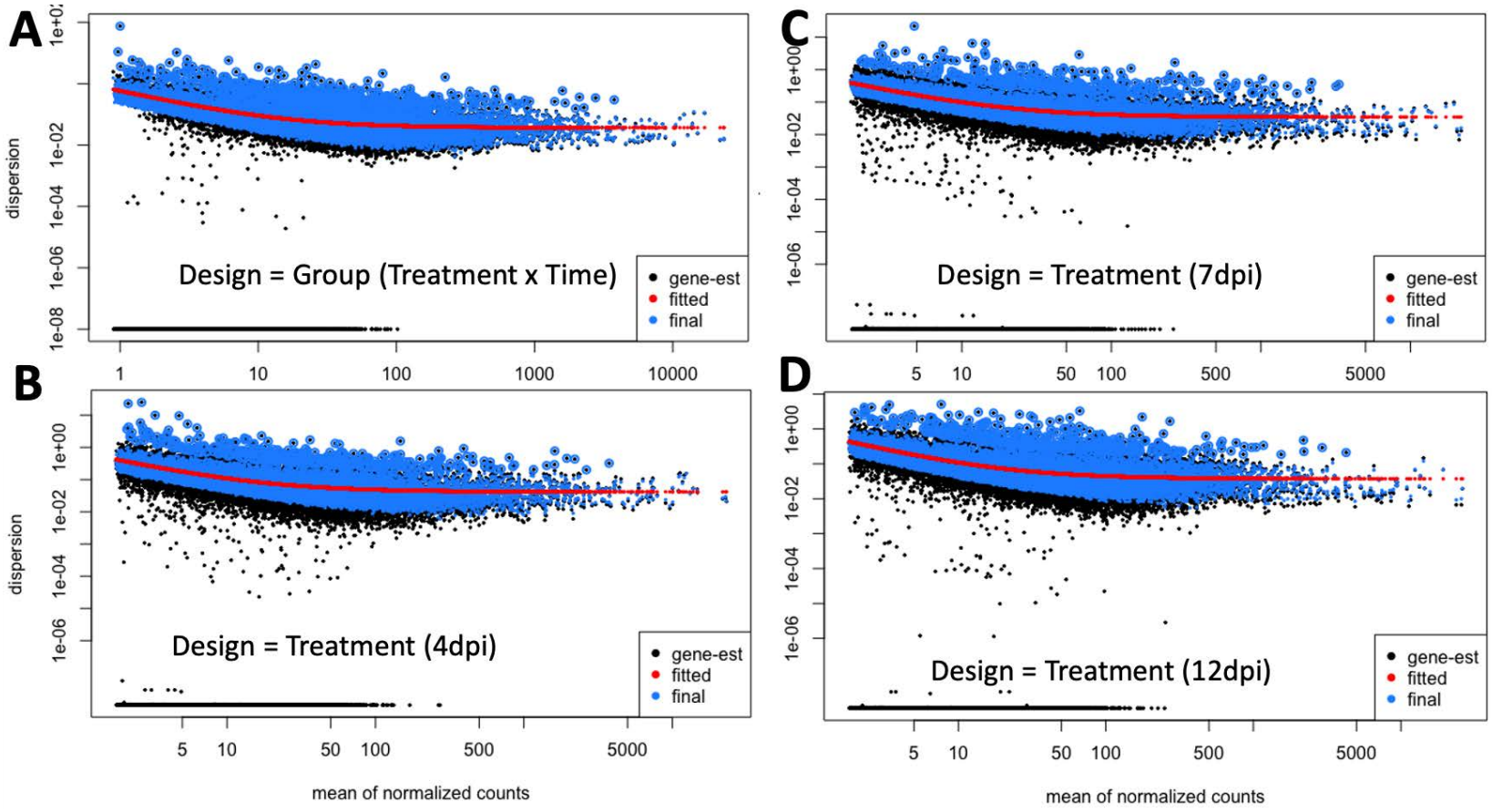
A
B
C
D
dispersion
mean of normalized counts
Design = Group (Treatment x Time)
Design = Treatment (4dpi)
Design = Treatment (7dpi)
Design = Treatment (12dpi)
gene-est
fitted
final
1
10
100
1000
10000
5
50
500
5000
1e-08
1e-06
1e-04
1e-02
1e+00

Figure 4-S9. Hierarchal clustering via McQuitty method for transcriptomic sample alignment files. This pair-wise clustering method shows samples with similar treatments and time points closely related with minimal cases of outliers. Notably the distinct phenotype group of wildtype grapevine fanleaf virus (GFLV) strain GHu at 7 days post inoculation of *Nicotiana benthamiana* is distinct from all other nodes (red box below). Mutant GFLV-F13 at 4 dpi is distinct from all others (blue boxes). Samples are also grouped by time points such as 4 dpi and 12 dpi (shown by black brackets), increasing the need to find further differences by creation of smaller summarized experiments by time point.

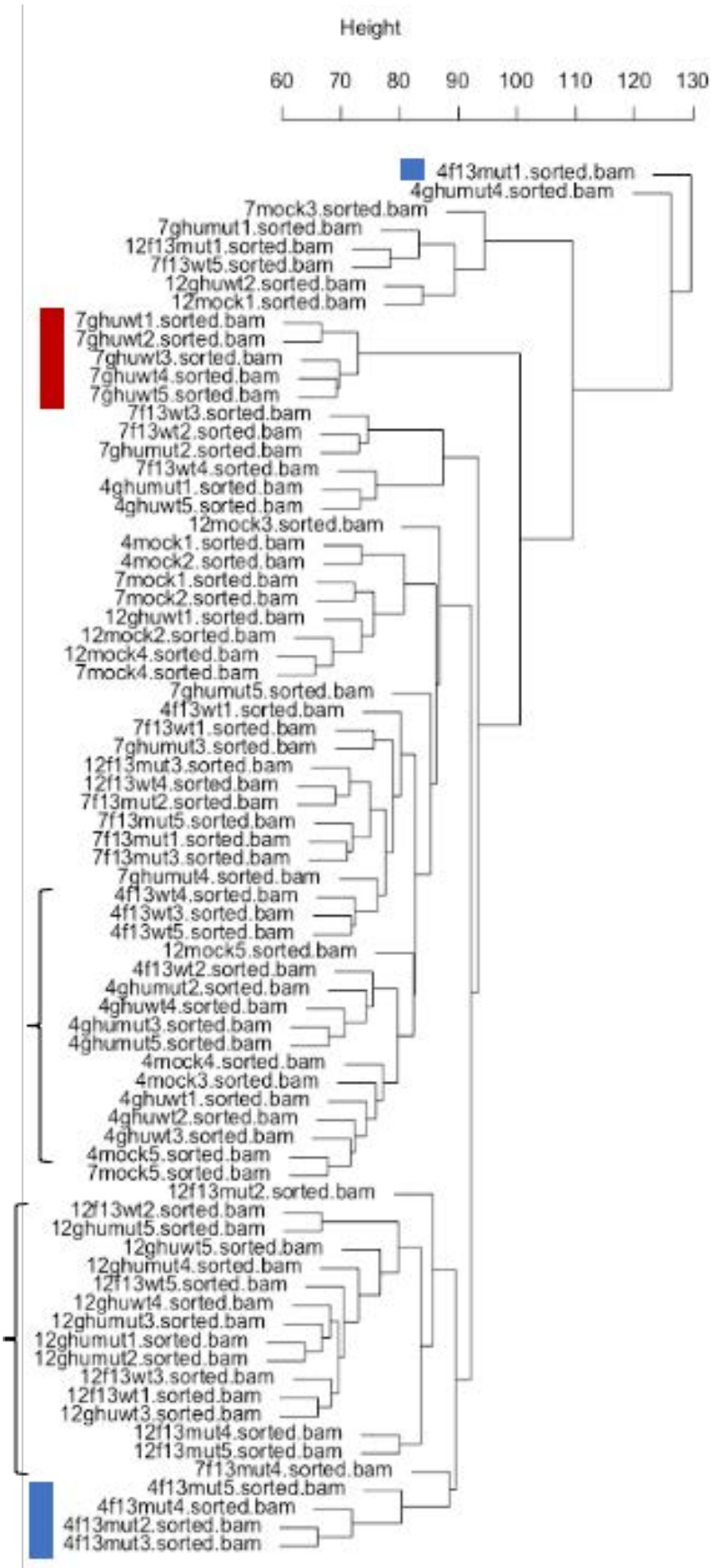
Height
60
70
80
90
100
110
120
130
4f13mut1.sorted.bam
4ghumut4.sorted.bam
7mock3.sorted.bam
7ghumut1.sorted.bam
12f13mut1.sorted.bam
7f13wt5.sorted.bam
12ghuwt2.sorted.bam
12mock1.sorted.bam
7ghuwt1.sorted.bam
7ghuwt2.sorted.bam
7ghuwt3.sorted.bam
7ghuwt4.sorted.bam
7ghuwt5.sorted.bam
7f13wt3.sorted.bam
7f13wt2.sorted.bam
7ghumut2.sorted.bam
7f13wt4.sorted.bam
4ghumut1.sorted.bam
4ghuwt5.sorted.bam
12mock3.sorted.bam
4mock1.sorted.bam
4mock2.sorted.bam
7mock1.sorted.bam
7mock2.sorted.bam
12ghuwt1.sorted.bam
12mock2.sorted.bam
12mock4.sorted.bam
7mock4.sorted.bam
7ghumut5.sorted.bam
4f13wt1.sorted.bam
7f13wt1.sorted.bam
7ghumut3.sorted.bam
12f13mut3.sorted.bam
12f13wt4.sorted.bam
7f13mut2.sorted.bam
7f13mut5.sorted.bam
7f13mut1.sorted.bam
7f13mut3.sorted.bam
7ghumut4.sorted.bam
4f13wt4.sorted.bam
4f13wt3.sorted.bam
4f13wt5.sorted.bam
12mock5.sorted.bam
4f13wt2.sorted.bam
4ghumut2.sorted.bam
4ghuwt4.sorted.bam
4ghumut3.sorted.bam
4ghumut5.sorted.bam
4mock4.sorted.bam
4mock3.sorted.bam
4ghuwt1.sorted.bam
4ghuwt2.sorted.bam
4ghuwt3.sorted.bam
4mock5.sorted.bam
7mock5.sorted.bam
12f13mut2.sorted.bam
12f13wt2.sorted.bam
12ghumut5.sorted.bam
12ghuwt5.sorted.bam
12ghumut4.sorted.bam
12f13wt5.sorted.bam
12ghuwt4.sorted.bam
12ghumut3.sorted.bam
12ghumut1.sorted.bam
12ghumut2.sorted.bam
12f13wt3.sorted.bam
12f13wt1.sorted.bam
12ghuwt3.sorted.bam
12f13mut4.sorted.bam
12f13mut5.sorted.bam
7f13mut4.sorted.bam
4f13mut5.sorted.bam
4f13mut4.sorted.bam
4f13mut2.sorted.bam
4f13mut3.sorted.bam

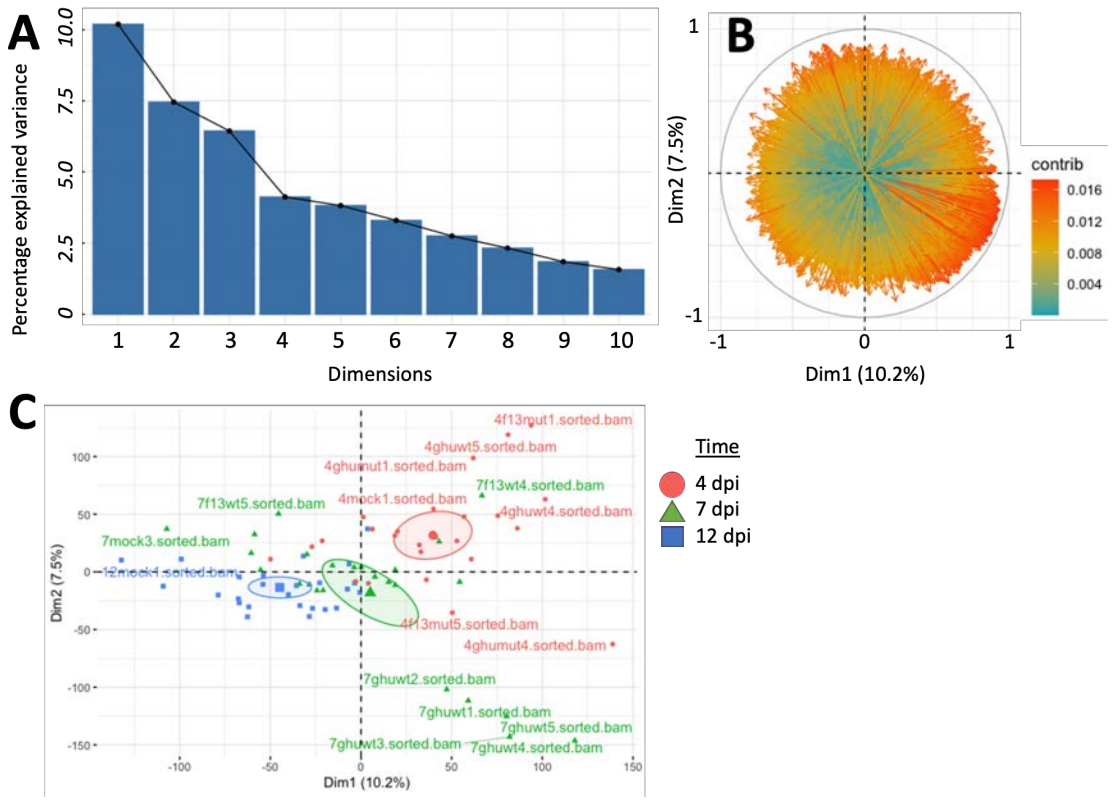

Figure 4-S10. Principal component analysis (PCA) of transcriptomics full experimental design shows separation by time with large contributions of separation by genes related to wildtype grapevine fanleaf virus (GFLV) strain GHu at seven days post inoculation (dpi). (A) Scree plot of principal component analysis for 500 top genes of transcriptomics reveals little variance explanation for entire 75 samples, starting with 10.2% variance explanation. (B) Gene loadings for explanation of variance shows higher contribution in lower right quadrant, which when compared with (C) wildtype GFLV-GHu samples group together in lower right quadrant also. PCA separates by time past infection as indicated by grouping ellipses and samples colored red circles for 4 dpi, green triangles for 7 dpi, and blue squares for 12 dpi. Labels of some samples were annotated to show general trends and sample names.

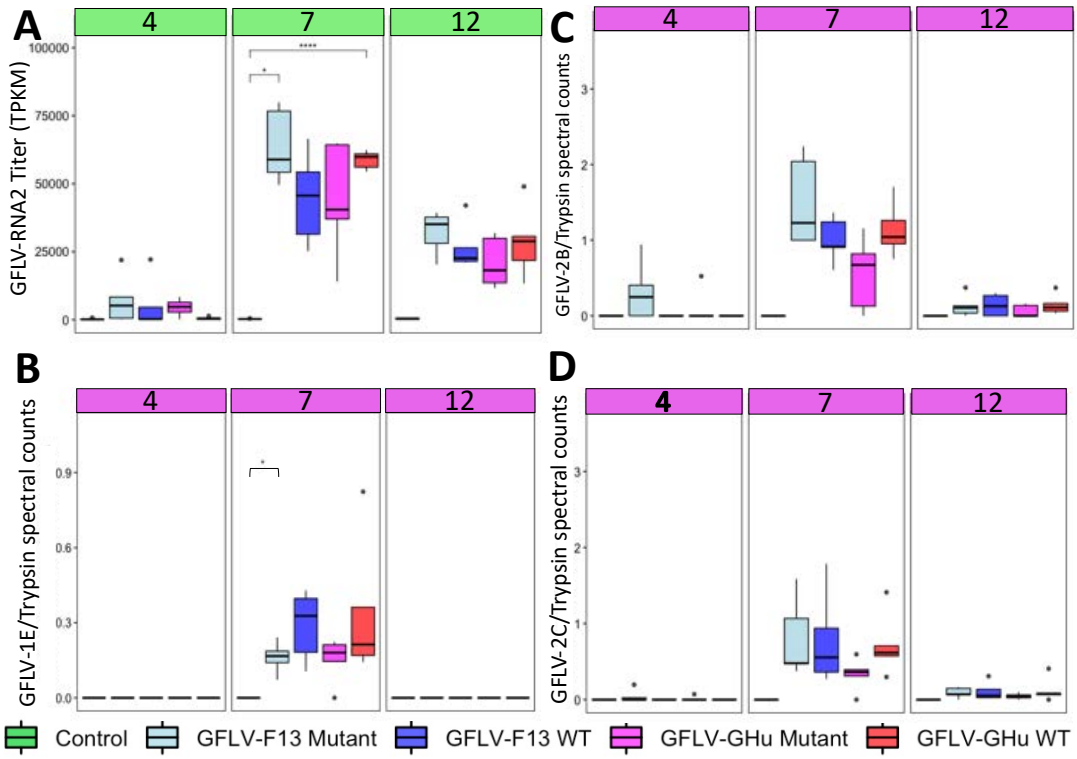

Figure 4-S11. Boxplots depicting grapevine fanleaf virus (GFLV) titer in infected *Nicotiana benthamiana* measured by RNA-Seq (A, green panels) and LC-MS/MS (C-D, pink panels). Each panel represents three time points (4-, 7-, and 12 days) post-inoculation. (A) GFLV RNA2 counts were extracted after normalization in DeSeq2 and are displayed as transcripts per kilobase million (TPKM). No statistical differences were found between viral treatments, however differences in viral titer were significant between mock control and two viral treatments, F13 mutant $1E_{G802K}$ ($p<0.05$) and wildtype GHu ($p<0.001$). Three viral proteins were detected through LC-MS/MS, and spectral counts of their matching peptides were plotted for GFLV proteins $1E^{Pol}$ (B), $2B^{MP}$ (C), and $2C^{CP}$ (D). None of the control samples indicated hits for any viral proteins. The data were normalized to the internal control of trypsin peptide spectral counts which was spiked into each sample for protein digestion.

Figure 4-S12. Additional transcriptomics data of *Nicotiana benthamiana* leaf tissue. Contrasts of wildtype grapevine fanleaf virus (GFLV) strain GHu and mutant F13 $1E^{Pol}_{K802G}$ treatments show large disruptions in the transcriptome at (A) 4 dpi, (B) 7 dpi, and (C) 12 dpi. Wildtype GFLV-GHu and mock control samples were also contrasted at (D) 4 dpi with little change in the transcriptome, (E) 7 dpi with a large amount of differentially abundant transcripts, and (F) 12 dpi with a reversion to little difference in transcriptome profiles. Contrasting wildtype GFLV strain F13 with mock controls resulted in moderate disruptions of the transcriptome at (G) 4 dpi, (H) 7 dpi, and (I) 12 dpi. Contrasts of mutant F13 $1E^{Pol}_{K802G}$ and controls showed a larger disruption than wildtype GFLV strain F13 at (J) 4 dpi, (K) 7 dpi, and (I) 12 dpi.

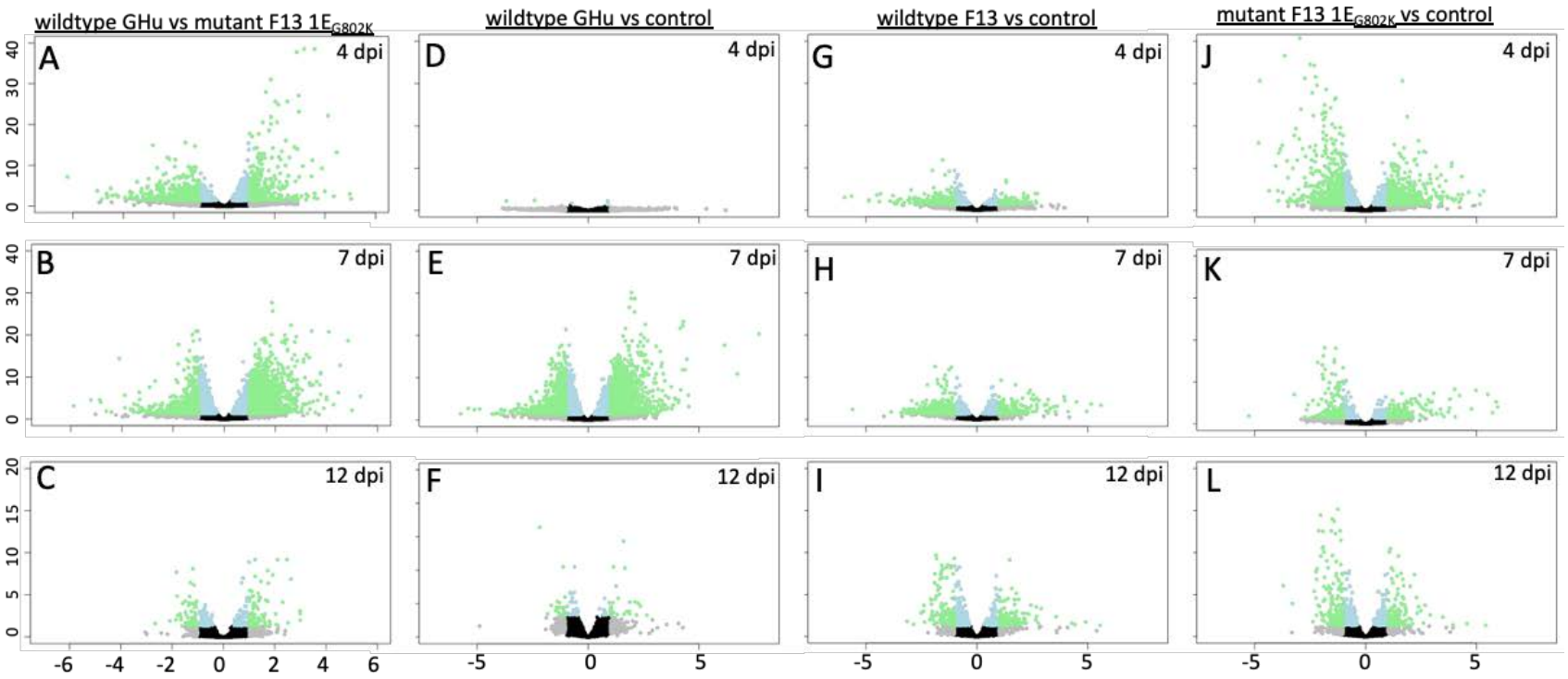
wildtype GHu vs mutant F13 1E$_{G802K}$
wildtype GHu vs control
wildtype F13 vs control
mutant F13 1E$_{G802K}$ vs control
A
4 dpi
B
7 dpi
C
12 dpi
D
4 dpi
E
7 dpi
F
12 dpi
G
4 dpi
H
7 dpi
I
12 dpi
J
4 dpi
K
7 dpi
L
12 dpi
0
10
20
30
40
0
5
10
15
20
-6
-4
-2
0
2
4
6
-5
0
5

Figure 4-S13. Additional volcano plots of proteomic contrasts. Wildtype grapevine fanleaf virus (GFLV) strain GHu and mutant F13 $1E^{Pol}_{K802G}$ treatments are contrasted at (A) 4 days post-inoculation (dpi), (B) 7 dpi, and (C) 12 dpi with the largest protein abundance differences appearing at 7 dpi. Volcano plots contrasting wildtype GFLV strain F13 and mutant GHu $1E^{Pol}_{K802G}$ treatments are shown at 4 dpi (D), 7 dpi (E), and 12 dpi (F). Contrasts of wildtype GFLV strain GHu and control are shown at 4 dpi (G), 7 dpi (H), and 12 dpi (I), where once again a large disruption in protein abundance is observed at 7 dpi. These contrasts are consistent and solidify the results observed in the major contrasts of interest (Figure 10).

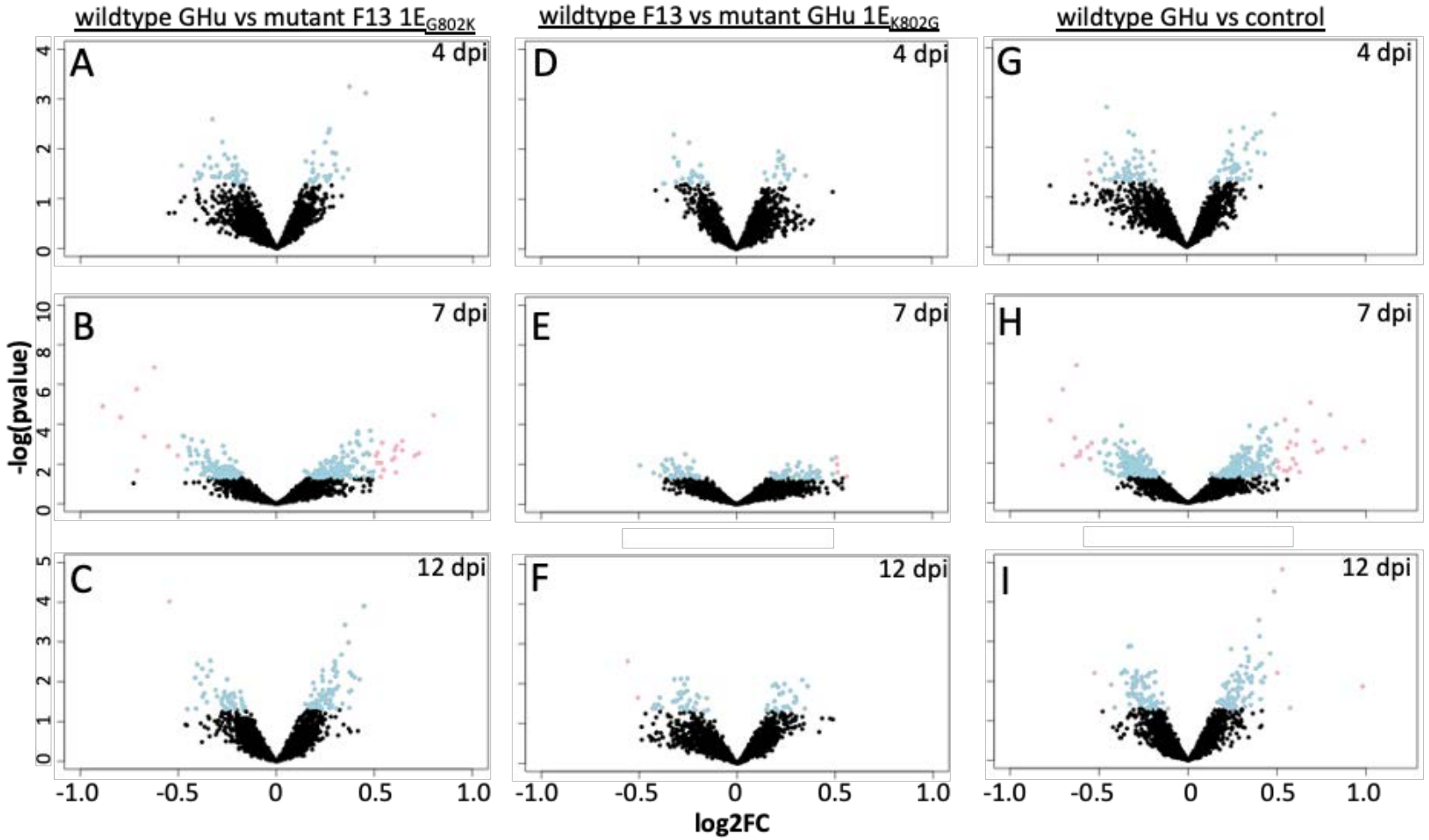
wildtype GHu vs mutant F13 1E$_{G802K}$
wildtype F13 vs mutant GHu 1E$_{K802G}$
wildtype GHu vs control
A
4 dpi
B
7 dpi
C
12 dpi
D
4 dpi
E
7 dpi
F
12 dpi
G
4 dpi
H
7 dpi
I
12 dpi
-log(pvalue)
log2FC
-1.0
-0.5
0
0.5
1.0

Figure 4-S14. Eigengene modules created from the transcriptomic dataset. MEgrey (top left) signifies genes that did not meet requirements to fit other modules. The modules following are ordered by the greatest number of genes that cluster together significantly by expression pattern across the three time point collections (4-, 7-, and 12-days post inoculation) following inoculation of *Nicotiana benthamiana* by various strains of grapevine fanleaf virus. The last fourteen modules highlight great dissimilarity amongst one treatment at one time point. while the larger modules are more similar in expression pattern between multiple groupings. Deviations in expression pattern indicate novel gene clusters for that treatment group.

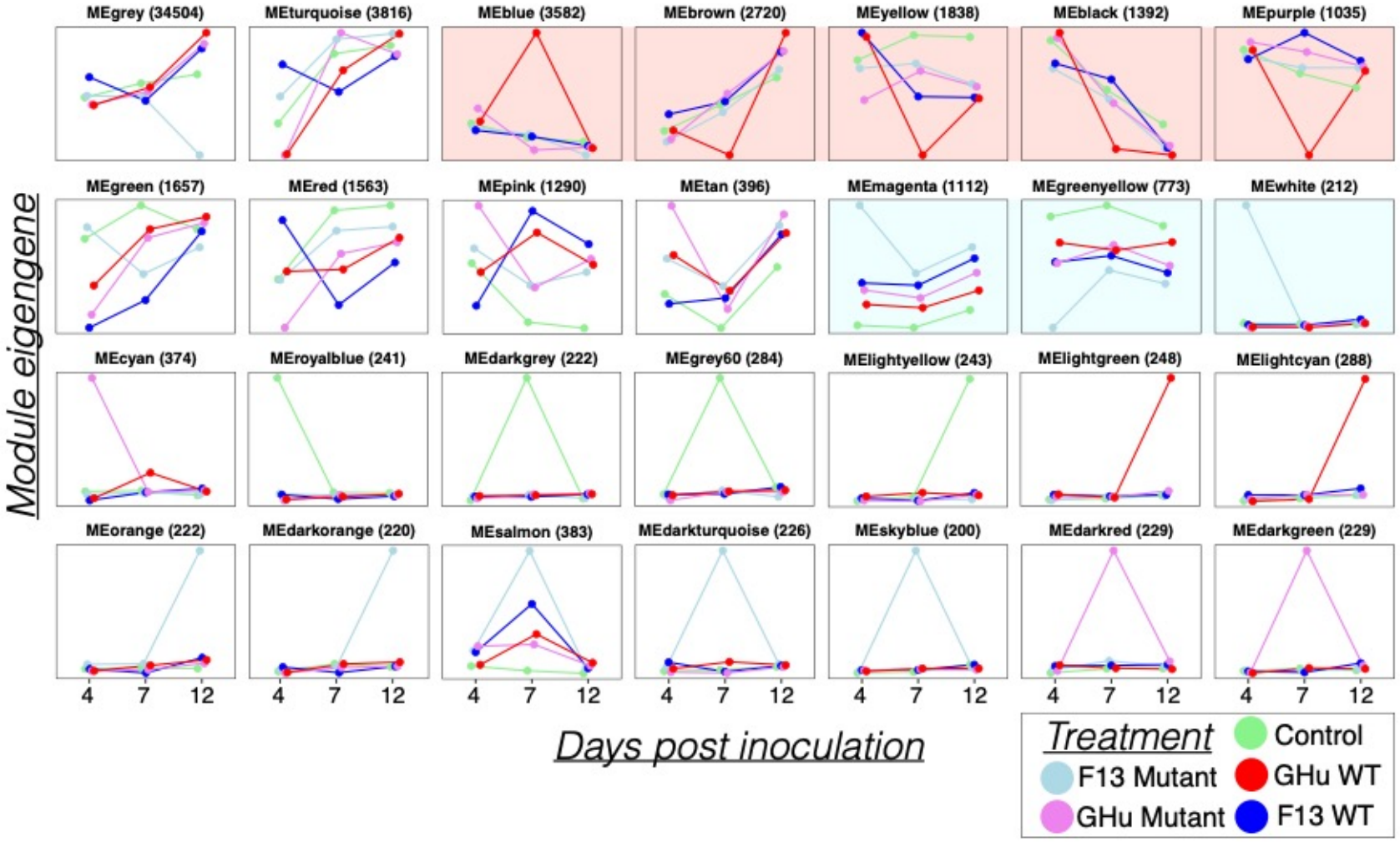
MEgrey (34504)
MEturquoise (3816)
MEblue (3582)
MEbrown (2720)
MEyellow (1838)
MEblack (1392)
MEpurple (1035)
MEgreen (1657)
MEred (1563)
MEpink (1290)
MEtan (396)
MEmagenta (1112)
MEgreenyellow (773)
MEwhite (212)
MEcyan (374)
MEroyalblue (241)
MEdarkgrey (222)
MEgrey60 (284)
MElightyellow (243)
MElightgreen (248)
MElightcyan (288)
MEorange (222)
MEdarkorange (220)
MEsalmon (383)
MEdarkturquoise (226)
MEskyblue (200)
MEdarkred (229)
MEdarkgreen (229)
4 7 12
Module eigengene
Days post inoculation
Treatment
Control
F13 Mutant
GHu WT
GHu Mutant
F13 WT

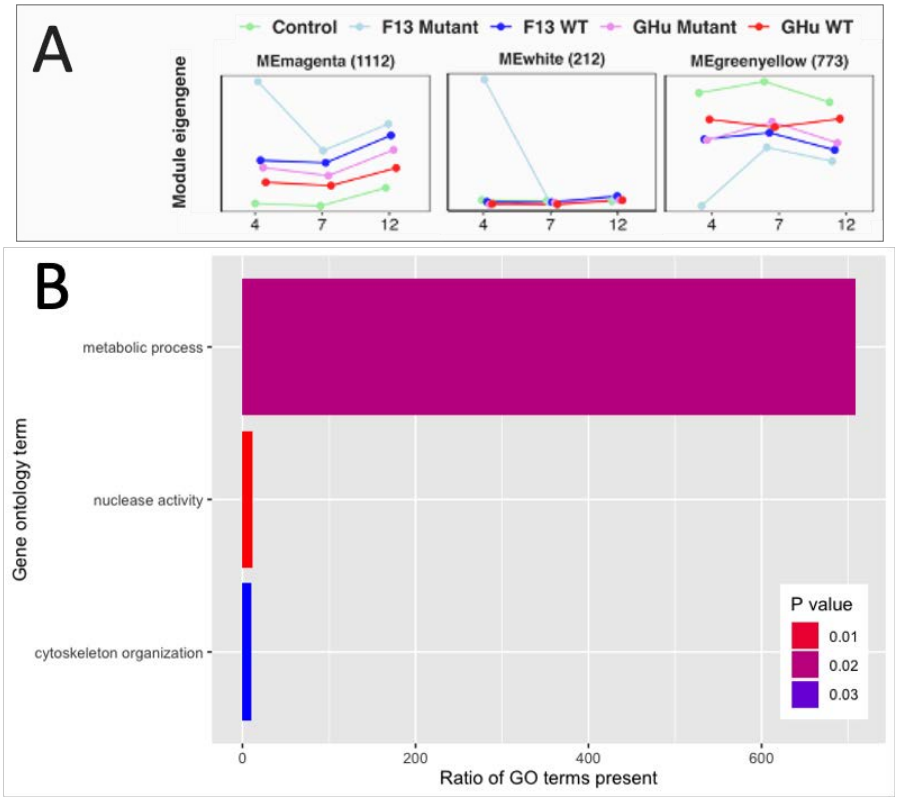

Figure 4-S15. Functional categorization of WGCNA eigengene modules unique to mutant grapevine fanleaf virus (GFLV) F13 $1E^{Pol}_{K802G}$ in *Nicotiana benthamiana* plants at 4 days post-inoculation, where four samples had raised GFLV presence. (A) Selected modules with unique expression patterns. (B) Gene ontologies overrepresented in the three modules subject to GSEA. Bars are colored by p-value as indicated by the in-plot legend.

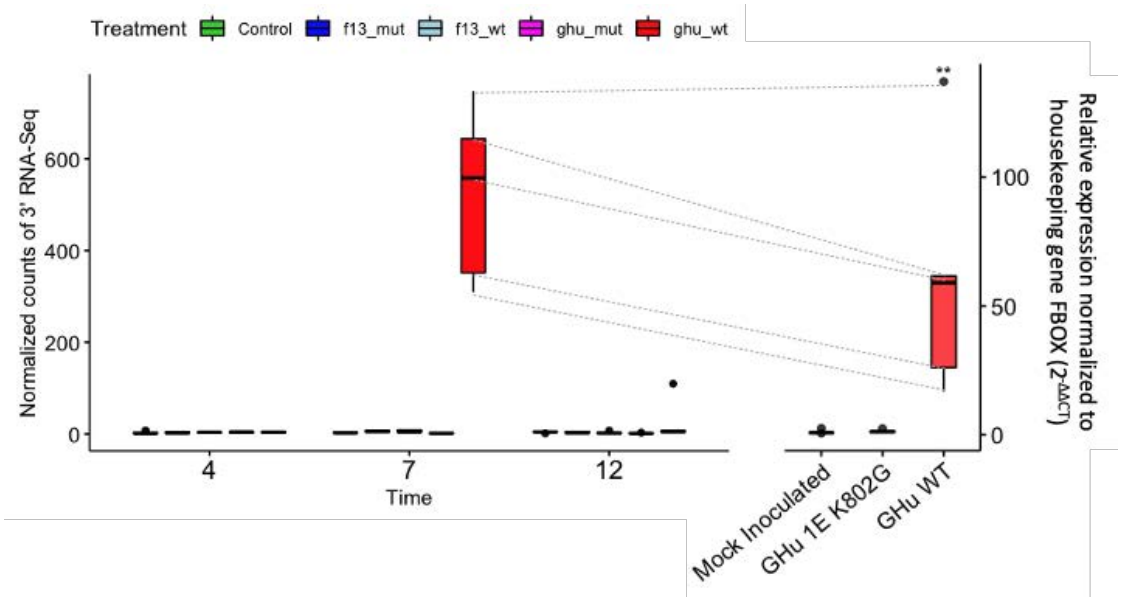

Figure 4-S16. RNA expression levels of Niben101Scf01478g00014, 60S acidic ribosomal protein P1 through 3'RNA-Seq normalized counts (left boxplot) and reverse transcription quantitative polymerase chain reaction (RT-qPCR) relative expression to housekeeping gene FBOX (right boxplot). All treatment groups and time points, except plants infected with wildtype grapevine fanleaf virus (GFLV) strain GHu at 7 days post inoculation (dpi), show very low abundance for this transcript in RNA-Seq data. Three treatments at 7 dpi and their five biological replicates from RNA-Seq experimentation were used for RT-qPCR analysis, where only *Nicotiana benthamiana* plants infected with wildtype GFLV-GHu shows high expression levels. Significant differences in relative expression were observed between wildtype GFLV-GHu and other treatments ($p<0.01$).

CHAPTER 5

A SINGLE VIRAL AMINO ACID SHAPES THE ROOT SYSTEM ARCHITECTURE OF A PLANT HOST UPON VIRUS INFECTION[5]

ABSTRACT

Background: Grapevine fanleaf virus (GFLV) is one of the most detrimental viral pathogens of grapevines worldwide but no information is available on its effect on the root system architecture (RSA) of plant hosts. We used two wildtype GFLV strains and their single amino acid mutants to assess RSA traits in infected *Nicotiana benthamiana* and evaluate transcriptomic changes in host root gene expression in replicated time course 3'RNA-Seq experiments. Mutations targeted the multi-functional GFLV-encoded protein $1E^{Pol*/Sd}$, a putative RNA-dependent RNA polymerase and determinant of foliar symptoms in *N. benthamiana* plants.

Results: Plant infection with wildtype GFLV strain GHu and mutant GFLV strain F13 $1E_{G802K}$, both carrying a lysine in position 802 of protein $1E^{Pol*/Sd}$, resulted in a significantly lower number of root tips (-30%), and a significantly increased average root diameter (+ 20%) at 17 days post inoculation (dpi) in comparison with roots of mock inoculated plants. In contrast, the RSA of plants infected with wildtype GFLV strain F13 and mutant GFLV strain GHu $1E_{K802G}$, both carrying a glycine in position 802 of protein $1E^{Pol*/Sd}$, resembled that of mock inoculated plants. Modifications of RSA traits were not associated with GFLV titer. Root tissue transcriptome analysis at 17 dpi indicated dysregulation of pattern recognition receptors, plant hormones, RNA silencing, and genes related to the production of reactive oxygen species (ROS). For

wildtype GFLV strain GHu, RSA modifications were correlated with an abundant accumulation of ROS in the pericycle of primary roots at 7 dpi and the duration of vein clearing symptom expression in apical leaves. Dysregulation of a hypersensitive response was an overarching gene ontology found through enrichment analyses of 3'RNA-Seq data.

Conclusions: Our findings revealed the causative role of lysine in position 802 of protein $1E^{Pol*/Sd}$ in a novel RSA phenotype during viral infection and documented GFLV-*N. benthamiana* interactions at the root level based on (i) antiviral response, (ii) receptor mediated production of ROS, and (iii) hormone regulation. A correlation between above and below ground symptoms was reported for the first time in plants infected with wildtype GFLV strain GHu. Further work is warranted to test whether the modified RSA of a plant host might impact GFLV acquisition and transmission by the ectoparasitic dagger nematode *Xiphinema index*.

---

[5]This chapter has been published: Roy, B.G., Fuchs, M. 2024. A single viral amino acid shapes the root system architecture of a plant host upon virus infection. *BMC Microbiol* **24**, 267.

INTRODUCTION

Roots play a crucial role in plant development, contributing largely to overall health and growth. Plants rely on this underground network of tissue to sequester nutrients, acquire water, provide energy sinks for long chain carbohydrates, and act as anchorage to combat adverse environmental stressors. The configuration of a root system in the soil is commonly referred to as root system architecture (RSA). The overall RSA is dynamically influenced by abiotic and biotic factors, including pathogens such as viruses that can negatively modify RSA upon infection of plant hosts (Peltier et al. 2011; Villordon et al. 2014; Vaisman et al. 2022).

Some plant viruses are transmitted by soil-borne vectors (Andika et al. 2016) and are known to manipulate host root systems. For example, tobacco rattle virus (TRV) alters RSA and root volatiles of *Nicotiana benthamiana*, affecting transmission characteristics by trichodorid nematode vectors (van Griethuysen et al. 2024). TRV manipulates the production pathway of 2-ethyl-1-hexanol to attract nematodes for feeding on infected tissue, and subsequentially to increase virus acquisition for more efficient transmission. Similarly, the RNA3-encoded p25 protein of beet necrotic yellow vein virus (BNYVV) determines both foliar and root symptoms in sugar beet (*Beta vulgaris* subsp. *vulgaris*) (Tamada et al. 1999). The constitutive expression of BNYVV protein p25 in *Arabidopsis thaliana* induces hormonal changes and a distinct RSA phenotype (Peltier et al. 2011).

Grapevine fanleaf virus (GFLV, species *Nepovirus foliumflabelli*, genus *Nepovirus*, family *Secoviridae,* order *Picornavirales*) is a causative agent of fanleaf degeneration disease, and the most detrimental viral pathogen of grapevines worldwide

(Andret-Link et al. 2004a). In the vineyard, GFLV is transmitted by the ectoparasitic dagger nematode *Xiphinema index* in an exclusive manner, solely dependent upon the viral coat protein (Belin et al. 2001; Andret-Link et al. 2004b; Schellenberger et al. 2010). The GFLV genome is bipartite with two single-stranded RNA molecules (RNA1 and RNA2). GFLV RNA1 encodes proteins involved in polyprotein processing (Margis et al. 1994), replication (Pinck et al. 1991; Ritzenthaler et al. 2002), and suppression of RNA silencing (Choi et al. 2023), while GFLV RNA2 encodes proteins involved in replication (Gaire et al. 1999), cell-to-cell movement (Belin et al. 1999), and encapsidation (Serghini et al. 1990). Performing experiments with GFLV in the natural host (*Vitis* spp.) can be laborious and time-consuming; therefore, herbaceous model hosts are commonly utilized for GFLV-plant interaction studies (Roy and Fuchs 2022). Among herbaceous hosts, *N. benthamiana* is frequently used to study virus-plant interactions because it can easily be infected via mechanically inoculation or through *Agrobacterium tumefaciens*-mediated infiltration of GFLV infectious clones, among other factors (Osterbaan et al. 2018).

Previous work revealed a single amino acid of GFLV strain GHu is responsible for a transient vein clearing phenotype in apical leaves of *N. benthamiana* plants (Vigne *et al.* 2013; Osterbaan et al. 2019). This symptom determinant (Sd) residue is located at position 802 (or position nts 2,404-2,406) of the GFLV RNA1-encoded putative RNA-dependent RNA polymerase (Pol*), refered to as protein $1E^{Pol*/Sd}$ (Vigne et al. 2013; Osterbaan et al. 2019; Roy et al. 2024). GFLV strain GHu encodes a lysine (K) at position 802 of protein $1E^{Pol*/Sd}$ which is necessary but not sufficient to produce these symptoms in GFLV strain F13 (Vigne et al. 2013; Osterbaan et al. 2019). The viral

symptom determinant region is hypothesized to interact with host components that ultimately elicit or repress an immune response, although structural or functional homologues could not be identified by advanced protein modeling techniques (Roy et al. 2024). A combined time-resolved transcriptomic and proteomic approach documented a reactive oxygen species (ROS) molecular pathway in addition to the dysregulation of transcripts and proteins of plant immune response, transcriptional regulation, and translational regulation in *N. benthamiana* leaves upon GFLV infection (Roy et al. 2023). Transient leaf symptoms can be observed on leaves of *Vitis* and *Nicotiana* species alike. Although experimental evidence of ROS production in *N. benthamiana* following GFLV infection is lacking, other studies have correlated ROS production with pronounced symptoms in GFLV-infected *Vitis* cultivars (Martin et al. 2021) or detected ROS in GFLV-infected *N. occidentalis* (Martin et al. 2018).

Studies on GFLV-host interactions have centered on above-ground plant tissue to investigate underpinnings of symptom development in leaves and determine how fruit yield and quality are affected by viral infection (Andret-Link et al. 2004a; Belin et al. 1999; Osterbaan et al. 2018, Vigne et al. 2013; Osterbaan et al. 2019; Roy et al. 2023; Martin et al. 2018; Martin et al. 2021). No research has investigated the effects of GFLV on the RSA of a plant host. The aim of this study was to explore below ground features of *N. benthamiana* plants and probe the molecular dysregulation of root tissue upon GFLV infection. We hypothesized that RSA traits follow similar phenotypic trends to foliar symptomology, and that GFLV elicits similar transcriptomic profiles in roots as previously observed with leaves (Vigne et al. 2013; Osterbaan et al. 2019; Roy et al. 2023). Here, we document GFLV protein $1E^{Pol*/Sd}$ single amino acid-specific

modifications of RSA traits, ROS production in roots, and root transcriptome dysregulation upon infection.

MATERIALS AND METHODS

Nicotiana benthamiana *plants*

Seeds of wildtype *N. benthamiana* were sown in Cornell LM-2 soil, transplanted ~14 days after germination, and maintained in a controlled growth chamber at 25 °C and 80% humidity, as previously documented (Osterbaan et al. 2018). Plants were watered daily and fertilized (Scotts Miracle-Gro® All Purpose Plant Food 24-8-16) weekly. Four independent experiments were performed with 75, 74, 107, and 80 plants referred to as cohorts 1-4, respectively.

Grapevine fanleaf virus (GFLV) strains

Four GFLV strains were selected for this study: wildtype GFLV strains GHu and F13, and their mutants carrying a single amino acid change at position 802 of the RNA1-encoded RNA-dependent RNA polymerase (Osterbaan et al. 2019). These strains will be referred herein to as wildtype GHu, wildtype F13, mutant GHu $1E^{Pol*/Sd}_{K802G}$, and mutant F13 $1E^{Pol*/Sd}_{G802K}$.

Plant mechanical inoculation with GFLV strains and leaf phenotyping

The genome of GFLV strains used in this study consisted of RNA1 of wildtype F13, wildtype GHu, mutant F13-$1E^{Pol*/Sd}_{G802K}$, or mutant GHu-$1E^{Pol*/Sd}_{K802G}$, alongside RNA2 of GFLV-GHu (Osterbaan et al. 2019). These combinations of GFLV RNA1 and RNA2 were selected for their high infection rates in *N. benthamiana* (Osterbaan et al.

2018). Infected plant tissue stored at -80 °C was used for mechanical inoculations (Vigne et al. 2013). The infection status of inoculated plants was confirmed in apical uninoculated leaves by double antibody sandwich enzyme-linked immunoassay (DAS-ELISA) at 14 days post inoculation (dpi) using GFLV specific antibodies (BIOREBA, Switzerland) (Osterbaan *et al.* 2018). At 4 dpi, the status of GFLV infection was tested in inoculated leaves through RT-PCR and in roots by both RT-qPCR and 3'RNA-Seq of total RNA.

Leaves of *N. benthamiana* plants inoculated with wildtype GHu were rated daily for vein clearing symptoms on a binary scale: 0 for asymptomatic, and 1 for symptomatic. No symptoms were observed on the other GFLV treatments or mock control plants, as previously reported (Osterbaan et al. 2019; Roy et al. 2023).

Root system excavation, image acquisition and processing, and root trait analysis

The root excavation pipeline used in this study was previously reported as an open access BioProtocol (Roy and Fuchs 2023). Briefly, potted plants were gently released of soil by hand and root systems were dipped in water until all soil was removed. If persistent soil was adhering to roots, a spray bottle of distilled water was used to remove excess debris. The roots were dried on a paper towel and immediately placed on clear plastic imaging trays (Roy and Fuchs 2023).

Imaging trays were placed on the scanning bed of an Epson Expression XL12000 photo scanner (Model:12000XL-PH) connected to a computer for image acquisition of the roots with the following parameters: ≥ 400 dpi, grayscale, and best quality. Images were analyzed in RhizoVision Explorer version 2.0.3 (Seethepalli and York 2020) with the following parameters: analysis mode (Broken roots), pixels

converted to physical units at ≥ 400 dpi, image thresholding level = 158, (158 for cohort 1, 186 for cohort 2, 182 for cohort 3) (manually adjusted per image ±10), filter non-root objects, enable edge smoothing = 2, feature extraction levels by root diameter (in pixel units) for fine (0.00 – 0.50), small (0.50 – 0.75), medium (0.75 – 1.75), and large (more than 1.75) roots. Using dpi and conversion factors of image acquisition, these measurements corresponded to thresholds of 0.00 mm, 0.32 mm, 0.48 mm, and 1.11 mm. Ultra-fine roots were not considered in this study because the excavation pipeline was optimized to analyze crown root tissue only pertaining to the first several orders of the root system including the primary root with secondary, and at least tertiary lateral roots extending off the primary. Output data was transferred to a Microsoft Excel file. All raw data, including images, are available on the GitHub page or within the supporting information.

Measurement of **N. benthamiana** *plant height and biomass*

The height of *N. benthamiana* plants was measured from the soil line barrier to the apical most part of the central stem with a ruler one day prior to root excavation. Shoots of *N. benthamiana* plants were collected into brown paper bags and thereafter roots were placed in the corresponding numbered bag. Dry biomass was measured after ~1 week in a drying oven at 105 °C. The ratio of root to shoot biomass was calculated for select cohort of *N. benthamiana* plants to assess biomass allocation.

3, 3'-diaminobenzidine (DAB) staining of **N. benthamiana** *primary roots*

Primary root samples of *N. benthamiana* plants were excavated from soil at 7- and 11-dpi for histological staining. For this, five plants per treatment were sacrificed

for tissue collection, where at least three or more of the plants tested true to infection status through RT-PCR. Roots were vacuum infiltrated with 1 mg/mL DAB solution for five minutes and kept in the dark at ambient conditions overnight (8-12 hours) (Vanacker et al. 2000). De-staining was not performed because there is no chlorophyll to extract, and roots produce high amounts of ROS when exposed to ethanol or other abiotic stressors. Cross-sections of roots were made by hand just above where lateral roots formed (e.g., first branching points of root system) and performed two centimeters from the cut made at the stem of plants during excavation. Root cross-sections were placed on a glass microscope slide (Fisher, Cat No. 12-550-A3) mounted with 0.1 mL of 50:50 v/v glycerol:PBST (137 mM NaCl, 2.7 mM KCl, 10 mM Na_2HPO_4, 1.8 mM KH_2PO_4), and protected with a coverslip (Fisher, Cat No. 12-545-88). Imaging of root cross sections was performed immediately following slide mounting to ensure no supplemental induction of ROS production due to additional stress. Images were acquired on an Olympus SZX12 microscope using the following parameters: Gamma 1.16, Contrast 0.79, Saturation 1.53, Color Temp 4188, Exposure 160-200, Gain 1.

N. benthamiana ***root tissue collection, nucleic acid extractions, RT-PCR, and RT-qPCR***

After root system images were acquired, five *N. benthamiana* plants that tested true to virus infection status were randomly chosen for GFLV titer analysis. Roots of mock inoculated *N. benthamiana* plants were used as controls in quantification assays. Approximately half of the root system was sectioned by excising primary, lateral, and fine roots with a sterile razor blade. Samples were placed in 2 mL Eppendorf tubes, flash frozen in liquid nitrogen, and stored at -80 °C until further processing. Total

nucleic acid was extracted from root samples using E.Z.N.A.® Plant RNA Kit (SKU:R6827-01) with a final elution volume of 120 µL nuclease-free water. Then, 40 µL of the eluted nucleic acids were used for DNAse I treatment at 20 °C for 15 minutes followed by RNA clean-up with Zymo Research RNA Clean & Concentrator®-5 (Cat #R1013). RNA integrity and quantity was assessed on an Agilent 2100 Bioanalyzer with the RNA 6000 Nano Kit Assay (No. 5067-1511) according to manufacturer instructions.

Total RNA was used to amplify the GFLV RNA1 nucleotide sequence region covering amino acid in position 802 of protein $1E^{Pol*/Sd}$ with the QIAGEN® OneStep RT-PCR Kit (No. 210210) for Sanger sequence confirmation, as previously described (Osterbaan et al. 2019). Total RNA was also used for GFLV titer analysis by Luna® Universal One-Step RT-qPCR (Cat. No. E3005) with primers specific to GFLV RNA1 (Osterbaan et al. 2019) and to the endogenous *N. benthamiana* control FBOX gene (Liu *et al.* 2012) (Supplementary Table 1). Samples were tested in triplicate, and quantification cycle (Cq) values for SYBR green were collected after each cycle, as previously reported (Osterbaan et al. 2019). GFLV treatments were compared with mock inoculated control samples to calculate ΔΔCq values, in which relative expression was calculated as $\log(2^{-\Delta\Delta Cq})$ values (Shipley 2006).

GFLV strain identification

Amplified RT-qPCR products of ~250 bp in size obtained with GFLV RNA1 primers from roots of two to four infected plants at 17- and 26 dpi were cleaned up with Zymo DNA Clean & Concentrator®-5 (Cat #D4004). The integrity of the two wildtype and two mutant GFLV strains was tested in roots through Sanger sequencing of the cleaned amplicons. Sequences obtained in this study were compared with GFLV

sequences deposited in GenBank (NC003615 for wildtype F13 RNA1 and JN391442 for wildtype GHu RNA1) using SeqMan Ultra™ (v.17.3.1) of the DNASTAR Navigator Package (v17.3.0.57) (DNASTAR, Inc., Madison, Wisconsin, USA).

3‘-ribonucleic acid sequencing

The transcriptome of *N. benthamiana* roots was characterized via 3’RNA-Seq for wildtype GHu, mutant GHu $1E^{Pol*/Sd}{}_{K802G}$, and mock control with samples collected at 4-, 17-, and 26 dpi. Three biological replicates for each time point per viral treatment were purified, concentrated, and DNAse I treated to produce a total of 27 samples. Libraries were prepared with the Illumina® TruSeq RNA Library Prep Kit (RS-122-200X) and sequenced via Illumina® NextSeq500/550. Transcript reads were trimmed with Trimmomatic (v0.39) (Bolger et al. 2014) and subsequently mapped to the host genome, as well as the previously curated GFLV library ‘Nepo’ (Roy et al. 2023) using HiSat2 (v2.2.1) (Kim et al. 2019). Sequences were checked for quality control using the FastQC program (v0.11.9) (Andrews 2010).

Bioinformatic analysis

Sequence reads were mapped to the *N. benthamiana* genome from two different sources: Niben v1.0.1 (Boyce Thompson Institute, Ithaca, NY, USA) (Bombarely et al. 2012) with 61,328 gene models and Nbe_v1 (Kurotani et al. 2023) with 57,583 high confidence gene models. Through a bioinformatic pipeline, the Niben v1.0.1 genome was reannotated in this study using an updated list of gene ontology identifiers by subjecting all protein encoding sequences to a BLAST search through EggNOG (v5.0) (Huerta-Cepas et al. 2019) [Supplementary Figure 1]. After curation of additional

annotation terms, the files were parsed and linked through the GO API (Open Biological and Biomedical Ontology Foundry, http://api.geneontology.org/api) to create a .gmt file for use in gene enrichment. Data files were then manually curated in RStudio and R (RStudio Team 2015; R Core Team 2013).

The DESeq2 package (v1.40.2) (Love *et al.* 2014) was used to normalize, test differential transcript abundance, and prepare data for downstream analysis, as performed previously (Roy et al. 2023). Gene set enrichment analysis was performed using gProfiler (v0.2.1) (Kolberg et al. 2020) and clusterProfiler (v4.8.2) (Wu et al. 2021) packages. Additional packages used for visualization and data analysis include the following: enrichplot (v1.20.1) (Yu 2021), pathview (v1.40.0) (Luo and Brouer 2013), dplyr (v1.3.1) (Wickham et al. 2018), ggplot2 (v3.4.3) (Wickham 2009), and GO.db (v3.16.0) (Bioconductor).

Statistical analyses

Matrices of acquired root traits were subject to Pearson's correlation analysis (Pearson 1931) with the hierarchal clustering method. RStudio package corrplot (v0.92) (Wei *et al.* 2021) was employed to calculate correlation coefficients (-1 to +1) and p-values at four significance intervals (* $p < 0.05$, ** $p < 0.01$, *** $p < 0.001$, **** $p < 0.0001$). In the instances of parametric data and normal distribution, root data were analyzed through analysis of variance (ANOVA) followed by student's t-test for mean testing differences amongst treatments to controls. The p-value for parametric data is reported through the adjustment of Holm's method. For instances of data with non-parametric or non-normal distributions, Kruskal-Wallis (Kruskal and Wallia 1952) tests followed by a Bonferroni correction (Etymologia: Bonferroni Correction 2015) were

performed. Tukey's HSD with associated letters of significance were utilized for follow up statistical testing in root phenotype analyses. A Dunn's test with Holm's method adjusted p-values was utilized for mean comparison testing in non-parametric data. For the analysis of virus titer by RT-qPCR, logarithmic transformed values were used in a geometric mean comparison (Williams and Crawford 1980) and multiple t-test. Further analysis of RNA-Seq data utilized native statistical testing within clusterProfiler, DESeq2, WGCNA, enrichplot, and gProfiler packages.

Days showing symptoms (DSS) on apical leaves of *N. benthamiana* plants infected with wildtype GHu were calculated by subtracting the first and last day of symptom observation, and this metric was used as a predictor variable for RSA traits. Subsequent linear models were constructed and visualized in RStudio through the intrinsic stats package (v4.1.3). Mixed models were also constructed by using the predictors of day first symptomatic (DFS), day last symptomatic (DLS), and the interaction of these two terms with regards to foliar symptoms of wildtype GHu.

RESULTS

Confirmation of GFLV infection status and strain integrity in N. benthamiana *plants*

At 4 dpi, GFLV was detected in most inoculated leaf samples of representative infected plants by RT-qPCR (75%, 15/20) or by RNA-Seq of root tissue (100%, 6/6), but was not detectable by DAS-ELISA, as expected for such an early infection stage. At 14 dpi, a high GFLV infection rate was observed in three cohorts of plants [100% (60/60) for cohort #1, 73% (52/71) for cohort #2, and 91% (85/93) for cohort #3] in apical leaves through DAS-ELISA. None (0%, 0/38) of the mock inoculated control

plants tested positive for GFLV in DAS-ELISA in any of the replicated experiments, as expected.

A glycine (GCC in RNA1 nt position 6,787-6,789) was found in the progeny of wildtype F13 and mutant GHu $1E^{Pol*/Sd}_{K802G}$, while a lysine (AAG in RNA1 nt position 6,797-6,799) was observed in the progeny of wildtype GHu and mutant F13 $1E^{Pol*/Sd}_{G802K}$, as anticipated (Table 4-S1). These analyses revealed high GFLV infection rates of inoculated *N. benthamiana* plants, and the genetic integrity of the GFLV progeny (Table 4-S2).

RSA trait acquisition and analysis

Roots of GFLV-infected and mock inoculated *N. benthamiana* plants were excavated to result in 263 crown root samples being scanned at ≥400 DPI. A total of 77 images captured a first and second side of the whole RSA per plant after a 180º rotation. The three time points of excavation, i.e., 4-, 17-, and 26 dpi, displayed distinct phenotypes with the most dramatic at 17 dpi for plants infected with wildtype GHu (Figures 5-1 and 5-2, Figure 5-S2).

By focusing on ten root traits (number of root tips, number of branch points, total root length, branching frequency, network area, average diameter, median diameter, perimeter, volume, and surface area) of the 32 metrics obtained by Rhizovision analysis, significant differences were found with several co-variable or often highly correlated traits (Figure 5-3a). Five root traits (number of root tips, root diameter, total root surface area, and root branching frequency) were selected for further analysis through pairwise treatment testing at each time point.

At 4 dpi, all GFLV strains indicated some level of initial RSA perturbation (Figure 5-S4d) with an overall 7-23% reduction in root tip number, a 20-25% increase in average diameter, and a 30-48% reduction in branching points, when compared with mock inoculated plants. However, no significant differences were observed for the number of root tips for virus strain, while the average diameter significantly differed between all viral strains compared to mock controls, as shown by Tukey's test and pairwise analysis (Figure 5-S4a,b). The number of branching points was less conclusive because all viral treatments, except wildtype GHu, were significantly different from mock inoculated plants, and wildtype GHu overlapped with all treatments according to Tukey's test (Figure 5-S4c). The limited changes in the overall RSA at 4dpi were likely due to younger plants being exposed to the effects of viral infection for a short period.

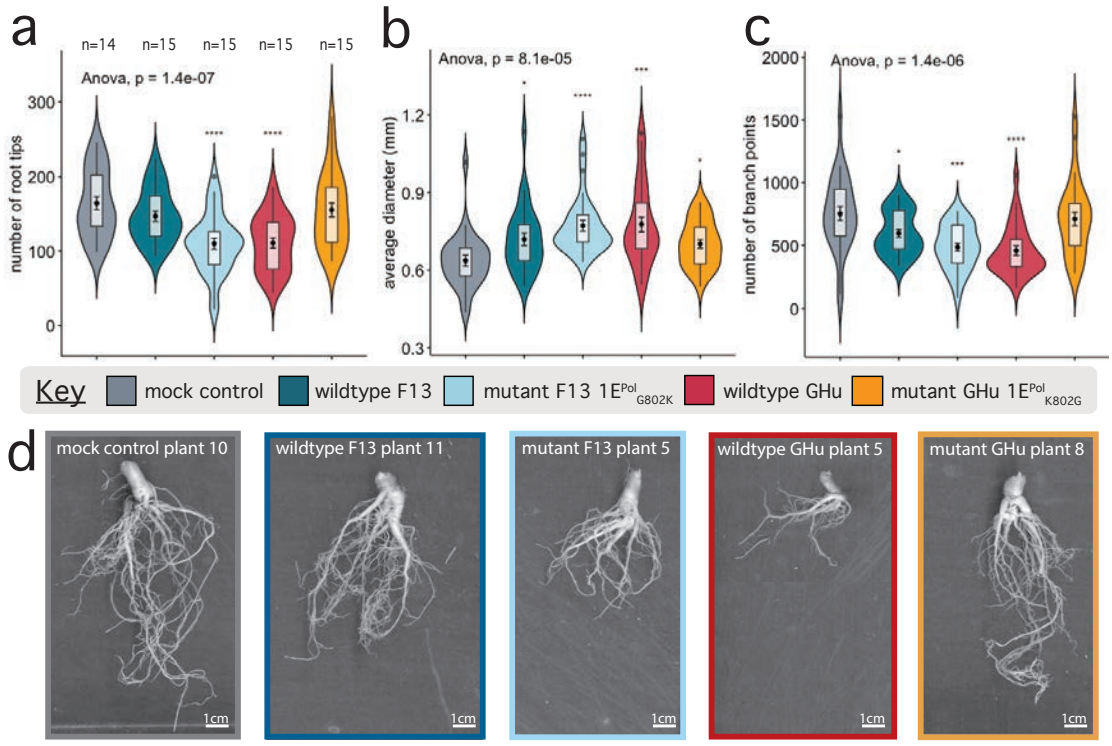

Figure 5-1. Root system architecture traits for *Nicotiana benthamiana* infected with four strains of grapevine fanleaf virus (i.e., wildtypes GHu and F13, and mutants GHu 1E$^{Pol*/Sd}_{K802G}$ and F13 1E$^{Pol*/Sd}_{G802K}$) at 17-days post-inoculation. (a) Number of root tips per plant, **(b)** average diameter in millimeters, and **(c)** number of branch points plotted per viral treatment group. Distribution of each continuous value is plotted along the y-axis as a violin plot with boxplot within, showing additional mean with standard error (central point with error bars). ANOVA significance values are displayed in the top left of each panel, as well as students t-test relative to control as significance values (p $< 0.05 = *, < 0.01 = **, < 0.001 = ***, < 0.0001 = ****$). The number of samples per treatment is displayed above panel A. **(d)** Representative images of mean phenotype observed between treatments, border color is indicative of treatment as in plots A, B, and C. White bar displayed in bottom right corner of each image is 1.0 centimeter, calculated in ImageJ software (v1.8.0.172).

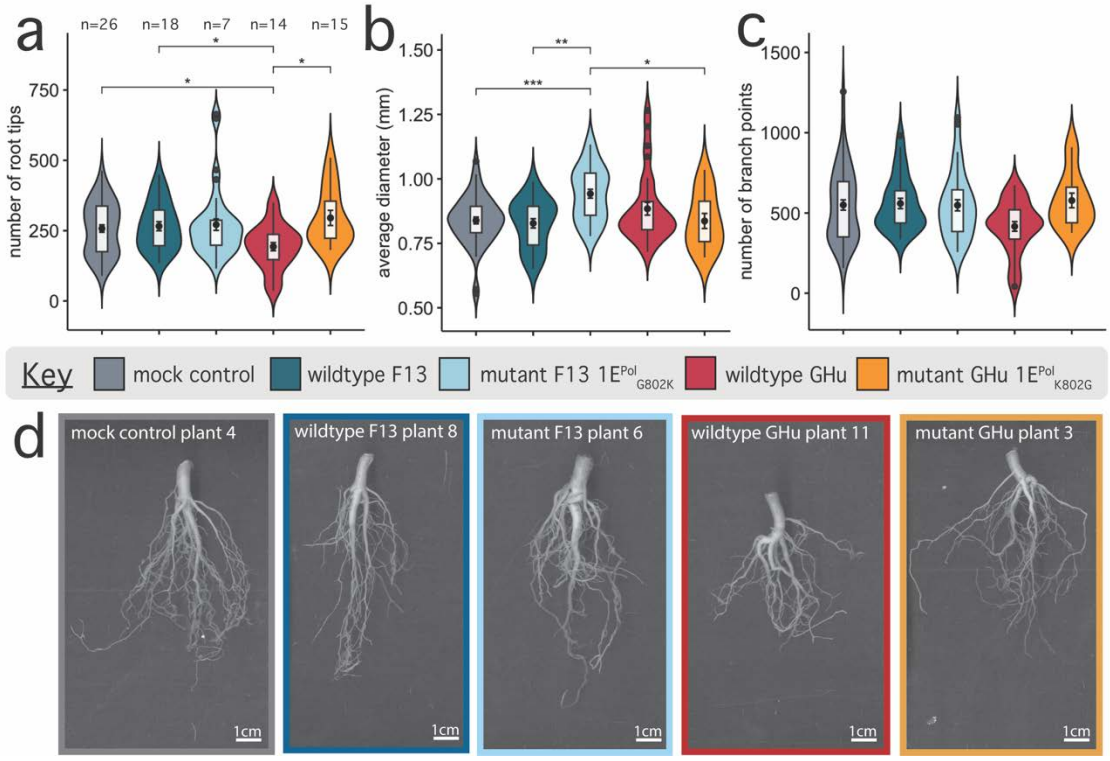

Figure 5-2. Root system architecture traits for *Nicotiana benthamiana* infected with four strains of grapevine fanleaf virus (i.e., wildtypes GHu and F13, and mutants GHu 1E$^{Pol*/Sd}_{K802G}$ and F13 1E$^{Pol*/Sd}_{G802K}$) at 26-days post-inoculation. (a) Number of root tips per plant, **(b)** average diameter in millimeters, and **(c)** number of branch points plotted per viral treatment group. Distribution of each continuous value is plotted along the y-axis as a violin plot with boxplot within, showing additional mean with standard error (central point with error bars). Pairwise Wilcox test results are displayed as significance values ($p < 0.05 = *, < 0.01 = **, < 0.001 = ***, < 0.0001 = ****$). The number of samples per treatment is displayed above panel A. **(d)** Representative images of mean phenotype observed between treatments, border color is indicative of treatment as in plots A, B, and C. White bar displayed in bottom right corner of each image is 1.0 centimeter, calculated in ImageJ software (v1.8.0.172).

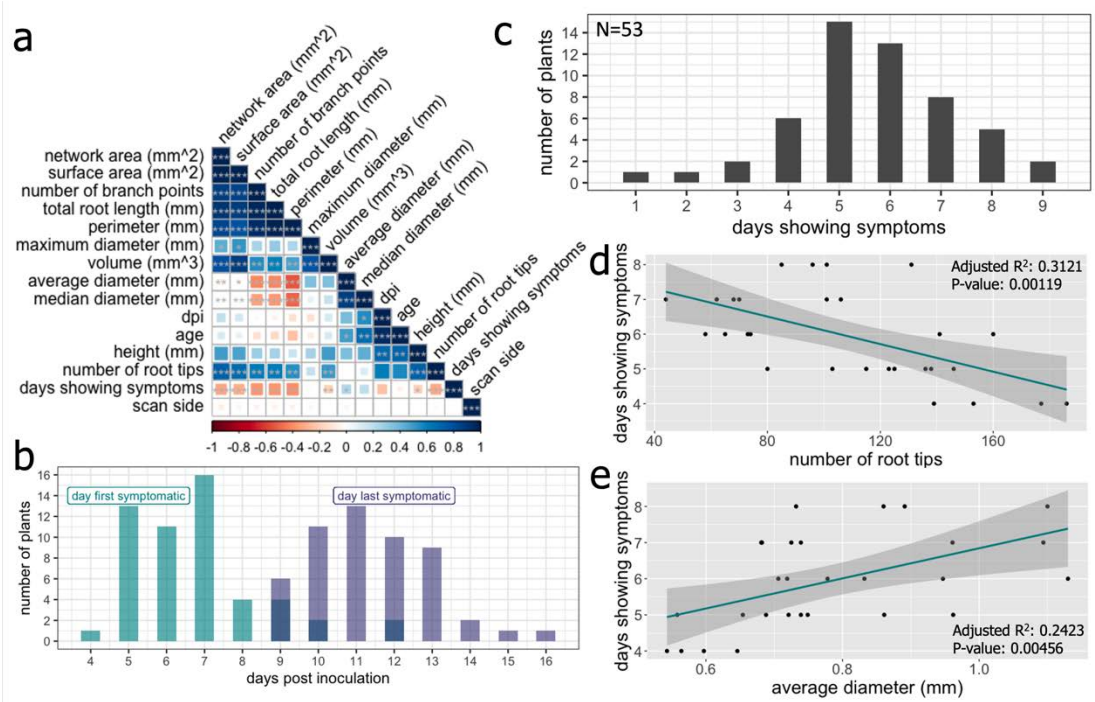

Figure 5-3. The root system architecture (RSA) of *Nicotiana benthamiana* plants upon grapevine fanleaf virus infection is dependent on the identity of amino acid 802 in protein 1E$^{Pol*/Sd}$. (a) RSA traits across four experimental replicates show highly correlated phenes that are dependent upon one another across all treatment groups. The variable `*days showing symptoms*` was calculated from observational documentation of vein clearing symptoms in apical leaves for wildtype GHu infected plants only. **(b)** A histogram displays the first and last day of symptoms (in teal and purple) before full recovery for apical leaves in wildtype GHu infected *N. benthamiana*. **(c)** A normal distribution appears when calculating the total days symptomatic across three experimental replicates ($n = 53$). At 17-days post inoculation **(d)** the number of days showing symptoms had a negative relationship with the number of total root tips and inversely, **(e)** the days showing symptoms in leaves had a positive relationship with the average diameter in millimeters.

At 17 dpi, wildtype GHu and mutant F13 $1E^{Pol*/Sd}_{G802K}$ caused up to a 33% reduction of the total number of root tips (****$p < 0.0001$, Figure 5-1a), and a 21%-22% increase in average root diameter compared with mock inoculated control plants (***$p < 0.001$, Figure 5-1b, Tables 5-S3, 5-S4). These two GFLV strains also decreased root branching frequency, a measure of the number of branch points per total root length by up to 10.1% (**$p < 0.01$, Figure 5-1c, Tables 5-S3, 5-S4). Reduced root tip numbers, less fibrous but thicker roots were visually apparent for wildtype GHu and mutant F13 $1E^{Pol*/Sd}_{G802K}$ compared with the other treatments (Figure 5-1d). Wildtype F13 and mutant GHu $1E^{Pol*/Sd}_{K802G}$ increased the average root diameter by 13% and 10%, respectively, compared with mock inoculated control plants ($p > 0.05$, Figure 5-1d). Dry root biomass was reduced in plants infected wildtype GHu (21%), wildtype F13 (9%), and mutant GHu $1E^{Pol*/Sd}_{K802G}$ (10%) when compared with mock controls while plants infected with mutant F13 $1E^{Pol*/Sd}_{G802K}$ had the same biomass as mock controls (Figure 5-S5). These results documented drastic changes in the RSA of plants infected with wildtype GHu and mutant F13 $1E^{Pol*/Sd}_{G802K}$, both containing K at position 802 of protein $1E^{Pol*/Sd}$, at 17 dpi.

At 26 dpi, plants infected with wildtype GHu exhibited a 25% reduction in the total number of root tips (*$p < 0.05$) and a 6.0% increase in average root diameter when compared with mock control plants (Figure 5-2a, b, Tables 5-S3, 5-S4). Plants infected with mutant F13 $1E^{Pol}_{G802K}$ displayed an increased average root diameter of 13% (***$p < 0.001$) but little change in the number of root tips ($p > 0.05$) when compared with mock control plants. Branching frequency was consistent across all treatment groups (Figure 5-2c). These characteristic RSA traits were apparent on pictures of

representative root systems (Figure 5-2d). Dry root and dry shoot biomass decreased by 26% and 20%, respectively, for plants infected with wildtype GHu, while an increase in these metrics was observed with all other virus strains in comparison with mock inoculated plants (Table 5-S5). These results documented drastic changes in the RSA of plants infected with wildtype GHu and to a lesser extent with mutant F13 $1E^{Pol}{}_{G802K}$, both containing K at position 802 of protein $1E^{Pol*/Sd}$, at 26 dpi. Additionally, many traits such as perimeter, surface area, root to shoot biomass, and plant height were less pronounced when comparing treatments at all time points (Figure 5-S5).

GFLV titer in root tissue

No significant differences in GFLV titer were found at 4 and 17 dpi, as shown by student's t-test of RT-qPCR data (Figure 5-S6a). At 26 dpi, the titer of wildtype F13 was significantly higher from both wildtype GHu and mutant GHu $1E^{Pol*/Sd}{}_{K802G}$, however no other viral treatments differed through student's t-test (Figure 5-S6a). The titer of wildtype F13 was significantly different between 17- and 26-dpi, as shown by a Wilcoxon test (*$p = 0.016$), however no other viral strain had significantly different titer between time points ($p > 0.05$) (Figure 5-S6a). As expected, mock control plants retained no viral titer. These data suggested that virus titer was unrelated to RSA traits during symptom development.

To complement RT-qPCR data, GFLV RNA1 and RNA2 reads from 3'RNA-Seq data were extracted and analyzed. No significant differences were observed amongst viral strains at 4 dpi or 17 dpi, but highly significant differences in RNA1 (**$p = 0.00014$) and RNA2 (****$p = 0.0000008$) were observed when comparing wildtype GHu to mutant GHu $1E^{Pol*/Sd}{}_{K802G}$ at 26 dpi, as shown by Tukey's HSD test (Figure 5-

S6b,c). This trend was numerically similar but not statistically significant in the RT-qPCR data. Together, these data suggested that GFLV titer is not directly correlated with root phenology at 17 dpi but differed amongst viral strains and corresponding root phenotype later in infection.

Effect of GFLV infection on plant height

At 4 dpi, plants infected with wildtype GHu and F13 had a 2% and 6% decrease in height, respectively, while plants infected with mutant GHu $1E^{Pol*/Sd}_{K802G}$ and F13 $1E^{Pol*/Sd}_{G802K}$ displayed a 1% and 9% increase in height, respectively (Table 5-S5, Figure 5-S5). At 17 dpi, GFLV-infected plants had increases in height (up to 18%) for asymptomatic strains and symptomatic wildtype GHu (up to 3%) (Table 5-S5, Figure 5-S5). At 26 dpi, height was reduced by an average of 16% and 9% for plants infected with wildtype GHu and F13, while mutant GFLV strains displayed no change or a minor increase in height when compared with mock inoculated plants (Figure 5-S5). These data revealed that GFLV infection had overall more drastic effects on plant height at late infection stages rather than during early infection.

Correlation of RSA traits and foliar symptomatology for wildtype GHu

A strong positive correlation was observed for root diameter and days showing symptoms (DSS) in apical leaves. Conversely, a strong negative correlation was found between DSS and root branching traits such as root tip number, number of branching points, and network area (Figure 3a, Supplementary Figure 3). At 17 dpi, dry biomass, network area, perimeter, and surface area were significantly reduced for plants infected with wildtype GHu, and to lesser extents across other viral strains several, illustrating

modifications above and below ground (Table 5-S5). At 26 dpi, additional traits were significantly impacted but not to the level described at 17 dpi (Table 5-S5). While plants infected with other viral strains remained close to mock control plants, wildtype GHu induced a lessened amount of root tips, number of branch points, total root length (mm), network area (mm^2), perimeter (mm), volume (mm^3), and surface area (mm^2) (Table 5-S5).

Since many RSA traits were significantly and strongly correlated (positively or negatively) with leaf symptomology in *N. benthamiana* infected with wildtype GHu, general linear models and mixed models were constructed to predict RSA traits. A relatively normal distribution of symptom emergence centered at 7 dpi (average 6.77 dpi) with symptom disappearance around 11 dpi (average 11.37 dpi) and vein clearing symptoms apparent for an average of 5.66 days across all 53 *N. benthamiana* plants infected by wildtype GHu (Figure 5-3b,c, Table 5-S6). A linear model constructed using the continuous response variables from acquired RSA traits against the predictor variable of days symptomatic documented an inverse relationship between the number of root tips and the number of days symptomatic in leaf tissue (RSE = 32.35, adjusted $R^2 = 0.254$, $p = 0.00266$, Figure 5-3d). The observed variance in average root diameter could be significantly explained by the symptomatic days (RSE = 0.1454, adjusted $R^2 = 0.1517$, $p = 0.01912$, Figure 5-3e), albeit explaining less variation compared with root tip number. These results illustrated an association between symptoms above and below ground for *N. benthamiana* infected with wildtype GHu.

A mixed model incorporating DFS and DLS as date component rather than difference of the two dates performed nearly twice as well for modeling root tip number

(RSE = 23.95, adjusted R^2 = 0.6067, p = 1.105E-5), and nearly as well for median root diameter prediction (RSE = 0.07733, adjusted R^2 = 0.3649, p = 0.002929). At 26 dpi, correlation analysis was strong although linear modeling returned insignificant results [p > 0.05] (Figure 5-S7). These observations suggested a correlation between apical leaf symptoms and long-term root phenotypes for wildtype GHu infected plants.

Reactive oxygen species are produced in roots during GFLV infection

ROS production was monitored in root tissue of *N. benthamiana* via histological cross sections of primary roots followed by DAB staining at 7 dpi (n=25) and 11 dpi (n=25) (Figure 5-4). Filamentous roots were very dark from DAB staining, likely due to the stress of digging up the plants from the soil and the abundance of ROS in emerging root tips (Figure 5-4a). At 7 dpi, roots of plants infected with wildtype GHu and mutant F13 $1E^{Pol*/Sd}_{G802K}$ contained a ring of dark stain bordering the pericycle and vascular bundle, but not the cortex (Figure 5-4b). This was not observed for any GFLV strain at 11 dpi. Roots of plants infected with wildtype F13 and mutant GHu $1E^{Pol*/Sd}_{K802G}$ did not have the same level of contrast but showed stain slightly darker than roots of control plants in the outermost parts of the vascular bundle (Figure 5-4b). Mock control plants at 7 dpi (n=5) and 11 dpi (n=5) yielded minimal background staining of any vasculature or cortex, but epidermal tissue consistently showed a dark brown or black color. These results suggested that the nature of residue 802 of protein $1E^{Pol*/Sd}$ largely influences the amount of ROS produced in the primary roots of *N. benthamiana.*

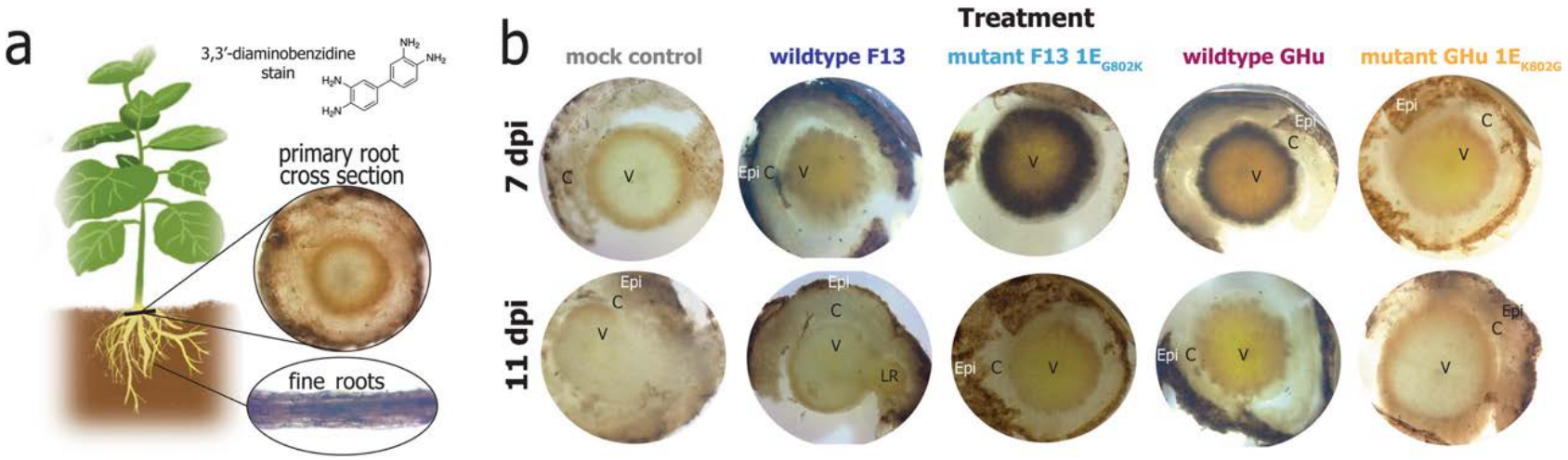

Figure 5-4. Reactive oxygen species (ROS) transiently produced in *Nicotiana benthamiana* primary root pericycle by four grapevine fanleaf virus (GFLV) strains (i.e., wildtypes GHu and F13, and mutants GHu 1E$^{Pol*/Sd}_{K802G}$ and F13 1E$^{Pol*/Sd}_{G802K}$) at 7- and 11- days post-inoculation (dpi). (a) Anatomical view of primary root cross sections from *N. benthamiana* immediately stained with 3′3-diaminobenzidine, dark portions represent tissue with high amounts of ROS reacting with the stain. Fine roots produced high amounts of ROS as expected from rapidly growing root tissue. **(b)** Primary root cross sections of virus treatments display high amounts of precipitated 3–3'-diaminobenzidine stain in the pericycle for both wildtype GHu and mutant F13 1E$^{Pol*/Sd}_{G802K}$ at 7 dpi and a diminished ROS abundance at 11 dpi. All other treatments have much lower levels of ROS detectable within the vasculature and cortex at both time points. (Epi = root epidermis, C = cortex, V = vascular bundle, LR = lateral root primordium). Images are representative of at least three individuals (n = 3) of five sacrificed plants per treatment

3'RNA-sequencing, and data curation

Twenty-seven *N. benthamiana* root samples were sequenced on Illumina 500/550 platform, three replicates of each treatment (wildtype GHu, mutant GHu $1E^{Pol*/Sd}{}_{K802G}$, mock control) at three time points (4-, 17-, 26 dpi). The average number of total reads per sample was 7,338,802. After identification of reads passing quality control thresholds and proper adapter trimming, an average of 7,271,449 reads remained per sample. Alignment to the Niben v1.0.1 genome (Bombarely et al. 2012) resulted in an average of 74.63% reads per sample, after outlier removal of sample mutant GHu $1E^{Pol*/Sd}{}_{K802G}$ 17 dpi replicate #3 (low alignment rate ~6%). Alignment to the Nbe_v1 genome resulted in an average of 5% less aligned reads, therefore, downstream analysis utilized the Niben v1.0.1 alignment. Quality control as reported through FastQC analysis of RNA-sequencing files returned average sequence lengths of 86 base pairs, 36-39% GC content, and Phred quality scores maintaining a majority above 30, with many sequences at 35 (1 in 5000 base pair call inaccuracy), which were all acceptable for downstream analysis (Table 5-S7). Re-annotation of the *N. benthamiana* genome was performed to retrieve 11525 GO terms that matched to the Niben v1.0.1 protein models (Figure 5-S1).

Initial statistical considerations of the 3'RNA-Seq dataset

FeatureCounts files were parsed to produce a gene count matrix that was utilized with a metadata matrix containing treatment, time, and a group factor of treatment*time for DESeq2 input. The resulting matrix represented 37,784 genes with a threshold of at least 20 counts across all samples. Count filtering, dispersion of counts, hierarchal clustering, and principal component analysis were performed on data prior to removal

of mutant GHu $1E^{Pol*/Sd}_{K802G}$ replicate #3 at 17 dpi, because it showed large separation from all other samples (Figure 5-S8a-d). After removal of this outlier, the analysis pipeline continued with the remaining 26 samples. Normalized counts returned roughly ~200,000 reads per sample across all time points and treatments (Figure 5-S9a). Further, dispersion estimate curves were largely normal across the DESeq2 experiment, indicating that the normalization of counts and quality of reads were acceptable. A strong grouping by both treatment and time in hierarchal clustering and principal component analysis was observed (Figure 5-S9c-d). All mock control samples grouped away from GFLV-infected samples, and GFLV-infected samples separated by time point through McQuitty method hierarchal clustering (Figure 5-S9c). Further, samples were discriminated by treatment and time through principal component analysis with PC1 of 29.89% and PC2 of 12.42%. Samples at 4 dpi grouped in the middle of the plot, loosely associated, while samples at 17 dpi grouped to the right of the plot. Samples collected at 26 dpi were located on the left of the PCA plot in tight association, suggesting that these samples were differentiated from the other time points based on PC1, but less discriminated by PC2. Based on these results, the dispersion of counts being acceptable after normalization (Figure 5-S9c), and the successful alignment of 201,108 reads per sample, data were deemed acceptable for further analysis.

Differential transcript abundance analysis

Contrasts were generated within the DESeq2 package to examine differences in the transcriptome between treatments. Thresholds of $p < 0.05$ and |Log2FoldChange|>1 were used for determining differentially abundant genes (DEGs). When comparing wildtype GHu to mutant GHu $1E^{Pol*/Sd}_{K802G}$ at 4-, 17- and 26 dpi, a total of 704, 761,

and 1041 transcripts was found to be differentially abundant, respectively (Table 5-1, Figure 5a-c). An increased number of differentially abundant transcripts was obtained when comparing viral treatments to the mock controls at each time point. When comparing wildtype GHu to mock control transcripts, a total of 713, 4351, and 1692 transcripts were differentially abundant at 4-, 17- and 26 dpi, respectively (Table 5-1, Figure 5-5d-f). Lastly, when comparing mutant GHu $1E^{Pol*/Sd}{}_{K802G}$ to mock control, a total of 437, 3293, and 2124 DEGs were found at 4-, 17-, and 26 dpi, respectively (Table 5-1, Figure 5-5g-i).

The top ten *N. benthamiana* root genes of differential abundance per treatment contrast and time point were identified (Table 5-2). By contrasting wildtype GHu and mutant GHu $1E^{Pol*/Sd}{}_{K802G}$, host root genes relating to immune response, signaling, disease resistance, hydrolase activity, and components of viral silencing were consistently found to be dysregulated. Transcripts for regulators of transcription, translation, and post-translational processes were most abundant (Table 5-2). When contrasting wildtype GHu to mock inoculated plants, host genes relating to transcription, mitochondria and signaling patterns, protein synthesis, and immune response were dysregulated in the top 10 DEGs across all time points. Further, glutamine synthase and phosphatidylinositol-related genes appeared in the top 10 DEGs at 17 dpi, consistent with previously identified candidates in apical leaf tissue during GFLV infection and foliar symptom development (Osterbaan *et al.* 2019). Additional regulators of transcription and translation, immune response and signaling genes were dysregulated in the contrast of mutant GHu $1E^{Pol*/Sd}{}_{K802G}$ and mock control across the three time points. Across all contrasts, genes relating to innate immune response were

consistently present, suggesting residue $1E^{Pol*/Sd}_{802}$ impacts the level in which immune responses are activated during infection. Notably, five unknown proteins were dysregulated to high magnitudes up to Log2FC of 14.66. These genes could have important functions related to morphology or viral infection not yet characterized in plant root tissue. All differentially abundant transcripts were documented (Table 5-S8).

Table 5-1. Differentially abundant transcripts as compared through DESeq2 analysis of *Nicotiana benthamiana* plant roots infected with two grapevine fanleaf virus strains, i.e., wildtype GHu and mutant GHu $1E^{Pol*/Sd}{}_{K802G}$) at 4-, 7- and 11 days post-inoculation (dpi). DEGs were defined as having both a p-value < 0.05 and an absolute Log2FoldChange > 1.

Treatment contrast	*wildtype GHu vs mutant GHu* $1E^{Pol*/Sd}{}_{K802G}$		*wildtype GHu vs mock control*		*mutant GHu* $1E^{Pol*/Sd}{}_{K802G}$ *vs mock control*	
Time	UP	DOWN	UP	DOWN	UP	DOWN
4 dpi	332	372	371	342	264	173
17 dpi	318	443	1548	2803	1483	1810
26 dpi	586	455	1043	649	1162	962

Table 5-2. The top ten differentially abundant transcripts present in each viral contrast with their respective gene ID, name, Log2FoldChange (Log2FC), and *p*-value, ranked by *p*-value.

a. Wildtype GHu contrasted with mutant GHu $1E^{Pol*/Sd}$ at 4-, 17-, and 26-days post-inoculation in *Nicotiana benthamiana*.
b. Wildtype GHu contrasted with mock controls at 4-, 17-, and 26-days post-inoculation in *N. benthamiana*.
c. Mutant GHu $1E^{Pol*/Sd}_{K802G}$ contrasted with mock controls at 4-, 17-, and 26-days post-inoculation in *N. benthamiana.*

Table 5-2a. Wildtype GHu contrasted with mutant GHu 1E$^{Pol*/Sd}$ at 4-, 17-, and 26-days post-inoculation in *N. benthamiana.*

Time		Name	GeneID	Log2FC	lfcSE	*p*-value
4 dpi	1	Mitochondrial protein	Niben101Scf04451g00027	5.6966875	1.2629942	6.47E-06
	2	Protein NRT1/ PTR FAMILY 4.3	Niben101Scf04119g03004	1.6205678	0.3728127	1.38E-05
	3	Isoflavone reductase family protein	Niben101Scf04113g17021	-3.0801945	0.7699946	6.33E-05
	4	Mitochondrial substrate carrier family protein	Niben101Scf02168g04008	-0.9887381	0.2482862	6.83E-05
	5	LOB domain-containing protein 41	Niben101Ctg14421g00002	1.6113985	0.4074446	7.66E-05
	6	Protein translocase subunit SecA	Niben101Scf01888g03004	2.4184992	0.6197774	9.53E-05
	7	Glutamate receptor 2.8	Niben101Scf00747g12032	-1.250575	0.3255952	1.23E-04
	8	FAD-binding Berberine family protein	Niben101Scf09217g00016	0.9738886	0.2592972	1.73E-04
	9	Proteinase inhibitor type-2	Niben101Scf07757g00001	-2.8053858	0.7484557	1.78E-04
	10	ATP-dependent RNA helicase eIF4A	Niben101Scf01998g00010	-1.8775588	0.5017108	1.82E-04
17 dpi	1	Protein kinase superfamily protein	Niben101Scf01450g01008	-1.8437026	0.3341768	3.45E-08
	2	Disease resistance protein I2	Niben101Scf03396g07026	-3.4940569	0.6487701	7.22E-08
	3	ABC transporter ATP-binding protein ARB1	Niben101Scf15836g04006	-0.6199358	0.129438	1.67E-06
	4	Beta-amylase	Niben101Scf10158g01036	1.9664738	0.4140633	2.04E-06
	5	Cytochrome c oxidase subunit 2	Niben101Scf04412g00017	-2.8547363	0.6198686	4.12E-06
	6	Xyloglucan endotransglucosylase/hydrolase protein 22	Niben101Scf14470g00001	-2.5754905	0.5690913	6.02E-06
	7	Patatin-like protein 7	Niben101Ctg15717g00003	2.465677	0.5483163	6.90E-06
	8	Unknown protein	Niben101Scf06105g01010	-2.0285676	0.4610409	1.08E-05
	9	40S ribosomal protein S4	Niben101Scf17473g00009	-1.4071685	0.3344886	2.59E-05
	10	glucan synthase-like 4	Niben101Scf00790g00004	-2.016389	0.4822456	2.90E-05
26 dpi	1	Glutamine synthetase	Niben101Scf00345g01021	1.7674997	0.2615045	1.39E-11
	2	Serine carboxypeptidase II-2	Niben101Scf02359g00009	1.2220252	0.2221445	3.78E-08
	3	Cupredoxin superfamily protein	Niben101Scf02393g02025	4.0739648	0.7475112	5.04E-08
	4	Pyrimidine-specific ribonucleoside hydrolase RihA	Niben101Scf04674g02018	2.2507337	0.4528093	6.67E-07
	5	nodulin MtN21 /EamA-like transporter family protein	Niben101Scf09197g00005	2.8514417	0.581598	9.45E-07
	6	Actin-2	Niben101Scf00672g00001	-1.392489	0.2851484	1.04E-06
	7	Pectinesterase 3	Niben101Scf03706g02006	-3.4769013	0.725795	1.66E-06
	8	Double-stranded RNA-binding protein 2	Niben101Scf01759g04003	-0.9927502	0.209516	2.16E-06
	9	Apyrase	Niben101Scf05918g03001	1.1004463	0.2379406	3.75E-06
	10	FAS-associated factor 2-B	Niben101Scf02972g07001	1.054296	0.231198	5.11E-06

Table 5-2b. Wildtype GHu contrasted with mock controls at 4-, 17-, and 26-days post-inoculation in *N. benthamiana.*

Time		Name	GeneID	Log2FC	lfcSE	*p*-value
4 dpi	1	Unknown protein (BLAST = Flocculation protein)	Niben101Scf03494g00002	16.827141	3.1119877	6.40E-08
	2	Heat shock 70 kDa protein 1A	Niben101Scf05389g00010	-0.992725	0.2053522	1.34E-06
	3	Mitochondrial protein	Niben101Scf04451g00027	6.6042454	1.3974789	2.29E-06
	4	Mitochondrial substrate carrier family protein	Niben101Scf02168g04008	-1.1086204	0.2481061	7.88E-06
	5	DNA-binding protein [Streptococcus suis]	Niben101Scf03528g03009	1.0295563	0.230432	7.90E-06
	6	ATP-dependent RNA helicase eIF4A	Niben101Scf01998g00010	-2.1936224	0.4975499	1.04E-05
	7	Thermosome subunit	Niben101Scf13415g00021	0.9343139	0.2119629	1.04E-05
	8	50S ribosomal protein L11	Niben101Scf01911g02007	-0.8416185	0.1963029	1.81E-05
	9	Heat shock 70 kDa protein 1-like	Niben101Scf12154g01009	-1.1372504	0.2653934	1.83E-05
	10	Tudor/PWWP/MBT superfamily protein	Niben101Scf01722g04010	1.2035777	0.2816975	1.93E-05
17 dpi	1	Sec14p-like phosphatidylinositol transfer family protein	Niben101Scf01018g03001	1.9836672	0.2093088	2.61E-21
	2	GATA transcription factor 2	Niben101Scf08635g02001	3.4384291	0.3744416	4.20E-20
	3	Low PSII Accumulation 3 isoform 3	Niben101Scf00715g09005	-4.0551673	0.4448789	7.85E-20
	4	cAMP-regulated phosphoprotein 19-related protein	Niben101Scf22015g02047	-0.9337399	0.1056044	9.41E-19
	5	Pentatricopeptide repeat-containing protein	Niben101Scf02525g02002	-3.5162577	0.4035648	2.96E-18
	6	UDP-D-glucuronate 4-epimerase 6	Niben101Scf02104g01010	2.9642438	0.3402434	2.98E-18
	7	evolutionarily conserved C-terminal region 5	Niben101Scf08176g00008	-2.337806	0.2850484	2.38E-16
	8	glucan synthase-like 4	Niben101Scf02725g02025	-2.7706434	0.3427949	6.34E-16
	9	Mitochondrial substrate carrier family protein	Niben101Scf02268g05007	-2.4230657	0.3058151	2.31E-15
	10	glucan synthase-like 4	Niben101Scf00790g00004	-3.4114818	0.430985	2.46E-15
26 dpi	1	Glutamine synthetase	Niben101Scf00345g01021	1.9631991	0.2618972	6.58E-14
	2	cAMP-regulated phosphoprotein 19-related protein	Niben101Scf22015g02047	-0.8186601	0.1099428	9.60E-14
	3	Glutamine synthetase	Niben101Scf01765g02012	1.9044151	0.2854461	2.53E-11
	4	Isoaspartyl peptidase/L-asparaginase	Niben101Scf05643g05001	3.032	0.4587894	3.88E-11
	5	expressed protein [Oryza sativa Japonica Group]	Niben101Scf04259g01024	-1.9964343	0.3061783	7.01E-11
	6	myb-like transcription factor family protein	Niben101Scf03942g02002	-1.6564299	0.2544056	7.47E-11
	7	5-methyltetrahydropteroyltriglutamate—homocysteine…	Niben101Scf09725g00022	1.7118145	0.2710982	2.71E-10
	8	Major facilitator superfamily protein	Niben101Scf04223g00001	2.5284428	0.4114759	8.01E-10
	9	Phospholipase A1-II 1	Niben101Scf10353g00011	2.4200058	0.3973735	1.13E-09
	10	Apyrase	Niben101Scf05918g03001	1.4397588	0.2381754	1.49E-09

Table 5-2c. Mutant GHu 1E$^{Pol*/Sd}_{K802G}$ contrasted with mock controls at 4-, 17-, and 26-days post-inoculation in *N. benthamiana.*

Time		Name	GeneID	Log2FC	lfcSE	*p*-value
4 dpi	1	Unknown protein	Niben101Scf00239g04001	1.3152369	0.2833667	3.46E-06
	2	Protein trichome birefringence-like 19	Niben101Scf02215g01004	2.5423049	0.5559715	4.81E-06
	3	Unknown protein	Niben101Scf03494g00002	14.655540	3.2427267	6.20E-06
	4	Adenylyl cyclase-associated protein	Niben101Scf13199g00006	-0.8376836	0.1854987	6.31E-06
	5	purple acid phosphatase 27	Niben101Scf03184g02002	1.293926	0.288435	7.26E-06
	6	Heat shock 70 kDa protein 1A	Niben101Scf05389g00010	-0.9033857	0.2042308	9.72E-06
	7	Unknown protein	Niben101Scf01881g02004	1.0296128	0.2370674	1.40E-05
	8	Proteinase inhibitor I-A	Niben101Scf09044g01003	4.0785915	0.9449667	1.59E-05
	9	Beta-D-xylosidase 4	Niben101Scf01894g02004	1.1060834	0.2607789	2.22E-05
	10	Leucine-rich repeat (LRR) family protein	Niben101Scf02422g02015	-0.8890076	0.2130283	3.00E-05
17 dpi	1	Sec14p-like phosphatidylinositol transfer family protein	Niben101Scf01018g03001	2.0325732	0.2335843	3.27E-18
	2	Calcium-binding protein 2	Niben101Scf01002g02005	1.251441	0.1616167	9.69E-15
	3	Heat shock 70 kDa protein 1A	Niben101Scf05389g00010	1.622938	0.2297735	1.63E-12
	4	Unknown protein	Niben101Scf00321g02008	-2.8658029	0.408885	2.40E-12
	5	cAMP-regulated phosphoprotein 19-related protein	Niben101Scf22015g02047	-0.8036557	0.1185462	1.21E-11
	6	Myb-related protein 306	Niben101Scf01013g01003	-2.4164981	0.3585196	1.58E-11
	7	UDP-D-glucuronate 4-epimerase 6	Niben101Scf02104g01010	2.5510918	0.3794764	1.78E-11
	8	Nutrient reservoir [Cucumis sativus]	Niben101Scf16997g00001	2.2587796	0.3442533	5.33E-11
	9	Beta-D-xylosidase 4	Niben101Scf01894g02004	2.1428993	0.3275848	6.09E-11
	10	Dormancy/auxin associated family protein	Niben101Scf01041g04001	-2.8642541	0.4492301	1.82E-10
26 dpi	1	WRKY transcription factor 1	Niben101Scf01833g00002	2.1014269	0.346101	1.27E-09
	2	Glycerol-3-phosphate dehydrogenase [NAD(P)+]	Niben101Scf01612g02014	1.3518906	0.2329634	6.51E-09
	3	Cyclin-U2-2	Niben101Scf00397g06001	1.5115199	0.2660277	1.33E-08
	4	Unknown protein	Niben101Scf01220g04008	1.4435006	0.2555505	1.62E-08
	5	Unknown protein	Niben101Scf04259g01024	-1.6340773	0.2988318	4.55E-08
	6	Boron transporter 1	Niben101Scf06412g01004	-1.4374495	0.2680706	8.22E-08
	7	Pentatricopeptide repeat-containing protein	Niben101Scf03076g02006	2.5436469	0.477935	1.03E-07
	8	Neutral ceramidase	Niben101Scf00978g09002	1.1002245	0.2070326	1.07E-07
	9	Ubiquitin-fold modifier-conjugating enzyme 1	Niben101Scf02593g00002	1.314139	0.2483603	1.21E-07
	10	Organ-specific protein P4	Niben101Scf03839g12008	3.1856642	0.6040954	1.34E-07

Figure 5-5. Volcano plot contrasts of *Nicotiana benthamiana* plants infected with two grapevine fanleaf virus (GFLV) strains (i.e., wildtype GHu and mutant GHu $1E^{Pol*/Sd}_{K802G}$) reveal perturbations of the root transcriptome at three time points; 4-, 17- and 26 days post-inoculation (dpi). Contrasts are divided by treatment in columns such as wildtype GHu vs mutant GHu $1E^{Pol*/Sd}_{K802G}$ (**a**, **b**, **c**), wildtype GHu vs mock control (**d**, **e**, **f**), and mutant GHu $1E^{Pol*/Sd}_{K802G}$ vs mock control (**g**, **h**, **i**) and by time (rows) at 4 dpi (**a**, **d**, **g**), 17 dpi (**b**, **e**, **h**) and 26 dpi (**c**, **f**, **i**). Logarithmic transformation of transcript abundance comparisons is shown on the x-axis. Confidence values as logarithmic transformations of *p*-value are represented on the y-axis. Genes shown as purple data points meet qualifications of $p\text{-value} < 0.05$ and absolute $\text{Log2FoldChange} \geq 1$. Genes in gray meet only one qualification, while black data points denote neither qualification was met.

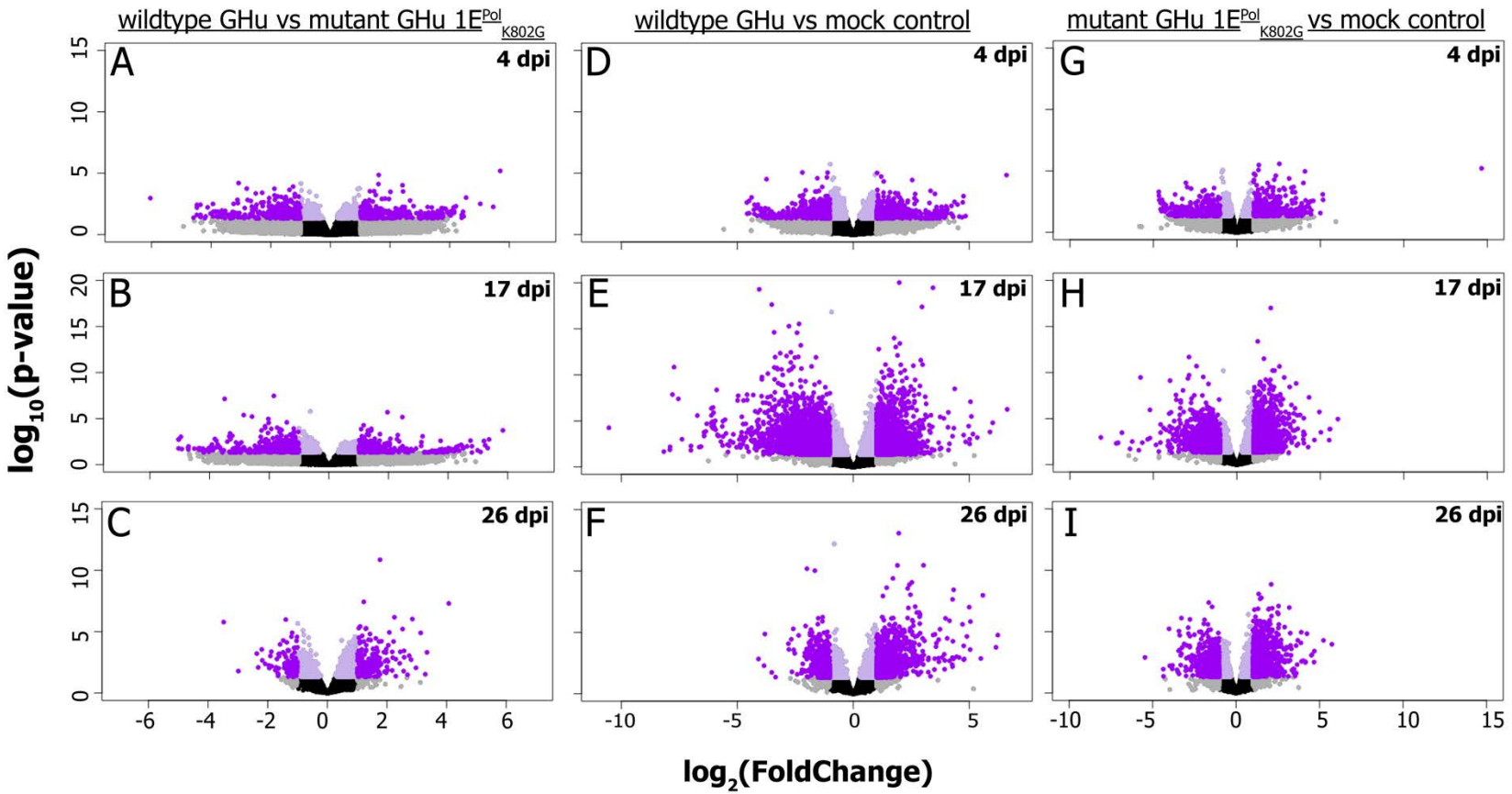
wildtype GHu vs mutant GHu 1E^Pol_K802G
wildtype GHu vs mock control
mutant GHu 1E^Pol_K802G vs mock control
A
4 dpi
B
17 dpi
C
26 dpi
D
4 dpi
E
17 dpi
F
26 dpi
G
4 dpi
H
17 dpi
I
26 dpi
log10(p-value)
log2(FoldChange)

Gene set enrichment analysis

From each of the treatment contrasts, DEGs were extracted and subject to GSEA to detect overrepresented gene ontology terms. An ordered list of DEGs was used to produce enriched terms between each contrast at each respective time point (Figure 5-S10). Few terms were produced during contrasts of wildtype GHu and mutant GHu $1E^{Pol*/Sd}{}_{K802G}$ root transcriptome profiles to include response to external stimulus (GO:0009605) and pigment binding (GO:0031409) at 4 dpi, negative regulation of plant-type hypersensitive response (GO:0034051) at 17 dpi, and regulation of steroid metabolic process (GO:0019218) at 26 dpi. The relatively low number of DEGs detected between these two treatment contrasts might have prevented further resolution of these data related to the observed changes in RSA.

Many more gene ontologies were detected through GSEA by contrasting wildtype GHu with mock inoculated control plants. At 4 dpi, ontologies related to dephosphorylation (GO:0016311) and phosphatase activity (GO:0016791) amongst other closely related GOs were overrepresented. Out of 59 total terms at 17 dpi, the top three GO's overrepresented according to p-value were DNA-binding transcription factor (GO:0003700), transcription regulator activity (GO:0140110), and response to stimulus (GO:0050896). Several terms relating to biosynthetic processes, phosphorylation, response to oxygen species, and hormone response were overrepresented at this time point as well (Figure 6a). Pigment binding (GO:0031409), obsolete anchored component of membrane (GO:0031225), and photosynthesis, light harvesting in photosystem I (GO:0009768) were the top three overrepresented GOs at

26 dpi (Figure 5-6a). Further terms related to photosynthetic components and secondary metabolite regulation were found at 26 dpi.

Contrasting mutant GHu $1E^{Pol*/Sd}_{K802G}$ and mock inoculated control plants revealed gene ontologies that were reminiscent of viral infection without all changes occurring to root morphology, as observed through the previously described RSA phenotyping (Figure 5-S10). Thylakoid (GO:0009579), photosynthetic membrane (GO:0034357), and singlet oxygen-mediated programmed cell death (GO:0010343) were among the overrepresented, non-redundant GO's present at 4 dpi. At 17 dpi, plasma membrane (GO:0005886), cell periphery (GO:0071944), and response to stimulus (GO:0050896) were the top three overrepresented GOs by p-value, with other terms relating to hormone response and phosphorylation activity also being abundant at this time. At 26 dpi, 29 terms were overrepresented with the top three by p-value being regulation of hormone levels (GO:0010817), hormone metabolic process (GO:0042445), and lipid metabolic process (GO:0006629). Other closely related terms of response to stimulus, plasma membrane, and phosphorylation were also present during late infection (Figure 5-S10).

A secondary evaluation of enrichment for differentially abundant transcripts found in roots was performed through Kyoto Encyclopedia of Genes and Genomes (KEGG) analysis. Significant KEGG terms were defined by the thresholds of $p<0.05$ and $q<0.05$ to evaluate the 3'RNA-Seq differentially abundant genes against the newly curated genome annotation. The enriched KEGG terms confirmed previous GSEA results to display terms of immune response, gene regulation, and signal transduction (Figure 5-6b-d, Figure 5-S11). Signaling genes such as calcium-binding protein CML

(ko:k13448), phosphatase 2C of the MAP kinase pathway (ko:k14497), and calcium dependent protein kinase (ko:k13412) were present at various contrasts and time points during GFLV infection (Figure 5-S11a,d,h). Interestingly, a new term relating to cell elongation and division appeared as well throughout multiple contrasts and time points: xyloglucan transferase (ko:k08235) (Figure 5-S11b,e,f). The results of the KEGG analysis further documented phytohormone pathways (ethylene, abscisic acid, transcription factor TGA) to be impacted upon viral infection although their relation to the development of root symptoms may not be immediately apparent. Several terms related to protein repair such as chaperone proteins, oxidases, and hormone regulators were found at 26 dpi from KEGG analysis (Figure 5-S11c,f,i).

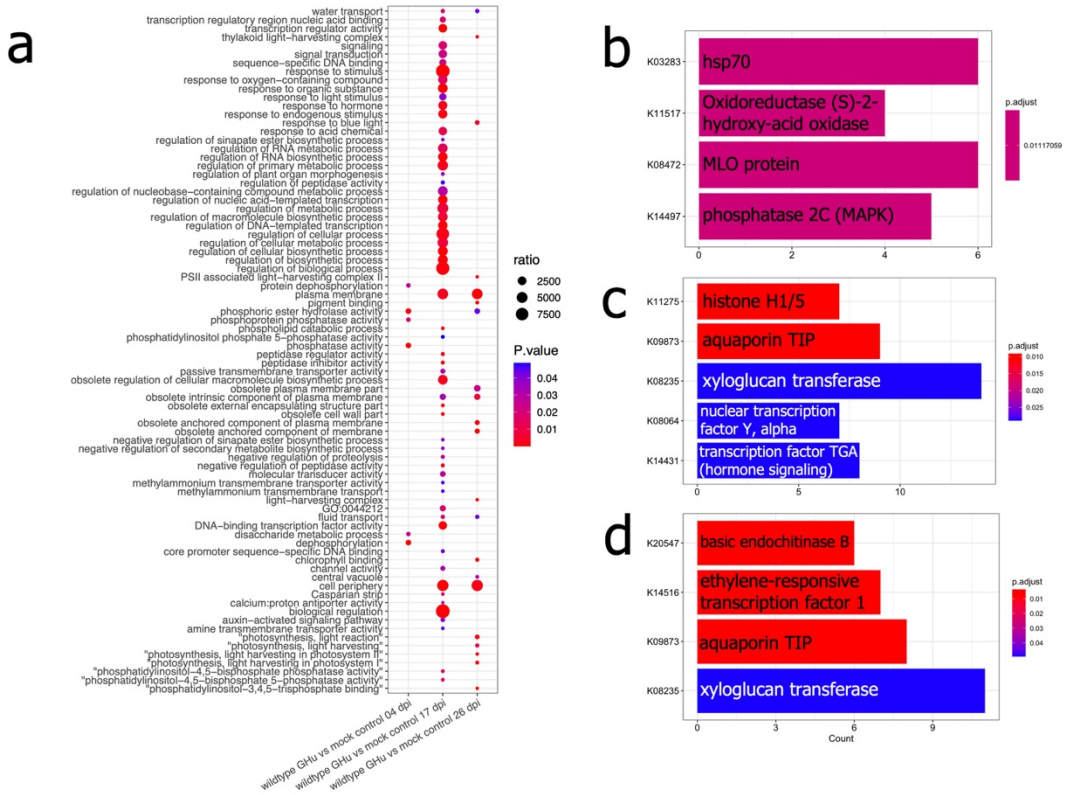

Figure 5-6. Downstream overabundance of transcript dysregulation in *Nicotiana benthamiana* roots infected with wildtype grapevine fanleaf virus strain GHu through gene set enrichment analysis and Kyoto Encyclopedia of Genes and Genomes (KEGG) reveals several conserved pathways of overabundance. (a) The dotplot representation of wildtype GHu infected plants against mock control GSEA shows pathways dysregulated at all three time points past inoculation. At early infection, 4 days post inoculation (dpi), categories related to signaling and phosphorylation are displayed. At 17 dpi, many components of metabolism, immune pathways, and signaling are overrepresented. Finally at 26 dpi, components related to physiology, photosynthesis, and signaling were significantly overrepresented. The size of each data point represents the ratio of genes dysregulated in this category related to the total number of genes in the genome. (b) KEGG analysis shows similar pathways at early infection for specific signaling and innate immune encoding genes. (c) At 17 dpi unique signaling molecules through gene regulation were overrepresented in addition to structural and transport genes. d Finally, similar genes were found at 26 dpi to 17 dpi, with the addition of differential abundance of plant hormone pathways and a general response factor chitinase.

Dysregulation of host pathways associated with viral infection and root symptom development

The three major host pathways resolved from GSEA, KEGG, and top candidates of differential abundance analysis were: (i) regulation of gene expression, (ii) immune signaling and oxidative response to pathogen invasion, and (iii) production of secondary metabolites (Figure 5-6). Substantial overlap of these pathways was previously identified in apical leaf tissue through transcriptomic and proteomic analysis (Roy *et al.* 2023). A fourth pathway of interest was considered based on the recent description of GFLV suppression of RNA silencing (Choi *et al.* 2023). From top gene candidates in root RNA-Seq analysis, immune signaling pathways were highly overrepresented, especially innate immune receptors (positive and negative dysregulation), cAMP phosphoprotein downregulated in both viral contrasts at 17 dpi, and proteinase inhibitors negatively regulated for wildtype GHu while upregulated for mutant GHu $1E^{Pol*/Sd}{}_{G802K}$ when compared against the mock controls (Figure 5-7). Several host-encoded gene silencing transcripts, including suppressor of gene silencing 3, SDE 1 and 2, AGO4, HEN1, and DRBP4, were less abundant in GFLV-infected *N. benthamiana* roots. Other members of the RNA-induced silencing complex such as AGO1 and AGO2 were upregulated, but other transcripts were either too low in number or provided orthologs with conflicting patterns to deduce a trend (Figure 5-7).

a

Contrast:	wildtype GHu vs mock control		mutant GHu vs mock control	
Gene | Time:	4 dpi	17 dpi	4 dpi	17 dpi
glucan synthase-like 4		DOWN		
short-chain dehydrogenase/reductase	DOWN	UP		UP
Leucine-rich repeat family protein			DOWN	
cAMP phosphoprotein		DOWN		DOWN
mitochondrial associated protein	UP/DOWN	DOWN	UP/DOWN	
***Receptors**	UP/DOWN	DOWN		
Proteinase inhibitor	DOWN		UP	

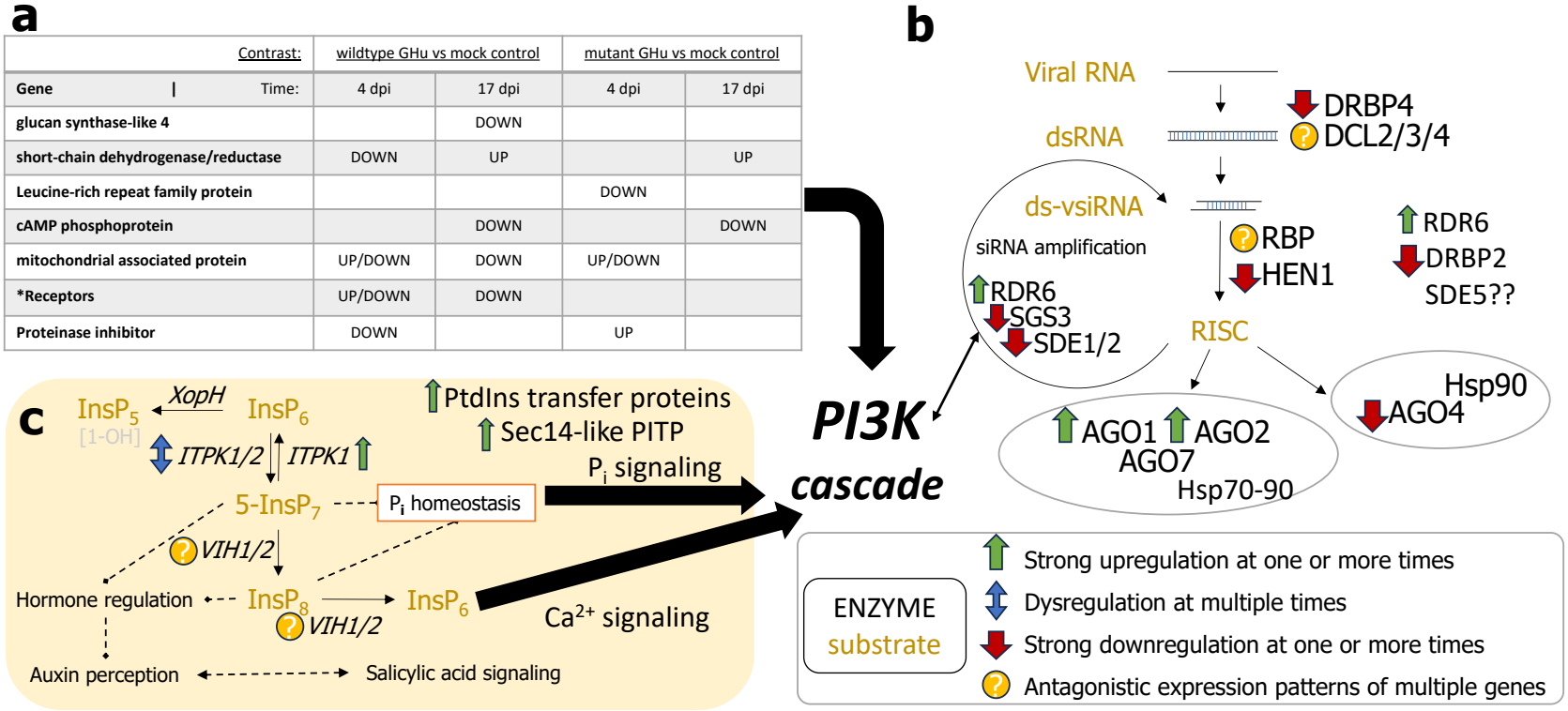

Figure 5-7. The dysregulation of three major pathways in the roots of *Nicotiana benthamiana* infected by grapevine fanleaf virus (GFLV) revealed by ontology and enrichment analysis. (**a**) Immune receptors and innate immune pathways were disrupted at 4- and 17-days post inoculation (dpi) when comparing viral treatments to mock inoculated plants. Further, wildtype GHu infected plants were more dysregulated across multiple types of innate immune pathways that feed into the PI3K cascade. (**b**) The host viral silencing pathway had several genes dysregulated throughout the course of GFLV infection, in that, either both viral treatments dysregulated or wildtype GHu altered expression to a greater extent. (**c**) Inositol biosynthesis was dysregulated in collected root RNA samples throughout the course of infection, in which the downstream effects of inositol metabolites can have profound signaling capabilities in hormone regulation, inorganic phosphate signaling, and calcium signaling that can amplify the PI3K cascade. Ultimately, these three pathways converge on the hallmarks of hypersensitive response during plant-pathogen interactions.

DISCUSSION

In this study, we documented changes in RSA traits in *N. benthamiana* upon GFLV infection (Figures 5-1 and 5-2). The average number of *N. benthamiana* root tips decreased by up to a third and the average root diameter increased over 20% upon infection by wildtype GHu and mutant F13 $1E^{Pol*/Sd}{}_{G802K}$ when compared with roots of mock inoculated plants (Figure 5-1a,b). The RNA1 of these two GFLV strains differ by 17% at the nucleotide sequence level (Vigne et al. 2013); however, the RNA1-encoded protein $1E^{Pol*/Sd}$ of both wildtype GHu and mutant F13 $1E^{Pol*/Sd}{}_{G802K}$ carry a lysine in position 802 (Osterbaan et al. 2019). In contrast, *N. benthamiana* plants infected with wildtype F13 and mutant GHu $1E^{Pol*/Sd}{}_{K802G}$, both carrying a glycine at position 802 of protein $1E^{Pol*/Sd}$ (Osterbaan et al. 2019), displayed RSA traits resembling those of mock control plants. These findings indicate that a single GFLV amino acid is associated with changes in RSA traits rather than other genetic differences of up to 17% between wildtype F13 and GHu. This is the first report of a single amino acid of a secovirus altering RSA traits of a plant host.

Efforts to correlate the vein clearing phenotype in apical leaves upon infection of *N. benthamiana* with wildtype GHu to RSA traits showed that the duration of foliar symptoms was significantly positively correlated with root diameter traits, and significantly negatively correlated with branching patterns, root tip number, and network metrics (Figures 5-3a, 5-S3). Linear models confirmed these correlated above and below ground symptoms (Figure 5-3d-e). The other three strains of GFLV used in this study were asymptomatic in *N. benthamiana* leaves (Vigne et al. 2013; Osterbaan

et al. 2019, Roy *et al.* 2023), preventing any comparison between above and below ground features.

The root phenotype was correlated to ROS produced in the pericycle of the primary roots (Figure 5-4) and the dysregulation of the host transcriptome (Figure 5-5). Abundant ROS production was specific to root systems infected with GFLV strains containing K at residue $1E^{Pol*/Sd}_{802}$ (Figure 5-4) with transcriptomic analysis confirming an active regulation of these transcripts across viral treatments (Figure 5-6). There was a direct correlation between the number of days showing symptoms in apical leaves and the severity of changes in RSA traits for plants infected by wildtype GHu (Figure 5-3), while a correlation of ROS production was shown in the roots infected with wildtype GHu and mutant F13 $1E^{Pol*/Sd}_{G802K}$ (Figure 5-4b). These results suggested a conserved reaction across tissue types that might be required for GFLV systemic infection and perhaps an evolutionarily conserved mechanism that elicits symptoms in *N. benthamiana*. Previous studies found that additional modifications to the amino acids in this region often reduced pathogenicity or virulence, or completely abolished the infectivity of the virus, indicating this protein's critical involvement in the infection process (Osterbaan et al. 2019; Osterbaan et al. 2021).

While several new host gene candidates were identified as most differentially abundant in root tissue of GFLV-infected *N. benthamiana*, general trends remained like those previously identified in apical leaves (Roy et al. 2023). The enrichment term of singlet oxygen-mediated programmed cell death (GO:0010343) was present in all GFLV-infected plants tested in this study. This result further supports the hypothesis that all GFLV strains elicit a certain level of ROS with symptomatic strains being the

most active. Additionally, five genes specified as PROTEIN OF UNKNOWN FUNCTION were among the top differentially abundant transcripts. Many of these candidate genes could benefit from follow up functional validation analysis in knock-out assays, with confirmation of gene classification and identification if resultant functions are specific to root tissue. The continued functional validation of root specific transcripts will aid in systems biology analyses for plant-pathogen interactions and provide genetic improvement resources for plant biologists (de Dorlodot et al. 2007).

Curated transcriptomics data and our updated annotation informed molecular mechanisms of the resultant *N. benthamiana* root phenotypes upon GFLV infection (Figure 5-7). In roots, upregulation of inositol-tetrakisphophate 1/2 kinase and the antagonistic expression patterns of other inositol synthesis genes prevented the full realization of a mechanism, although an imbalance of this signaling molecule could explain similar events occurring for the transient ROS production in root tissue (Figure 5-7). Rather than a 1:1 model, we hypothesize synergistic effects of inositol-mediated signaling, immune receptors, and hormones to contribute to the observed root modifications. Interestingly, the top DEGs return to phosphatidylinositol and extended pathways that relate to the PI3 kinase cascade. This central innate immune response regulator is widely involved in host–pathogen interactions. The top gene according to p-value at 17 dpi when contrasting wildtype GFLV-GHu to mock control is the SEC14P-LIKE PHOSPATIDYLINOSITOL TRANSFER FAMILY PROTEIN, with a Log2FoldChange of 1.98 (Table 5-2). This gene is a key regulator of many downstream biological processes (Huang et al. 2016), further supporting the proposed hypersensitive response during GFLV infection. As with the innate mammalian immune system (Fukao

and Koyasu 2003), the PI3K cascade was identified as a major factor in bacterial plant-pathogen hypersensitive response (Zhang et al. 2020). It is notable that genes related to this pathway were documented in both shoot (Roy et al. 2023) and root tissue (this study), making evident that the combination of signaling pathways are utilized to mount the robust production of ROS (Figure 5-7). Future work could address the benefit of ROS accumulation to the host and the pathogen, and how this cascade might have influenced the evolutionary adaptation of the virus in plant hosts.

It is known that plant viruses proficiently manipulate host gene regulatory pathways (Ramesh et al. 2021). Generally, transcriptional and translational regulators can be activated or repressed, directly or indirectly, by RNA/protein binding plant hormones, metabolites, or proteins in plant root tissue. Some factors described in the literature to great extents include abscisic acid, indole 3-butyric acid, ethylene, gibberellic acid, brassinosteroids, nitrogen, glutamate, nitrous oxide, phosphate, sulfate, temperature, and water availability (López-Bucio et al. 2003, Osmont et al. 2007; Lynch et al. 2012). The manipulation of one or more of these factors can alter the way in which root systems are formed, usually in a dose-dependent manner. The underlying molecular mechanisms behind abiotic factor changes have been identified in many systems from model plants like *Arabidopsis thaliana* (Oláh et al. 2020; Jacobsen et al. 2021) to perennial crop systems like grape, apple, and orange (Lynch et al. 2012). A summary of historically understood models expands upon gene regulation, hormone pathways, and nutrient availability to determine root structure (Osmont et al. 2007). The documentation of modified root morphology upon virus infection overlaps considerably with nutrient deficiencies/toxicities such as phosphorus (Fang et al. 2009), nitrogen (Qin

et al. 2019), calcium (Simon 1978), and others. As our study was performed in controlled conditions, the impacts of nutrient, light, or temperature differences were limited. Thus, root traits could be ascribed to a single amino acid of the GFLV-encoded protein $1E^{Pol*/Sd}$. We further hypothesize that the severity of symptoms occurs in a similar manifestation to dose-dependent concentrations of stressors (i.e., secondary signaling molecules, nutrient availability, plant hormones, etc.), but in this instance to be dependent upon the protein encoding factor(s) of the virus exposed to the host machinery.

GFLV-host interactions documented at the root level by 3'RNA-Seq included multiple overlapping pathways of immune response and hormone regulation. The upregulation of oxidoreductases in roots at 17 dpi indicate lessened ROS levels and a diminished effect on plant response thereafter (Figure 5-6). Tolerance of oxidative stress and respective signaling patterns to auxin mediate large morphological changes in plants (Krishnamurthy and Rathinasabapathi 2013), which might explain the root phenotype in GFLV-infected *N. benthamiana*. Overall, ROS production due to a hypersensitive response (HR) agrees with current understandings of virus-host interactions at the molecular level (Piau and Schmitt-Keichinger 2023). The regulation of HR is not linear and can utilize any combination of RNA silencing, pattern triggered immunity, and effector triggered immunity to elicit such responses (Piau and Schmitt-Keichinger 2023). Overall, HR, ROS burst, hormone manipulation are documented as common denominators in symptomatic viral infections (Jiang and Zhou 2023) but the appearance and disappearance of ROS and symptomology above and below ground depending on a single viral amino acid is unique to GFLV.

Other plant systems have documented changes in RSA upon viral infection. For example, single infections of sweet potato chlorotic stunt virus or multiple infections of sweet potato feathery mottle virus, sweet potato virus 2, sweet potato virus C, and sweet potato virus G decrease lateral root development and adventitious roots of sweet potatoes (*Ipomoea batatas*) (Villordon and Clark 2014). In a similar study, viral co-infections reduced the total marketable yield between 60–95% depending on the level of tolerance or susceptibility of the sweet potato variety (Mulabisana et al. 2019). Additionally, tomato (*Solanum lycopersicum* L.) infected with tomato brown rugose fruit virus differ in multiple RSA traits when compared with uninfected plants with a 15% reduction in root diameter, and a 30% decrease in root tip number at three weeks post inoculation (Vaisman et al. 2022). Cassava brown streak virus (CBSV) causes root necrosis and tuber yield loss (Tomilson et al. 2017). Almost all (99%) of above ground symptomatic cassava plants display necrotic lesions below ground due to the presence of CBSV, while only 16% of asymptomatic infection events above ground also have root necrosis (Hillocks et al. 1996). Cassava mosaic disease is associated with at least ten different viral species and has been shown to have anywhere from minor changes to up to 87% losses in tuber yield in the most aggressive instances (Chikoti and Tembo 2022). While cassava and sweet potato are tuber crops, significant impacts to above ground crop production can be associated with total root health, and thereby increasing the importance on documenting the most resilient and sturdy roots for prolonged cropping systems such as with perennial crops. In the case of BNYVV, three viral amino acids are crucial to determine a resistant or a susceptible phenotype in beets, with amino acid 68 of p25 being of critical stature for host-genotype interactions (Chiba et al. 2008).

Our findings on GFLV strain-specific alterations in *N. benthamiana* RSA have direct implications in transmission biology. The ectoparasitic dagger nematode vector of GFLV, *X. index*, acquires GFLV in a non-circulative, non-propagative manner by feeding on infected plant roots (Raski and Hewitt 1960; Cohn 1970; Wyss 1978). We hypothesize that the phenotype of RSA induced by wildtype GHu and mutant F13 $1E^{Pol*/Sd}_{G802K}$ deter continued feeding of *X. index* on *N. benthamiana* roots. This is because plants with significantly less root tips and increased root diameter are less appetent to *X. index*, which prefers fibrous over mature roots for sustained feeding and reproduction (Cohn 1970). Modified RSA traits of plants infected with wildtype GHu or mutant F13 $1E^{Pol*/Sd}_{G802K}$ could push nematode vectors away from an already infected host and increase the likelihood of feeding on neighboring healthy plants at a faster rate than unperturbed root systems of healthy plants or plants infected with other GFLV strains such as wildtype F13 or mutant GHu $1E^{Pol*/Sd}_{K802G}$. Virus manipulation of plants and vectors to enhance acquisition and/or promote transmission to new plants is well documented for hemipteran-transmitted viruses (Carr et al. 2020). It would be interesting to test how modified *N. benthamiana* RSA traits influence *X. index*-mediated GFLV transmission in controlled assays with different virus strains. Additionally, if modified RSA traits induced by specific GFLV strains are observed in the natural host *Vitis* spp., and *X. index* feeding strategies altered by GFLV-induced changes in root morphology are confirmed, new management strategies of GFLV based on changes in the host rhizosphere could be explored to reduce transmission events.

It is unknown if the GFLV-mediated root phenotype in *N. benthamiana* fully manifests in the natural host, *Vitis* spp. In the instance of BNYVV, the transient

expression of protein p25 induced similar effects in *A. thaliana* as observed for the natural host, sugar beet (Chiba et al. 2008; Peltier et al. 2011). It would be interesting to investigate if distinct GFLV strains, including some that cause severe foliar symptoms in *Vitis* spp., affect RSA traits of infected grapevines over the vineyard's lifespan. Similarly, a correlation analysis of above and below-ground traits in grapevines would be beneficial to better understand the mechanism of disease induced by GFLV. Such work could inform new management strategies for growers experiencing the impacts of fanleaf degeneration.

CONCLUSIONS

We documented for the first time the impact of GFLV on RSA traits of infected *N. benthamiana*. The most notable changes in roots were observed in plants infected with wildtype GHu and mutant F13 $1E^{Pol*/Sd}_{G802K}$, both carrying a lysine at the 802nd position of the putative RNA-dependent RNA polymerase (protein $1E^{Pol*/Sd}$). These two GFLV strains caused a significant reduction in the number of root tips (up to 30%), an increased root average diameter (up to a 20%), and an abundant accumulation of ROS in the pericycle of the primary roots when compared with roots of mock inoculated control plants. The severity of root phenotypic changes was associated with ROS production in the root pericycle. Transcriptomic analysis revealed potential host gene candidates related to viral immune response, RNA silencing, and plant hormone pathways that could contribute to the observed root phenotype. More work is needed to understand any potential downstream impacts of root morphology, particularly on GFLV transmission by the ectoparasitic nematode vector *X. index*. Finally, unknown root transcripts dysregulated due to a single GFLV amino acid should be validated through reverse genetic assays to improve our understanding of how GFLV manipulates root architecture.

REFERENCES

Andika, I. B., Kondo, H., and Sun, L. 2016. Interplays between Soil-Borne Plant Viruses and RNA Silencing-Mediated Antiviral Defense in Roots. Frontiers in Microbiology 7.

Andret-Link, P., Laporte, C., Valat, L., Ritzenthaler, C., Demangeat, G., Vigne, E., Laval, V., Pfeiffer, P., Stussi-Garaud, C., and Fuchs, M. 2004a. Grapevine fanleaf virus: Still a major threat to the grapevine industry. Journal of Plant Pathology 86:183–195.

Andret-Link, P., Schmitt-Keichinger, C., Demangeat, G., Komar, V., and Fuchs, M. 2004b. The specific transmission of Grapevine fanleaf virus by its nematode vector *Xiphinema index* is solely determined by the viral coat protein. Virology 320:12–22. https://doi.org/10.1016/j.virol.2003.11.022.

Andrews, S. 2010. FastQC: a quality control tool for high throughput sequence data. .

Belin, C., Schmitt, C., Demangeat, G., Komar, V., Pinck, L., and Fuchs, M. 2001. Involvement of RNA2-encoded proteins in the specific transmission of *Grapevine fanleaf virus* by its nematode vector *Xiphinema index*. Virology 291:161–171. https://doi.org/10.1006/viro.2001.1216.

Belin, C., Schmitt, C., Gaire, F., Walter, B., Demangeat, G., and Pinck, L. 1999. The nine C-terminal residues of the grapevine fanleaf nepovirus movement protein are critical for systemic virus spread. Journal of General Virology 80:1347–1356. https://doi.org/10.1099/0022-1317-80-6-1347.

Bolger, A. M., Lohse, M., and Usadel, B. 2014. Trimmomatic: a flexible trimmer for Illumina sequence data. Bioinformatics 30:2114–2120. https://doi.org/10.1093/bioinformatics/btu170.

Bombarely, A., Rosli, H. G., Vrebalov, J., Moffett, P., Mueller, L. A., and Martin, G. B. 2012. A draft genome sequence of *Nicotiana benthamiana* to enhance molecular plant-microbe biology research. MPMI 25:1523–1530. https://doi.org/10.1094/MPMI-06-12-0148-TA.

Carr, J. P., Tungadi, T., Donnelly, R., Bravo-Cazar, A., Rhee, S.-J., Watt, L. G., Mutuku, J. M., Wamonje, F. O., Murphy, A. M., Arinaitwe, W., Pate, A. E., Cunniffe, N. J., and Gilligan, C. A. 2020. Modelling and manipulation of aphid-mediated spread of non-persistently transmitted viruses. Virus Research 277:197845. https://doi.org/10.1016/j.virusres.2019.197845.

Chiba, S., Miyanishi, M., Andika, I. B., Kondo, H., and Tamada, T. 2008. Identification of amino acids of the beet necrotic yellow vein virus p25 protein required for induction of the resistance response in leaves of *Beta vulgaris* plants. Journal of General Virology 89:1314–1323. https://doi.org/10.1099/vir.0.83624-0.

Chikoti, P. C., and Tembo, M. 2022. Expansion and impact of cassava brown streak and cassava mosaic diseases in Africa: A review. Frontiers in Sustainable Food Systems 6.

Choi, J., Pakbaz, S., Yepes, L. M., Cieniewicz, E. J., Schmitt-Keichinger, C., Labarile, R., Minutillo, S. A., Heck, M., Hua, J., and Fuchs, M. 2023. Grapevine fanleaf virus RNA1-encoded proteins 1A and $1B^{Hel}$ suppress RNA silencing. Mol Plant Microbe Interact. https://doi.org/10.1094/MPMI-01-23-0008-R.

Cohn, E. 1970. Observations on the Feeding and Symptomatology of Xiphinema and Longidorus on Selected Host Roots. J Nematol 2:167–173.

Dorlodot, S. de, Forster, B., Pagès, L., Price, A., Tuberosa, R., and Draye, X. 2007. Root system architecture: opportunities and constraints for genetic improvement of crops. Trends in Plant Science 12:474–481. https://doi.org/10.1016/j.tplants.2007.08.012.

Etymologia: Bonferroni Correction. 2015. Emerg. Infect. Dis. 21. https://doi.org/10.3201/eid2102.ET2102.

Fang, S., Yan, X., and Liao, H. 2009. 3D reconstruction and dynamic modeling of root architecture in situ and its application to crop phosphorus research. The Plant Journal 60:1096–1108.

Fukao, T., and Koyasu, S. 2003. PI3K and negative regulation of TLR signaling. Trends in Immunology 24:358–363. https://doi.org/10.1016/S1471-4906(03)00139-X.

Gaire, F., Schmitt, C., Stussi-Garaud, C., Pinck, L., and Ritzenthaler, C. 1999. Protein 2A of grapevine fanleaf nepovirus is implicated in RNA2 replication and colocalizes to the replication site. Virology 264:25–36. https://doi.org/10.1006/viro.1999.9927.

GO.db. Bioconductor. http://bioconductor.org/packages/GO.db/ (accessed 5 Jul 2023).

van Griethuysen, P.-A. 2020. Plant–virus–vector interactions: Tobacco rattle virus infection alters root volatile emissions to attract nematode vectors.

Hillocks, R. J., Raya, M., and Thresh, J. M. 1996. The association between root necrosis and above-ground symptoms of brown streak virus infection of cassava in

southern Tanzania. International Journal of Pest Management 42:285–289. https://doi.org/10.1080/09670879609372008.

Huang, J., Ghosh, R., and Bankaitis, V. A. 2016. Sec14-like Phosphatidylinositol Transfer Proteins and the Biological Landscape of Phosphoinositide Signaling in Plants. Biochim Biophys Acta 1861:1352–1364. https://doi.org/10.1016/j.bbalip.2016.03.027.

Huerta-Cepas, J., Szklarczyk, D., Heller, D., Hernández-Plaza, A., Forslund, S. K., Cook, H., Mende, D. R., Letunic, I., Rattei, T., Jensen, L. J., von Mering, C., and Bork, P. 2019. eggNOG 5.0: a hierarchical, functionally and phylogenetically annotated orthology resource based on 5090 organisms and 2502 viruses. Nucleic Acids Research 47:D309–D314. https://doi.org/10.1093/nar/gky1085.

Jacobsen, A. G. R., Jervis, G., Xu, J., Topping, J. F., and Lindsey, K. 2021. Root growth responses to mechanical impedance are regulated by a network of ROS, ethylene and auxin signalling in *Arabidopsis*. New Phytologist 231:225–242. https://doi.org/10.1111/nph.17180.

Jiang, T., and Zhou, T. 2023. Unraveling the Mechanisms of Virus-Induced Symptom Development in Plants. Plants (Basel) 12:2830. https://doi.org/10.3390/plants12152830.

Kim, D., Paggi, J. M., Park, C., Bennett, C., and Salzberg, S. L. 2019. Graph-based genome alignment and genotyping with HISAT2 and HISAT-genotype. Nat Biotechnol 37:907–915. https://doi.org/10.1038/s41587-019-0201-4.

Kolberg, L., Raudvere, U., Kuzmin, I., Vilo, J., and Peterson, H. 2020. gprofiler2 -- an R package for gene list functional enrichment analysis and namespace conversion toolset g:Profiler. F1000Res 9:ELIXIR-709. https://doi.org/10.12688/f1000research.24956.2.

Krishnamurthy, A., and Rathinasabapathi, B. 2013. Oxidative stress tolerance in plants. Plant Signaling & Behavior 8:e25761. https://doi.org/10.4161/psb.25761.

Kruskal, W. H., and Wallis, W. A. 1952. Use of Ranks in One-Criterion Variance Analysis. Journal of the American Statistical Association 47:583–621. https://doi.org/10.1080/01621459.1952.10483441.

Kurotani, K.-I., Hirakawa, H., Shirasawa, K., Tanizawa, Y., Nakamura, Y., Isobe, S., and Notaguchi, M. 2023. Genome Sequence and Analysis of *Nicotiana benthamiana*, the Model Plant for Interactions between Organisms. Plant Cell Physiol 64:248–257. https://doi.org/10.1093/pcp/pcac168.

Liu, D., Shi, L., Han, C., Yu, J., Li, D., and Zhang, Y. 2012. Validation of reference genes for gene expression studies in virus-infected *Nicotiana benthamiana* using quantitative real-time PCR. PLoS One 7:e46451. https://doi.org/10.1371/journal.pone.0046451.

López-Bucio, J., Cruz-Ramírez, A., and Herrera-Estrella, L. 2003. The role of nutrient availability in regulating root architecture. Current Opinion in Plant Biology 6:280–287. https://doi.org/10.1016/S1369-5266(03)00035-9.

Love, M. I., Huber, W., and Anders, S. 2014. Moderated estimation of fold change and dispersion for RNA-seq data with DESeq2. Genome Biol 15:550. https://doi.org/10.1186/s13059-014-0550-8.

Luo, W., and Brouwer, C. 2013. Pathview: an R/Bioconductor package for pathway-based data integration and visualization. Bioinformatics 29:1830–1831. https://doi.org/10.1093/bioinformatics/btt285.

Lynch, J., Marschner, P., and Rengel, Z. 2012. Chapter 13 - Effect of Internal and External Factors on Root Growth and Development. In *Marschner's Mineral Nutrition of Higher Plants (Third Edition)*, ed. Petra Marschner. San Diego: Academic Press, pp. 331–346. https://doi.org/10.1016/B978-0-12-384905-2.00013-3.

Margis, R., Viry, M., Pinck, M., Bardonnet, N., and Pinck, L. 1994. Differential proteolytic activities of precursor and mature forms of the 24K proteinase of Grapevine fanleaf nepovirus. Virology 200:79–86. https://doi.org/10.1006/viro.1994.1165.

Martin, I. R., Vigne, E., Berthold, F., Komar, V., Lemaire, O., Fuchs, M., and Schmitt-Keichinger, C. 2018. The 50 distal amino acids of the $2A^{HP}$ homing protein of *Grapevine fanleaf virus* elicit a hypersensitive reaction on *Nicotiana occidentalis*. Molecular Plant Pathology 19:731–743. https://doi.org/10.1111/mpp.12558.

Martin, I. R., Vigne, E., Velt, A., Hily, J.-M., Garcia, S., Baltenweck, R., Komar, V., Rustenholz, C., Hugueney, P., Lemaire, O., and Schmitt-Keichinger, C. 2021. Severe Stunting Symptoms upon Nepovirus Infection Are Reminiscent of a Chronic Hypersensitive-like Response in a Perennial Woody Fruit Crop. Viruses 13:2138. https://doi.org/10.3390/v13112138.

Mulabisana, M. J., Cloete, M., Laurie, S. M., Mphela, W., Maserumule, M. M., Nhlapo, T. F., Cochrane, N. M., Oelofse, D., and Rey, M. E. C. 2019. Yield evaluation of multiple and co-infections of begomoviruses and potyviruses on sweet potato varieties under field conditions and confirmation of multiple infection by NGS. Crop Protection 119:102–112. https://doi.org/10.1016/j.cropro.2019.01.009.

Oláh, D., Feigl, G., Molnár, Á., Ördög, A., and Kolbert, Z. 2020. Strigolactones Interact With Nitric Oxide in Regulating Root System Architecture of *Arabidopsis thaliana*. Frontiers in Plant Science 11.

Osmont, K. S., Sibout, R., and Hardtke, C. S. 2007. Hidden Branches: Developments in Root System Architecture. Annual Review of Plant Biology 58:93–113. https://doi.org/10.1146/annurev.arplant.58.032806.104006.

Osterbaan, L. J., Choi, J., Kenney, J., Flasco, M., Vigne, E., Schmitt-Keichinger, C., Rebelo, A. R., Heck, M., and Fuchs, M. 2019. The identity of a single residue of the RNA-dependent RNA polymerase of grapevine fanleaf virus modulates vein clearing in *Nicotiana benthamiana*. Molecular Plant-Microbe Interactions 32:790–801. https://doi.org/10.1094/MPMI-12-18-0337-R.

Osterbaan, L. J., Hoyle, V., Curtis, M., DeBlasio, S., Rivera, K. D., Heck, M., and Fuchs, M. 2021. Identification of protein interactions of grapevine fanleaf virus RNA-dependent RNA polymerase during infection of *Nicotiana benthamiana* by affinity purification and tandem mass spectrometry. Journal of General Virology 102. https://doi.org/10.1099/jgv.0.001607.

Osterbaan, L. J., Schmitt-Keichinger, C., Vigne, E., and Fuchs, M. 2018. Optimal systemic grapevine fanleaf virus infection in *Nicotiana benthamiana* following

agroinoculation. Journal of Virological Methods 257:16–21. https://doi.org/10.1016/j.jviromet.2018.04.006.

Pearson, E. S. 1931. The analysis of variance in cases of non-normal variation. Biometrika 114–133.

Peltier, C., Schmidlin, L., Klein, E., Taconnat, L., Prinsen, E., Erhardt, M., Heintz, D., Weyens, G., Lefebvre, M., Renou, J.-P., and Gilmer, D. 2011. Expression of the Beet necrotic yellow vein virus p25 protein induces hormonal changes and a root branching phenotype in *Arabidopsis thaliana*. Transgenic Res 20:443–466. https://doi.org/10.1007/s11248-010-9424-3.

Piau, M., and Schmitt-Keichinger, C. 2023. The Hypersensitive Response to Plant Viruses. Viruses 15:2000. https://doi.org/10.3390/v15102000.

Pinck, M., Reinbolt, J., Loudes, A. M., Le Ret, M., and Pinck, L. 1991. Primary structure and location of the genome-linked protein (VPg) of grapevine fanleaf nepovirus. FEBS Letters 284:117–119. https://doi.org/10.1016/0014-5793(91)80775-X.

Qin, L., Walk, T. C., Han, P., Chen, L., Zhang, S., Li, Y., Hu, X., Xie, L., Yang, Y., and Liu, J. 2019. Adaption of roots to nitrogen deficiency revealed by 3D quantification and proteomic analysis. Plant physiology 179:329–347.

R Core Team, R. 2013. R: A language and environment for statistical computing. .

Ramesh, S. V., Yogindran, S., Gnanasekaran, P., Chakraborty, S., Winter, S., and Pappu, H. R. 2021. Virus and Viroid-Derived Small RNAs as Modulators of Host Gene Expression: Molecular Insights Into Pathogenesis. Frontiers in Microbiology 11.

Raski, D. J., and Hewitt, W. M. B. 1960. Experiments With Xiphinema Index as a Vector of Fanleaf of Grapevines. Nematologica 5:166–170. https://doi.org/10.1163/187529260X00316.

Ritzenthaler, C., Laporte, C., Gaire, F., Dunoyer, P., Schmitt, C., Duval, S., Piéquet, A., Loudes, A.-M., Rohfritsch, O., Stussi-Garaud, C., and Pfeiffer, P. 2002. Grapevine fanleaf virus replication occurs on endoplasmic reticulum-derived membranes. Journal of Virology 76:8808–8819. https://doi.org/10.1128/JVI.76.17.8808-8819.2002.

Roy, B. G., Choi, J., and Fuchs, M. F. 2024. Predictive Modeling of Proteins Encoded by a Plant Virus Sheds a New Light on Their Structure and Inherent Multifunctionality. Biomolecules 14:62. https://doi.org/10.3390/biom14010062.

Roy, B. G., DeBlasio, S., Yang, Y., Thannhauser, T., Heck, M., and Fuchs, M. 2023. Profiling Plant Proteome and Transcriptome Changes during Grapevine Fanleaf Virus Infection. J. Proteome Res. 22:1997–2017. https://doi.org/10.1021/acs.jproteome.3c00069.

Roy, B. G., and Fuchs, M. 2022. Herbaceous plant hosts as supermodels for grapevine viruses: a historical perspective. J Plant Pathol 1–30. https://doi.org/10.1007/s42161-022-01267-z.

Roy, B. G., and Fuchs, M. 2023. Processing and maintenance of Nicotiana benthamiana tissue for phenotypic, histological, and ribonucleic acid analysis *v1*. https://protocols.cloud/view/processing-and-maintenance-of-nicotiana-benthamian-cvssw6ee (accessed 28 Aug 2023).

Schellenberger, P., Andret-Link, P., Schmitt-Keichinger, C., Bergdoll, M., Marmonier, A., Vigne, E., Lemaire, O., Fuchs, M., Demangeat, G., and Ritzenthaler, C. 2010. A stretch of 11 amino acids in the βB- βC loop of the coat protein of *Grapevine fanleaf virus* is essential for transmission by the nematode *Xiphinema index*. Journal of Virology 84:7924–7933. https://doi.org/10.1128/JVI.00757-10.

Seethepalli, A., and York, L. M. 2020. RhizoVision Explorer - Interactive software for generalized root image analysis designed for everyone. . https://doi.org/10.5281/ZENODO.4095629.

Serghini, M., Fuchs, M., Pinck, M., Reinbolt, J., Walter, B., and Pinck, L. 1990. RNA2 of grapevine fanleaf virus: sequence analysis and coat protein cistron location. Journal of General Virology 71:1433–1441.

Shipley, G. L. 2006. Real-Time Quantitative PCR: Theory and Practice. In *Reviews in Cell Biology and Molecular Medicine*, John Wiley & Sons, Ltd. https://doi.org/10.1002/3527600906.mcb.200500012.

Simon, E. W. 1978. The Symptoms of Calcium Deficiency in Plants. New Phytologist 80:1–15. https://doi.org/10.1111/j.1469-8137.1978.tb02259.x.

Tamada, T., Uchino, H., Kusume, T., and Saito, M. 1999. RNA 3 Deletion Mutants of Beet Necrotic Yellow Vein Virus Do Not Cause Rhizomania Disease in Sugar Beets. Phytopathology 89:1000–1006. https://doi.org/10.1094/PHYTO.1999.89.11.1000.

Team, Rs. 2015. RStudio: integrated development for R. (No Title).

Tomlinson, K. R., Bailey, A. M., Alicai, T., Seal, S., and Foster, G. D. 2017. Cassava brown streak disease: historical timeline, current knowledge and future prospects. Mol Plant Pathol 19:1282–1294. https://doi.org/10.1111/mpp.12613.

Vaisman, M., Hak, H., Arazi, T., and Spiegelman, Z. 2022. The Impact of Tobamovirus Infection on Root Development Involves Induction of *Auxin Response Factor 10a* in Tomato. Plant and Cell Physiology 63:1980–1993. https://doi.org/10.1093/pcp/pcab179.

Vanacker, H., Carver, T. L. W., and Foyer, C. H. 2000. Early H2O2 Accumulation in Mesophyll Cells Leads to Induction of Glutathione during the Hyper-Sensitive Response in the Barley-Powdery Mildew Interaction. Plant Physiol 123:1289–1300.

Vigne, E., Gottula, J. W., Schmitt-Keichinger, C., Komar, V., Ackerer, L., Belval, L., Rakotomalala, L., Lemaire, O., Ritzenthaler, C., and Fuchs, M. 2013. A strain-specific segment of the RNA-dependent RNA polymerase of grapevine fanleaf virus determines symptoms in *Nicotiana* species. Journal of General Virology 94:2803–2813. https://doi.org/10.1099/vir.0.057646-0.

Villordon, A. Q., and Clark, C. A. 2014. Variation in Virus Symptom Development and Root Architecture Attributes at the Onset of Storage Root Initiation in 'Beauregard' Sweetpotato Plants Grown with or without Nitrogen. PLoS One 9:e107384. https://doi.org/10.1371/journal.pone.0107384.

Wei, T., Simko, V., Levy, M., Xie, Y., Jin, Y., Zemla, J., Freidank, M., Cai, J., and Protivinsky, T. 2021. corrplot: Visualization of a Correlation Matrix. .

Wickham, H. 2009. *ggplot2: Elegant Graphics for Data Analysis*. New York, NY: Springer. https://doi.org/10.1007/978-0-387-98141-3.

Wickham, H., François, R., Henry, L., and Müller, K. 2018. dplyr: A Grammar of Data Manipulation. R package version 0.7. 6. Computer software]. https://CRAN. R-project. org/package= dplyr.

Williams, C., and Crawford, G. 1980. *Analysis of subjective judgment matrices.* RAND CORP SANTA MONICA CA.

Wu, T., Hu, E., Xu, S., Chen, M., Guo, P., Dai, Z., Feng, T., Zhou, L., Tang, W., Zhan, L., Fu, X., Liu, S., Bo, X., and Yu, G. 2021. clusterProfiler 4.0: A universal enrichment tool for interpreting omics data. The Innovation 2:100141. https://doi.org/10.1016/j.xinn.2021.100141.

Wyss, U. 1978. Root and cell response to feeding by *Xiphinema index*. Nematologica 24:159–166.

Yu, G. 2021. Enrichplot: visualization of functional enrichment result. R package version 1.

Zhang, H., Liu, X., Zhang, X., Qin, N., Xu, K., Yin, W., Zheng, Y., Song, Y., Zeng, R., and Liu, J. 2020. Phosphoinositide 3-Kinase Promotes Oxidative Burst, Stomatal Closure and Plant Immunity in Bacterial Invasion. Frontiers in Plant Science 10.

Table 5-S1. Grapevine fanleaf virus (GFLV) RNA1 sequence analyses of DNA amplicons obtained from root tissue of *Nicotiana benthamiana* by RT-qPCR. Sequences were aligned with UGENE (v45.1) and consensus sequences were aligned to sequences of wildtype GFLV strains F13 and GHu. DPI = days post inoculation. Average alignment was 98.6% identity at the nucleotide level to sequences available in NCBI.

GFLV inoculum	DPI	Primer	Reference	E-value	% Identity	Nt	802 ID[a]
mutant F13 $1E^{Pol}_{G802K}$	17	FWD	NC_003615.1 (F13 RNA1)	4.00E-99	98.98	395	K
mutant F13 $1E^{Pol}_{G802K}$	17	REV		3.00E-100	99.49	414	K
wildtype F13	17	FWD		2.00E-97	98.48	396	G
wildtype F13	17	REV		8.00E-101	99.49	410	G
mutant GHu $1E^{Pol}_{K802G}$	17	FWD	JN391442.1 (GHu RNA1)	1.00E-94	97.96	205	G
mutant GHu $1E^{Pol}_{K802G}$	17	REV		1.00E-94	97.96	203	G
wildtype GHu	17	FWD		2.00E-97	98.01	202	K
wildtype GHu	17	REV		5.00E-98	98.97	204	K
mutant F13 $1E^{Pol}_{G802K}$	26	FWD	NC_003615.1 (F13 RNA1)	1.00E-99	98.51	474	K
mutant F13 $1E^{Pol}_{G802K}$	26	REV		1.00E-99	99.49	339	K
wildtype F13	26	FWD		2.00E-97	98.48	394	G
wildtype F13	26	REV		2.00E-96	98.47	347	G
mutant GHu $1E^{Pol}_{K802G}$	26	FWD	JN391442.1 (GHu RNA1)	6.00E-97	97.54	204	G
mutant GHu $1E^{Pol}_{K802G}$	26	REV		3.00E-100	99.49	203	G
wildtype GHu	26	FWD		8.00E-96	97.07	205	K
wildtype GHu	26	REV		5.00E-98	98.97	211	K

[a]Identity of amino acid residue 802 of the $1E^{Pol}$ protein confirmed via Sanger sequencing of RT-PCR amplicon (Osterbaan et al. 2019).

Table 5-S2. Primer sets used in RT-qPCR for grapevine fanleaf virus RNA1 using *Nicotiana benthamiana* FBOX as a reference gene.

Primer Name	Assay	Target	Sequence (5'-3')	Reference
Nb-FBOX-F	RT-qPCR	*N. benthamiana* FBOX gene	ggcactcacaaacgtctatttc	Liu et al. 2012
Nb-FBOX-R			acctgggaggcatcctgcttat	
GFLV-RNA1-F		GFLV RNA1 sequence across coding regions of proteins $1D^{Pro}$-$1E^{Pol}$	cccaaaagtcatcgcaatgct	Osterbaan et al. 2019
GFLV-RNA1-R			ggatcaggatatggaaagcac	
GFLV-F13-1-F	RT-PCR	Sequence determinant region of GFLV RNA1	tgttgggaccaaatcagaggaatg	
GFLV-F13-1-R			gaaactgggttatttaaacttggt	
GFLV-GHu-1-F			tgctaggaccaaatcagaggaacg	
GFLV-GHu-1-R			aaacttggttatcccagtacca	

Table 5-S3. Root system architecture traits of *Nicotiana benthamiana* plants infected with four grapevine fanleaf virus strains (i.e., wildtypes GHu and F13, and mutants $1E^{Pol*/Sd}_{K802G}$ and F13 $1E^{Pol*/Sd}_{G802K}$) **at three time points following mechanical inoculation of leaves, i.e., 4-, 17-, and 26-days post-inoculation, as extracted from Rhizovision Explorer**. Statistical comparison of means to mock control plants with significance thresholds of p-value < 0.05 (*); < 0.01 (**), < 0.001 (***), and <0.0001 (****) with Holm's method adjustment. Plants at 4- and 17-dpi were compared through pairwise t-test for parametric data while plants at 26 dpi were compared through Dunn's test for non-parametric data.

Table 5-S3. (continued)

days post inoculation	treatment	n	number of root tips	number of branch points	total root length (mm)	branching frequency	network area (mm^2)	average diameter (mm)	median diameter (mm)	perimeter (mm)	volume (mm^3)	surface area (mm^2)
4 dpi	mock control	15	83	135	222.2	0.573	103.8	0.656	0.426	332.3	154.8	467.3
	wildtype F13	15	63	70***	147.2*	0.461**	84.7	0.786**	0.467	228.9	140.5	370.0
	mutant F13 $1E^{Pol*/Sd}_{G802K}$	15	77	88*	201.4	0.415***	116.7	0.806***	0.486	318.8	214.7	513.6
	wildtype GHu	15	73	94	202.9	0.436***	119.2	0.822***	0.526*	312.1	208.3	523.6
	mutant GHu $1E^{Pol*/Sd}_{K802G}$	15	73	90*	207.5	0.419***	118.3	0.809***	0.501	325.8	206.3	519.8
17 dpi	mock control	14	164	754	1366.3	0.550	545.5	0.637	0.405	2099.0	922.8	2653.9
	wildtype F13	15	147	597	1216.9	0.486**	556.9	0.720	0.466*	1862.8	1000.6	2698.6
	mutant F13 $1E^{Pol*/Sd}_{G802K}$	15	110****	488***	1009.1**	0.478**	477.2	0.773***	0.494****	1505.2**	997.3	2389.6
	wildtype GHu	15	111****	460****	918.1***	0.494**	434.5*	0.777***	0.507****	1369.2****	881.7	2169.6
	mutant GHu $1E^{Pol*/Sd}_{K802G}$	15	155	712	1287.5	0.541	554.7	0.702	0.447	1918.3	1060.4	2776.7
17 dpi	mock control	14	188	460	936.8	0.482	526.0	0.893	0.584	1297.4	1354.7	2652.5
	wildtype F13	22	165	391	803.4	0.477	476.4	0.963	0.639	1076.2	1221.3	2432.0
	mutant F13 $1E^{Pol*/Sd}_{G802K}$	22	163	402	815.0	0.486	444.4	0.874	0.570	1127.4	1038.2	2230.0
	wildtype GHu	23	132**	351*	738.7*	0.460	414.9*	0.911	0.606	1016.4	942.2	2076.0
	mutant GHu $1E^{Pol*/Sd}_{K802G}$	19	163	368	779.5	0.462	463.3	0.974	0.643	1063.7	1126.7	2334.3
26 dpi	mock control	26	257	550	1072.9	0.506	588.2	0.839	0.601	1501.4	1093.3	2804.2
	wildtype F13	14	266	559	1073.2	0.518	576.3	0.828	0.572	1497.6	1116.0	2795.2
	mutant F13 $1E^{Pol*/Sd}_{G802K}$	18	271	548	1066.7	0.511	631.3	0.942***	0.644	1443.3	1418.1*	3130.5
	wildtype GHu	15	193*	416*	819.5**	0.500	461.4**	0.884	0.642	1143.6	831.6	2184.2**
	mutant GHu $1E^{Pol*/Sd}_{K802G}$	7	295	578	1135.2	0.506	617.0	0.837	0.580	1584.9	1236.9	3019.7

Table 5-S4. Relative percentage change of root system architecture traits of *Nicotiana benthamiana* plants infected with four distinct grapevine fanleaf virus strains (i.e., wildtypes GHu and F13, and mutants GHu $1E^{Pol*/Sd}_{K802G}$ and F13 $1E^{Pol*/Sd}_{G802K}$) **compared with mock control at three time points** (i.e., 4, 17 and 26 days post-inoculation) **following mechanical inoculation of leaves**. Statistical comparison of means to mock control plants with significance thresholds of p-value < 0.05 (*); < 0.01 (**), < 0.001 (***), and <0.0001 (****) with Holm's method adjustment. Plants at 4- and 17-dpi were compared through pairwise t-test for parametric data while plants at 26 dpi were compared through Dunn's test for non-parametric data.

Table 5-S4. (continued)

days post inoculation	treatment	n	number of root tips	number of branch points	total root length (mm)	branching frequency	network area (mm^2)	average diameter (mm)	median diameter (mm)	perimeter (mm)	volume (mm^3)	surface area (mm^2)
4 dpi	mock control	15	0%	0%	0%	0%	0%	0%	0%	0%	0%	0%
	wildtype F13	15	-23%	-48%***	-34%*	-20%**	-18%	20%**	10%	-31%	-9%	-21%
	mutant F13 $1E^{Pol*/Sd}_{G802K}$	15	-7%	-35%*	-9%	-28%***	12%	23%***	14%	-4%	39%	10%
	wildtype GHu	15	-12%	-30%	-9%	-24%***	15%	25%***	*23%	-6%	35%	12%
	mutant GHu $1E^{Pol*/Sd}_{K802G}$	15	-12%	-33%*	-7%	-27%***	14%	23%***	18%	-2%	33%	11%
17 dpi	mock control	14	0%	0%	0%	0%	0%	0%	0%	0%	0%	0%
	wildtype F13	15	-11%	-21%	-11%	-12%**	2%	13%	15%*	-11%	8%	2%
	mutant F13 $1E^{Pol*/Sd}_{G802K}$	15	-33%****	-35%***	-26%**	-13%***	-13%	21%***	22%****	-28%**	8%	-10%
	wildtype GHu	15	-32%****	-39%****	-33%***	-10%**	-20%*	22%***	25%****	-35%****	-4%	-18%
	mutant GHu $1E^{Pol*/Sd}_{K802G}$	15	-5%	-6%	-6%	-2%	2%	10%	10%	-9%	15%	5%
17 dpi	mock control	14	0%	0%	0%	0%	0%	0%	0%	0%	0%	0%
	wildtype F13	22	-12%	-15%	-14%	-1%	-9%	8%	9%	-17%	-10%	-8%
	mutant F13 $1E^{Pol*/Sd}_{G802K}$	22	-13%	-13%	-13%	1%	-16%	-2%	-2%	-13%	-23%	-16%
	wildtype GHu	23	-30%**	-24%*	-21%*	-5%	-21%*	2%	4%	-22%	-30%	-22%
	mutant GHu $1E^{Pol*/Sd}_{K802G}$	19	-13%	-20%	-17%	-4%	-12%	9%	10%	-18%	-17%	-12%
26 dpi	mock control	26	0%	0%	0%	0%	0%	0%	0%	0%	0%	0%
	wildtype F13	14	3%	2%	0%	2%	-2%	-1%	-5%	0%	2%	0%
	mutant F13 $1E^{Pol*/Sd}_{G802K}$	18	5%	0%	-1%	1%	7%	12%***	7%	-4%	30%*	12%
	wildtype GHu	15	-25%*	-24%*	-24%**	-1%	-22%**	6%	7%	-24%	-24%	-22%**
	mutant GHu $1E^{Pol*/Sd}_{K802G}$	7	15%	5%	6%	0%	5%	0%	-3%	6%	13%	8%

Table 5-S5. Root system architecture (RSA) metrics of *Nicotiana benthamiana* at 4-, 17-, and 26 days post inoculation (dpi) with grapevine fanleaf virus (GFLV), organized by viral treatment group. Differences were observed largely between asymptomatic plants (mock control, wildtype GFLV-F13 and mutant GFLV-GHu $1E^{Pol}_{K802G}$) and symptomatic plants (wildtype GFLV-GHu and mutant GFLV-F13 $1E^{Pol}_{G802K}$), where symptomatic plants had significantly less root tips, a larger root diameter, and decreased root branching points. Other metric averages include branching frequency, network area, median diameter, perimeter, root volume, and surface area. These data are also present on GitHub repository for ease of analysis with R Markdown files. **(.xlsx)**

Sheet 1. Summary of metrics from Rhizovision analysis.

Sheet 2. Metrics of data from Rhizovision and metadata measurements for plants inoculated with GFLV at 4 dpi.

Sheet 3. Metrics of data from Rhizovision and metadata measurements for plants inoculated with GFLV at 17 dpi.

Sheet 4. Metrics of data from Rhizovision and metadata measurements for plants inoculated with GFLV at 17 dpi, replicate 2.

Sheet 5. Metrics of data from Rhizovision and metadata measurements for plants inoculated with GFLV at 26 dpi.

This table is provided online at the following link:

https://static-content.springer.com/esm/art%3A10.1186%2Fs12866-024-03399-x/MediaObjects/12866_2024_3399_MOESM2_ESM.xlsx

---

Table 5-S6. Symptomology observations of *Nicotiana benthamiana* plants from infection of grapevine fanleaf virus (GFLV) strain wildtype GHu. Symptomology recordings represent three replicated experiments with confirmed infection status through DAS-ELISA, and strain specific infection status through RT-PCR amplicon sequencing for a subset of individuals. All experiments have at least three individuals sequenced and all individuals displaying symptoms of vein clearing were true to infection status. **(.xlsx)**

3A. Summary of grapevine fanleaf virus infected plants according to when they were first symptomatic, last symptomatic, and total days symptomatic.

3B. Binary rating (0=asymptomatic, 1=symptomatic) of three replicated experiments for vein-clearing symptoms of GFLV wildtype GHu infected plants from 0 to 17 days post inoculation.

This table is provided online at the following link:

https://static-content.springer.com/esm/art%3A10.1186%2Fs12866-024-03399-x/MediaObjects/12866_2024_3399_MOESM3_ESM.xlsx

---

Table 5-S7. Metrics corresponding to 3'RNA-Seq data acquisition, trimming (Trimmomatic), alignment/gene encoding product (HiSat2, FeatureCounts), and quality (FastQC) per sample. Alignment was performed against two *Nicotiana benthamiana* genomes at HiSat2, but only Niben101 (Bombarely et al. 2012) was utilized for performance. Viral counts were acquired through the "Nepo" curated database as performed previously (Osterbaan et al. 2021; Roy et al. 2023).

Treatment	DPI	Sample	Total raw reads	Trimmomatic	HISAT2 Alignment		
					Nbe_v1	Niben101	Nepo
mock control	4	04c1	6217836	6173503	78.06	81.97	0.03
mock control	4	04c2	8011427	7952623	79.62	83.88	0
mock control	4	04c3	6701481	6622577	78.26	82.52	0
mutant GHu $1E_{K802G}$	4	04gm1	6656499	6602426	73.17	77.63	0.03
mutant GHu $1E_{K802G}$	4	04gm2	7131063	7081983	78.99	82.64	0
mutant GHu $1E_{K802G}$	4	04gm3	8141591	8045949	77.09	82.34	0.02
wildtype GHu	4	04g1	7709192	7627005	79.05	83.75	0
wildtype GHu	4	04g2	6867052	6798673	72.98	77.98	0
wildtype GHu	4	04g3	6054255	5997005	68.78	74.32	0
mock control	17	17c1	8103805	8013077	75.92	80.71	0
mock control	17	17c2	7991139	7928576	71.98	76.54	0
mock control	17	17c3	6416814	6361303	74.24	79.3	0
mutant GHu $1E_{K802G}$	17	17gm1	7694521	7634873	64.28	68.47	13.64
mutant GHu $1E_{K802G}$	17	17gm2	8534701	8462990	71.47	75.57	8.31
mutant GHu $1E_{K802G}$	17	17gm3	8855058	8728814	*6.44*	*9.21*	*0.57*
wildtype GHu	17	17g1	15074782	14947611	68.89	72.61	10.27
wildtype GHu	17	17g2	7160207	7099684	68.08	71.56	10.06
wildtype GHu	17	17g3	5786029	5737186	72.13	75.85	2.92
mock control	26	26c1	6154012	6099810	65.37	73.07	0
mock control	26	26c2	6667623	6615207	67.95	74.61	0
mock control	26	26c3	5960107	5909375	65.14	71.77	0
mutant GHu $1E_{K802G}$	26	26gm1	6095382	6042797	69.76	75.84	0.19
mutant GHu $1E_{K802G}$	26	26gm2	6073605	6006985	54.95	61.72	0.28
mutant GHu $1E_{K802G}$	26	26gm3	6773979	6680729	62.65	71.63	0.03
wildtype GHu	26	26g1	7200438	7143528	51.9	58.4	16.54
wildtype GHu	26	26g2	7552687	7498423	57.86	62.9	14.47
wildtype GHu	26	26g3	6562379	6516407	57.05	62.97	13.9
	Average:		**7338802**	**7271448**	**67.11**	**72.21**	
	Average after removal of outliers:				**69.45**	**74.64**	

Table 5-S8. All differentially abundant genes across all contrasts generated in DESeq2 analysis. (.xlsx)

This table is provided online at the following link:

https://static-content.springer.com/esm/art%3A10.1186%2Fs12866-024-03399-x/MediaObjects/12866_2024_3399_MOESM5_ESM.xlsx

---

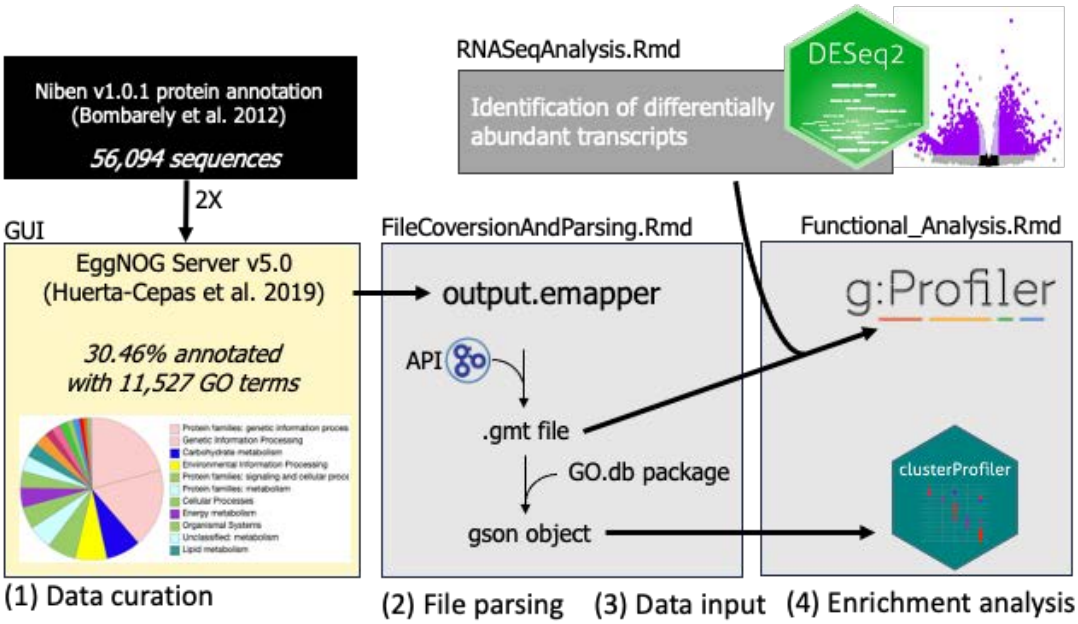

Figure 5-S1. Reannotation of the *Nicotiana benthamiana* genome from data curation to enrichment analysis at the terminal end of transcriptomic analysis. Over 50,000 protein encoding sequences were subject to the EggNOG server (Huerta-Cepas et al. 2019) where 30.46% of the sequences were annotated with 11,527 GO terms used once or more. (2) The output was cross-referenced to the GO API server in which a .gmt file was created for all genes annotated as protein. Further, the .gmt file was parsed to include term2name and gsid2gene as required for the creation of a gson object by the use of the GO.db package. (3) RNA-Seq differential abundance analysis was performed with DESeq2 and the resulting output of gene lists were used for (4) enrichment analysis. The curated .gmt file and gson object were used as input for use in gProfiler2 and clusterProfiler, respectively. All code utilized in steps 2, 3, and 4 are found in as R markdown files in the supplementary information.

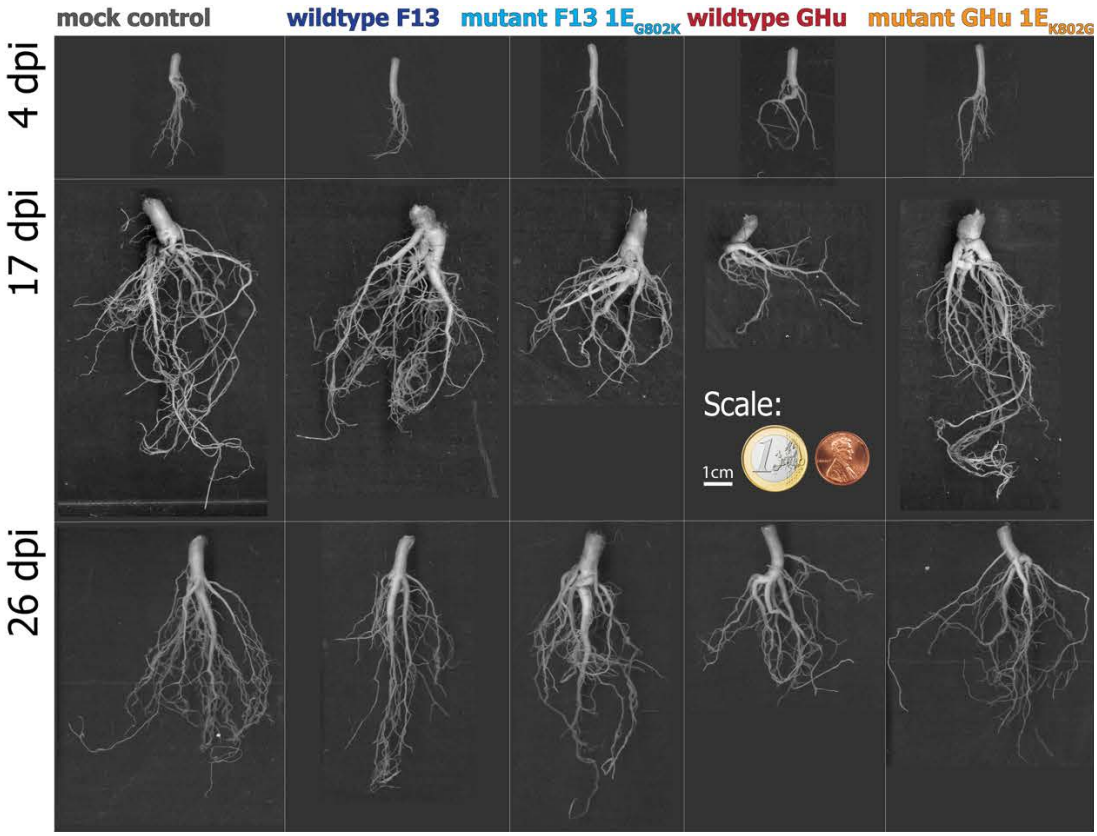

Figure 5-S2. Representative root phenotypes of *Nicotiana benthamiana* upon differential grapevine fanleaf virus strain (wildtype GFLV-F13 and wildtype GFLV-GHu) **and mutant** (GFLV-F13 $1E^{Pol}_{G802K}$ and GFLV-GHu $1E^{Pol}_{K802G}$) **infections at four-, 17-, and 26 days post inoculation (dpi).** All roots are scaled to 1 cm through pixels per square inch and using ImageJ, with reference coins for visualization purposes.

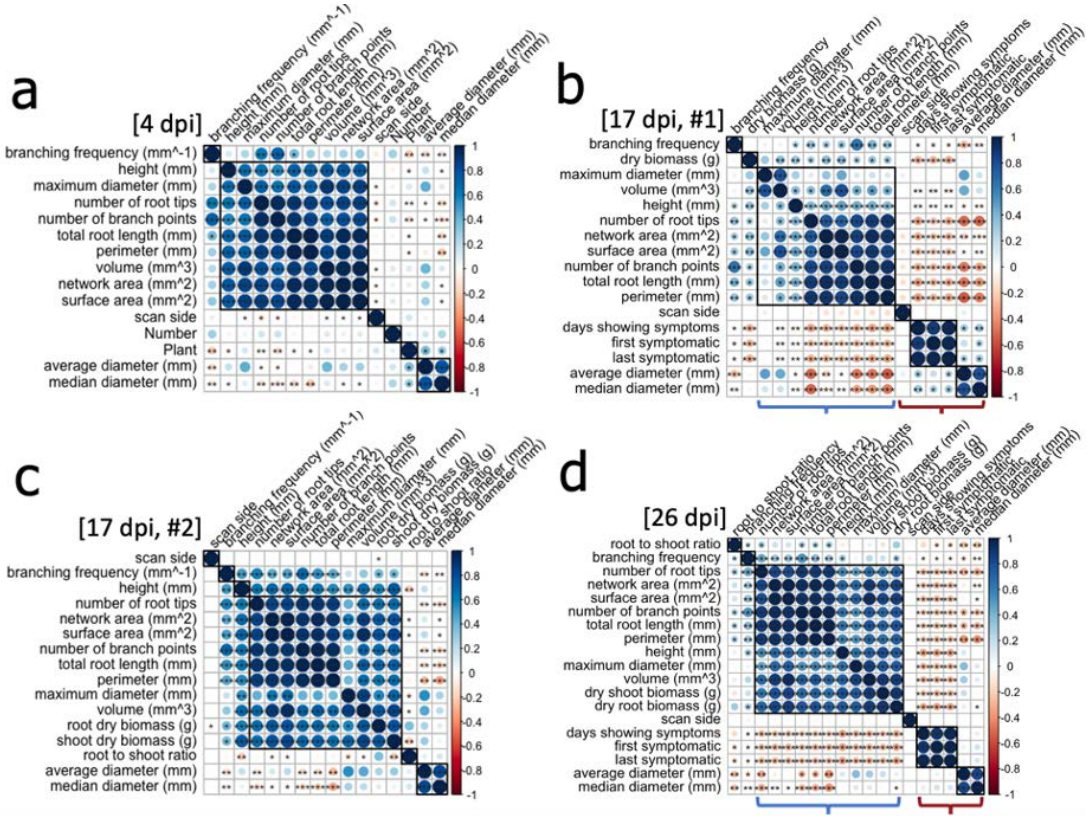

Figure 5-S3. Correlation matrices of acquired root phenotypic data for *Nicotiana benthamiana* infected with grapevine fanleaf virus (GFLV) (a) Correlation of root system and total plant metrics at 4 days post inoculation (dpi), **(b)** 17 dpi, **(c)** 17 dpi replicate 2, and **(d)** 26 dpi. Positively and negatively correlated metrics are denoted in blue and red, respectively, with color opaqueness and size increasing with larger absolute correlation. Significant correlation of traits is denoted by p-value as asterisks with increasing intensity (* $P < 0.05$, ** $P < 0.01$, *** $P < 0.001$). Hierarchal clustering method was employed through corrplot in RStudio, with square groupings assigned through clustering (rect = 6). Two 'phene' groups were assigned based on large, significant positive or negative correlation with each other as phene 1 (blue bracket) and phene 2 (red bracket). These phene group traits were consistently observed as highly correlated upon GFLV infection in *Nicotiana benthamiana* for all time points.

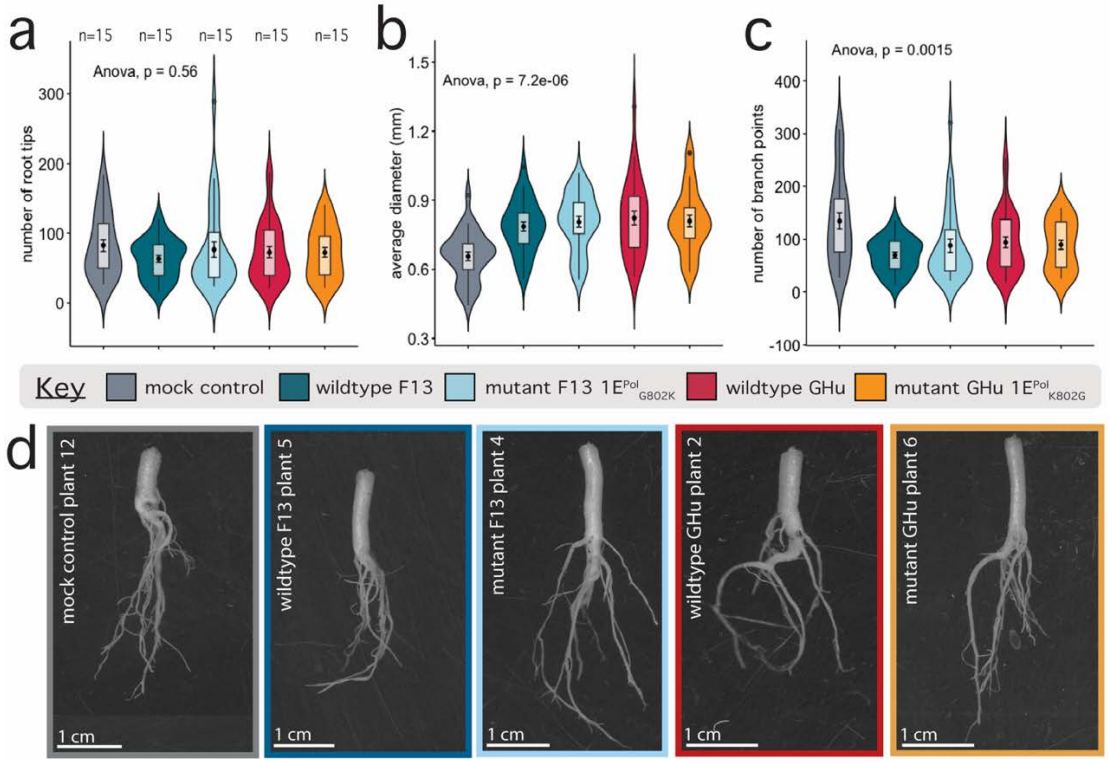

Figure 5-S4. Root system architecture traits for *Nicotiana benthamiana* infected with four strains of grapevine fanleaf virus at 4 days post inoculation (dpi). (a) Number of root tips per plant, **(b)** average diameter in millimeters, and **(c)** number of branch points plotted per viral treatment group. Distribution of each continuous value is plotted along the y-axis as a violin plot with boxplot within, showing additional mean with standard error (central point with error bars). Pairwise Wilcox test results are displayed as significance values ($P < 0.05$=*, $P < 0.01$=**, $P < 0.001$=***, $P < 0.0001$=****). Number of samples per treatment are displayed once above panel (a). **(d)** Representative images of mean phenotype observed between treatments, border color is indicative of treatment as in plots A, B, and C. White bar displayed in bottom left corner of each image is 1.0 centimeters, calculated in ImageJ software (v1.8.0.172).

Figure 5-S5. Additional traits of *Nicotiana benthamiana* infected with grapevine fanleaf virus (GFLV) strains at various days post inoculation (dpi). Height of plant from soil-barrier line in millimeters at (a) 4 dpi, (b) 17 dpi, (c) 17 dpi, and (d) 26 dpi show more statistically validated dissimilarities later in infection. Biomass tissue in grams at (e) 4 dpi with no data, (f) 17 dpi for total dry biomass, and dry root biomass for (g) 17 dpi (h) 26 dpi show significant differences for several treatments. The network area of root system in square millimeters at (i) 4 dpi, (j) 17 dpi, (k) 17 dpi, and (l) 26 dpi show minor separation by treatment. The perimeter of root system in millimeters at (m) 4 dpi, (n) 17 dpi, (o) 17 dpi, and (p) 26 dpi show transient significant differences. The calculated surface area in square millimeters at (q) 4 dpi, (r) 17 dpi, (s) 17 dpi, and (t) 26 dpi show separation of wildtype GHu starting at 17 dpi. The projected volume of root system in cubed millimeters per viral treatment group at (u) 4 dpi, (v) 17 dpi, (w) 17 dpi, and (x) 26 dpi show again sustained differences for wildtype GHu according to Tukey tests. No significant differences were observed for root to shoot ratio at 17 dpi (y) or 26 dpi (z). Distribution of each continuous value is plotted along the y-axis as a box plot. Tukey's honest significant difference test was performed across all treatments to assign Tukey letters and display above each treatment.

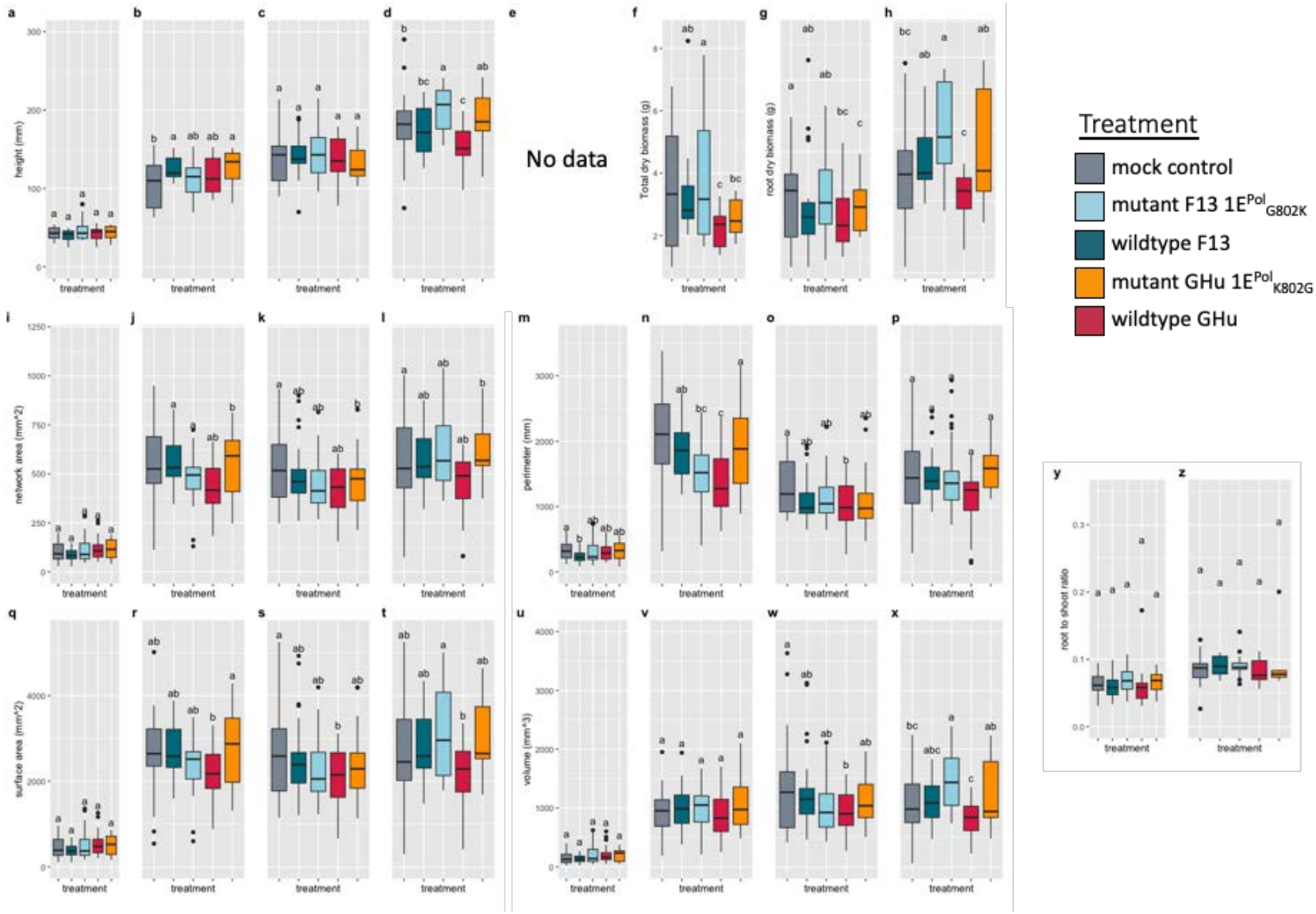
No data
Treatment
mock control
mutant F13 1E^Pol G802K
wildtype F13
mutant GHu 1E^Pol K802G
wildtype GHu
height (mm)
Total dry biomass (g)
root dry biomass (g)
network area (mm^2)
perimeter (mm)
surface area (mm^2)
volume (mm^3)
root to shoot ratio
treatment

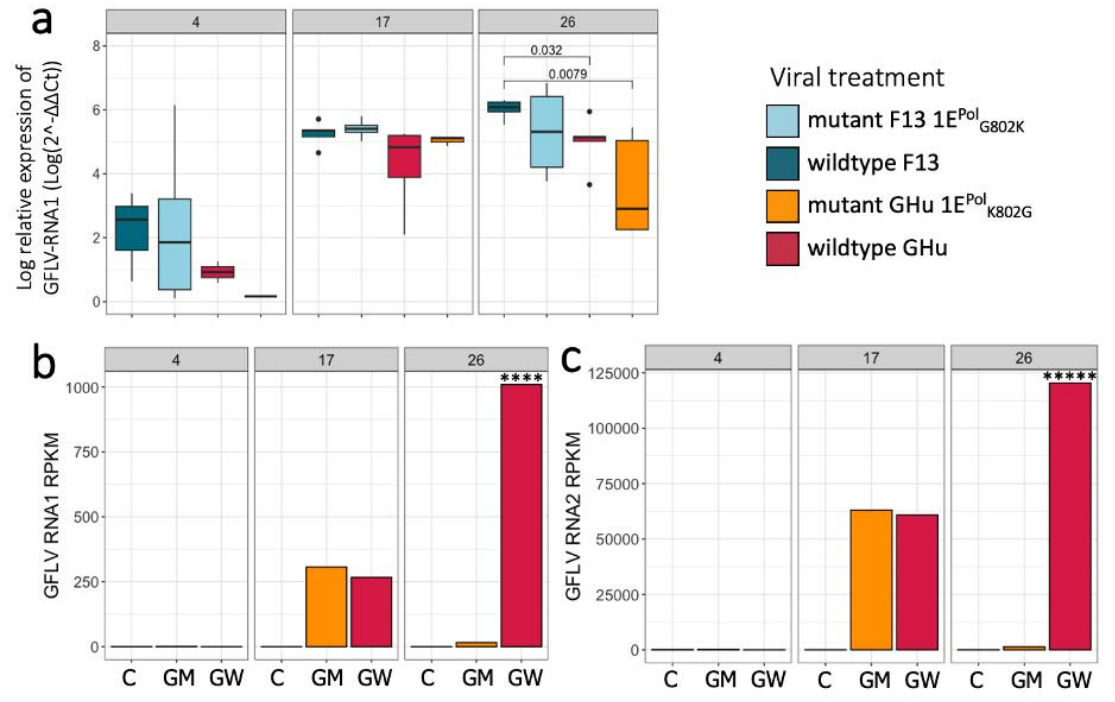

Figure 5-S6. Quantitative real-time polymerase chain reaction- and 3'RNA-sequencing-based detection of grapevine fanleaf virus (GFLV) from *Nicotiana benthamiana* root tissue samples reveal differences in viral titer by strain late in infection. (a) Treatment-wise comparison at 4-, 17-, and 26 days post inoculation (dpi) show treatments do not vary in viral RNA1 titer by Wilcoxon geometric comparison of means except for wildtype GFLV-F13 strain ($P \leq 0.032$) at 26 dpi when compared to either GFLV-GHu strain. **(b)** Normalized GFLV RNA1 reads per kilobase million (RPKM) extracted from RNA-Seq data reveal significantly more abundant reads of wildtype GFLV-GHu when compared to mutant GFLV-GHu $1E^{Pol}{}_{K802G}$ at 26 dpi (Tukey's HSD, $p = 0.00014$), and **(c)** an increased retrieval amount of GFLV-RNA2 reveal a similar comparison at 26 dpi (Tukey's HSD, $p = 0.0000008$).

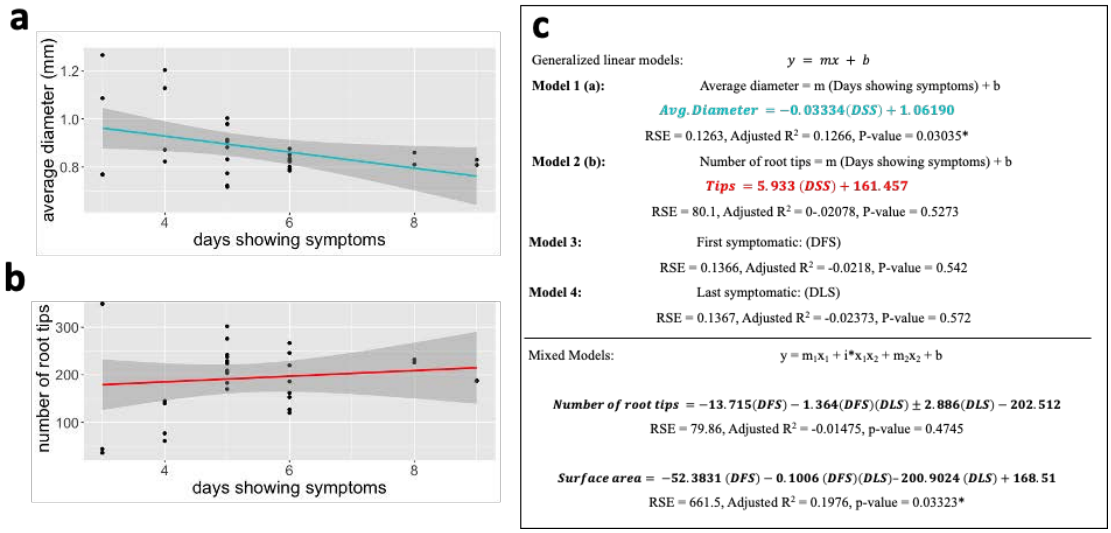

Figure 5-S7. Linear model generation for *Nicotiana benthamiana* infected with wildtype grapevine fanleaf virus strain GHu at 26 days post inoculation (dpi) returns mostly insignificant predictions of above and below ground phenotypes. **(a)** Using the number of days showing symptoms, a predictive linear model was generated to reflect the average diameter on the y-axis. This model retained a significant p-value however other metrics were of low quality (RSE and adjusted R^2 values). **(b)** In a similar way, days showing symptoms were plotted against the number of root tips, however retained a poor *p*-value (0.5273) and was inconsistent with previous findings. **(c)** Linear model formulaic construction considered several biologically important parameters, however few had acceptable metrics for a complete model to be considered at this time point.

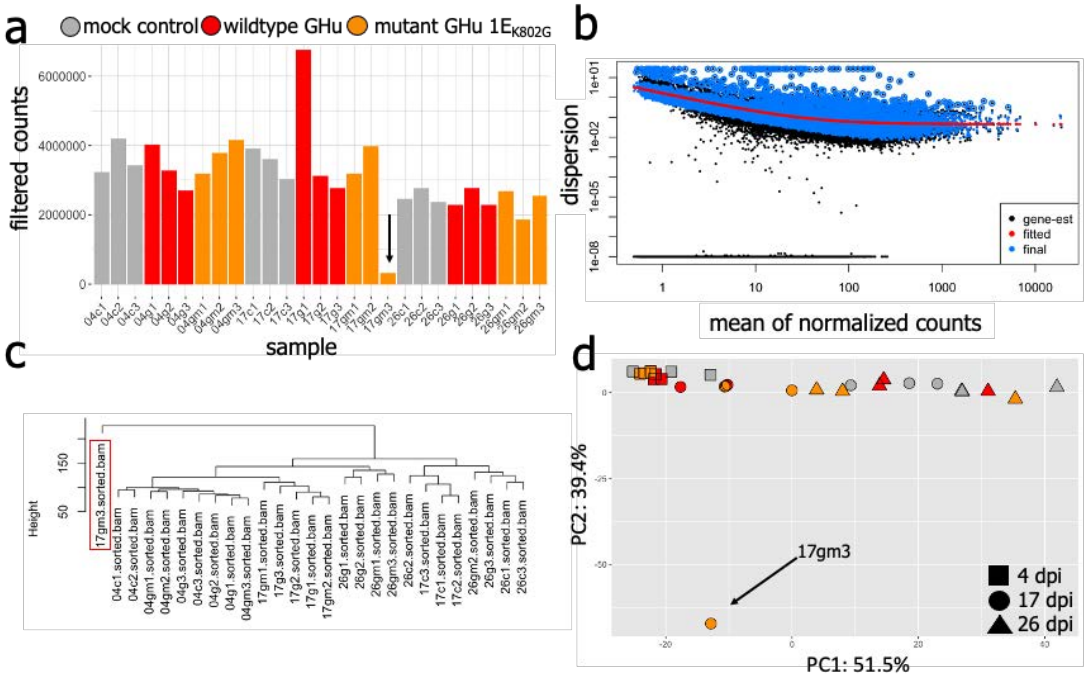

Figure 5-S8. Primary analysis of input RNA-Seq data shows presence of outlier of mutant GFLV-GHu 1E$^{Pol}_{K802G}$ at 17 dpi due to low counts acquired. (a) Filtered reads per sample show many samples around 3,000,000 reads except for '17g1' and '17gm3', towering red bar and small orange bar indicated by arrow, respectively. Treatments are colored gray for mock control, red for wildtype GFLV-GHu treated plants, and orange for mutant GFLV-GHu 1E$^{Pol}_{K802G}$ treated plants. Time scale from 4-, 17-, and 26-days post inoculation (dpi) are visualized from left to right in groups of nine samples. **(b)** Dispersion estimates output of DESeq2 package analysis of RNA-Seq reads. Many reads diverge from fitted line in red, which may correspond to dissonance of samples with varying read number. **(c)** Hierarchal clustering (McQuitty method) groups samples by time except for outlier of '17gm3', indicated by red box, post-normalization. **(d)** Principal component analysis of samples post-normalization through 'vsd' method native to DESeq2 package shows outlier '17gm3' separating from all other samples.

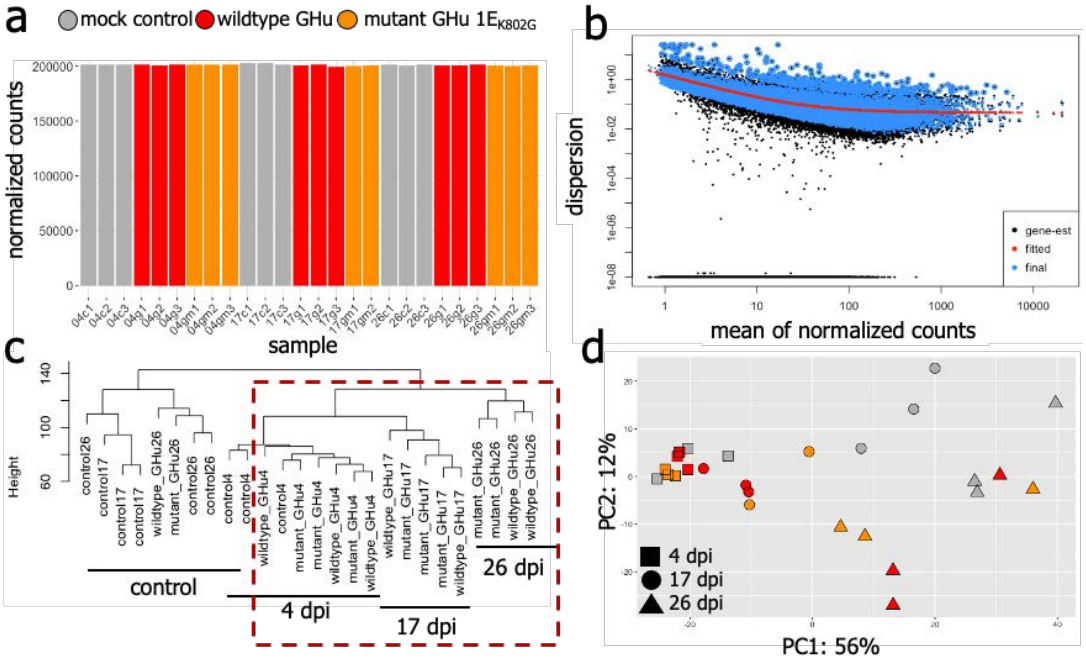

Figure 5-S9. Analysis of input RNA-Seq data shows grouping of viral treated individuals and acceptable input for differential abundance testing after removal of outlier. (a) Bar plot depiction of total counts after filtering and normalization per sample. Left to right colored gray, red, and orange are treatments mock control, wildtype GHu, and mutant GHu $1E^{Pol}{}_{K802G}$, by times of 4-, 17-, and 26 dpi. **(b)** Dispersion estimates of counts plot shows fitted line with decreased final values placed above or below y-axis bounds **(c)** Hierarchal clustering of samples through McQuitty method after removal of outlier (wildtype GHu #3). Virally infected samples at 4-, 17-, and 26 dpi group to the right while mock inoculated control plants group together on the left. **(d)** Principal component analysis of all samples shows distinct separation by time through PC1 [56%], and additional but not complete separation of treatment through PC2 [12%].

Figure 5-S10. Experiment wide gene set enrichment analysis (GSEA) shows small overlaps of treatment-wise comparisons of overrepresentation and many unique attributes over time. Input parameters required differentially expressed genes with *p*-value < 0.05 and |Log2FoldChange| > 0.75.

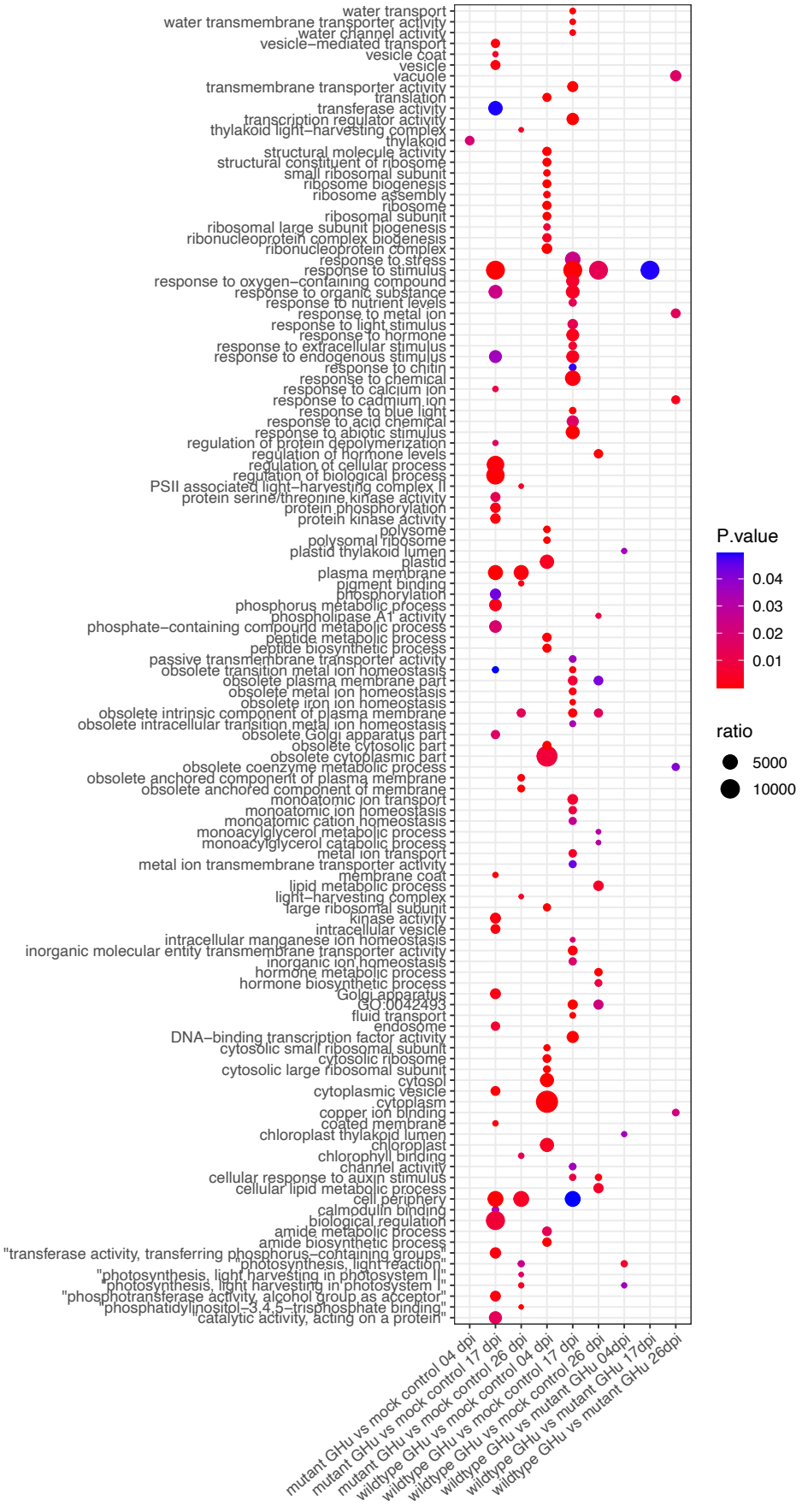
water transport
water transmembrane transporter activity
water channel activity
vesicle−mediated transport
vesicle coat
vesicle
vacuole
transmembrane transporter activity
translation
transferase activity
transcription regulator activity
thylakoid light−harvesting complex
thylakoid
structural molecule activity
structural constituent of ribosome
small ribosomal subunit
ribosome biogenesis
ribosome assembly
ribosome
ribosomal subunit
ribosomal large subunit biogenesis
ribonucleoprotein complex biogenesis
ribonucleoprotein complex
response to stress
response to stimulus
response to oxygen−containing compound
response to organic substance
response to nutrient levels
response to metal ion
response to light stimulus
response to hormone
response to extracellular stimulus
response to endogenous stimulus
response to chitin
response to chemical
response to calcium ion
response to cadmium ion
response to blue light
response to acid chemical
response to abiotic stimulus
regulation of protein depolymerization
regulation of hormone levels
regulation of cellular process
regulation of biological process
PSII associated light−harvesting complex II
protein serine/threonine kinase activity
protein phosphorylation
protein kinase activity
polysome
polysomal ribosome
plastid thylakoid lumen
plastid
plasma membrane
pigment binding
phosphorylation
phosphorus metabolic process
phospholipase A1 activity
phosphate−containing compound metabolic process
peptide metabolic process
peptide biosynthetic process
passive transmembrane transporter activity
obsolete transition metal ion homeostasis
obsolete plasma membrane part
obsolete metal ion homeostasis
obsolete iron ion homeostasis
obsolete intrinsic component of plasma membrane
obsolete intracellular transition metal ion homeostasis
obsolete Golgi apparatus part
obsolete cytosolic part
obsolete cytoplasmic part
obsolete coenzyme metabolic process
obsolete anchored component of plasma membrane
obsolete anchored component of membrane
monoatomic ion transport
monoatomic ion homeostasis
monoatomic cation homeostasis
monoacylglycerol metabolic process
monoacylglycerol catabolic process
metal ion transport
metal ion transmembrane transporter activity
membrane coat
lipid metabolic process
light−harvesting complex
large ribosomal subunit
kinase activity
intracellular vesicle
intracellular manganese ion homeostasis
inorganic molecular entity transmembrane transporter activity
inorganic ion homeostasis
hormone metabolic process
hormone biosynthetic process
Golgi apparatus
GO:0042493
fluid transport
endosome
DNA−binding transcription factor activity
cytosolic small ribosomal subunit
cytosolic ribosome
cytosolic large ribosomal subunit
cytosol
cytoplasmic vesicle
cytoplasm
copper ion binding
coated membrane
chloroplast thylakoid lumen
chloroplast
chlorophyll binding
channel activity
cellular response to auxin stimulus
cellular lipid metabolic process
cell periphery
calmodulin binding
biological regulation
amide metabolic process
amide biosynthetic process
"transferase activity, transferring phosphorus−containing groups"
"photosynthesis, light reaction"
"photosynthesis, light harvesting in photosystem II"
"photosynthesis, light harvesting in photosystem I"
"phosphotransferase activity, alcohol group as acceptor"
"phosphatidylinositol−3,4,5−trisphosphate binding"
"catalytic activity, acting on a protein"
mutant GHu vs mock control 04 dpi
mutant GHu vs mock control 17 dpi
mutant GHu vs mock control 26 dpi
wildtype GHu vs mock control 04 dpi
wildtype GHu vs mock control 17 dpi
wildtype GHu vs mock control 26 dpi
wildtype GHu vs mutant GHu 04dpi
wildtype GHu vs mutant GHu 17dpi
wildtype GHu vs mutant GHu 26dpi
P.value
0.04
0.03
0.02
0.01
ratio
5000
10000

Figure 5-S11. Enrichment results of differentially abundant host genes through Kyoto Encyclopedia of Genes and Genomes (KEGG) analysis of grapevine fanleaf virus infected *Nicotiana benthamiana*. Each panel is representative of an individual treatment contrast per time point in which differentially abundant genes were tested for overrepresentation of KEGG terms. Manual labels were curated to each data point according to the corresponding KEGG identifier. From blue to red, the color shows increased significance of enrichment while the size of the datapoint is relative to the number of genes in that category. The distance from the x-axis intercept is relative of the gene ratio or the relative amount of genes found in that category to the total number of genes subject to the test. The contrast of wildtype GHu against mutant GHu $1E^{Pol}{}_{K802G}$ is observed at **(a)** 4 days post inoculation (dpi), **(b)** 17 dpi, and **(c)** 26 dpi. Similarly, the contrast of wildtype GHu versus mock inoculated control plants are shown for overrepresented KEGG terms at **(d)** 4 dpi, **(e)** 17 dpi, and **(f)** 26 dpi. **(g)** No significant KEGG terms returned at 4 dpi for the contrast of mutant GHu against mock control plants, however several terms were significant in this contrast at **(h)** 17dpi and **(i)** 26 dpi.

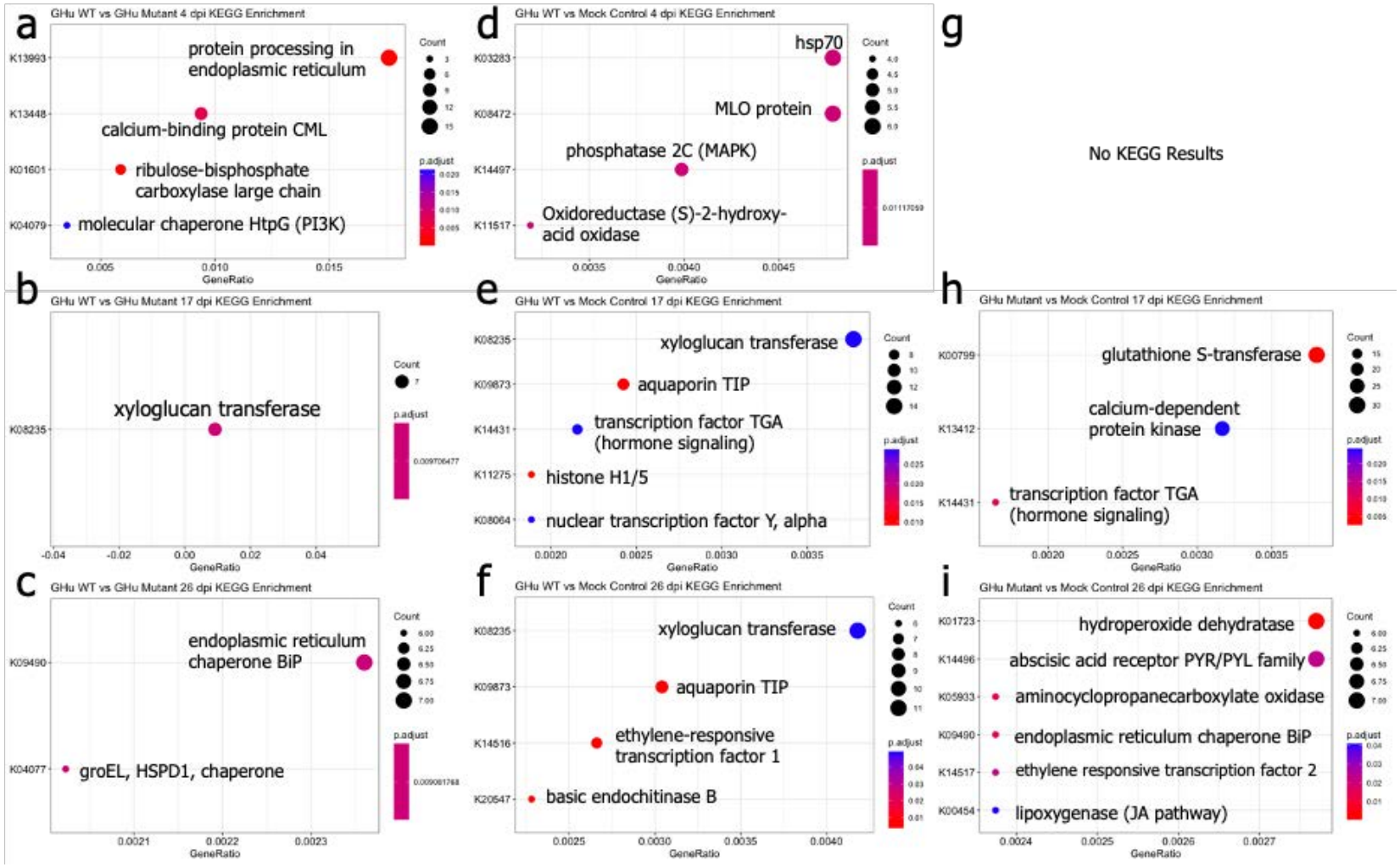
a
GHu WT vs GHu Mutant 4 dpi KEGG Enrichment
protein processing in endoplasmic reticulum
calcium-binding protein CML
ribulose-bisphosphate carboxylase large chain
molecular chaperone HtpG (PI3K)
K13993
K13448
K01601
K04079
GeneRatio
Count
p.adjust
b
GHu WT vs GHu Mutant 17 dpi KEGG Enrichment
xyloglucan transferase
K08235
GeneRatio
c
GHu WT vs GHu Mutant 26 dpi KEGG Enrichment
endoplasmic reticulum chaperone BiP
groEL, HSPD1, chaperone
K09490
K04077
GeneRatio
d
GHu WT vs Mock Control 4 dpi KEGG Enrichment
hsp70
MLO protein
phosphatase 2C (MAPK)
Oxidoreductase (S)-2-hydroxy-acid oxidase
K03283
K08472
K14497
K11517
GeneRatio
e
GHu WT vs Mock Control 17 dpi KEGG Enrichment
xyloglucan transferase
aquaporin TIP
transcription factor TGA (hormone signaling)
histone H1/5
nuclear transcription factor Y, alpha
K08235
K09873
K14431
K11275
K08064
GeneRatio
f
GHu WT vs Mock Control 26 dpi KEGG Enrichment
xyloglucan transferase
aquaporin TIP
ethylene-responsive transcription factor 1
basic endochitinase B
K08235
K09873
K14516
K20547
GeneRatio
g
No KEGG Results
h
GHu Mutant vs Mock Control 17 dpi KEGG Enrichment
glutathione S-transferase
calcium-dependent protein kinase
transcription factor TGA (hormone signaling)
K00799
K13412
K14431
GeneRatio
i
GHu Mutant vs Mock Control 26 dpi KEGG Enrichment
hydroperoxide dehydratase
abscisic acid receptor PYR/PYL family
aminocyclopropanecarboxylate oxidase
endoplasmic reticulum chaperone BiP
ethylene responsive transcription factor 2
lipoxygenase (JA pathway)
K01723
K14496
K05933
K09490
K14517
K00454
GeneRatio

CHAPTER 6

MECHANISTIC UNDERPINNINGS OF ABOVE AND BELOW-GROUND PLANT SYMPTOM DEVELOPMENT UPON INFECTION BY GRAPEVINE FANLEAF VIRUS[6]

ABSTRACT

Grapevine fanleaf virus (GFLV) causes fanleaf degeneration, an endemic soil-borne disease in most vineyards worldwide. GFLV is transmissible to herbaceous plant hosts, including *Nicotiana benthamiana*, which display various temporal foliar and root phenotypes upon infection. The molecular mechanisms of symptom development in GFLV-infected plant hosts are not well characterized. To address mechanistic underpinnings of symptom development, we investigated the impact of 14 GFLV strains on foliar and root system architecture traits with an emphasis on the C-terminus of protein $1E^{Pol*/Sd}$, the putative viral RNA-dependent RNA polymerase, for which the C-terminus is a documented symptom determinant. An in-depth analysis of four different transcriptomics and proteomics datasets previously obtained upon GFLV infection and the use of an updated annotated genome of *N. benthamiana* suggested initial callose deposition and a dysregulation of the hormone and phosphatidylinositol signaling pathways correlated to symptom elicitation. During the initial stages of GFLV infection, protein $1E^{Pol*/Sd}$ was shown to alter pathogen triggered immunity and induced temporal, viral strain-dependent production of reactive oxygen species. Additionally, protein structure prediction and functional mapping tools revealed a putative phosphatase domain located centrally in GFLV protein $1E^{Pol*/Sd}$ with low sequence similarity (<10%)

but relatively confident structural alignment to tyrosine phosphatases (TM-score > 0.50). Interaction of the symptom determinant region with the phosphatase domain of protein $1E^{Pol*/Sd}$ is hypothesized to dysregulate host signaling cascades upon GFLV infection. Based on the spatial positioning of the phosphatase and symptom determinant domains within the C-terminus of protein $1E^{Pol*/Sd}$, protein-protein interactions could explain the temporal foliar and root phenotypes for symptomatic GFLV strains, or inversely, a lack thereof for asymptomatic GFLV strains. This work provided new insights into molecular GFLV-plant host interactions.

---

[6]This chapter has been submitted for publication: Roy, B.G., Mutisya, T., Osterbaan, L.J., Hoyle, V., Choi, J., DeBlasio, S.L., Julkowska, M., Heck, M., & Fuchs, M. 2025. Mechanistic underpinnings of above and below-ground plant symptom development upon infection by grapevine fanleaf virus.

INTRODUCTION

Plant viruses cause devastating disease and crop losses estimated upwards of $30 billion USD each year (Jones 2021). In an arms race with their hosts, plant viruses dysregulate several cellular pathways to facilitate replication, translation, and movement (Heinlein 2015; Laliberté and Sanfaçon 2010). As obligate intracellular parasites, viruses enter host cells and commandeer multiple host proteins, RNA, lipids, and enzymes to complete their infection cycle (Grangeon et al. 2012; Huang et al. 2012; Ivanov and Mäkinen 2012; Whitham and Wang 2004). The successful manipulation of cellular processes can result in symptomatic and/or asymptomatic infections depending on host and viral genetic factors, as well as environmental conditions (García and Pallás 2015; Ghoshal and Sanfaçon 2015; Jiang and Zhou 2023; Pallas and García 2011). A great deal of advances has been made to understand susceptibility and resistance factors for viral infection, but transient protein-protein interactions and the multifunctionality of viral proteins convolute the traditional gene-for-gene concept. Transcriptomics, proteomics, and metabolomics techniques are commonly employed to profile host responses to viral infection and provide further mechanistic insight into the arms race between plants and viruses (Ahmad et al. 2024; Das et al. 2021).

Viral disease symptoms typically vary in onset, severity, and duration. Grapevine (*Vitis* spp.) hosts over one hundred viruses (Fuchs 2020; Roy and Fuchs 2022), most of which cause latent or asymptomatic infections. Grapevine fanleaf virus (GFLV, species *Nepovirus foliumflabelli*, genus *Nepovirus*, family *Secoviridae*, order *Picornavirales*) and closely related viruses, including Arabis mosaic virus (ArMV, species *Nepovirus arabis,* genus *Nepovirus*, family *Secoviridae*) and grapevine

deformation virus (GDeV, species species *Nepovirus deformationis,* genus *Nepovirus*, family *Secoviridae*), cause fanleaf degeneration disease for which symptoms represent the semantic leaf fanning, with variance in leaf mottling, chlorosis, uneven berry ripening, and internode shortening (Andret-Link et al. 2004). However, fanleaf degeneration disease is primarily caused by GFLV. This virus has a bipartite positive sense, single-stranded RNA (+ssRNA) genome with a viral genome-linked protein ($1C^{VPg}$) at the 5' end and a poly(A) tract that is mono-uridylated at the 3' end (Joly et al. 2023). GFLV RNA1 and RNA2 encode five and three mature proteins, respectively, that are produced by proteolytic cleavage of their polyproteins by the viral-encoded cysteine protease ($1D^{Pro}$) upon translation (Margis et al. 1994). By analogy with other picornaviruses, the replication of the GFLV genome is hypothesized to adopt a double-stranded RNA (dsRNA) intermediate before the amplification of +ssRNA molecules at viral replication complexes (VRCs) *in planta*, where the putative viral RNA-dependent RNA polymerase (RdRP, protein $1E^{Pol*/Sd}$) and putative helicase (protein $1B^{Hel*/VSR}$) sequester host proteins to replicate the viral genome. GFLV encodes three viral suppressors of RNA silencing (VSRs) (Choi et al. 2023, 2024) identified as protein $1A^{VSR}$, protein $1B^{Hel*/VSR}$, and a precursor protein $1AB^{VSR}$. The three GFLV VSRs are not pathogenicity factors.

GFLV biology has been studied in the model herbaceous host species *Nicotiana benthamiana* (Vigne et al. 2013), a common herbaceous host plant for grapevine virus studies (Roy and Fuchs 2022), to understand nuanced differences in pathogenicity between strains F13 and GHu. These two strains both systemically infect *N. benthamiana,* with strain F13 remaining asymptomatic and strain GHu inducing

transient vein clearing in apical leaf tissue (Osterbaan et al. 2019; Vigne et al. 2013). In GFLV-GHu infections, transient production of reactive oxygen species (ROS) is associated with an increased average root diameter and lessened root tip number (Roy and Fuchs 2024). ROS production is a hallmark anti-viral response of plant hosts (Xu et al. 2024). The phenotypic display upon infection of GFLV-GHu was mapped to the C-terminus of the RNA1-encoded protein $1E^{Pol*/Sd}$ (92 kDa), the coined symptom determinant (Vigne et al. 2013), particularly its amino acid in position 802 at its C-terminus (Osterbaan et al. 2019). A positive and polar amino acid, lysine (K), in position 802 of protein $1E^{Pol*/Sd}$ is necessary for GFLV-GHu to induce foliar and root symptoms in *N. benthamiana*, but not sufficient for GFLV-F13 (Osterbaan et al. 2019; Vigne et al. 2013) to cause symptoms (Osterbaan et al. 2019; Roy and Fuchs 2024). These results suggested that symptom determinants other that the amino acid in position 802 of protein $1E^{Pol*/Sd}$ are yet to be identified. Previous *in silico* analyses showed that residue 802 of protein $1E^{Pol*/Sd}$ is flanked by an ordered region at the N-terminus and a conserved LLKTHLKTLR motif at the C-terminus (Osterbaan et al. 2019). Furthermore, GFLV protein $1E^{Pol*/Sd}$ was predicted to contain at least three globular protein domains (Roy et al. 2024). The N-terminal domain is approximately 500 amino acids in length and contains the conserved putative RdRP domain. The central domain of protein $1E^{Pol*/Sd}$ is roughly 200 amino acids in length and was predicted to contain a parathyroid hormone motif, although the presence or biological relevance of this domain is questionable in higher plants. Finally, the C-terminal domain of protein $1E^{Pol*/Sd}$ (about 100 amino acids in length) contains the leaf and root symptom determinant region, including the 802^{nd} residue (Osterbaan et al. 2019). The exact

mechanism of how protein $1E^{Pol*/Sd}$ functions in leaf and root symptom development is unclear.

Possible mechanisms in which GFLV symptoms arise were previously investigated from an iterative approach on the virus side (Osterbaan et al. 2019; Vigne et al. 2013), and a global profiling approach on the plant host side (Roy et al. 2023; Roy and Fuchs 2024). Four omics datasets were previously produced within the realm of GFLV-*N. benthamiana* interactions from three independent studies (Osterbaan et al. 2021; Roy et al. 2023; Roy and Fuchs 2024). Two datasets were of 3'RNA-Seq, and two were of proteomic approaches with liquid chromatography tandem mass spectrometry (LC-MS/MS). Three omics studies focused on leaf tissue and one on root tissue of *N. benthamiana*. These studies all focused on the symptom-inducing wildtype GFLV-GHu strain with a few asymptomatic strains. Differential abundance analysis in these individual datasets indicated a pronounced hypersensitive response in symptomatic GFLV-infected plants, whereas this response was weaker in asymptomatic GFLV-infected plants (Roy et al. 2023; Roy and Fuchs 2024). Further network analysis revealed the dysregulation of several signaling molecule pathways, however the involvement of protein $1E^{Pol*/Sd}$ in symptom development remains unclear. Viruses manipulate many host pathways simultaneously at the RNA and protein levels, which decrease the precision of 'omics techniques when considered alone. The intersect of these approaches has yet to be fully explored to understand how GFLV protein $1E^{Pol*/Sd}$ alters the host immune response.

Virus-host interaction studies have considered the regulation of host components, RNA silencing, susceptibility factors, and immune receptors as the

foundational host factors responsible for symptom expression and repression tactics of the host immune system (Ghoshal and Sanfaçon 2015; Jiang and Zhou 2023; Osterbaan and Fuchs 2019; Tsuda 2020). Due to a virus' limited genetic coding capacity, it is essential for viral proteins to possess multiple functions. For example, GFLV protein $1B^{Hel*/VSR}$ is a putative helicase and a viral silencing suppressor; and protein $1E^{Pol*/Sd}$ is the putative RdRP and symptom determinant in leaves and roots of *N. benthamiana*. It is plausible that additional functionalities in many GFLV proteins elude our understandings.

The aim of this research was to advance our understanding of the role of GFLV protein $1E^{Pol*/Sd}$, particularly its C-terminus, in foliar and root symptomatology in *N. benthamiana* by integrating four previously obtained omics datasets. Furthermore, dysregulated metabolomic pathways were linked with new quantitative phenotypic data of leaf and root tissue upon GFLV infection. We hypothesized that (i) interactions of host and viral proteins trigger symptomatic and asymptomatic infections, (ii) protein $1E^{Pol*/Sd}$ may contain a hitherto undescribed functional enzymatic domain potentially involved in symptom induction, and (iii) leaf and root phenotypes can be predicted based on viral symptom determinant sequence identities. To address these hypotheses, we conducted an extensive *in silico* integration of the previously generated 'omics data and present new experimental evidence to support converging trends. Finally, novel comparative analysis of protein structure predictions identified a domain with high structural similarity to dual-specificity phosphatases in GFLV protein $1E^{Pol*/Sd}$. Predicted confirmations of this domain in the central region of protein $1E^{Pol*/Sd}$ could be involved in symptomatology.

METHODS

Plant growth

Wildtype *Nicotiana benthamiana* seeds were sown in Cornell LM-3 soilless media for two to three weeks before transplant in a similar growth medium (4:1:1, LM-3:perlite:vermiculite), as previously reported (Osterbaan et al. 2018, 2019; Roy et al. 2023). Seedlings were fertilized weekly with Scott's Miracle Grow. Growing conditions were constantly maintained at a 16:8 hour light:dark period at 25ºC and 70% relative humidity.

GFLV strains and plant inoculation

Infectious clones of GFLV RNA1 and RNA2 in *Agrobacterium tumefaciens* strain GV3301 were utilized to establish initial systemic infection *in planta* (Osterbaan et al. 2018, 2019). Wildtype strains F13 (GenBank accession number NC003615) and GHu (JN391442), and their respective mutant clones of RNA1 in combination with GFLV-GHu RNA2 were selected for this study. *Agrobacterium tumefaciens*-mediated inoculation was performed on plants at the four to six leaf stage and tested for systemic infection by double antibody sandwich enzyme-linked immunosorbent assay (DAS-ELISA) using specific antibodies (Bioreba, Reinach, Switzerland) at two weeks post-inoculation.

A total of 13 GFLV strains were used in this study, including wildtype GFLV strains GHu (Vigne et al. 2013) and F13 (Ritzenthaler et al. 1991), and 11 GFLV mutants (Osterbaan et al. 2019, 2021) (Figure 6-1). Three GFLV mutants carried protein $1E^{Pol*/Sd}$ tagged with V5 at the C-terminus (GHu, F13, and GHu-$1E_{K802G}$) (Osterbaan et

al. 2021). Four GFLV mutants carried a single (802nd or 804th) or double (802nd and 804th) amino acid swap between protein 1E$^{Pol*/Sd}$ of wildtype strains GHu and F13, or a 20-nucleotide swap (2404-2424) (Figure 6-1). Additionally, lyophilized plant material infected with pepper ringspot virus (PepRSV, species *Tobravirus capsica*, genus *Tobravirus*, family *Virgaviridae*) strain CAM (NC003669) was mechanically transmitted into *N. benthamiana* and passaged across multiple experiments from original source material.

Confirmation of viral infection status

GFLV progeny was characterized in infected plants via reverse transcription (RT) polymerase chain reaction (PCR) and Sanger sequencing to verify the genetic stability of protein 1E$^{Pol*/Sd}$. Apical leaf tissue infected with sequence-confirmed isolates were collected and maintained at -80^{o}C until further use as inoculum in mechanical inoculations (Osterbaan et al. 2019; Roy et al. 2023; Roy and Fuchs 2024). Leaves and roots of plants inoculated with GFLV or PepRSV were collected for RNA extraction through the Omega E.Z.N.A. Plant RNA Mini Kit (cat no. R6827) and used to characterize viruses by RT-PCR using the QIAGEN One-Step RT-PCR Kit (Cat. No. 210212) with specific primers (Jones et al. 2008) (Table 6-S1). PCR products were resolved through gel electrophoresis on 1.5% agarose for 45 minutes at 100 V and visualized under UV after GelRed staining. Following gel purification (Zymo, cat. no. D4007), isolated amplicons were characterized by Sanger sequencing at the Cornell Institute of Biotechnology in Ithaca, NY.

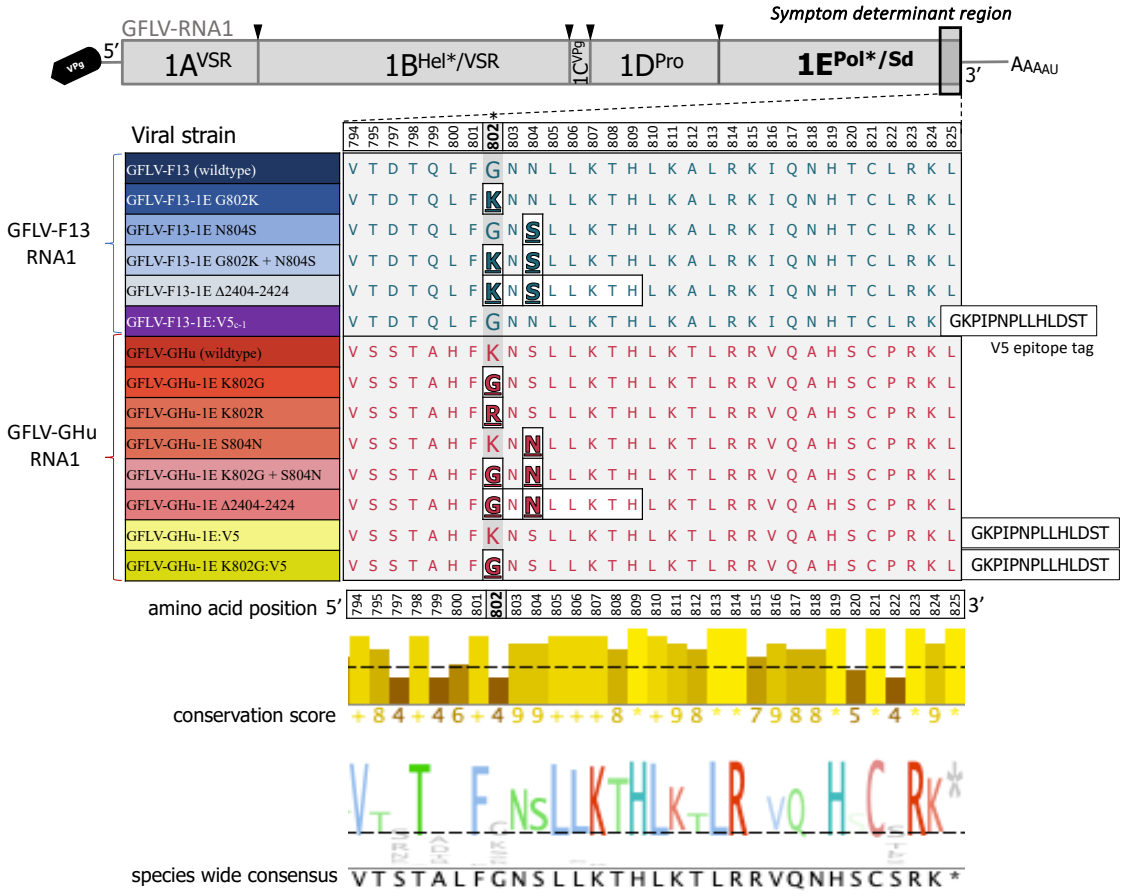

FIGURE 6-1. Strains of grapevine fanleaf virus (GFLV) utilized in this study. The GFLV RNA1-encoded polyprotein is proteolytically cleaved *in cis* by GFLV protease 1D^{Pro} to produce five mature proteins (1A^{VSR}, 1B$^{Hel*/VSR}$, 1C^{VPg}, 1D^{Pro}, and 1E$^{Pol*/Sd}$) following translation. The zoomed in box at the C-terminal region of GFLV-GHu protein 1E$^{Pol*/Sd}$ shows the critical amino acid residue (802) for foliar vein clearing symptoms in *Nicotiana benthamiana* (Vigne et al. 2013; Osterbaan et al. 2019) with extended range to depict conservation of amino acids. The derived mutants (GFLV-F13 strains in cool colors, and GFLV-GHu strains in warm colors) were selected based on their composition at the 802nd and 804th amino acids, with additional strains based on nucleotide identity. The select amino acids that have altered identity are highlighted in bold and underlined while nucleotide changes are indicated with box outlines. Amino acid sequences of a V5 epitope tag at the C-terminus of protein 1E$^{Pol*/Sd}$ are depicted by white boxes with the appropriate amino acid sequence for three GFLV strains.

Quantitative chlorophyll measurements in leaves

Chlorophyll content was measured on *N. benthamiana* leaves using a SPAD-502DL meter (Minolta Chlorophyl Meter SKU #2900PDL) following inoculation with different GFLV strains. Leaves of *N. benthamiana* were excised at 10 days post inoculation (dpi) and repeated measures were captured on the lamina (left and right) and midrib of apical leaves through three technical replicates of five randomly selected plants per treatment group. The average SPAD reading of the three leaf areas and technical replicates was used for statistical analysis. Considering previous observations of vein clearing symptom development from four to ten dpi in *N. benthamiana* infected with GFLV-GHu (Osterbaan et al. 2019; Vigne et al. 2013), repeated readings were taken from two- to sixteen-dpi on three to five individual plants per treatment group. Readings were conducted on leaves still connected to each plant.

Reactive oxygen species production in* Nicotiana benthamiana *leaf tissue

3,3'-diaminobenzidine (DAB) staining was performed to quantify reactive oxygen species (ROS) production in apical leaf tissue of *N. benthamiana* infected with GFLV. Leaf tissue was collected at 2-, 3-, 4-, 5-, 6-, 7-, 9-, 11-, and 13 dpi and subject to either whole leaf or leaf disc assays for ROS detection. Leaf samples were placed in a 2 mL Eppendorf tube with 1 mg/mL 3,3′-diaminobenzidine staining (DAB) solution (pH 5.8) and then vacuum infiltrated for one minute. After an incubation in the dark at ambient conditions for two hours, leaf samples were de-stained in boiling ethanol (90%) for one minute. Whole leaves or leaf discs were placed on a glass microscope slide (Fisher, Cat No. 12-550-A3) mounted with 0.1 mL of 50:50 v/v glycerol:PBST

(phosphate-buffered saline supplemented with Tween), and covered with a coverslip for observation (Fisher, Cat No. 12-545-88).

Foliar applications of inositol and effects on GFLV infection

Myo-inositol (#J62886-30, ThermoFisher Scientific, USA) was applied to three cohorts of *N. benthamiana* plants to understand how this signaling molecule could impact GFLV infection. A foliar spray of 10 mM or 25 mM myo-inositol was applied daily for seven consecutive days either immediately prior to mechanical inoculation of the plants with GFLV or immediately following inoculation with GFLV. Wildtype GFLV strains F13 and GHu, and mutant GFLV strains GHu 1E:V5, GHu $1E_{K802G}$, GHu_{K802R}, F13 $1E_{G802K}$, and F13 $1E_{G802K+N804S}$ were evaluated for symptomatology type and severity, and infection rates by DAS-ELISA.

Foliar applications of phytohormones and effects on GFLV infection

Salicylic acid (#A12253-36, ThermoFisher Scientific, USA) and abscisic acid (A102, PhytoTech Labs, USA) were applied as foliar sprays at two days or at 18-19 days post mechanical inoculation. Both phytohormones were applied at a concentration of 50 µM in water, and rinsed off by a thorough water spray 15 min later. Wildtype GFLV strains F13 and GHu, and mutant GFLV strains F13 $1E_{G802K}$, GHu $1E_{K802G+S804N}$, and GHu $1E_{K802R}$ were evaluated for symptomatology type and severity, and infection rates by DAS-ELISA.

Excavation of root systems and root system architecture analysis

Whole crown root systems of *N. benthamiana* plants infected with GFLV strains and PepRSV or uninoculated plants were excavated by hand and processed according

to our previously described methodology (Roy and Fuchs 2023, 2024). Data on key root trait metrics, such as total number of root tips, average diameter (mm), number of branch points, and total volume (cubic mm) with minimal pre-processing and no normalization were compared. PepRSV-infected plants acted as a positive control. For plants infected with GFLV strains for which experimental replicates were grown for slightly different amount of time, a z-score normalization of the RSA traits across all replicates was performed and standardized to the non-infected plants.

X-ray tomography of Nicotiana benthamiana *roots*

Root samples of *N. benthamiana* plants were analyzed by X-ray tomography. At least three individual samples were selected per treatment (wildtype GFLV-F13, mutant GFLV-F13-1E$_{G802K}$, wildtype GFLV-GHu, mutant GFLV-GHu-1E$_{K802G}$, and PepRSV infected plants) based on the closeness of their average diameter (mm) and average number of root tips. Root tissue was excised from the full root systems in two cm long pieces, just above the area where adventitious branching began. Samples were then prepared in a 2.0 mL Eppendorf tube by stacking multiple root system regions of interest separated by packaging foam. Then, samples were submerged in an organic iodine stain consisting of 1% iodine crystals (w:v), 2% potassium iodine (w:v), 90% ethanol (v:v), in water for two days. To increase the penetrative ability of the iodine solution to the root system, samples were rehydrated with distilled water and subject again to staining with equal concentrations of iodine crystals and potassium iodine. The same iodine stain was retained in the tubes to prevent dehydration of cells during imaging. Four to five root samples were stacked in this manner for consecutive scanning on a micro-CT Bruker Skyscan 1276 (Ithaca, NY, USA). A total of 20 scans was obtained per sample

for analysis in Dragonfly (v2024.1, Comet Technologies Canada Inc.) to visualize and quantify the primary root vasculature.

Samples were analyzed the Cornell Imaging Facility (Cornell University, Ithaca, NY, USA) following root tissue staining with iodine. DICOM images were imported to Dragonfly (Object Research Systems, version 2022.2) for view in 2D and 3D modes. Briefly, 2D images were processed through a custom pseudo-colored palette called `root cross section` from black to purple to yellow to white from lowest to highest pixel intensity. A bi-gated ramp (gamma gain of 2.00) was placed starting at the midpoint of signal distribution and adjusted to a range of ~20,000 units to provide the most contrast with reduced background signal. The noise was further negated by using a slab average of the XY view (vertical cross section of root). Root cross-sections obtained from x-ray scans were subject to further image analysis in ImageJ (1.53k, NIH, USA) with Java (v1.8.0). Images of 2D cross sections down the stem of the plant were imported and scaled to the 1 mm bar, roughly 175 pixels in each image. Then, perimeter and area measurements were acquired using the `oval` and `measure` functions.

For 3D analysis, a bi-gated, inversed ramp of a new palette called ‘ctscan’ was derived from Dragonfly’s native palette ‘vegetal’. This palette contains increased contrasting colors from lowest intensity signal to highest by colors blue, brown, green, orange, and black when inversed in the thresholding window. To reduce background signal, the lower threshold was placed slightly above the midpoint of signal distribution until little to no pixels remained outside of stained root samples. Activated preset parameters across all 3D image generation included tone mapping, filtered gradient, specular boost, edge contrast maximized, high quality, render mode default,

interpolation cubic, orthographic projections, and scale bar. Images were acquired through the software and exported in .png file format.

In silico *integration of transcriptomics and proteomics datasets*

Transcriptomics files of bulk mRNA expression in *N. benthamiana* leaves and roots under NCBI accession numbers PRJNA838211 (SRX15277918-SRX15277992) and PRJNA984296 (SRX24939862-SRX24939888) were reanalyzed. Similarly, proteomics data from the PRIDE database of ProteomeXChange under NCBI identifier PXD037185 and DOI: 10.6019/PXD037185 were reanalyzed. Previous proteomics data[27] were also uploaded to ProteomeXChange under the identifier PXD054729 and DOI: 10.6019/PXD054729.

Data pre-processing and alignment remained identical to previous reports (Roy et al. 2023; Roy and Fuchs 2024). A threshold of counts was placed at ≥1 count per sample. Differentially abundant genes were then detected from transcriptomics of leaves and roots, and proteomics of leaves, by setting thresholds of p-value < 0.05 and |Log2FoldChange| > 1. For the proteomics dataset, interactants were extracted with two levels of confidence: the first set was for host protein interactants of V5 tagged GFLV proteins (wildtype GFLV-F13:$V5_{c\text{-}1}$, wildtype GFLV-GHu:V5, mutant GFLV-GHu $1E_{K802G}$:V5) in contrast to non-tagged control proteins, and the second set was for the quantitative spectral counts for specific proteins.

Contrasts of each viral treatment against mock inoculated plants were selected to then extract differentially abundant transcripts (DATs) or differentially abundant proteins (DAPs). For functional gene analysis, approaches in identifying enriched gene clusters were conducted by considering the contrasts of interest with the default

parameters for Gene Set Enrichment Analysis (GSEA). For Kyoto Encyclopedia of Genes and Genomes (KEGG) analysis using clusterProfiler(Wu et al. 2021), the enricher function was employed with pvalueCutoff =0.05, pAdjustMethod = "BH" (Bonferonni), and minGSSize = 10 as default. The argument TERM2GENE was fulfilled with the custom KEGG annotation recently reported (Roy and Fuchs 2024).

GFLV protein 1E$^{Pol*/Sd}$ structure prediction

As of September 2024, 214 full-length nucleotide sequences of the coding region of GFLV RNA1-encoded protein 1E$^{Pol*/Sd}$ were publicly available. FASTA files corresponding to these sequences were downloaded, aligned, and trimmed to the 824 amino acid length of the 92 kDa protein 1E$^{Pol*/Sd}$. Corresponding sequences of the closely related ArMV and GDeV were also included for protein sequence alignment, and a GFLV consensus sequence was extracted. The GFLV consensus sequence along with sequences of ArMV, GDeV, wildtype GFLV-F13, wildtype GFLV-GHu, and GFLV-GHu mutant 1E$_{K802G}$ were submitted to the I-TASSER-MTD server (Zhang 2008) for structural and functional protein predictions. For analysis to the C-terminus of protein 1E$^{Pol*/Sd}$, the putative RdRP domain was removed from the protein 1E$^{Pol*/Sd}$ structural files and the resultant coordinate files were subject to the FoldSeek (Van Kempen et al. 2024) algorithm for structural and sequence similarity scoring.

Post-hoc analysis of resultant PDB files from this study and a previous study (Roy et al. 2024) was performed. Resultant functional gene annotations were parsed and compiled to assess putative functions of protein 1E$^{Pol*/Sd}$. Sequence specific data from I-TASSER-MTD were retained for comparative analysis between GFLV, ArMV, and GDeV. Further, PDB files of GFLV, ArMV, and GDeV protein 1E$^{Pol*/Sd}$ were submitted

to DeepFRI (Gligorijević et al. 2021) to extrapolate catalytic motifs and residues of interest. For this, DeepFRI result files (JSON) were parsed using a custom function to extract residue by residue confidence metrics for each predicted gene ontology. These extracted values were used to create heatmaps across all PDB files generated through I-TASSER-MTD prediction software.

Statistical analyses and visualization

All data was analyzed in R (R Core Team 2013) and RStudio (Team 2015). Libraries for specific statistical analysis include corrplot (Wei and Simko 2017) (v0.92), lme4 (Bates et al. 2015) (v1.1-35.5), FSA (Ogle et al. 2023) (v0.9.5), emmeans (Lenth 2024) (v1.10.3), DESeq2 (Love et al. 2014) (v1.44.0), clusterProfiler (Wu et al. 2021) (v4.12.2), enrichplot (Yu 2021) (v1.24.2), gprofiler2 (Kolberg et al. 2020) (v0.2.3), WGCNA(Langfelder and Horvath 2008) (v1.72-5), GSEABase (Subramanian et al. 2005) (v1.66.0). Visualization was accomplished with the additional libraries ggplot2 (Wickham 2009) (v3.5.1) and scatterplot3d (Ligges and Mächler 2003) (v0.3-44). All code and Rmarkdown files are available on the associated Github page (https://github.com/brandon-roy/ExtendedRootPhenotyping).

RESULTS

Symptomatic, GFLV-infected **N. benthamiana** *plants display reduced photosynthetic potential*

A total of 1,438 plants were analyzed for leaf symptomatology, root traits, chlorophyll content, and/or reactive oxygen species (ROS) production across 18 independent experiments with 13 GFLV strains (Figure 6-1). GFLV infection rates per experimental replicate per treatment varied with a low of 32% and a high of 100% of plants inoculated testing positive for GFLV at 14-18 days post inoculation (dpi) in DAS-ELISA (Table 6-S2). For further analysis, any individual plant that was inoculated yet held no detectable virus was placed in a treatment group called 'inoculated, non-infected' to differentiate from mock inoculated plants during phenotype analysis of roots were simply excluded from leaf phenotype analyses.

Plants inoculated with wildtype GFLV-GHu, mutant GFLV-GHu-1E$_{S804N}$, and mutant GFLV-GHu-1E:V5 that tested positive for GFLV in DAS-ELISA all displayed vein clearing symptoms on apical leaves, as expected (Osterbaan et al. 2019, 2021) (Figure 6-2a). Daily ratings of GFLV-GHu symptoms across all experimental replicates showed vein clearing symptoms first appearing at four dpi, most pronounced around nine dpi, and all plants recovered by 17 dpi (Figure 6-2b). These observations were consistent with previous reports (Osterbaan et al. 2019; Roy et al. 2023; Vigne et al. 2013). Mutants GFLV-GHu-1E$_{S804N}$ and GFLV-GHu-1E:V5 displayed vein clearing symptoms for a similar duration (Figure 6-2b). Plants infected with any other wildtype or mutant GFLV strains did not show any apical leaf symptoms at any point during infection, as previously reported (Osterbaan et al. 2019) (Figure 6-2a,b).

FIGURE 6-2. Visual and quantitative assessment of vein clearing symptoms after infection of *Nicotiana benthamiana* with several grapevine fanleaf virus (GFLV) strains. (a) Apical *N. benthamiana* leaves of similar size were excised 11 days post inoculation (dpi) and used for documenting vein clearing symptom severity. Treatments from left to right are: mock control, wildtype GFLV-F13, mutant GFLV-F13 $1E^{G802K}$, wildtype GFLV-GHu, and mutant GFLV-GHu $1E^{K802G}$. A mock control leaf is labeled with the three areas of sampling through SPAD meter readings, LL = left lamina, M = midrib, and RL = right lamina. **(b)** Symptom development rating in 194 individual *N. benthamiana* plants over the course of infection with wildtype GFLV-GHu (*n=145*), mutant GFLV-GHu-$1E^{S804N}$ (*n=20*), and mutant GHu-1E:V5 (*n=29*), showed a bell-shaped curve with a peak of vein clearing at 9 dpi and symptom recovery at 14 dpi. The percentage of plants infected with GFLV and showing symptoms is displayed over time, with standard deviation as the encompassing lines of the same color. **(c)** Output readings of the three leaf areas show significant differences in chlorophyll content at 10 dpi through a SPAD meter. Error bars show standard error of mean reading, Tukey's HSD letter system is represented above as performed on a treatment comparison. **(d)** Time-course chlorophyll measurements indicate a brief period from 7 to 10 dpi of statistically significant difference of symptomatic vein clearing when compared to asymptomatic infection and mock controls. The same five treatments are similarly color coded as in panels b and c. Absolute bounds of vein clearing were determined by visual assessment to be 5 dpi to 13 dpi, and all plants fully recovered by 14 dpi.

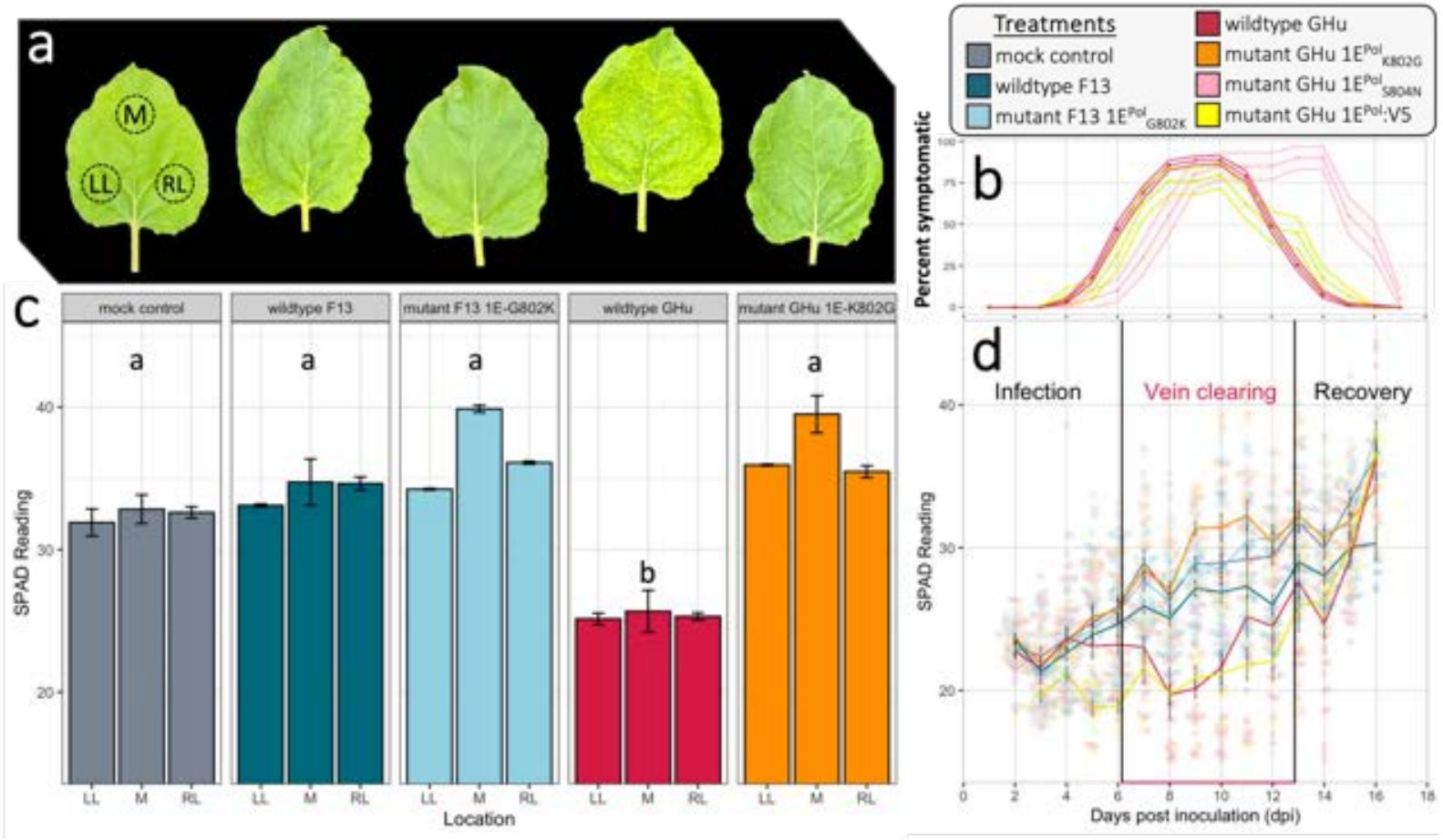
a
M
LL
RL
Treatments
mock control
wildtype F13
mutant F13 1E^Pol G802K
wildtype GHu
mutant GHu 1E^Pol K802G
mutant GHu 1E^Pol S804N
mutant GHu 1E^Pol:V5
b
Percent symptomatic
c
mock control
wildtype F13
mutant F13 1E-G802K
wildtype GHu
mutant GHu 1E-K802G
a
a
a
b
a
SPAD Reading
Location
LL
M
RL
d
Infection
Vein clearing
Recovery
SPAD Reading
Days post inoculation (dpi)

Analysis of chlorophyll content in leaves of symptomatic (wildtype GFLV-GHu) and asymptomatic (wildtype GFLV-F13, mutant GFLV-F13-1E$_{G802K}$, and mutant GFLV-GHu-1E$_{K802G}$) GFLV-infected plants using a SPAD meter separated treatments into two statistically supported groups of plants (≥ 95% confidence, Tukey's HSD, Figure 6-2c). These two groups included symptomatic plants infected with wildtype GFLV-GHu on one hand, and asymptomatic plants infected with wildtype GFLV-13, mutants GFLV-F13 1E$_{G802K}$ and GFLV-GHu 1E$_{K802G}$, and mock controls on the other hand (Figure 6-2c). Chlorophyll content increased over time for each GFLV strain with measurements of symptomatic leaves of plants infected with wildtype GFLV-GHu remaining statistically different from all other strains from eight to 10 dpi ($p \leq 0.0001$, Figure 6-2d). The first and last instance of a significant difference in chlorophyll content between wildtype GFLV-GHu and any other GFLV strains with regards to mock inoculated control was at six dpi ($p = 0.0298$) and 14 dpi ($p = 0.0077$), respectively (Table 6-S5). These results provided insights into a substantially reduced photosynthetic potential of GFLV-infected plants displaying vein clearing symptoms.

Reactive oxygen species are produced in leaves of GFLV-infected N. benthamiana *plants*

Previous transcriptomic work (Roy et al. 2023) suggested ROS production in leaf tissue of *N. benthamiana* infected with GFLV but had yet to be experimentally tested. Here, all GFLV-infected *N. benthamiana* plants exhibited some level of ROS production compared with mock controls (Figure 6-S1). The most striking differences were at five dpi, when plants infected with wildtype GFLV-GHu and mutant GFLV-F13 1E$_{G802K}$ produced large amounts of ROS compared with plants infected with

wildtype GFLV-F13 and mutant GFLV-GHu $1E_{K802G}$ (Figure 6-S1). The highest and longest production of ROS was observed in leaves of plants infected with wildtype GFLV-GHu, particularly during vein clearing symptom display from two to seven dpi. These results revealed ROS production in leaves of *N. benthamiana* infected with GFLV (Roy and Fuchs 2024) and confirmed previous observations on ROS production depending on both the GFLV strain and the nature of residue 802 of protein $1E^{Pol*/Sd}$ in root tissue of *N. benthamiana* (Roy and Fuchs 2024).

Root system architecture traits are differentially modified by GFLV species

A total of 342 scans of *N. benthamiana* roots was obtained on a flatbed scanner and 2,555 parsed images were subsequentially segmented and analyzed in Rhizovision Explorer, as previously described (Roy and Fuchs 2023, 2024). RSA traits were extracted per experimental replicate and saved in Microsoft Excel files (DOI: 10.5281/zenodo.14844388). Outlier experimental replicates (3 and 13) contained too little plants per treatment; these were excluded from further analyses. Additional outliers were detected upon interquartile range (IQR) exemption, where individuals more than 1.5 times the distance of the IQR from the mean were excluded. Manual exemption of eight additional samples resulted in a new matrix of 1,298 individual plant root systems. The entire dataset is represented by files 'RhizoAllCompiled.xlsx' for raw data and 'RhizoAllNormalized.xlsx' for normalized and adjusted data (DOI: 10.5281/zenodo.14844388). A total of 1,298 root systems are represented in the z-score adjusted, normalized data. After normalization, unsupervised cluster analysis was conducted by extracting data with non-zero values across all normalized traits and by subjecting these to dimension reduction analysis. A principal component analysis

explained 46.3% of the data in PC1, 18.7% in PC2, and 12% in PC3. The data grouping within a 3D scatter plot of the principal components showed some associations by GFLV strain, while 2D PCA dissections exhibited grouping by experimental replicate or 'cohort' (Figure 6-3a-b, Figure 6-S2a-d). Therefore, future models retained the experimental replicate term.

The correlation of RSA traits was analyzed in corrplot with diameter traits (average diameter, median diameter, etc.) and network traits (number of root tips, number of branch points, surface area, etc.) (Figure 6-3c). These two groupings of highly correlated traits were used to justify further analyses on specific traits in each subset, namely average diameter, number of branch points, number of root tips, surface area, and volume (Figure 6-3d-h). The average root diameter differed among plants infected by GFLV strains and non-infected individuals. Wildtype GFLV-F13, and mutants GFLV-F13-1E$_{G802K-N804S}$ and GFLV-GHu-1E$_{S804N}$ caused a significant decrease in average diameter, and mutants GFLV-F13-1E:V5$_{c-1}$ and GFLV-GHu-1E$_{2404-2424}$ had an increased average root diameter when compared with non-infected plants (Figure 6-3d). Plants infected by mutants GFLV-F13-1E$_{N804S}$ and GFLV-F13-1E-G802K$_{N804S}$ displayed an increased number of branch points, while plants infected with wildtype GFLV-GHu and mutant GFLV-GHu-1E$_{2404-2424}$ exhibited reduced branching points (Figure 6-3e). Plants infected with wildtype GFLV-F13, wildtype GFLV-GHu, and mutant GHu-1E$_{2404-2424}$ also had a reduction in root tip number per plants, while plants infected with mutants GFLV-F13-1E$_{N804S}$, GFLV-F13-1E:V5$_{c-1}$, GFLV-GHu-1E$_{S804N}$, and GFLV-GHu-1E$_{K802G-S804N}$ displayed an increase in the number of root tips per plant (Figure 6-3f). For root surface area and volume, plants

infected with mutant GFLV-F13-1E:V5 showed an increase in both metrics and mutant GFLV-F13-1E$_{N804S}$ had an increase only in total volume. Plants infected with wildtype GFLV-GHu and mutant GFLV-GHu-1E$_{S804N}$ had a significant decrease in both traits, while plants infected with mutant F13-1E$_{N804S}$ had a decrease in root volume (Figure 6-3g-h). For PepRSV, the average root diameter was not affected in infected plants, but the number of branch points was significantly decreased (Figure 6-3g-h). As expected, plants infected with PepRSV had a significantly reduced number of root tips when compared with non-infected plants, and a drastic reduction in surface area and volume ($p < 0.0001$). Kruskal-Wallis rank sum test indicated a significant modification explained by treatment ($p < 2.2$ E-16) and average root diameter ($p < 6.94$ E-16). Together these results revealed GFLV strain-specific changes in RSA traits. They also indicated that changes in RSA traits were not solely dependent upon residue 802 of GFLV protein 1E$^{Pol*/Sd}$, suggesting additional amino acids within the C-terminus of this protein contribute to phenotypic differences.

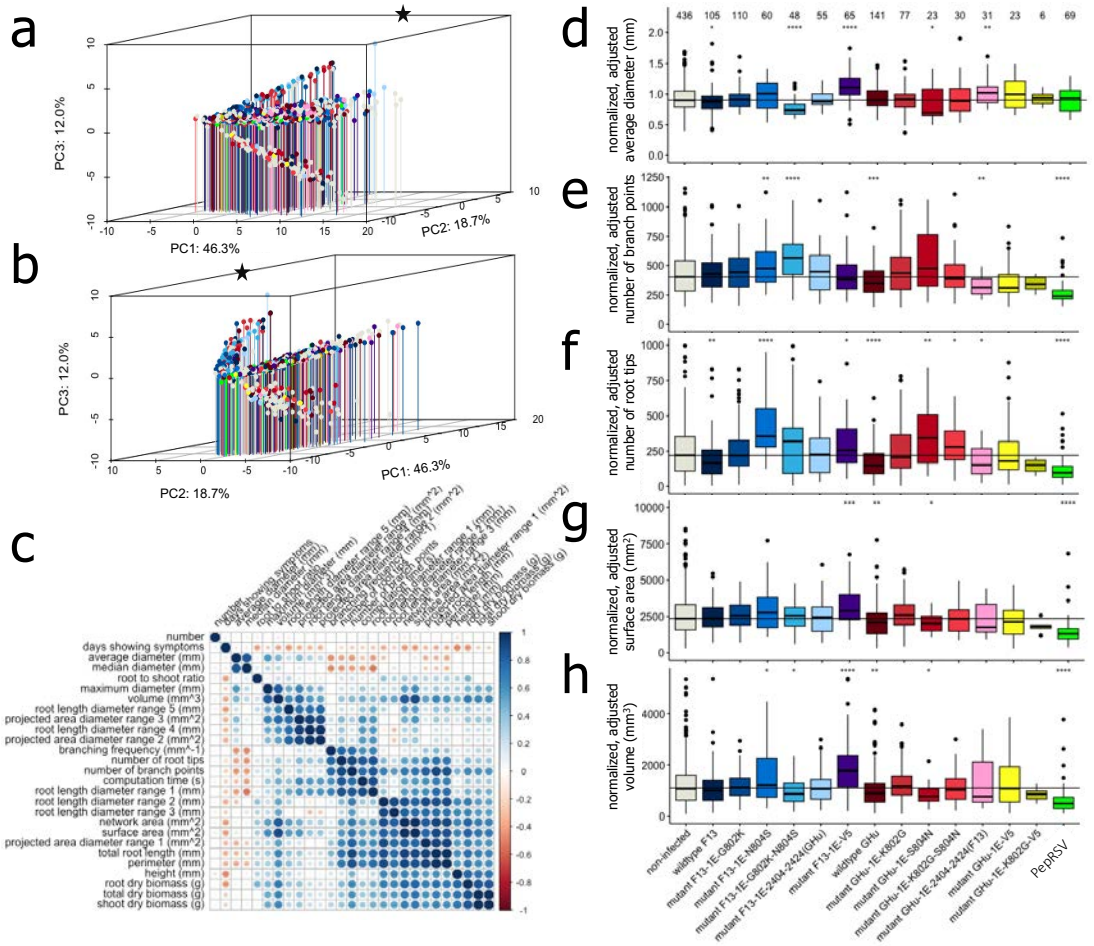

FIGURE 6-3. Root system architecture (RSA) traits of *Nicotiana benthamiana* with overlapping data structures depending on GFLV infection status and the amino acid identity in the symptom determinant region of protein 1E$^{Pol*/Sd}$. (a) Principal component analysis (PCA) in three dimensional projections reveals minor grouping of viral strains; **(b)** PCA is 90 degrees shifted about the z-axis to show more of the data structure (star shape highlights the same side between a and b). **(c)** Correlation analysis of RSA traits with major grouping of diameter traits versus network traits (Pearson's correlation, $p < 0.05$ *, $p < 0.01$ **, $p < 0.001$ ***). Plotting normalized, z-score adjusted RSA traits of **(d)** average diameter (mm), **(e)** number of branch points, **(f)** number of root tips, **(g)** surface area (mm^2), and volume (mm^3) shows differences amongst viral treatment types (number of individuals, n is displayed above panel d, paired-Wilcox test in each panel d-h, p-values 0.05, 0.01,0.001, 0.0001; *, **, ***, ****).

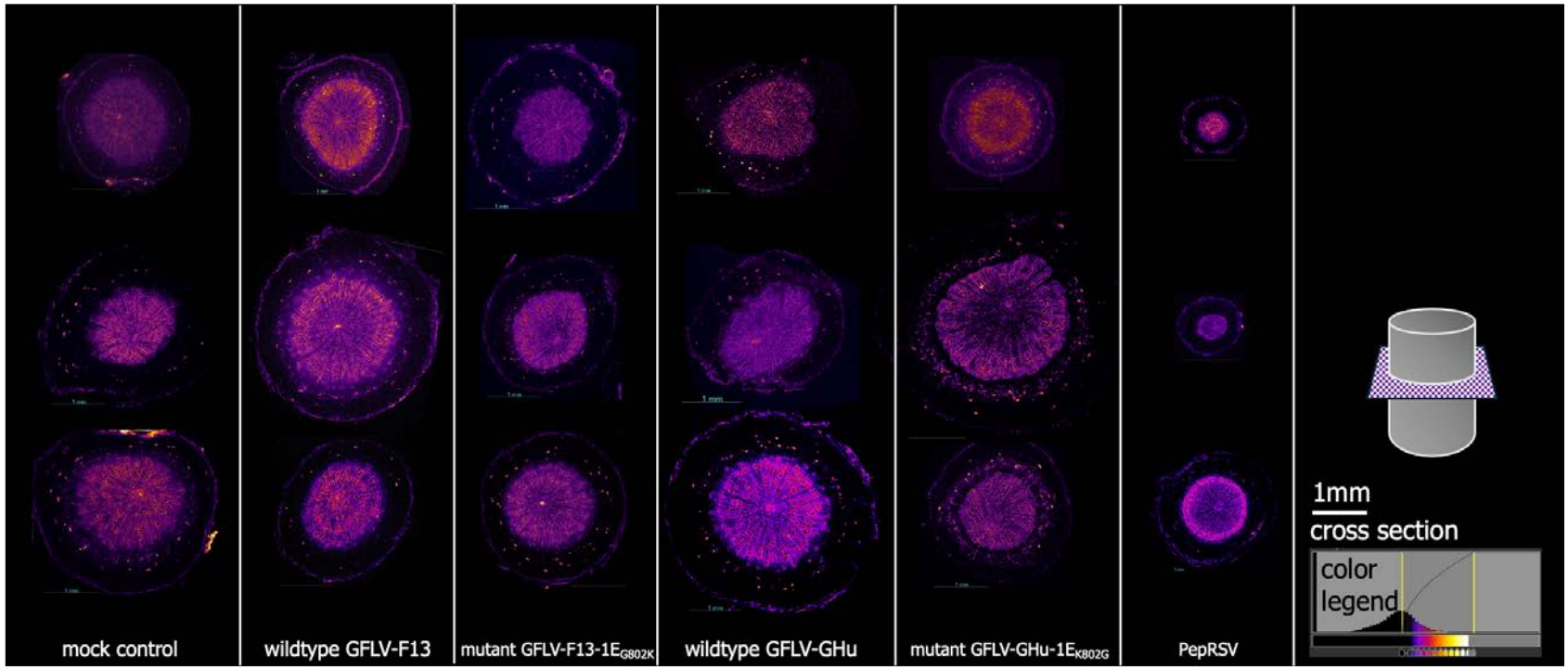

FIGURE 6-4. Root cross section images of *Nicotiana benthamiana* plants infected with wildtype grapevine fanleaf virus (GFLV) strains GHu and F13, mutants GFLV-GHu 1E$_{K802G}$ and GFLV-F13 1E$_{G802K}$, and pepper ringspot virus (PepRSV). Treatments shown per column of images from left to right as mock inoculated controls, plants infected with wildtype GFLV-F13, mutant GFLV-F13-1E$_{G802K}$, wildtype GFLV-GHu, mutant GFLV-GHu-1E$_{K802G}$, and PepRSV. Relative intensity of pixel is correlated to iodine stain intensity and was standardized by midpoint calculations as shown by the color legend thresholding window (bottom right) in Dragonfly software (Object Research Systems, v2022.2).

Modeling RSA traits confirmed the causative role of the C-terminus of protein $1E^{Pol*/Sd}$ in root phenotypes

Statistical modeling approaches were used to test the impact of GFLV strain on root traits. Analysis of RSA traits utilized non-adjusted and non-normalized data. RSA traits were modeled with the explanatory variables of amino acid identity at positions 802 and 804 of protein $1E^{Pol*/Sd}$, their respective interactions (802*804), age of the plants, viral infection status (GFLV, PepRSV, or none), virus strain, tag (V5 epitope or none), and dpi. The variables `cohort` and `plant` denote experiment number and individual identifier per experiment. These variable predictors were represented as a linear model in the following equation:

$$RSA\ Trait = \text{`}1E\ 802\ identity\text{`} * \text{`}1E\ 804\ identity\text{`} + Background + age + dpi + Tag + Virus + (1\ |cohort/plant)$$

Significant modifications of root tip number by 43% ($p < 0.0001$) and average diameter ($p < 0.0001$) were observed for wildtype and mutant GFLV-F13 strains based on the identity of amino acid in position 802 of protein $1E^{Pol*/Sd}$. The modification of residue 804 also significantly modified these traits for the two GFLV-F13 strains by up to 34% ($p = 0.0019$). Similarly, the number of root tips increased by up to 68.5% when changing the native 802 residue but not the 804 residue ($p < 0.0001$), and modification of both residues lessened that effect to 37.3% ($p = 0.0005$) for wildtype and mutant GFLV-GHu strains. Overall, linear modeling showed consistent significance of both amino acids at positions 802 and 804 of protein $1E^{Pol*/Sd}$ on root tip number and average diameter, suggesting that these two residues, or this region of the C-terminal end of

protein $1E^{Pol*/Sd}$ that contains these two residues, may have a combined function for eliciting root symptoms. Together with ROS production in leaf tissue, root phenotyping contextualizes previous findings of GFLV protein $1E^{Pol*/Sd}$ residue 802 being necessary but not sufficient for vein clearing symptoms in leaves (Roy and Fuchs 2024).

X-ray tomography revealed callose deposition and modified cell walls in roots of symptomatic, GFLV-infected plants

To analyze *N. benthamiana* roots in a non-destructive manner, root sections were stained with iodine and cross-sections were imaged. Iodine binding to lignified tissue, from callose deposition and modifications of cell walls, is a visualization of the host response to limit virus movement. Scan voxel size (3D pixel length, width, and height) ranged from 3.33 µm to 5.12 µm. Two dimensional cross sections of roots were visualized by correcting the XY coordinate view to look down the stem towards the root system and observed the distribution of the stele (xylem and phloem), pericycle, cortex, parenchyma cells, and epidermis in the primary roots (Figure 6-4). The primary vasculature bundle of the primary root retained the iodine stain the best, as visualized from both cross sections and 3D top views of root scans (Figure 6-4). Roots of non-infected plants had overall darker vascular bundles, indicating less iodine binding (Figure 6-4), while roots of plants infected with GFLV strains showed a variable distribution and intensity of iodine staining across the vasculature. Overall, wildtype GFLV-GHu and mutant GFLV-F13 $1E_{G802K}$ retained higher intensity pixels across all vasculature tissue while wildtype GFLV-F13 and mutant GFLV-GHu $1E_{K802G}$ retained overall less intensity pixels that were more concentrated towards the pericycle. Roots of plants infected with PepRSV retained a very bright display of pixels bordering the

pericycle. These results suggested that residue 802 of GFLV protein $1E^{Pol*/Sd}$ is involved in modulating lignin production.

By taking the cross sections and outlining the vasculature and overall root structure, circumference and area measurements were acquired for each sample (Table 6-S6). While numeric differences were apparent, differences between GFLV-infected plants and non-infected plants were not statistically supported through ANOVA or t-test (Figure 6-S4).

Inositol reduces GFLV infection rates and symptom expression

Treatment of *N. benthamiana* leaves with myo-inositol for seven consecutive days prior to inoculation resulted in reduced rates of infection in a dose dependent manner for wildtype and mutant GFLV-GHu strains (Table 6-1), although a reduction at 10 mM inositol and a return to baseline at 25 mM inositol was observed for mutant GFLV-F13 $1E_{G802K}$. The severity of vein clearing symptom expression (Figure 6-5a-c) and percent of plants displaying symptoms over time (Figure 6-5d-e) was myo-inositol dose dependent for symptomatic GFLV strains, including wildtype GFLV-GHu. In addition, instead of one or two leaves displaying symptoms, up to nine leaves displayed symptoms when myo-inositol was applied to wildtype GFLV-GHu inoculated plants (data not shown). As expected, foliar application of myo-inositol did not result in phenotypic changes for mock inoculated plants. In contrast, treatment with myo-inositol for seven days following inoculation resulted in decreased infection rates across all GFLV strains tested, as well as decreased visual symptoms and decreased longevity for wildtype GFLV-GHu symptoms, although not consistently dose-dependent (Table 6-1). These results revealed that the application of inositol affects the rate of GFLV infection

and symptom severity in *N. benthamiana* and validated previous hypotheses derived from proteomics and transcriptomics studies (Roy et al. 2023; Roy and Fuchs 2024).

Phytohormones affect GFLV infection and modify symptom expression

Foliar application of salicylic acid (SA) delayed symptom expression by about two days in plants infected with wildtype GFLV-GHu but increased the proportion of plants displaying symptoms for 8-16 days (Table 6-2, Figure 6-5f). Vein clearing phenotypes were observed in all *N. benthamiana* plants infected with wildtype GFLV-GHu, however the intensity was greatly increased with SA applications (Figure 6-5l,m). Necrotic lesions were observed for several, but not all wildtype GFLV-F13 infected *N. benthamiana* plants when SA was applied (Figure 6-5n). Application of abscisic acid (ABA) largely reduced symptom persistence (Table 6-3), sometimes clearing infection that was symptomatic in lower leaves with undetectable GFLV in apical leaves, as shown by DAS-ELISA (Figure 6-5f). Phenotypes of leaf cupping or curling were apparent in all plants treated with ABA (Figure 6-5g,i,k) and occasionally necrotic lesions would appear for plants infected with wildtype GFLV-F13 and GFLV-F13 mutant $1E_{G802K}$ (Figure 6-5j). Vein-clearing phenotypes were not produced from strains that are observed to typically be asymptomatic. These results revealed that phytohormones affect the rate of GFLV infection and symptom production in *N. benthamiana* and validated previous hypotheses (Roy et al. 2023; Roy and Fuchs 2024).

TABLE 6-1. Grapevine fanleaf virus (GFLV) infection rates in apical leaves of myo-inositol treated *Nicotiana benthamiana* plants.

	Cohort 1 (*n=142*) treated *prior* to inoculation			**Cohort 2 (*n=105*) treated *post*-inoculation**			**Cohort 3 (*n=131*) treated *post*-inoculation**		
	Inositol conc. (mM)			**Inositol conc. (mM)**			**Inositol conc. (mM)**		
Viral treatment	**0**	**10**	**25**	**0**	**10**	**25**	**0**	**10**	**25**
wildtype GFLV-GHu	66% (10/15)[a]	53% (8/15)	55% (12/22)	47% (7/15)	47% (7/15)	6% (1/15)	27% (3/11)	0% (0/11)	0% (0/11)
wildtype GFLV-F13	nt	nt	nt	50% (5/10)	0% (0/10)	60% (6/10)	20% (2/10)	0% (0/11)	18% (0/11)
mutant GFLV-GHu 1E$_{K802G}$	47% (7/15)	40% (6/15)	26% (4/15)	nt	nt	nt	nt	nt	nt
mutant GFLV-GHu 1E$_{K802R}$	nt	nt	nt	nt	nt	nt	64% (7/11)	36% (4/11)	27% (3/11)
mutant GFLV-F13 1E$_{G802K}$	60% (9/15)	47% (7/15)	60% (9/15)	nt	nt	nt	nt	nt	nt
mutant GFLV-F13 1E$_{G802K + N804S}$	nt	nt	nt	nt	nt	nt	73% (8/11)	27% (3/11)	36% (4/11)
mutant GFLV-GHu 1E:V5	nt	nt	nt	90% (9/10)	60% (6/10)	40% (4/10)	nt	nt	nt

[a]Fractions indicate the number of plants testing positive for GFLV in DAS-ELISA over the total number of plants tested
nt: not tested

TABLE 6-2. Grapevine fanleaf virus (GFLV) infection in apical leaves of phytohormone-treated *N. benthamiana* plants.

	Cohort 1 (*n=180*)			Cohort 2 (*n=165*)		
Viral treatment	*H_2O*	*ABA*[a]	*SA*[b]	*H_2O*	*ABA*	*SA*
wildtype GFLV-GHu	27% (4/15)c	27% (4/15)	53.3% (8/15)	29% (6/21)	24% (5/21)	55% (11/20)
wildtype GFLV-F13	53% (8/15)	13% (2/15)	53% (8/15)	nt	nt	nt
mutant GFLV-GHu $1E_{K802G+S804N}$	nt	nt	nt	nt	29% (6/21)	67% (14/21)
mutant GFLV-GHu $1E_{K802R}$	73% (11/15)	20% (3/15)	67% (10/15)	nt	nt	nt
mutant GFLV-F13 $1E_{G802K}$	nt	nt	nt	80% (16/20)	70% (14/20)	67% (14/21)
mock inoculated	0% (0/15)	0% (0/15)	0% (0/15)	nt	nt	nt

[a]ABA: Abscisic acid applied at 50 µM
[b]SA: Salicylic acid applied at 50 µM
[c]Fractions indicate the number of plants testing positive for GFLV in DAS-ELISA over the total number of plants tested
Nn: not tested

TABLE 6-3. Average persistence of symptomology for grapevine fanleaf virus (GFLV) strain GHu in phytohormone-treated *Nicotiana benthamiana* plants.

Viral treatment	***Hormone treatment***	**Cohort 1** Persistence (days showing symptoms/plant infected)[a]	**Cohort 2**
Wildtype GFLV-GHu	*H_2O*	10.8 ± 3.49	12.83 ± 2.17
	ABA	8.25 ± 6.18	7.40 ± 1.52
	SA	9.25 ± 4.09	7.73 ± 2.24

[a]The average days showing symptoms is shown with one standard deviation.

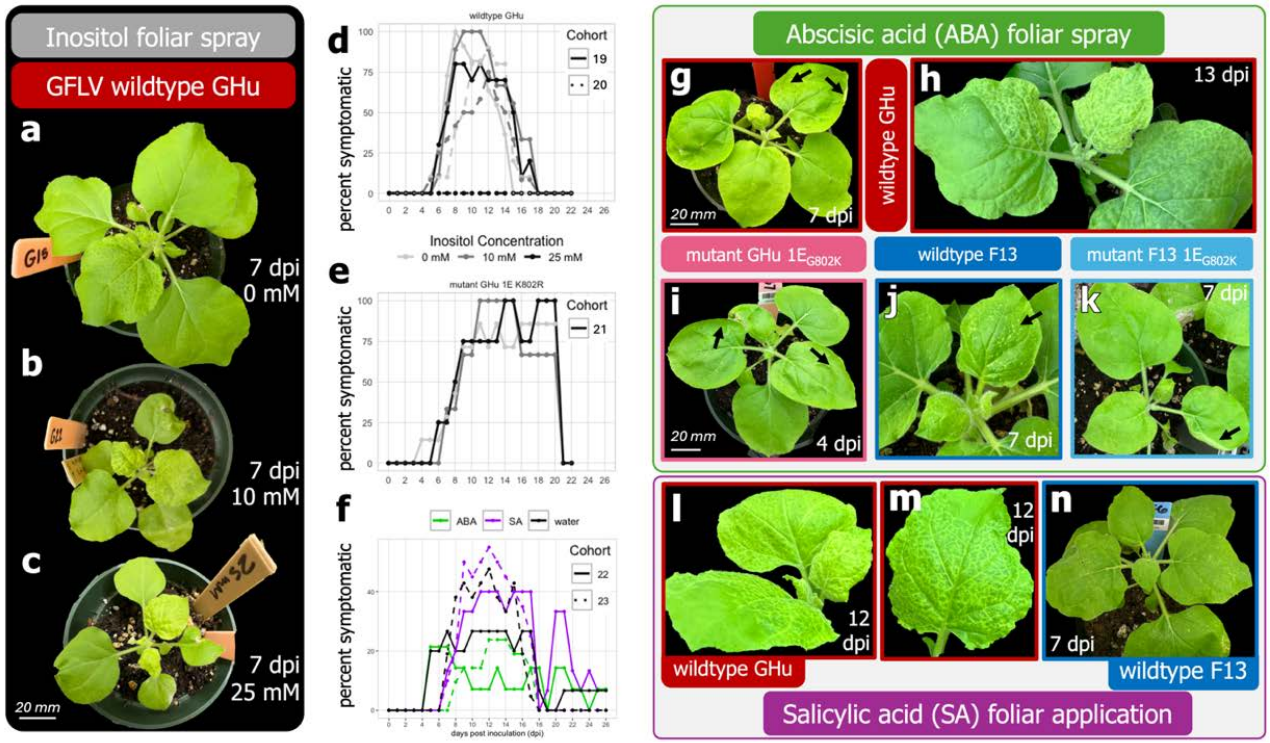

FIGURE 6-5. Effect of foliar application of signaling molecule inositol and phytohormones abscisic acid (ABA) and salicylic acid (SA) on the expression of vein clearing symptoms upon grapevine fanleaf virus (GFLV) infection in *Nicotiana benthamiana*. (a-c) With increasing concentration of myo-inositol, an increased intensity of vein clearing is visible on plants infected with wildtype GFLV-GHu at 7 dpi, however, **(d)** no increased longevity or proportion of plants displaying symptoms were apparent. **(e)** A similar trend was observed for mutant GFLV GHu 1E$_{K802R}$. **(f)** The application of salicylic acid (SA) increased the proportion and longevity for plants displaying symptoms when infected with wildtype GFLV strain GHu, while abscisic acid (ABA) had the opposite effect. In addition to typical vein clearing **(h),** leaf cupping was frequently observed in ABA-treated GFLV-infected plants (black arrows, **g,i,k**), while necrotic lesions also appeared across all treatments in non-inoculated apical leaves (black arrow, **j**). Vein-clearing appeared more severe under SA treatment (**l,m**), but was not induced for GFLV-F13 infected plants **(n)**. Non-infected plants did not display any symptoms (not pictured).

FIGURE 6-6. Four 'omics datasets on grapevine fanleaf virus (GFLV) in *Nicotiana benthamiana* provide insights on virus host-interactions (Osterbaan et al. 2021; Roy et al. 2023; Roy and Fuchs 2024). (a) Identified proteins in GFLV-1E:V5 epitope pull-downs of leaf proteins across three different viral strains contrast (Osterbaan et al. 2021) with expanded time point collections in leaf tissue in **(b)** shotgun proteomics (Roy et al. 2023) and **(c)** 3'RNA-Seq approaches (Roy et al. 2023). **(d)** 3'RNA-Seq was also employed to analyze the differences between root phenotypes in GFLV-GHu strains (Roy and Fuchs 2024). **(e)** A circular chord diagram was modified to display matching overlap of 'omics datasets for grapevine fanleaf virus symptomology studies in *N. benthamiana*. The outer ring denotes the relative size of enriched or differentially abundant transcripts or proteins, compared with mock control plants at different days post-inoculation (dpi), colored and separated by dataset origin. The inner ring denotes the viral treatment group for infected *N. benthamiana* and time post inoculation (white number). Ribbons connecting each dataset signify identical genes detected in both groupings, and blue/red ribbons are that of matching viral treatments. (**f**) Upset plots of intersecting contrasts across leaf transcriptomics work and (**g**) root transcriptomics work and again seen contrasted through Venn diagrams for (**h**) leaf transcriptomics at 4-, 7-, and 12 dpi and for (**i**) root transcriptomics at 4-, 17-, and 26 dpi. Colors are respective to GFLV strains (i.e. maroon for wildtype GHu, red for mutant GHu $1E_{K802G}$, dark blue for wildtype F13, and light blue for mutant F13 $1E_{G802K}$.)

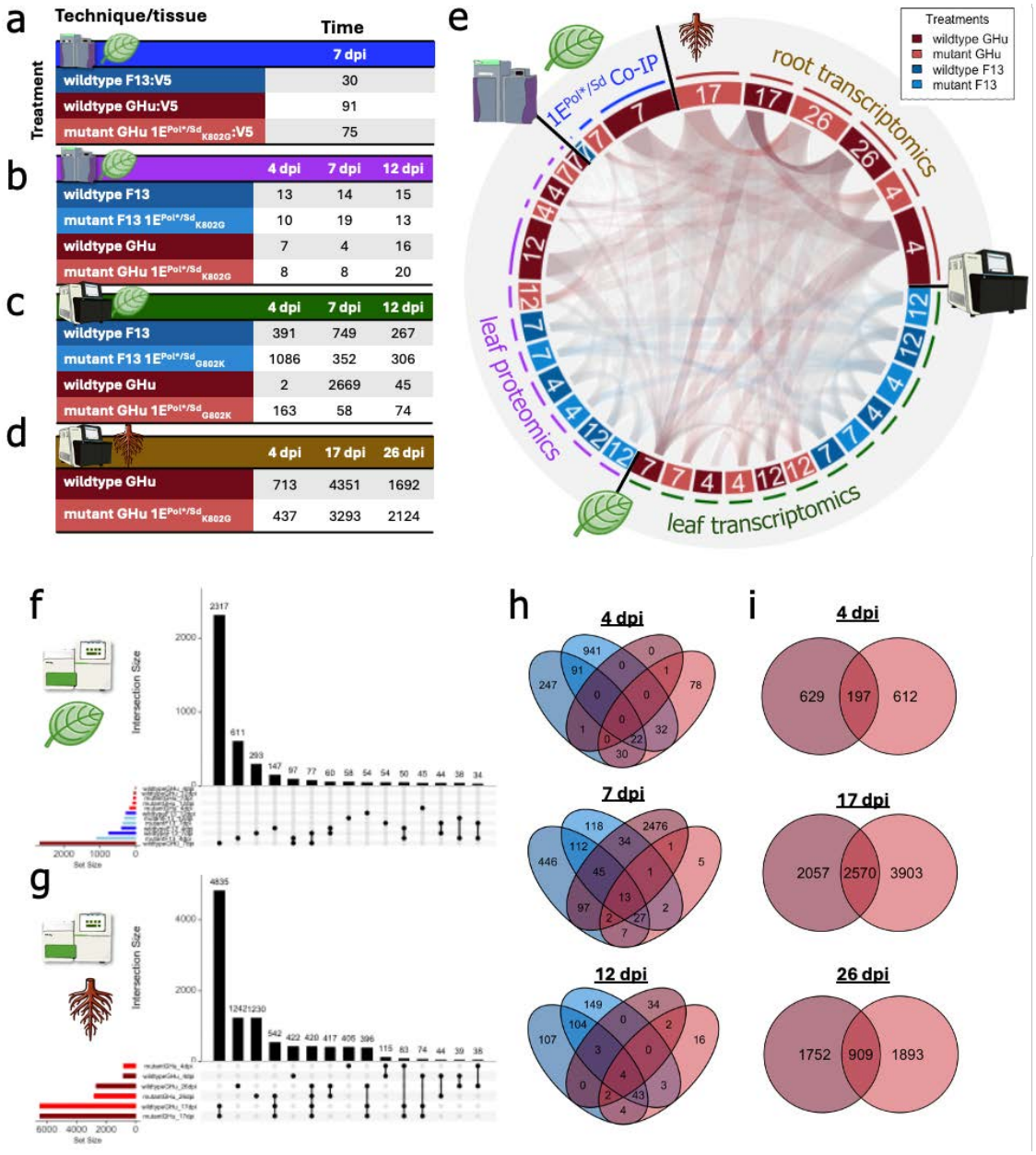
a
Technique/tissue
Time
Treatment
7 dpi
wildtype F13:V5
30
wildtype GHu:V5
91
mutant GHu 1E^Pol*/Sd_K802G:V5
75
b
4 dpi
7 dpi
12 dpi
wildtype F13
13
14
15
mutant F13 1E^Pol*/Sd_K802G
10
19
13
wildtype GHu
7
4
16
mutant GHu 1E^Pol*/Sd_K802G
8
8
20
c
4 dpi
7 dpi
12 dpi
wildtype F13
391
749
267
mutant F13 1E^Pol*/Sd_G802K
1086
352
306
wildtype GHu
2
2669
45
mutant GHu 1E^Pol*/Sd_G802K
163
58
74
d
4 dpi
17 dpi
26 dpi
wildtype GHu
713
4351
1692
mutant GHu 1E^Pol*/Sd_K802G
437
3293
2124
e
Treatments
wildtype GHu
mutant GHu
wildtype F13
mutant F13
1E^Pol*/Sd Co-IP
root transcriptomics
leaf proteomics
leaf transcriptomics
f
Intersection Size
Set Size
g
Intersection Size
Set Size
h
4 dpi
7 dpi
12 dpi
i
4 dpi
629
197
612
17 dpi
2057
2570
3903
26 dpi
1752
909
1893

Processing and comparative analysis of omics datasets

Previous transcriptomic and proteomic datasets on GFLV-*N. benthamiana* interactions (Osterbaan et al. 2021; Roy et al. 2023; Roy and Fuchs 2024) were re-processed for a more granular understanding of mechanisms of symptom expression upon GFLV infection (Figure 6-S7). Extracting host protein interactants of GFLV protein $1E^{Pol*/Sd}$ across three GFLV strains resulted in 30, 81, and 75 host proteins from co-immunoprecipitation tandem mass spectrometry data (Figure 6-6a). All viral contrasts in the time-course proteomic and transcriptomic work in leaves (wildtypes GFLV-F13 and -GHu, mutants GFLV-F13 $1E_{G802K}$ and -GHu $1E_{K802G}$) were re-analyzed against mock control plants to produce differentially abundant proteins (DAPs) ranging from four to 20 in high confidence, and differentially abundant transcripts (DATs) from two to 2,669 (Figure 6-6b-c). The transcriptomics work in root tissue (wildtype GFLV-GHu and mutant GFLV-GHu $1E_{K802G}$) resulted in 437 to 4,351 DATs detected, with a lower confidence threshold placed to account for variance across this difficult to standardize and compare tissue type (Figure 6-6d).

Many common dysregulated genes were identified, as visualized on a modified circos plot (Figure 6-6e, Supp File X. *Shared Gene Identities*). Further comparative analysis of transcriptomics work was conducted through upset plots of leaf (Figure 6-6f) and root tissue (Figure 6-6g), which indicated an overwhelmingly large number of dysregulated transcripts for wildtype GFLV-GHu, but an overlap between all categories upon GFLV infection regardless of the viral strain. This was further visualized for leaf (Figure 6-6h) and root (Figure 6-6i) transcriptomes at different time points. The complementary nature of these omics datasets justified pursuing more detailed

mechanistic underpinnings of GFLV infection and symptom development by gene set enrichment analysis (GSEA) and KEGG grouping of gene sets.

GFLV protein 1E$^{Pol*/Sd}$ predictably interacts with host proteins and modifies host expression

To elucidate pathways important to the function of GFLV protein 1E$^{Pol*/Sd}$, the first focus was placed on the proteins identified in co-immunoprecipitation experiments (Osterbaan et al. 2021). In plants infected with symptomatic GFLV-GHu, six host proteins were found to be enriched with statistical support when comparing spectral counts: Plastid transcriptionally active 14 SET domain protein, Splicing factor 3B subunit 1, Dynamin-related protein 5A, WD40 domain-containing protein, Translation initiation factor IF-2, and P-type ATPase PMA1 (Table 6-4). These data were consistent with previous results[27]. The expression of the transcripts corresponding to these proteins in shoot and root tissue of GFLV-infected *N. benthamiana* plants was confirmed (Figure 6-S8). Translation initiation factor IF-2 was substantially downregulated for wildtype GFLV-GHu at 7 dpi in leaves but upregulated in root tissue at 4 and 17 dpi. P-type ATPase (PMA1) was observed in higher abundance at earlier infection time points for both wildtype GFLV-GHu and mutant GFLV-F13 1E$_{G802K}$ in leaf tissue, as well as upregulated in root tissue for wildtype GFLV-GHu. Plastid transcriptionally active 14 was significantly enriched in wildtype GFLV-GHu:V5 plants (4.33 spectral counts) when compared with other treatments of ≤1.33 spectral counts.

TABLE 6-4. Summary of genes corresponding to putative host protein interactants of GFLV protein 1E$^{Pol*/Sd}$ through co-immunoprecipitation assays (Osterbaan et al. 2021) and their subcellular localization.

Grouping	Gene ID (Niben101)	Name	[e]Subcellular localization/complex
[a]Statistical support for enrichment in wildtype GFLV-GHu 1E:V5 pulldowns	Niben101Scf01006g03016	Dynamin-related protein 5A	Cytoplasm/membrane
	Niben101Scf00593g01002	P-type ATPase (PMA1)/ ATPase 3	Plasma membrane
	Niben101Scf03607g00009	Plastid transcriptionally active 14 SET domain protein	Chloroplast
	Niben101Scf06128g00004	Splicing factor 3B subunit 1	Spliceosome
	Niben101Scf01814g05011	Transducin/WD40 domain-containing protein	Chloroplast
	Niben101Scf04225g02007	Translation initiation factor IF-2	Chloroplast
[b]Detected in all GFLV 1E:V5 pulldowns	Niben101Scf09512g04024	NAD(P)-binding Rossmann-fold superfamily protein	Cytoplasm/microtubules
	Niben101Scf04328g00049	Photosystem II D2 protein	Chloroplast
	Niben101Scf03607g00009	Plastid transcriptionally active 14 SET domain protein	Chloroplast
	Niben101Scf02622g10003	Pyruvate kinase family protein	Cytoplasm
	Niben101Scf06128g00004	Splicing factor 3B subunit 1	Spliceosome
	Niben101Scf03693g01008	Succinate dehydrogenase flavoprotein subunit	Mitochondria
[c]Detected in all GFLV 1E:V5 pulldowns except wildtype GFLV-GHu	Niben101Scf01374g15012	Acid phosphatase 1	Unknown
	Niben101Scf04007g01012	Cathepsin B-like cysteine proteinase	Extracellular space/lysosome
	Niben101Scf07008g03009	Chaperone DnaJ-domain superfamily protein	Cytoplasm/vesicles (Auxillin)
	Niben101Scf02373g04023	Serine/arginine-rich splicing factor 12 (SC35-like)	Nucleus
	Niben101Scf00595g02005	Short-chain dehydrogenase/reductase 2b	Chloroplast
	Niben101Scf01341g03006	[d]Unknown protein	Unknown

[a]Spectral counts of six host proteins were statistically enriched in comparison to other tagged and untagged samples (Osterbaan et al. 2021).
[b]Proteins identified in all viral tagged isolates, minus any background proteins from untagged samples.
[c]Proteins identified in wildtype F13 $1E_{c\text{-}1}$:V5 and mutant GHu $1E_{K802G}$:V5 affinity purification samples, but not present in wildtype GHu 1E:V5 samples.
[d]MotifFinder returns low confidence result of G-protein coupled receptor that interacts with parathyroid hormone and other factors (cd15263, e-value of 9.2).
[e]Extracted from genome annotation or from NCBI BLAST closest homologue

In all viral treatments (wildtype GFLV-GHu 1E:V5, wildtype GFLV-F13 1E:V5, and mutant GFLV-GHu $1E_{K802G}$:V5), eight additional protein clusters were enriched; GFLV protein $2B^{Hel/VSR}$, GFLV protein $1D^{Pro}$, pyruvate kinase family protein, plastid transcriptionally active 14, succinate dehydrogenase flavoprotein subunit, photosystem II D2 protein, splicing factor 3B subunit 1, and NAD(P)-binding Rossmann-fold superfamily protein . The expression of the genes corresponding to these proteins was extracted from the other omics datasets, validating their identification. The only exceptions were the GFLV genes and photosystem II D2 protein, which were undetected (Figure 6-S8). Of particular interest, the pyruvate kinase family protein was upregulated in root tissue early in infection (4 dpi) but was less abundant in leaf tissue for several GFLV strains.

Proteins found in other GFLV 1E:V5 co-immunoprecipitation pull-downs, except for wildtype GFLV-GHu 1E:V5, were considered (Table 6-4). These proteins included acid phosphatase 1, Cathepsin B-like cysteine proteinase, chaperone DnaJ-domain superfamily protein, serine/arginine-rich splicing factor 12, short-chain dehydrogenase/reductase 2b, and an unknown protein. These proteins lacked statistical differences in treatments but were different from non-tagged treatments. Gene enrichment analysis was performed on the six resulting possible contrasts (each of the three individual treatments plus the overlapping combinations). First, proteins enriched by all three GFLV:V5 tagged strains included KEGG terms of pyruvate kinase (K00873) and photosystem II CP43 chlorophyll apoprotein (K02705). Second, asymptomatic infections of GFLV (wildtype F13 and mutant GHu $1E_{K802G}$) showed enrichment of four KEGG terms; replication factor C subunit 3/5 (K10756), cofilin

(K05765), eukaryotic translation initiation factor 2C (K11593), and endoglucanase (K01179). For symptomatic infection in wildtype GFLV-GHu 1E:V5, the most abundant number of enriched terms was found at 19 KEGG categories. Of note were ribosomal proteins (K02937), fructose-1,6-bisphosphatase I (K03841), lipoxygenases (K15718, K00454), pyruvate kinase (K00873), and reticulon proteins (K20721, K20723, K20720). KEGG ontologies shared between wildtype GFLV-GHu and mutant GFLV-GHu $1E_{K802G}$:V5 pulldowns included F-type ATPase subunit beta (K02112), DNA-directed RNA polymerase subunit beta (K03043), cell division protease FtsH (K03798), glycine hydroymethyltransferase (K00600), clathrin coat assembly protein AP180 (K20043), myosin V (K10357), and thioredoxin (K03671) (Table 6-S7C). GFLV-GHu mutant $1E_{K802G}$:V5 alone showed enrichment of H+ antiporter (K07300), far upstream element-binding protein (K13210), histone H1/5 (K11275), F-type ATPase subunit alpha (K02111), beta-glucosidase (K05349), heterogenous nuclear ribonucleoprotein A1/A3 (K12741), potassium channel (K21867), and mitochondrial mTERF domain-containing protein (K15032) (Table 6-S7C). Analyzing the temporal transcript expression profiles for these host proteins provided a wider range of potential interactants for GFLV $1E^{Pol*/Sd}$ to elicit symptoms than previously reported. Further, these proteins were predicted to be in various subcellular compartments, either through direct annotations (Bombarely et al. 2012) or identified homologues (Table 6-4). The locations of these putative host interactors of GFLV $1E^{Pol*/Sd}$ correlated to the dysregulation of bulk transcriptome profiling in apical leaves and roots during GFLV infection.

GFLV induces transcriptome-wide changes across tissue types over the course of infection

A follow up analysis on the transcriptomic data was necessary to track the regulation of transcript production over time against mock inoculated control plants. For plants infected with wildtype GFLV-GHu, 2, 2269, and 45 transcripts were detected as differentially abundant at 4-, 7-, and 12 dpi (Figure 6-5c). This was confirmatory to the drastic difference in phenotype observed at 7 dpi for wildtype GFLV-GHu infected plants. For asymptomatic strains mutant GFLV-GHu $1E_{K802G}$, wildtype GFLV-F13, and mutant GFLV-F13 $1E_{G802K}$ there were 163, 58, and 74 transcripts, 391, 749, and 267 transcripts, and 1086, 352, and 306 transcripts detected as differentially abundant at 4-, 7-, and 12 dpi, respectively. An overlap between omics datasets was observed at differing levels, dependent upon time, GFLV strain, and acquisition type (Figure 6e, Table 6-S8). When comparing transcript abundance in leaves of plants infected with wildtype GFLV-GHu and mock control, a set of 3,667 DATs was identified. For the same contrast in roots, a set of 4,627 DATs was identified. For these two datasets, 659 common DATs were found (Table 6-5). In the comparison of mutant GFLV-GHu-$1E_{K802G}$ to mock control, 117 DATs overlapped between roots and shoots, 3,883 DATs were root-specific, and 847 DATs were leaf-specific (Table 6-5).

TABLE 6-5. Comparative differential abundance of transcripts in apical leaves and roots of *Nicotiana benthamiana* infected with grapevine fanleaf virus (GFLV) strains GHu and F13. High amounts of unique transcript abundance per tissue type were observed with large amounts of overlap according to treatment contrast. GFLV-infected apical leaf transcriptomic data were extracted (Roy et al. 2023) and gene identifiers matching *p*-value < 0.05 and absolute Log2FoldChange > 1 were counted against mock inoculated controls at 7 days post inoculation (dpi). Similarly, root transcriptomic data were parsed for the number of differentially abundant genes in contrasts against mock controls at 17 dpi (Roy and Fuchs 2024). A total of 28,001 gene IDs were identical between the two datasets at ≥1 count per sample.

Tissue type			**Root tissue (17 dpi)**	
	Treatment contrast versus mock		**wildtype GFLV-GHu**	**mutant GFLV-GHu 1E$_{K802G}$**
		DATs	4,627 (1,670)[a]	3,883 (1,201)
Apical leaf (7 dpi)	**wildtype GFLV-GHu**	3,667 (246)[a]	**659**[b]	334
	mutant GFLV-GHu 1E$_{K802G}$	847(63)	146	**117**[b]
	wildtype GFLV-F13	2,105 (135)	365	344
	mutant GFLV-F13 1E$_{G802K}$	1,457 (88)	265	254

[a]Total number of genes differentially abundant with the number of genes unique to the apical leaves or roots in parentheses.
[b]Gray highlighted boxes show two treatment contrasts of interest for GFLV-GHu and mutant GFLV-GHu 1E$_{K802G}$.

A gene set enrichment analysis on the 659 DATs (Table 6-5) revealed six terms significantly over-represented to include response to inorganic substance (GO:0010035), response to zinc ion (GO:0010043), regulation of reactive oxygen species metabolic process (GO:2000377 and GO:2000379), obsolete iron ion homeostasis (GO:0055072), and manganese ion transport (GO:0006828). With these terms being represented in the two datasets alone, it was not surprising to see them again in the overlap.

Different contrasts were considered to further understand the host response to GFLV infection over time. The first contrast considered was mutant GFLV-F13 $1E_{G802K}$ at 4 dpi since an overabundant number of dysregulated genes was present at this time point (605 up and 481 down). Of the upregulated genes, only ko:K07375 corresponding to tubulin beta was found through KEGG analysis. No gene ontologies of significance were identified as overabundant. Of the downregulated transcripts, 13 KEGG terms were found to be significantly abundant. These included 4-coumarate--CoA ligase (K01904), solute carrier family 25 (mitochondrial carnitine/acylcarnitine transporter) (K15109), 3-deoxy-7-phosphoheptulonate synthase (K01626), phosphoenolpyruvate carboxylase (K01595), aquaporin PIP (K09872), hydroquinone glucosyltransferase (K08237), ammonia-lyase (K10775), phenylalanine/tyrosine ammonia-lyase (K13064), solute carrier family 15 (peptide/histidine transporter) (K14638), E3 ubiquitin-protein ligase RFWD2 (K10143), jasmonic acid-amino synthetase (K14506), mechanosensitive ion channel protein (K22048), and ferric-chelate reductase (K00521) (Table 6-S11A). Further, similarly named gene ontologies were significant and overabundant to include response to karrikin (GO:0080167), small molecular biosynthetic process

(GO:0044283), trans-cinnamate 4-monooxygenase activity (GO:0016710), secondary metabolic process (GO:0019748), and inositol biosynthetic process (GO:0006021), amongst 40 others (Table 6-S11B). These dysregulated genes are involved in the repression of precursors for lignin deposition, inositol biosynthesis, and the shikimate pathway (explored further in Figures 6-S9, S10).

The lipid signaling molecule pathways were further explored by dissecting the inositol immune signaling cascade, which is more known as the PI3K cascade, a general innate immune response (Figure 6-S10). A differential abundance of transcripts in various steps in the PI3K pathway directly linked to ROS production previously identified was observed (Roy and Fuchs 2024) (Figure 6-S10). Further, cumulative counts of transcripts for enzymes in the callose and lignin deposition pathways revealed the consistent downregulation of phenylalanine ammonia-lyase, cinnamate 4-hydroxylase, 4-coumarate:CoA ligase, hydroxycinnamoyl-CoA shikimate transferase, cinnamoyl-CoA reductase, and cinnamyl alcohol dehydrogenase (Figure 6-S10). The activation of this cascade is frequently correlated with callose deposition in other virus-host interaction studies (Feng et al. 2024; Góra-Sochacka et al. 2019).

Total cumulative transcript counts showed the perturbed expression of three key genes in the signaling cascade, including phosphatidylinositol synthase, inositol monophosphatase, and protein kinase c (Figure 6-S9). The downregulation of these terms contained some overlap with downregulated terms of wildtype GFLV-GHu at 7 dpi, where vein clearing symptoms peak and begin to fade on leaves. For KEGG analysis, 30 terms were upregulated, and 22 terms were downregulated. Of the upregulated terms, 14 were large ribosomal subunits (L7e, L10Ae, L19e, L23e, L23Ae,

L24e, L30e, L32e, L35e, L36e, L37Ae, L44e, LP1, and LP2) and six were small ribosomal subunits (S4e, S6e, S8e, S15e, S15Ae, and S27e). Further upregulated KEGG terms included chaperonin GroEL, heterogeneous nuclear ribonucleoprotein A1/A3, elongation factor 1-alpha, mitochondrial Q subcomponent-binding protein, ribose 5-phosphate isomerase A, ferredoxin, CTP synthase, cold-inducible RNA-binding protein and endoribonuclease Dicer (Table 6-S11A). GSEA returned similar trends with 225 upregulated and 62 downregulated enrichment terms, and included many of the same ribosomal, signaling, and metabolic components identified through KEGG analysis (Table 6-S11B). The large transcriptome perturbations observed in wildtype GFLV-GHu were not matched by any other GFLV strain in leaf tissue.

Common trends amongst all GFLV-infected plants when compared to mock inoculated plants showed a significant upregulation of two terms at 12 dpi, regardless of the virus strain: cellular response to selenium (GO:0071291) and sulfate assimilation (GO:0000103). All asymptomatic plants at 12 dpi, but not wildtype GFLV-GHu, showed a significant downregulation of five overlapping terms: response to karrikin (GO:0080167), fatty acid desaturase 4 (delta 3-trans-hexadecenoic acid phosphatidylglycerol desaturase activity, GO:0052637), ketone biosynthetic process (GO:0042181) trans-cinnamate 4-monooxygenase activity (GO:0016710), and oxidoreductase activity (GO:0016491). These pathways highlighted differences in the downregulation of a host immune response by upregulating the assimilation of sulfate and selenium. It is possible that selenoproteins could sequester and neutralize ROS production, thereby preventing GFLV symptom expression. This hypothesis is bolstered by the predicted interaction of wildtype GFLV-GHu $1E^{Pol*/Sd}$ with ribosomal subunit

L7Ae of the 60S ribosomal subunit (Osterbaan et al. 2021), a factor in selenoprotein production (Labunskyy et al. 2014).

Together, a detailed analysis of dysregulated cellular pathways suggested that GFLV-F13 strains quickly suppress host immune responses in apical leaf tissue, while GFLV-GHu strains are less proactive in the initial stages of infection. Cellular dysregulations in the root transcriptome incurred more noise, but followed similar trends for expression of the host innate immune response. In addition, residue 802 of GFLV protein $1E^{Pol*/Sd}$ was correlated to how quickly the host response was turned off, although the exact mechanism cannot be determined from these data.

Structural and functional prediction analysis of GFLV protein $1E^{Pol*/Sd}$

The structure of protein $1E^{Pol*/Sd}$ of wildtype GFLV-F13 and -GHu, and their respective mutants at residue 802, ArMV, GDeV, and a GFLV consensus sequence was modeled using I-TASSER-MTD. Protein $1E^{Pol*/Sd}$ structural alignment to known structures ranged in overall TM-scores from 0.55 to 0.57, aligning extensively to the polymerase domain (Table 6-S12). The top resultant protein predictions are available at ModelArchive (https://modelarchive.org/) under accession numbers ma-6uzpp, ma-gl0zp, ma-gf9js, ma-75llk, ma-lniyd, ma-h4tyx and ma-pufyr.

From these predictions and previous phylogenetic analyses (Fuchs et al. 2017), GFLV protein $1E^{Pol*/Sd}$ shares similarities with ArMV and GDeV (Table 6-6) and up to five distinct globular domains. For wildtype GFLV strain F13, FUPred returned domain classification of the putative RdRP (D1, 1-465), D2 (466-696), D3 (679-696;775-824), D4 (697-741), and D5 (742-774). To contrast, wildtype GFLV strain GHu contained four predicted domains: the putative RdRP (1-465), D2 (466-685), D3 (686-783), and

D4 (784-824) (Table 6-6). D1 consistently returned RdRP domains and catalytic sites for RNA synthesis for all GFLV strains, with homologues detected in other ssRNA viruses, as anticipated (Figure 6-7a, Table 6-S12). Previous prediction analysis suggested multi-component subcellular localization patterns, with little indication of nuclear localization signals or transmembrane domains that are typical of viral polymerases and viral proteins involved in replication, respectively (Roy et al. 2024).

TABLE 6-6. Domain prediction of protein $1E^{Pol*/Sd}$ of grapevine fanleaf virus (GFLV), Arabis mosaic virus (ArMV), and grapevine deformation virus (GDeV). Four or five globular protein domains were identified in protein $1E^{Pol*/Sd}$, with high conservation of the first domain (RNA-dependent RNA polymerase) and second domain (predicted phosphatase).

Virus-strain	RdRP	Domain 2	Domain 3	Domain 4	Domain 5
ArMV	1-465	466-697	698-738	739-774	775-825
GFLV-F13	1-465	466-678	679-696;775-824	697-741	742-774
GFLV-F13 $1E_{G802K}$	1-465	466-678	679-696;775-824	697-741	742-774
GFLV-GHu	1-465	466-685	686-783	784-824	-
GFLV-GHu $1E_{K802G}$	1-465	466-685	686-783	784-824	-
GDeV	1-457	458-685	686-783	784-823	-

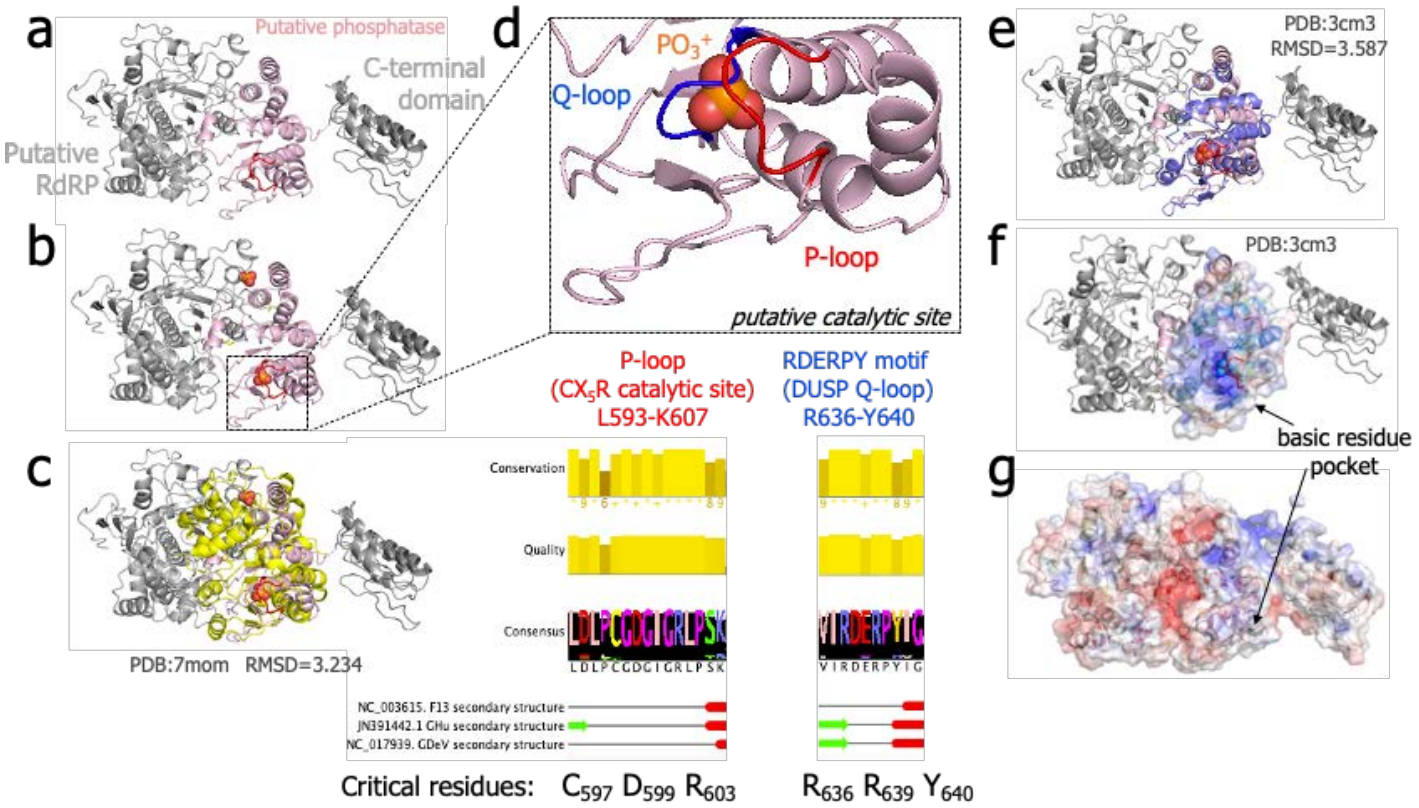

FIGURE 6-7. ***In silico*** **modeling of a structurally predicted, low sequence homology phosphatase domain in grapevine fanleaf virus (GFLV) protein 1E$^{Pol*/Sd}$.** **(a)** Globular domain profile of the putative RdRP at the N-terminus, putative phosphatase in the central domain, and C-terminal domain highlighted on I-TASSER-MTD prediction of protein 1E$^{Pol*/Sd}$ of wildtype GFLV-GHu. **(b)** Predicted ligand binding sites extracted from PDB:7MOM align with potential active sites in protein 1E$^{Pol*/Sd}$. **(c)** Pymol superalign function aligns PDB:7MOM to central phosphatase domain with RMSD=3.234. **(d)** The putative phosphatase catalytic site of GFLV protein 1E$^{Pol*/Sd}$ contains two structurally conserved features; the CX_5R catalytic cysteine and nucleophilic arginine in the P-loop, and the positively charged Q-loop (aa 636-640). **(e)** Evaluation of GFLV protein 1E$^{Pol*/Sd}$ against other homologs such as PDB:3CM3 display typical basic residues present at the catalytic pocket in **(f)** and **(g)** with electrostatic surface potential displayed.

Queried protein $1E^{Pol*/Sd}$ sequences returned consistent results for domain 2 (Figure 6-7a, pink). This domain is a newly predicted phosphatase domain, which is not yet documented for GFLV or any other nepoviruses. Structure 5XW4, referred to as protein phosphatase Cdc14p, yielded the highest confidence alignment in all submitted structures (TM ≥ 0.66, Table 6-S13) (Kobayashi and Matsuura 2017). Structure 1OHE (Gray et al. 2003) is also a phosphatase within the Cdc14b classification (TM ≥ 0.65). These two structures represented the top two hits for each of the predicted structures and were both isolated from yeast (Table 6-S13). Structures 4Y7I, 1ZVR, and 4YFE were the third ranked structural alignments to myotubularin phosphoinositide phosphatases, two isolated from humans (Begley et al. 2006; Yoo et al. 2015) and the later of proteobacteria (TM ≥ 0.56) (Yamagata et al. 2015). Sequence similarity scores of the predicted phosphatases were all lower than 10%, explaining why protein $1E^{Pol*/Sd}$ was never annotated with such a domain prior to *in silico* structure prediction analyses (Table 6-S13). Functional predictions of the protein $1E^{Pol*/Sd}$ C-terminus of the consensus GFLV sequence (amino acids 466 to 824 without the polymerase domain) with DALI showed strong alignments to phosphatase structures (RMSD 2-4), including the previously mentioned Cdc14 (PDB:5XW4), a dual specificity protein phosphatase 23 (2JMG), and tyrosine protein phosphatase YIL113W (2J17).

Independent alignment of D2 to known protein structures showed high structural similarity to protein-tyrosine phosphatase (TM:0.45-0.68), protein-serine/threonine phosphatase (TM:0.45-0.68), 3-phytase (TM:0.48-0.50), formate C-acetyltransferase (TM:0.48), and methane monooxygenase (TM:0.41-0.49). Most predictions were indicative of protein-tyrosine phosphatase (83% of total predictions) and protein-

serine/threonine phosphatase domains (26% of predictions) (Table 6-S14). A total of 29 amino acid positions within D2 was classified as functional residues with respect to the structural alignment templates. Of note were two distinct regions in protein phosphatases known as the P-loop and Q-loop, where several residues are expected to participate in the dephosphorylation through critical residues (Table 6-S15). These residues are encoded at the 597-603 positions and 636-640 positions of GFLV protein $1E^{Pol*/Sd}$, respectively (Figure 6-7d). Analysis of similar proteins such as 7MOM and 3CM3 indicates alignment of dual specificity phosphatase active sites (Figure 6-7c), and electrostatic potential basic residue pocket (Figure 6-7e-g), characteristic of this enzyme family.

In D3, structural alignments were less confident (TM:0.31-0.55) and varied more widely across viruses and strains. These predictions spanned nearly all enzyme classes to include oxidoreductases (EC:1.-.-.-), transferases (EC:2.-.-.-), hydrolases (EC:3.-.-.-), isomerases (EC:4.-.-.-), and ligases (EC:5.-.-.-). The strongest and most consistently predicted structural homology was found in the oxidoreductase category as polyamine oxidase (TM:0.55) and dihydrolipyl dehydrogenase (six hits). It is possible that this domain interacts with the neighboring two domains, which would be supported by the abundance of NAD(P)H functional predictions and lipid/sugar specific enzymes with high structural similarity.

The C-terminal D4/D5 domains (GFLV symptom determinant region) are of the lowest predicted confidence in protein $1E^{Pol*/Sd}$ (TM:0.23-0.59), with less than 50 residues having ambiguous and unreliable structural alignment. This elusive region also contains the symptom determinant residue at position 802 (Osterbaan et al. 2019).

Alignment to representative structures across all six classes of enzymes may be interpreted poorly since this region is also the smallest predicted domain. Notably, the protein of mutant GFLV-GHu $1E_{K802G}$ prediction revealed an RNA glycosylase activity with high confidence (C-score 0.48) and a binding site to isopentenyl pyrophosphate at residues 6, 7, and 10 of the C-terminal 41 residues. The lack of resolved structure and low sequence homology prevents further functional investigations of the C-terminus. However, structural predictions indicated a loose association of the D4/D5 domains (GFLV symptom determinant region) with other globular domains for wildtype GFLV-GHu, but a stronger association for asymptomatic GFLV strains, as illustrated by a longer or a shorter distance between the different domains (Figure 6-8a-c). The two types of association could modulate the phosphatase activity of domain D2 or the unknown function(s) across domains D4/D5 with the conformation of protein $1E^{Pol*/Sd}$ modulating interactions with host components.

Sequence-based analysis of GFLV protein $1E^{Pol*/Sd}$ after structural modeling

A ScanProsite custom database created for GFLV sequences revealed other interesting features of GFLV protein $1E^{Pol*/Sd}$ (Figure 6-S11b-c). The predicted tyrosine phosphatase domain of CX_5R was confirmed for the sequence conservation noted by structural predictions (Hsu and Mao 2015) (Figure 6-7). A leucine zipper pattern with the typical leucine at an increment of seven amino acids between residues 604 and 625 was identified in 71 GFLV isolates, including GFLV-GHu (Figure 6-S11b). Additionally, a multicopper oxidase catalytic motif was noted between residues 643 and 663; however, several typically preserved residues of this motif were absent (Figure 6-S11c).

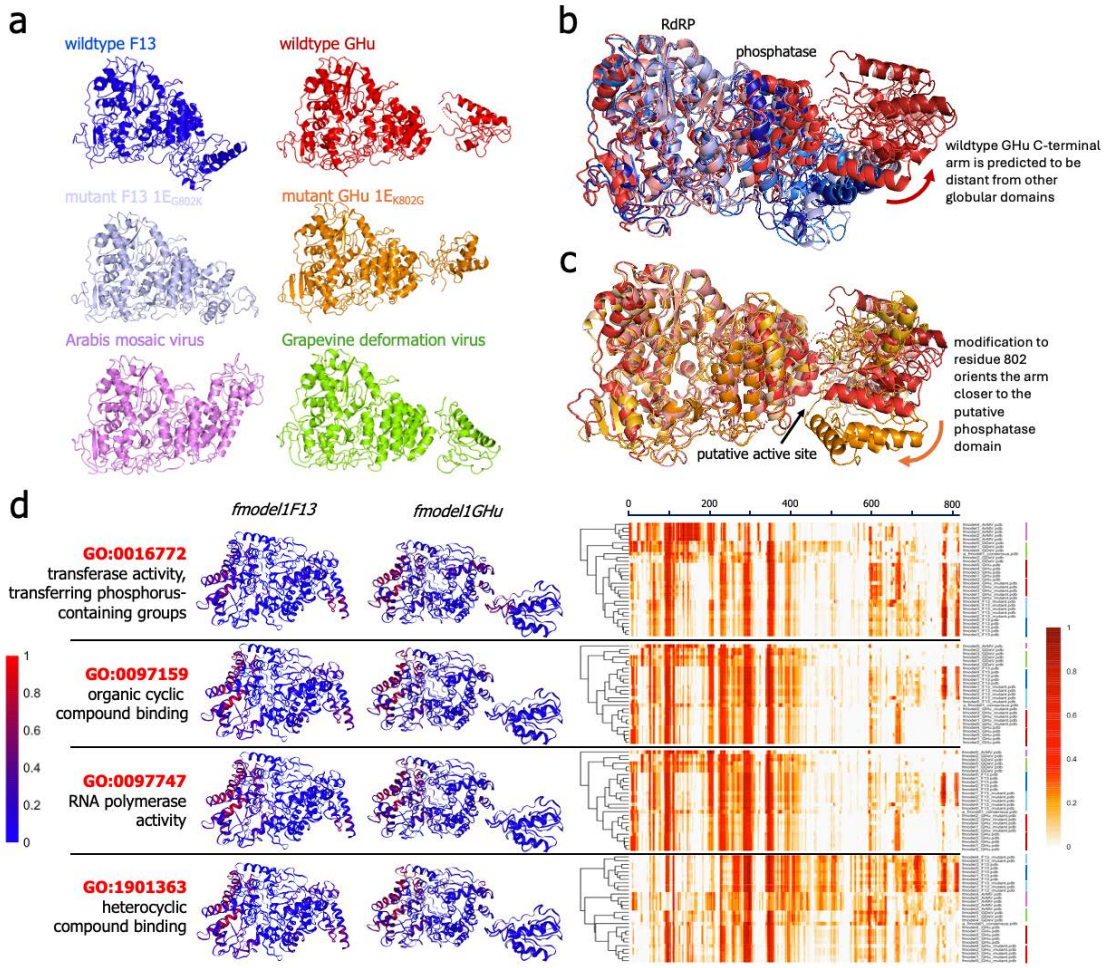

FIGURE 6-8. Top structural predictions of the C-terminus of nepovirus protein 1E show distinct conformational and catalytic activity differences. (a) Seven separate models of GFLV consensus (black), wildtype GFLV-F13 (blue), mutant GFLV-F13 1E$_{G802K}$, wildtype GFLV-GHu (red), Arabis mosaic virus (pink), mutant GFLV-GHu 1E$_{K802G}$ (orange), and grapevine deformation virus (yellow) display nuanced C-terminal associations of the D4 domain with the central phosphatase domain, likely due to differences in the amino acid identity within the proximal areas. **(b)** Overlay and alignment of the top three structural predictions between wildtype GFLV-F13 (blue shades) and wildtype GFLV-GHu (red shades) display a differential association with the phosphatase domain for wildtype GFLV-GHu. **(c)** The overlay and alignment of wildtype GFLV-GHu (red shades) with the single amino acid mutant GFLV-GHu 1E$_{K802G}$ (orange shades) displays a possible conformational change that would allow the association of the C-terminus with the phosphatase domain, hypothesized to restore the function. **(d)** Integration of structure with DeepFRI prediction software indicates RdRP motifs and differentially predicted catalytic components within the C-terminal domains. Three-dimensional structures of GFLV protein 1E$^{Pol*/Sd}$ are colored according to confidence or salience (blue to red; low to high) with respective molecular function (left). Heatmap depiction of the GFLV protein 1E$^{Pol*/Sd}$ coding sequence and salience of molecular function for each submitted protein structure, virus and virus strain clusters indicated by color (right).

Several phosphoserine and phosphothreonine phosphorylation sites were identified in wildtype GFLV-F13, wilrftype GHu and consensus $1E^{Pol*/Sd}$ protein sequences using Scansite 4.0. GFLV-F13 returned a single motif at residue S319, which was an Aurora A site. GFLV-GHu returned three unique sites of S82 (a 14-3-3 motif), S609 (an AMP kinase motif), and T812 (a Nek4 motif). The consensus returned the same S319 site as GFLV-F13, the same S609 and T812 sites as GFLV-GHu, and returned an additional T717 (PLK1 kinase motif). These unique post-translational modifications may be required for exacting the function in any of the domains across protein $1E^{Pol*/Sd}$.

A novel functional residue prediction analysis was conducted on protein $1E^{Pol*/Sd}$ using DeepFRI, a graph convolution network that assigns confidence values to each amino acid in a submitted sequence (Figure 6-8d). The gene ontology predictions of transferase activity (GO:0046772) and heterocyclic compound binding (GO:1901363) were the most informative about hot spots in the newly predicted phosphatase domains and involvement of the C-terminal 50 amino acids with these functions (Figure 6-9d). Several other functions such as organic cyclic compound binding (GO:0097159) and RNA polymerase activity (GO:0097747) were extracted across all submitted queries. Further, assignment to general functions such as ion binding (GO:0043167), cation binding (GO:0043169), metal ion binding (GO:0046872). Minor differences in catalytic 'hotspots' assigned through the DeepFRI predictions were observed among protein $1E^{Pol*/Sd}$ of different GFLV strains, ArMV and GDeV. Of note was the high confidence for these predicted functions within the C-terminus of the polymerase domain, residues surrounding the P-loop in the predicted phosphatase domain, and the C-terminal domain

containing the symptom determinant. These results suggested important features for the predicted phosphatase activity within the tertiary conformation of protein $1E^{Pol*/Sd}$.

Together, the new structural and functional protein predictions suggested that GFLV protein $1E^{Pol*/Sd}$ contains at least three globular domains, including the putative RdRP domain, a predicted novel phosphatase domain in the center, and the C-terminal domain that may impact the catalytic functions predicted with DeepFRI.

Contextualizing protein-protein interactions from omics data, and proposed functions of GFLV protein $1E^{Pol*/Sd}$ for symptom expression

Integrating data on protein-protein interactions with the new putative phosphatase function of protein $1E^{Pol*/Sd}$ was used to imagine a potential mechanism of GFLV symptom development in *N. benthamiana* (Figure 6-9). Asymptomatic GFLV strains display the ability to downregulate initial immune responses at 4 dpi by putatively interacting with eIF2a (Table 6-4). This correlation was not observed at an early stage of infection with symptomatic wildtype GFLV-GHu. For hepatitis E virus, the protease inhibits eIF2 alpha kinase 4 to promote viral survival (Kumar et al. 2023). This is part of an integrated stress response, a hypothesis that was proposed for GFLV in previous work (Roy et al. 2023). The dysregulation of host ribosomal subunits upon GFLV infection strongly supports this hypothesis (Table 6-S11).

A SH3 domain was noted in protein structural predictions for wildtype GFLV-GHu at the far C-terminus of protein $1E^{Pol*/Sd}$ (i.e. symptom determinant region). SH3 domains are known to interact with dynamin-related protein 5A with GTPase activity, via a proline arginine rich domain. Dynamin-related protein 5A was identified as a potential interactant of GFLV protein $1E^{Pol*/Sd}$ (Table 6-4) and a 50S ribosome-binding

GTPase domain was found upregulated upon GFLV infection (Table 6-S11). Further, the newly phosphatase domain predicted in protein $1E^{Pol*/Sd}$ could provide context to the interaction with kinases and signaling proteins (Table 6-4). Moreover, the perturbed expression of three key genes in the PI3K signaling cascade, including phosphatidylinositol synthase, inositol monophosphatase, and protein kinase c, was documented (Figure 6-S9). This disruption in signaling could impact multiple host pathways involved in general stress response. Finally, the amount of ROS produced is proposed to manifest into different phenotypic presentations depending on the amino acid identity at position 802 of protein $1E^{Pol*/Sd}$ (Figure 6-9b). This hypothesis is supported by the phenotypic differences in root morphology (Figure 6-3) and ROS production in leaves (Figure 6-S1) and roots (Roy and Fuchs 2024).

Recovery from symptoms could be explained by the cumulative effects of ribosomal regulation, suppression of RNA silencing, and additional viral protein-protein interactions (Figure 6-9a). These are only plausible ways possible models of GFLV-host interactions that could result in the manifestation of symptoms during infection. More work is needed to better understand the events of the GFLV infection cycle and the events leading to symptom presentation *in planta*.

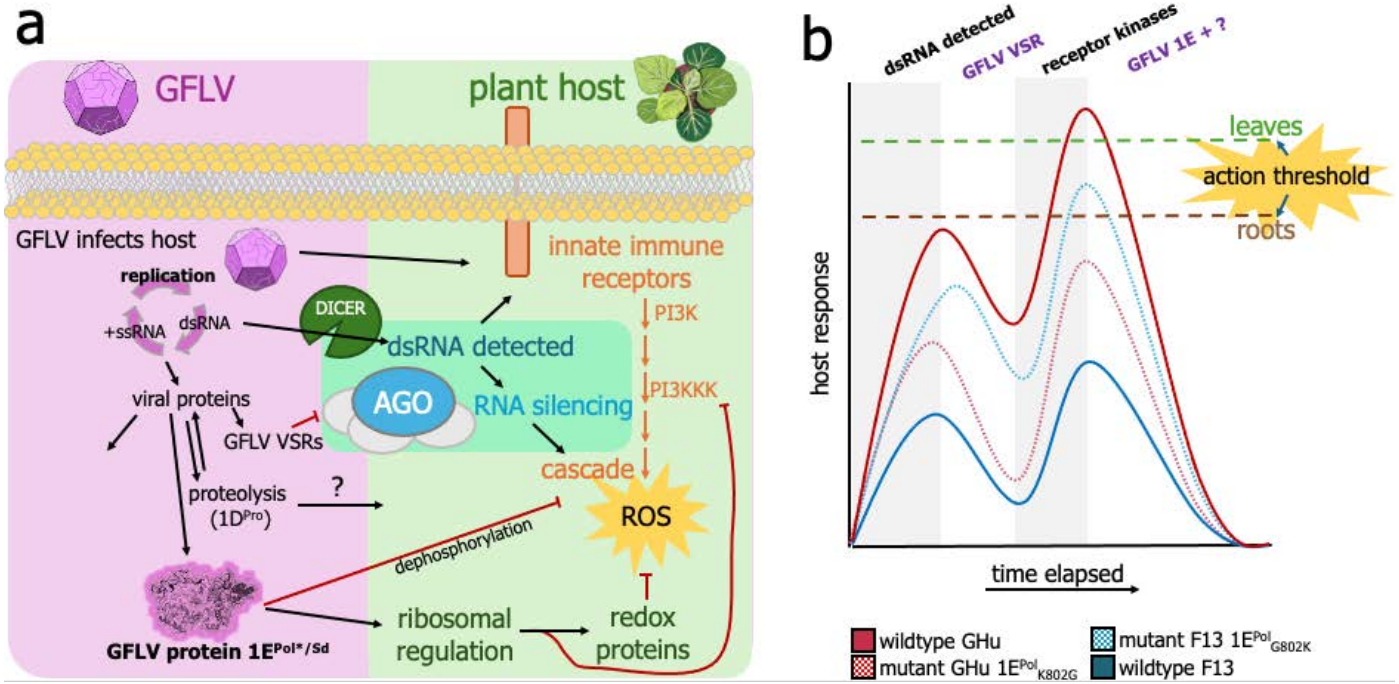

FIGURE 6-9. A hypothesized mechanism of grapevine fanleaf virus (GFLV) interference with the host immune system during infection in *Nicotiana benthamiana*. (a) GFLV replication begins upon its entry into the host cell. Antiviral RNA silencing initiates when host endoribonuclease DICER binds and cleaves viral double-stranded RNA intermediates produced during replication. To counter, GFLV encodes three suppressors of viral silencing (VSR) that repress the host RNA silencing response. Other viral proteins or changes in host can elicit an immune response independent of the dsRNA recognition, potentially leading to the activation of the phosphatidylinositol 3-kinase (PI3K) cascade. From the integrative omics and structural analyses, we hypothesize that GFLV protein $1E^{Pol*/Sd}$ utilizes the predicted phosphatase activity to negate this signal for reactive oxygen species (ROS) production. The GFLV strain and amino acid identity of the symptom determinant region of protein $1E^{Pol*/Sd}$ appear to modulate the efficiency of this interaction. **(b)** A similar depiction of the host response (y-axis) is explained for the ability to elicit a hypersensitive response depending on multiple viral and host factors. The strains of GFLV used across multiple studies are depicted to relate the efficiency of host immune activation and repression over time.

DISCUSSION

The expression of plant virus disease symptoms often involves the dysregulation of many host cellular pathways (Ahmad et al. 2024; Ghoshal and Sanfaçon 2015; Grangeon et al. 2012; Jiang and Zhou 2023; Osterbaan and Fuchs 2019; Pallas and García 2011; Palukaitis and Yoon 2024; Tsuda 2020). The integration gene expression, protein expression, phenotypic, and microscopic data has shed light on different immune responses of *N. benthamiana* activated by GFLV upon infection. Changes in host phenotype were described following infection of differing GFLV strains and mutants (Figure 6-1). Plants infected with symptomatic strains of GFLV induced statistical difference in chlorophyll content when the foliar vein clearing phenotype was apparent (Figure 6-2). The production of ROS in leaf tissue was correlated to the vein clearing phenotype (Figure 6-S1) and to the previously observed phenotype in root tissue (Roy and Fuchs 2024). Analysis of RSA traits in an expanded screening of GFLV mutants illustrated distinct modifications to root branching, surface area, and volume (Figure 6-3). Linear regression analysis confirmed that amino acid 802 of protein $1E^{Pol*/Sd}$ affects the number of root tips, and that the GFLV strain and amino acid 804 of protein $1E^{Pol*/Sd}$ also plays a role in the overall root system phenotype (Figure 6-3).

Phenotypic root system architecture analysis and micro-CT scans of a subset of GFLV-infected plant roots showed quantitative and qualitative differences in root morphology and vasculature (Figure 6-4, Figure 6-S4-6). GFLV isolates with a lysine in position 802 of protein $1E^{Pol*/Sd}$ incurred the most changes to the host root architecture and vasculature, but additional variance in the GFLV strains may have convoluted

further conclusions. A recent study documented GFLV alleviated host incurred xylem occlusions, seemingly priming the response to other stressors by maintaining viral infection (Jež-Krebelj et al. 2022). We observed similar numeric differences in vasculature, but similarly, our data did not indicate significant differences in root vasculature at a tissue level scale (Jež-Krebelj et al. 2022). Future advances in temporal, non-destructive phenotyping strategies may reveal larger differences in primary root vasculature than observed in this study. Although there are limitations in the long-term growth of GFLV-infected grapevines, it still is unknown if GFLV alone can manifest symptoms in grapevine root systems, which are typically attributed to the ectoparasitic dagger nematode vector, *Xiphinema index* (Djennane et al. 2021; Raski et al. 1983).

Ectopic sprays of inositol and phytohormones documented the involvement of these molecules during the host response to GFLV, as previously hypothesized (Roy et al. 2023; Roy and Fuchs 2024). The application of inositol decreased infection rates across multiple GFLV strains (Table 6-1) and exacerbated symptom expression in plants infected with wildtype GFLV-GHu (Figure 6-5a-e). The application of ABA generally decreased GFLV infection rates (Table 6-2), while the application of SA increased GFLV infection rates (Table 6-3). Both phytohormones decreased the longevity of symptom expression and manifested unique phenotypic symptomologies (Figure 6-5f-n). Given that plant viruses have been documented to modulate major phytohormone pathways (Zhao and Li 2021), more work is needed to explore the effect of SA and ABA on GFLV infection, and expand into jasmonic acid, ethylene, brassinosteroids, and other phytohormones to probe transient disease symptom expression patterns. In a recent study, apple stem grooving virus and apple stem pitting virus impacted the rate

of root induction for tissue culture-grown plants of a single cultivar of pear (*Pyrus* spp.) (Chen et al. 2017). Phytohormone concentrations, namely cytokinins and ABA, were perturbed for the infected cultivar with delayed induction, but not another cultivar. Even though these viruses are not related to GFLV, they manipulate these canonical pathways to sustain infection and replicate (Alazem and Lin 2014; Pasin et al. 2020; Zhao and Li 2021). It has been shown that the ABA, PI3K cascade, and callose deposition pathways are heavily connected to combat biotic and abiotic stressors in plants (Palukaitis and Yoon 2024), as was seen in integrative host profiling analysis during GFLV infection. The application of phytohormones confirmed a priming for systemic host response to viral infection and provided preliminary results to link phenotypic and molecular data surmounted thus far.

Many dysregulated cellular pathways beyond phytohormones were observed for GFLV-infected *N. benthamiana* plants. During the initial stages of systemic infection (4 dpi, leaves), asymptomatic GFLV strains downregulate one or several (many in the case of GFLV-F13 mutant $1E_{G802K}$) immune signaling pathways such as response to wounding, phytohormone, and glucosinolate metabolic processes. No ontologies were significantly changed at 4 dpi for wildtype GFLV-GHu, the symptomatic strain, however, the host activated RNA silencing, callose deposition at the cell plasmodesmata, and ROS production as antiviral responses. Further, the expression of two upstream regulators in the PI3 kinase cascade, phosphatidylinositol synthase and inositol monophosphatase, were downregulated during GFLV infection, with the latter being downregulated only later in infection for symptomatic wildtype GFLV-GHu.

Enrichment analysis indicated the downregulation of both ABA and JA pathways in asymptomatic GFLV-infected plants at 4- and 7-dpi (Table 6-S11).

In the symptom expression phase of wildtype GFLV-GHu in leaves and roots, a large shift in the expression of ribosomal proteins, cell structure components, and metabolic pathways (such as inositol, peptide production, and nucleotides) was observed. The upregulation of 14 large and six small ribosomal subunits observed for GFLV was documented for other plant viruses and reported as crucial to viral development, spread, and replication (Li 2019). Our data suggested the ability of wildtype GFLV-GHu to suppress symptoms through an alternative pathway not necessarily utilized by other GFLV strains. It cannot be deduced if this stage of infection is controlled solely by protein $1E^{Pol*/Sd}$ or if other factors aid in the suppression of the host immune system for the recovery from symptoms. In cases of asymptomatic infection at the same time, host gene enrichment analysis indicated a continued repression of ABA, JA, signaling pathways, lignin deposition, ubiquitin mediated degradation, and other innate immune pathways (Table 6-S11). Some studies indicate post-translational modifications of PtdIn-catalysing enzymes in response to stress (Westergren et al. 2001). For example, phosphorylation of PIP5K6 by mitogen-activated protein kinase (MAPK) MPK6 upon PAMP (pathogen-associated molecular patterns) perception reduces the activity of PIP5K6 kinases (Menzel et al. 2019). In our study, an initial uptick of the PI3K cascade was observed for symptomatic wildtype GFLV-GHu with a downregulation later into infection across tissue types and for other strains (Figure 6-S9) Late-stage infection across all GFLV strains (symptomatic and asymptomatic) showed an increased overabundance of sulfate assimilation, and

‘cellular response to selenium’, which could be related to the long-term suppression of host responses to sustain GFLV infection (Table 6-S11). Some selenoproteins are glutathione reductases that promote redox homeostasis to avoid oxidative burst and damage. Oxidoreductases were heavily dysregulated at earlier time points of GFLV infection and are considered to be linked with the recovery phase and/or suppression of symptoms in both leaves and roots (Table 6-S11) (Roy et al. 2023; Roy and Fuchs 2024).

Varying transcript abundance levels for putative interactants of protein $1E^{Pol*/Sd}$ (Figure 6-S8) suggest an affinity for pyruvate kinase (Table 6-4, Table 6-S7C). This is consistent with the polymerase of tomato bushy stunt virus (species *Tombusvirus lycopersici,* genus *Tombusvirus*, family *Tombusviridae*) that recruits cytosolic pyruvate kinase to facilitate viral replication (Chuang et al. 2017). Several enriched proteins shared signaling and host regulation capacities, particularly within the KEGG analysis (Table 6-S7C). Succinate dehydrogenase may impact oxidative burst and energy availability during GFLV infection. This may be a mechanism in which the succinate dehydrogenase flavoprotein subunit is targeted for suppression, leading to a halt in ROS production. Protein phosphatase 1 (PP1) has been documented in viral-host interaction studies (Corda et al. 2024). PP1 interactions have been largely documented to occur through the RVxF motif and expanded to include other variations of charged, hydrophobic, and bulky amino acids present at the first, second, and fourth positions of the motif (Hendrickx et al. 2009). The expanded motif is repeatedly found within the C-terminus of GFLV protein $1E^{Pol*/Sd}$ and may contribute to the putative interaction of acid phosphatase 1 with protein $1E^{Pol*/Sd}$ (Table 6-4). To a great deal, targeting of host protein

phosphatases is documented in other viruses (Barski et al. 2021). By interacting with host proteins, viral phosphatases can disrupt normal signaling cascades to promote viral infection. The interactants of the PP1 motif RVxF in GFLV protein $1E^{Pol*/Sd}$ needs further resolution and testing through knockout host mutants or coupled immunofluorescence assays (e.g. BiFC, FRET).

Through sequence and structure prediction modeling, a combination of canonical and unique features was identified in protein $1E^{Pol*/Sd}$ compared with other viral polymerases. The presence of key polymerase domains was confirmed in all analyzed strains of GFLV (Figure 6-S11), most of which are not suspected to be involved with symptom development through previous sequence analysis and experiments (Osterbaan et al. 2019; Vigne et al. 2013). Predictive protein modeling suggested a putative phosphatase domain in GFLV $1E^{Pol*/Sd}$ that is structurally homologous to dual-specificity phosphatases in humans, bacteria, yeast, and plants, yet with less than 10% amino acid identity to resolved structural homologues (Figure 6-7, Table 6-S13). The highest protein similarity to the D2 domain of protein $1E^{Pol*/Sd}$ was a phosphatase Cdc14p (PDB:5XW4) from *Saccharomyces cerevisiae*. 5XW4 was shown to interact with mitotic cyclin-dependent kinases in yeast to modulate the cell cycle (Kobayashi and Matsuura 2017). Human Cdc14b (PDB:1OHE), the second closest structure, was shown to antagonize cyclin-dependent kinases in cell cycle maintenance (Gray et al. 2003). These key regulators of cellular functions could be antagonized by GFLV protein $1E^{Pol*/Sd}$ and the newly predicted phosphatase domain D2.

By performing *in silico* analysis, the centrally located phosphatase domain of protein $1E^{Pol*/Sd}$ was predicted to be proximal to the C-terminal domain, which could

facilitate putative catalytic activity through the CX_5R motif, P-loop, Q-loop, and C-terminal threonine residue (Figure 6-7). Modifications to the 802nd residue induced conformational changes in the predicted structures (Figure 6-8), which could interrupt the predicted phosphatase activity when the amino acid lysine, and other positive amino acids are present. In the instance that wildtype GFLV-GHu is mutated to encode a glycine, this structural protrusion was relaxed and positioned the C-terminus more closely to the phosphatase domain. A leucine zipper sequence and a multicopper oxidase domain were also observed within the 1E$^{Pol*/Sd}$ C-terminus (Figure 6-S11).

The putative phosphatase domain of GFLV protein 1E$^{Pol*/Sd}$ should be considered in the context of protein-protein interactions and pathogenicity. Phosphatase domains have been noted in other viral pathogens. Herpes simplex virus-1 protein pUL21 is a viral phosphatase adaptor that aids in replication and movement through hosts (Benedyk et al. 2021). The small P7 protein of tomato chlorosis virus has been shown to recruit a MAP kinase to inhibit the plant immune response (Feng et al. 2024). Wheat yellow mosaic virus protein P1 is another pathogenicity determinant that modulates ROS production *in planta* (Zhao et al. 2025). Cassava brown streak virus and Ugandan cassava brown streak virus encode atypical Ham1 proteins that are co-factors for replication (Valli et al. 2022). Cassava torrado-like virus, within the same viral family as GFLV, also encodes a Maf/Ham1 domain within the RNA1 C-terminal sequence, which was documented to aid in the mechanical transmission to *N. benthamiana* (Jimenez et al. 2023). Sequence comparison of the GFLV protein 1E$^{Pol*/Sd}$ shows similarity of the identified Ham1 sequence, but their distant relationship and rapid mutation of viral sequences convolutes the exact origin. Additionally, cleavage of

the GFLV 1E$^{Pol*/Sd}$ C-terminus results in non-infectious transcripts, which may be indicative of a key viral event to suppress the host immune response (Vigne et al. 2013). Perhaps most documented is that of VH1 dual-specificity phosphatase protein of vaccinia virus (Liu et al. 1995), which has been shown to block phosphorylation events of the canonical Stat1 immune pathway (Najarro et al. 2001). Given that the Janus kinase-signal transducer of activators of transcription (JAK-STAT) pathway is not present in plants, other targets must be considered for the predicted phosphatase of GFLV. The downregulation of several general immune response pathways in GFLV-F13 strains suggests protein 1E$^{Pol*/Sd}$ could dampen any preemptive host response. This would require work in asymptomatic GFLV strains at the onset of infection.

To validate the predicted phosphatase domain, future research should focus on the purification of GFLV protein 1E$^{Pol*/Sd}$ of strains F13 and GHu due to their predicted differences in structure and enzymatic activity. Upon expression and purification of protein 1E$^{Pol*/Sd}$, *in vitro* assays could be conducted to examine the activity of the putative polymerase, predicted phosphatase, multicopper oxidase, and leucine zipper domains/motifs. By using protein 1E$^{Pol*/Sd}$ of multiple GFLV strains, or other nepoviruses, the molecular mechanism behind GFLV induced symptom development could be elucidated. It can be imagined that future work could investigate inhibitory molecules of protein 1E$^{Pol*/Sd}$ to engineer new forms of resistance and curtail the impacts of viral disease. For example, a resolved crystal structure and purified protein product would be helpful to confirm this putative catalytic pocket and any associated enzymatic function(s).

Independent analysis of host and viral components suggested several ways of GFLV protein $1E^{Pol*/Sd}$ manipulation of the host. By interacting with several host components, GFLV reprograms the entire host for structural modification, evades kinase cascades and ROS production (sometimes partially). In the event of symptom development in *N. benthamiana*, these interactions are less proactive to suppress host components and take additional time to compensate against host antiviral strategies (Figure 6-9). This is supported by the early downregulation of canonical immune response genes in asymptomatic viral infections (Table 6-S11). Notably, several layers of virus-host interactions have been elucidated, including activated RNA silencing and innate immune receptors, as well as how GFLV counter-acts host defense strategies (Figure 6-9b). Based on the initial downregulation of innate immune pathways, the delayed suppression in symptomatic wildtype GFLV-GHu, and structural proximity of residue 802 to the phosphatase domain, we hypothesize that the dephosphorylation activity of protein $1E^{Pol*/Sd}$ could be linked to symptom expression in *N. benthamiana* (Figure 6-9a). When considering the four GFLV strains analyzed in host profiling experiments, a simplified model can depict plant host responses over the course of infection with an activation threshold for phenotypic displaying, including the phosphatase activity of protein $1E^{Pol*/Sd}$ involved in the arms race between GFLV and its host (Figure 6-9b).

REFERENCES

Ahmad, N., Hussain, H., Naeem, M., Rahman, S. ur, Khan, K. A., Iqbal, B., and Umar, A. W. 2024. Metabolites-induced co-evolutionary warfare between plants, viruses, and their associated vectors: So close yet so far away. Plant Science 346:112165. https://doi.org/10.1016/j.plantsci.2024.112165.

Alazem, M., and Lin, N. 2014. Roles of plant hormones in the regulation of host–virus interactions. Mol Plant Pathol 16:529–540. https://doi.org/10.1111/mpp.12204.

Andret-Link, P., Laporte, C., Valat, L., Ritzenthaler, C., Demangeat, G., Vigne, E., Laval, V., Pfeiffer, P., Stussi-Garaud, C., and Fuchs, M. 2004. Grapevine fanleaf virus: Still a major threat to the grapevine industry. Journal of Plant Pathology 86:183–195.

Barski, M. S., Minnell, J. J., and Maertens, G. N. 2021. PP2A Phosphatase as an Emerging Viral Host Factor. Front. Cell. Infect. Microbiol. 11. https://doi.org/10.3389/fcimb.2021.725615.

Bates, D., Mächler, M., Bolker, B., and Walker, S. 2015. Fitting Linear Mixed-Effects Models Using lme4. Journal of Statistical Software 67:1–48. https://doi.org/10.18637/jss.v067.i01.

Begley, M. J., Taylor, G. S., Brock, M. A., Ghosh, P., Woods, V. L., and Dixon, J. E. 2006. Molecular basis for substrate recognition by MTMR2, a myotubularin family phosphoinositide phosphatase. Proceedings of the National Academy of Sciences 103:927–932. https://doi.org/10.1073/pnas.0510006103.

Benedyk, T. H., Muenzner, J., Connor, V., Han, Y., Brown, K., Wijesinghe, K. J., Zhuang, Y., Colaco, S., Stoll, G. A., Tutt, O. S., Svobodova, S., Svergun, D. I.,

Bryant, N. A., Deane, J. E., Firth, A. E., Jeffries, C. M., Crump, C. M., and Graham, S. C. 2021. pUL21 is a viral phosphatase adaptor that promotes herpes simplex virus replication and spread. PLoS Pathogens 17:e1009824. https://doi.org/10.1371/journal.ppat.1009824.

Bombarely, A., Rosli, H. G., Vrebalov, J., Moffett, P., Mueller, L. A., and Martin, G. B. 2012. A draft genome sequence of *Nicotiana benthamiana* to enhance molecular plant-microbe biology research. MPMI 25:1523–1530. https://doi.org/10.1094/MPMI-06-12-0148-TA.

Chen, J., Tang, H.-H., Li, L., Qin, S.-J., Wang, G.-P., and Hong, N. 2017. Effects of virus infection on plant growth, root development and phytohormone levels in in vitro-cultured pear plants. Plant Cell Tiss Organ Cult 131:359–368. https://doi.org/10.1007/s11240-017-1289-1.

Choi, J., Browning, S., Schmitt-Keichinger, C., and Fuchs, M. 2024. Mutations in the WG and GW motifs of the three RNA silencing suppressors of grapevine fanleaf virus alter their systemic suppression ability and affect virus infectivity. Front. Microbiol. 15. https://doi.org/10.3389/fmicb.2024.1451285.

Choi, J., Pakbaz, S., Yepes, L. M., Cieniewicz, E. J., Schmitt-Keichinger, C., Labarile, R., Minutillo, S. A., Heck, M., Hua, J., and Fuchs, M. 2023. Grapevine fanleaf virus RNA1-encoded proteins 1A and 1BHel suppress RNA silencing. Mol Plant Microbe Interact. https://doi.org/10.1094/MPMI-01-23-0008-R.

Chuang, C., Prasanth, K. R., and Nagy, P. D. 2017. The Glycolytic Pyruvate Kinase Is Recruited Directly into the Viral Replicase Complex to Generate ATP for RNA

Synthesis. Cell Host & Microbe 22:639-652.e7. https://doi.org/10.1016/j.chom.2017.10.004.

Corda, P. O., Bollen, M., Ribeiro, D., and Fardilha, M. 2024. Emerging roles of the Protein Phosphatase 1 (PP1) in the context of viral infections. Cell Communication and Signaling 22:65. https://doi.org/10.1186/s12964-023-01468-8.

Das, P. P., Rana, S., Muthamilarasan, M., Kannan, M., and Ghazi, I. A. 2021. Omics Approaches for Understanding Plant Defense Response. In *Omics Technologies for Sustainable Agriculture and Global Food Security Volume 1*, eds. Anirudh Kumar, Rakesh Kumar, Pawan Shukla, and Manish K. Pandey. Singapore: Springer, pp. 41–83. https://doi.org/10.1007/978-981-16-0831-5_3.

Djennane, S., Prado, E., Dumas, V., Demangeat, G., Gersch, S., Alais, A., Gertz, C., Beuve, M., Lemaire, O., and Merdinoglu, D. 2021. A single resistance factor to solve vineyard degeneration due to grapevine fanleaf virus. Commun Biol 4:1–8. https://doi.org/10.1038/s42003-021-02164-4.

Feng, L., Luo, X., Huang, L., Zhang, Y., Li, F., Li, S., Zhang, Z., Yang, X., Wang, X., OuYang, X., Shi, X., Zhang, D., Tao, X., Chen, J., Yang, J., Zhang, S., and Liu, Y. 2024. A viral protein activates the MAPK pathway to promote viral infection by downregulating callose deposition in plants. Nat Commun 15:10548. https://doi.org/10.1038/s41467-024-54467-9.

Fuchs, M. 2020. Grapevine viruses: a multitude of diverse species with simple but overall poorly adopted management solutions in the vineyard. J Plant Pathol 102:643–653. https://doi.org/10.1007/s42161-020-00579-2.

Fuchs, M., Schmitt-Keichinger, C., and Sanfaçon, H. 2017. A renaissance in nepovirus research provides new insights into their molecular interface with hosts and vectors. In *Advances in Virus Research*, eds. Margaret Kielian, Thomas C. Mettenleiter, and Marilyn J. Roossinck. Cambridge, MA, USA: Academic Press, pp. 61–105. https://doi.org/10.1016/bs.aivir.2016.08.009.

García, J. A., and Pallás, V. 2015. Viral factors involved in plant pathogenesis. Current Opinion in Virology 11:21–30. https://doi.org/10.1016/j.coviro.2015.01.001.

Ghoshal, B., and Sanfaçon, H. 2015. Symptom recovery in virus-infected plants: Revisiting the role of RNA silencing mechanisms. Virology 479–480:167–179. https://doi.org/10.1016/j.virol.2015.01.008.

Gligorijević, V., Renfrew, P. D., Kosciolek, T., Leman, J. K., Berenberg, D., Vatanen, T., Chandler, C., Taylor, B. C., Fisk, I. M., Vlamakis, H., Xavier, R. J., Knight, R., Cho, K., and Bonneau, R. 2021. Structure-based protein function prediction using graph convolutional networks. Nat Commun 12:3168. https://doi.org/10.1038/s41467-021-23303-9.

Góra-Sochacka, A., Więsyk, A., Fogtman, A., Lirski, M., and Zagórski-Ostoja, W. 2019. Root Transcriptomic Analysis Reveals Global Changes Induced by Systemic Infection of Solanum lycopersicum with Mild and Severe Variants of Potato Spindle Tuber Viroid. Viruses 11:992. https://doi.org/10.3390/v11110992.

Grangeon, R., Jiang, J., and Laliberté, J.-F. 2012. Host endomembrane recruitment for plant RNA virus replication. Current Opinion in Virology 2:683–690. https://doi.org/10.1016/j.coviro.2012.10.003.

Gray, C. H., Good, V. M., Tonks, N. K., and Barford, D. 2003. The structure of the cell cycle protein Cdc14 reveals a proline-directed protein phosphatase. The EMBO Journal 22:3524–3535. https://doi.org/10.1093/emboj/cdg348.

Heinlein, M. 2015. Plant virus replication and movement. Virology 479–480:657–671. https://doi.org/10.1016/j.virol.2015.01.025.

Hendrickx, A., Beullens, M., Ceulemans, H., Abt, T. D., Eynde, A. V., Nicolaescu, E., Lesage, B., and Bollen, M. 2009. Docking Motif-Guided Mapping of the Interactome of Protein Phosphatase-1. Chemistry & Biology 16:365–371. https://doi.org/10.1016/j.chembiol.2009.02.012.

Hsu, F., and Mao, Y. 2015. The structure of phosphoinositide phosphatases: Insights into substrate specificity and catalysis. Biochimica et Biophysica Acta (BBA) - Molecular and Cell Biology of Lipids 1851:698–710. https://doi.org/10.1016/j.bbalip.2014.09.015.

Huang, Y.-W., Hu, C.-C., Lin, N.-S., and Hsu, Y.-H. 2012. Unusual roles of host metabolic enzymes and housekeeping proteins in plant virus replication. Current Opinion in Virology 2:676–682. https://doi.org/10.1016/j.coviro.2012.10.002.

Ivanov, K. I., and Mäkinen, K. 2012. Coat proteins, host factors and plant viral replication. Current Opinion in Virology 2:712–718. https://doi.org/10.1016/j.coviro.2012.10.001.

Jež-Krebelj, A., Rupnik-Cigoj, M., Stele, M., Chersicola, M., Pompe-Novak, M., and Sivilotti, P. 2022. The Physiological Impact of GFLV Virus Infection on Grapevine Water Status: First Observations. Plants (Basel) 11:161. https://doi.org/10.3390/plants11020161.

Jiang, T., and Zhou, T. 2023. Unraveling the Mechanisms of Virus-Induced Symptom Development in Plants. Plants (Basel) 12:2830. https://doi.org/10.3390/plants12152830.

Jimenez, J., Leiva, A. M., and Cuellar, W. J. 2023. Cassava torrado-like virus encodes a gene that facilitates the mechanical transmission to Nicotiana benthamiana of Cassava virus X. Sci. agropecu. 14:213–221. https://doi.org/10.17268/sci.agropecu.2023.019.

Joly, A. C., Garcia, S., Hily, J.-M., Koechler, S., Demangeat, G., Garcia, D., Vigne, E., Lemaire, O., Zuber, H., and Gagliardi, D. 2023. An extensive survey of phytoviral RNA 3' uridylation identifies extreme variations and virus-specific patterns. Plant Physiol 193:271–290. https://doi.org/10.1093/plphys/kiad278.

Jones, D., Farreyrol, K., Clover, G. R. G., and Pearson, M. N. 2008. Development of a generic PCR detection method for tobraviruses. Australasian Plant Pathology 37:132–136. https://doi.org/10.1071/AP07091.

Jones, R. A. C. 2021. Global Plant Virus Disease Pandemics and Epidemics. Plants (Basel) 10:233. https://doi.org/10.3390/plants10020233.

Kobayashi, J., and Matsuura, Y. 2017. Structure and dimerization of the catalytic domain of the protein phosphatase Cdc14p, a key regulator of mitotic exit in Saccharomyces cerevisiae. Protein Science 26:2105–2112. https://doi.org/10.1002/pro.3244.

Kolberg, L., Raudvere, U., Kuzmin, I., Vilo, J., and Peterson, H. 2020. gprofiler2 -- an R package for gene list functional enrichment analysis and namespace

conversion toolset g:Profiler. F1000Res 9:ELIXIR-709. https://doi.org/10.12688/f1000research.24956.2.

Kumar, A., Subramani, C., Raj, S., Ranjith-Kumar, C. T., and Surjit, M. 2023. Hepatitis E Virus Protease Inhibits the Activity of Eukaryotic Initiation Factor 2-Alpha Kinase 4 and Promotes Virus Survival ed. J.-H. James Ou. J Virol 97:e00347-23. https://doi.org/10.1128/jvi.00347-23.

Labunskyy, V. M., Hatfield, D. L., and Gladyshev, V. N. 2014. Selenoproteins: Molecular Pathways and Physiological Roles. Physiological Reviews 94:739–777. https://doi.org/10.1152/physrev.00039.2013.

Laliberté, J.-F., and Sanfaçon, H. 2010. Cellular Remodeling During Plant Virus Infection. Annual Review of Phytopathology 48:69–91. https://doi.org/10.1146/annurev-phyto-073009-114239.

Langfelder, P., and Horvath, S. 2008. WGCNA: an R package for weighted correlation network analysis. BMC Bioinformatics 9:559. https://doi.org/10.1186/1471-2105-9-559.

Lenth, R. V. 2024. *emmeans: Estimated Marginal Means, aka Least-Squares Means*.

Li, S. 2019. Regulation of Ribosomal Proteins on Viral Infection. Cells 8:508. https://doi.org/10.3390/cells8050508.

Ligges, U., and Mächler, M. 2003. Scatterplot3d - an R Package for Visualizing Multivariate Data. Journal of Statistical Software 8:1–20. https://doi.org/10.18637/jss.v008.i11.

Liu, K., Lemon, B., and Traktman, P. 1995. The dual-specificity phosphatase encoded by vaccinia virus, VH1, is essential for viral transcription in vivo and in vitro. J Virol 69:7823–7834. https://doi.org/10.1128/jvi.69.12.7823-7834.1995.

Love, M. I., Huber, W., and Anders, S. 2014. Moderated estimation of fold change and dispersion for RNA-seq data with DESeq2. Genome Biol 15:550. https://doi.org/10.1186/s13059-014-0550-8.

Margis, R., Viry, M., Pinck, M., Bardonnet, N., and Pinck, L. 1994. Differential proteolytic activities of precursor and mature forms of the 24K proteinase of Grapevine fanleaf nepovirus. Virology 200:79–86. https://doi.org/10.1006/viro.1994.1165.

Menzel, W., Stenzel, I., Helbig, L., Krishnamoorthy, P., Neumann, S., Eschen-Lippold, L., Heilmann, M., Lee, J., and Heilmann, I. 2019. A PAMP -triggered MAPK cascade inhibits phosphatidylinositol 4,5-bisphosphate production by PIP 5K6 in *Arabidopsis thaliana*. New Phytologist 224:833–847. https://doi.org/10.1111/nph.16069.

Najarro, P., Traktman, P., and Lewis, J. A. 2001. Vaccinia Virus Blocks Gamma Interferon Signal Transduction: Viral VH1 Phosphatase Reverses Stat1 Activation. J Virol 75:3185–3196. https://doi.org/10.1128/JVI.75.7.3185-3196.2001.

Ogle, D. H., Doll, J. C., Wheeler, A. P., and Dinno, A. 2023. FSA: Simple Fisheries Stock Assessment Methods. .

Osterbaan, L. J., Choi, J., Kenney, J., Flasco, M., Vigne, E., Schmitt-Keichinger, C., Rebelo, A. R., Heck, M., and Fuchs, M. 2019. The identity of a single residue

of the RNA-dependent RNA polymerase of grapevine fanleaf virus modulates vein clearing in Nicotiana benthamiana. Molecular Plant-Microbe Interactions 32:790–801. https://doi.org/10.1094/MPMI-12-18-0337-R.

Osterbaan, L. J., and Fuchs, M. 2019. Dynamic interactions between plant viruses and their hosts for symptom development. J Plant Pathol 101:885–895. https://doi.org/10.1007/s42161-019-00323-5.

Osterbaan, L. J., Hoyle, V., Curtis, M., DeBlasio, S., Rivera, K. D., Heck, M., and Fuchs, M. 2021. Identification of protein interactions of grapevine fanleaf virus RNA-dependent RNA polymerase during infection of Nicotiana benthamiana by affinity purification and tandem mass spectrometry. Journal of General Virology 102. https://doi.org/10.1099/jgv.0.001607.

Osterbaan, L. J., Schmitt-Keichinger, C., Vigne, E., and Fuchs, M. 2018. Optimal systemic grapevine fanleaf virus infection in *Nicotiana benthamiana* following agroinoculation. Journal of Virological Methods 257:16–21. https://doi.org/10.1016/j.jviromet.2018.04.006.

Pallas, V., and García, J. A. 2011. How do plant viruses induce disease? Interactions and interference with host components. Journal of General Virology 92:2691–2705. https://doi.org/10.1099/vir.0.034603-0.

Palukaitis, P., and Yoon, J.-Y. 2024. Chapter Two - Defense signaling pathways in resistance to plant viruses: Crosstalk and finger pointing. In *Advances in Virus Research*, eds. Robin M. MacDiarmid, Benhur Lee, and Martin Beer. Academic Press, pp. 77–212. https://doi.org/10.1016/bs.aivir.2024.01.002.

Pasin, F., Shan, H., García, B., Müller, M., San León, D., Ludman, M., Fresno, D. H., Fátyol, K., Munné-Bosch, S., Rodrigo, G., and García, J. A. 2020. Abscisic Acid Connects Phytohormone Signaling with RNA Metabolic Pathways and Promotes an Antiviral Response that Is Evaded by a Self-Controlled RNA Virus. Plant Communications 1:100099. https://doi.org/10.1016/j.xplc.2020.100099.

R Core Team, R. 2013. R: A language and environment for statistical computing. .

Raski, D. J., Goheen, A. C., Lider, L. A., and Meredith, C. P. 1983. Strategies Against Grapevine Fanleaf Virus and Its Nematode Vector. Plant Dis. 67:335. https://doi.org/10.1094/PD-67-335.

Ritzenthaler, C., Viry, M., Pinck, M., Margis, R., Fuchs, M., and Pinck, L. 1991. Complete nucleotide sequence and genetic organization of grapevine fanleaf nepovirus RNA1. Journal of General Virology 72:2357–2365. https://doi.org/10.1099/0022-1317-72-10-2357.

Roy, B. G., Choi, J., and Fuchs, M. F. 2024. Predictive Modeling of Proteins Encoded by a Plant Virus Sheds a New Light on Their Structure and Inherent Multifunctionality. Biomolecules 14:62. https://doi.org/10.3390/biom14010062.

Roy, B. G., DeBlasio, S., Yang, Y., Thannhauser, T., Heck, M., and Fuchs, M. 2023. Profiling Plant Proteome and Transcriptome Changes during Grapevine Fanleaf Virus Infection. J. Proteome Res. 22:1997–2017. https://doi.org/10.1021/acs.jproteome.3c00069.

Roy, B. G., and Fuchs, M. 2024. A single viral amino acid shapes the root system architecture of a plant host upon virus infection. BMC Microbiol 24:267. https://doi.org/10.1186/s12866-024-03399-x.

Roy, B. G., and Fuchs, M. 2022. Herbaceous plant hosts as supermodels for grapevine viruses: a historical perspective. J Plant Pathol 1–30. https://doi.org/10.1007/s42161-022-01267-z.

Roy, B. G., and Fuchs, M. 2023. *Processing and maintenance of Nicotiana benthamiana tissue for phenotypic, histological, and ribonucleic acid analysis v1*. https://protocols.cloud/view/processing-and-maintenance-of-nicotiana-benthamian-cvssw6ee (accessed 28 Aug 2023).

Subramanian, A., Tamayo, P., Mootha, V. K., Mukherjee, S., Ebert, B. L., Gillette, M. A., Paulovich, A., Pomeroy, S. L., Golub, T. R., Lander, E. S., and Mesirov, J. P. 2005. Gene set enrichment analysis: A knowledge-based approach for interpreting genome-wide expression profiles. Proc. Natl. Acad. Sci. U.S.A. 102:15545–15550. https://doi.org/10.1073/pnas.0506580102.

Team, Rs. 2015. RStudio: integrated development for R. (No Title).

Tsuda, S. 2020. Development of plant virus symptoms and attenuated virus strains to control viral disease. J Gen Plant Pathol 86:538–542. https://doi.org/10.1007/s10327-020-00951-1.

Valli, A. A., García López, R., Ribaya, M., Martínez, F. J., Gómez, D. G., García, B., Gonzalo, I., Gonzalez De Prádena, A., Pasin, F., Montanuy, I., Rodríguez-Gonzalo, E., and García, J. A. 2022. Maf/ham1-like pyrophosphatases of non-canonical nucleotides are host-specific partners of viral RNA-dependent RNA

polymerases ed. Weifeng Gu. PLoS Pathog 18:e1010332. https://doi.org/10.1371/journal.ppat.1010332.

Van Kempen, M., Kim, S. S., Tumescheit, C., Mirdita, M., Lee, J., Gilchrist, C. L. M., Söding, J., and Steinegger, M. 2024. Fast and accurate protein structure search with Foldseek. Nat Biotechnol 42:243–246. https://doi.org/10.1038/s41587-023-01773-0.

Vigne, E., Gottula, J. W., Schmitt-Keichinger, C., Komar, V., Ackerer, L., Belval, L., Rakotomalala, L., Lemaire, O., Ritzenthaler, C., and Fuchs, M. 2013. A strain-specific segment of the RNA-dependent RNA polymerase of grapevine fanleaf virus determines symptoms in *Nicotiana* species. Journal of General Virology 94:2803–2813. https://doi.org/10.1099/vir.0.057646-0.

Wei, T., and Simko, V. 2017. *R package "corrplot": Visualization of a Correlation Matrix*.

Westergren, T., Dove, S. K., Sommarin, M., and Pical, C. 2001. AtPIP5K1, an Arabidopsis thaliana phosphatidylinositol phosphate kinase, synthesizes PtdIns(3,4)P2 and PtdIns(4,5)P2 in vitro and is inhibited by phosphorylation. Biochemical Journal 359:583–589. https://doi.org/10.1042/bj3590583.

Whitham, S. A., and Wang, Y. 2004. Roles for host factors in plant viral pathogenicity. Current Opinion in Plant Biology 7:365–371. https://doi.org/10.1016/j.pbi.2004.04.006.

Wickham, H. 2009. *ggplot2: Elegant Graphics for Data Analysis*. New York, NY: Springer. https://doi.org/10.1007/978-0-387-98141-3.

Wu, T., Hu, E., Xu, S., Chen, M., Guo, P., Dai, Z., Feng, T., Zhou, L., Tang, W., Zhan, L., Fu, X., Liu, S., Bo, X., and Yu, G. 2021. clusterProfiler 4.0: A universal enrichment tool for interpreting omics data. The Innovation 2:100141. https://doi.org/10.1016/j.xinn.2021.100141.

Xu, Y., Zhang, S., Zhang, M., Jiao, S., Guo, Y., and Jiang, T. 2024. The role of reactive oxygen species in plant-virus interactions. Plant Cell Rep 43:197. https://doi.org/10.1007/s00299-024-03280-1.

Yamagata, A., Yoshida, T., Sato, Y., Goto-Ito, S., Uemura, T., Maeda, A., Shiroshima, T., Iwasawa-Okamoto, S., Mori, H., Mishina, M., and Fukai, S. 2015. Mechanisms of splicing-dependent trans-synaptic adhesion by PTPδ–IL1RAPL1/IL-1RAcP for synaptic differentiation. Nat Commun 6:6926. https://doi.org/10.1038/ncomms7926.

Yoo, K.-Y., Son, J. Y., Lee, J. U., Shin, W., Im, D.-W., Kim, S. J., Ryu, S. E., and Heo, Y.-S. 2015. Structure of the catalytic phosphatase domain of MTMR8: implications for dimerization, membrane association and reversible oxidation. Acta Cryst D 71:1528–1539. https://doi.org/10.1107/S139900471500927X.

Yu, G. 2021. Enrichplot: visualization of functional enrichment result. R package version 1.

Zhang, Y. 2008. I-TASSER server for protein 3D structure prediction. BMC Bioinformatics 9:40. https://doi.org/10.1186/1471-2105-9-40.

Zhao, S., and Li, Y. 2021. Current understanding of the interplays between host hormones and plant viral infections ed. Xiaofeng Wang. PLoS Pathog 17:e1009242. https://doi.org/10.1371/journal.ppat.1009242.

Zhao, Y., Yang, J., Liu, Y., Hu, X., Wang, X., Yang, J., and Liu, J. 2025. Wheat Yellow Mosaic Virus P1 Inhibits ROS Accumulation to Facilitate Viral Infection. IJMS 26:1455. https://doi.org/10.3390/ijms26041455.

TABLE 6-S1. Primers used in this study for the detection of grapevine fanleaf virus (GFLV) or pepper ringspot virus (PepRSV) by RT-PCR or RT-qPCR.

Name	Assay	Target	Sequence (5'-3')	Reference
GFLV-RNA1-qF GFLV-RNA1-qR	RT-qPCR	GFLV protein coding sequence ($1D^{Pro}$-$1E^{Pol*/Sd}$)	ccc-aaa-agt-cat-cgc-aat-gct gga-tca-gga-tat-gga-aag-cac	
GFLV-F13-1-F GFLV-F13-1-R GFLV-GHu-1-F GFLV-GHu-1-R	RT-PCR	GFLV C-terminal symptom determinant region in protein $1E^{Pol*/Sd}$	tgt-tgg-gac-caa-atc-aga-gga-atg gaa-act-ggg-tta-ttt-aaa-ctt-ggt tgc-tag-gac-caa-atc-aga-gga-acg aaa-ctt-ggt-tat-ccc-agt-acc-a	Osterbaan et al. 2019
Tobra-F3 Tobra-R2	RT-PCR	Tobravirus 194K RNA polymerase gene	ggt-ggk-caa-tgg-tct-twt-tgg gtc-agc-tgy-tga-tca-gat-aac-c	Jones et al. 2008

TABLE 6-S2. Experimental design and infection of grapevine fanleaf virus strain and pepper ringspot virus into *Nicotiana benthamiana* plants across multiple experiments.

Treatment	Exp. Reps	1	2	3	4	5	6	7	8	9	10	11	12	13	14	15	16	17	18	n
GFLV-F13	11	15	10	15	7	5	14		21					`1`		1	13	18		119
GFLV-F13 1E G802K	7	15					18	1	22					`1`		14	17			87
GFLV-F13 1E N804S	3												21		21				18	60
GFLV-F13 1E G802K + N804S	3		10					19											18	47
GFLV-F13 1E Δ2404-2424	4			5		11		19					18							53
GFLV-GHu	13	15	9	12	8	13	14		23		2			`1`	24	4	12	15		151
GFLV-GHu 1E K802G	9	15	4	4			6	18	19					`1`		5	19			90
GFLV-GHu 1E S804N	2														8				15	23
GFLV-GHu 1E K802G S804N	3										8		2						9	19
GFLV-GHu 1E Δ2404-2424	3					17					10	9								36
GFLV-GHu 1E:V5	3				9								10				4			23
GFLV-GHu 1E K802G:V5	1				6															6
GFLV-F13 1E:V5	4										18	12			24		10			64
Mock Inoculated	12	14	5	15		15	11	16	14		8			`1`		15	37	12		162
Inoculated, non-infected	16		7	24	12	25	19	23	5		42	22	37		9	52	30	27	22	356
Pepper ringspot virus (pos control)	4									`1`					15	`1`	`1`			17
number of individuals	74	45	75	42	86	82	96	104	25	88	43	88	75	101	92	143	72	82		1413
infection rate	1	0.83	0.6	0.71	0.64	0.73	0.71	0.94	-	0.48	0.48	0.58	-	0.89	0.31	0.71	0.55	0.73		0.683

TABLE 6-S3. Repeated SPAD meter readings performed on apical leaves of *Nicotiana benthamiana* plants infected with wildtype or mutant grapevine fanleaf virus (GFLV) strains. SPAD readings were taken in three locations: left lamina (LL), midrib (M), and right lamina (RL) to negate any major sources of variation within the leaf anatomy. Average across three technical replicates and respective standard deviation are reported. The highest amount of variation was ~3%.

Treatment	Location	Technical replicate			Average	STDEV
		1	2	3		
mutant F13 1E$_{G802K}$	LL	34.2	34.2	34.3	34.23	0.058
mutant F13 1E$_{G802K}$	M	40.1	39.6	39.9	39.87	0.252
mutant F13 1E$_{G802K}$	RL	36.1	36	36.2	36.1	0.1
wildtype F13	LL	33.2	33	33.1	33.1	0.1
wildtype F13	M	35.3	36	32.9	34.73	1.626
wildtype F13	RL	34.9	34.9	34.1	34.63	0.462
mock control	LL	31.3	31.4	33	31.9	0.954
mock control	M	34	32.3	32.2	32.83	1.012
mock control	RL	32.6	32.2	33	32.6	0.4
mutant GHu 1E$_{K802G}$	LL	35.9	36	35.9	35.93	0.058
mutant GHu 1E$_{K802G}$	M	40.4	40.1	38	39.5	1.308
mutant GHu 1E$_{K802G}$	RL	35.8	35.6	35	35.47	0.416
wildtype GHu	LL	25.5	24.7	25.2	25.13	0.404
wildtype GHu	M	26.2	24	26.8	25.67	1.474
wildtype GHu	RL	25.5	25.4	25	25.3	0.265

TABLE 6-S4. Chlorophyll quantification with SPAD meter across grapevine fanleaf virus treatments from 2 to 16 days post inoculation. Measurements were conducted across experimental cohorts 15 and 16.

This table is provided online at the following link:

https://doi.org/10.5281/zenodo.15115514

TABLE 6-S5. Pairwise comparison output of SPAD meter readings for all timepoints across treatments. (ANOVA followed by Tukey's HSD post-hoc test reported.)

DPI	Contrast	Estimate	t-ratio	*p* value
2	Mock control - Wildtype GHu	0.2867	0.266	0.9989 .
2	Mutant F13 1E G802K - Wildtype GHu	0.2600	0.241	0.9992 .
2	Mutant GHu 1E K802G - Wildtype GHu	0.9667	0.898	0.8978 .
2	Wildtype F13 - Wildtype GHu	0.8133	0.755	0.9431 .
3	Mock control - Wildtype GHu	1.2333	1.145	0.7824 .
3	Mutant F13 1E G802K - Wildtype GHu	-0.9867	-0.916	0.8907 .
3	Mutant GHu 1E K802G - Wildtype GHu	0.1733	0.161	0.9998 .
3	Wildtype F13 - Wildtype GHu	-0.5133	-0.477	0.9895 .
4	Mock control - Wildtype GHu	-0.3467	-0.322	0.9977 .
4	Mutant F13 1E G802K - Wildtype GHu	-2.4133	-2.241	0.1656 .
4	Mutant GHu 1E K802G - Wildtype GHu	-2.2400	-2.080	0.2296 .
4	Wildtype F13 - Wildtype GHu	-2.3333	-2.167	0.1934 .
5	Mock control - Wildtype GHu	1.3400	1.244	0.7253 .
5	Mutant F13 1E G802K - Wildtype GHu	0.6400	0.594	0.9760 .
5	Mutant GHu 1E K802G - Wildtype GHu	1.2133	1.127	0.7925 .
5	Wildtype F13 - Wildtype GHu	-0.4000	-0.371	0.9959 .
6	Mock control - Wildtype GHu	3.1400	2.916	0.0298 *
6	Mutant F13 1E G802K - Wildtype GHu	2.6133	2.427	0.1091 .
6	Mutant GHu 1E K802G - Wildtype GHu	2.9000	2.693	0.0557 .
6	Wildtype F13 - Wildtype GHu	1.9733	1.832	0.3555 .
7	Mock control - Wildtype GHu	5.4267	5.039	<.0001 ***
7	Mutant F13 1E G802K - Wildtype GHu	2.5133	2.334	0.1351 .
7	Mutant GHu 1E K802G - Wildtype GHu	5.0867	4.723	<.0001 ***
7	Wildtype F13 - Wildtype GHu	1.1400	1.059	0.8277 .
8	Mock control - Wildtype GHu	6.7800	6.295	<.0001 ***
8	Mutant F13 1E G802K - Wildtype GHu	6.1000	5.664	<.0001 ***
8	Mutant GHu 1E K802G - Wildtype GHu	6.8400	6.351	<.0001 ***
8	Wildtype F13 - Wildtype GHu	4.7067	4.370	0.0001 **
9	Mock control - Wildtype GHu	8.2867	7.694	<.0001 ***
9	Mutant F13 1E G802K - Wildtype GHu	6.9400	6.444	<.0001 ***
9	Mutant GHu 1E K802G - Wildtype GHu	9.9200	9.211	<.0001 ***
9	Wildtype F13 - Wildtype GHu	5.6600	5.255	<.0001 ***
10	Mock control - Wildtype GHu	6.9600	6.463	<.0001 ***

DPI	Contrast	Estimate	t-ratio	*p* value
10	Mutant F13 1E G802K - Wildtype GHu	5.7133	5.305	<.0001 ***
10	Mutant GHu 1E K802G - Wildtype GHu	8.9067	8.270	<.0001 ***
10	Wildtype F13 - Wildtype GHu	3.6733	3.411	0.0061 **
11	Mock control - Wildtype GHu	3.1467	2.922	0.0292 *
11	Mutant F13 1E G802K - Wildtype GHu	3.9600	3.677	0.0023 **
11	Mutant GHu 1E K802G - Wildtype GHu	6.6067	6.134	<.0001 ***
11	Wildtype F13 - Wildtype GHu	0.7867	0.730	0.9494 .
12	Mock control - Wildtype GHu	2.3867	2.216	0.1745 .
12	Mutant F13 1E G802K - Wildtype GHu	3.2467	3.015	0.0221 *
12	Mutant GHu 1E K802G - Wildtype GHu	4.3533	4.042	0.0005 **
12	Wildtype F13 - Wildtype GHu	0.2267	0.210	0.9996 .
13	Mock control - Wildtype GHu	1.0467	0.972	0.8679 .
13	Mutant F13 1E G802K - Wildtype GHu	0.3800	0.353	0.9967 .
13	Mutant GHu 1E K802G - Wildtype GHu	2.6067	2.420	0.1107 .
13	Wildtype F13 - Wildtype GHu	-3.1867	-2.959	0.0262 *
14	Mock control - Wildtype GHu	3.6000	3.343	0.0077 **
14	Mutant F13 1E G802K - Wildtype GHu	1.4133	1.312	0.6836 .
14	Mutant GHu 1E K802G - Wildtype GHu	2.4600	2.284	0.1508 .
14	Wildtype F13 - Wildtype GHu	0.3133	0.291	0.9984 .
15	Mock control - Wildtype GHu	2.3467	2.179	0.1885 .
15	Mutant F13 1E G802K - Wildtype GHu	0.1867	0.173	0.9998 .
15	Mutant GHu 1E K802G - Wildtype GHu	0.0800	0.074	1.0000 .
15	Wildtype F13 - Wildtype GHu	-1.3467	-1.250	0.7216 .

TABLE 6-S6. Measurements of primary root traits of *Nicotiana benthamiana* infected with grapevine fanleaf virus (GFLV) strains or pepper ringspot virus extracted from micro-CT scans.

Sample code[a]	Treatment	Plant code[b]	Vascular bundle		Full diameter		Circumference ratio	Area ratio
			Circum. (mm)	Area (mm^2)	Circum. (mm)	Area (mm^2)		
1A	pepper ringspot virus	P1	1.786	0.254	3.426	0.925	0.521	0.275
1B		P2	1.538	0.186	3.621	1.038	0.425	0.179
1C		P3	3.671	1.073	6.427	3.287	0.571	0.326
1D		P4	3.752	1.12	6.824	3.7	0.550	0.303
1E	non-infected	M4	5.009	1.997	7.387	4.343	0.678	0.460
2A		C7	4.927	1.913	9.676	7.409	0.509	0.258
2B		C10	6.597	3.409	10.073	8.066	0.655	0.423
FM12	mutant GFLV F13-1E$_{G802K}$	FM12	4.409	1.543	6.947	3.841	0.635	0.402
2C		FM7	4.363	1.514	8.761	6.108	0.498	0.248
2D		FM9	4.506	1.616	8.105	5.228	0.556	0.309
2E		FM14	4.838	1.863	8.348	5.545	0.580	0.336
3A	wildtype GFLV F13	F11	4.999	1.969	7.401	4.342	0.675	0.453
3B		F13	4.881	1.88	7.738	4.697	0.631	0.400
3C		F16	6.974	3.871	10.181	8.238	0.685	0.470
3D	mutant GFLV GHu-1E$_{K802G}$	GM3	4.211	1.409	6.328	3.186	0.665	0.442
4A		GM5	4.479	1.596	8.339	5.533	0.537	0.288
4B		GM10	7.203	4.114	12.999	13.326	0.554	0.309
4C	wildtype GFLV GHu	G1	4.263	1.393	7.407	4.265	0.576	0.327
4D		G3	5.606	2.489	8.677	5.928	0.646	0.420
4E		G10	7.602	4.536	12.211	11.847	0.623	0.383

[a]Sample code pertains to zip file name of original scans, delineated from tube number and the order in which the samples were scanned.
[b]Plant code represents a letter coding scheme in combination with the plant ID number in experimental replicate #16.

TABLE 6-S7. Proteins identified through co-immunoprecipitation assays of grapevine fanleaf virus (GFLV) protein $1E^{Pol*/Sd}$.

A. All identified proteins and associated metadata to include the contrasting and overlapping treatments of wildtype GFLV-GHu:V5, mutant GFLV-GHu $1E_{K802G}$:V5, and wildtype GFLV-F13:$V5_{c\text{-}1}$, filtered by untagged controls (Osterbaan et al. 2021).

B. Condensed comparison and contrast of 7A, only to include the condense gene names for input into KEGG analysis pipeline.

C. Enrichment analysis of gene ontologies separated by viral treatment within the co-immunoprecipitation data (Osterbaan et al. 2021).

This table is provided online at the following link:

https://doi.org/10.5281/zenodo.15101797

TABLE 6-S8. *Nicotiana benthamiana* genes that play a role in grapevine fanleaf virus infection identified via ‘omics datasets. The identified genes were simplified to their gene ID numbers to provide a contrast matrix that counts the overlap of each dataset’s extracted gene ID for the production of a pseudo-correlation matrix. The categories were split by experiment, and further dissected to time point, viral treatment, and specifying the tissue type and correlating protein or transcript technology for acquisition.

Technique	Dataset, Treatment, Time	CO–IP, wildtype GHu:V5, T7	CO–IP, mutant GHu:V5, T7	CO–IP, wildtype F13:V5, T7	Leaf RNA, wildtype GHu, T4	Leaf RNA, wildtype GHu, T7	Leaf RNA, wildtype GHu, T12	Leaf RNA, mutant GHu, T4	Leaf RNA, mutant GHu, T7	Leaf RNA, mutant GHu, T12	Leaf RNA, wildtype F13, T4	Leaf RNA, wildtype F13, T7	Leaf RNA, wildtype F13, T12	Leaf RNA, mutant F13, T4	Leaf RNA, mutant F13, T7	Leaf RNA, mutant F13, T12	Leaf protein, wildtype GHu, T4	Leaf protein, wildtype GHu, T7	Leaf protein, wildtype GHu, T12	Leaf protein, mutant GHu, T4	Leaf protein, mutant GHu, T7	Leaf protein, mutant GHu, T12	Leaf protein, wildtype F13, T4	Leaf protein, wildtype F13, T7	Leaf protein, wildtype F13, T12	Leaf protein, mutant F13, T4	Leaf protein, mutant F13, T7	Leaf protein, mutant F13, T12	Root RNA, wildtype GHu, T4	Root RNA, wildtype GHu, T17	Root RNA, wildtype GHu, T26	Root RNA, mutant GHu, T4	Root RNA, mutant GHu, T17	Root RNA, mutant GHu, T26
CO-IP	CO–IP, wildtype GHu:V5, T7		25	14	0	15	0	0	0	0	0	2	0	0	1	0	0	0	0	0	0	0	0	0	0	0	0	5	9	3	1	15	4
	CO–IP, mutant GHu:V5, T7	25		13	1	9	1	1	1	1	2	2	2	3	1	1	1	1	2	1	1	2	1	1	3	1	1	2	3	8	2	3	13	4
	CO–IP, wildtype F13:V5, T7	14	13		1	3	1	1	1	1	1	2	2	3	2	2	1	1	2	1	1	1	1	1	2	1	1	1	2	8	4	1	9	5
Leaf 3'RNA-Seq	Leaf RNA, wildtype GHu, T4	0	1	1		0	1	2	1	1	2	2	1	1	1	1	1	1	1	1	1	0	1	1	1	1	1	1	2	1	1	1	0	1
	Leaf RNA, wildtype GHu, T7	15	9	3	0		11	23	17	13	35	157	54	169	93	50	1	0	2	1	0	1	2	1	1	1	2	0	187	289	155	46	396	136
	Leaf RNA, wildtype GHu, T12	0	1	1	1	11		3	2	9	6	6	10	6	2	8	1	1	1	1	1	0	1	1	1	1	1	1	2	9	2	2	13	4
	Leaf RNA, mutant GHu, T4	0	1	1	2	23	3		18	15	53	79	20	55	41	29	1	1	1	1	1	0	1	1	1	1	1	1	14	35	25	5	44	21
	Leaf RNA, mutant GHu, T7	0	1	1	1	17	2	18		18	16	50	24	34	44	24	1	1	1	1	1	0	1	1	1	1	1	1	3	12	9	6	13	8
	Leaf RNA, mutant GHu, T12	0	1	1	1	13	9	15	18		19	36	54	36	34	51	1	1	1	1	1	0	1	1	1	1	1	1	4	19	8	3	15	5
	Leaf RNA, wildtype F13, T4	0	2	1	2	35	6	53	16	19		141	40	114	62	41	1	1	1	1	1	0	1	1	1	1	1	1	19	89	39	4	128	29
	Leaf RNA, wildtype F13, T7	2	2	2	2	157	6	79	50	36	141		94	142	198	90	1	1	1	1	1	0	1	3	1	1	3	1	57	159	76	18	219	71
	Leaf RNA, wildtype F13, T12	0	2	2	1	54	10	20	24	54	40	94		124	84	155	1	1	1	1	1	0	1	2	1	1	2	1	16	58	36	8	65	27
	Leaf RNA, mutant F13, T4	0	3	3	1	169	6	55	34	36	114	142	124		175	175	1	1	2	2	1	1	2	2	2	2	2	2	77	205	108	37	258	113
	Leaf RNA, mutant F13, T7	1	1	2	1	93	2	41	44	34	62	198	84	175		99	1	1	1	1	1	0	1	2	1	1	2	1	21	79	38	13	97	36
	Leaf RNA, mutant F13, T12	0	1	2	1	50	8	29	24	51	41	90	155	175	99		1	1	1	1	1	0	1	2	1	1	2	1	25	70	34	11	87	29
Leaf LC-MS/MS	Leaf protein, wildtype GHu, T4	0	1	1	1	1	1	1	1	1	1	1	1	1	1	1		1	1	7	1	0	8	1	1	7	1	1	1	3	3	1	1	2
	Leaf protein, wildtype GHu, T7	0	1	1	1	0	1	1	1	1	1	1	1	1	1	1	1		1	1	4	0	1	5	1	1	5	1	1	1	1	1	0	1
	Leaf protein, wildtype GHu, T12	0	2	2	1	2	1	1	1	1	1	1	1	2	1	1	1	1		2	1	12	2	1	10	2	1	9	1	6	3	3	1	2
	Leaf protein, mutant GHu, T4	0	1	1	1	1	1	1	1	1	1	1	1	2	1	1	7	1	2		1	1	8	1	2	8	1	2	1	3	2	2	0	2
	Leaf protein, mutant GHu, T7	0	1	1	1	0	1	1	1	1	1	1	1	1	1	1	1	4	1	1		0	1	7	1	1	9	1	3	1	1	1	0	1
	Leaf protein, mutant GHu, T12	0	2	1	0	1	0	0	0	0	0	0	0	1	0	0	0	0	12	1	0		1	0	15	1	0	11	0	4	2	2	1	1
	Leaf protein, wildtype F13, T4	0	1	1	1	2	1	1	1	1	1	1	1	2	1	1	8	1	2	8	1	1		1	2	9	1	2	1	4	3	2	3	2
	Leaf protein, wildtype F13, T7	0	1	1	1	1	1	1	1	1	1	1	1	2	2	2	1	5	1	1	7	0	1		1	1	15	1	3	3	3	1	2	2
	Leaf protein, wildtype F13, T12	0	3	2	1	1	1	1	1	1	1	1	1	2	1	1	1	1	10	2	1	15	2	1		2	1	12	1	5	3	3	1	2
	Leaf protein, mutant F13, T4	0	1	1	1	1	1	1	1	1	1	1	1	2	1	1	7	1	2	8	1	1	9	1	2		1	2	1	4	3	2	2	2
	Leaf protein, mutant F13, T7	0	1	1	1	2	1	1	1	1	1	3	2	2	2	2	1	5	1	1	9	0	1	15	1	1		1	3	3	3	1	2	2
	Leaf protein, mutant F13, T12	0	2	1	1	0	1	1	1	1	1	1	1	2	1	1	1	1	9	2	1	11	2	1	12	2	1		1	4	3	3	1	2
Root 3'RNA-Seq	Root RNA, wildtype GHu, T4	5	3	2	2	187	2	14	3	4	19	57	16	77	21	25	1	1	1	1	3	0	1	3	1	1	3	1		251	153	215	371	162
	Root RNA, wildtype GHu, T17	9	8	8	1	289	9	35	12	19	89	159	58	205	79	70	3	1	6	3	1	4	4	3	5	4	3	4	251		824	224	2570	880
	Root RNA, wildtype GHu, T26	3	2	4	1	155	2	25	9	8	39	76	36	108	38	34	3	1	3	2	1	2	3	3	3	3	3	3	153	824		108	875	910
	Root RNA, mutant GHu, T4	1	3	1	1	46	2	5	6	3	4	18	8	37	13	11	1	1	3	2	1	2	2	1	3	2	1	3	215	224	108		175	107
	Root RNA, mutant GHu, T17	15	13	9	0	396	13	44	13	15	128	219	65	258	97	87	1	0	1	0	0	1	3	2	1	2	2	1	371	2570	875	175		1028
	Root RNA, mutant GHu, T26	4	4	5	1	136	4	21	8	5	29	71	27	113	36	29	2	1	2	2	1	1	2	2	2	2	2	2	162	880	910	107	1028	

TABLE 6-S9. Overlap of root and shoot transcriptomic data for contrasts, extended with names.

This table is provided online at the following link:

https://zenodo.org/records/15077180

TABLE 6-S10. Dysregulated genes for all treatment contrasts and techniques of host profiling, documenting the commonalities of grapevine fanleaf virus infection across all strains.

This table is provided online at the following link:

https://zenodo.org/records/15077180

TABLE 6-S11. Functional enrichment analysis of leaves infected with various grapevine fanleaf virus (GFLV) strains.

A. KEGG enrichment analysis of leaf transcriptomics data upon infection with GFLV strains indicates perturbed pathways specific to each viral strain and time point of analysis.

B. Gene set enrichment analysis of leaf transcriptomics data upon infection with GFLV strains, updated with new annotation and contrasts of viral infection against mock control plants.

This table is provided online at the following link:

https://zenodo.org/records/15077180

TABLE 6-S12. Top PDB hits for overall structural protein alignment across grapevine fanleaf virus, Arabis mosaic virus and grapevine deformation virus to include three RNA-dependent RNA polymerases (RdRPs) from distantly related RNA viruses.

Viral RdRP	PDB	TM-score range	RMSD range	Seq ID range	Structural coverage
Norwalk virus	1SH0	0.5605-0.5670	2.36-2.63	0.1820-0.2040	0.5934-0.5947
Murine norovirus	3NAH	0.5537-0.5572	2.08-2.22	0.1930-0.2030	0.5777-0.5796
Rabbit hemorrhagic disease virus	1KHV	0.5497-0.5532	2.49-2.61	0.1680-0.1810	0.5830-0.5857

TABLE 6-S13. Top three models resulting from I-TASSER-MTD structural predictions of domain 2 in the nepovirus RNA-dependent RNA polymerase (protein 1E). The provided eTM value is the top-resulting model that received the best TM-align scores to known structures.

Virus	eTM	PDB Hit – common name	TM-score	RMSD	Seq ID	Coverage
Arabis mosaic virus	0.48 ± 0.15	5xw4A – Cdc14p phosphatase	0.71	3.59	0.075	0.918
		1oheA – Cdc14b phosphatase	0.69	3.81	0.085	0.905
		4y7iA – phosphoinositide phosphatase	0.60	3.89	0.055	0.784
GFLV consensus	0.52 ± 0.15	5xw4A – Cdc14p phosphatase	0.72	3.19	0.091	0.895
		1oheA – Cdc14b phosphatase	0.70	3.39	0.091	0.895
		1zvrA – phosphoinositide phosphatase	0.58	4.06	0.043	0.791
GFLV-F13	0.43 ± 0.14	5xw4A – Cdc14p phosphatase	0.66	4.16	0.081	0.915
		1oheA – Cdc14b phosphatase	0.65	4.14	0.072	0.897
		4fyeA – phosphoinositide phosphatase	0.56	4.47	0.059	0.789
GFLV-GHu	0.50 ± 0.15	5xw4A – Cdc14p phosphatase	0.72	3.45	0.075	0.909
		1oheA – Cdc14b phosphatase	0.70	3.47	0.061	0.891
		1zvrA2 – phosphoinositide phosphatase	0.59	4.01	0.078	0.791
Grapevine deformation virus	0.42 ± 0.14	5xw4A – Cdc14p phosphatase	0.70	3.93	0.085	0.921
		1oheA – Cdc14b phosphatase	0.68	3.92	0.082	0.903
		4y7iA – phosphoinositide phosphatase	0.57	3.69	0.070	0.750

TABLE 6-S14. Enzyme commission (EC) classification predictions for domain 2 of protein 1E structure predictions in I-TASSER-MTD, their respective functions, and chemical reactions. Predictions are cumulative across predictions made for wildtype grapevine fanleaf virus strains F13 and GHu, Arabis mosaic virus (ArMV) and grapevine deformation virus (GDeV).

Structural model query prediction				Total	Percent	EC Number	Common enzyme name
ArMV	GDeV	F13	GHu				
34	19	17	31	101	83%	3.1.3.48	protein-tyrosine-phosphatase
	2	2		4	3%	1.14.13.25	methane monooxygenase (soluble)
16	3	1	12	32	26%	3.1.3.16	protein-serine/threonine phosphatase
	1			1	1%	3.1.3.8	3-phytase
	1			1	1%	2.3.1.54	formate C-acetyltransferase

Enzyme name	Enzymatic reaction
protein-tyrosine-phosphatase	H_2O + O-phospho-L-tyrosyl-[protein] = L-tyrosyl-[protein] + phosphate
methane monooxygenase (soluble)	H(+) + methane + NADH + O_2 = H_2O + methanol + NAD(+)
protein-serine/threonine phosphatase	H_2O + O-phospho-L-seryl-[protein] = L-seryl-[protein] + phosphate
3-phytase	1D-myo-inositol hexakisphosphate + H_2O = 1D-myo-inositol 1,2,4,5,6-pentakisphosphate + phosphate
formate C-acetyltransferase	acetyl-CoA + formate = CoA + pyruvate

TABLE 6-S15. The prediction results of grapevine fanleaf virus (GFLV) protein 1E$^{Pol*/Sd}$ of wildtype strains F13 and GHu through I-TASSER-MTD indicates several residues within the second globular domain to have confidence behind functional residues. Many of these residues reside within the two predicted enzymatic motifs of the P-loop and Q-loop.

Amnio acid position	Predicted as functional across six query predictions	Motif	amnio acid composition in GFLV strains of interest	
			GFLV-F13	GFLV-GHu
520	1		C	C
566	1		G	G
570	3		I	I
580	1		L	L
592	3		K	K
595	1		P	P
597	4	**P-loop with active site Cys (CxxxxxR)**	**C**	**C**
599	1		**D**	**D**
602	4		**G**	**G**
603	1		**R**	**R**
604	1		**L**	**L**
610	1		**I**	**I**
613	1		**L**	**L**
615	2		**K**	**K**
619	1		**V**	**V**
621	1		**R**	**N**
622	3		**L**	**L**
635	3		**I**	**I**
638	5	**(Q-loop) DERPY**	**E**	**E**
639	1		**R**	**R**
641	3		**Y**	**Y**
646	1		**A**	**A**
648	3		**A**	**A**
649	1		**C**	**C**
665	4		L	L
666	1		Y	Y
671	3		G	G
674	1		Q	Q
678	0		L	L

TABLE 6-S16. Predicted protein models of the RNA-dependent RNA polymerase of wildtype and mutant grapevine fanleaf virus (GFLV) strains F13 and GHu, Arabis mosaic virus (ArMV) and grapevine deformation virus (GDeV), as obtained in this work and previous studies (Vigne et al. 2013; Osterbaan et al. 2019, Roy et al. 2024**).**

Virus	**Strain,** accession number	**Amino acid length**	**TM-Score**[a]	**QMEANDisCo**	**ModelArchive ID**	**Reference**
ArMV	"**Colmar**", MN599984.1	825	0.5609	0.44 ± 0.05	ma-6uzpp	This study
GDeV	**N66**, NC017939.1	823	0.5670	0.44 ± 0.05	ma-gl0zp	This study
GFLV	**Consensus**, generated multiple sequence alignment	824	0.5555	0.46 ± 0.05	ma-gf9js	This study
GFLV	**F13**, NP619689.1	824	0.5605	0.43 ± 0.05	ma-h4tyx	(Roy et al. 2024)
GFLV	**GHu**, AFM91094.1	824	0.5659	0.46 ± 0.05	ma-pufyr	
GFLV	**mutant F13 1E$_{G802K}$**	824	0.5616	0.44 ± 0.05	ma-75llk	This study
GFLV	**mutant GHu 1E$_{K802G}$**	824	0.5594	0.46 ± 0.05	ma-lniyd	This study

[a]Top match in PDB files against highest confidence model from I-TASSER MTD protein prediction software, identified by TM-align.

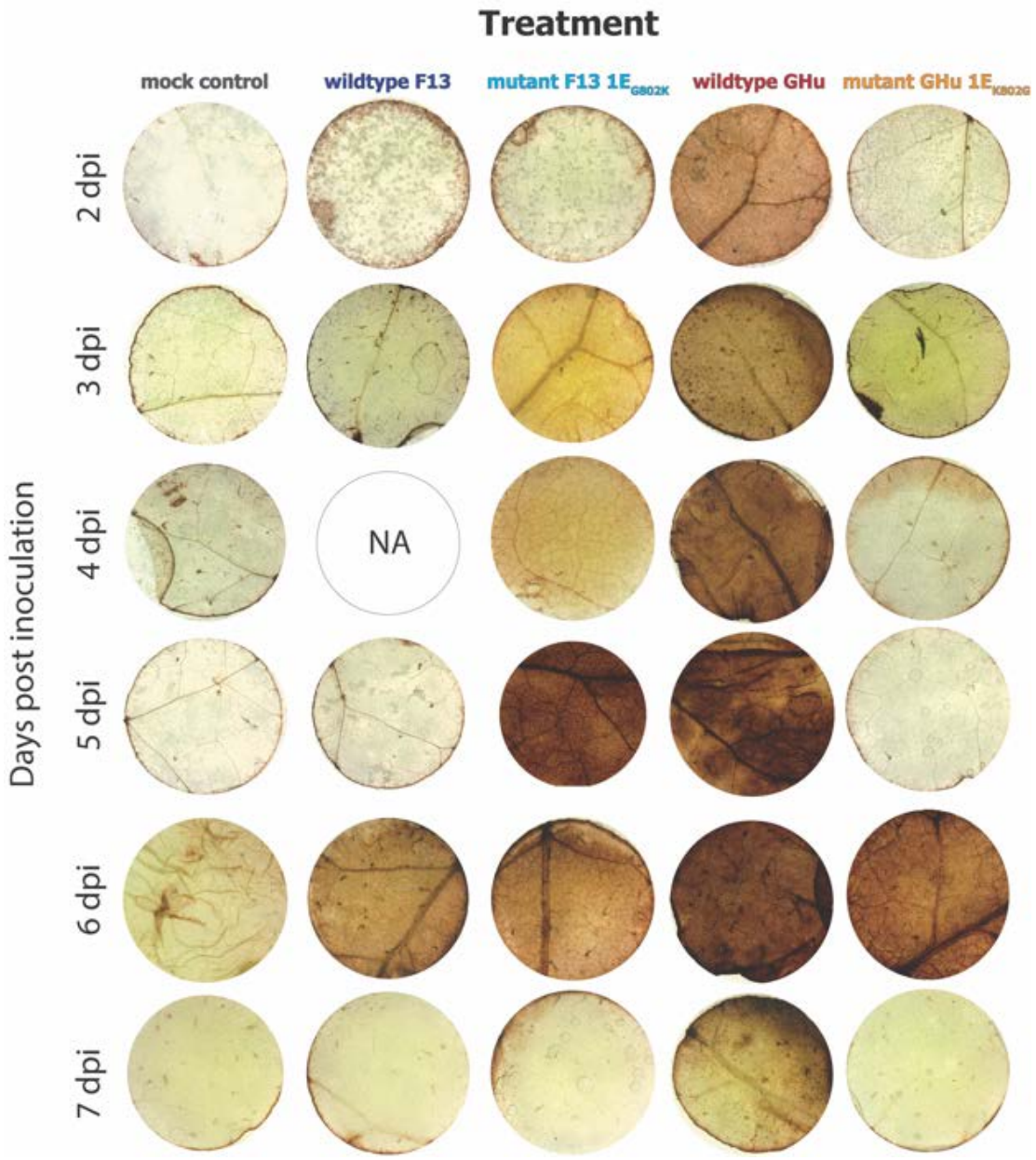

FIGURE 6-S1. 3-3' diaminobenzidine staining of leaf discs from *Nicotiana benthamiana* plants infected with wildtype grapevine fanleaf virus (GFLV) strains GHu and F13, and mutants GFLV GHu-1E$_{K802G}$ and F13-1E$_{G802K}$. A transient production of reactive oxygen species depending majorly on the amino acid in position 802 of protein 1E$^{Pol*/Sd}$ is observed. Each leaf disc is a representative example of the majority phenotype for plants testing positive true to treatment group. Images of leaf discs were cropped in Adobe Illustrator 2023® using clipping masks, no adjustment of brightness or contrast was performed. Each leaf disc is 7 millimeters in diameter. NA: data not captured.

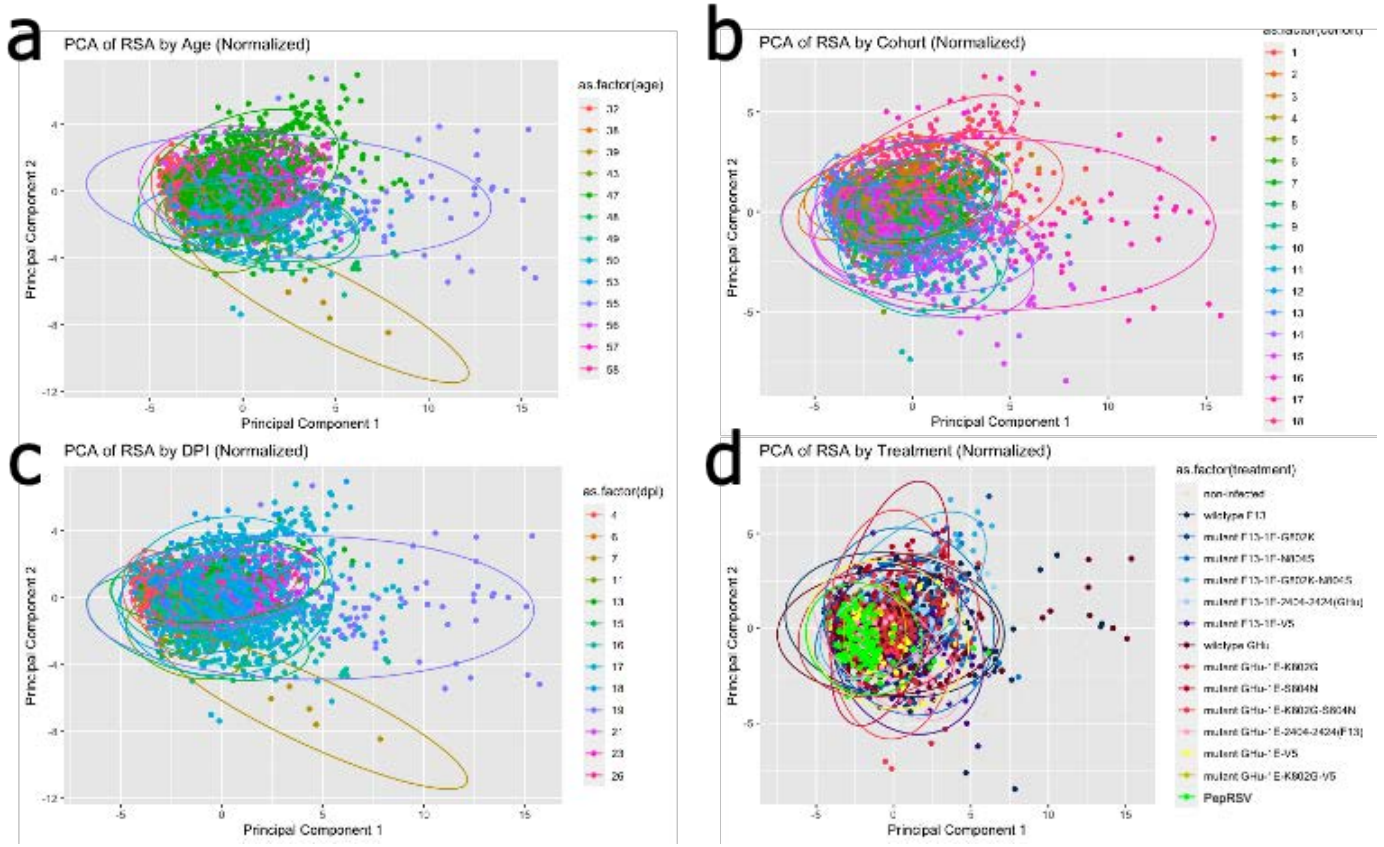

FIGURE 6-S2. Principal component analysis of *Nicotiana benthamiana* plant root system architecture traits after normalization. Minor grouping by several explanatory variables is revealed, but major overlap in continuous variables within the dataset are noted. (a) A large variance explained by PC2 can be associated with age but less so by **(b)** days post-inoculation (dpi). **(c)** Grouping by cohort or experimental replicate has minor attributions to RSA, but **(d)** treatment shows the most separation when considering the density of each treatment.

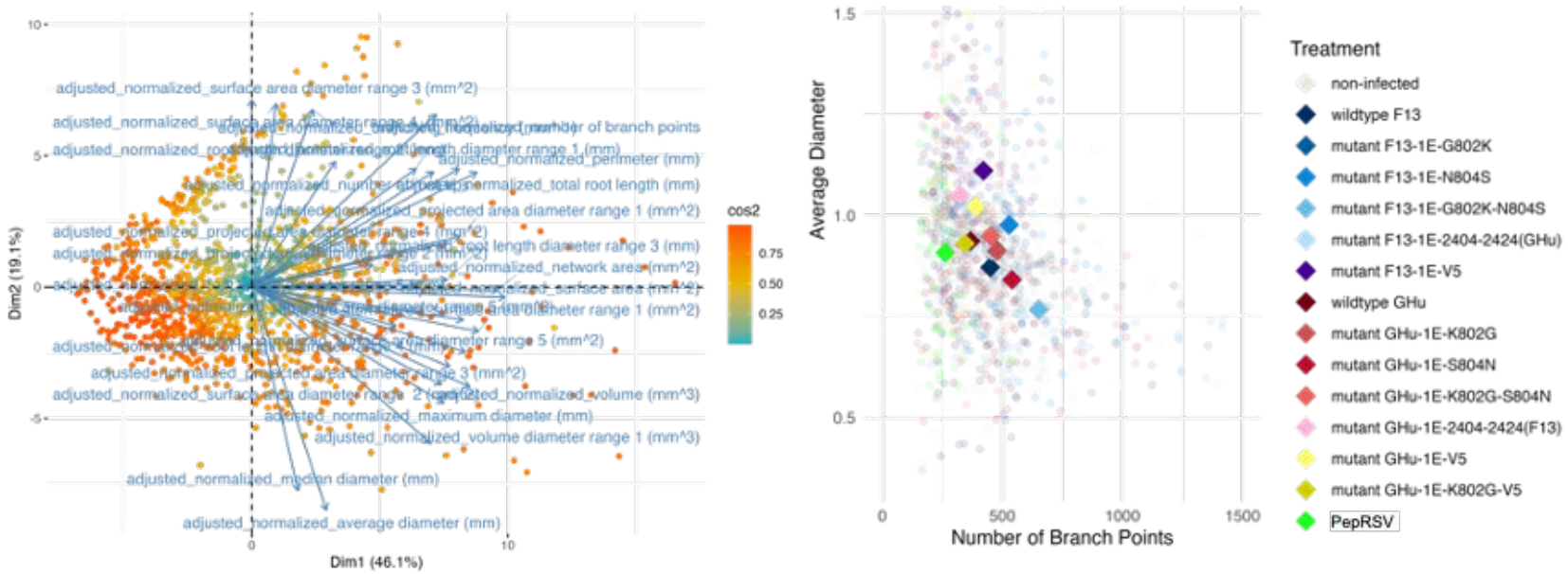

FIGURE 6-S3. Principal component analysis (PCA) biplot indicates that *Nicotiana benthamiana* root diameter traits are largely attributed in dim2 while network traits are associated in dim1 (left). A simple scatter plot with average values of number of branch points and average diameter shows similar structure to the observations in PCA assignment for treatment group dispersion (right).

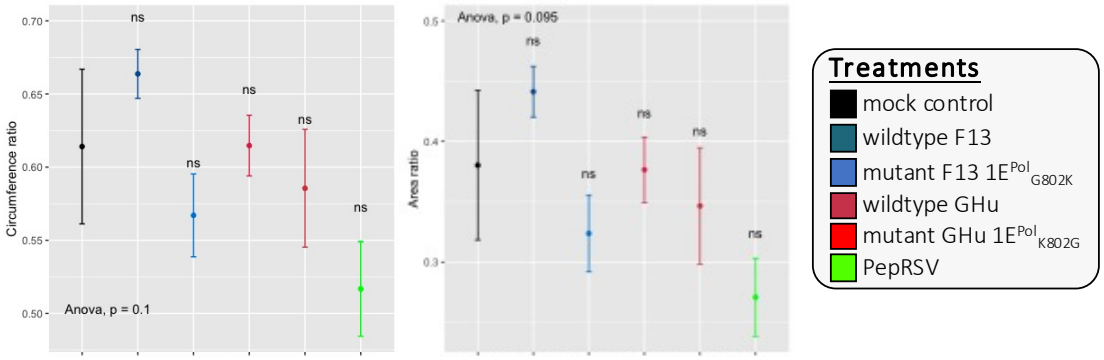

FIGURE 6-S4. Total root circumference (left panel) and area (right panel) of *Nicotiana benthamiana* plants infected with wildtype and mutant grapevine fanleaf virus (GFLV) strains. No statistically supported differences in root system architecture traits between viral treatment and non-infected *N. benthamiana* plant primary root (T-test, $p > 0.05$; ANOVA, $p > 0.05$) were observed, although numerical differences of root vasculature to total root circumference and area are present.

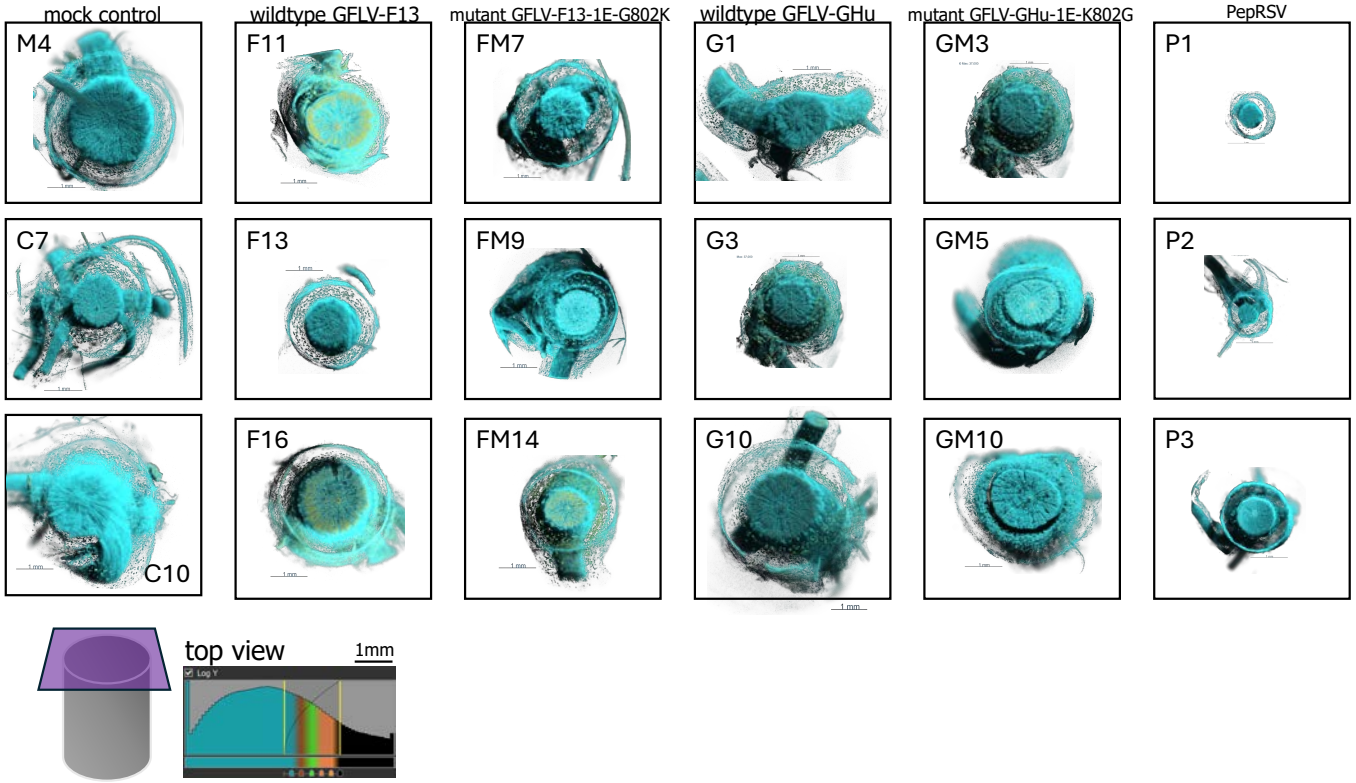

FIGURE 6-S5. Three-dimensional (stem down) view of primary roots of *Nicotiana benthamiana* plants infected with wildtype grapevine fanleaf virus (GFLV) strains GHu and F13, mutants GFLV GHu-1E^{K802G} and F13-1E^{G802K}, and pepper ringspot virus (PepRSV). Treatments shown per column of images from left to right are: mock inoculated controls (M4, C7, C10), plants infected with wildtype GFLV-F13 (F11, F13, F16), mutant GFLV-F13-1E^{G802K} (FM7, FM9, FM14), wildtype GFLV-GHu (G1, G3, G10), mutant GFLV-GHu-1E^{K802G} (GM3, GM5, GM10), and PepRSV (P1, P2, P3). Relative intensity of pixel is correlated to iodine stain intensity and was standardized by calculations as shown by the color legend thresholding window (bottom left) in Dragonfly software (Object Research Systems, v2022.2). Size of 1 millimeter is indicated by scale bar in each respective image and in the bottom left legend.

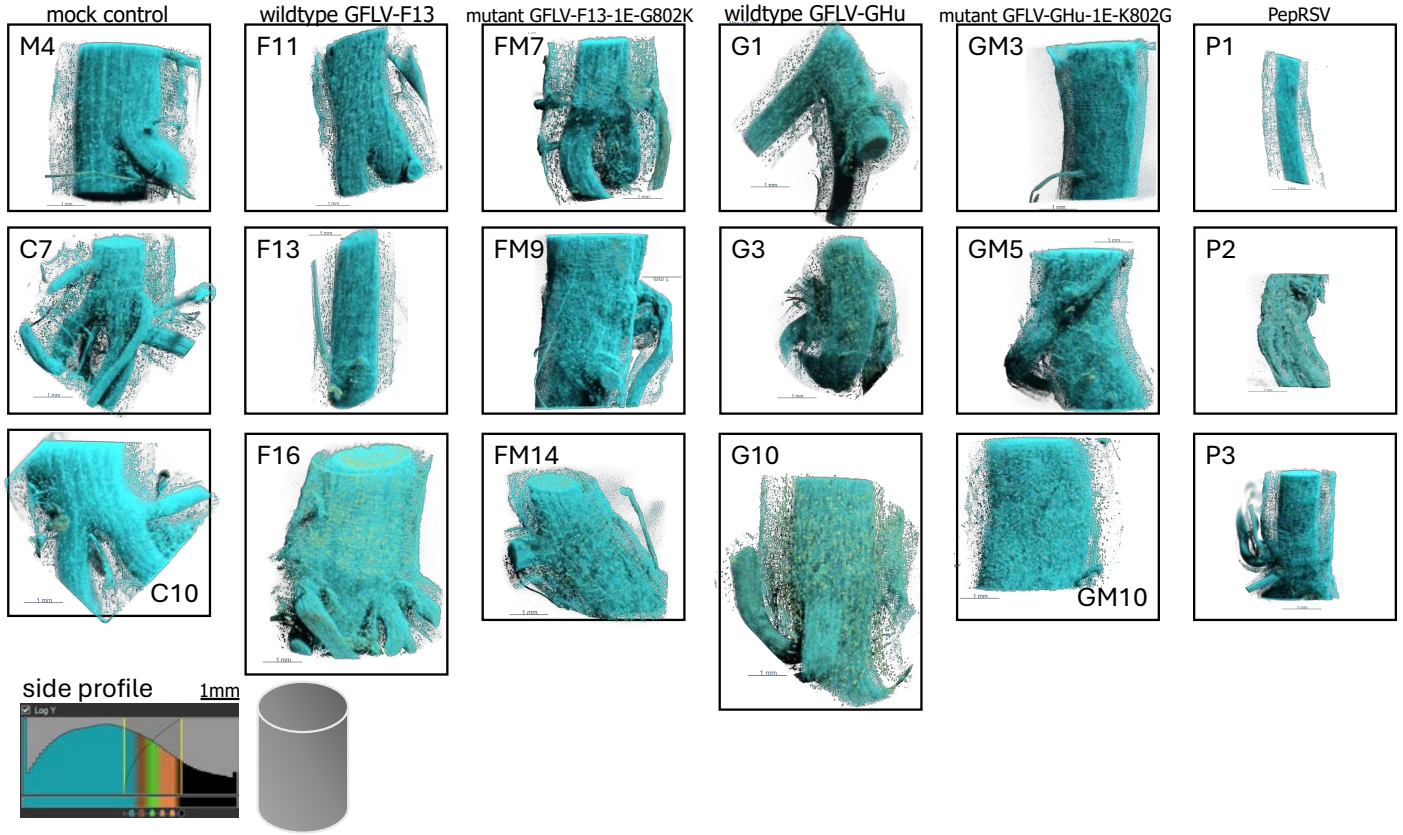

FIGURE 6-S6. Three-dimensional side view of primary root of *Nicotiana benthamiana* plants infected with wildtype grapevine fanleaf virus (GFLV) strains GHu and F13, mutants GFLV GHu-1E$_{K802G}$ and F13-1E$_{G802K}$, and pepper ringspot virus (PepRSV). Treatments shown per column of images from left to right are: mock inoculated controls (M4, C7, C10), plants infected with wildtype GFLV-F13 (F11, F13, F16), mutant GFLV-F13-1E$_{G802K}$ (FM7, FM9, FM14), wildtype GFLV-GHu (G1, G3, G10), mutant GFLV-GHu-1E$_{K802G}$ (GM3, GM5, GM10), and PepRSV (P1, P2, P3). Relative intensity of pixel is correlated to iodine stain intensity and was standardized by calculations as shown by color legend thresholding window (bottom left) in Dragonfly software (Object Research Systems, v2022.2). Size of 1 millimeter is indicated by scale bar in each respective image and in the bottom left legend.

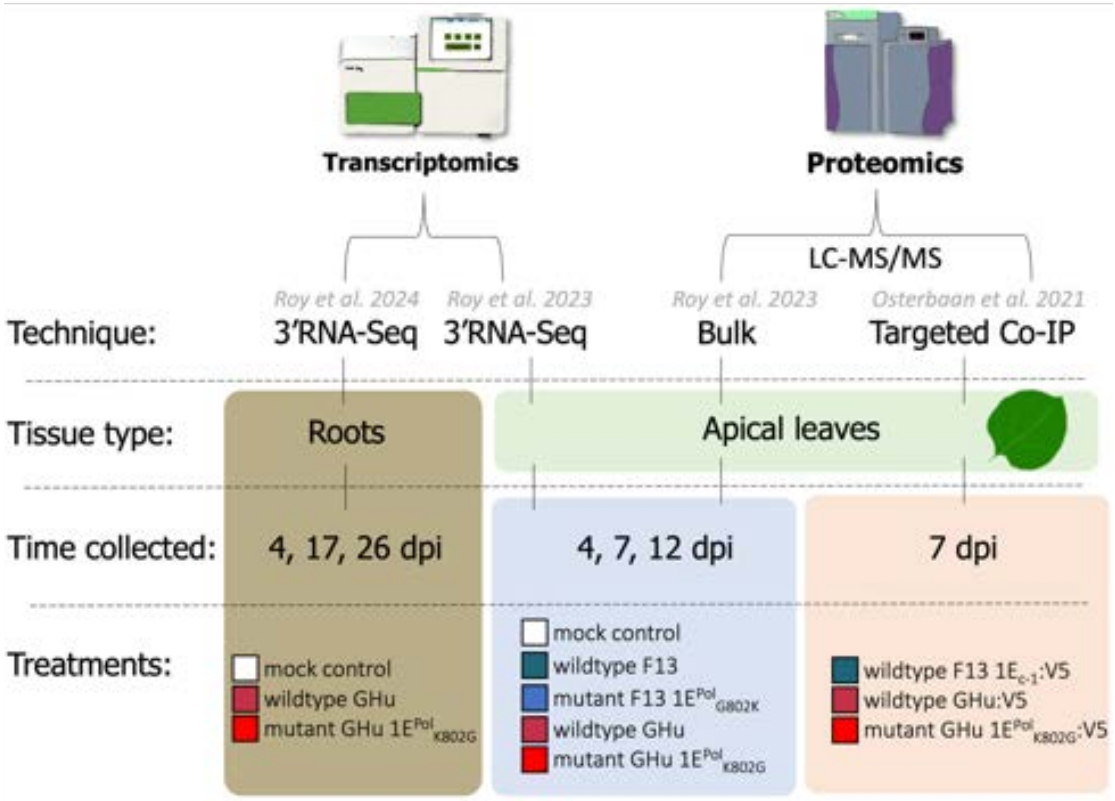

FIGURE 6-S7. Schematic representation of four independent studies on grapevine fanleaf virus (GFLV)-*Nicotiana benthamiana* interactions that were previously performed (Osterbaan et al. 2021; Roy et al. 2024; Roy and Fuchs 2024). These studies can be broken down into the technique used to acquire data (3'RNA-Seq or LC-MS/MS) with additional specification to bulk or targeted co-immunoprecipitation capture based proteomics. Two different tissue types, root or apical leaf tissue, were targeted in these experiments. Tissue collection times after inoculation with virus varied across these experiments from 4 dpi to 26 dpi. Treatment groups also differed with GFLV strains being centered around symptomatic wildtype strain GFLV-GHu.

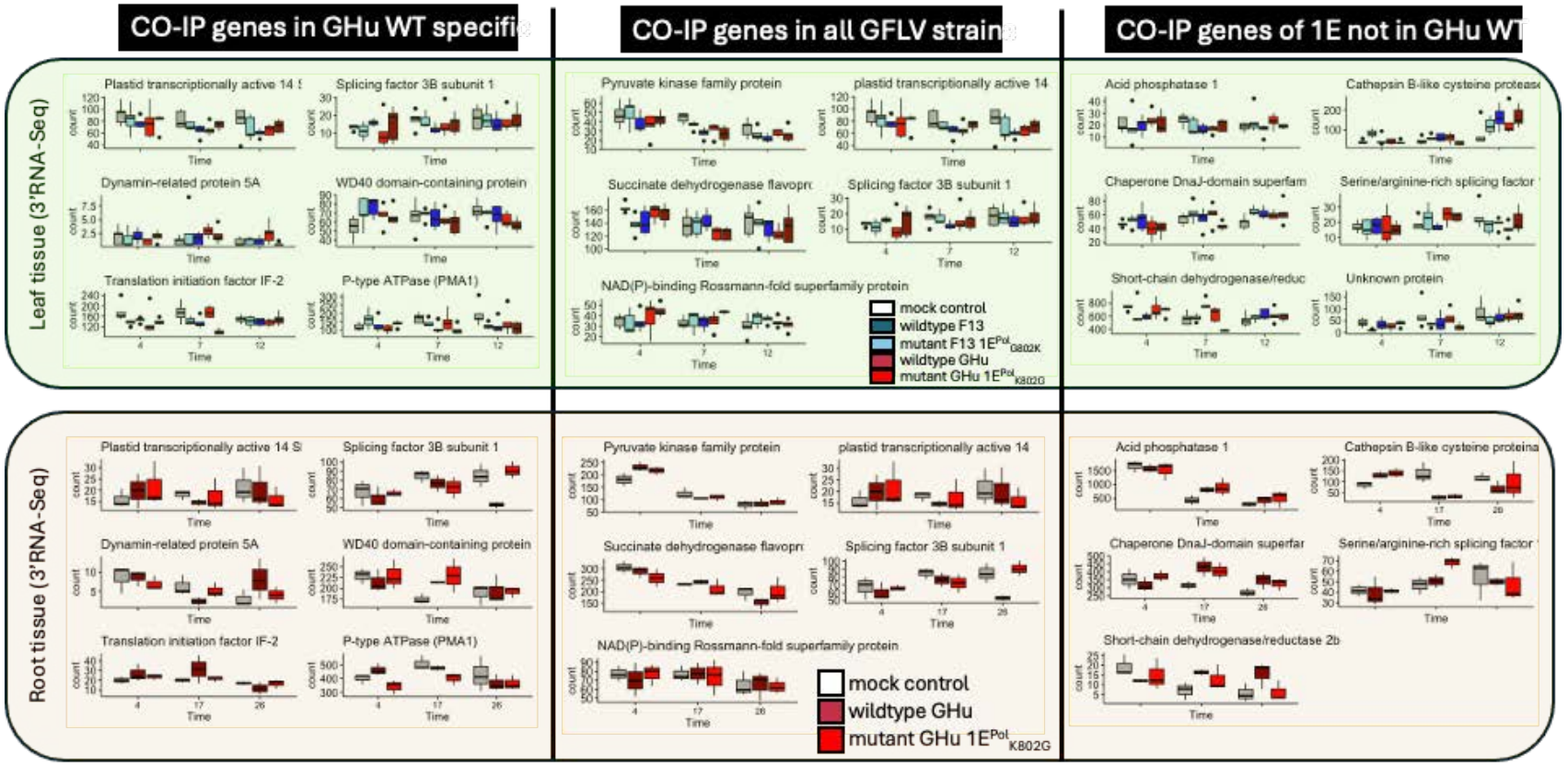

FIGURE 6-S8. Transcript abundance profiles of corresponding host proteins identified in co-immunoprecipitation (Osterbaan et al. 2021) with grapevine fanleaf virus (GFLV) protein $1E^{Pol*/Sd}$. From left to right, three groupings were extracted, where genes were (1) shown to interact with wildtype GFLV strain GHu with statistical enrichment, (2) detected in all GFLV:V5 pulldowns, and (3) detected in all treatments except for wildtype GFLV-GHu pulldowns. Above are the transcript boxplots across three time points and five treatments for leaf 3'RNA-Seq data (Roy et al. 2023), and bottom displays the same except for only three treatments in root tissue (Roy and Fuchs 2024).

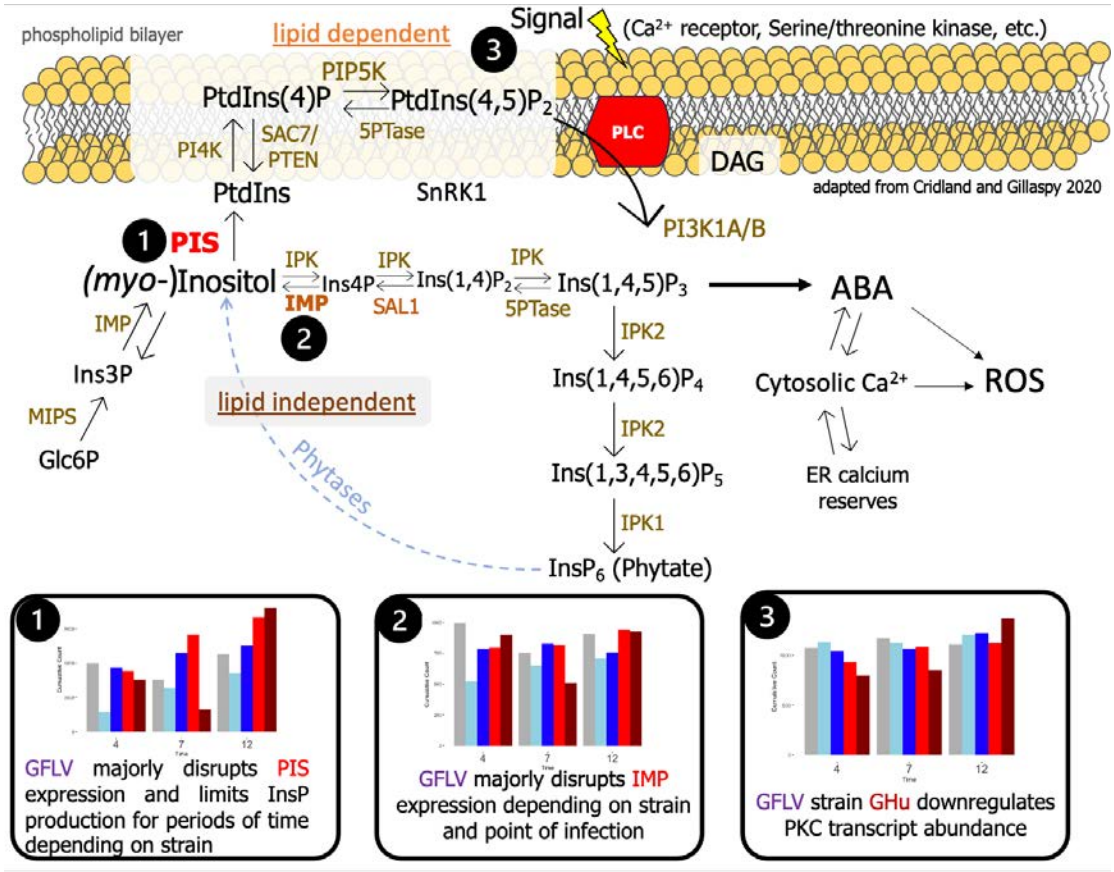

FIGURE 6-S9. The inositol signaling pathway is disrupted differentially upon grapevine fanleaf virus (GFLV) infection in *Nicotiana benthamiana* dependent upon viral strains and the identity of the 802nd amino acid in protein 1E$^{Pol*/Sd}$. (1) Phosphatidylinositol synthase is majorly repressed at 4 days post inoculation (dpi) for mutant GFLV-F13 and at 7 dpi for wildtype GFLV-GHu. **(2)** Inositol monophosphatase is similarly downregulated by these strains at the same time points. **(3)** Protein kinase c, a potential signal provider in this cascade is downregulated during wildtype GFLV-GHu infection until 12 dpi.

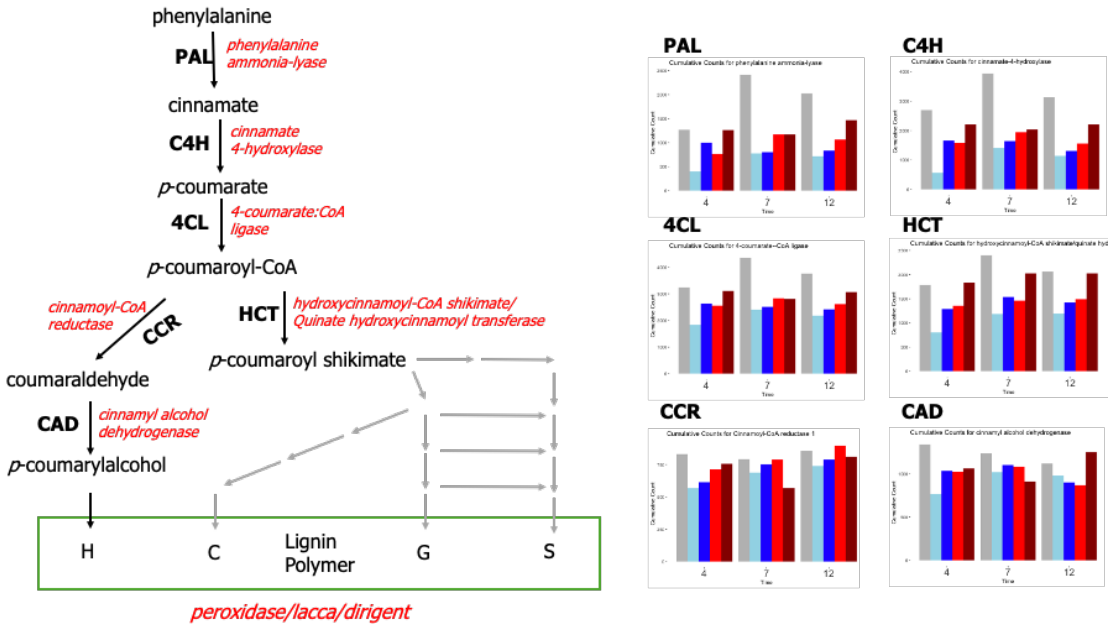

FIGURE 6-S10. A simplified metabolic pathway from phenylalanine to synthesized lignin polymer (left) follows four distinct polymer organization styles (right) upon grapevine fanleaf virus (GFLV) infection in *Nicotiana benthamiana* with six of the enzymes in this pathway being repressed to different extents compared with mock control plants. Lignin deposition is a common response of plants to limit viral movement from cell to cell.

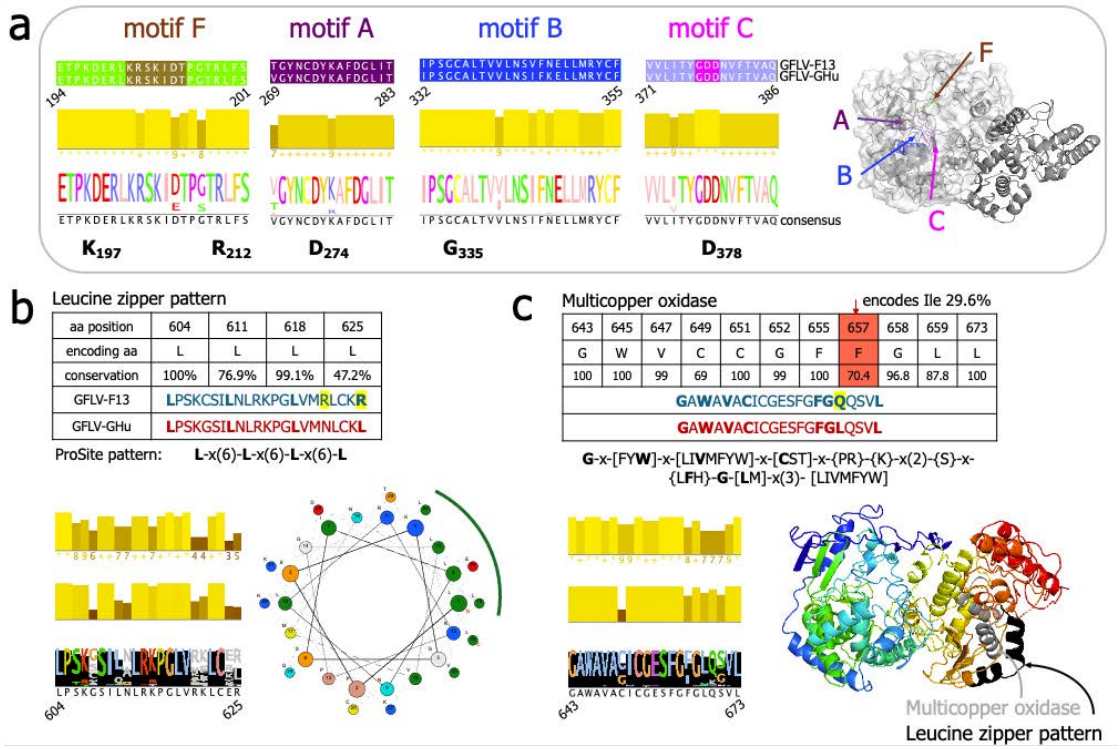

FIGURE 6-S11. Detailed mapping of predicted motifs of grapevine fanleaf virus (GFLV) protein 1E$^{Pol*/Sd}$ informed by sequence alignment of 214 NCBI accessions. **(a)** Four highly conserved catalytic motifs (F, A, B, and C) of the polymerase were manually extracted and annotated based on closely related picornaviruses. Two additional motifs within globular domain A of GFLV protein 1E$^{Pol*/Sd}$ suggest a (b) leucine zipper pattern with spacer intervals of six amino acids in 71 of 214 GFLV isolates, including GFLV-GHu, (c) multicopper oxidase signature in two isolates of GFLV, including GFLV-GHu. The position 657 residue of the multicopper oxidase domain encodes an unexpected amino acid for this motif over seventy percent of the time.

ProSite patterns:
[LIV] = residue can be either leucine, isoleucine, or valine
{LFH} = residue can be anything except leucine, phenylalanine, or histidine

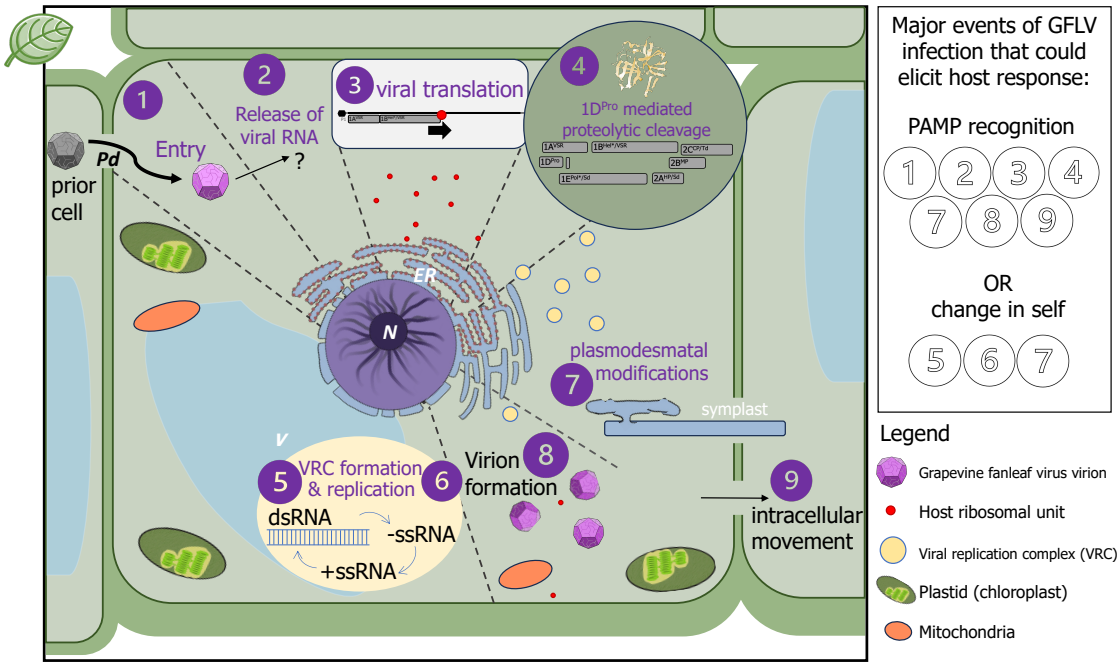

FIGURE 6-S12. Schematic representation of grapevine fanleaf virus (GFLV) replication, translation, and cell-to-cell movement. (1) GFLV enters *Nicotiana benthamiana* cells through modified plasmodesmata where **(2)** virions release viral RNAs. **(3)** Translation occurs immediately by recruiting host ribosomes. After monocistronic translation, **(4)** the viral protease ($1D^{Pro}$) cleaves RNA1 and RNA2 polyproteins into mature final protein products. These proteins are shuttled to respective parts of the cell and eventually **(5)** viral replication complexes (VRC) bud from the endoplasmic reticulum to allow for **(6)** replication through the putative RNA-dependent RNA polymerase. **(7)** RNA2 proteins such as $2B^{MP}$ and $2C^{CP}$ are suspected to be readily translated to mediate **(8)** virion formation from 60 coat protein units and **(9)** movement protein-mediated modification to plasmodesmata, allowing spread to the next cell and/or vasculature for long systemic transport.

CHAPTER 7

A SOIL-BORNE VIRUS MODIFIES THE ROOT SYSTEM ARCHITECTURE OF A PLANT HOST VIA A SINGLE AMINO ACID TO INFLUENCE NEMATODE TRANSMISSION[7]

ABSTRACT

Grapevine fanleaf virus (GFLV) is the main causative agent of fanleaf degeneration disease. Transmission of GFLV is exclusively accomplished by the ectoparasitic dagger nematode *Xiphinema index* in a non-circulative, non-propagative mode. Recent advances in GFLV-host interactions revealed strain- and viral amino acid-specific changes to the root system architecture (RSA) in *Nicotiana benthamiana*. First, a two-step assay revealed the suitability of *N. benthamiana* in comparison to *Vitis* sp. for the transmission of GFLV by *X. index*. Then, a novel one-step assay revealed strain- and viral amino acid-specific differences in transmission between wildtype GFLV strains F13 and GHu, and their respective mutants with single residue changes to position 802 of the RNA-dependent RNA polymerase (protein $1E^{Pol*/Sd}$). Lower transmission rates were obtained with symptomatic wildtype GFLV-GHu (25.53%, 12/47) and mutant GFLV-F13 $1E_{G802K}$ (51.28%, 20/39), while higher rates were obtained with asymptomatic wildtype GFLV-F13 (75%, 30/40) and mutant GFLV-GHu $1E_{K802G}$ (33.33%,16/48). These results documented that *X. index*-mediated transmission is influenced by the GFLV strain and the identity of the amino acid in position 802 of protein $1E^{Pol*/Sd}$ with a glycine favoring transmission and a lysine reducing transmission. As expected, GFLV transmission was significantly correlated with

differences in RSA traits such as the number of root tips and total root length, but not to GFLV titer in *X. index* or in roots of donor plants. This is the first report of a soil-borne virus manipulating the RSA of a plant host via a single viral amino acid to influence its transmission by a dagger nematode.

---

[6]This chapter has been submitted for publication: Roy, B.G., Demangeat, G., Meyer, S., Gertz, C., Komar, V., Martin, I.R., Fuchs, M. 2025. A soil-borne virus modifies the root system architecture of a plant host via a single amino acid to influence nematode transmission.

INTRODUCTION

Transmission is arguably the most important step in the viral infection cycle. This is particularly true for plant viruses for which hosts have extremely limited, if any, mobility compared with most viruses of humans or animals. Therefore, the transfer of a virus from an infected plant to a healthy plant is essential for its survival and persistence. Additionally, plant viruses are known to evolve specific molecular functions to modify host phenotypes for promoting transmission via a vector such as insects, mites, nematodes, fungi, and plasmodiophores (Mauck et al. 2018; Whitfield et al. 2015), as proposed by the adaptive host manipulation concept (Poulin 2010). This concept has been thoroughly explored with viruses transmitted by aphids, leafhoppers, thrips, and whiteflies (Blanc and Michalakis 2016; Callaway et al. 2001; Gray et al. 2014; Mauck et al. 2018; Ng and Falk 2006; Whitfield et al. 2015). For example, viruses manipulate plant hosts to attract and/or deter aphid feeding, most commonly through the production of volatile organic compounds (VOCs) by infected plants (Falla and Cunniffe 2024; Milonas et al. 2023). Plant viruses have also been observed to manipulate whiteflies to increase transmission (Moreno-Delafuente et al. 2013) and decrease host defenses against herbivories (Su et al. 2015). Overall, both positive and negative interactions have been documented in virus-vector arthropod relationships regarding transmission (Colvin et al. 2006). While many studies have been performed on plant viruses with aerial vectors, information on plant host manipulation by soil-borne viruses to influence their transmission is scarce.

Grapevine fanleaf virus (GFLV, species *Nepovirus foliumflabelli,* genus *Nepovirus*, family *Secoviridae*) is a causative agent of fanleaf degeneration disease. This

disease is present in most vineyards worldwide. It severely affects vine health, reduces fruit yield by up to 80% and substantially limits the productive lifespan of vineyards (Andret-Link et al. 2004a). The economic toll of GFLV was estimated to more than 1 billion euros in 2015 in France alone (Fuchs and Lemaire 2017). GFLV is transmitted by the ectoparasitic dagger nematode *Xiphinema index* (family *Longidoridae*) in an exclusive manner (Hewitt et al. 1958). *X. index* preferentially feeds on actively growing root tips of plant hosts (Wyss 1978), where it can acquire nutrients and GFLV particles alike (Hewitt et al. 1958). The combinatorial presence of GFLV and *X. index* in a vineyard ultimately lead to secondary spread.

GFLV has a bipartite single-stranded positive RNA genome that encodes eight proteins upon monocistronic translation and proteolytic cleavage (Margis et al. 1994; Ritzenthaler et al. 1991; Serghini et al. 1990). Both GFLV RNA1 and RNA2 are required for systemic infection of plant hosts (Viry et al. 1993). RNA2 encodes the coat protein, $2C^{CP/Td}$, which forms virions that encapsulate the two viral RNAs and determine transmission by *X. index* (Margis et al. 1993; Schellenberger et al. 2011). The structure of protein $2C^{CP/Td}$ was determined and has elucidated regions crucial for self-assembly, movement in the plant host, and transmission by *X. index* (Belval et al. 2019; Schellenberger et al. 2011). The regions of note for transmission constitute a positively charged cavity at the external surface of GFLV virions where amino acids T258, M260, D261, G297 and R301 are hypothesized to be binding sites for *X. index*. The loss of transmissibility through mutations of these residues confirmed their specificity for GFLV-*X. index* interactions, and indicated that protein $2C^{CP/Td}$ facilitates binding to feeding parts of the nematode (Belval et al. 2019). These data were supported by the

presence of GFLV particles in the cuticular lining of nematode mouthparts (Taylor and Robertson 1970), and the use of recombinant viruses with coat protein chimeras of GFLV and Arabis mosaic virus (ArMV, species *Nepovirus arabis*, genus *Nepovirus*, family *Secoviridae*), a closely related nepovirus, in transmission assays (Schellenberger et al. 2010; 2011).

GFLV can also be transferred by mechanical inoculation from infected grapevine tissue to herbaceous indicator plants (Cadman et al. 1960; Dias 1963). Herbaceous plant hosts are excellent models to study vector-mediated virus transmission (Roy and Fuchs 2022). For example, infected *Chenopodium quinoa* and *Chenopodium amaranticolor* have been used for the acquisition of GFLV by *X. index* (Brown et al. 1995, Roberts and Brown 1980). Similarly, *Petunia hybrida* has been used as a source and a recipient plant for GFLV acquisition and transmission assays (Belin et al. 2001, Roberts and Brown 1980). Herbaceous plant hosts are also excellent models to study virus biology (Roy and Fuchs 2022). For example, wildtype and mutant strains of GFLV display distinct symptomatology on *Nicotiana benthamiana* (Martin et al. 2018; Osterbaan et al. 2019; Vigne et al. 2013). Wildtype GFLV strain GHu elicits transient vein clearing symptoms in apical leaves of *N. benthamiana* (Osterbaan et al. 2019; Vigne et al. 2013) and a modified RSA with lessened root tips and increased average root diameter (Roy and Fuchs 2024). In contrast, wildtype GFLV strain F13 infection does not lead to any symptoms in leaves or roots of *N.* benthamiana (Osterbaan et al. 2019; Roy and Fuchs 2024; Vigne et al. 2013). Through reverse genetics approaches followed by plant inoculation of infectious cDNA clones, amino acid in position 802 of the RNA-dependent RNA polymerase ($1E^{Pol}$) of GFLV-GHu was

associated with both leaf (Osterbaan et al. 2019) and root symptoms (Roy and Fuchs 2024). This single amino acid is referred to as a symptom determinant (Sd) in protein $1E^{Pol*/Sd}$ (Osterbaan et al. 2019; Roy et al. 2024). Foliar and root symptoms of wildtype GFLV-GHu and mutant GFLV-F13 $1E^{Pol*/Sd}_{G802K}$ in *N. bethamiana* are transient with foliar vein clearing symptoms most notable at eight days post-inoculation (dpi) and marked root symptoms at 17 dpi, followed by recovery in leaves and lessened differences in root traits at later time points (Osterbaan et al. 2019; Roy and Fuchs 2024).

Given the differences in root morphology in relation to the GFLV strain and identity of the amino acid in position 802 of protein $1E^{Pol*/Sd}$ (Roy and Fuchs 2024), as well as the preferred feeding of *X. index* on actively growing root tips (Wyss 1978), distinct *X. index*-mediated transmission rates were hypothesized across viral strains. In other words, the RSA of a plant host with less root tips and thinker roots such as observed in *N. benthamiana* plants infected with GFLV-GHu (Roy and Fuchs 2024), is anticipated to be less desirable for *X. index* feeding, thus potentially reducing transmission. In contrast, the RSA of *N. benthamiana* plants infected with GFLV-F13 should not be repulsive for *X. index* feeding, resulting in more efficient transmission. The aim of our research was to test if GFLV strains, depending on the identity of amino acid in position 802 of protein $1E^{Pol*/Sd}$ that influence the RSA of *N. benthamiana,* modulate transmission by *X. index*. We hypothesized that GFLV strains differ in their transmission efficiency by specifically eliciting root symptoms that affect the behavior of *X. index*. Here we summarize our findings on the ability of protein $1E^{Pol*/Sd}$ to modify RSA traits for influencing *X. index*-mediated transmission of GFLV.

MATERIALS AND METHODS

Plant material

Fig (*Ficus carica*) plants were used for rearing of aviruliferous *Xiphinema index*. Fig is an reproductive host for *X. index* but does not sustain GFLV infection (Esmenjaud et al. 1993; Taylor and Raski 1964). Similarly, aviruliferous *X. index* were reared on GFLV-free *Vitis* rootstock Kober 5BB (*V. berlandieri* x *V. riparia*). Aviruliferous *X. index* were reared on plants grown in 10 liter pots containing a sand:loess (4:1) soil mixture in the greenhouse. Fig and grapevine material were propagated from green cuttings on rockwool in an environmental growth chamber under controlled temperature (26ºC) and light (16:8, light:dark) conditions. After five weeks, rooted fig and grapevine plants were transferred to sandy soil (2:1, sand:loess, wt:wt) and used for nematode rearings or for virus transmission assays, respectively. Herbaceous plants such as *Chenopodium quinoa*, *C. amaranticolor*, and *Nicotiana benthamiana* were sown in the greenhouse, transferred two weeks later in sandy soil, and maintained in greenhouse conditions at 25 °C ± 3 °C with supplemental lighting (16:8, light:dark). Plants were watered twice daily and supplemented with liquid fertilizer once weekly.

Viruses and plant infection

GFLV strain F13 (Vuittenez et al. 1964) and Arabis mosaic virus (ArMV) strain S (Huss et al. 1989) were transferred by mechanical inoculation from infected grapevines to *Chenopodium quinoa*, a systemic herbaceous host for both viruses. Leaf tissue of infected *C. quinoa* plants was then used to infect *N. benthamiana* and *C. amaranticolor* plants at the four to six leaf stage via mechanical inoculation.

Establishment of infection in herbaceous plants was confirmed through double antibody sandwich enzyme-linked immunosorbent assay (DAS-ELISA) using specific antibodies (BIOREBA, Switzerland). Virus-infected Kober 5BB (*Vitis berlandieri* x *V. riparia*) grapevines were generated through *in vitro* heterologous grafting (Belin et al. 2001). Infected green cuttings of grapevine were maintained under greenhouse conditions and used in two-step transmission experiments with *X. index*.

Infectious clones of GFLV RNA1 and RNA2 of strains GHu and F13 in *Agrobacterium tumefaciens* were introduced to *N. benthamiana* plants at the four to six leaf stage (Osterbaan et al. 2018, 2019; Roy et al. 2023). The infection status of inoculated plants was determined through DAS-ELISA and reverse transcription (RT) polymerase chain reaction (PCR) of apical leaves. Leaves of GFLV sequence confirmed, infected plants were then frozen in liquid nitrogen and maintained at -80ºC until use in mechanical inoculation in one-step transmission experiments. For transmission assays, *N. benthamiana* plants were mechanically inoculated with RNA2 of wildtype GFLV strain GHu and with RNA1 of one of four different GFLV strains: wildtype F13, mutant F13 $1E^{Pol*/Sd}_{G802K}$, wildtype GHu, and mutant GHu $1E^{Pol*/Sd}_{K802G}$.

Xiphinema index *isolation*

X. index were extracted from soil samples (~0.5 kg) of rearings on figs and grapevines through elutriation using an adapted Oostenbrink method and sieves of different sizes (Flegg 1967; Hooper et al. 2005) (Figure 7-S1A-K). First, soil samples were rinsed with water into a bucket through 2.00 mm and 1.00 mm sieves (Figure 7-S1A-K). Then the collected water volume was reduced using 80 µm sieves. The *X. index* nematodes from the 80 µm sieves were elutriated along with the soil and water retained

in the bucket (Figure 7-S1A-K). Constant water pressure was supplied to a custom-built Oostenbrink elutriator capped with a rubber stopper with the sample added to the top of the funnel (Figure 7-S1A-K). After a complete volume of water had almost filled the apparatus, the suspension was emptied into a collection bucket (Figure 7-S1A-K). This new bucket of water containing *X. index* was further elutriated using the 150 µm and 80 µm sieves to collect nematodes from each of these two sieves into a clean beaker. Isolated nematodes from aviruliferous rearings were used in one-step or two-step transmission assays.

Nematodes were similarly elutriated from soil samples at the completion of the one-step transmission assays. Isolated nematodes were counted and randomly pooled cohorts of 3-20 individuals proximal to either donor or recipient plants were used for GFLV detection by RT-qPCR.

Two-step (discontinuous)* X. index-*mediated transmission assay

A discontinuous transmission assay was utilized to test the efficiency of GFLV transmission by *X. index* using different plant hosts (Figure 7-S1A). Nematodes were exposed to infected plants for a six-week acquisition access period (AAP) with ~300 nematodes per potted plant (0.5 L). Infected plants of *Vitis* rootstock Kober 5BB, *N. benthamiana*, *C. quinoa*, and *C. amaranticolor* were used as virus source plants. After the APP, the virus source plant was removed from the 0.5 L pot and replaced by a healthy recipient grapevine or herbaceous plant for a six-week inoculation access period (IAP). Recipient plants were healthy *Vitis* rootstock Kober 5BB or healthy *N. benthamiana*, *C. quinoa*, and *C. amaranticolor*. Transmission assays were replicated

twice. ArMV was used as a negative control in two-step transmission assays because this virus is specifically transmitted by *X. diversicaudatum* rather than *X. index*.

One-step (continuous)* X. index-*mediated transmission assay

A continuous transmission assay with *N. benthamiana* plants was performed to limit soil manipulation after initial setup (Figure 7-1B). The first iteration of this experiment utilized a 3x4 grid pattern where GFLV-inoculated source *N. benthamiana* plants were centrally located, while healthy recipient *N. benthamiana* plants were placed 10-12 cm away on the perimeter of a large plastic bin (32 cm x 40 cm). Central source plants were previously mechanically inoculated with distinct strains of GFLV and transplanted into the experimental plastic bin. Then, approximately 900 nematodes were placed two days after transplant on the roots of the central donor plants. The continuous AAP and IAP steps were allowed to proceed for seven and a half weeks. Transmission assays were replicated three times.

A second iteration of this experimental approach utilized a 2x3 grid pattern in a smaller bin (27 cm x 27 cm), using two infected central source *N. benthamiana* plants and four perimeter recipient *N. benthamiana* plants. Donor and recipient plants were 10 cm away from each other. Approximately 550 *X. index* were placed in each bin two days after transplanting. Treatments were replicated four times for wildtype GFLV-F13, mutant GFLV-F13 $1E_{G802K}$, and mock controls, and replicated six times for viral treatments wildtype GFLV-GHu and mutant GFLV-GHu $1E_{K802G}$. This continuous AAP and IAP was allowed to progress for eight weeks. Overall, transmission assay treatments were replicated eight to ten times.

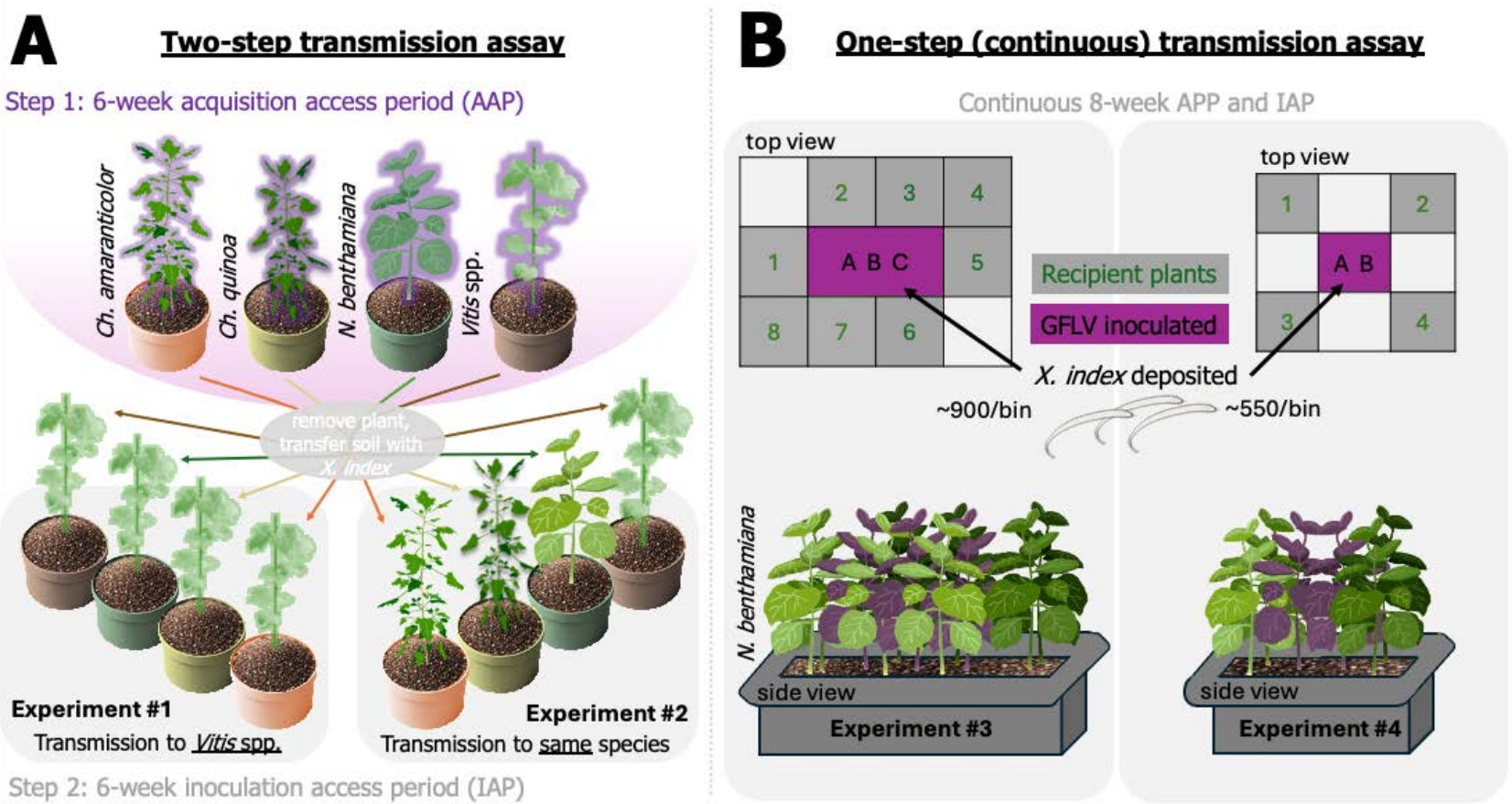

FIGURE 7-1. Experimental schematic of two transmission assays of grapevine fanleaf virus (GFLV) with *Xiphinema index* to investigate virus-vector-host interactions. (A) A traditional two-step (discontinuous) transmission assay used four GFLV-infected source plant species for the acquisition access period (AAP) and healthy recipient grapevine plants for experiment #1 or healthy recipient herbaceous host species for experiment #2 for the inoculation access period (IAP). **(B)** To contrast, a one-step (continuous) transmission assay was developed with centrally placed GFLV-inoculated *Nicotiana benthamiana* plants surrounded by four to eight healthy recipient *N. benthamiana* plants during an eight-week tandem AAP and IAP.

Plant tissue collection and GFLV detection

Root and leaf tissue of *N. benthamiana* plants were assessed for GFLV infection at multiple time points. Apical leaf tissue of inoculated plants was collected at two weeks post-inoculation and tested through DAS-ELISA with GFLV specific antibodies (Osterbaan et al. 2018). The apical leaf tissue of recipient (uninoculated) plants was collected at seven weeks post inoculation for RT-PCR detection of GFLV using specific primers (Table 7-S1). At the completion of the transmission assays, apical leaf and root tissue of each plant in every bin were collected for GFLV infection by DAS-ELISA. Root tissue of each plant was also used for GFLV detection by RT-PCR (Figure 7-S1).

Total nucleic acid extractions from plant and nematode samples for virus detection by RT-PCR

Nucleic acid extractions of plant leaf and root tissue were performed using a King Fischer 96 Well-Plate Extraction Kit (Cat. No. R2141-E). The purified RNA was subject to RT-PCR with GFLV primers specific to the $1E^{Pol*/Sd}$ symptom determinant genomic region (Table 7-S1) (Osterbaan et al. 2019). The reaction utilized the QIAGEN One-Step RT-PCR kit (Cat. No. 210212) according to manufacturer's instructions with the following thermocycler protocol; 50°C for 30 minutes; 95°C for 15 minutes; 30 cycles of 94°C, 52°C, and 72°C for 30s, 30s, and 1 minute; with a final extension at 72°C for 10 minutes. PCR amplicons were visualized on 1.5% gel agarose by electrophoresis at 100V for 40 minutes, stained in GelRed® for 10 minutes, and imaged under UV light. Select resulting bands were excised, gel purified, and subject to Sanger sequencing to confirm both viral strain identity (F13 vs GHu) and stability of amino acid 802 in protein $1E^{Pol*/Sd}$ (Osterbaan et al. 2019; Roy and Fuchs 2024).

Purification of *X. index* RNA was performed using the QIAGEN RNeasy Plant Mini Kit (Cat. No. 74904) according to the manufacturer's protocols with a 15 minute on-column DNAse digestion (QIAGEN, Cat. No./ID: 79256). Briefly, samples of 2-30 *X. index* were pooled into 2 mL Eppendorf tubes with 100-120 mg of glass beads, 200 µL RTL lysis buffer, and 10 µL 1M dithiothreitol. Nematode samples with lysis buffer were homogenized at 30 Hz for three minutes in a QIAGEN TissueLyser II (Cat. No. 85300) and then column purified according to manufacturer protocol. A final elution volume of 45 µL was collected using RNAse-free water and then flash frozen for storage at -80C. The purified RNA was used for GFLV quantification by RT-qPCR.

GFLV quantification in plant roots and* X. index *by RT-qPCR

Purified RNA samples were thawed on ice where 100 ng plant RNA or 11 µL of nematode RNA were subject to cDNA production with random primers and Invitrogen Superscript IV Reverse Transcriptase (Cat. No. 18090050). The reaction was stopped by heat inactivation, and the cDNA was used immediately for qPCR or kept at -20^{o}C until further use. Nematode cDNA was used for qPCR with primers specific to GFLV RNA1 and *X. index* actin sequences (Table 7-S1) (Vigne et al. 2018).

For quantification purposes, aviruliferous *X. index* from colonies reared on fig plants and viruliferous *X. index* nematodes from GFLV-infected grapevines (Table 7-S2) were used as negative and positive controls, respectively, for RT-qPCR. Additionally, a standard curve was obtained from an RNA extraction of purified GFLV-F13 (Pinck et al. 1988; Schellenberger et al. 2011) (Table 7-S3). Each qPCR microplate was normalized using inter-plate standards. Briefly, the correlation of Cq value and GFLV RNA was used to generate slope and intercept values (Figure 7-S4). The actual

RNA concentration of the standard was then used as an adjustment factor at a Cq value 25 (centroid to most data) which produced new intercept values. The difference in intercept between the assigned reference plate allowed normalization of all samples to each other (Figure 7-S5C-D). These standard curves were utilized in downstream quantification of GFLV in nematode samples. Any nematode samples not meeting a Cq value of 37.5 after standardization were considered to not contain detectable levels of GFLV, as serial dilution limits became less confident for GFLV detection at this threshold.

Root system architecture analysis

Root systems of individual *N. benthamiana* plants were excavated, as previously described (Roy and Fuchs 2023, 2024) for the one-step transmission assays, except that a plastic cylindrical tube (27 cm x 10 cm, h x d) was used to first isolate the root system, similar to taking a soil core. Root systems were incubated at ambient conditions in reverse osmosis water for ten minutes to release excess sand, nematodes, and debris. Root systems were imaged using a 48-megapixel camera (iPhone 14 Pro, Apple Inc.) on a black background, and with a meter stick for reference. Images were processed first in ImageJ (v1.53k, National Institutes of Health, USA) to extract pixel density (Table 7-S4) and then subject to the Rhizovision Explorer analysis software (Seethepalli and York 2020) with custom parameters; custom pixel resolution input per image, contrast threshold (160±5 or 140±5), filter non-root at 1, edge smoothing at 2, and feature extraction (Roy and Fuchs 2024). Given the spatial configuration and phenotyping of all root systems in the experiments, RSA traits from virus donor and recipient plants were used to predict total transmission events in a bin and transmission from a donor

plant to a neighboring recipient plant. These two levels of analysis were then evaluated in linear models against root traits calculated in Rhizovision.

Statistical analysis and visualization

Data from two-step transmission assays were analyzed through paired t-test and post-hoc Tukey's HSD test. RT-qPCR data for plant samples were processed according to the standard ΔΔCq method and log transformed for comparison by treatment using analysis of variance, t-test, and Tukey's HSD post-hoc test. Standard curves from GFLV purifications and nematode extractions of viruliferous and aviruliferous nematodes were used as references and inter-plate standards to compare samples across plates and experiments. A standard linear modeling approach was used on log transformed viral concentration in nematode samples, as well as a mixed modeling approach when considering multiple locations to contribute to transmission characteristics.

Data on nematode counts, GFLV acquisition by nematodes, RSA traits, and transmission were aggregated from continuous transmission assays to allow for correlation analysis through the corrplot [v0.95] package (Wei et al. 2021; Wei and Simko 2017). This allowed for spatial correlation specifically for the second replicate of the continuous transmission assay that included viral titer analysis of centrally located plant roots. Each factor was tested individually and then in mixed model approaches to explain differences in transmission efficiency between viral treatments. Nematode count data was considered as a proportion of the starting nematodes per basin.

Data parsing and statistical testing were performed in RStudio [v4.4.0] (Team 2015) through packages dplyr [v1.1.4] (Wickham et al. 2018), emmeans [v1.10.6] (Lenth and Lenth 2018), FSA [v0.9.5] (Ogle et al. 2023), glmmTMB [v1.1.10] (Brooks

et al. 2017), lme4 [v35.5] (Bates et al. 2015), multcomp [v1.4-26] (Hothorn et al. 2008), and tidyr [v1.3.1]. Visualization was accomplished through packages ggplot2 (v3.5.1) (Wickham 2009), ggbeeswarm [v0.7.2] (Clarke et al. 2016), ggpubr [v0.6.0], ggstats [v0.7.0], and patchwork [v1.3.0] (Pedersen 2019).

RESULTS

Two-step (discontinuous) GFLV transmission assays reveal N. benthamiana *as a suitable donor and recipient plant for* X. index.

Herbaceous and *Vitis* plants were first examined as virus source plants in discontinuous transmission assays with GFLV-F13 and *X. index*. After a six-week IAP on GFLV-infected source *Vitis* plants, most recipient grapevines tested positive for GFLV (93%, 13/14) (Table 7-1). In comparison, with herbaceous source plants, the transmission of GFLV-F13 by *X. index* to recipient *Vitis* plants was slightly lower for *N. benthamiana* (86%, 12/14) and *C. quinoa* (83%, 15/18), and reduced for *C. amaranticolor* (61%, 11/18) (Table 7-1). These results revealed that *Vitis*, *N. benthamiana*, and *C. quinoa* were equally effective as source plants for transmission of GFLV-F13 by *X. index*, with *C. amaranticolor* having a lower performance, as shown by ANOVA and Tukey's HSD post-hoc test (Table 7-1). As expected, no *X. index*-mediated transmission from ArMV-infected plants (0%, 0/26) or mock controls (0%, 0/26) was obtained (Table 7-1). These findings confirmed the specificity of GFLV-*X. index* transmission (Andret-Link et al. 2004b) and showed the suitability of two herbaceous host species, i.e., *N. benthamiana*, and *C. quinoa,* as donor plants for GFLV transmission to grapevine.

TABLE 7-1. Transmission rates of grapevine fanleaf virus (GFLV) and Arabis mosaic virus (ArMV) by *Xiphinema index* from various GFLV-infected source plants to recipient *Vitis* rootstock Kober 5BB (*V. berlandieri* x *V. riparia*).

Source plant	Recipient plant	Virus-strain	Replicate #1	Replicate #2	Overall	Percent	Tukey
Vitis rootstock Kober 5BB	*Vitis* rootstock Kober 5BB	GFLV-F13	7/7[a]	6/7	13/14	93%	a
		ArMV-S	0/3	0/3	0/6	0%	c
		mock	0/3	0/2	0/5	0%	c
Nicotiana benthamiana		GFLV-F13	8/9	4/5	12/14	86%	a
		ArMV-S	0/4	0/3	0/7	0%	c
		mock	0/3	0/2	0/5	0%	c
Chenopodium quinoa		GFLV-F13	7/9	8/9	15/18	83%	a
		ArMV-S	0/3	0/3	0/6	0%	c
		mock	0/3	0/2	0/5	0%	c
C. amaranticolor		GFLV-F13	5/9	6/9	11/18	61%	b
		ArMV-S	0/3	0/4	0/7	0%	c
		mock	0/3	0/2	0/5	0%	c

[a]Fractions represent the total number of plants that tested positive for GFLV in DAS-ELISA at the conclusion of the transmission assays over the total number of plants tested.

TABLE 7-2. Transmission rates of grapevine fanleaf virus (GFLV) and Arabis mosaic virus (ArMV) by *Xiphinema index* from various infected source plants to recipient plants of the same species.

Source plant	Recipient plant	Virus-strain	Replicate #1	Replicate #2	Overall	Percent	Tukey
Vitis rootstock Kober 5BB	*Vitis* rootstock Kober 5BB	GFLV-F13	8/9[a]	7/8	15/17	88%	a
		ArMV-S	0/3	0/3	0/6	0%	c
		mock	0/3	0/2	0/5	0%	c
Nicotiana benthamiana	*N. benthamiana*	GFLV-F13	6/9	3/5	9/14	64%	ab
		ArMV-S	0/4	0/3	0/7	0%	c
		mock	0/3	0/2	0/5	0%	c
Chenopodium quinoa	*C. quinoa*	GFLV-F13	6/9	4/9	10/18	56%	b
		ArMV-S	0/3	0/3	0/6	0%	c
		mock	0/3	0/2	0/5	0%	c
C. amaranticolor	*C. amaranticolor*	GFLV-F13	2/8	0/7	2/15	13%	c
		ArMV-S	0/4	0/4	0/8	0%	c
		mock	0/3	0/3	0/6	0%	c

[a]Fractions represent the total number of plants that tested positive for GFLV in DAS-ELISA at the conclusion of the transmission assays over the total number of plants tested.

Herbaceous and *Vitis* plants were then examined both as virus donor and recipient plants of the same species in discontinuous transmission assays with GFLV-F13 and *X. index* (Table 2). Results revealed a high (88%, 15/17) transmission rate from *Vitis* to from *Vitis*. For herbaceous plants, transmission rates were highest for *N. benthamiana* to *N. benthamiana* (64%, 9/14), moderate for *C. quinoa* to *C. quinoa* (56%, 10/18), and low for *C. amaranticolor* to *C. amaranticolor* (13%, 2/15) (Table 7-2). The transmission rate of GFLV-F13 was statistically similar with *Vitis* and *N. benthamiana*, as indicated by ANOVA and Tukey's HSD post-hoc test (Table 7-2). The transmission was also statistically similar with *N. benthamiana* and *C. quinoa*, as well as with *C. amaranticolor* and negative controls such as ArMV-S and mock plants (Table 7-2). The presence of GFLV was confirmed by RT-PCR with primers CNR and CPS (Table 7-S1) in all nematodes exposed to GFLV-infected plants with the amplification of an expected 650 bp DNA fragment in size, and no amplicon from *X. index* that fed on ArMV-infected plants. These findings revealed *N. benthamiana* to be the most suitable and statistically supported herbaceous host both as a donor and a recipient plant for transmission assays of GFLV by *X. index*.

***One-step (continuous) transmission of wildtype GFLV strains and their mutants by X. index occurs from* N. benthamiana *to* N. benthamiana *at different rates*.**

Two wildtype GFLV strains (F13 and GHu) and their respective mutants in protein $1E^{Pol*/Sd}$ were used in continuous transmission assays with *N. benthamiana* and *X. index*. Virus donor plants in the center of each bin were all infected by GFLV at 14 dpi, as shown by DAS-ELISA with apical leaves (100%, 36/36 in replicate 1 and 100%, 40/40 in replicate 2). As expected, none (0%, 0/36) of the recipient plants in the

perimeter of the bins were positive for GFLV in DAS-ELISA two weeks into the experiment when testing apical leaves. Three central plants infected with GFLV did not survive through the completion of the experiment and were excluded from further analysis.

At the completion of the assays at 55-65 dpi, transmission occurred for all wildtype strains and mutants, as shown by GFLV detection in leaves and roots of recipient plants by DAS-ELISA (Table 7-3). Testing the same recipient plants by RT-PCR consistently revealed higher GFLV infection rates, thus higher levels of transmission (Table 7-3). Mapping the location of GFLV-infected recipient plants in individual bins did not suggest any spatial trends in transmission patterns (Figure 7-S2). Furthermore, the integrity of the two wildtype GFLV strains and two mutants was confirmed by RT-PCR with primers GFLV-SymDetF and GFLV-SymDetR (Table 7-S1) and Sanger sequencing of the GFLV RNA1-encoded symptom determinant region. All randomly selected donor and recipient plants (100%, 20/20) returned both the expected nucleotide sequence of the GFLV strain (F13 or GHu) and the expected amino acid in position 802 of protein $1E^{Pol*/Sd}$ (K or G). These results indicated that roots of recipient plants testing positive for GFLV through RT-PCR were the best indicator of *X. index*-mediated transmission, and that the four GFLV strains used in continuous transmission assays were genetically stable.

Significantly higher transmission rates were obtained for wildtype and mutant GFLV-F13 when compared with wildtype and mutant GFLV-GHu (Table 7-3, Figure 7-2A), indicating that distinct GFLV strains can be differentially transmitted by *X. index*. Moreover, the highest transmission rate (75%, 30/40) was obtained with wildtype

GFLV-F13, and a lower rate (51.28%, 20/39) with mutant GFLV-F13 $1E^{Pol*/Sd}_{G802K}$ (Table 3). For GFLV-GHu, the transmission rate was lowest with the wildtype strain (25.53%, 12/47) and slightly higher with the mutant $1E^{Pol*/Sd}_{K802G}$ (33.33%, 16/48) (Table 7-3). These results were consistent with the identity of amino acid in position 802 of protein $1E^{Pol*/Sd}$ influencing *X. index*-mediated transmission rates. A lysine in position 802 of protein $1E^{Pol*/Sd}$ reduced the transmission rate of GFLV-F13 from 75% to 51%, and a glycine in position 802 of protein $1E^{Pol*/Sd}$ slightly reduced the transmission rate of GFLV-GHu from 33% to 25%. These results also revealed lower transmission rates with wildtype GFLV-GHu and mutant GFLV-F131E$_{G802K}$ that cause leaf and root symptoms in *N. benthamiana* (Osterbaan et al. 2019; Roy and Fuchs 2024), while higher transmission rates were obtained with asymptomatic wildtype GFLV-F13 and mutant GFLV-GHu 1E$_{K802G}$ (Osterbaan et al. 2019; Roy et al. 2024), although these differences were not always statistically supported. Indeed, post-hoc Tukey's HSD indicated statistical groupings between viral treatments with wildtype GFLV-F13 being distinct from wildtype GFLV-GHu and mutant GFLV-GHu $1E^{Pol*/Sd}_{K802G}$, but not mutant GFLV-F13 $1E^{Pol*/Sd}_{G802K}$ (Table 7-3). No transmission events were detected from mock-inoculated plants, as expected (0%, 0/20) (Table 7-3, Figure 7-2A). These results revealed for the first time both GFLV strain and protein $1E^{Pol*/Sd}$ amino acid-specific differences in *X. index*-mediated transmission.

TABLE 7-3. Transmission of wildtype and mutant grapevine fanleaf virus (GFLV) by *Xiphinema index* from inoculated *Nicotiana benthamiana* plants to recipient *N. benthamiana* plants in a one-step continuous assay.

Experiment #1					
Inoculum Source	**Replicates**	**n[a]**	**DAS-ELISA**	**RT-PCR**	**Tukey[c]**
healthy control	1	4	0% (0/4)[b]	0% (0/4)	**-**
mutant GFLV-F13 $1E_{G802K}$	3	23	4.3% (1/23)	52% (12/23)	**bc**
wildtype GFLV-F13	3	24	8.3% (2/24)	75% (18/24)	**c**
mutant GFLV-GHu $1E_{K802G}$	3	24	4.2% (1/24)	17% (4/24)	**ab**
wildtype GFLV-GHu	3	23	4.3% (1/23)	13% (3/23)	**a**
Experiment #2					
Inoculum Source	**Replicates**	**n**	**DAS-ELISA**	**RT-PCR**	**Tukey**
healthy control	4	16	0% (0/16)	0% (0/16)	**-**
mutant GFLV-F13 $1E_{G802K}$	4	16	18.75% (3/16)	50% (8/16)	**ab**
wildtype GFLV-F13	4	16	50% (8/16)	75% (12/16)	**a**
mutant GFLV-GHu $1E_{K802G}$	6	24	58.33% (14/24)	50% (12/24)	**ab**
wildtype GFLV-GHu	6	24	33.33% (8/24)	37.5% (9/24)	**ab**
Overall					
Inoculum Source	**Replicates**	**n**	**DAS-ELISA**	**RT-PCR**	**Tukey**
healthy control	5	20	0% (0/20)	0% (0/20)	**-**
mutant GFLV-F13 $1E_{G802K}$	7	39	10.26% (4/39)	51.28% (20/39)	**ab**
wildtype GFLV-F13	7	40	25% (10/40)	75% (30/40)	**b**
mutant GFLV-GHu $1E_{K802G}$	9	48	31.25% (15/48)	33.33% (16/48)	**a**
wildtype GFLV-GHu	9	47	19.14% (9/47)	25.53% (12/47)	**a**

[a]The total number of plants analyzed at the end of the experiment.
[b]Fractions represent the total number of plants that tested positive for GFLV in DAS-ELISA at the conclusion of the transmission assays over the total number of plants tested.
[c]Logistic regression was performed on viral treatments excluding healthy controls, followed by Post-Hoc Tukey's Honest Significance testing to determine compact letter display.

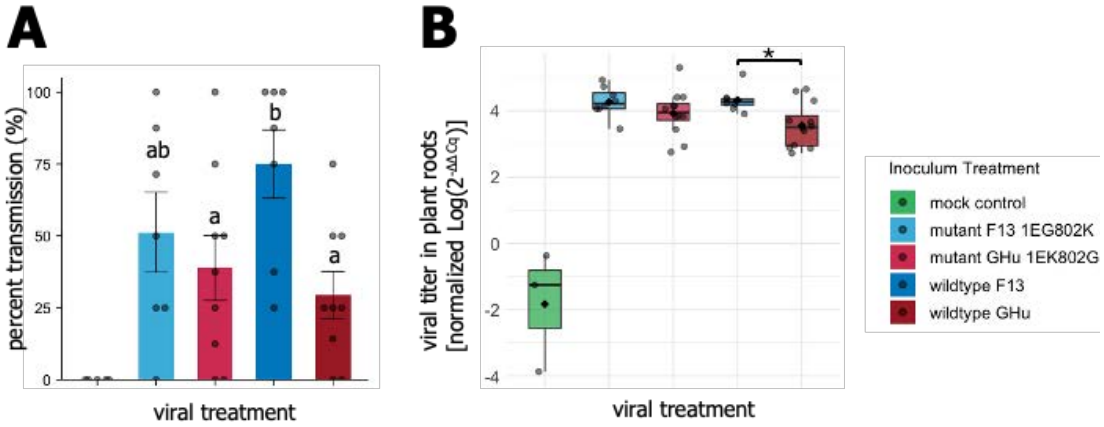

FIGURE 7-2. Transmission of grapevine fanleaf virus (GFLV by *Xiphinema index* is influenced by the identity of GFLV RNA1 (F13 or GHu) and the identity of the amino acid at position 802 of protein 1E$^{Pol*/Sd}$ (K or G). (A) Differential transmission rates across two experimental replicates for wildtype GFLV-F13, wildtype GFLV-GHu, and mutants GFLV-GHu and GFLV-F13 in the 802nd amino acid in protein 1E$^{Pol*/Sd}$. **(B)** Relative GFLV titer in *Nicotiana benthamiana* roots of donor plants determined by RT-qPCR at two months post inoculation suggests minor differences in RNA1 levels, but significant differences between wildtype GFLV-F13 and wildtype GFLV-GHu (Tukey's HSD).

Root system architecture traits are associated with the rate of GFLV transmission

The RSA traits of *N. benthamiana* plants were examined at the completion of continuous transmission assays to analyze any correlations with GFLV transmission rates by *X. index*. Virus donor plants sustained minor perturbations in multiple root traits, although these were not specific to GFLV treatment, bin, or experimental replicate (Figure 7-S3). Nonetheless, multiple linear regression of root traits confidently predicted transmission rates with the number of root tips, root surface area (mm^2), and total root length (mm) being positively and significantly associated with GFLV transmission by *X. index* ($p \leq 0.033$, Figure 7-3A). These three RSA traits were significant across virus donor and virus recipient plants when considered separately, and together (Figure 3A). Additional traits of virus donor plants such as average diameter and total root volume were positively, but not significantly associated with transmission ($p > 0.05$). A mixed model indicated the largest contribution to transmission from differences in root tip number ($p < 0.001$). Together, these results suggested that GFLV transmission by *X. index* is highly influenced by the configuration and expansiveness of the plant root system.

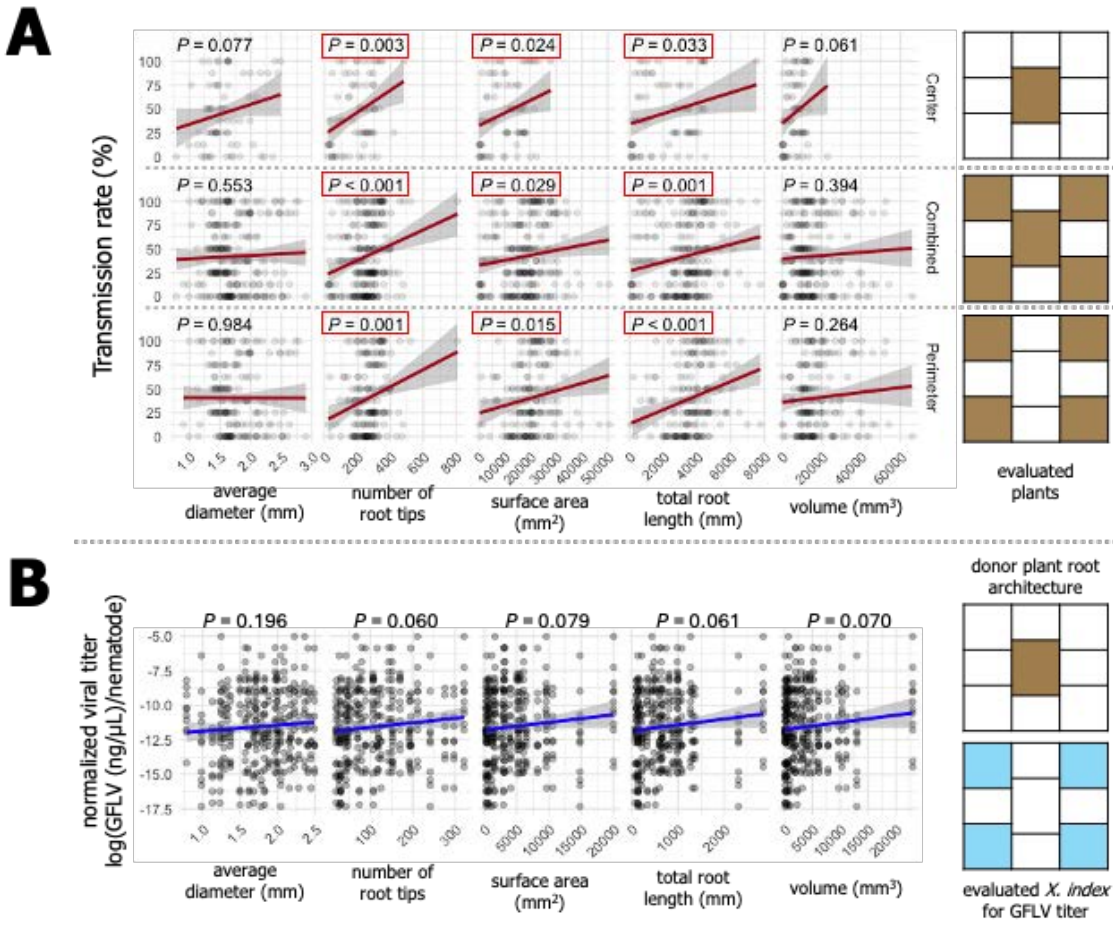

FIGURE 7-3. Relationships between root system architecture traits of *Nicotiana benthamiana* and transmission of grapevine fanleaf virus (GFLV) in continuous assays with *Xiphinema index*. (A) Root traits were used as explanatory variables for transmission rates across experimental replicates, where number of root tips, surface area (mm^2) and total root length (mm) but not diameter (mm) and volume (mm^3) were significantly and positively associated with transmission. RSA traits of donor plants (center, top panels), recipient plants (perimeter, bottom panels) and all plants (combined, middle panels) were considered. **(B)** Root traits of donor plants were positively associated but not significantly associated with GFLV titer in nematodes. The configuration of experimental bins is depicted on the right, where cells highlighted in brown are representing the locations used for correlative analysis. Boxes highlighted in light blue depict nematode samples evaluated for GFLV titer against root traits of donor plants.

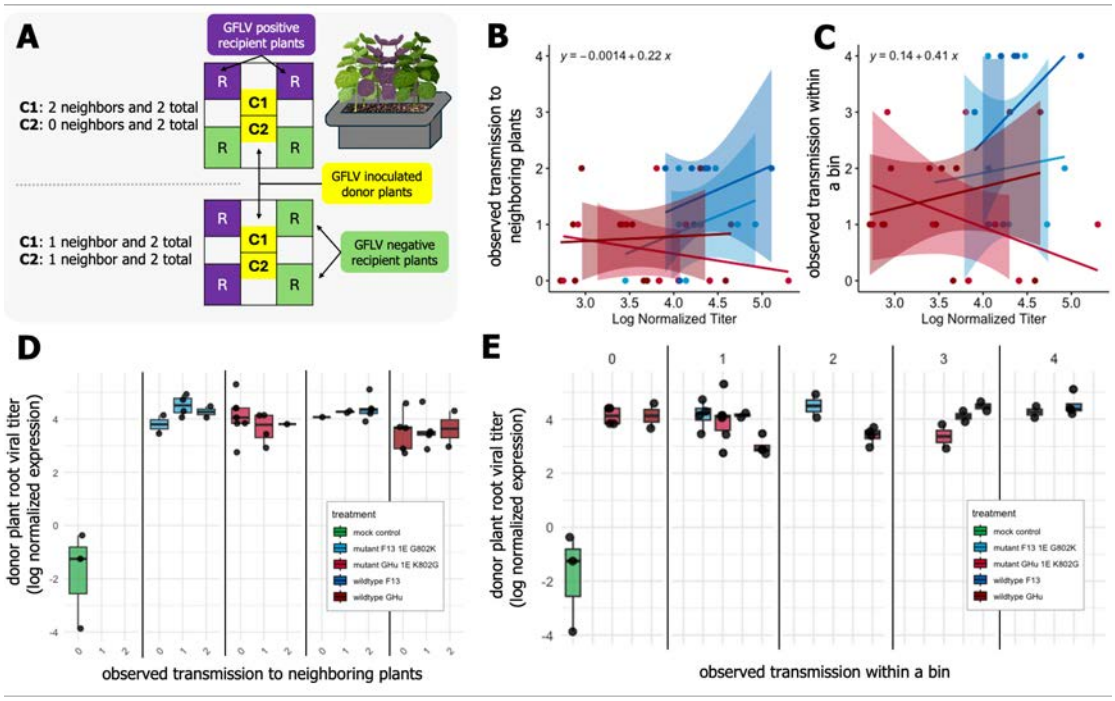

FIGURE 7-4. Spatial modeling of GFLV transmission indicates viral titer in roots of *Nicotiana benthamiana* donor plants is not correlated with transmission rates. **(A)** Schematic depicting of a bin with two GFLV-infected *Nicotiana benthamiana* donor plants in the center (C1 and C2) for transmission to healthy recipient *N. benthamiana* plants that tested negative (green) or positive (purple) for GFLV by RT-qPCR at the conclusion of the transmission assays. **(B,D)** Transmission from a donor plant to a neighboring recipient lant were not explained by the relative GFLV titer in the roots of donor plants. **(C,E)** Transmission at the bin level was not explained by relative GFLV titer in roots of donor plants.

GFLV titer in roots of donor and recipient plants is not an indicator for transmission

At the conclusion of the continuous transmission assays at 55-65 days post-inoculation, GFLV titer was analyzed by RT-qPCR in root samples of central donor plants. A pairwise comparison using the Wilcox test with a Benjamin-Hochberg correction was performed because the healthy control displayed a negatively skewed distribution in the normalized, log transformed GFLV titer. These tests indicated a difference in viral titer between wildtype GFLV-GHu and wildtype GFLV-F13 (p = 0.04) (Figure 7-2B). This result contrasted previous work that indicated no statistical difference in titer between these two GFLV strains in leaves of infected *N. benthamiana* at 14 dpi (Osterbaan et al. 2019). It is possible that GFLV titer fluctuates over time and varies in leaves versus roots during infection. As expected, all GFLV strains retained a statistically significant higher normalized titer when compared with mock control plants (Figure 7-2B).

GFLV titer in roots of donor plants was further explored through mixed-modeling approaches to evaluate a possible correlation with transmission donor to neighboring recipient plants or overall transmission in each bin paired with GFLV titer in donor plant roots (Figure 7-4A). Results indicated that instances of transmission from donor to neighboring recipient plants were not associated with GFLV titer in donor plants (Figure 7-4B,D, $p > 0.05$). Similarly, no correlation was observed between GFLV titer in roots of donor plants and transmission to recipient plants at a bin level (Figure 7-4C,E). Further, no statistical support was found for GFLV titer in roots of donor plants when spatial positioning was considered through linear mixed models (Figure 7-4B-C).

Together, these data rejected GFLV titer in plant roots to impact transmission rates by *X. index*.

The presence of GFLV but not GFLV titer in* X. index *is associated with transmission rates

Nematodes were isolated from soil samples (0.5 L) proximal to donor and recipient *N. benthamiana* plants separately from each bin at the end of the continuous transmission assays (Table 7-4). There was a significantly higher average number of nematodes recovered close to donor plants when compared with recipient plants for mutant GFLV-F13 $1E_{G802K}$ (p = 0.044), with strong numeric but insignificant differences for wildtype GFLV-GHu (p = 0.093) (Figure 7-5A). No significant difference was found in the average number of nematodes close to donor and recipient plants for wildtype GFLV-F13 and mutant GFLV-GHu $1E_{k802g}$ (Figure 7-5A). These results indicated less nematodes on recipient plants close to symptomatic donor plants infected with wildtype GFLV-GHu and mutant GFLV-F13 $1E_{G802K}$ at 55-65 days post-inoculation, while the same number of nematodes was isolated from recipient plants close to asymptomatic donor plants infected with wildtype GFLV-F13 and mutant GFLV-GHu $1E_{K802G}$.

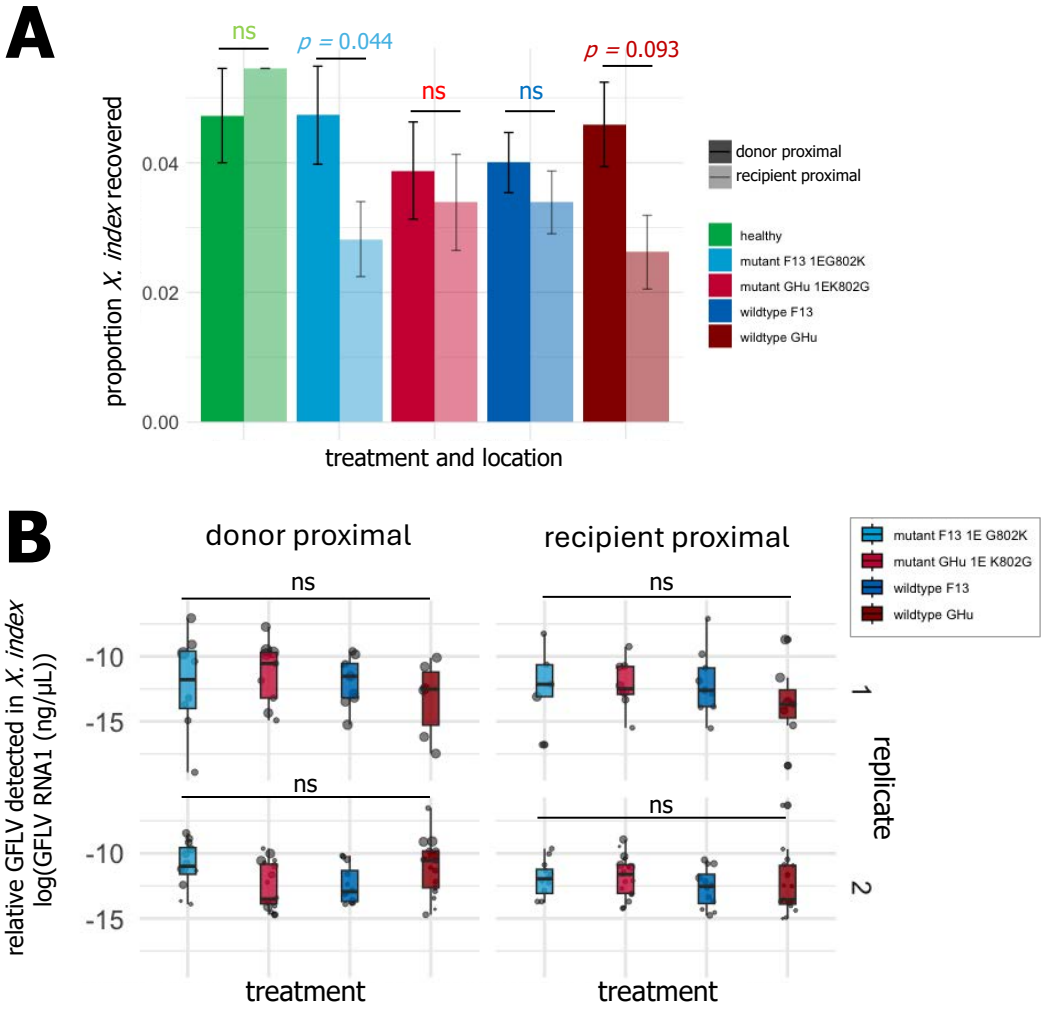

FIGURE 7-5. Number of *Xiphinema index* in donor and recipient *Nicotiana benthamiana* plants and titer of grapevine fanleaf virus (GFLV) in 2-30 pooled *X. index* samples at the conclusion of duplicated continuous transmission assays. (A) A larger proportion of nematodes was isolated close to donor plants compared with recipient plants across all viral treatments, particularly for wildtype GFLV-GHu and mutant GFLV-F13 $1E_{G802K,}$ with a statistically supported difference only for mutant GFLV-F13 $1E_{G802K}$. **(B)** The relative GFLV titer in *X. index* close to donor and recipient plants was not informative of transmission.

TABLE 7-4. Number of *Xiphinema index* from soil samples proximal to recipient *Nicotiana benthamiana* that did not test positive for grapevine fanleaf virus in RT-qPCR at the conclusion of duplicated continuous transmission assays.

Treatment	Experiment #1 *X. index* samples	Experiment #2 *X. index* samples	Overall *X. index* samples
mutant GFLV-F13 $1E_{G802K}$	1/9[a]	0/12	3/21 (14%)
wildtype GFLV-F13	0/9	2/12	2/21 (9%)
mutant GFLV-GHu $1E_{K802G}$	0/9	2/17	2/26 (8%)
wildtype GFLV-GHu	1/9	5/18	6/27 (22%)

[a]Fractions represent the total number of pooled nematode samples (2 to 30 per sample) that tested negative for GFLV in RT-qPCR at the conclusion of the transmission assays over the total number of pooled nematode samples tested.

Pooled *X. index* samples with undetectable levels of GFLV proximal to recipient plants were compiled across the duplicated continuous transmission assays as an indirect assessment of nematode feeding behavior on donor plants. Aviruliferous nematodes were essentially found on roots of non-infected recipient plants in bins with below average transmission rates (Figure 7-S2). The highest count of aviruliferous *X. index* was for wildtype GFLV-GHu (22%, 6/27) and mutant GFLV-F13 $1E_{G802K}$ (14%, 3/21), while lower counts were obtained for wildtype GFLV-F13 (9%, 2/21) and mutant GHu $1E_{K802G}$ (8%, 2/26) (Table 7-4). These results were suggestive of distinct feeding behaviors *of X. index* on *N. benthamiana* roots infected with different strains of GFLV in relation to amino acid in position 802 of protein $1E^{Pol*/Sd}$.

GFLV was quantified in pooled samples of 3-20 *X. index* by RT-qPCR to evaluate if transmission was influence by the virus titer in nematodes. Standard curves across plates obtained with purified GFLV-F13 allowed for standardization and normalization across all experimental samples (Figure 7-S4A-E). The correlation of all standards obtained R^2 values above 0.97, which were deemed suitable for quantification in experimental samples (Figure 7-S4F). The normalized quantification of actin in *X. index* samples then followed a logarithmic regression, as expected (Figure 7-S4G). The viral concentration determined from the standard curve allowed for treatment-wise comparisons of GFLV RNA in pooled nematode samples. The response variable 'detected RNA' deviated from normality assumptions and required the use of a Gamma general linear mixed model to explain GFLV levels as a response from viral treatment and number of nematodes. As expected, the number of nematodes positively correlated to the detectable amount of GFLV across all experimental samples. Treatment

differences were not statistically supported on nematodes from either donor or recipient plants (Dunnett's Test, $p > 0.05$) (Figure 7-5B). Furthermore, the relative amount of GFLV detected in *X. index* for each viral treatment was statistically similar, although numerical trends showed that *X. index* close to recipient plants infected with wildtype GFLV-GHu contained the lowest amount of GFLV (Kruskall-Wallis, $p > 0.05$) (Figure 7-5B). These results suggested that GFLV titer in *X. index* is not associated with transmission.

***Suggested mechanism in which GFLV modulates its transmission by* X. index**

Wildtype GFLV-F13 had the highest *X. index*-mediated transmission rate when compared with wildtype GFLV-GHu and mutant strains. Transmission correlated strongly with *N. benthamiana* root traits, i.e. number of root tips, reduced branching, and total root length, that were previously documented to be impacted by wildtype GFLV-GHu and mutant GFLV-F13 $1E_{G802K}$ infections, but not by GFLV-F13 and mutant GFLV-GHu $1E_{K802G}$ infections (Roy and Fuchs 2024). These findings suggested that the root network can impact transmission by influencing nematode feeding on root systems of multiple plants (Figure 7-6). In the case of asymptomatic infections, the physical proximity of root systems promotes nematode feeding on several plants, thus facilitating GFLV acquisition from donor plants and subsequent transmission to recipient plants. This scenario applies to wildtype GFLV-F13 and mutant GFLV-GHu $1E_{K802G}$. In contrast, in the case of symptomatic infections, nematode feeding on donor plants is reduced and the physical distance between root systems of donor and recipient plants further reduces nematode feeding on multiple plants, thus limiting GFLV

transmission from plant to plant by *X. index*. This scenario applies to wildtype GFLV-GHu and mutant GFLV-F13 1E$_{G802K}$.

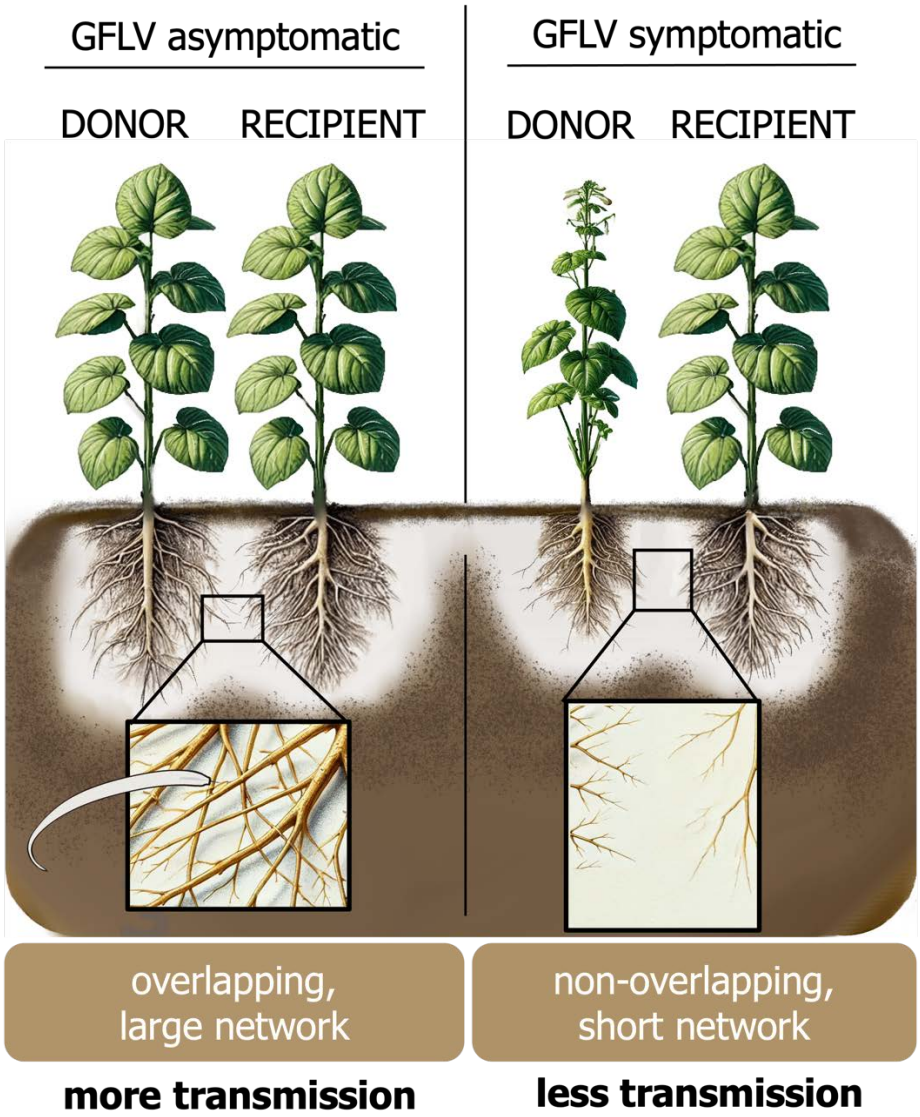

FIGURE 7-6. Possible role of modified root system architecture (RSA) traits of *Nicotiana benthamiana* in grapevine fanleaf virus (GFLV) transmission by *Xiphinema index*. Asymptomatic GFLV strains sustain normal RSA, similar to that of non-infected plants, and provide optimal conditions for transmission with large and overlapping root networks. This scenario applies to wildtype GFLV-F13 and mutant GFLV-GHu 1E$_{K802}$. Symptomatic GFLV strains elicit perturbations in total root length, root surface area, and root tip number to reduce transmission due to short and non-overlapping root networks. This scenario applies to wildtype GFLV-GHu and mutant GFLV-F13 1E$_{G802K}$.

DISCUSSION

Studies on virus-host-vector interactions have shown how a virus can manipulate its plant host to modulate transmission, one of the most important steps in a virus' infection cycle. For aerial vectors such as aphids, whiteflies, and leafhoppers, several viruses have been shown to manipulate their plant hosts to facilitate transmission (Colvin et al. 2006; Falla and Cunniffe 2024; Milonas et al. 2023). For soil-borne viruses, protein p31 encoded by RNA4 of beet necrotic yellow vein virus (BNYVV, genus *Benyvirus*, family *Benyviridae*) exponentiates transmission by its protist vector *Polymyza betae* (Rahim et al. 2007). Further, BYNVV RNA3 protein p25 modifies the RSA through plant hormone response pathways (Peltier et al. 2011). While modifications of root traits were documented, their correlation to transmission was nnot modeled for BNYVV. Another example is tobacco rattle virus (TRV, genus *Tobravirus*, family *Virgaviridae*) that manipulates root VOC expression profiles in *N. benthamiana* to modify vector behavior by enhancing its attraction to plants treated with 2-ethyl-1-hexanol (Van Griethuysen et al. 2024). TRV RNA2 non-structural proteins 2b and 2c impact transmission (Macfarlane et al. 1996; Visser and Bol 1999) with mutations of these genes modifying 2-ethyl-1-hexanol production (Van Griethuysen et al. 2024). Again, symptoms in roots and transmission rates were independently observed, but not correlated to each other for TRV. Additionally, modification of the pea early browning virus (PEBV, genus *Tobravirus*, family *Virgaviridae*) RNA2 genes 2a (coat protein), 2b (VSR) and 2c (unknown function) have been associated with transmission efficiency of its trichodorid nematode vector, however, the exact mechanism has not been described

(Macfarlane et al. 1996). It will be interesting to observe if RSA traits in these systems are associated with viral transmission.

Here, we built on previous studies centering on virus manipulations of plant hosts for transmission by using a virus transmitted by an ectoparasitic dagger nematode. We first evaluated several herbaceous host species to determine *N. benthamiana* as a suitable plant for GFLV transmission by *X. index* (Table 7-1). Then, different transmission rates by *X. index* were observed based on the GFLV strain and the identity of the amino acid in position 802 of GFLV protein $1E^{Pol*/Sd}$ (Tables 7-2 and 7-3). Lower transmission rates were obtained with symptomatic wildtype GFLV-GHu and mutant GFLV-F13 $1E_{G802K}$, while higher transmission rates were obtained with asymptomatic wildtype GFLV-F13 and mutant GFLV-GHu $1E_{K802G}$. Relative GFLV titer in roots of donor plants was significantly different for wildtype GFLV strains F13 and GHu (Figure 7-2D), however spatial correlation of transmission rejected virus titer as a contributing factor to influence transmission (Figure 7-4, Figure 7-S5B). These findings validated our hypothesis on GFLV strains and amino acid-specific modifications to RSA resulting in differential transmission rates. Indeed, transmission rates were associated with the number of root tips, root system surface area (mm^2), and total root length (mm) (Figure 7-3A). These RSA traits are modified by the amino acid in position 802 of GFLV protein $1E^{Pol*/Sd}$ at 17 days post-inoculation (Roy and Fuchs 2024), but are no longer apparent after two months of infection (this study). This is the first report on the ability of a plant virus to differentially manipulate the RSA of its plant host to influence nematode-mediated transmission. Similarly, to our knowledge, this report reflects the first instance of viral strain differences in transmission of a plant virus by a dagger nematode vector.

Previous work suggested strain differences in tomato ringspot virus (species *Nepovirus lycopersici*, genus *Nepovirus*, family *Secoviridae*) transmission by *X. californicum* (Hoy et al. 1984); however, transmission assays were not replicated, and roots of donor and recipient cucumber plants were not examined in this study.

Several *X. index* samples close to recipient plants were avirulifeous at the conclusion of the continuous transmission assays, suggesting that they had not acquired or retained GFLV. Such nematode samples were present across all viral treatments, indicating that not all *X. index* acquired GFLV while feeding on donor plants during the eight-week experiment (Table 7-4). This was disproportionately true for symptomatic wildtype GFLV-GHu and to a lesser extent for symptomatic mutant GFLV-F13 $1E_{G802K}$. It is plausible that the root morphology of donor plants infected with wildtype GFLV-GHu and mutant GFLV-F13 $1E_{G802K}$ deterred *X. index* feeding, hence a higher proportion of aviruliferous specimens found on recipient plants for these two viral treatments (Table 7-4). Alternatively, other factors such as root metabolites could impact nematode feeding behavior. More detailed studies will be needed to address *X. index* feeding preferences on different root systems.

Viruses have evolved multiple strategies to accomplish transmission, essentially through a CP or a CP and a helper compoment mode (Hamelin et al. 2016; Shi et al. 2021; Whitfield et al. 2015). In the case of GFLV, protein $2C^{CP/Td}$ determines GFLV transmission by *X. index* (Andret-Link et al. 2004b; Schellenberger et al. 2010) and protein $1E^{Pol*/Sd}$ modulates transmission rates by *X. index* through modifications of the plant root morphology (Figure 7-3 and Figure 7-5A). Further, protein $2C^{CP/Td}$ is not known to be associated with protein $1E^{Pol*/Sd}$ in GFLV-infected *N. benthamiana*, as

shown by co-immunoprecipitation assays (Osterbaan et al. 2021). Therefore, although interactions between protein $1E^{Pol*/Sd}$ and nematode components cannot be ruled out, the role of protein $1E^{Pol*/Sd}$ in transmission seems unrelated to protein-protein interactions (Andret-Link et al. 2004b; Belin et al. 2001; Gray et al. 2014; Schellenberger et al. 2011). Instead, protein $1E^{Pol*/Sd}$ likely influences transmission by modifying RSA traits of plant hosts and/or activating the production of VOCs that may attract or eventually repel *X. index*, as recently described for TRV (Van Griethuysen et al. 2024).

In this study, a novel nematode transmission assay was developed to test how GFLV influences its transmission by *X. index* (Figure 7-1B). This assay relied on continuous AAP and IAP with minimal soil disturbance. It was designed to mimic natural *X. index*-mediated transmission of GFLV in the vineyard where infected and non-infected plants are continuously grown in close spatial proximity. This modification was vital to investigate intricate plant host-virus-nematode vector interactions. Our continuous assays lasted 7-8-weeks to establish secondary spread. This is a substantially shorter period than the most conventional 6-week APP combined with a 6-week IAP (Schellenberger et al. 2011). For tobraviruses, a two-step transmission assay typically involves four-week AAPs followed by one-week IAPs and three-week incubation periods to detect transmission when nematodes are placed directly on young root systems almost immediately after germination (MacFarlane and Neilson 2009). A previous study based on a two-step assay with seven single-female *X. index* lines documented similar transmission rates of wildtype GFLV-GHu and -F13 from Kober 5BB to Kober 5BB (Demangeat et al. 2010). This assay, unlike our one-step approach,

was likely saturated with transmission rates ranging from 88% to 96% compared with 17% to 75% (this study). In addition, modifications to the RSA of grapevines were not considered in the previous study (Demangeat et al. 2010).

It would be interesting to perform GFLV transmission studies with the natural host, *Vitis* spp., beginning with examining RSA of GFLV-infected grapevines. It is currently unknown if GFLV impacts the RSA of *Vitis*, and further, if differences in RSA are observed between distinct viral strains. Similarly, it would be interesting to characterize the metabolome of grapevine roots infected by distinct GFLV strains to determine whether specific VOCs may influence *X. index*-mediated transmission rates in addition to RSA traits modified by protein $1E^{Pol*/Sd}$. Metabolic changes of various grapevine cultivars, with and without viral infection, have been profiled (Mandrile et al. 2022; Rienth et al. 2021) but none have yet focused on grapevine roots. If root exudates differ between plants infected with various GFLV strains and are shown to impact the olfactory behavior of *X. index*, choice assays, as documented for TRV (Van Griethuysen et al. 2024), could be insightful to determine their role in GFLV transmission. Furthermore, *X. index* has been suggested to induce changes in root morphology, particularly at high population density, that contribute to decline of grapevine (Cohn 1970; Wyss 1978). The results presented here indicate that GFLV reprograms RSA to influence transmission by *X. index* (Figure 7-6). Future work could disentangle the respective impacts of GFLV and *X. index* on root architecture with singularly GFLV-infected or *X. index*-infested grapevines over extended periods.

Natural GFLV infection in the vineyard usually displays vines with varying degrees of foliar symptoms and a patchy distribution (Andret-Link et al. 2004a). Such

aggregation of symptomatic vines often leads to hotspots of infection. In the center of these hotspots are typically dead vines that succumbed from the infection. Beyond the center is a circle of symptomatic vines that exhibit severe disease symptoms such as mosaic, interveinal chlorosis and leaf deformations, and are infected with GFLV. Beyond this circle of symptomatic vines is often another circle of vines that display no symptoms or very mild disease symptoms but are infected with GFLV (Martelli 1978). Assuming our findings on *N. benthamiana* directly apply to grapevines, *X. index*-mediated GFLV transmission is likely more efficient among vines located in the outer circle than among vines in the inner circle. It would be interesting to test this hypothesis in fanleaf diseased vineyards from an epidemiological standpoint.

REFERENCES

Andret-Link, P., Laporte, C., Valat, L., Ritzenthaler, C., Demangeat, G., Vigne, E., Laval, V., Pfeiffer, P., Stussi-Garaud, C., and Fuchs, M. 2004a. Grapevine fanleaf virus: Still a major threat to the grapevine industry. Journal of Plant Pathology 86:183–195.

Andret-Link, P., Schmitt-Keichinger, C., Demangeat, G., Komar, V., and Fuchs, M. 2004b. The specific transmission of Grapevine fanleaf virus by its nematode vector *Xiphinema index* is solely determined by the viral coat protein. Virology 320:12–22. https://doi.org/10.1016/j.virol.2003.11.022.

Bates, D., Mächler, M., Bolker, B., and Walker, S. 2015. Fitting Linear Mixed-Effects Models Using lme4. Journal of Statistical Software 67:1–48. https://doi.org/10.18637/jss.v067.i01.

Belin, C., Schmitt, C., Demangeat, G., Komar, V., Pinck, L., and Fuchs, M. 2001. Involvement of RNA2-encoded proteins in the specific transmission of *Grapevine fanleaf virus* by its nematode vector *Xiphinema index*. Virology 291:161–171. https://doi.org/10.1006/viro.2001.1216.

Belval, L., Marmonier, A., Schmitt-Keichinger, C., Gersch, S., Andret-Link, P., Komar, V., Vigne, E., Lemaire, O., Ritzenthaler, C., and Demangeat, G. 2019. From a Movement-Deficient Grapevine Fanleaf Virus to the Identification of a New Viral Determinant of Nematode Transmission. Viruses 11:E1146. https://doi.org/10.3390/v11121146.

Blanc, S., and Michalakis, Y. 2016. Manipulation of hosts and vectors by plant viruses and impact of the environment. Current Opinion in Insect Science 16:36–43. https://doi.org/10.1016/j.cois.2016.05.007.

Brooks, M. E., Kristensen, K., Van Benthem, K. J., Magnusson, A., Berg, C. W., Nielsen, A., Skaug, H. J., Mächler, M., and Bolker, B. M. 2017. glmmTMB balances speed and flexibility among packages for zero-inflated generalized linear mixed modeling. .

Cadman, C. H., Dias, H. F., and Harrison, B. D. 1960. Sap-Transmissible Viruses Associated With Diseases of Grape Vines in Europe and North America. Nature 187:577–579. https://doi.org/10.1038/187577a0.

Callaway, A., Giesman-Cookmeyer, D., Gillock, E. T., Sit, T. L., and Lommel, S. A. 2001. THE MULTIFUNCTIONAL CAPSID PROTEINS OF PLANT RNA VIRUSES. Annual Review of Phytopathology 39:419–460. https://doi.org/10.1146/annurev.phyto.39.1.419.

Clarke, E., Sherrill-Mix, S., and Dawson, C. 2016. ggbeeswarm: Categorical scatter (violin point) plots. CRAN: Contributed Packages.

Cohn, E. 1970. Observations on the Feeding and Symptomatology of *Xiphinema* and *Longidorus* on Selected Host Roots. J Nematol 2:167–173.

Colvin, J., Omongo, C. A., Govindappa, M. R., Stevenson, P. C., Maruthi, M. N., Gibson, G., Seal, S. E., and Muniyappa, V. 2006. Host-Plant Viral Infection Effects on Arthropod-Vector Population Growth, Development and Behaviour: Management and Epidemiological Implications. In *Advances in Virus Research*, Elsevier, pp. 419–452. https://doi.org/10.1016/S0065-3527(06)67011-5.

Dias, H. F. 1963. Host range and properties of grapevine fanleaf and grapevine yellow mosaic viruses. Ann Applied Biology 51:85–95. https://doi.org/10.1111/j.1744-7348.1963.tb03677.x.

Esmenjaud, D., Walter, B., Minot, J., Voisin, R., and Cornuet, P. 1993. Biotin-avidin ELISA detection of grapevine fanleaf virus in the vector nematode *Xiphinema index*. Journal of Nematology 25:401.

Falla, E. K., and Cunniffe, N. J. 2024. Why aphid virus retention needs more attention: Modelling aphid behaviour and virus manipulation in non-persistent plant virus transmission ed. Claudio José Struchiner. PLoS Comput Biol 20:e1012479. https://doi.org/10.1371/journal.pcbi.1012479.

Flegg, J. 1967. Extraction of *Xiphinema* and *Longidorus* species from soil by a modification of Cobb's decanting and sieving technique. Annals of applied Biology 60:429–437.

Fuchs, M., and Lemaire, O. 2017. Novel Approaches for Viral Disease Management. In *Grapevine Viruses: Molecular Biology, Diagnostics and Management*, eds. Baozhong Meng, Giovanni P. Martelli, Deborah A. Golino, and Marc Fuchs. Cham: Springer International Publishing, pp. 599–621. https://doi.org/10.1007/978-3-319-57706-7_29.

Gray, S., Cilia, M., and Ghanim, M. 2014. Circulative, "Nonpropagative" Virus Transmission. In *Advances in Virus Research*, Elsevier, pp. 141–199. https://doi.org/10.1016/B978-0-12-800172-1.00004-5.

Hamelin, F. M., Allen, L. J. S., Prendeville, H. R., Hajimorad, M. R., and Jeger, M. J. 2016. The evolution of plant virus transmission pathways. Journal of Theoretical Biology 396:75–89. https://doi.org/10.1016/j.jtbi.2016.02.017.

Hewitt, W., Raski, D., and Goheen, A. 1958. Transmission of fanleaf virus by Xiphinema index Thorne and Allen. In AMER PHYTOPATHOLOGICAL SOC 3340 PILOT KNOB ROAD, ST PAUL, MN 55121, pp. 393–394.

Hooper, D. J., Hallmann, J., and Subbotin, S. A. 2005. Methods for extraction, processing and detection of plant and soil nematodes. In *Plant parasitic nematodes in subtropical and tropical agriculture*, CABI Publishing Wallingford UK, pp. 53–86.

Hothorn, T., Bretz, F., and Westfall, P. 2008. Simultaneous inference in general parametric models. Biometrical Journal: Journal of Mathematical Methods in Biosciences 50:346–363.

Hoy, J. W., Mircetich, S. M., and Lownsbery, B. F. 1984. Differential Transmission of Prunus Tomato Ringspot Virus Strains by *Xiphinema californicum*. Phytopathology 74:332. https://doi.org/10.1094/Phyto-74-332.

Huss, B., Walter, B., and Fuchs, M. 1989. Cross-protection between arabis mosaic virus and grapevine fan leaf virus isolates in *Chenopodium quinoa*. Annals of Applied Biology 114:45–60.

Lenth, R., and Lenth, M. R. 2018. Package 'lsmeans.' The American Statistician 34:216–221.

MacFarlane, S. A., and Neilson, R. 2009. Testing of Transmission of Tobraviruses by Nematodes. CP Microbiology 12. https://doi.org/10.1002/9780471729259.mc16b05s12.

Macfarlane, S. A., Wallis, C. V., and Brown, D. J. F. 1996. Multiple Virus Genes Involved in the Nematode Transmission of Pea Early Browning Virus. Virology 219:417–422. https://doi.org/10.1006/viro.1996.0267.

Mandrile, L., D'Errico, C., Nuzzo, F., Barzan, G., Matić, S., Giovannozzi, A. M., Rossi, A. M., Gambino, G., and Noris, E. 2022. Raman Spectroscopy Applications in Grapevine: Metabolic Analysis of Plants Infected by Two Different Viruses. Front. Plant Sci. 13:917226. https://doi.org/10.3389/fpls.2022.917226.

Margis, R., Ritzenthaler, C., Reinbolt, J., Pinck, M., and Pinck, L. 1993. Genome organization of grapevine fanleaf nepovirus RNA2 deduced from the 122K polyprotein P2 *in vitro* cleavage products. Journal of General Virology 74:1919–1926.

Margis, R., Viry, M., Pinck, M., Bardonnet, N., and Pinck, L. 1994. Differential proteolytic activities of precursor and mature forms of the 24K proteinase of Grapevine fanleaf nepovirus. Virology 200:79–86. https://doi.org/10.1006/viro.1994.1165.

Martelli, G. P. 1978. Nematode-borne viruses of grapevine, their epidemiology and control. Nematologia Mediterranea.

Martin, I. R., Vigne, E., Berthold, F., Komar, V., Lemaire, O., Fuchs, M., and Schmitt-Keichinger, C. 2018. The 50 distal amino acids of the $2A^{HP}$ homing protein of *Grapevine fanleaf virus* elicit a hypersensitive reaction on *Nicotiana*

occidentalis. Molecular Plant Pathology 19:731–743. https://doi.org/10.1111/mpp.12558.

Mauck, K. E., Chesnais, Q., and Shapiro, L. R. 2018. Evolutionary Determinants of Host and Vector Manipulation by Plant Viruses. In *Advances in Virus Research*, Elsevier, pp. 189–250. https://doi.org/10.1016/bs.aivir.2018.02.007.

Milonas, P. G., Anastasaki, E., Psoma, A., Partsinevelos, G., Fragkopoulos, G. N., Kektsidou, O., Vassilakos, N., and Kapranas, A. 2023. Plant viruses induce plant volatiles that are detected by aphid parasitoids. Sci Rep 13:8721. https://doi.org/10.1038/s41598-023-35946-3.

Moreno-Delafuente, A., Garzo, E., Moreno, A., and Fereres, A. 2013. A Plant Virus Manipulates the Behavior of Its Whitefly Vector to Enhance Its Transmission Efficiency and Spread ed. Murad Ghanim. PLoS ONE 8:e61543. https://doi.org/10.1371/journal.pone.0061543.

Ng, J. C. K., and Falk, B. W. 2006. Virus-Vector Interactions Mediating Nonpersistent and Semipersistent Transmission of Plant Viruses. Annu. Rev. Phytopathol. 44:183–212. https://doi.org/10.1146/annurev.phyto.44.070505.143325.

Ogle, D. H., Doll, J. C., Wheeler, A. P., and Dinno, A. 2023. FSA: Simple Fisheries Stock Assessment Methods. .

Osterbaan, L. J., Choi, J., Kenney, J., Flasco, M., Vigne, E., Schmitt-Keichinger, C., Rebelo, A. R., Heck, M., and Fuchs, M. 2019. The identity of a single residue of the RNA-dependent RNA polymerase of grapevine fanleaf virus modulates vein clearing in *Nicotiana benthamiana*. Molecular Plant-Microbe Interactions 32:790–801. https://doi.org/10.1094/MPMI-12-18-0337-R.

Osterbaan, L. J., Hoyle, V., Curtis, M., DeBlasio, S., Rivera, K. D., Heck, M., and Fuchs, M. 2021. Identification of protein interactions of grapevine fanleaf virus RNA-dependent RNA polymerase during infection of *Nicotiana benthamiana* by affinity purification and tandem mass spectrometry. Journal of General Virology 102. https://doi.org/10.1099/jgv.0.001607.

Osterbaan, L. J., Schmitt-Keichinger, C., Vigne, E., and Fuchs, M. 2018. Optimal systemic grapevine fanleaf virus infection in *Nicotiana benthamiana* following agroinoculation. Journal of Virological Methods 257:16–21. https://doi.org/10.1016/j.jviromet.2018.04.006.

Pedersen, T. L. 2019. Package 'patchwork.' R package http://CRAN. R-project. org/package= patchwork. Cran.

Peltier, C., Schmidlin, L., Klein, E., Taconnat, L., Prinsen, E., Erhardt, M., Heintz, D., Weyens, G., Lefebvre, M., Renou, J.-P., and Gilmer, D. 2011. Expression of the Beet necrotic yellow vein virus p25 protein induces hormonal changes and a root branching phenotype in *Arabidopsis thaliana*. Transgenic Res 20:443–466. https://doi.org/10.1007/s11248-010-9424-3.

Pinck, L., Fuchs, M., Pinck, M., RAVELONANDROI, M., and WALTER, B. 1988. A satellite RNA in Grapevine Fanleaf Virus strain F13. Journal of General Virology - J GEN VIROL 69:233–239. https://doi.org/10.1099/0022-1317-69-1-233.

Poulin, R. 2010. Parasite Manipulation of Host Behavior. In *Advances in the Study of Behavior*, Elsevier, pp. 151–186. https://doi.org/10.1016/S0065-3454(10)41005-0.

Rahim, M. D., Andika, I. B., Han, C., Kondo, H., and Tamada, T. 2007. RNA4-encoded p31 of beet necrotic yellow vein virus is involved in efficient vector transmission, symptom severity and silencing suppression in roots. Journal of General Virology 88:1611–1619. https://doi.org/10.1099/vir.0.82720-0.

Rienth, M., Vigneron, N., Walker, R. P., Castellarin, S. D., Sweetman, C., Burbidge, C. A., Bonghi, C., Famiani, F., and Darriet, P. 2021. Modifications of Grapevine Berry Composition Induced by Main Viral and Fungal Pathogens in a Climate Change Scenario. Front. Plant Sci. 12. https://doi.org/10.3389/fpls.2021.717223.

Ritzenthaler, C., Viry, M., Pinck, M., Margis, R., Fuchs, M., and Pinck, L. 1991. Complete nucleotide sequence and genetic organization of grapevine fanleaf nepovirus RNA1. Journal of General Virology 72:2357–2365. https://doi.org/10.1099/0022-1317-72-10-2357.

Roy, B. G., Choi, J., and Fuchs, M. F. 2024. Predictive Modeling of Proteins Encoded by a Plant Virus Sheds a New Light on Their Structure and Inherent Multifunctionality. Biomolecules 14:62. https://doi.org/10.3390/biom14010062.

Roy, B. G., DeBlasio, S., Yang, Y., Thannhauser, T., Heck, M., and Fuchs, M. 2023. Profiling Plant Proteome and Transcriptome Changes during Grapevine Fanleaf Virus Infection. J. Proteome Res. 22:1997–2017. https://doi.org/10.1021/acs.jproteome.3c00069.

Roy, B. G., and Fuchs, M. 2024. A single viral amino acid shapes the root system architecture of a plant host upon virus infection. BMC Microbiol 24:267. https://doi.org/10.1186/s12866-024-03399-x.

Roy, B. G., and Fuchs, M. 2022. Herbaceous plant hosts as supermodels for grapevine viruses: a historical perspective. J Plant Pathol 1–30. https://doi.org/10.1007/s42161-022-01267-z.

Roy, B. G., and Fuchs, M. 2023. Processing and maintenance of *Nicotiana benthamiana* tissue for phenotypic, histological, and ribonucleic acid analysis *v1*. https://protocols.cloud/view/processing-and-maintenance-of-nicotiana-benthamian-cvssw6ee.

Schellenberger, P., Andret-Link, P., Schmitt-Keichinger, C., Bergdoll, M., Marmonier, A., Vigne, E., Lemaire, O., Fuchs, M., Demangeat, G., and Ritzenthaler, C. 2010. A stretch of 11 amino acids in the βB- βC loop of the coat protein of *Grapevine fanleaf virus* is essential for transmission by the nematode *Xiphinema index*. Journal of Virology 84:7924–7933. https://doi.org/10.1128/JVI.00757-10.

Schellenberger, P., Sauter, C., Lorber, B., Bron, P., Trapani, S., Bergdoll, M., Marmonier, A., Schmitt-Keichinger, C., Lemaire, O., Demangeat, G., and Ritzenthaler, C. 2011. Structural insights into viral determinants of nematode mediated Grapevine fanleaf virus transmission. PLoS Pathogens 7:e1002034. https://doi.org/10.1371/journal.ppat.1002034.

Seethepalli, A., and York, L. M. 2020. RhizoVision Explorer - Interactive software for generalized root image analysis designed for everyone. . https://doi.org/10.5281/ZENODO.4095629.

Serghini, M. A., Fuchs, M., Pinck, M., Reinbolt, J., Walter, B., and Pinck, L. 1990. RNA2 of grapevine fanleaf virus: sequence analysis and coat protein cistron location. Journal of General Virology 71:1433–1441. https://doi.org/10.1099/0022-1317-71-7-1433.

Shi, X., Zhang, Z., Zhang, C., Zhou, X., Zhang, D., and Liu, Y. 2021. The molecular mechanism of efficient transmission of plant viruses in variable virus–vector–plant interactions. Horticultural Plant Journal 7:501–508. https://doi.org/10.1016/j.hpj.2021.04.006.

Su, Q., Preisser, E. L., Zhou, X. M., Xie, W., Liu, B. M., Wang, S. L., Wu, Q. J., and Zhang, Y. J. 2015. Manipulation of Host Quality and Defense by a Plant Virus Improves Performance of Whitefly Vectors. Journal of Economic Entomology 108:11–19. https://doi.org/10.1093/jee/tou012.

Taylor, C. E., and Robertson, W. M. 1970. Sites of virus retention in the alimentary tract of the nematode vectors, *Xiphinema diversicaudatum* (Micol.) and *X. index* (Thorne and Allen). Annals of Applied Biology 66:375–380. https://doi.org/10.1111/j.1744-7348.1970.tb04616.x.

Taylor, C., and Raski, D. 1964. On the transmission of grape fanleaf by *Xiphinema index*. .

Team, Rs. 2015. RStudio: integrated development for R. (No Title).

Van Griethuysen, P., Redeker, K. R., MacFarlane, S. A., Neilson, R., and Hartley, S. E. 2024. Virus-induced changes in root volatiles attract soil nematode vectors to infected plants. New Phytologist 241:2275–2286. https://doi.org/10.1111/nph.19518.

Vigne, E., Garcia, S., Komar, V., Lemaire, O., and Hily, J.-M. 2018. Comparison of Serological and Molecular Methods With High-Throughput Sequencing for the Detection and Quantification of Grapevine Fanleaf Virus in Vineyard Samples. Front. Microbiol. 9:2726. https://doi.org/10.3389/fmicb.2018.02726.

Vigne, E., Gottula, J. W., Schmitt-Keichinger, C., Komar, V., Ackerer, L., Belval, L., Rakotomalala, L., Lemaire, O., Ritzenthaler, C., and Fuchs, M. 2013. A strain-specific segment of the RNA-dependent RNA polymerase of grapevine fanleaf virus determines symptoms in *Nicotiana* species. Journal of General Virology 94:2803–2813. https://doi.org/10.1099/vir.0.057646-0.

Viry, M., Serghini, M. A., Hans, F., Ritzenthaler, C., Pinck, M., and Pinck, L. 1993. Biologically active transcripts from cloned cDNA of genomic grapevine fanleaf nepovirus RNAs. Journal of General Virology 74:169–174. https://doi.org/10.1099/0022-1317-74-2-169.

Visser, P. B., and Bol, J. F. 1999. Nonstructural proteins of Tobacco rattle virus which have a role in nematode-transmission: expression pattern and interaction with viral coat protein. Journal of General Virology 80:3273–3280. https://doi.org/10.1099/0022-1317-80-12-3273.

Vuittenez, A., Munck, M., and Kuszala, J. 1964. Demonstration of the infectious degeneration virus by serological tests and observation of characteristic particles from extracts of diseased Vine leaves. .

Wei, T., and Simko, V. 2017. *R package "corrplot": Visualization of a Correlation Matrix*.

Wei, T., Simko, V., Levy, M., Xie, Y., Jin, Y., Zemla, J., Freidank, M., Cai, J., and Protivinsky, T. 2021. corrplot: Visualization of a Correlation Matrix. .

Whitfield, A. E., Falk, B. W., and Rotenberg, D. 2015. Insect vector-mediated transmission of plant viruses. Virology 479–480:278–289. https://doi.org/10.1016/j.virol.2015.03.026.

Wickham, H. 2009. *ggplot2: Elegant Graphics for Data Analysis*. New York, NY: Springer. https://doi.org/10.1007/978-0-387-98141-3.

Wickham, H., François, R., Henry, L., and Müller, K. 2018. dplyr: A Grammar of Data Manipulation. R package version 0.7. 6. Computer software]. https://CRAN. R-project. org/package= dplyr.

Wyss, U. 1978. Root and cell response to feeding by *Xiphinema index*. Nematologica 24:159–166.

TABLE 7-S1. Primers used in this study for the detection of grapevine fanleaf virus (GFLV), Arabis mosaic virus (ArMV), and *Xiphinema index* sequences by RT-PCR or RT-qPCR.

Technique	Primer name	Target gene	Sequence 5'-3'	Reference(s)
RT-PCR	AR2	ArMV RNA2	GAGTTTGAGGCAGCAAAGAG	Loudes et al. 1995
	CNR	GFLV RNA2, ArMV RNA2	CAAGTCTAGACAAAGGACA AACAACACACTGTCGC	Serghini et al. 1990; Loudes et al. 1995
	CPS	GFLV RNA2	TTGTGCGCCCAGATCTCTCTTTACCA	Demangeat et al. 2004
	GFLV-SymDetF	GFLV RNA1	TGCTAGGACCAAATCAGAGGAACG	Osterbaan et al. 2019
	GFLV-SymDetR	GFLV RNA1	AAACTTGGTTATCCCAGTACCA	
RT-qPCR	q1G5680fwd	GFLV RNA1	ATTGCTTCAARAARATAGTNCCYCC	Vigne et al. 2018
	q1G5802reva	GFLV RNA1	CAGTRAAATRYTGCATRACAGAYTGTGC	
	q2G2720fwd	GFLV RNA2	TGTGTBYTRGGWATGGGAGGYACT	Garcia et al. 2019
	q2G2835rev	GFLV RNA2	TTCCARTCCATVGTGGTCCCGTT	
	Actin-nem-qfwd	*X. index* actin	ACACTGTGCCCATCTATGAAG	
	Actin-nem-qrev	*X. index* actin	TAACCACGTTCAGTGAGGATTT	

TABLE 7-S2. Experimental design for inter-plate standards and normalization across plate runs for the quantification of grapevine fanleaf virus (GFLV) by RT-qPCR in *Xiphinema index* used in continuous transmission assays.

Assay	Plate	Nematode[a]	Virus dilution[b]
1	1	All viruliferous (N) and aviruliferous (AV) standards	10^{-1} to 10^{-7}
1	2	N_{10} (x3) and N_{20} (x3)	10^{-9} to 10^{-11}
1	3	N_{10} (x3), N_{20} (x3), AV1 to AV3, and AV5	10^{-5} to 10^{-9}
2	1	AV1 to AV15	10^{-4} to 10^{-10}
2	2	AV1 to AV4, AV13 to AV15	10^{-5} to 10^{-8}
2	3	AV5 to AV10, AV12, entire viruliferous standard curve	10^{-5} to 10^{-8}
2	4	AV1 to AV3	10^{-4} to 10^{-9}

[a]Samples pertaining to nematode actin reference gene
[b]Samples pertaining to serial dilutions of GFLV RNA isolated from purified particles

TABLE 7-S3. Calculations of grapevine fanleaf virus (GFLV) RNA1 concentrations in standard curves for RT-qPCR. Purified GFLV particles were subject to RNA column extraction which resulted in starting solutions of 374.8 ng/µL viral RNA and 362.6 ng/µL viral RNA in replicates #1 and #2, respectively.

Sample in RT-qPCR	GFLV RNA (ng/µL) in replicate #1	GFLV RNA (ng/µL) in replicate #2
[V] x 10^{-1}	37.48	36.26
[V] x 10^{-2}	3.748	3.626
[V] x 10^{-3}	3.748 x 10^{-1}	3.626 x 10^{-1}
[V] x 10^{-4}	3.748 x 10^{-2}	3.626 x 10^{-2}
[V] x 10^{-5}	3.748 x 10^{-3}	3.626 x 10^{-3}
[V] x 10^{-6}	3.748 x 10^{-4}	3.626 x 10^{-4}
[V] x 10^{-7}	3.748 x 10^{-5}	3.626 x 10^{-5}
[V] x 10^{-8}	3.748 x 10^{-6}	3.626 x 10^{-6}
[V] x 10^{-9}	3.748 x 10^{-7}	3.626 x 10^{-7}
[V] x 10^{-10}	3.748 x 10^{-8}	3.626 x 10^{-8}

TABLE 7-S4. Number of *Xiphinema index* elutriated from soil samples around donor and recipient *Nicotiana benthamiana* plants used at the conclusion of continuous transmission assays.

Replicate	Bin	Treatment	*X. index* on donor			*X. index* on recipient		
			#1	#2	#3	#1	#2	#3
1	1	mutant GFLV-GHu 1E$_{K802G}$	9	8	9	19	20	20
	2	mutant GFLV-F13	20	20	20	15	15	10
	3[a]	wildtype GFLV-GHu 1E$_{K802G}$	12	12	10	15	15	15
	4	wildtype GFLV-F13	15	15	15	10	10	10
	5	mutant GFLV-GHu 1E$_{K802G}$	19	19	19	20	13	12
	6	mutant GFLV-F13	10	10	0	10	10	0
	7	wildtype GFLV-GHu 1E$_{K802G}$	15	15	15	15	15	15
	8	wildtype GFLV-F13	16	15	15	8	7	7
	9	mutant GFLV-GHu 1E$_{K802G}$	10	10	10	8	7	0
	10	mutant GFLV-F13	10	10	10	0	0	0
	11	wildtype GFLV-GHu 1E$_{K802G}$	15	15	15	12	11	11
	12	wildtype GFLV-F13	15	15	15	8	8	8
	13[a]	healthy	20	20	30	20	0	0
2	1	wildtype GFLV-F13	7	7	7	7	5	5
	2	mutant GFLV-F13 1E$_{G802K}$	12	12	11	5	6	1
	3	wildtype GFLV-GHu	10	2	0	5	5	2
	4	mutant GFLV-GHu 1E$_{K802G}$	5	5	1	7	5	0
	5	wildtype GFLV-F13	10	7	7	9	8	8
	6	mutant GFLV-F13 1E$_{G802K}$	11	11	11	6	6	7
	7	wildtype GFLV-GHu	10	7	7	5	4	5
	8	mutant GFLV-GHu 1E$_{K802G}$	7	6	7	7	7	8
	9	wildtype GFLV-F13	6	5	1	6	5	7
	10	mutant GFLV-F13 1EG802K	5	5	3	7	7	7
	11	wildtype GHu	7	7	7	3	2	0
	12	mutant GFLV-GHu 1E$_{K802G}$	5	5	12	6	5	6
	13	wildtype GFLV-F13	7	8	9	11	10	10
	14	mutant GFLV-F13 1E$_{G802K}$	12	11	11	7	7	7
	15	wildtype GFLV-GHu	8	8	8	5	5	6
	16	mutant GFLV-GHu 1E$_{K802G}$	10	10	10	6	5	5
	17	wildtype GFLV-GHu	9	5	5	7	7	6
	18	mutant GFLV-GHu 1E$_{K802G}$	15	15	15	12	12	12
	19	wildtype GFLV-GHu	16	16	15	2	5	0
	20	mutant GFLV-GHu 1E$_{K802G}$	5	5	5	5	5	2
	21	healthy	10	10	10	10	10	10
	22	healthy	10	10	10	10	10	10
	23	healthy	5	5	4	10	10	10
	24	healthy	10	10	10	10	10	10

[a]Total soil from individual bins was utilized for nematode elutriation.

TABLE 7-S5. Quantitative metadata of images of *Nicotiana benthamiana* root systems at the completion of continuous transmission assays of grapevine fanleaf virus by *Xiphinema index*. Images were standardized using a metric ruler to obtain pixel density and resolution for use in downstream root system architecture analysis.

Replicate	Basin	Picture name	Mean pixels per 10 cm	Mean pixels per inch (dpi)
1	1	Bin1_all.1 copy	68.81	174.77
1	1	Bin1_all.2 copy	72.15	183.26
1	1	Bin1_all.3 copy	70.64	179.42
1	1	Bin1_all.4 copy	73.60	186.94
1	2	Bin2_all.1 copy	63.82	162.11
1	2	Bin2_all.2 copy	63.22	160.57
1	2	Bin2_all.3 copy	65.41	166.14
1	3	Bin3_1_4.1 copy	63.50	161.29
1	3	Bin3_1_4.2 copy	71.50	181.61
1	3.5	Bin3_5_8.1 copy	67.50	171.46
1	3.5	Bin3_5_8.2 copy	71.37	181.28
1	4	Bin4_all.1 copy	63.70	161.80
1	4	Bin4_all.2 copy	61.70	156.73
1	4	Bin4_all.3 copy	65.70	166.88
1	5	Bin5_all.1 copy	63.80	162.06
1	5	Bin5_all.2 copy	65.24	165.71
1	5	Bin5_all.3 copy	66.52	168.95
1	6	Bin6_all.1 copy	63.78	162.01
1	6	Bin6_all.2-copy	66.75	169.54
1	6	Bin6_all.3 copy	65.41	166.13
1	6	Bin6_all.4 copy	64.73	164.42
1	7	Bin7_all.1 copy	61.82	157.02
1	7	Bin7_all.2 copy	61.82	157.02
1	7	Bin7_all.3 copy	61.82	157.02
1	8	Bin8_all.1 copy	62.47	158.67
1	8	Bin8_all.2 copy	61.74	156.81
1	8	Bin8_all.3 copy	60.21	152.94
1	9	Bin9_all.1 copy	50.71	128.79
1	9	Bin9_all.2 copy	50.40	128.02
1	9	Bin9_all.3 copy	63.38	160.97
1	9.5	Bin9_3and4.1 copy	63.70	161.80
1	10	Bin10_1to8.1 copy	52.70	133.87
1	10	Bin10_1to8.2 copy	53.05	134.73
1	10	Bin10_1to8.3 copy	52.70	133.87
1	10	Bin10_inoculated.1	55.40	140.72
1	11	Bin11_all.1 copy	57.10	145.04
1	11	Bin11_all.2 copy	57.10	145.04
1	11/12	Bin11&12_center.1	61.39	155.94
1	11/12	Bin11_12_center.2-	61.39	155.94
1	12	Bin12_1to8.1-	60.19	152.87
1	12	Bin12_1to8.2-	60.04	152.50
2	1	bin1_2	64.5	163.7
2	1	bin1_4	66.1	167.8

TABLE 7-S5. (continued)

Replicate	Basin	Picture name	Mean pixels per 10 cm	Mean pixels per inch (dpi)
2	2	bin2_1	58.3	148.0
2	2	bin2_3	64.3	163.4
2	3	bin3_1	67.3	171.0
2	3	bin3_3	64.7	164.3
2	4	bin4_2	61.1	155.1
2	4	bin4_3	66.1	168.0
2	5	bin5_2	67.2	170.7
2	5	bin5_3	66.7	169.3
2	6	bin6_2	58.8	149.4
2	6	bin6_3	58.8	149.4
2	7	bin7_1	68.2	173.2
2	7	bin7_3	67.2	170.7
2	8	bin8_2	64.8	164.6
2	8	bin8_3	64.6	164.1
2	9	bin9_2	60.8	154.4
2	9	bin9_4	62.6	159.0
2	10	bin10_1	66.0	167.6
2	10	bin10_2	71.2	180.8
2	11	bin11_1	66.0	167.6
2	11	bin11_2	65.6	166.6
2	12	bin12_1	65.4	166.1
2	12	bin12_3	66.2	168.1
2	13	bin13_1	62.8	159.5
2	13	bin13_2	62.2	158.0
2	14	bin14_1	65.6	166.6
2	14	bin14_4	65.6	166.6
2	15	bin15_1	69.2	175.8
2	15	bin15_3	64.6	164.1
2	16	bin16_1	61.2	155.4
2	16	bin16_2	64.4	163.6
2	17	bin17_1	66.6	169.2
2	17	bin17_2	64.6	164.1
2	18	bin18_1	63.0	160.0
2	18	bin18_2	64.0	162.6
2	19	bin19_1	66.4	168.7
2	19	bin19_2	65.0	165.1
2	20	bin20_1	65.1	165.4
2	20	bin20_2	66.5	168.8
2	21/22	bin21_22_2	63.5	161.2
2	21/22	bin21_22_1	64.8	164.6
2	23/24	bin23_24_2	63.2	160.5
2	23 & 24	bin24_24_1	65.4	166.1

TABLE 7-S6. Root system architecture traits of *Nicotiana benthamiana* at the termination of two independent, continuous transmission assays.

This table is provided online at the following link:

https://zenodo.org/records/15077180

FIGURE 7-S1. The isolation of *Xiphinema index* was performed using a standard nematode isolation methodology in a ten-step process. (A) Plants were gently excised from soil samples and placed into small beakers of water to release any active nematodes in the immediate surroundings, then **(B)** the beaker and surrounding soil were subject to 2.00 mm and 1.00 mm sieves to remove large soil debris. **(C)** The soil-water suspension was reduced by filtering with 80 µm sieves to be used in the elutriation apparatus. **(D)** The set-up of the elutriation funnel requires the hose to be inserted at the bottom of the funnel, **(E)** water turned on **(F)** to fill the first chamber. **(G)** At this point the water pressure is adjusted to a gentle, solid stream and a rubber stopper is used to start filling the second chamber. Immediately the soil sample was added to the top of the funnel and **(H)** water was allowed to fill nearly to the top. **(I)** The water was turned off and the stopper was immediately removed to collect the nematode suspension into a clean bucket. **(J)** The collected bucket was reduced in volume using two sieves of sizes 250 µm, and 80 µm. **(K)** The nematodes on the two smallest sieves were collected into a beaker.

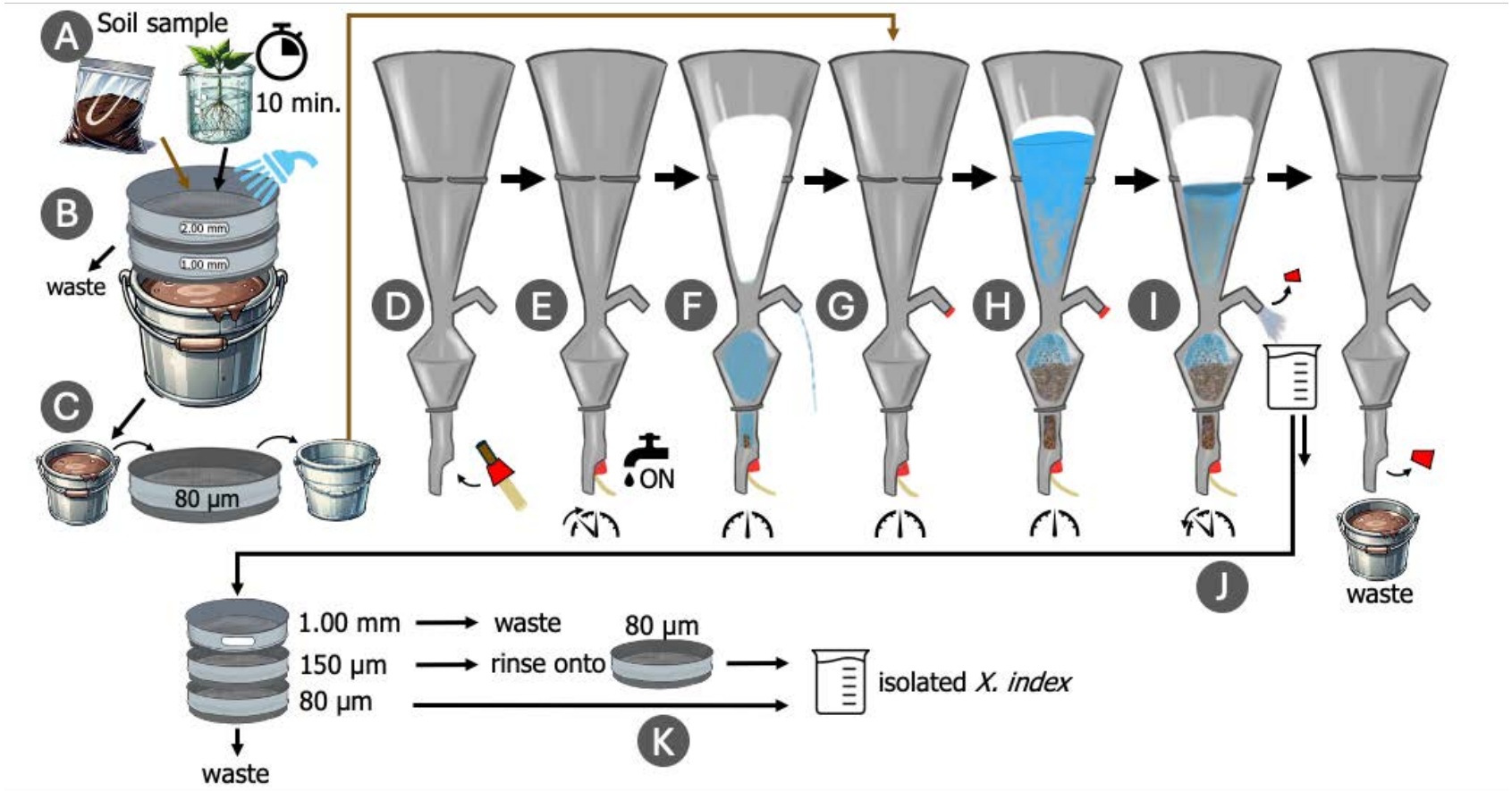
A
Soil sample
10 min.
B
2.00 mm
1.00 mm
waste
C
80 µm
D
E
ON
F
G
H
I
J
waste
1.00 mm
waste
150 µm
rinse onto
80 µm
80 µm
isolated X. index
K
waste

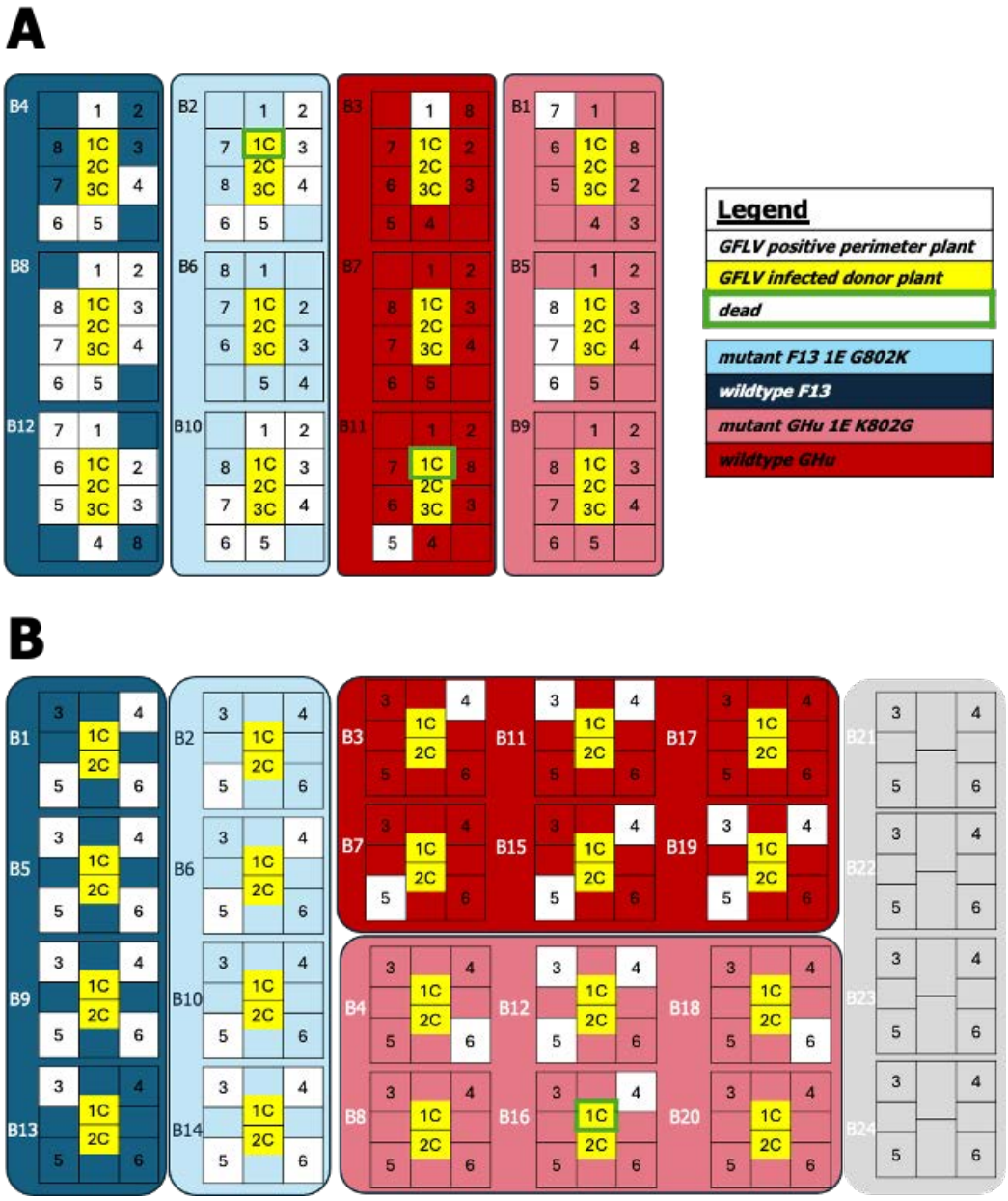

FIGURE 7-S2. Spatial distribution of continuous transmission assays for each GFLV treatment. Grapevine fanleaf virus (GFLV)-infected donor *Nicotiana benthamiana* plants are highlighted in yellow at the center of each bin replicate while recipient *N. benthamiana* plants testing positive for GFLV by RT-PCR at the end of the experiment are indicated in white. Plants with a number but no white background did not test positive, and spaces with no number did not have a plant at this position. **(A)** The first continuous assay consisted of a 3x4 grid with three central donor plants, while **(B)** the second assay adopted a smaller bin size with a 2x3 grid and two central donor plants. Viral treatment is indicated by color, and numbers outside each grid represent bin numbers.

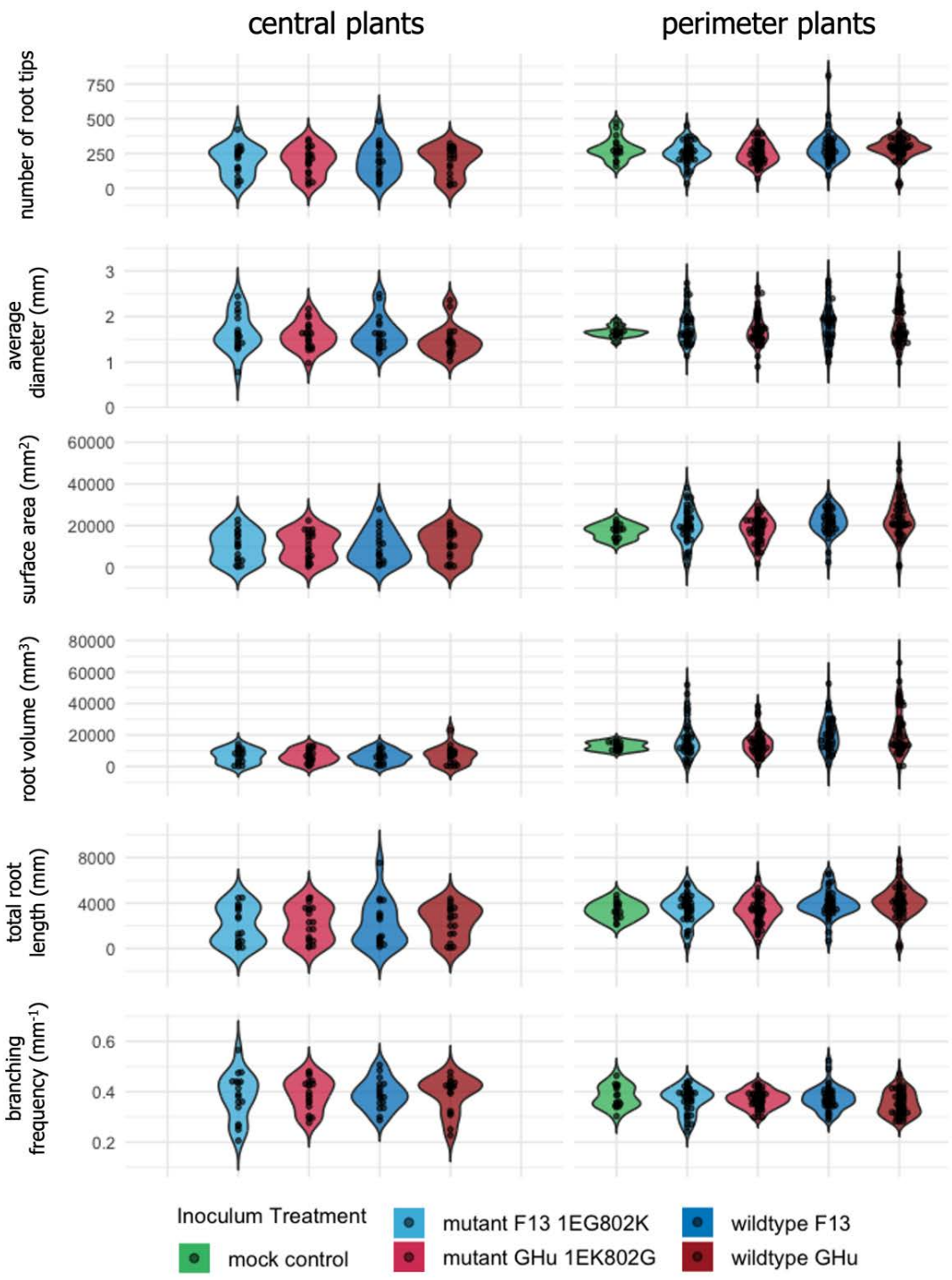

FIGURE 7-S3. Root system architecture traits of donor and recipient *Nicotiana benthamiana* plants used in continuous transmission assays of wildtype (F13 and GHu) and mutant (GFLV-GHu $1E_{K802G}$ and mutant GFLV-F13 $1E_{G802}$) grapevine fanleaf virus strains with *Xiphinema index* and at 55-65 days post-inoculation.

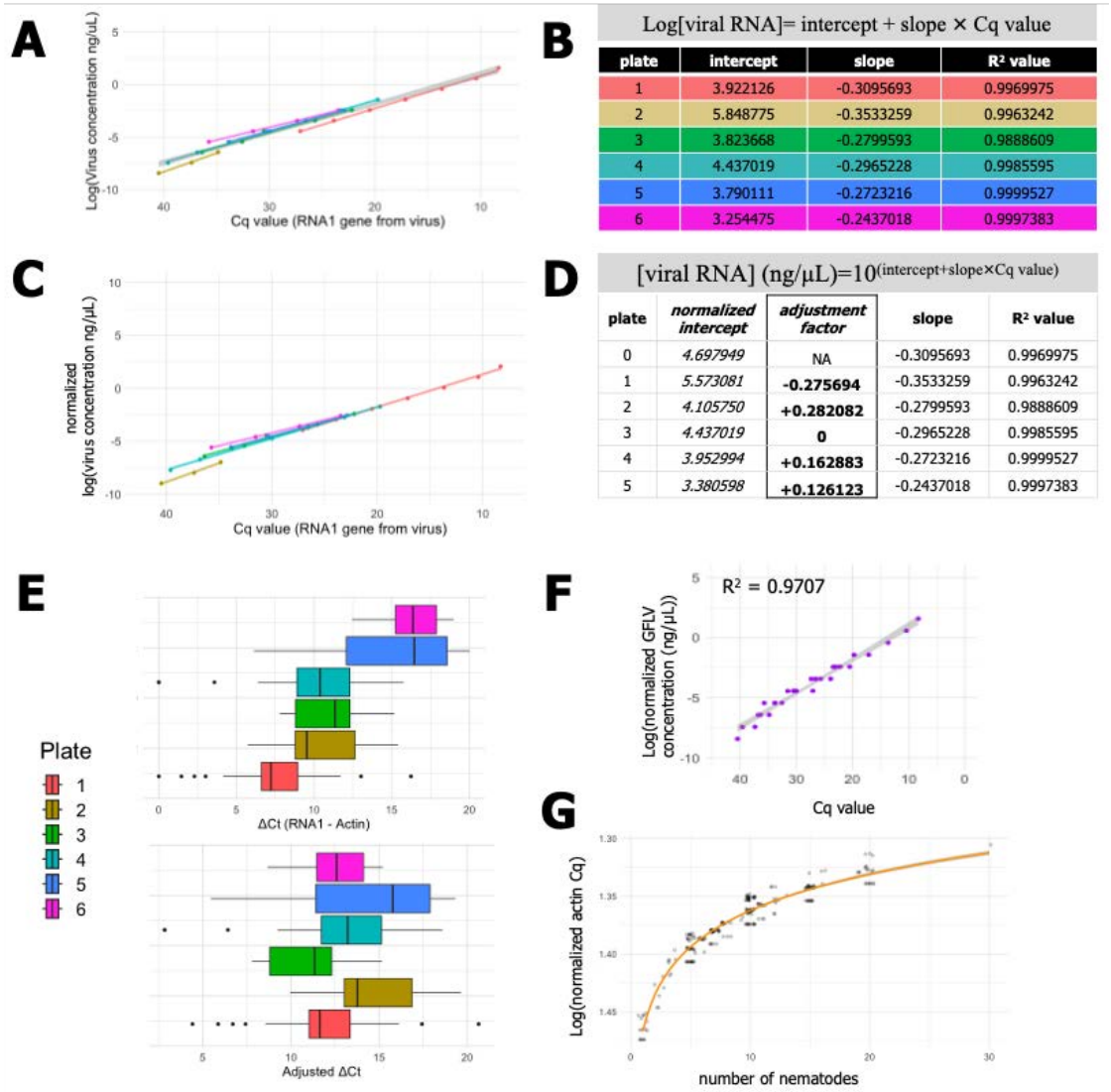

plate	intercept	slope	R² value
1	3.922126	-0.3095693	0.9969975
2	5.848775	-0.3533259	0.9963242
3	3.823668	-0.2799593	0.9888609
4	4.437019	-0.2965228	0.9985595
5	3.790111	-0.2723216	0.9999527
6	3.254475	-0.2437018	0.9997383

plate	*normalized intercept*	*adjustment factor*	slope	R² value
0	*4.697949*	NA	-0.3095693	0.9969975
1	*5.573081*	**-0.275694**	-0.3533259	0.9963242
2	*4.105750*	**+0.282082**	-0.2799593	0.9888609
3	*4.437019*	**0**	-0.2965228	0.9985595
4	*3.952994*	**+0.162883**	-0.2723216	0.9999527
5	*3.380598*	**+0.126123**	-0.2437018	0.9997383

FIGURE 7-S4. Inter-plate normalization of RT-qPCR for comparative analysis of relative abundance of grapevine fanleaf virus (GFLV) in *Xiphinema index* samples. **(A-B)** Serial dilution of purified GFLV displayed a strong correlation of Cq values, allowing for inter-plate adjustment factors to be calculated **(C-D). (E)** The distribution of Cq values across plates indicates that the adjustment factors indeed corrected and centralized the data. **(F)** The log regression of viral standard curves after normalization returned a strong R^2 value of 0.9707. **(G)** The normalized data were used to assess the log expression against nematode count per sample.

CHAPTER 8

CONCLUSIONS, PROSPECTIVES, AND FUTURE DIRECTIONS FOR GRAPEVINE FANLEAF VIRUS-HOST-VECTOR INTERACTIONS

Grapevine fanleaf virus (GFLV, species *Nepovirus foliumflabelli*, genus *Nepovirus*, family *Secoviridae*) is known as a devastating pathogen of grapevine with limited methods to subdue symptoms of infection. This dissertation aimed to track host components involved in symptom elicitation upon GFLV infection and provide new information regarding the host response to multiple viral strains. By conducting experiments across host, virus, and vector, I uncovered host immune pathways that result in the phenotypic manifestation of symptoms upon infection with GFLV, which then was linked to differential transmission rates of several GFLV strains. Although this work shed light on multiple layers of virus-host interactions for GFLV protein $1E^{Pol*/Sd}$, there is much more to learn about the interplay of virus and host proteins during symptom elicitation. Here I suggest possible routes to learn more about GFLV induced symptomology, with a particular focus on the symptom inducing C-terminal region of protein $1E^{Pol*/Sd}$.

GRAPEVINE FANLEAF VIRUS PROTEIN $1E^{POL*/SD}$ HAS MULTIPLE PREDICTED PRO-VIRAL FUNCTIONS

As a result of the previous chapters, there was a substantial amount of data surmounted for work on GFLV in *N. benthamiana* in addition to substantial root

phenotyping that covered select mutants from Osterbaan *et al.* (2019). By integrating 'omics' datasets (Osterbaan et al. 2019, Roy et al. 2023, Roy and Fuchs 2024), I identified common dysregulated pathways across host profiling techniques, viral protein structure predictions, and posed new hypotheses relating to a phosphatase function in the center of protein $1E^{Pol*/Sd}$. While one function has been understood from sequence similarity (the putative RNA-dependent RNA polymerase), the C-terminal ~350 amino acids have not been described with any predicted function. The result of this work proposed to assign a predicted phosphatase domain to the $1E^{Pol*/Sd}$ protein, which was further hypothesized in dampening the plant immune response in varying capacities to elicit differing symptomatic or asymptomatic infections. This predicted structural homology is supportive to rename protein $1E^{Pol*/Sd}$ to $1E^{Pol*/PTP*/Sd}$, to indicate the new putative phosphatase activity. In the following sections, I briefly describe future plausible experiments to test and validate these hypothesized functions.

FUTURE WORK

Despite the work conducted so far, many questions remain in the GFLV pathosystem. In the broadest scope, variables impacting the successful transmission based on the plant host, virus strain, nematode population, and environment can be considered in a web of influences (Figure 8-1). Volatile organic compounds (VOCs) of plant host roots have not been evaluated for GFLV-infected root tissue. The volatile expression profile of GFLV-infected roots could be associated with nematode behaviors such as dispersal and feeding, which would facilitate or hinder transmission. I conducted preliminary work to analyze the root system architecture (RSA) of *N. benthamiana* in a hydroponic growth system, which could be adapted to an aeroponic growth system that

any residual liquid could be collected and analyzed through liquid chromatography tandem mass spectrometry. Alternatively, the protocol described by van Griethuysen et al. (2024) would be appropriate, particularly for the use of *N. benthamiana* and adaptation of a sealed chamber to capture VOCs of plant roots during infection. Multiple time point samplings and using both viral and mock inoculated controls would be necessary to delineate VOCs specific to symptomatic GFLV infection. It will be important to understand any differences in VOC profiles exist that could impact nematode mediated transmission of GFLV, which could shift the current focus for reducing viral spread. To test this, simple choice assays with *X. index* should be conducted with live plants or with purified extracts of infected plant roots in sandy loess soil to allow for nematode movement. Attention is needed to dissect host-vector interactions for what factors contribute to *X. index* feeding behaviors.

It will be important to delineate physical and biochemical (metabolic) processes that contribute to GFLV transmission. Soil-borne plant viruses contain additional barriers to understand the vector, virus, and host which may explain the large gaps of understanding in this discipline. While not technically challenging to complete, evaluation of plant RSA requires methodical and time-consuming analyses that disrupt, if not destroy, the plant upon measurement. Sacrificing plants required increasing experiment size, but was still the most appropriate method to analyze differences in RSA upon GFLV infection. While imaging root systems could be accomplished slightly later than the discovery of GFLV, throughput phenotyping platforms for complex traits are only just beginning to be implemented. Several programs have been shown to be acceptable against manual trait measurements, and Rhizovision proved to be the most

accurate across these platforms (Sabety et al. 2024). Despite initial barriers, root phenotyping has opened new doors for investigating the transmission of GFLV and should be considered for virus-host-vector interactions in other soil-borne systems.

It has also remained quite challenging to document transient symptomatology induced by GFLV. The vein-clearing leaf phenotype and perturbations in root morphology suggest a cell type specific interaction between GFLV and host components. It would be beneficial to distinguish cell specific events that are less pronounced in bulk tissue sequencing technologies. The studies I performed are unable to differentiate mRNA or proteins produced in different cells, where other cell types could be considered as 'noise' in these data. As technologies advance and sequencing costs come down, a finer resolution on time, and cell type would resolve further understandings into plant-virus interactions. The implementation of single-cell sequencing technologies into plant virology research would undoubtedly provide targeted insights for GFLV-host interactions with respect to tissue specific symptomatology. It is continuously hypothesized that the protein-protein interactions of GFLV and its plant host facilitate the elicitation of symptoms in *N. benthamiana* and other plant hosts. Hereafter I propose several immediate ways with established tools to reveal biological characteristics of GFLV protein $1E^{Pol*/Sd}$ and its impact on plant hosts.

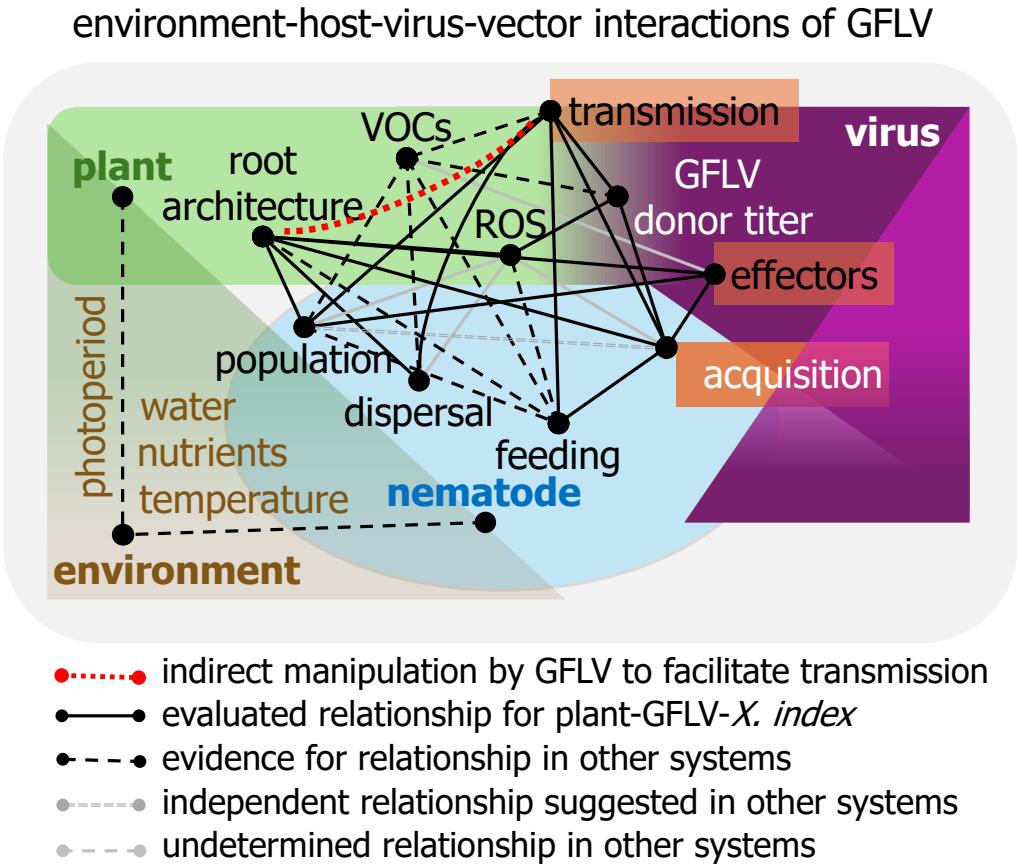

FIGURE 8-1. The cumulative understandings of grapevine fanleaf virus (GFLV) interactions with plant host and its vector *Xiphinema index*, and the unexplored capacities of environmental factors that facilitate viral replication and spread. The contribution of each respective component results in dynamic disease spread and should continue to be evaluated for novel intervention strategies.

PROTEIN PURIFICATION, BIOLOGICAL ASSAYS, AND EFFORTS FOR CRYSTALLIZATION OF PROTEIN 1E$^{POL*/SD}$

Appendix 2 describes efforts at the purification of grapevine fanleaf virus (GFLV) protein 1E$^{Pol*/Sd}$. Two vectors were successfully created for the expression and subsequent purification of protein 1E$^{Pol*/Sd}$, one of wildtype GFLV strain F13 and the other of wildtype GFLV strain GHu. The constructs contain both NusA and histidine tags for protein stabilization and affinity tag purification, respectively. Initial considerations in the purification process are also detailed in Appendix 2.

After obtaining purified GFLV protein 1E$^{Pol*/Sd}$, several assays should be employed to explore the enzymatic properties of this multifunctional protein. If protein 1E$^{Pol*/Sd}$ of multiple strains of GFLV is successfully cloned and purified, comparative assays could be explored. First, an RNA polymerase assay should be conducted to examine transcriptional efficiency. Existing methods provide a platform to conduct *in vitro* viral polymerase assays to assess incorporation of nucleotides through autoradiography (Filomatori et al. 2011), however a fluorescence-based method would be more suitable given its safer implementation and reproducibility across several viral polymerases (Sáez-Álvarez et al. 2019). Demonstrating the polymerase activity alone will be sufficient to graduate 1E$^{Pol*/Sd}$ from putative to confirmed RNA-dependent RNA polymerase (and become 1E$^{Pol/Sd}$). Viral replication is considered equivalent according to viral titer data (Osterbaan et al. 2019; Chapter 4), however a side-by-side *in vitro* comparison could be considered as another measure of fitness between the viral polymerases of different strains.

Secondly, the putative phosphatase function discussed in Chapter 5 should be investigated further. A screening panel of several phosphorylation types, molecules, and co-factors should be explored for this predicted function. Typical assays employ phosphorylated peptide substrates and evaluate the released phosphate groups, like that seen in the validation of chicken anemia virus (species *Gyrovirus chickenanemia,* genus *Gyrovirus*, family *Anelloviridae*) protein VP2 (Peters et al. 2002). This could be further investigated through site-directed mutagenesis of predicted critical amino acids in the P-loop, Q-loop, and C-terminus to deduce functional components of the protein. Deletion mutants proposed in Appendix 2 isolate individual domains of protein $1E^{Pol*/Sd}$, where the activity could be further explored for the RdRP and phosphatase domains. Given the aligned protein matches of the three-dimensional protein structure and the confidence metrics provided by DeepFRI (Chapter 5), I hypothesize that the phosphatase domain functions via the P-loop (residues: 297, 599, 603), Q-loop (residues: 636, 639, 640), and additional residues in the C-terminal globular domain.

The phosphatase and symptom determinant region approximately cover the C-terminal half of GFLV protein $1E^{Pol*/Sd}$. With this, it would be highly informative to obtain crystal protein structures of the N-terminal and C-terminal halves to understand the actual configuration of the protein's globular domains, oligomerization, and if these properties impact enzymatic efficiency. Based on other viral systems, dimerization is a key tactic employed for dephosphorylation of immune receptors (Koksal and Cingolani 2011).

Based on protein prediction analysis and alignment of $1E^{Pol*/Sd}$, I hypothesize homologous tertiary protein structures present in viruses, plants, and/or unicellular

organisms have divergent sequence identity but conserved structure. The protein repertoire of a virus is limited in size and provides an evolutionary bottleneck to maintain essential and important proteins. This selective pressure is dictated by the combinatorial effects of plant host, environment, and transmission. I anticipate that this protein interacts with components of the plant immune system, possible explaining why symptoms are produced by some GFLV strains and not others.

Structures of protein $1E^{Pol*Sd}$ will be informative to the protein-protein interactions that occur *in planta* and will provide context to the functional/non-functional aspects of this protein during infection. One preliminary way to dissect differences in sequence and functional evolution of GFLV protein $1E^{Pol*/Sd}$ is to perform multiple sequence alignment of protein sequences across related viruses. For this, I performed a preliminary analysis of RdRP proteins across nepoviruses with complete coding sequences of either RNA1 or the RdRP coding region (Figure 8-2).

This analysis showed the distribution of several domains including the catalytic core and polymerase motifs associated with viral RdRP proteins. Of note, many of the viral sequences encompass a size range from 690 amino acids for grapevine Bulgarian latent virus to 1370 amino acids for cassava torrado-like virus. The catalytic core in red across domain predictions was centrally aligned and with N- and C-terminal domains identified across the nepoviruses (Figure 8-2). It would be interesting to conduct a more systematic analysis of the three domains and correlate these to host range, similar to that conducted for ArMV and GFLV, differentiating host range on grapevine only or to herbaceous hosts (Hily et al. 2021). For GFLV, some mutations in the C-terminus of protein $1E^{Pol*/Sd}$ perturb the ability to replicate and sustain infection (Osterbaan et al.

2019). There is a need to understand the functional capacities of the C-terminal domain in respect to viral replication, antagonization of anti-viral host defenses, and pathogenicity. Given the tools and advances seen in GFLV, the application of this knowledge could then be applied to other viruses within and beyond nepoviruses.

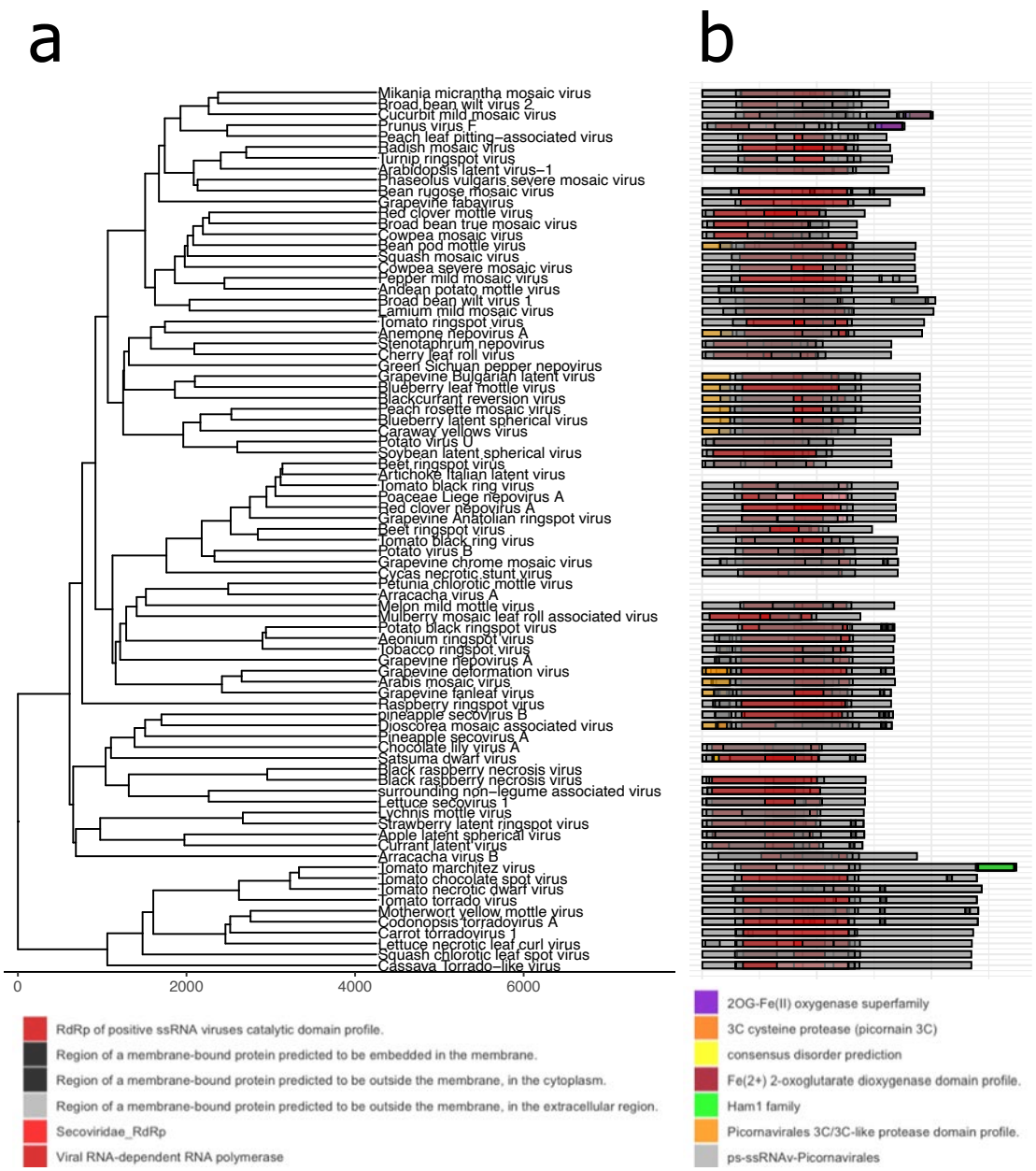

FIGURE 8-2. Phylogenetic relationship of viral RNA-dependent RNA polymerase (RdRP) protein sequences in viruses of the genus *Nepovirus*. Sequences for RNA1 within the NCBI Virus Database were extracted in December 2024. A preliminary manual alignment by the GDD and (S/T)GXXXTXXXN(S/T) sequences was conducted to trim the sequences of the RdRP to the appropriate length. 98 representative sequences that were curated were submitted to InterProScan for domain identification and protein motif analysis. The resulting files were used to curate a phylogenetic tree (Average distance BLOSUM62) and corresponding domain plot that were constructed in R using the packages ape (v5.8), ggtree (v3.12.0), stringr (v1.5.1), patchwork (v1.2.0), and ggplot2 (v3.5.1).

IN PLANTA *ANALYSIS OF PREDICTED ACTIVE RESIDUES IN GFLV 1E$^{POL*/SD}$ THROUGH SITE-DIRECTED MUTAGENESIS*

Infectious clones of GFLV are available and have been optimized for infection in *Nicotiana benthamiana* (Osterbaan et al. 2018; 2019). To explore the importance of predicted catalytic residues for GFLV avoidance of host defenses, these residues should be first targeted for single amino acid swaps (Gly or Ala). These methods have been thoroughly detailed to perform Q5 mutagenesis on the infectious clones of GFLV and then infiltrate *N. benthamiana* with *Agrobacterium tumefaciens* harboring the new RNA1 derived construct and strain GHu RNA2 for ideal infection rates (Osterbaan et al. 2018; 2019).

Like *in vitro* enzymatic assays proposed in the last section, the activity of the predicted phosphatase domain is particularly interesting with regards to a possible association with a symptom determinant on protein 1E$^{Pol*/Sd}$. After mutating residues of the phosphatase domain in wildtype GFLV-F13 and wildtype GFLV-GHu backgrounds, it would be informative to observe the infectivity at local and systemic levels, and symptomology in *N. benthamiana*. I hypothesize the involvement of protein 1E$^{Pol*/Sd}$ with dephosphorylating host enzymes that are implicated in pattern triggered immunity. I further hypothesize the abolishment of this activity will either (1) render the virus non-infectious, resulting in no infections, or (2) elicit symptoms in typically asymptomatic GFLV strains and/or extend the symptom duration for already symptomatic GFLV strains. Alternatively, mutations to these residues could display a non-functional, redundant, or obsolete function, where neither infectivity nor symptomology is impacted. This is hypothesized by analogy with other dual specificity phosphatases

encoded in other viral systems like vaccina virus protein VH1, where mutation to the catalytic Cys residue abolished Ser/Tyr phosphatase activity (Guan et al. 1991). Further, disruption of this function significantly compromised viral replication ability, rendering most vaccina virus particles non-infectious (Liu et al. 1995). If the C-terminus of GFLV protein $1E^{Pol*/Sd}$ is implicated in the enzymatic activity of the putative phosphatase, this could explain the many non-infectious GFLV mutants previously generated (Vigne et al. 2013, Osterbaan et al. 2019).

ISOLATION OF GFLV THROUGH AFFINITY PURIFICATION COUPLED WITH ULTRACENTRIFUGATION TECHNIQUES

The distribution of GFLV protein $1E^{Pol*/Sd}$ in distinct cell types and subcellular localization(s) is still unknown. I hypothesize that the localization and/or lack of localization to cell types and/or subcellular compartments of $1E^{Pol*/Sd}$ is involved with transient symptoms observed in *Nicotiana. benthamiana*. Several other GFLV proteins and protein complexes have been documented for their subcellular localization and structure to include assembled virions (Belval et al. 2016), coat protein subunits (Shellenberger et al. 2011), viral silencing suppressors with dynamic movement (Choi et al. 2024), the movement protein (Amari et al. 2010), and replication complexes (Ritzenthaler et al. 2002). The observed subcellular localizations of these GFLV proteins overlapped with current protein prediction tool analyses (Chapter 3).

From predictive analysis, it is hypothesized that GFLV protein $1E^{Pol*/Sd}$ has a nucleocytoplasmic distribution with an additional anchor to viral replication complex membranes derived from the endoplasmic reticulum (Roy et al. 2024). Interestingly, transmembrane domains were not predicted for both F13 and GHu strains of GFLV but

will be necessary to document for ruling out these differences and their association with symptom development *in planta*.

Infectious GFLV clones have been engineered to encode a V5 epitope tag at the C-terminus of protein $1E^{Pol*/Sd}$ (Osterbaan et al. 2021). Clones for transient expression of GFLV protein $1E^{Pol*/Sd}$ with an eGFP tag have also been developed (Berthold 2015). From these previously engineered tools, it would be interesting to perform temporal apical and local analysis of GFLV protein $1E^{Pol*/Sd}$ subcellular localization. Using the wildtype GFLV-F13 and -GHu with a 1E:V5 epitope tag, a temporal subcellular localization experiment could be performed to understand the presence of $1E^{Pol*/Sd}$ in various subcellular niches during the onset of symptoms. The time course should target apical leaves from two days post-inoculation (dpi) to 10 dpi, at a minimum once daily tissue sample collection. Then, protein extractions utilizing established methods for *N. benthamiana* can be followed on mirrored samples for plant subcellular differential centrifugation techniques. Total protein extracts could then be compared to the abundance of V5-tagged protein $1E^{Pol*/Sd}$ in subcellular fractions to determine the relative abundance and localization of protein $1E^{Pol*/Sd}$. This technique has been employed for cherry leaf roll virus (species *Nepovirus avii*, genus *Nepovirus*, family *Secoviridae*), where antibodies against the coat protein were used to detect viral presence in multiple subcellular locations (Más et al. 2000). A similar approach could be accomplished using V5 epitope specific antibodies that have been optimized for detection in *N. benthamiana* leaf tissue (Osterbaan et al. 2021). Western blot analysis paired with subcellular fractionation of infected tissue would be anticipated to resolve subcellular localization of protein $1E^{Pol*/Sd}$. A successful instance of this technique was

employed for the subcellular localization of the NTB protein of tomato ringspot virus (species *Nepovirus lycopersici*, genus *Nepovirus*, family *Secoviridae*) (Han and Sanfaçon 2003; Zhang and Sanfaçon 2006).

In the instance that this approach is unsuccessful, immunohistochemical approaches can be used to target the localization and distribution of protein $1E^{Pol*/Sd}$ in inoculated leaves, apical leaves, and root tissue. This will rely on an equally methodical approach that will require more optimization than the previous methods described.

PROTEIN-PROTEIN INTERACTIONS IN ROOT TISSUE

Nepoviruses are soil-borne transmissible pathogens in the presence of their nematode vectors. I hypothesize the molecular mechanism of symptomology to be increasingly prevalent within the root tissue of plant hosts, and that protein interactants of importance related to systemic signaling are yet to be identified. To this end, I hypothesize that major silencing suppression and basal immune response networks to link symptomatology observations of above and below ground. With the already described tools, one direct method would be to conduct co-immunoprecipitation of the GFLV $1E^{Pol*/Sd}$ protein with V5 epitope tags in root tissue. It is currently unknown if GFLV protein $1E^{Pol*/Sd}$ interacts with similar or different components in different tissue types. Considering the transmission mode of GFLV, I would expect that viral replication and evasion of host defense would be most evolved in root tissue. Examining host interactants of GFLV protein $1E^{Pol*/Sd}$ would involve a level of optimization for isolation of proteins in root tissue, which could be impacted by soil type and smaller particles interfering with extraction buffers and downstream LC-MS/MS applications. Careful preparation and consideration to these factors should provide an improved

understanding of the symptom determinant protein and host interactors that are involved in symptomology *in planta*. It is imperative to determine the host factors that interact with GFLV protein $1E^{Pol*/Sd}$ in root tissue to better understand how symptoms are transiently elicited and imagine new molecular pathways that can be manipulated to stop or slow the spread of GFLV.

REFERENCES

Amari, K., Boutant, E., Hofmann, C., Schmitt-Keichinger, C., Fernandez-Calvino, L., Didier, P., Lerich, A., Mutterer, J., Thomas, C. L., Heinlein, M., Mély, Y., Maule, A. J., and Ritzenthaler, C. 2010. A Family of Plasmodesmal Proteins with Receptor-Like Properties for Plant Viral Movement Proteins. PLOS Pathogens 6:e1001119. https://doi.org/10.1371/journal.ppat.1001119.

Belval, L., Marmonier, A., Schmitt-Keichinger, C., Gersch, S., Andret-Link, P., Komar, V., Vigne, E., Lemaire, O., Ritzenthaler, C., and Demangeat, G. 2019. From a Movement-Deficient Grapevine Fanleaf Virus to the Identification of a New Viral Determinant of Nematode Transmission. Viruses 11:E1146. https://doi.org/10.3390/v11121146.

Choi, J., Browning, S., Schmitt-Keichinger, C., and Fuchs, M. 2024. Mutations in the WG and GW motifs of the three RNA silencing suppressors of grapevine fanleaf virus alter their systemic suppression ability and affect virus infectivity. Front. Microbiol. 15. https://doi.org/10.3389/fmicb.2024.1451285.

Filomatori, C. V., Iglesias, N. G., Villordo, S. M., Alvarez, D. E., and Gamarnik, A. V. 2011. RNA Sequences and Structures Required for the Recruitment and Activity of the Dengue Virus Polymerase. Journal of Biological Chemistry 286:6929–6939. https://doi.org/10.1074/jbc.M110.162289.

Guan, K., Broyles, S. S., and Dixon, J. E. 1991. A Tyr/Ser protein phosphatase encoded by vaccinia virus. Nature 350:359–362. https://doi.org/10.1038/350359a0.

Han, S., and Sanfaçon, H. 2003. *Tomato Ringspot Virus* Proteins Containing the Nucleoside Triphosphate Binding Domain Are Transmembrane Proteins That

Associate with the Endoplasmic Reticulum and Cofractionate with Replication Complexes. J Virol 77:523–534. https://doi.org/10.1128/JVI.77.1.523-534.2003.

Hily, J. M., Poulicard, N., Kubina, J., Reynard, J. S., Spilmont, A. S., Fuchs, M., Lemaire, O., and Vigne, E. 2021. Metagenomic analysis of nepoviruses: diversity, evolution and identification of a genome region in members of subgroup A that appears to be important for host range. Arch Virol 166:2789–2801. https://doi.org/10.1007/s00705-021-05111-0.

Más, P., Sánchez-Pina, M. A., Balsalobre, J. M., and Pallás, V. 2000. Subcellular localisation of cherry leaf roll virus coat protein and genomic RNAs in tobacco leaves. Plant Science 153:113–124. https://doi.org/10.1016/S0168-9452(99)00253-8.

Orlov, I., Hemmer, C., Ackerer, L., Lorber, B., Ghannam, A., Poignavent, V., Hleibieh, K., Sauter, C., Schmitt-Keichinger, C., Belval, L., Hily, J.-M., Marmonier, A., Komar, V., Gersch, S., Schellenberger, P., Bron, P., Vigne, E., Muyldermans, S., Lemaire, O., Demangeat, G., Ritzenthaler, C., and Klaholz, B. P. 2020. Structural basis of nanobody recognition of grapevine fanleaf virus and of virus resistance loss. PNAS 117:10848–10855. https://doi.org/10.1073/pnas.1913681117.

Osterbaan, L. J., Choi, J., Kenney, J., Flasco, M., Vigne, E., Schmitt-Keichinger, C., Rebelo, A. R., Heck, M., and Fuchs, M. 2019. The identity of a single residue of the RNA-dependent RNA polymerase of grapevine fanleaf virus modulates

vein clearing in Nicotiana benthamiana. Molecular Plant-Microbe Interactions 32:790–801. https://doi.org/10.1094/MPMI-12-18-0337-R.

Osterbaan, L. J., Hoyle, V., Curtis, M., DeBlasio, S., Rivera, K. D., Heck, M., and Fuchs, M. 2021. Identification of protein interactions of grapevine fanleaf virus RNA-dependent RNA polymerase during infection of Nicotiana benthamiana by affinity purification and tandem mass spectrometry. Journal of General Virology 102. https://doi.org/10.1099/jgv.0.001607.

Osterbaan, L. J., Schmitt-Keichinger, C., Vigne, E., and Fuchs, M. 2018. Optimal systemic grapevine fanleaf virus infection in *Nicotiana benthamiana* following agroinoculation. Journal of Virological Methods 257:16–21. https://doi.org/10.1016/j.jviromet.2018.04.006.

Roy, B. G., Choi, J., and Fuchs, M. F. 2024. Predictive Modeling of Proteins Encoded by a Plant Virus Sheds a New Light on Their Structure and Inherent Multifunctionality. Biomolecules 14:62. https://doi.org/10.3390/biom14010062.

Roy, B. G., DeBlasio, S., Yang, Y., Thannhauser, T., Heck, M., and Fuchs, M. 2023. Profiling Plant Proteome and Transcriptome Changes during Grapevine Fanleaf Virus Infection. J. Proteome Res. 22:1997–2017. https://doi.org/10.1021/acs.jproteome.3c00069.

Roy, B. G., and Fuchs, M. 2024. A single viral amino acid shapes the root system architecture of a plant host upon virus infection. BMC Microbiol 24:267. https://doi.org/10.1186/s12866-024-03399-x.

Roy, B. G., and Fuchs, M. 2022. Herbaceous plant hosts as supermodels for grapevine viruses: a historical perspective. J Plant Pathol 1–30. https://doi.org/10.1007/s42161-022-01267-z.

Sabety, J., Serrano, A., and Khan, A. 2024. A root system architecture measurement pipeline for apple rootstocks. The Plant Phenome Journal 7:e70011. https://doi.org/10.1002/ppj2.70011.

Schellenberger, P., Andret-Link, P., Schmitt-Keichinger, C., Bergdoll, M., Marmonier, A., Vigne, E., Lemaire, O., Fuchs, M., Demangeat, G., and Ritzenthaler, C. 2010. A stretch of 11 amino acids in the βB- βC loop of the coat protein of *Grapevine fanleaf virus* is essential for transmission by the nematode *Xiphinema index*. Journal of Virology 84:7924–7933. https://doi.org/10.1128/JVI.00757-10.

Schellenberger, P., Sauter, C., Lorber, B., Bron, P., Trapani, S., Bergdoll, M., Marmonier, A., Schmitt-Keichinger, C., Lemaire, O., Demangeat, G., and Ritzenthaler, C. 2011. Structural insights into viral determinants of nematode mediated Grapevine fanleaf virus transmission. PLoS Pathogens 7:e1002034. https://doi.org/10.1371/journal.ppat.1002034.

Zhang, G., and Sanfaçon, H. 2006. Characterization of Membrane Association Domains within the *Tomato Ringspot Nepovirus* X2 Protein, an Endoplasmic Reticulum-Targeted Polytopic Membrane Protein. J Virol 80:10847–10857. https://doi.org/10.1128/JVI.00789-06.

APPENDIX I

PROCESSING AND MAINTENECE OF *NICOTIANA BENTHAMIANA* TISSUE FOR PHENOTYPIC, HISTOLOGICAL, AND RIBONUCELIC ACID ANALYSIS*

ABSTRACT

Nicotiana benthamiana is extensively used as a model herbaceous plant for virus-host interactions and systems biology research. Here we describe a methodology to phenotype the root system architecture of *N. benthamiana* plants following infection with grapevine fanleaf virus (GFLV). GFLV is an economically important soil-borne virus that is present in vineyards globally. Upon completion of this protocol, images of whole root crowns can be analyzed with root phenotyping software. Following image acquisition, root tissue can be directly processed for cross sectioning and/or ribonucleic acid extraction. Additional data (plant height, dry biomass, and leaf symptoms) were collected for correlation analysis. Documentation of root system architecture is an important first step to understand how a virus can manipulate its plant host below ground when most research is focusing on disease symptomology in leaves and fruits. This protocol allows for utilization of other viruses that infect *N. benthamiana* and adaptation to other plant hosts.

*This appendix has been submitted into a public repository as: Brandon G Roy, Marc Fuchs 2023. Processing and maintenance of *Nicotiana benthamiana* tissue for phenotypic, histological, and ribonucleic acid analysis. protocols.io https://dx.doi.org/10.17504/protocols.io.261gedpqwv47/v1

MATERIALS

Plant growth

- *Nicotiana benthamiana* seed
- Soil/plant growth medium
- Pots
- Potting stick labels
- Fertilizer (Scott's Miracle Grow)

Inoculation

- Inoculum source of grapevine fanleaf virus (GFLV) in either infected plant tissue (Roy et al. 2023) or infectious clones of GFLV RNA1 and RNA2 in *Agrobacterium tumefaciens* (Osterbaan et al. 2018; 2019)
- Mortar and pestle
- Potassium dihydrogen phosphate (KH_2PO_4)
- Disodium phosphate (Na_2HPO_4)
- Deionized water

Excavation of crown root systems

- Bucket(s)
- Water
- Scissors
- EPSON 12000XL Scanner
- Clear scanning trays (12" X 18", 30.48 cm X 45.72 cm)
- Solid color background (we utilized a black felt on cardboard, 14” X 20”, 35.56 cm X 50.8 cm)

Root phenotyping

- Windows computer for Rhizovision Software, all other software is cross-compatible, including;
    - EPSON Scanner 2 Software
    - R and RStudio
    - Microsoft Excel or Google Sheets

Tissue Collection

- 10% bleach
- 70% ethanol
- RNAse Away
- Sterilized steel BBs
- Razor blade
- Tweezers
- Nuclease-free or molecular grade water
- Nuclease-free 1.5 mL Eppendorf tubes
- Sterilized 2 mL Eppendorf tubes
- Pipettes (P10, P20, P200, P1000)
- Omega E.Z.N.A. Plant RNA Mini Kit (cat no. R6827)

METHODS

Plant production and growth

Seeds of *Nicotiana benthamiana* were sown in Cornell LM-2 soil, and seedlings were transplanted after ~14 days into individual pots. Throughout all growth stages, plants were maintained in controlled growth chamber conditions (16:8 light:dark photoperiod, 25 °C, 70% humidity). Plants were watered daily and provided Scotts Miracle-Gro® All Purpose Plant Food 24-8-16 once weekly. Experiments consisted typically of 100 plants.

Viral inoculation

Plants at the ~5 leaf stage were mechanically inoculated with GFLV using infected *N. benthamiana* leaf tissue as inoculum (Roy et al. 2023). Briefly, carborundum powder was dusted onto the leaves of each plant. The inoculum was prepared by macerating the infected leaf tissue with a mortar and pestle in a phosphate buffer (0.15 M KH2PO4, 0.35 M Na2HPO4, pH 7.0) and rub inoculated onto the two basal leaves. Water was generously applied to each plant using a spray bottle to eliminate the carborundum power and prevent additional abiotic stress. After the inoculation step, plants were monitored for phenotypical changes and tested for the presence of the virus in apical, uninoculated leaves. Mock inoculated plants, e.g., plants rubbed with phosphate buffer only, were used as controls.

Alternatively, *Agrobacterium tumefaciens*-mediated inoculation with infectious clones of grapevine fanleaf virus can be performed to infect *N. benthamiana* plants according to Osterbaan et al. (2018).

Testing viral infection status

Leaf and root tissue was used to test GFLV infection status by RT-PCR or RT-qPCR with specific primers beyond 4 days post-inoculation, and by DAS-ELISA with specific antibodies beyond 14 days post-inoculation, as previously reported (Osterbaan et al. 2018; 2019, Roy et al. 2023).

Excavation of root systems

Gloves are recommended during all steps of root excavation.

Note: It is easier to excavate roots when the soil is dry.

1. **Excise shoots from roots.** Height of plants were measured prior to root excavation. The, the shoots were cut at the soil boundary line and samples were placed into a brown paper bag labeled with treatment and plant number.
2. **Remove soil.** Pots of *N. benthamiana* plant were squeezed on the side to loosen soil, and then inverted to release the soil and plant. The soil was then removed from the crown root system by gently rotating the root system in a dynamic motion.
3. **Wash root system**. Roots were submerged by hand in a bucket filled with distilled water to remove the remaining soil still attached to the more fiberous roots. The root system was then rotated within the water to shake off excess soil. Finally, any excess soil particles were removed by carefully massaging the root system.
4. (*Optional*) If soil was difficult to remove, a spray bottle with distilled water was used on troublesome areas, especially at junction points too small for hands to reach.

5. **Dry roots.** Roots clean of soil particles were placed on a towel to briefly remove water.

Root system architecture phenotyping

1. **Place clean roots on a scanning tray.** Clean roots were placed on clear scanning trays compatible with the EPSON 12000XL Scanner bed size. Between eight to fifteen *N. benthamiana* root systems could fit depending on respective size of roots. Pot labels were placed neatly beside each root system to document the order of individuals on each image acquired.
2. **Place tray and background on scanner.** Scanning tray was placed on the EPSON 12000XL Scanner bed and the black background (black felt and cardboard in our case) was placed on top of the scanning tray.
3. **Acquire image(s).** A computer with the EPSON Scan 2 software connected to the scanner was used with the following software parameters for image acquisition: ≥400 dpi and grayscale 16-bit. Roots were flipped 180 degrees to acquire images of the two sides of the root system.
4. **Save images for future analysis.** Files were saved in .tiff file format. Each image was saved with the date of acquisition, treatment, and side of the root system.
5. Depending on the next step(s) of tissue preservation it is important to immediately complete future steps for optimal results.

Collection of tissue for histological or ribonucleic acid use

After confirmation of the viral infection status, the root system of a random subset of *N. benthamiana* individuals were used for the following three analyses: (1) dry mass measurement, (2) tissue staining, and (3) RNA extraction.

For dry mass measurement, crown root systems were placed in the corresponding brown paper bag with the previously excised shoot system. The bags of shoots and/or roots were placed in a drying oven at 105 °C for 1 week and dry biomass measurements were taken. Shoot and root dry biomass were taken independently on a scale.

For root tissue staining, two methods were used in which the only difference was the final preservation step. In the instance of fresh tissue, whole root systems were placed into a 15 mL conical tube for immediate staining to detect reactive oxygen species (ROS). For preserving samples, the top half of the root system was excised with a razor blade and placed into a pre-labeled 2.0 mL Eppendorf tube filled with 70% ethanol. Only fresh samples were used in the ROS assay described below, however, preserved samples were used in histological stains specific to xylem and/or phloem. Root tissue was stained to detect ROS using diaminobenzidine (DAB) staining methods.

For RNA extraction, the bottom half of the root system of individual plants was collected on a weighing tray using a razor blade. Collected root samples were placed into a pre- labeled RNAse free 2.0 mL Eppendorf tube containing two sterile steel BBs using sterile tweezers. Samples were flash frozen in liquid nitrogen and stored at -80 °C until RNA extraction and processing. Total RNA was extracted from root samples as previously described for leaves of *N. benthamiana* (Roy et al. 2023). Briefly, tissue was flash frozen before maceration with sterile steel BBs in a Retsch Mixer Mill MM400

(Model 04182-09, Retsch USA, Verder Scientific, Inc.) at a frequency of 60 Hertz for two minutes, and then, total RNA was isolated by using an Omega E.Z.N.A. Plant RNA Mini Kit (cat no. R6827). A final elution was performed in molecular grade water.

Executing the above steps yields tissue suitable for cross section analysis under a microscope or purified total RNA isolation for viral diagnostic RT-PCR or RT-qPCR, or root transcript analyses by 3'RNA-Seq or RT-qPCR. Data from these analyses were used to complement root phenotypic information collected by excavating root systems in combination with image analyses with the Rhizovision Explorer software.

REFERENCES

Daudi, A., and O'Brien, J. A. 2012. Detection of Hydrogen Peroxide by DAB Staining in Arabidopsis Leaves. Bio Protoc 2:e263.

Osterbaan, L. J., Choi, J., Kenney, J., Flasco, M., Vigne, E., Schmitt-Keichinger, C., Rebelo, A. R., Heck, M., and Fuchs, M. 2019. The identity of a single residue of the RNA-dependent RNA polymerase of grapevine fanleaf virus modulates vein clearing in Nicotiana benthamiana. Molecular Plant-Microbe Interactions 32:790–801. https://doi.org/10.1094/MPMI-12-18-0337-R.

Osterbaan, L. J., Schmitt-Keichinger, C., Vigne, E., and Fuchs, M. 2018. Optimal systemic grapevine fanleaf virus infection in *Nicotiana benthamiana* following agroinoculation. Journal of Virological Methods 257:16–21. https://doi.org/10.1016/j.jviromet.2018.04.006.

Roy, B. G., DeBlasio, S., Yang, Y., Thannhauser, T., Heck, M., and Fuchs, M. 2023. Profiling Plant Proteome and Transcriptome Changes during Grapevine Fanleaf Virus Infection. J. Proteome Res. 22:1997–2017. https://doi.org/10.1021/acs.jproteome.3c00069.

Vanacker, H., Carver, T. L. W., and Foyer, C. H. 2000. Early H2O2 Accumulation in Mesophyll Cells Leads to Induction of Glutathione during the Hyper-Sensitive Response in the Barley-Powdery Mildew Interaction. Plant Physiol 123:1289–1300.

APPENDIX II

EFFORTS TO PURIFY AND CHARACTERIZE THE GRAPEVINE FANLEAF VIRUS ENCODED PROTEIN $1E^{POL*/SD}$, PUTATIVE VIRAL RNA-DEPENDENT RNA POLYMERASE, PREDICTED PHOSPHATASE, AND SYMPTOM DETERMINANT

ABSTRACT

The genome of grapevine fanleaf virus (GFLV, species *foliumflabelli,* genus *Nepovirus*, family *Secoviridae*) is comprised of two single-stranded positive RNA particles, RNA1 and RNA2. Five proteins are encoded by RNA1, lettered A-E, where protein $1E^{Pol*/Sd}$ encodes the putative RNA-dependent RNA polymerase (RdRP) and a determinant of apical vein clearing in the model plant host *Nicotiana benthamiana*. The N-terminus of the protein carries a conserved RdRP motif. The C- terminal ~300 amino acids surrounding the symptom determinant have no homology outside nepoviruses where only one virus has a similar sequence with undetermined function. The resolving of the structure of GFLV protein $1E^{Pol*/Sd}$ would provide additional information to better understand the mechanism of symptom development *in planta*. A cloning scheme was developed and implemented GFLV protein $1E^{Pol*/Sd}$ to aid in this endeavor. After the execution and confirmation of transforming two constructs, pCAV4:$1E_{GHu}$ and pCAV4:$1E_{F13}$, protein expression $1E^{Pol*/Sd}$ was induced, and a standard protein purification protocol was followed. This is a report of the cumulative efforts to obtain purified GFLV protein $1E^{Pol*/Sd}$ from an *Escherichia coli* expression system.

MATERIALS AND METHODS

Sequence acquisition and predictive analysis of globular protein domains

Sequence alignment was conducted on the protein coding regions of grapevine fanleaf virus (GFLV) protein $1E^{Pol*/Sd}$ strains F13 (Vuittenez et al. 1964) and GHu (Vigne et al. 2013) from GenBank identifiers NC_003615.1 and JN391442.1, respectively. The regions pertaining to protein $1E^{Pol*/Sd}$ (92 kDa, 824 amino acids) were extracted and subject to AlphaFold protein prediction for globular domain identification (Jumper et al. 2021). Primers (Table A2-1) were designed based on the respective target vector expression system (pET-15b, Novagen; pET-21b(+), Novagen; pCAV4.1, and custom modified for T7 expression vector (Schiltz et al. 2022, Adams et al. 2022).

Amplification of grapevine fanleaf virus target sequences

Polymerase chain reaction (PCR) amplification of target sequences was performed using template pCLEAN plasmids containing GFLV-F13 and GFLV-GHu RNA1 coding sequences (Osterbaan et al. 2019). All PCR utilized Phusion® High-Fidelity DNA Polymerase (New England BioLabs® Inc., M0530) with primers at recommended concentrations of 10 μM each. Thermocycler parameters were as follows: 35 cycles of denaturation (1 minute, 98°C), primer-specific annealing (20 seconds, 62-72°C), extension (25 seconds to 3 minutes, 72°C) followed by a final extension (5 minutes, 72°C). Resulting amplicons were resolved through gel electrophoresis and subsequently visualized under UV illumination after ethidium bromide staining on 1% agarose in TAE buffer. Resulting amplicons were excised and purified using manufacturer protocols (Zymoclean Gel DNA Recovery Kit, Zymo Research, USA).

Table A2-1. Primers designed to target various segments of grapevine fanleaf virus (GFLV) protein 1E$^{Pol*/Sd}$.

Primer	Sequence (5'-3')
R1_PET15_GHu	GAC GTC GGA TCC TTA ACC ACT CTC TCC ACT C
R2_PET15_GHu	GAG CGT GGA TCC TTA ACT TTC AAA ATC AG
R3_PET15_GHu	GGC AGC GGA TCC TTA CTT CCT CGG GCA TGA GTG
R1_PET15_F13	GAG GCG GGA TCC TTA ACC ACT CTC TCC ACT CTT C
R2_PET15_F13	GGA GCG GGA TCC TTA ACT TTC AAA ATC AGA AAA AT
R3_PET15_F13	GGA CGT GGA TCC TTA TTT CCT CAG GCA TGT ATG ATT CTG
F1_PET21_GHu	GGA GAT CAT ATG GGA GAA GTG CCG TAC GTG CCA GAA
F2_PET21_GHu	GGA GAG CAT ATG AGT CAT GGA GCG GCT TTT G
F3_PET21_GHu	GGA GGA CAT ATG CCC GTG TAT ATT CAG AAA ATC
R1_PET21_GHu	GCT GAC CTC GAG ACC ACT CTC TCC ACT CTT ATG ACA
R2_PET21_GHu	GGA GAG CTC GAG ACT TTC AAA ATC AGA AAA ATA GC
R3_PET21_GHu	GGA GAG CTC GAG CTT CCT CGG GCA TGA GTG AG
F1_PET21_F13	GGA GGA CAT ATG GGA GAA GTG CCG TAC GTA CCA G
F2_PET21_F13	GGA GAG CAT ATG AGT CAT GGA GCA GCT TTT G
F3_PET21_F13	GTG ACG CAT ATG CCC ATT CAT ATC AAG AAA GTC C
R1_PET21_F13	GCT GAC CTC GAG ACC ACT CTC TCC ACT CTT CTG ACA
R2_PET21_F13	GGA GAG CTC GAG ACT TTC AAA ATC AGA AAA ATA AC
R3_PET21_F13	GGA GAG CTC GAG TTT CCT AAG GCA TGT ATG ATT C
F1_pCAV_GHu	GGA GGA GAA TTC ATG GGA GAA GTG CCG TAC GTG CCA G
F2_pCAV_GHu	GTG GTA GAA TTC ATG AGT CAT GGA GCT GCT TTT GCC
F3_pCAV_GHu	GTG CTG GAA TTC ATG CCC GTG TAT ATT CAG AAA ATC C
R1_pCAV_GHu	GTC AGT GTC GAC TTA GCC GGA CTC TCC ACT CTT ATG ACA
R2_pCAV_GHu	GGA GAG GTC GAC TTA ACT TTC AAA ATC AGA AAA ATA GCA
R3_pCAV_GHu	GGA TGG GTC GAC TTA CTT CCT CGG GCA TGA GTG
F1_pCAV_F13	GGA GGA GAA TTC ATG GGA GAA GTG CCG TAT GTG CC
F2_pCAV_F13	GGA GAG GAA TTC ATG AGT CAC GGA GCA GCT TTC GCC
F3_pCAV_F13	GGA GCG GAA TTC ATG CCC ATC CAT ATC AAG AAA GTC
R1_pCAV_F13	GAG CGT GTC GAC TTA ACC ACT CTC TCC ACT CTT CTG ACA
R2_pCAV_F13	GGA GAG GTC GAC TTA ACT TTC AAA ATC AGA AAA ATA ACT
R3_pCAV_F13	GGA GAG GTC GAC TTA TTT CCT AAG GCA TGT ATG ATT CTG

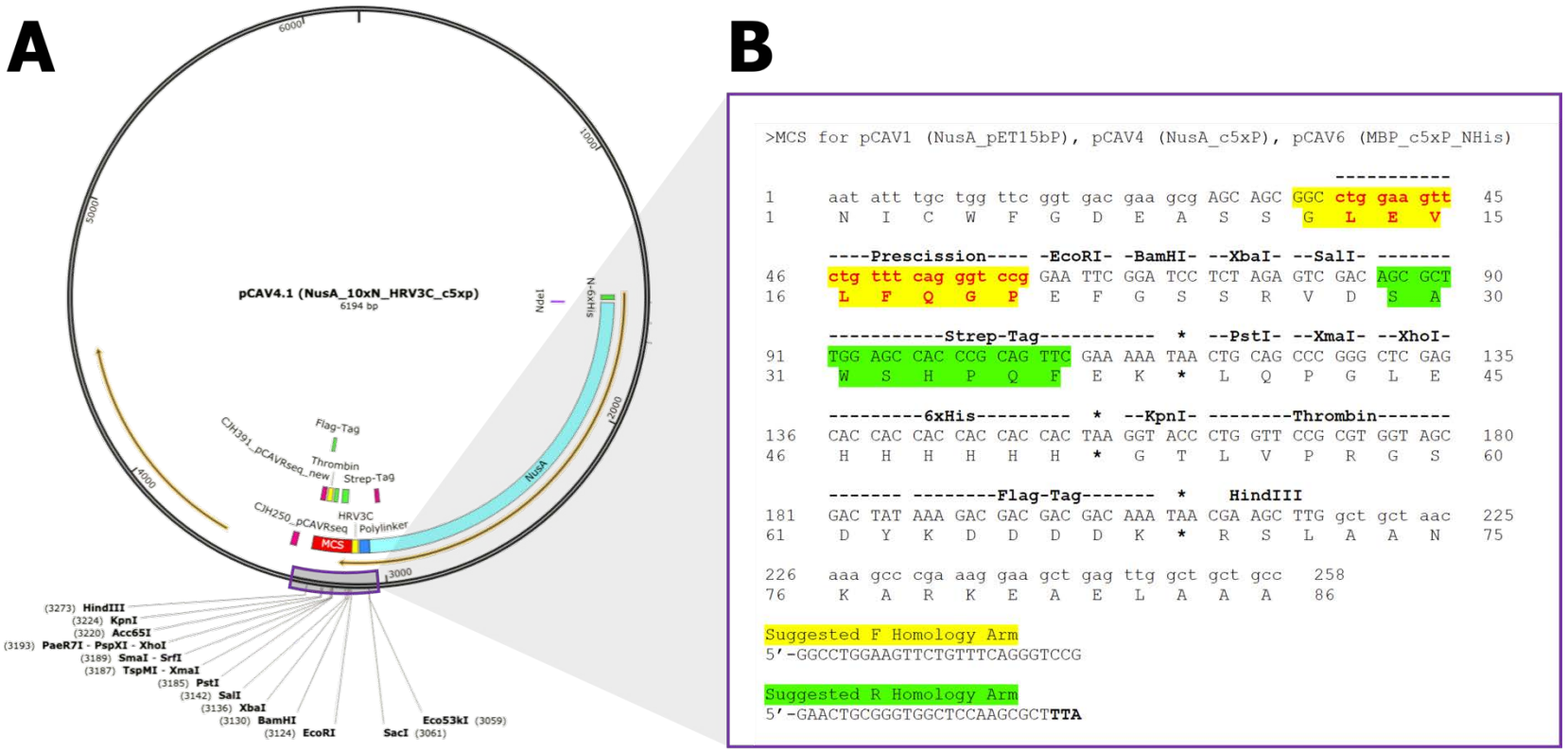

Figure A2-1. The multiple cloning site (MCS) for pCAV4 vector includes several features that increase efficiency in protein purification. (A) The vector map including major restriction cut sites at the MCS, and (B) sequence of the MCS includes the presence of several restriction enzyme sites, a Strep Tag, Thrombin cleavage site proximal to a C-terminal Flag-Tag provide multiple strategies for cloning. (Schilitz et al. 2022)

Restriction enzyme cloning

For *in vitro* expression of GFLV protein $1E^{Pol*/Sd}$, inserts were designed with a 6-10 base pair extension to match respective multiple cloning site target vectors. For each recipient plasmid and insert pair, specific restriction enzyme insertions were used (pET15b with NdeI and BamHI, pET21b with NedI and XhoI; pCAV4.1 with EcoRI and SalI). All restriction enzyme digestions were performed in either NEBuffer™ r3.1 (New England Biolabs®, #B6003S) or rCutSmart™ Buffer (New England Biolabs®, #B6004S) at 37°C for five to 15 minutes.

Using restriction enzyme cloning, digested plasmid and PCR products were ligated overnight at 12°C and transformed into 10ß-line competent *Escherichia coli* cells (New England Biolabs®, #C3019H) according to manufacturer specifications. Single colony PCR was performed on resulting colonies from transformed cells plated on selective media. For pET-derived vectors, primers T7Seq and T7Term were used; while for pCAV4 backbones, primers pCAVSeq and pCAVSeqR were used (Table A2-2). Resulting single colonies that tested positive through PCR were isolated, preserved in sterilized 30% glycerol-LB, and stored at -80°C.

Bacterial transformation

Sequence confirmed constructs were heat shock transformed into *E. coli* Rosetta™ 2 (DE3) competent cells (Millipore Sigma, 71400-M) according to manufacturer specifications.

Protein expression

From sequence confirmed inserts of the pCAV4.1 vector transformed into Rosetta 2 cells, the following protocol was exacted for protein expression and purification. Transformed Rosetta cells with the desired pCAV4.1 vector were grown in 125 mL of sterile Luria-Bertani (LB) with chloramphenicol and ampicillin. The culture was incubated at 37°C for twelve hours to an optical density of 2.0 at 600 nm (OD_{600nm}). A portion of the culture in LB was transferred to 2 liters of sterile Terrific Broth with chloramphenicol (Research Products International, C61000-25.0) and ampicillin and incubated at 37°C until an OD_{600nm} of 1.0 was reached (roughly four hours). The temperature was then dropped to 19°C for one hour and then induced with 0.3 mM isopropyl β-D-thiogalactopyranoside (IPTG) overnight for protein expression for 16 to 18 hours.

The following day, the resulting 2 L culture was subject to ultracentrifugation at 4000 rpm for 15 minutes. The clear supernatant was decanted and 50 mL of nickel loading buffer (20 mM HEPES, pH 7.5, 500 mM NaCl, 30 mM imidazole, 5% glycerol (v:v) and 5 mM ß-mercaptoethanol) was added to each pellet, where the cells were allowed to equilibrate at 4°C for at least 30 minutes but no longer than six hours. Cells were resuspended using a serological pipette and through vortexing. The resuspended cells were transferred to 50 mL conical tubes and subject to centrifugation once more at 4000 rpm for 10 minutes at 4°C. After decanting the supernatant, the cells were either flash frozen in liquid nitrogen or used immediately in protein purification.

Protein purification

Frozen pellets were reconstituted in 50.0 mL nickel buffer with 10 mM $MgCl_2$, 26 µg/mL lysozyme, 0.5 mM PMSF, Roche protease inhibitor, and 130 µg/mL DNAse. Lysozyme was added to a final concentration of 1 mg/mL and the resulting suspension was incubated at 4°C for 10 minutes with constant agitation. Cells were then lysed on ice by probe sonication for a total of four minutes with alternating amplitude to avoid denaturing of target protein (20 seconds amplitude 20; 20 seconds amplitude 0). The resulting lysate was then subject to centrifugation at 13000 rpm at 4°C for 10 minutes. The supernatant was decanted and stored at 4°C as `Post-13k supernatant` and the pellet was resuspended in 50 mL of nickel buffer as `Post 13k pellet` for downstream comparison of relative protein abundance of target protein $1E^{Pol*/Sd}$. The supernatant sample was filtered using a 0.45 µm filter and stored at 4°C.

Filtered supernatant of the previous step was the subject to affinity column purification on a BioLogic low-pressure chromatography system with BioFrac fraction collector (BIO-RAD, #7318304EDU) using a 5 mL HiTrap™ HP His tag protein purification column (Cytiva Life Sciences, #17524801) charged with 0.1 M $NiSO_4$ and flushed with nickel loading buffer. The protein sample was loaded onto the column and eluted through an imidazole gradient (50 to 500 mM) over ten column volumes.

Resulting combined aliquots containing protein $1E^{Pol*/Sd}$ were then subject to simultaneous human rhinovirus 3C mediated proteolytic cleavage of the NusA tag and membrane dialysis overnight at 4°C against Q buffer (20 mM Tris-HCl, 1 mM EDTA, 1 mM DTT, 5% glycerol (v:v)). Soluble cleaved protein was the subject to ion exchange chromatography with Tris-HCl pH 8.0 and a 5 mL HiTrap™ Q HP column (Cytiva Life

Sciences #17115401). Protein was bound to the charged column and then eluted using an NaCl gradient of 50 – 500 mM over five column volumes (25 mL). Collected 1 mL fractions containing GFLV protein $1E^{Pol*/Sd}$ (92 kDa band) were combined and dialysis was performed as before in minimal NaCl concentration HEPES buffer.

The dialyzed protein sample was then subject to size exclusion chromatography on a Superdex™ 75 10/300 GL sizing column (Cytiva Life Sciences #29148721) that was first equilibrated with SEC buffer (20 mM HEPES pH 7.5, 150 mM KCl, 1 mM DTT). Resulting aliquots were resolved by SDS-PAGE electrophoresis, pooled, and concentrated through membrane dialysis.

Western blot analysis of protein samples

Samples obtained at multiple points during protein purification were subject to sodium dodecyl sulfate polyacrylamide gel electrophoresis (SDS-PAGE) with Mini-PROTEAN® TGX Stain-Free™ Protein Gels (BIO-RAD, #4568026). Generally, the respective protein sample was diluted in elution buffer (1:2, vol:vol) with NuPAGE™ LDS 4X Sample Buffer (Invitrogen™, #NP0007) for electrophoresis. Resolved proteins were visualized through Coomassie Brilliant Blue staining for 1 hour and overnight destaining in 1X buffer with Kimwipes®.

Crystallization predictions

The sequences for wildtype GFLV strains F13 and GHu were submitted to the XTalPred-RF server (https://xtalpred.godziklab.org/XtalPred-cgi/xtal.pl) to predict solubility and crystallization propensity using default parameters.

RESULTS

Analysis of grapevine fanleaf virus protein 1E$^{Pol*/Sd}$ domains

Protein structure prediction resulted in the identification of three domains that were noted as the RNA-dependent RNA polymerase (RdRP) domain, middle domain, and C-terminal domain (Figure A2-2). These three domains concurrently are documented in Chapters 3 and 5 of this dissertation with more information on their respective predicted functions. The full-length protein 1E$^{Pol*/Sd}$ was 2472 nucleotides (824 amino acids) in length, and individually the RdRP, middle, and C-terminus domains were 1581 (527 amino acids), 453 (288 amino acids), and 411 (137 amino acids) nucleotides long (Table A2-2).

TABLE A2-2. Protein traits of grapevine fanleaf virus protein 1E$^{Pol*//Sd}$ domains targeted for cloning and crystallization.

wildtype GFLV-GHu protein 1E$^{Pol*/Sd}$						
Domain	**Range**	**Length**	**Da (g/mol)**	**Theoretical pI**	**Cys**	**Met**
RdRP	1–527	527	59306.08	5.61	10	13
C-terminal half	537–824	288	31256	8.17	13	2
Middle	537–687	151	16107.61	6.68	6	1
C-terminus	688–824	137	15166.41	8.55	7	1
wildtype GFLV-F13 protein 1E$^{Pol*/Sd}$						
Domain	**Range**	**Length**	**Da**	**Theoretical pI**	**Cys**	**Met**
RdRP	1–527	527	59366.05	5.33	11	15
C-terminal half	537–824	288	31582.33	8.37	13	5
Middle	537–687	151	16324.71	7.56	6	1
C-terminus	688–824	137	15275.63	8.56	7	4

These GFLV protein $1E^{Pol*/Sd}$ sequences were subject to further analysis with the AlphaFold prediction server for three-dimensional predictions with confidence metrics (Figure A2-2). Contact maps and predicted alignment error indicated the confident association of residues between three distinct globular protein domains (Figure A2-2A). The highest returned prediction (Figure A2-2B) was high confidence prediction areas was for the RdRP domain, while less confident was obtained for the C-terminal domain (Figure A2-2C). The multiple sequence alignment indicated a lack of references to build the C-terminal residues (Figure A2-2D). This resulted in the final determination of domains that were used in the cloning scheme (Figure A2-2E).

The sequences for GFLV protein $1E^{Pol*/Sd}$ were subject to additional secondary structure analysis. Single amino acid sequence changes are not hypothesized to impact the conformational structure using AlphaFold (Jumper et al. 2021), however, minor differences can be tested with secondary structure prediction software. Indeed, the C-terminal modification of position 802 from lysine to glycine resulted in a change in alpha helix predictions for wildtype GFLV-GHu to mutant GFLV-GHu $1E_{K802G}$ (Figure A2-3). This information should be considered during the crystallization process if any discrepancies are noticed.

Finally, the relative ease to crystallize protein $1E^{Pol*/Sd}$ was considered. Using the tool XTalPred, GFLV protein $1E^{Pol*/Sd}$ was determined to be in the most difficult class of enzymes to produce a crystal for. This was associated with the relative length of the protein and the solubility.

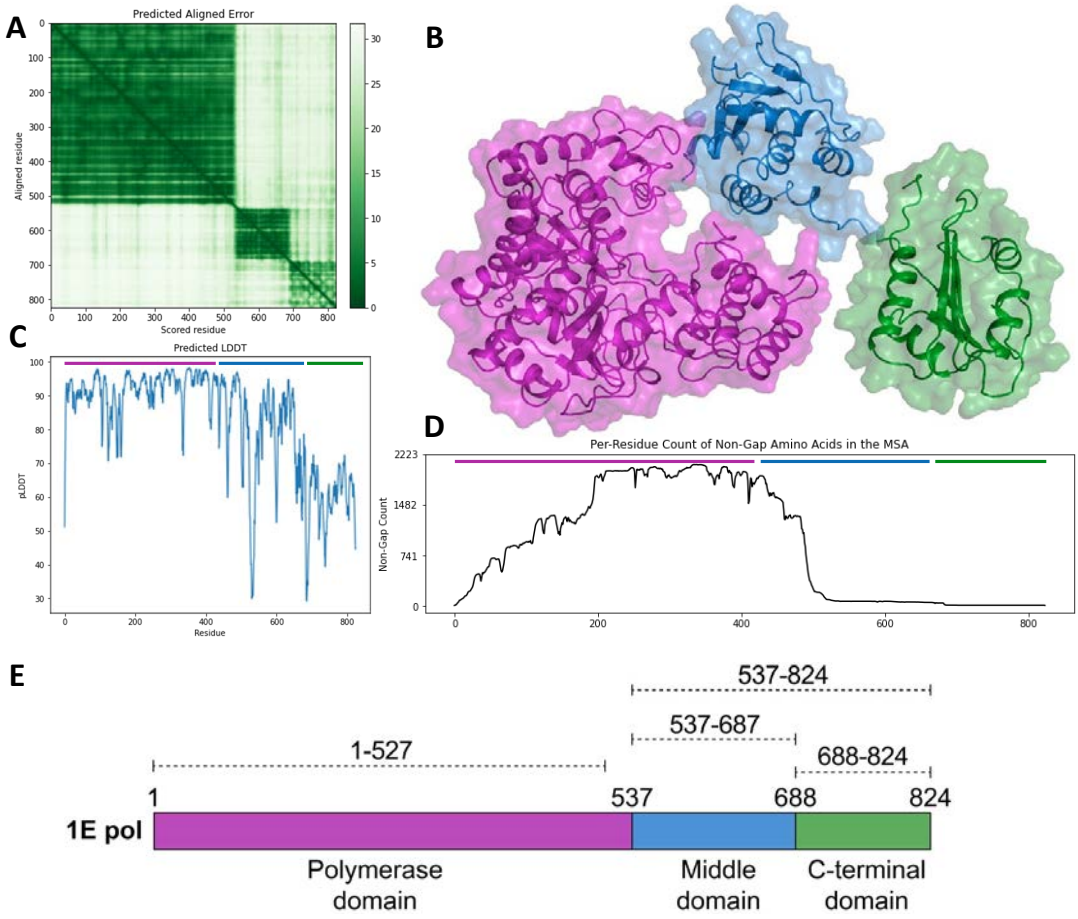

FIGURE A2-2. AlphaFold prediction analysis of grapevine fanleaf virus protein $1E^{Pol*/Sd}$ determined three globular domains with varying levels of confidence. (A) Contact-residue map confidence is shown where the most confident predicted association is depicted in dark green, suggesting three individual protein domains. (B) The most confident protein model provided by AlphaFold, colored by suggested domains. (C) The confidence of prediction as pLDDT over the entire protein $1E^{Pol*/Sd}$ sequence shows the highest confidence for the polymerase domain, where (D) most aligned sequences are found in publicly available databases. (E) The results of three-dimensional protein prediction suggested a three-domain approach to cloning to segment and achieve higher probability of segmented protein crystallization.

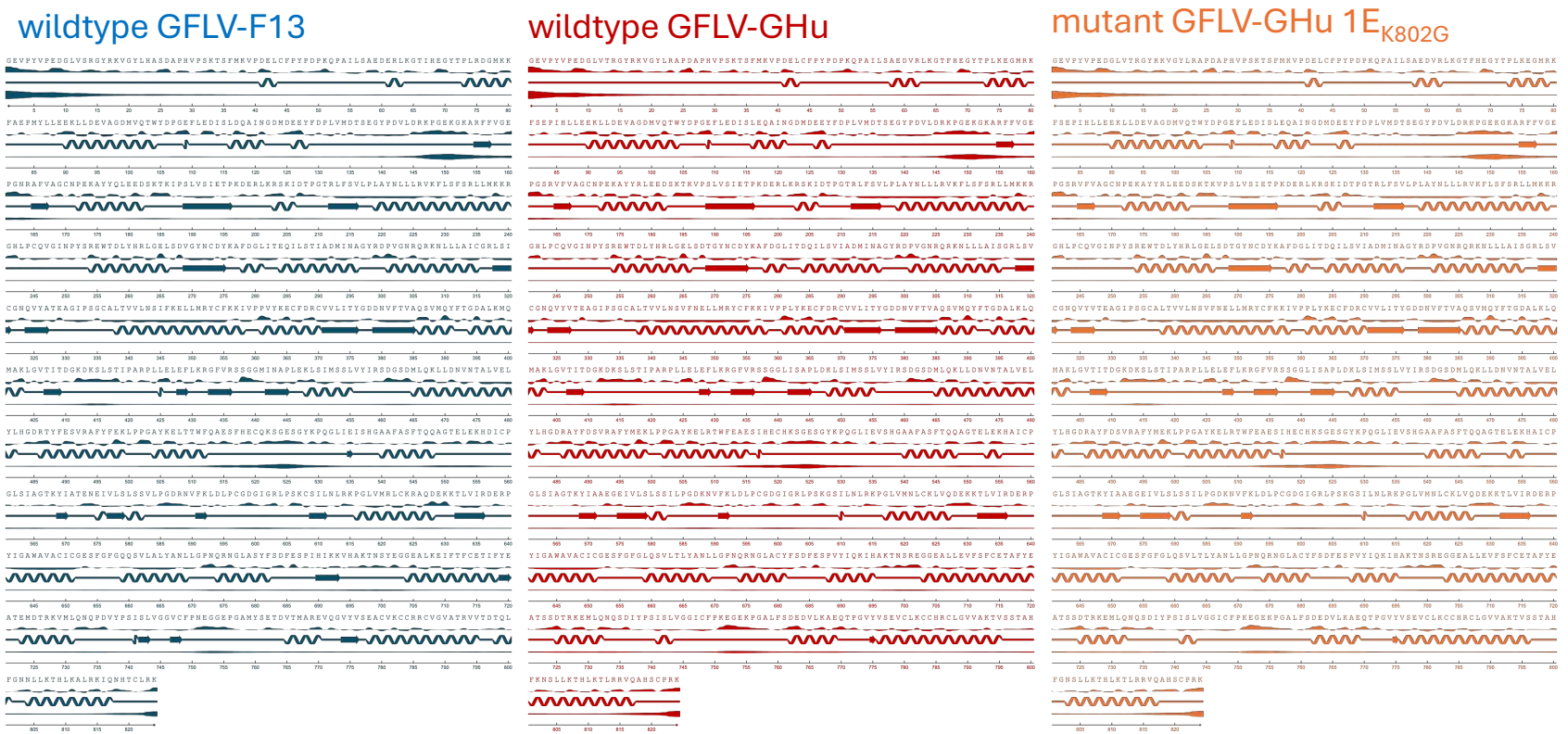

FIGURE A2-3. Predicted secondary structure and solvent accessibility metrics of grapevine fanleaf virus (GFLV) protein 1E$^{Pol*//Sd}$. Sequences were analyzed through the NetSurfP 3.0 Server (https://services.healthtech.dtu.dk/services/NetSurfP-3.0/). Surface accessibility is represented by the first line under each amino acid, where above the centroid line is exposed, and below the line is a buried residue. Secondary structure is represented by helices and beta sheets, and disorder is represented as the relative thickness of the third line, where a thinner line is more ordered. Color of the sequences represent individual strains of GFLV.

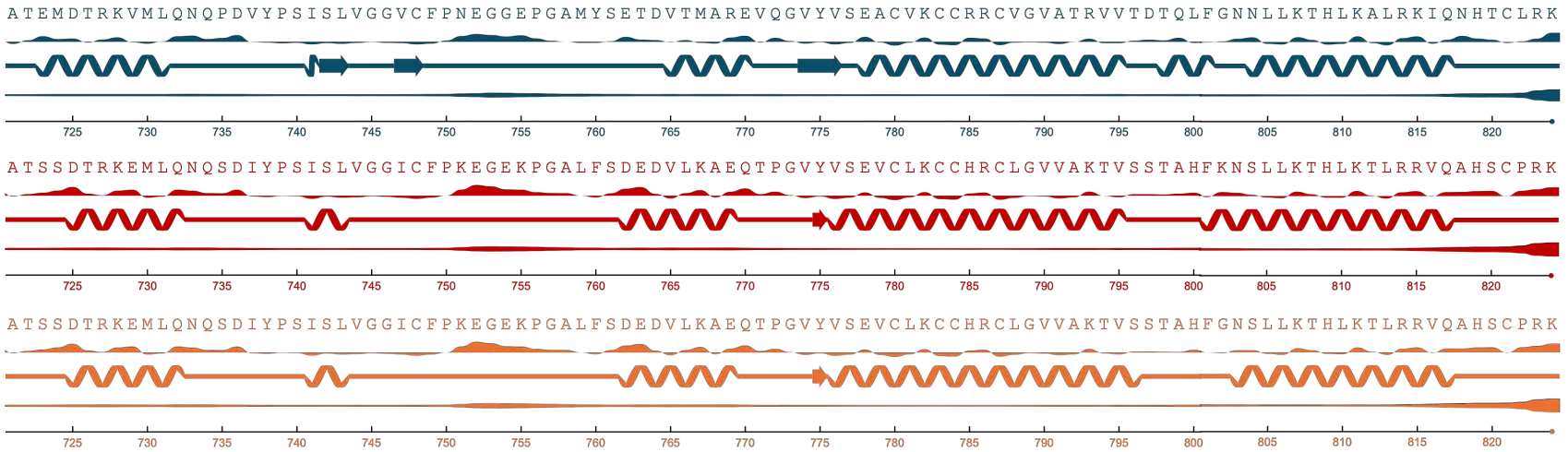

FIGURE A2-3. (continued). A closer look at the final 50 C-terminal residues of protein $1E^{Pol*/Sd}$ show predicted difference in secondary structure around residues 798 to 804.

Cloning

Protein encoding sequences were successfully amplified for protein $1E^{Pol*/Sd}$ of wildtype GFLV-GHu and wildtype GFLV- F13 strains with respective primers (Table A2-1) into backbones pET15 and pCAV4. The amplicons for the full protein were isolated via gel purification and ligated into the pCAV4 expression vector. The ligation reaction was then transformed into BL21 competent cells, plated, and confirmed through sequencing of single colony PCR products. Confirmed expression of inserts allowed for the isolation of the plasmid through miniprep, and transformation into the Rosetta-2 protein expression cells. While other constructs were evaluated, the downstream purification concentrated on full-length proteins $1E^{Pol*/Sd}$ for the two wildtype GFLV strains.

GFLV $1E^{Pol*/Sd}$ protein expression and purification

Transformed Rosetta cells were grown and protein expression was induced. After cell lysis and centrifugation, a detectable protein with the anticipated 124 kDa band for 1E-NusA-6xHis was produced (Figure A2-4A, arrow). Based on background expression of Rosetta™ 2(DE3) cells (Figure A2-4A, right), the expression pattern for GFLV-1E-All-NusA was convincing for further purification. Full 2L culture expressions were performed and showed similar results with increased abundance of all proteins, correlated with the increased number of cells lysed (Figure A2-4B, lanes 4, 5, 13, 14).

Protein samples were collected through Nickel column purification via 6X His tagged protein, where the same ~124kDa band remained. The protein collected was subject to dialysis (Buffer: 20 mM HEPES, 5% glycerol, 1 mM EDTA, 1 mM DTT)

and human Rhinovirus 3C protease mediated proteolytic cleavage of the NusA-6xHis tag of the 3' end (Figure A2-4D, lanes 12 and 13). No protein 'crashing-out' of solution was visible in the dialysis tube upon cleavage, indicating protein solubility after NusA removal. The cleaved protein $1E^{Pol*/Sd}$ resulted in a prominent ~92kDa band, as expected.

Ion exchange chromatography followed using Tris-HCl pH 8.0 and HiTrapQ HP Columns to elute protein based on isoelectric charge. The collected aliquots are visualized as bands in Figure A2-5, lanes 4-14, where lanes 9, 10 and 11 display the most abundant levels of the cleaved GFLV-1E-All at ~92kDa. The purification process was halted at this point for a transition period. Size exclusion chromatography (SEC) has yet to be performed on these samples and is expected to resolve out additional unwanted proteins, mostly two bands of lower molecular weight (70kDa and 45kDa, seen in Figure A2-5).

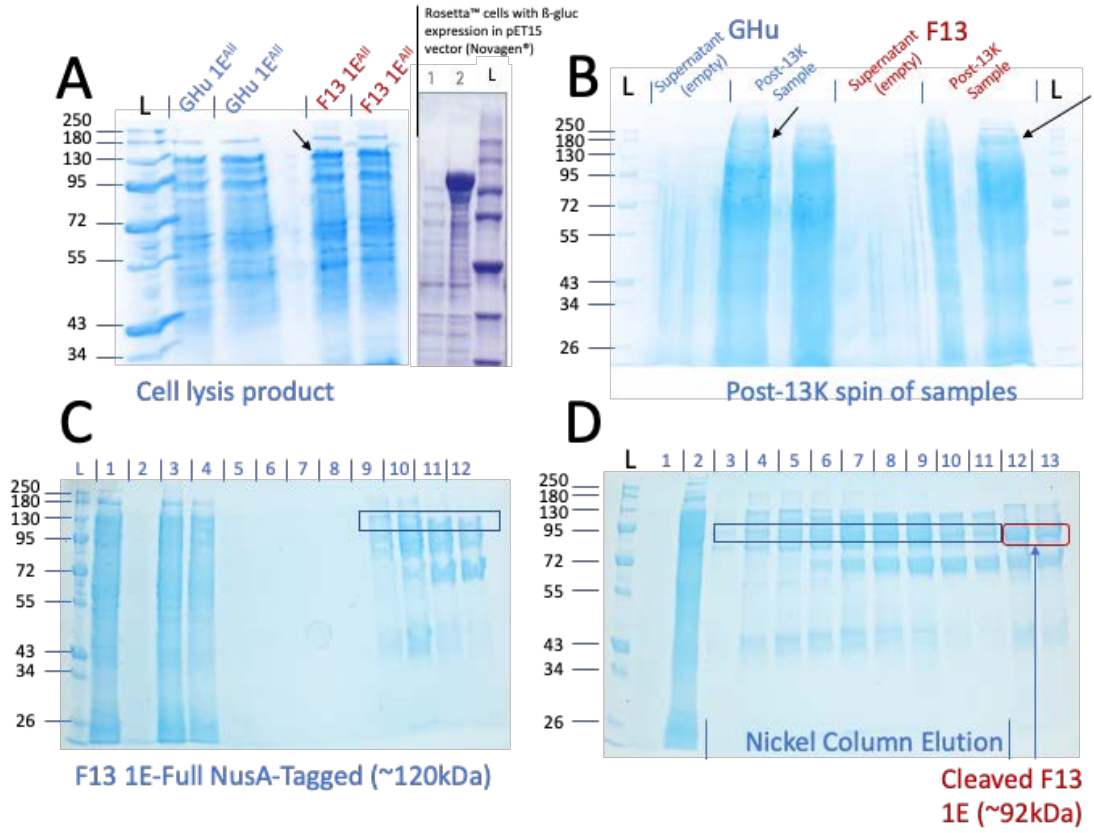

Figure A2-4. SDS-PAGE gel electrophoresis of protein products from Rosetta™ 2 (DE3) *E. coli* cells expressing pCAV4-GFLV-1E-All constructs. (A) Diluted 1:10 protein product after initial cell lysis test for which lanes are as follows: L=Ladder, GHu 1E-All-NusA for two cultures grown containing the GFLV-GHu-1E coding region within pCAV4, [empty lane] and F13 1E-All-NusA for two cultures grown containing the GFLV-F13 1E coding region within pCAV4. To illustrate the background protein expression of Rosetta™ cells, a cropped image of Rosetta™ 2(DE3) cells are shown to the right with lane 2 showing induced expression of a desired protein at ~100 kDa next to a ladder marker. Relative background expression is lower than what we observe which could indicate the need for optimization of expression. **(B)** Protein expression is contained within the pellet of cells prior to lysis. After overnight expression of 2.0L cultures, cells were pelleted and showed most of the expression within pellet fraction, with little in supernatant. Ladders flank this gel with lanes labeled for GFLV-GHu construct in blue and GFLV-F13 in red. **(C)** Nickel column purification of pCAV4-GFLV-1E-GHu-All construct. Lanes are as follows: L = ladder, 1 = Post-13K sample, 2 = supernatant, 3-5 = Loading sample flow-through, 6-12 = Nickel column elutions of column volumes #9-35. **(D)** Pre- and post-cleavage of 1E-GHu-All from NusA-6x-His across several column volumes showed that the HRV3C protease was successful in cleaving NusA tag from 1E. Lanes are as follows: L = ladder, 1 = supernatant, 2 = post-13K pellet, 3-11 = Nickel column elution volumes #16-24, 12 and 13 = Post-dialysis and HRV3C cleavage sample.

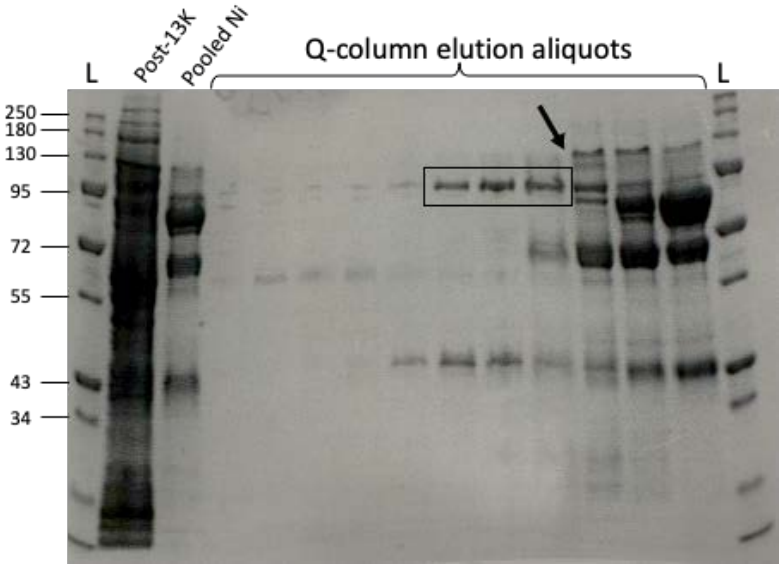

Figure A2-5. SDS-PAGE gel electrophoresis of protein elution aliquots after ion exchange chromatography. Purified product indicates expected band of GFLV-1E-All (92kDa) with black box across four column volumes (4 mL), and uncleaved product GFLV-1E-All-NusA-6xHis (~120kDa) by black arrow in last three sample lanes. Lanes are as follows: **1, 15** - NEB Ladder (11-250kDa), **2** – Post 13K sample, **3** – Pooled Nickel purification samples in single lane, **4 through 14** – Ion exchange Q Column aliquots collected over 10 volumes predicted from Biologic instrument detection of flow through of protein (utilizing UV sensor for protein absorbance).

CONCLUSIONS

Purification efforts of GFLV protein $1E^{Pol*/Sd}$ indicate that the full protein product is stable in solution with low salt concentrations, and that expression of the full-length protein is feasible. More work is needed to isolate a homogenous protein and to increase the total yield to perform downstream crystal trays. A few modifications could be made to the protein purification process (i.e., induction time, dialysis volume, IPTG concentration to 1mM as directed by Novagen) for increased yield upon expression. With a higher abundance of protein, sufficient protein might be utilized for structure determination. Upon the completion of size exclusion chromatography, it would be advantageous to confirm the specific expression of protein $1E^{Pol*/Sd}$ by mass spectrometry analysis of excised bands after SDS-PAGE gel visualization. Unfortunately, the length and size of the protein may impede upon crystallization of the full protein as indicated by the XTalPred server. Therefore, the truncated domains should also be targeted in future efforts to purify this protein.

The crystal structure of $1E^{Pol*/Sd}$ is hypothesized to reveal more about the molecular interactions of the protein, specifically in the association with symptoms elicited in *Nicotiana benthamiana* during plant infection (Vigne et al. 2013; Osterbaan et al. 2021; Roy et al. 2024). More work is needed to determine these biological functions and shed light on the nonhomologous and peculiar C-terminus of GFLV protein $1E^{Pol*/Sd}$.

REFERENCES

Adams, M. C., Schiltz, C. J., Heck, M. L., and Chappie, J. S. 2022. Crystal structure of the potato leafroll virus coat protein and implications for viral assembly. Journal of Structural Biology 214:107811. https://doi.org/10.1016/j.jsb.2021.107811.

Jumper, J., Evans, R., Pritzel, A., Green, T., Figurnov, M., Ronneberger, O., Tunyasuvunakool, K., Bates, R., Žídek, A., Potapenko, A., Bridgland, A., Meyer, C., Kohl, S. A. A., Ballard, A. J., Cowie, A., Romera-Paredes, B., Nikolov, S., Jain, R., Adler, J., Back, T., Petersen, S., Reiman, D., Clancy, E., Zielinski, M., Steinegger, M., Pacholska, M., Berghammer, T., Bodenstein, S., Silver, D., Vinyals, O., Senior, A. W., Kavukcuoglu, K., Kohli, P., and Hassabis, D. 2021. Highly accurate protein structure prediction with AlphaFold. Nature 596:583–589. https://doi.org/10.1038/s41586-021-03819-2.

Osterbaan, L. J., Hoyle, V., Curtis, M., DeBlasio, S., Rivera, K. D., Heck, M., and Fuchs, M. 2021. Identification of protein interactions of grapevine fanleaf virus RNA-dependent RNA polymerase during infection of Nicotiana benthamiana by affinity purification and tandem mass spectrometry. Journal of General Virology 102. https://doi.org/10.1099/jgv.0.001607.

Roy, B. G., Choi, J., and Fuchs, M. F. 2024. Predictive Modeling of Proteins Encoded by a Plant Virus Sheds a New Light on Their Structure and Inherent Multifunctionality. Biomolecules 14:62. https://doi.org/10.3390/biom14010062.

Schiltz, C. J., Wilson, J. R., Hosford, C. J., Adams, M. C., Preising, S. E., DeBlasio, S. L., MacLeod, H. J., Van Eck, J., Heck, M. L., and Chappie, J. S. 2022. Polerovirus N-terminal readthrough domain structures reveal molecular strategies for mitigating virus transmission by aphids. Nat Commun 13:6368. https://doi.org/10.1038/s41467-022-33979-2.

Vigne, E., Gottula, J. W., Schmitt-Keichinger, C., Komar, V., Ackerer, L., Belval, L., Rakotomalala, L., Lemaire, O., Ritzenthaler, C., and Fuchs, M. 2013. A strain-specific segment of the RNA-dependent RNA polymerase of grapevine fanleaf virus determines symptoms in *Nicotiana* species. Journal of General Virology 94:2803–2813. https://doi.org/10.1099/vir.0.057646-0.

Vuittenez, A., Munck, M., and Kuszala, J. 1964. Demonstration of the infectious degeneration virus by serological tests and observation of characteristic particles from extracts of diseased Vine leaves. .

APPENDIX III

GRAPEVINE RED BLOTCH VIRUS IS TRANSMITTED BY THE THREE-CORNERED ALFALFA HOPPER IN A CIRCULATIVE, NONPROPAGATIVE MODE WITH UNIQUE ATTRIBUTES*

ABSTRACT

The transmission mode of grapevine red blotch virus (GRBV, genus *Grablovirus*, family *Geminiviridae*) by *Spissistilus festinus*, the three-cornered alfalfa hopper, is unknown. By analogy with other members in the family *Geminiviridae*, we hypothesized circulative, nonpropagative transmission. Time course experiments revealed GRBV in dissected guts, hemolymph and heads with salivary glands following a 5-, 8- and 10-day exposure to infected grapevines, respectively. After a 15-day acquisition on infected grapevines and subsequent transfer on alfalfa, a non-host of GRBV, the virus titer decreased over time in adult insects, as shown by qPCR. Snap bean proved to be a feeding host of *S. festinus* and a pseudo-systemic host of GRBV following *Agrobacterium tumefaciens*-mediated delivery of an infectious clone. The virus was efficiently transmitted by *S. festinus* from infected snap bean plants to excised snap bean trifoliates (90%) or grapevine leaves (100%) but less efficiently from infected grapevine plants to excised grapevine leaves (10%) or snap bean trifoliates (67%). Transmission of GRBV also occurred trans-stadially but not via seeds. The virus titer was significantly higher in guts and hemolymph relative to heads with salivary glands, and in adults emanating from third compared with first instars that emerged on infected

grapevine plants and developed on snap bean trifoliates. This study demonstrated circulative, nonpropagative transmission of GRBV by *S. festinus* with an extended acquisition access period compared with other viruses in the family *Geminiviridae* and marked differences in transmission efficiency between grapevine, the natural host, and snap bean, an alternative herbaceous host.

---

*This appendix has been published: Flasco, M., Hoyle, V., Cieniewicz, E.J., Roy, B., McLane, H., Perry, K.L., Loeb, G., Nault, B., Heck, M., and Fuchs, M. (2021). Grapevine red blotch virus is transmitted by the three-cornered alfalfa hopper in a circulative, nonpropagative mode with unique attributes. *Phytopathology* 111:1851-1861.

INTRODUCTION

Grapevine red blotch disease was recognized as a new threat to viticulture in the mid- to late 2000s in the state of California in the United States (Cieniewicz et al. 2017b; Sudarshana et al. 2015). Subsequently, grapevine red blotch virus (GRBV) was identified in diseased vines (Al Rwahnih et al. 2013; Krenz et al. 2012) and later shown to be the causal agent of the disease (Yepes et al. 2018). GRBV causes red or chlorotic blotches on leaves of red- and white-berried *Vitis vinifera* cultivars, respectively (Cieniewicz et al. 2017a; Sudarshana et al. 2015). The virus delays fruit ripening and reduces fruit quality. It also affects wine composition and sensory attributes (Blanco-Ulate et al. 2017; Cauduro Giradello et al. 2020; Cieniewicz et al. 2017a; Martínez-Lüscher et al. 2019). GRBV is also reported to occasionally reduce fruit yield and vine growth (Cieniewicz et al. 2017a). The estimated economic impact of red blotch disease ranges from U.S. $2,200 to $19,500 per hectare over a predicted 25-year life span of a vineyard (Ricketts et al. 2017).

GRBV is the type member of the genus *Grablovirus* in the plant virus family *Geminiviridae* (Rojas et al. 2018; Varsani et al. 2017). Its genome consists of a single-stranded, circular DNA molecule that bi-directionally codes for seven open reading frames (ORFs): four in the viral sense orientation and three in the complementary sense orientation (Cieniewicz et al. 2017b; Vargas-Asencio et al. 2019). ORF V0 is of unknown function (Vargas-Asencio et al. 2019); ORF V1 is predicted to code for the coat protein (Buchs et al. 2018; Krenz et al. 2014; Vargas-Asencio et al. 2019); ORFs V2 and V3 are suspected to be involved in virus movement (Guo et al. 2015); ORF C1 codes for a replication-associated protein (RepA); ORF C2 is the C terminus of RepA

expressed from a spliced C1:C2 transcript; and the function of ORF C3 is not known (Guo et al. 2015; Krenz et al. 2014; Vargas-Asencio et al. 2019). Analysis of the genetic diversity among GRBV isolates indicates two phylogenetic groups with up to 8.5% nucleotide sequence divergence (Krenz et al. 2014). Isolates of both phylogenetic groups are involved in the etiology of red blotch disease (Yepes et al. 2018).

GRBV has been reported in vineyards throughout the United States (Adiputra et al. 2018; Cieniewicz et al. 2020; Hoffmann et al. 2020; Krenz et al. 2014; Soltani et al. 2020) and Canada (Fall et al. 2020; Poojari et al. 2017; Xiao e t al. 2015). The widespread distribution of GRBV in North America vineyard results from the dissemination of infected propagation material (Cieniewicz et al. 2017a; Sudarshana et al. 2015). Beyond North America, the virus has been described in Switzerland (Reynard et al. 2018), South Korea (Lim et al. 2016), Mexico (Gasperin-Bulbarela et al. 2019), Argentina (Luna et al. 2019), and India (Marwal et al. 2019).

Vitis spp. are the only known hosts of GRBV (Bahder et al. 2016b; Cieniewicz et al. 2017a). The virus was isolated from wine grape cultivars and rootstocks (Cieniewicz et al. 2017a; Sudarshana et al. 2015), as well as from table grapes (Al Rwahnih et al. 2015a), interspecific hybrids (Schoelz et al. 2020) and Muscadine grapes (Soltani et al. 2020). GRBV was further found in an archival *V. vinifera* herbarium sample collected in 1940 in California (Al Rwahnih et al. 2015b) and in free-living *Vitis* spp. in Northern California (Bahder et al. 2016b; Cieniewicz et al. 2018b; Perry et al. 2016).

Secondary spread of GRBV in vineyards has been documented but only in Northern California (Cieniewicz et al. 2017a, 2018a, b, 2019) and Oregon (Dalton et al.

2019). No evidence of secondary spread has been obtained in vineyards of New York (Cieniewicz et al. 2019) or Switzerland (Reynard et al. 2018). Patterns of spatiotemporal increase of GRBV-infected vines in diseased California and Oregon vineyards suggested the existence of an aerial hemipteran vector capable of acquiring and transmitting the virus (Cieniewicz et al. 2018a, b, 2019; Dalton et al. 2019). A few vector candidates, including *Spissistilus festinus* (Say, 1830; Hemiptera: Membracidae), the three-cornered alfalfa hopper, were identified in diseased California vineyards in which spread was documented (Cieniewicz et al. 2018a, b, 2019). This treehopper species was reported to transmit GRBV from infected to healthy grapevines under greenhouse conditions (Bahder et al. 2016b). Nonetheless, these results have not been independently confirmed and no information is available on the transmission mode of GRBV by *S. festinus.*

By analogy with other viruses of the family *Geminiviridae* (Czosnek et al. 2017; Fiallo-Olivé et al. 2018; Gray et al. 2014; Nault 1997; Rojas et al. 2018; Whitfield et al. 2015), we hypothesized that *S. festinus* is a vector of GRBV and transmission is circulative and nonpropagative. Here, we describe our efforts to confirm *S. festinus* as a vector of GRBV, develop a reliable transmission assay, and investigate fundamental attributes of transmission biology.

MATERIALS AND METHODS

Plant materials

Cuttings of healthy and GRBV-infected *V. vinifera* were collected during the winters of 2015 to 2018 and grown to mature plants in the greenhouse. Healthy and GRBV-infected vines were used as recipient and donor vines in transmission assays with *S. festinus*, respectively, as well as controls in diagnostic PCR. Grapevines that were previously inoculated with GRBV via *Agrobacterium tumefaciens*-mediated delivery of infectious partial dimer virus clones (Yepes et al. 2018) were also used as infected material in this study.

Seedlings of *Solanum lycopersicum* 'Florida Lanai', *Nicotiana benthamiana*, *Phaseolus vulgaris* 'Hystyle', and *Medicago sativa* (Galaxy 100 Brand, a blend of cultivars) were used to identify alternative hosts of GRBV. Tomato cultivar Florida Lanai was selected for this study because it is an excellent host of several members of the family Geminiviridae (Rajabu et al. 2018); *N. benthamiana* was selected as a model host, as it is commonly used in plant virology studies (Goodin et al. 2008); and alfalfa and snap bean were selected because leguminous plants in the family Fabaceae are preferred hosts of *S. festinus* (Beyer et al. 2017; Bick et al. 2020; Kron and Sisterson 2020; Preto et al. 2018a, 2018b, 2019; Wilson et al. 2020).

GRBV inoculation of herbaceous plants via pinpricking of A. tumefaciens-*carrying infectious clones*

Two- to three-week-old *P. vulgaris* 'Hystyle' plants received pinpricks at the petiole-leaf junction of each trifoliate using a sterile dissecting needle dipped in a solid

culture (Luria-Bertani medium supplemented with agar and kanamycin) of recombinant *A. tumefaciens* harboring an infectious partial dimer clone corresponding to either GRBV isolate NY175 from phylogenetic clade 1 or GRBV isolate NY358 from phylogenetic clade 2 (Yepes et al. 2018). Alternatively, petioles of snap bean plants were pinpricked three times at 2-cm intervals along the petiole. Seedlings of *S. lycopersicum* 'Florida Lanai', *M. sativa* and *N. benthamiana* were similarly inoculated by pinpricking of petioles and midribs. Mock-inoculated snap bean, tomato, alfalfa, and *N. benthamiana* seedlings were used as controls. Inoculated and uninoculated plants were visually monitored for virus-like symptoms for 3 to 8 weeks and tested for GRBV.

Establishment of a* Spissistilus festinus *colony on alfalfa plants

S. festinus specimens were collected in alfalfa fields from Yolo County in California in October of 2015 and established on alfalfa within screened insect cages (BugDorm 6E610 Insect Rearing Cage, MegaView Science, Taichung, Taiwan) maintained in a controlled environmental chamber at Cornell Agritech in Geneva, NY with rearing conditions set at 26°C, 14:10 light/dark photoperiod, and 85% RH. These conditions were adapted from those described in Meisch and Randolph (1965) to promote nymph development and prevent diapause. The colony population was supplemented with field-collected adults from alfalfa fields in Yolo or San Joaquin Counties in California in October of 2016 to 2019. In addition, specimens from alfalfa in Fresno County in California were kindly provided to us by Dr. Mark Sisterson, U.S. Department of Agriculture, Agricultural Research Service, Parlier, CA, in November of 2015. Because the *S. festinus* populations collected in Yolo, San Joaquin, and Fresno

Counties were morphologically and genetically identical (Cieniewicz et al. 2020), they were combined over time to constitute a California-derived *S. festinus* colony.

Time-course experiments to assess the movement of GRBV in dissected Spissistilus festinus *organs and determine the acquisition access period*

Replicated time-course experiments were carried out to determine the acquisition access period (AAP) of GRBV by *S. festinus* after exposure to infected plants for 1 to 15 days on grapevines kept in screened cages (BugDorm 2400F Insect Rearing Tent). After the AAP, insects were collected using a D cell-powered aspirator and transferred to alfalfa plants, a nonhost for GRBV (see Results section), for a period of 48 h to clear the gut content. Individual specimens were dissected to test for the presence of GRBV in heads with salivary glands, hemolymph, and guts.

For organ dissections, individual *S. festinus* specimens were frozen first at −80°C for 5 to 10 min or −20°C for 20 to 60 min. Then, heads with salivary glands and guts were dissected in phosphate buffered saline (PBS) under an SZX16 stereoscope (Olympus, Center Valley, PA). Specimens were first stabilized with sterile tweezers and one of the forelegs was removed to release the hemolymph, which was collected using a glass capillary tubule, in efforts to quickly extract hemolymph before any organs were disrupted. Next, the insects were moved to a fresh drop of PBS and heads with salivary glands attached were gently removed using a new set of sterilized tweezers. The abdomens and remaining parts were again moved to a fresh drop of PBS. Finally, the gut tissue was removed using a pair of sterile tweezers by removal of the wings from one side of the insect followed by separation of the abdomen from the thorax to release

the intact gut containing the entire alimentary canal from foregut through hindgut. Dissected organs and collected hemolymph from a single insect were individually transferred to 2-ml microfuge tubes or tubes of a 96-well collection microtube plate (cat. no. 95040455; Thermo Fisher Scientific), for genomic DNA extraction and virus testing by multiplex PCR (Krenz et al. 2014) or quantitative PCR (qPCR) (Setiono et al. 2018).

Time-course experiment to quantify the amount of virus in **Spissistilus festinus** *after feeding and removal from GRBV-infected plants*

Another time-course experiment with *S. festinus* adults and fourth and fifth instars was carried out to determine if transmission is nonpropagative. Adults and nymphs were deposited on GRBV-infected grapevines for 2 weeks in insect rearing cages (BugDorm 2400F Insect Rearing Tent). Then, all specimens were transferred to caged (BugDorm 6E610 Insect Rearing Cage) alfalfa plants, a nonhost for GRBV (see Results), for the duration of the experiment. The day of transfer to alfalfa was time 0 (T0). At 3-day intervals (T1 = 3 days, T2 = 6 day, T3 = 9 days, and T4 = 12 days), cohorts of six adults that had acquired GRBV as nymphs, and six adults that had acquired GRBV as adults, were removed from the alfalfa plants using a D cell-powered aspirator and frozen at −80°C for whole insect testing of GRBV by qPCR with endogenous heterologous (Setiono et al. 2018) and exogenous homologous controls (Cieniewicz et al. 2019, 2020). Grapevine and alfalfa plants were maintained in a greenhouse at 25 ± 2°C and a 16:8 light/dark photoperiod.

Trans-stadial transmission of GRBV by Spissistilus festinus

Adults of *S. festinus* were exposed to caged GRBV-infected *V. vinifera* until nymphs emerged. Then, the different nymphal stages were separately transferred with a fine-tipped paint brush to caged snap bean trifoliates. Experimental conditions were identical to those described for transmission assays. Next, as soon as the nymphs molted into adults, they were collected and tested for GRBV by qPCR (Setiono et al. 2018).

Transmission assays of GRBV with Spissistilus festinus

Three types of transmission experiments of GRBV by *S. festinus* were conducted to develop a reliable assay and determine transmission attributes (**Figure A3-1**). Transmission assay-1 used *P. vulgaris* as the virus donor plant and excised trifoliates of *P. vulgaris* as the virus recipient tissue (**Figure A3-1**). Transmission assay-2 used *P. vulgaris* as the virus donor plant and excised leaves of *V. vinifera* 'Cabernet franc' as the virus recipient tissue (**Figure A3-1**). Transmission assay-3 used potted GRBV-infected *V. vinifera* 'Cabernet franc' as the virus donor plant and excised leaves of *V. vinifera* 'Cabernet franc' as the virus recipient tissue (**Figure A3-1**).

For transmission assays-1 and -2, *S. festinus* adults were allowed to feed for 2 to 12 days on caged (BugDorm 6E610 Insect Rearing Cage) *P. vulgaris* after the bottom segment of the inoculated stem was wrapped in cheesecloth to direct insect feeding on areas of GRBV inoculation, i.e., the petiole-leaf junction of trifoliates. After the AAP, *S. festinus* specimens were transferred to caged (BugDorm 6E610 Insect Rearing Cage) alfalfa plants, a nonhost of GRBV (see Results section), using a D cell-powered aspirator, for 48 h to remove nonacquired virus from the lumen of the gut (referred to as "gut clearing"). Cohorts of 8 to 10 or 6 to 8 insects were then moved from alfalfa to

healthy, excised *P. vulgaris* trifoliates or *V. vinifera* 'Cabernet franc' leaves, respectively, for a 4-day inoculation access period (IAP). For the IAP, excised leaves of *P. vulgaris* or *V. vinifera* were placed in parafilm-covered 20-ml collection vials containing sterile water with a hole poked through the parafilm to hold the petiole upright, and the petiole was submerged in the water. Detached leaves in vials were then enclosed in a clear polypropylene 950-ml container (cat. no. PK32T, Fabri-Kal, Kalamazoo, MI) sealed with a polypropylene donut lid carrying a nylon screen (BugDorm 5002). This setting forced *S. festinus* to feed and inoculate GRBV on the leaf and petiole/leaf junction. The collection vials were regularly replenished with sterile water, as appropriate. For transmission assay-3, *S. festinus* adults were exposed to caged (BugDorm 6E610 Insect Rearing Cage) GRBV-infected grapevines for at least 15 days. Then *S. festinus* specimens were transferred to alfalfa for 48-h to clear the gut. Next, cohorts of six to eight insects were moved from alfalfa to healthy *V. vinifera* 'Cabernet franc' leaves for a 4-day IAP, as performed for transmission assays-1 and -2.

For the three transmission assays, individual insects were collected at the completion of the IAP for GRBV testing by multiplex PCR (Krenz et al. 2014) or qPCR (Setiono et al. 2018), while detached *P. vulgaris* trifoliates or *V. vinifera* leaves remained in the IAP chambers to allow for GRBV multiplication for up to 2 weeks. Next, leaf and petiole tissue were collected for GRBV testing by PCR (Krenz et al. 2014) or qPCR (Setiono et al. 2018). The AAP and gut-clearing steps were carried out in the greenhouse at 22 ± 3°C with a 16:8 light/dark photoperiod and the IAP and virus multiplication steps were done in an environmental chamber at 24°C with a 16:8 light/dark photoperiod and 50% RH.

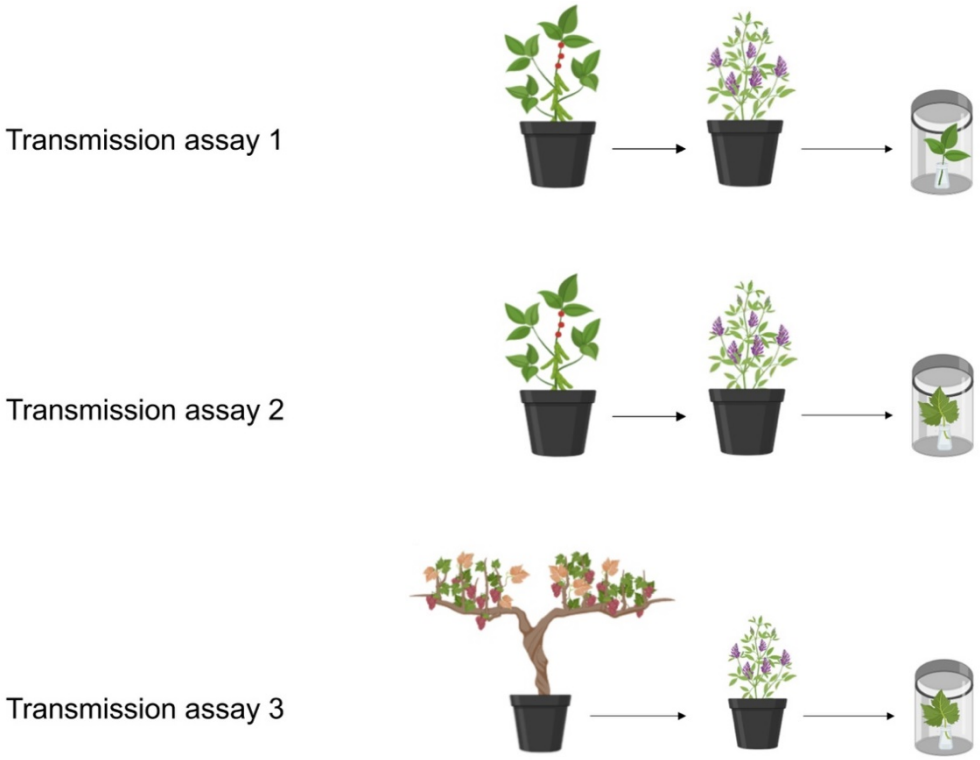

Figure A3-1 Schematic representation of the transmission assays performed in this study. Transmission assay 1 used *Phaseolus vulgaris* 'Hystyle' as virus donor plant and excised trifoliates of *P. vulgaris* 'Hystyle' as virus recipient tissue. Transmission assay 2 used *P. vulgaris* 'Hystyle' as virus donor plant and excised leaves of *Vitis vinifera* 'Cabernet franc' as virus recipient tissue. Transmission assay 3 used potted *V. vinifera* 'Cabernet franc' as virus donor plant and excised *V. vinifera* 'Cabernet franc' leaves as virus recipient tissue. Virus donor plants were either infected by *Agrobacterium tumefaciens*-mediated inoculation of an infectious grapevine red blotch virus (GRBV) partial dimer clone (Yepes et al. 2018) or rootings of GRBV-infected *V. vinifera* from the vineyard. Agroinoculation sites on *P. vulgaris* plants via pinpricking are indicated by red dots. Excised leaves of *P. vulgaris* or *V. vinifera* were placed in parafilm-covered 20-ml collection vials containing sterile water, and then enclosed in a sealed polypropylene container for exposure to *Spissistilus festinus*. The artwork was produced using the program BioRender (Toronto, CA).

Transmission of GRBV through seeds

Mature fruits of GRBV-infected 'Cabernet franc' and 'Cabernet Sauvignon' (Cieniewicz et al. 2017a, 2019) were collected from vineyards in Napa County in California in October 2015 to assess seed transmission of the virus. Seeds from mature fruits of healthy 'Cabernet franc' were used as negative control. Seeds were extracted and cleaned as described in Ellis et al. (1983). After a stratification at 4°C for at least a month, seeds were germinated on wet filter paper at 30°C and transferred to soil in a greenhouse at 22 ± 3°C and a 16:8 light/dark photoperiod. Seedlings were tested for GRBV by multiplex PCR (Krenz et al. 2014).

Pods and seeds produced by healthy and GRBV-infected *P. vulgaris* 'Hystyle' were also collected then germinated in the greenhouse, and seedlings were tested for GRBV by multiplex PCR (Krenz et al. 2014).

Nucleic acid extraction from plant and **Spissistilus festinus** *tissue*

Genomic DNA was isolated from plant tissue using the H.P. Plant DNA Mini Kit (Omega Bio-Tek, Norcross, GA) or the MagMAX-96 Al/ND Isolation Kit (Thermo Fisher Scientific, Waltham, MA) on a KingFisher instrument (Thermo Fisher Scientific). Genomic DNA was isolated from *S. festinus* using the E.Z.N.A. Insect DNA kit (Omega Bio-Tek) or the MagMAX DNA Multi-Sample Ultra Kit (Thermo Fisher Scientific) on a KingFisher instrument.

Total RNA was isolated from plant tissue using the Plant RNA Kit (Omega Bio-Tek) or the MagMAX-96 Al/ND Isolation Kit (Thermo Fisher Scientific) on a KingFisher instrument.

GRBV detection by PCR, qPCR, and reverse transcription PCR

The presence of GRBV in plant tissue, whole *S. festinus* bodies, and dissected *S. festinus* organs was tested by multiplex PCR using genomic DNA and primer pairs designed in the ORFs coding for the coat protein and RepA proteins, as described in Cieniewicz et al. (2018a, b, 2019) and Krenz et al. (2014). DNA amplicons were analyzed by gel electrophoresis and visualized under UV illumination after staining with GelRed (Biotium, Fremont, CA).

GRBV was also tested in nucleic acids from plant tissue by qPCR with SYBR Green reagents (iTaq Universal SYBR Green Supermix, Bio-Rad, Hercules, CA), GRBV primers pREP3v and pREP4v designed in ORF C1 coding RepA, and a primer pair designed in the plant nicotinamide adenine dinucleotide phosphate gene (Setiono et al. 2018). GRBV testing in *S. festinus* by qPCR required GRBV primers pREP3v and pREP4v (Setiono et al. 2018), *S. festinus* primers Sf18SFor and Sf18SRev (Cieniewicz et al. 2020), SYBR Green reagents, and 50 ng of genomic DNA from individual specimens. Negative controls included sterile water and nucleic acids from healthy grapevines and *S. festinus* from the colony maintained on alfalfa or *P. vulgaris.* Each DNA sample was run in triplicate (three technical replicates) on a model no. C1000 Touch thermocycler (Bio-Rad). GRBV was quantified using the relative ΔΔCt method to calculate the fold difference of GRBV DNA between two samples. Quantification of GRBV was also performed according to the absolute method with exogenous homologous controls using a dilution series containing 1×10^9 to 1×10^2 copies of the GRBV monomer maintained in Escherichia coli to calculate the amount of GRBV DNA in each sample (Setiono et al. 2018).

GRBV replication in *P. vulgaris* was tested by reverse transcription PCR (RT-PCR), using total RNA and a primer pair that bridges the confirmed splice site of the GRBV C1-C2 ORFs to amplify an unspliced 369-bp cDNA fragment and a spliced 206-bp cDNA fragment (Vargas-Asencio et al. 2019; Yepes et al. 2018). This assay was used to distinguish GRBV replication from expression mediated by the recombinant *A. tumefaciens* clone carrying an infectious clone of GRBV after plant inoculation. RT-PCR amplicons were resolved by gel electrophoresis and visualized under UV illumination after staining with the product GelRed. Controls for RT-PCR included a no-template control, a healthy plant control, an inoculated plant control collected immediately after pinpricking (unspliced amplicon only), a bacterium colony from the partial dimer GRBV clone in *A. tumefaciens* (unspliced amplicon only), and a positive control from GRBV-infected grapevine (spliced and unspliced amplicons).

Statistical analyses

Statistical comparisons were performed on titers of GRBV in insects according to qPCR Ct values determined with analysis of variance (ANOVA) in the program RStudio (The R Project for Statistical Computing). Fold changes were based on ΔΔCt values. Statistically significant differences between mean ΔΔCt values in dissected insect organs and collected hemolymph were determined using Tukey's Honestly Significant Difference test. The significance level was set at $\alpha = 0.05$. A two-way ANOVA was used to determine the level of interaction between insect tissue type and AAP for virus titer. Statistically significant differences between mean ΔΔCt values in adults that emerged from different instar stages were determined using Tukey's honestly significant difference test.

RESULTS

Initial failures at transmitting GRBV with Spissistilus festinus

Our initial attempts at transmission using naturally infected grapevines and grapevines infected after *A. tumefaciens*-mediated delivery of an infectious virus clone repeatedly failed to reproducibly achieve GRBV infection in recipient grapevines when applying the experimental conditions reported in Bahder et al. (2016a). Indeed, after a 48-h AAP and a 48-h IAP (Bahder et al. 2016a), none (0%, 0 of 48 in eight independent transmission experiments) of the recipient grapevines became infected with GRBV in the greenhouse even when tested after one or two dormancy periods, although most tested *S. festinus* individuals (95%, 35 of 37) had ingested the virus after exposure to infected grapevines. In separate experiments with dissected *S. festinus* organs, none of the heads with salivary glands (0%, 0 of 13) tested positive while all (100%, 20 of 20) dissected guts tested positive for GRBV in PCR after a 48-h AAP. Similar results were obtained after a 5- to 10-day AAP and a 5- to 8-day IAP. The absence of detectable GRBV in salivary glands explained our repeated failures at accomplishing transmission. Therefore, we decided to determine the persistence of GRBV in *S. festinus* and optimize the AAP.

Persistence of GRBV in Spissistilus festinus *after clearing the gut content of insects by feeding on alfalfa*

To circumscribe GRBV acquisition by *S. festinus*, we selected alfalfa, which is a nonhost of GRBV (see Results section), to clear the gut content of insects after feeding on infected grapevines. This was to assess virus acquisition resulting in virus transit to

the salivary glands, rather than virus ingestion in the gut, when whole insect bodies were tested by PCR after exposure to GRBV-infected plants. Most *S. festinus* individuals (58%, 18 of 31 in three independent experiments) tested positive for GRBV after a 2-week AAP on infected grapevines followed by 2 weeks on alfalfa in the greenhouse, as shown by multiplex PCR using specific primers and genomic DNA from whole specimens. Retaining the virus after a 2-week gut-clearing period on alfalfa clearly documented acquisition of GRBV and suggested circulative transmission. Similar results were obtained after 2 days of feeding on alfalfa (41%, 35 of 85 in six independent experiments), and after 2 weeks on GRBV-infected grapevines in the greenhouse. With no gut-clearing period on alfalfa, nearly twice as many *S. festinus* adults (79%, 223 of 284 in 13 independent experiments) tested positive for GRBV after a 2-week exposure to infected grapevines when whole insects were tested by multiplex PCR. An artificially higher percentage of *S. festinus* tested positive for the virus without gut clearing, because GRBV contained in plant sap residing in the gut and salivary glands was detected. These results demonstrated that GRBV persists in *S. festinus* even after a considerable period of gut clearing, consistent with circulative transmission.

***Identification of alternative hosts of GRBV and* Spissistilus festinus**

Carrying out GRBV research on *Vitis* spp. can be tedious and time-consuming. To address the limitation of *Vitis* spp. as a natural host of GRBV, we investigated herbaceous hosts as potential alternative hosts. GRBV replication was confirmed in inoculated but not in uninoculated apical leaves of *S. lycopersicum* (8 of 10) and *N. benthamiana* (9 of 10) at 7, 14, and 21 dpi, suggesting local but no systemic infection on these herbaceous plants (**Table A3-1**). GRBV replication was also detected in

inoculated petioles (11 of 16) and corresponding trifoliates (6 of 12) of snap bean plants, but not in uninoculated trifoliates of the same plants (**Table A3-2**). Remarkably, the accumulation of spliced GRBV C1:C2 transcripts was readily detected 1 to 5 cm away from the inoculated site on the stem and trifoliate of the inoculated snap bean tissue but not in the petiole and trifoliate of uninoculated snap bean tissue (**Table A3-2**). These data indicated *P. vulgaris* 'Hystyle' as a pseudo-systemic host of GRBV, based on its limited long-distance virus movement and the lack of systemic infection in trifoliates of infected plants in which the petiole had not been inoculated by pinprick delivery of an *A. tumefaciens* culture carrying an infectious virus clone. The GRBV titer in infected *P. vulgaris* was high, with qPCR Ct values of 18 to 23. No virus-like symptoms were apparent in inoculated or apical leaves of tomato, snap bean, or *N. benthamiana* after pinprick inoculation. Additionally, GRBV was never detected in inoculated *M. sativa* by RT-PCR or PCR in repeated experiments, indicating alfalfa is not a host of GRBV (**Table A3-1**).

To test if these herbaceous plants are feeding hosts of *S. festinus*, adult specimens from the colony maintained on alfalfa were allowed to feed for 2 to 8 weeks. Snap bean cultivar Hystyle and *M. sativa* are excellent feeding and reproductive hosts of *S. festinus* (data not shown). In contrast, *S. festinus* did not survive on tomato or *N. benthamiana*. Based on these results, snap bean plants were used in transmission assays as an alternative herbaceous host of GRBV and a feeding host of *S. festinus*

Table A3-1. Detection of grapevine red blotch virus (GRBV) in herbaceous hosts following *Agrobacterium tumefaciens*-mediated inoculation of GRBV infectious clones NY175 and NY358.

Plant Species	Local GRBV Infection[a]		Apical GRBV Infection[b]	
	NY175	NY358	NY175	NY358
Nicotiana benthamiana	5/5[c]	3/5	0/5	0/5
Solanum lycopersicum	5/5	4/5	0/5	0/5
Phaseolus vulgaris	6/8	5/8	4/6[d]	2/6[d]
Medicago sativa	0/11	0/9	0/8	0/12

[a]Local infection was detected in inoculated leaves by RT-PCR at 7 days post-inoculation (dpi).
[b]Systemic infection was tested at 14-21 dpi by PCR and RT-PCR in uninoculated, apical leaves.
[c]Number of plants that tested positive for GRBV over the total number of plants that were inoculated.
[d]Some of the inoculated snap bean trifoliates for which the petiole was inoculated tested positive for GRBV whereas all the snap bean trifoliates for which the petiole was uninoculated were negative for GRBV.

Table A3-2. Detection of grapevine red blotch virus (GRBV) by RT-PCR in *Phaseolus vulgaris*, a pseudo-systemic host, following Agrobacterium tumefaciens-mediated inoculation of infectious clone NY175.

		Tissue collection		GRBV detection[c]	
Time (week)[a]	Agroinoculation	Direction	Distance (cm)[b]	N	%
1	+	Acropetal	1-2	14/18	78
	-			0/3	0
	+		4-5 (Trifoliate)	2/2	100
	-			0/4	0
	+	Basipetal	1-2	33/43	77
	-			0/5	0
2	+		2-3	19/34	56
	-			0/3	0
3	+		4-5	15/21	71
	-			0/3	0

[a]The petiole of *P. vulgaris* cv. 'Hystyle' was pinpricked (+) or not (-) at inoculation sites close to the petiole/leaf junction of a single trifoliate with a solid culture of recombinant *Agrobacterium tumefaciens* carrying a partial dimer clone of GRBV.
[b]Tissue fragments were collected above (acropetal) and below (basipetal) the inoculation site at 1-3 weeks post-inoculation to test the accumulation of spliced GRBV C1:C2 transcripts by RT-PCR. Trifoliates were also tested by RT-PCR or PCR at one-week post-inoculation.
[c]Number (N) of stem or petiole fragments or trifoliates that tested positive for GRBV over the total number tested by RT-PCR and percent (%) of petiole fragments or trifoliates with detectable spliced C1:C2 transcripts.

GRBV is transmitted from *Phaseolus vulgaris* to *P. vulgaris* by *Spissistilus festinus*

To determine if snap bean cultivar 'Hystyle' can serve as a host plant source of virus inoculum and virus recipient material for *S. festinus*-mediated transmission of GRBV, replicated transmission assays were carried out. Snap bean plants were inoculated by pinpricking petioles with an infectious GRBV clone of isolate NY175 from phylogenetic clade 1 (**Figure A3-1**). When S. *festinus* had a minimum AAP of 6 days, GRBV was detected by multiplex PCR in almost all excised petioles and trifoliates (90%, 27 of 30), exclusive of a 2-day feeding on alfalfa (**Table A3-3**). Neither petioles (0%, zero of four) nor trifoliates (0%, zero of four) of snap beans exposed to *S. festinus* from the colony maintained on alfalfa (the uninfected negative control) tested positive for GRBV in PCR. No transmission occurred if the feeding period was <6 days (**Table A3-3**). These results demonstrated a high transmission rate of GRBV from infected snap bean plants to excised snap bean trifoliates.

The majority of *S. festinus* specimens tested positive for GRBV at the completion of the 4-day IAP after at least a 6-day AAP on infected snap bean plants (81%, 109 of 134 in three independent experiments). In contrast, none (0%, 0 of 24 in three independent experiments) and two-thirds (66%, 25 of 38 in three independent experiments) of *S. festinus* individuals tested positive for GRBV in PCR after a 2- and a 4-day AAP and a 2-day feeding period on alfalfa, respectively. As expected, none of the insects from the colony maintained on alfalfa that fed on healthy snap bean (0%, 0 of 15) tested positive for GRBV in PCR. In parallel, GRBV presence was ascertained in the gut and head with salivary glands of dissected *S. festinus* organs after a 4- and 6-

day AAP on infected *P. vulgaris*, respectively (**Table A3-4**). These results were consistent with a 6-day AAP on snap bean plants.

Table A3-3. Transmission of grapevine red blotch virus (GRBV) on excised *Phaseolus vulgaris* and *Vitis vinifera* leaves following acquisition by *Spissistilus festinus* on infected *P. vulgaris* during various acquisition access periods.

		Experiment 1[a]		Experiment 2		Experiment 3		Total[c]	
Virus recipient tissue	AAP[b]	Petiole[d]	Leaf	Petiole	Leaf	Petiole	Leaf	N	%
P. vulgaris	2	0/2	0/2	nt	nt	nt	nt	0/4	0
	4	0/2	0/2	nt	nt	nt	Nt	0/4	0
	6	6/7	7/7	6/8	8/8	nt	Nt	27/30	90
	12	nt	Nt	nt	nt	7/8	7/8	14/16	88
V. vinifera	6	5/5	5/5	nt	nt	nt	Nt	10/10	100

[a]Acquisition access period (AAP) in days.
[b]*S. festinus* adults fed on *P. vulgaris* plants infected by *Agrobacterium tumefaciens*-mediated delivery of infectious GRBV clone NY175 for a 2-, 4-, 6-, or 12-day AAP and then for 48 h on alfalfa for gut clearing. Cohorts of 8 to 10 specimens were used for a 4-day inoculation access period on excised *P. vulgaris* or *V. vinifera* leaves.
[c]Total number of petioles or leaf samples testing positive for GRBV over the total number tested by PCR across experiments. Percentage of GRBV-infected petioles or leaf samples.
[d]Number of petioles or leaf samples testing positive for GRBV over the total number tested by PCR. nt = not tested.

Table A3-4. Detection of grapevine red blotch virus (GRBV) in dissected organs (gut and head with salivary glands) of *Spissistilus festinus* following virus acquisition on infected *Phaseolus vulgaris.*

	GRBV detection[a]	
AAP[b]	Gut[c]	Head[c]
0	0/4	0/10
2	0/9	0/9
4	6/9	0/9
6	8/11	8/11
8	1/1	1/1

[a]*S. festinus* fed for 0-8 days on *P. vulgaris* infected by *Agrobacterium tumefaciens*-mediated delivery of infectious GRBV clone NY175 and then on alfalfa for 48 hrs.
[b]Acquisition access period (AAP) on GRBV-infected snap beans in days.
[c]Number of insect guts (Gut) and heads with salivary glands (Head) that tested positive for GRBV over the total number of insect tissue tested in PCR or qPCR.

***GRBV is transmitted from* Vitis vinifera *to* V. vinifera *by* Spissistilus festinus**

This experiment was designed to verify the capacity of our *S. festinus* population to transmit GRBV from *V. vinifera* 'Cabernet franc' naturally infected with GRBV isolate NY358 from phylogenetic clade 2 to healthy *V. vinifera* 'Cabernet franc' (**Figure A3-1**). The GRBV titer in infected *V. vinifera* was high with qPCR Ct values ranging from 15 to 26. After a 15-day AAP on grapevine and 2 days on alfalfa, GRBV was detected by PCR in a limited number of excised grapevine leaves (10%, 4 of 39) after a 4-day IAP with transmission observed in two of six independent experiments. As controls, none of the excised, healthy grapevine leaves exposed to *S. festinus* specimens from the colony (0%, 0 of 17) and none of the *S. festinus* specimens from the colony that were exposed to excised, healthy grapevine leaves (0%, 0 of 19) tested positive for GRBV in PCR. Concurrently, the same experimental conditions using excised trifoliates of snap bean plants as recipient tissue resulted in a higher rate of GRBV detection (67%, two of three). These results documented the capacity of our *S. festinus* colony to transmit GRBV from grapevine to grapevine under laboratory conditions.

***A 10-day AAP is required for detection of the virus in the head and salivary glands of* Spissistilus festinus *after feeding on* V. vinifera**

To test if transmission of GRBV by *S. festinus* is circulative, replicated time-course experiments were performed with *S. festinus* adults exposed to GRBV-infected *V. vinifera*. The virus presence was tested in dissected insect organs over time by PCR or qPCR. A minimum of a 5-day AAP was required before the virus could be detected in the gut with the majority (68%, 17 of 25) of insects testing positive for GRBV after a 5-day AAP versus none (0%, 0 of 80) after a 1- to 4-day AAP (**Table A3-5**). GRBV

was not detected in the hemolymph before an 8-day AAP (in two of eight insects, 25%). A 10-day AAP was required for virus detection in the head with salivary glands (from 8 of 40 insects, 20%; **Table A3-5**). As negative controls, none of the insects that were exposed to healthy *V. vinifera* (controls) ever tested positive for GRBV in the gut (0%, 0 of 14), hemolymph (0%, 0 of 8), or head with salivary glands (0%, 0 of 13). These results supported a circulative model for transmission with 10 days on infected *V. vinifera* required for GRBV to be detectable in heads with salivary glands of *S. festinus*, exclusive of a 2-day feeding on alfalfa.

Table A3-5. Detection of grapevine red blotch virus (GRBV) in dissected organs (guts and heads with salivary glands) and collected hemolymph of *Spissistilus festinus* after virus acquisition on naturally infected *Vitis vinifera.*

AAP[a]	Experiment 1[b]			Experiment 2[b]			Experiment 3[b]			Total		
	Gut[c]	Hem	Head	Gut	Hem	Head	Gut	Hem	Head	Gut	Hem	Head
0	0/7	0/12	0/13	0/4	0/5	0/3	0/13	0/9	0/11	0/24	0/26	0/27
1	nt	nt	Nt	0/8	0/8	0/8	0/10	0/10	0/10	0/18	0/18	0/18
2	0/10	nt	0/10	0/8	0/8	0/8	0/10	0/10	0/10	0/28	0/18	0/28
4	0/10	nt	0/10	nt	nt	nt	nt	nt	nt	0/10	nt	0/10
5	7/10	nt	0/5	3/8	0/8	0/8	7/7	0/7	0/7	17/25	0/15	0/20
8	9/11	nt	0/15	3/8	0/8	0/8	nt	nt	nt	11/19	2/8	0/23
10	13/15	nt	1/15	3/8	4/8	3/8	12/17	0/17	4/17	28/40	4/25	8/40
12	6/7	nt	1/8	4/8	2/8	1/8	nt	nt	nt	10/15	2/8	2/16
15	nt	nt	nt	5/8	2/8	1/8	21/22	5/22	10/22	26/30	7/30	11/30

[a]Acquisition access period (AAP) measured on GRBV-infected grapevines in days.
[b]*S. festinus* were allowed to feed on *V. vinifera* for 0 to 15 days and then on alfalfa for 48 h.
[c]Number of insect organs (guts [Gut] and heads with salivary glands [Head]) and hemolymph (Hem) that tested positive for GRBV over the total number of insect tissues tested in PCR or quantitative PCR. nt = not tested.

The titer of GRBV in individual* S. festinus *decreases after insect removal from GRBV-infected plants

To quantify the amount of GRBV in *S. festinus* over time, insects were exposed to an infected *V. vinifera* for 2 weeks and then transferred to alfalfa, a nonhost of GRBV, for the remainder of the experiment. Insects were then collected on alfalfa at 3-day intervals and tested for GRBV by qPCR. A decreasing GRBV titer was obtained over time when *S. festinus* individuals that ingested GRBV as nymphs or adults were no longer exposed to a GRBV-infected plant, as shown by the absolute quantification method using a dilution series of known GRBV DNA derived from a GRBV monomer maintained in *E. coli* as heterologous reference (**Figure A3-2A**). Low and steady levels of virus accumulated in insects at 9 (T3) and 12 (T4) days post-transfer on alfalfa. The relative quantification method based on an internal reference (*S. festinus* 18S) confirmed these results with the ratio of GRBV-Rep threshold cycle number (Ct) values compared with *S. festinus*-18S Ct values remaining steady or increasing over time, in particular at 9 (T3) and 12 (T4) days post transfer on alfalfa (**Figure A3-2B**). An increasing ratio of GRBV-Rep Ct values over *S. festinus*-18S Ct values revealed a decreasing virus titer over time. These results are consistent with a nonpropagative transmission mode of GRBV by *S. festinus*.

A substantial higher virus titer in *S. festinus* that ingested GRBV as nymphs compared with adults, in particular at early time points, e.g., T0 (0 days on alfalfa after ingestion) and T1 (3 days on alfalfa after ingestion), suggested that nymphs may ingest more GRBV than adults and be more efficient phloem feeders compared with adults. At later time points, e.g., T3 (9 days on alfalfa after ingestion) and T4 (12 days on alfalfa

after ingestion), no statistical difference in virus titer between adults and nymphs was found (**Figure A3-2B**). The fact that significantly more GRBV was overall detected at T0 and T1 compared with T2, T3, and T4, in particular for nymphs (**Figure A3-2**), suggested a limited fraction of the virus that is ingested is capable of crossing the insect gut epithelium.

A comparative analysis of the GRBV titer in the dissected organs and collected hemolymph after a 15-day AAP revealed that mean ΔΔCt values were significantly different depending on the insect tissue type ($F_{2,34} = 24.366$, $Pr = 2.721e\text{-}07$, $P < 0.01$, $R2 = 0.589$), in particular, between heads with salivary glands in comparison with guts ($P < 0.0001$) and hemolymph ($P = 0.000242$; **Figure A3-3A**). A higher virus titer was obtained in the gut relative to the hemolymph, but the difference was not statistically significant ($P = 0.941109$; **Figure A3-3A**). In addition, a two-way ANOVA did not support a significant interaction between insect tissue type and AAP (5, 10, and 15 days; $P = 0.70169$), although both tissue type ($P = 1.42e\text{-}09$) and AAP ($P = 0.00057$) significantly influenced virus titer. These results are consistent with a higher GRBV titer in gut and hemolymph compared with heads with salivary glands, suggesting an inefficient transit of the virus from hemolymph to heads with salivary glands.

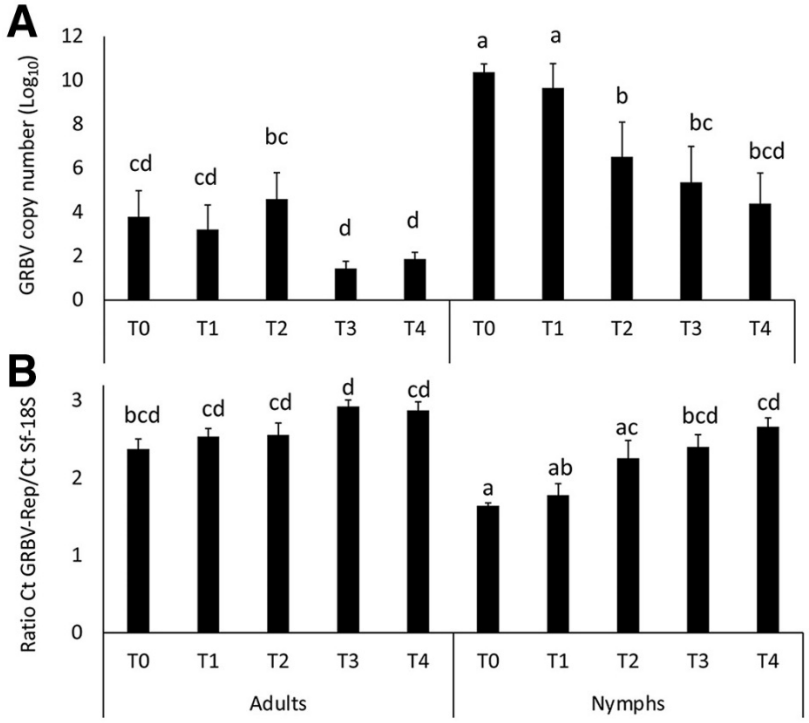

Figure A3-2. Quantitative determination of grapevine red blotch virus (GRBV) in *Spissistilus festinus* after exposure to infected *Vitis vinifera* for 15 days and transfer to alfalfa for 0 to 12 days. (**A**) Comparative copy number of GRBV in *S. festinus* adults exposed to GRBV-infected grapevines for 2 weeks as adults (left five bars) or as fourth or fifth instars (right four to five bars). (**B**) Ratios of quantitative PCR Ct values of GRBV RepA over *S. festinus* 18S in *S. festinus* adults exposed to infected grapevines for 2 weeks as adults (left five bars) or as fourth or fifth instars (right four or five bars). Individual adult insects (n = 6 for each time point) were tested for GRBV by quantitative PCR immediately (T0) and at 3 (T1), 6 (T2), 9 (T3), and 12 (T4) days posttransfer on alfalfa. Vertical axes are set on logarithmic scales. Error bars indicate standard error of the mean. Letters above standard error bars indicate significant groups as determined by analysis of variance in the software R.

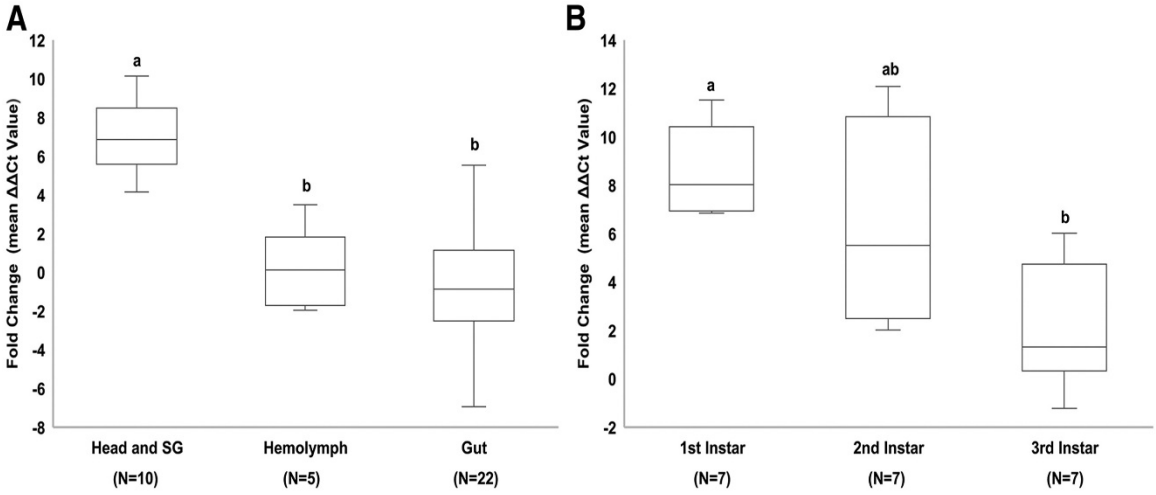

Figure A3-3. Quantification of grapevine red blotch virus (GRBV) by quantitative PCR in (**A**) dissected organs (head and salivary glands [SG], gut) and collected hemolymph of *Spissistilus festinus* individuals exposed to grapevine red blotch virus (GRBV)-infected *Vitis vinifera* for 15 days and then for 48 h on alfalfa. (**B**) *S. festinus* adults derived from first, second, and third instars that emerged on GRBV-infected grapevines, were separately transferred to *Phaseolus vulgaris* trifoliates and tested as adults. Vertical axes are set on logarithmic scales. Error bars indicate standard error of the mean. Lowercase lettering for significant differences between mean $\Delta\Delta Ct$ values as determined by Tukey's honestly significant difference test ($P < 0.05$) are indicated above standard error bars.

GRBV persists in* S. festinus *through molting

To test trans-stadial transmission, insects were exposed to GRBV-infected *V. vinifera* and emerging first, second, and third instars were transferred to excised snap bean trifoliates as soon as they developed. Adults from the three instars were collected on excised snap bean trifoliates and tested for GRBV by qPCR. All adults derived from first (100%, seven of seven), second (100%, seven of seven), and third (100%, seven of seven) instars tested positive for GRBV. As expected, none (0%, 0 of 10) of the adults derived from first, second, and third instars from the colony maintained on alfalfa which were transferred to excised, healthy snap bean trifoliates, tested positive for GRBV in qPCR. At the time of adult insect collection, none of the excised snap bean petioles and trifoliates onto which first instars fed (zero of three) were positive for GRBV in qPCR and only a few petioles and trifoliates onto which second (one of three) and third (one of three) instars fed, were positive for GRBV. These results showed virus transmission by nymphs from infected grapevines to excised snap bean trifoliates. They also suggested primary virus acquisition on infected grapevines at the nymphal stage, with limited acquisition from infected snap bean tissue in these experiments because all the adults (100%, 21 of 21) carried the virus at the end of the experiment. This rate of virus detection in insects is in contrast to the 77 to 81% of the insects feeding on infected snap bean plants that are routinely found to contain the virus (cf. results of transmission assays from *P. vulgaris* to *P. vulgaris* and from *P. vulgaris* to *V. vinifera*).

The virus titer increased with older instars, as shown by ANOVA ($F_{2,14} = 7.9479$, $P < 0.01$, $R2 = 0.4648$) and illustrated by decreasing mean ΔΔCt values with older instars (**Figure A3-3B**). Statistically significant differences between mean ΔΔCt

values were obtained between adults from the first and third instars (**Figure A3-3B**). This result suggested that the time of exposure to GRBV-infected grapevines increased the virus titer in nymphs and subsequently in the adult progeny because the feeding time and capacity to acquire the virus was less limited for third instars relative to first instars. Together, these findings were consistent with trans-stadial transmission of GRBV through *S. festinus* molting, in agreement with circulative transmission of viruses in the family *Geminiviridae* (Czosnek et al. 2017; Gray et al. 2014; Nault 1997; Whitfield et al. 2015).

GRBV is not seed transmitted

To assess seed transmissibility of GRBV, seedlings derived from GRBV-infected *V. vinifera* and GRBV-infected snap beans were tested for the presence of GRBV by multiplex PCR. None of the seedlings from GRBV-infected 'Cabernet franc' (0%, 0 of 200) and Cabernet Sauvignon (0%, 0 of 79) had detectable GRBV, as shown by PCR. Similarly, all the seedlings (0%, 0 of 16) derived from pods of GRBV-infected snap bean plants tested negative for GRBV in PCR. As controls, none of the seedlings from healthy 'Cabernet franc' (0%, 0 of 96) or healthy snap beans (0%, 0 of 37) showed GRBV amplicons in PCR. These findings were consistent with a lack of vertical transmission of GRBV via seeds, as expected by analogy with most geminiviruses (Czosnek et al. 2017; Fiallo-Olivé et al. 2018; Rojas et al. 2018).

DISCUSSION

We obtained evidence consistent with circulative, nonpropagative transmission of GRBV by *S. festinus*. This means the virus initially moves from the insect mouthparts into the food canal after feeding on the phloem sap of a GRBV-infected plant. Then, GRBV egresses from the gut epithelium of *S. festinus* into the hemolymph and finally is acquired into the salivary gland epithelium to be transmitted to a plant via the salivary canal. During this process, there is no evidence of viral replication in the vector, a phenomenon only reported for one geminivirus (He et al. 2020). This mode of transmission is a first for a grapevine virus (Fuchs 2020). Indeed, the other grapevine viruses for which the transmission mode is characterized are transmitted semi-persistently. These include nepoviruses transmitted by ectoparasitic nematodes (Andret-Link et al. 2017), ampeloviruses and vitiviruses transmitted by mealybugs and soft scale insects (Herrbach et al. 2017), and trichoviruses transmitted by eriophyid mites (Kunugi et al. 2000; Malagnini et al. 2016).

We found clear evidence of an extended AAP for GRBV in comparison with other members of the family *Geminiviridae*, as determined by the time needed for the virus to be detectable in the salivary glands. In the literature, it has taken 4 h to up to 3 days of AAP for viruses to be detected in the salivary glands of their respective insect vector (Briddon et al. 1996; Czosnek et al. 2017; Ryckebusch et al. 2020; Simons and Coe 1958; Soto and Gilbertson 2003). For example, beet curly top virus from the genus Curtovirus is detected in the salivary glands of the beet leafhopper, *Circulifer tenellus* within 4 to 7 h of AAP (Soto and Gilbertson 2003). A similar short AAP is described for tomato yellow leaf curl virus from the genus *Begomovirus* in the whitefly, *Bemisia*

tabaci (Czosnek et al. 2017). Also, an 8-h AAP is sufficient to identify tomato pseudocurly top virus (TPCTV) from the genus *Topocuvirus* in the treehopper, *Micrutalis malleifera* (Briddon et al. 1996; Simons and Coe 1958) and a 3-day AAP to detect alfalfa leaf curl virus from the genus *Capulavirus* in heads with salivary glands of the cowpea aphid, *Aphis craccivora* (Ryckebusch et al. 2020). GRBV is unique among geminiviruses as it requires the vector to have a 10-day AAP on V. vinifera (**Table A3-5**) and a 6-day AAP on *P. vulgaris* (**Table A3-4**) to reach the salivary glands of *S. festinus*.

At least a 10-day AAP on a GRBV-infected *V. vinifera* was necessary for the virus to be detectable in the salivary glands (**Table A3-5**). Knowing that grapevine is not a preferred feeding host of *S. festinus* (Preto et al. 2018a, b), it is reasonable to assume only occasional insect feeding during a 10-day exposure to *V. vinifera*. Indeed, our observations indicate less efficient feeding of *S. festinus* on *V. vinifera* compared with feeding on *P. vulgaris* (Hoyle et al. unpublished data). The observed sporadic feeding behavior of *S. festinus* on *V. vinifera*, a host that does not support reproduction (Preto et al. 2018a), may limit the potency of *S. festinus* at acquiring and transmitting the virus.

At the tissue level, transmission of GRBV may be impeded because the virus crosses the gut-hemolymph barrier of *S. festinus* with low efficiency, which is consistent with some of our results (**Figure A3-2A**). GRBV was detectable by PCR in only 21% (13 of 63) of the hemolymph samples and 24% (21 of 86) of the heads with salivary glands, but in 75% (64 of 85) of the gut samples tested after 10 to 15 days AAP on infected *V. vinifera* (**Table A3-5**). A virus presence in the hemolymph of a few adults

(21%) compared with its presence in the gut of the majority of adults (75%) provides support for the hypothesized poor transit from the gut to the hemolymph, although a similar virus titer was found in the hemolymph and gut (**Figure A3-3A**). In addition, a limited efficiency of GRBV crossing the hemolymph-salivary gland barrier is also plausible. The fact that a significantly higher virus titer was found in the hemolymph compared with the heads and salivary glands supports this hypothesis (**Figure A3-3A**). Monitoring the localization of GRBV within *S. festinus* tissue after acquisition, for instance via fluorescence in situ hybridization (Di Mattia et al. 2020; Kliot et al. 2014), could be carried out to address tissue tropism in the vector. In addition, in light of the discovery that tomato yellow leaf curl virus replicates in the salivary glands of *B. tabaci* by recruiting essential whitefly factors to establish a replication-competent environment (He et al. 2020), it would be interesting to expand our findings and determine GRBV titer over time in dissected salivary glands rather than whole *S. festinus* specimens after virus acquisition. Furthermore, a nonstructural helper component could potentially be involved in *S. festinus*-mediated transmission of GRBV, as described for the related nanovirus, faba bean necrotic stunt (Di Mattia et al. 2020). This hypothesis could be investigated with regard to the level of GRBV accumulation in gut cells. This work would lead to a better understanding of the behavior of GRBV within its vector.

The natural and heritable variation of vectoring *S. festinus* is unknown at this time, although two distinct insect genotypes have been described in Cieniewicz et al. (2020). For other insect vectors, vectoring capacity, including aspects of acquisition, trans-cytosis and inoculation, is highly variable within a species (Linak et al. 2020; Yang et al. 2008). In addition, within a vector species, insect genes control virus

movement across the different barriers to transmission such as the gut, the hemolymph, and the salivary glands (Dietzgen et al. 2016; Gray et al. 2014; Heck 2018; Qin et al. 2018). This is an important area for future research on GRBV–*S. festinus* interactions.

The atypically long AAP suggests that *S. festinus* is not an efficient vector of GRBV. This hypothesis agrees with the low *S. festinus*-mediated transmission rate (10%, 4 of 39) obtained from infected to healthy *V. vinifera* when excised leaves were used as virus recipient tissue. Interestingly, this transmission rate is consistent with the low annual rate of increase (1 to 2%) of newly infected vines in some vineyards in California (Cieniewicz et al. 2017a, 2019). Higher annual rates of increase of newly infected vines (4 to 16%) were observed in some vineyards where many spatially aggregated GRBV-infected vines are in close proximity, suggesting a high virus supply in a conglomerate formation can substantially contribute to higher rates of virus spread in some vineyards (Cieniewicz et al. 2017a; Dalton et al. 2019), particularly in areas where *S. festinus* is abundant (Cieniewicz et al. 2019). The low *V. vinifera* to *V. vinifera* transmission rate obtained in only two of six independent transmission assays underscores the need to characterize additional transmission biology attributes such as the latency period, i.e., time between acquisition and transmission, and retention period, i.e., time during which *S. festinus* remains viruliferous after acquisition. Nonetheless, despite low transmission rates from *V. vinifera* to *V. vinifera*, we documented transmission of GRBV isolates NY175 and NY358 from phylogenetic clades 1 and 2, respectively. This result is consistent with the transmission of isolates from both phylogenetic clades observed in vineyards of Northern California (Cieniewicz et al. 2019).

In agreement with the detection of GRBV in salivary glands of *S. festinus* no sooner than 10 days postexposure to infected *V. vinifera* followed by 2 days on alfalfa, we never confidently achieved transmission from *V. vinifera* to *V. vinifera* with shorter than 10-day AAPs. Moreover, given that *S. festinus* causes severe necrosis at feeding sites and girdling of petioles and shoots on *V. vinifera* (Bahder et al. 2016a, b; Preto et al. 2018a, b, 2019; Wilson et al. 2020), minimizing feeding damage for optimal virus acquisition and inoculation, as well as efficient virus multiplication in the inoculated grape tissue exposed to *S. festinus*, was a constant challenge in this study. For this reason, cohorts of no more than six to eight *S. festinus* specimens were deposited on excised *V. vinifera* leaves. Transferring more insects created physical damage to grapevine tissue such that the inoculation step of the transmission assay, and consequently, virus replication, might have been suboptimal. Similarly, the IAP was limited to 4 days for GRBV to be detectable after inoculation in plant tissue with minimal feeding damage. Furthermore, a high number of *S. festinus* was required for every transmission assay from *V. vinifera* to *V. vinifera* because the mortality rate (approximately 10 to 20% within 48 h of exposure) was substantial on this nonpreferred host. Consequently, approximately 30 to 40 specimens were routinely required to feed on GRBV-infected *V. vinifera* to obtain six to eight insects for transfer onto a single excised *V. vinifera* leaf.

Differences in AAP between two plant hosts of GRBV, i.e., *P. vulgaris* (6 days) and *V. vinifera* (10 days), merits further investigations. Such differences could result from a differential virus titer and/or a distinct feeding behavior of *S. festinus* on the two plant species. Interestingly, a similar GRBV titer was observed in infected *P. vulgaris*

and *V. vinifera* with qPCR Ct values ranging from 18 to 23 and 15 to 26, respectively, dismissing the role of virus supply in determining AAP. However, a higher feeding propensity of *S. festinus* is repeatedly observed on *P. vulgaris* compared with *V. vinifera* (Hoyle et al. unpublished data). These results are consistent with leguminous plants in the family Fabaceae as preferred feeding and reproductive hosts of *S. festinus* (Beyer et al. 2017; Bick et al. 2020; Kron and Sisterson 2020; Preto et al. 2018b; Wilson et al. 2020). The differential behavior of the vector on distinct plant species likely explains a markedly higher *S. festinus*-mediated GRBV transmission rate on excised *V. vinifera* leaves when the virus is acquired from infected snap bean plants (100%, 5 of 5) compared with infected grapevines (10%, 4 of 39). Similarly, when GRBV is acquired from infected *V. vinifera*, the transmission rate is higher on excised snap bean trifoliates (67%, 2 of 3) than excised grapevine leaves (10%, 4 of 39). These results underscore a clear feeding preference of *S. festinus* for snap bean compared with *V. vinifera*. In the green peach aphid*, Myzus persicae,* host plants influence transmission rates of the circulative potato leafroll virus, by modulating levels of cysteine proteases in the aphid midgut, the site of virus acquisition. *M. persicae* reared on turnip, a nonhost of potato leafroll virus, transmit the virus less efficiently as compared with individuals from the same clonal lineage reared on *Physalis floridana*, a host of both the aphid and the virus (Pinheiro et al. 2016).

The discovery of *P. vulgaris* as an alternative herbaceous pseudo-systemic host of GRBV greatly facilitated the development of a reliable transmission assay and the study of transmission attributes. The fact that GRBV moves 4 to 5 cm away from the inoculation site on the petiole after pinprick delivery of a virus infectious clone in *A.*

tumefaciens provided an opportunity to direct the feeding of *S. festinus* on infected tissue. This technical advancement enabled us to confidently ascertain *S. festinus* as a vector of GRBV, consistent with an earlier report (Bahder et al. 2016a). It also provided a solid means to characterize important steps of transmission, such as the AAP and trans-cytosis through the insect's hemocoel. A reliable transmission assay of GRBV on *P. vulgaris*, an alternative host of the virus, required ≤8 to 10 *S. festinus* specimens per excised leaf. This was critical to minimize feeding damage while sustaining optimal virus acquisition and inoculation. A transmission assay of GRBV from snap bean to snap bean was key for subsequently being able to investigate transmission parameters on *V. vinifera*, the natural host of GRBV.

The use of excised leaves was also paramount to assess attributes of GRBV transmission biology. A similar approach was described for the transmission of *Candidatus* Liberibacter asiaticus by *Diaphorina citri* (Ammar et al. 2018). Detached leaves enabled us to restrict the tissue onto which viruliferous *S. festinus* specimens fed and potentially released the virus, thus increasing opportunities to detect minute amounts of virus after inoculation and virus replication. In addition to snap bean, tomato and *N. benthamiana* were identified in this study as experimental herbaceous hosts of GRBV. This was not actually surprising, as these plant species are commonly described as hosts of viruses in the family *Geminiviridae* (Paplomatas et al. 1994; Rajabu et al. 2018; Sun et al. 2020). Nonetheless, these two hosts did not sustain systemic GRBV infection or serve as feeding or reproductive hosts to *S. festinus*, and thus were not further used in this study.

GRBV is the second treehopper-vectored geminivirus for which transmission is characterized. TPCTV was the first account of geminivirus transmitted by a treehopper, and the vector *M. malleifera* was the first membracid reported as vector of a plant virus (Simons and Coe 1958). *M. malleifera* nymphs retain TPCTV after molting, with adults and nymphs vectoring the virus (Ammar and Nault 2002). Our results on the trans-stadial transmission of GRBV by *S. festinus* and on the capacity of *S. festinus* adults and nymphs at transmitting GRBV agree with these findings.

We documented that GRBV is not seed-transmitted, making it similar to most other viruses in the family *Geminiviridae* (Czosnek et al. 2017; Fiallo-Olivé et al. 2018; Rojas et al. 2018). This result has profound implications for disease epidemiology, as the contribution of *S. festinus* and other potential vector candidates of GRBV to the spatiotemporal increase of infected vines in the vineyard becomes more relevant. Here we confirm *S. festinus* as a vector of GRBV under laboratory conditions. This treehopper species is also suspected as a vector of epidemiological relevance in vineyards, which is based on a statistically significant association between the co-occurrence and covariation between the spatial distribution of GRBV-infected vines and *S. festinus* that have ingested GRBV (Cieniewicz et al. 2018a, b); a relative association between differential GRBV spread dynamics and the abundance of *S. festinus* populations; a higher rate of spread that occurred with higher *S. festinus* populations (Cieniewicz et al. 2019); and a lack of spread in vineyards where *S. festinus* is not found (Cieniewicz et al. 2019; Reynard et al. 2018). Expanding on these observations and on the results of this study will lead to the assessment of the epidemiological role of *S. festinus* in the vineyard.

In addition to *S. festinus*, surveys of insects in diseased vineyards identified *Colladonus reductus* (Cicadellidae), *Osbornellus borealis* (Cicadellidae), and a *Melanoliarus* sp. (Cixiidae) as vector candidates. This planthopper and the two leafhopper species were identified based on a relatively high ingestion rate of GRBV by specimens caught on sticky cards in diseased vineyards that had documented spread (Cieniewicz et al. 2018a, b, 2019). The capacity of the two cicadellids and the cixiid species, and of other potential vector candidates, at transmitting GRBV needs to be addressed to determine if insects other than *S. festinus* can vector this virus. Earlier, the Virginia creeper leafhopper (*Erythroneura ziczac*) was reported to transmit GRBV from infected to healthy vines under greenhouse conditions (Poojari et al. 2013). However, epidemiological studies in California did not support this finding, as none of the *E. ziczac* specimens captured in diseased vineyards with documented spread had ingested GRBV over several growing seasons (Cieniewicz et al. 2018a, 2019). In addition, an independent study failed to confirm the vector capacity of this leafhopper species (Bahder et al. 2016a).

In summary, we confirmed *S. festinus* as a vector of GRBV under laboratory conditions and provided empirical evidence of circulative, nonpropagative transmission with a distinct AAP of 10 days on *V. vinifera*, the natural perennial host, and of 6 days on *P. vulgaris*, an alternative herbaceous host. The identification of snap bean as a pseudo-systemic host and its use in conjunction with infectious clones of GRBV and colony-reared *S. festinus* sets a solid foundation to further investigate transmission biology attributes and virus–vector–host relationships.

REFERENCES

Adiputra, J., Kesoju, S.R. and Naidu, R.A. 2018. The relative occurrence of *Grapevine leafroll-associated virus 3* and *Grapevine red blotch virus* in Washington state vineyards. Plant Disease 102:2129-2135.

Al Rwahnih, M., Rowhani, A., Golino, D., Islas, C., Preece, J. and Sudarshana, M.R. 2015a. Detection and genetic diversity of Grapevine red blotch-associated virus isolates in table grape accessions in the National Clonal Germplasm Repository in California. Canadian Journal of Plant Pathology 37:130-135.

Al Rwahnih, M., Rowhani, A. and Golino, D. 2015b. First report of Grapevine red blotch-associated virus in archival grapevine material from Sonoma County, California. Plant Disease 99:895.

Al Rwahnih, M., Dave, A., Anderson, M., Rowhani, A., Uyemoto, J.K., and Sudarshana, M.R. 2013. Association of a DNA virus with grapevines affected by red blotch disease in California. Phytopathology 10:1069-1076.

Ammar, E.D. and Nault, L.R. 2002. Virus transmission by leafhoppers, planthoppers and treehoppers (Auchenorrhyncha, Homoptera). Advances in Botanical Research 36:141-167.

Ammar, E.D., Hall, D.G., Hosseinzadeh, S. and Heck, M. 2018. The quest for a non-vector psyllid: Natural variation in acquisition and transmission of the huanglongbing pathogen '*Candidatus* Liberibacter asiaticus' by Asian citrus psyllid isofemale lines. PLoS One https://doi.org/10.1371/journal.pone.0195804.

Andret-Link, P., Marmonier, A., Belval, L., Hleibieh, K., Ritzenthaler, C. and Demangeat, G. 2017. Ectoparasitic nematode vectors of grapevine viruses. In: Grapevine Viruses: Molecular Biology, Diagnostics and Management. Meng, B., Martelli, G.P., Golino, D.A. and Fuchs, M.F (eds). Springer Verlag, pp. 505-530.

Bahder, B.W., Zalom, F.G. and Sudarshana, M.R. 2016a. An evaluation of the flora adjacent to wine grape vineyards for the presence of alternative host plants of Grapevine red blotch-associated virus. Plant Disease 100:1571-1574.

Bahder, B., Zalom, F., Jayanth, M. and Sudarshana, M. 2016b. Phylogeny of geminivirus coat protein sequences and digital PCR aid in identifying *Spissistilus festinus* (Say) as a vector of Grapevine red blotch-associated virus. Phytopathology 106:1223-1230.

Beyer, B.A., Srinivasan, R., Roberts, P.M. and Abney, M.R. 2017. Biology and management of the threecornered alfalfa hooper (Hemitera: Membracidae) in alfalfa, soybean, and peanut. Journal of Integrated Pest Management 8:1-10.

Bick, E.N., Kron, C.R. and Zalom, F.G. 2020. Timing the implementation of cultural practices for *Spissistilus festinus* (Hemiptera: Membracidae) in California vineyards using a stage-structure degree-day model. Journal of Economic Entomology https://doi.org/10.1093/jee/toaa165

Blanco-Ulate, B. Hopfer H., Figueroa-Balderas, R., Ye, Z., Rivero, R.M., Albacete, A., Pérez-Alfocea, F., Koyama, R., Anderson, M.M., Smith, R.J., Ebeler, S.E. and Cantu, D. 2017. Red blotch disease alters grape berry development and

metabolism by interfering with the transcriptional and hormonal regulation of ripening. Journal f Experimental Botany 68:1225-1238.

Buchs, N., Braga-Lagache, S., Uldry, A-C., Brodard, J., Debonnneville, C., Reynard, J-S. and Heller, M. 2018. Absolute quantification of *Grapevine red blotch virus* in grapevine leaf and petiole tissues by proteomics. Frontiers in Plant Science https://doi.org/10.3389/fpls.2018.01735

Briddon, R.W., Bewdford, I.D., Tsai, J.H., and Markham, P.G. 1996. Analysis of the nucleotide sequence of the treehopper-transmitted geminivirus, tomato pseudo-curly top virus, suggests a recombinant origin. Virology 219:387-394.

Cauduro Giaradello, R., Rich, V., Smith, R.J., Brennenman, C., Heymann, H., and Oberhoslter, A. 2020. The impact of grapevine red blotch disease on *Vitis vinifera* L. Chardonnay grape and wine composition and sensory attributes over three seasons. Journal of the Science of Food and Agriculture 100:1436-1447.

Cieniewicz, E., Poplaski, V., Brunelli, M., Dombroswkie, J. and Fuchs, M. 2020. Two distinct *Spissistilus festinus* genotypes in the United States revealed by phylogenetic and morphological analyses. Insects 11:80; doi:10.3390/insects11020080.

Cieniewicz, E., Flasco, M., Brunelli, M., Onwumelu, A., Wise, A. and Fuchs, M. 2019. Differential spread of grapevine red blotch virus in California and New York vineyards. Phytobiomes Journal 3:203-211.

Cieniewicz, E., Pethybridge S.J., Loeb, G.M., Perry, K.L. and Fuchs, M. 2018a. Insights into the ecology of grapevine red blotch virus in a diseased vineyard. Phytopathology 108:94-102.

Cieniewicz, E., Thompson, J.R., McLane, H., Perry, K.L., Dangl, G.S., Corbett, Q., Martinson, T., Wise, A., Wallis, A., O'Connell, J., Dunst, R., Cox, K. and Fuchs, M. 2018b. Prevalence and diversity of grabloviruses in free-living *Vitis* spp. Plant Disease 102:2308-2316.

Cieniewicz, E.J., Perry, K.L. and Fuchs, M. 2017a. Grapevine red blotch virus: Molecular biology of the virus and management of the disease. In: Grapevine Viruses: Molecular Biology, Diagnostics and Management. Meng, B., Martelli, G.P., Golino, D.A. and Fuchs, M.F (eds). Springer Verlag, pp. 303-314.

Cieniewicz, E., Pethybridge S., Gorny, A., Madden, L., Perry, K.L., McLane, H. and Fuchs, M. 2017b. Spatiotemporal spread of grapevine red blotch-associated virus in a California vineyard. Virus Research 230:59-62.

Czosnek, H., Hariton-Shalev, A., Sobol, I., Gorovits, R. and Ghanim, M. 2017. The incredible journey of begomoviruses in their whitefly vector. Viruses 9:273, doi:10.3390/v910027

Dalton, D.T., Hilton, R.J., Kaiser, C., Daane, K.M., Sudarshana, M.R., Vo, J., Zalom, F.G., Buser, J.Z. and Walton, V.M. 2019. Spatial associations of vines infected with grapevine red blotch virus in Oregon vineyards. Plant Disease 103:1507-1514.

Di Mattia, J., Vernerey, M-S, Yvon, M., Pirolles, E., Villegas, M., Gaafar, Y, Ziebell, H., Michalakis, Y., Zeddam, J-L. and Blanc, S. 2020. Route of a multipartite nanovirus across the body of its aphid vector. Journal of Virology 94:9 e01998-19.

Dietzgen, R.G., Mann, K.S. and Jonson, K.N. 2016. Plant virus-insect vector interactions: current and potential future research directions. Viruses 8:303, https://doi.org/10.3390/v8110303

Ellis, R.H., Hong, T.D. and Roberts, E.H. 1983. A note on the development of a practical procedure for promoting the germination of dormant seed of grape *(Vitis* spp.). *Vitis* 22:211-219.

Fall, M.L., Xu, D., Lemoyene, P., Ben Moussa, I.E., Beaulieu C. and Carisse, O. 2020. A diverse virome of leafroll-infected grapevine unveiled by dsRNA sequencing. Viruses 12:1142, https://doi.org/10.3390/v12101142

Fiallo-Olivé, E., Zerbini, F.M., Briddon, R.W., Martin, D.P., Navas-Castillo, J., Roumagnac, P. and Varsani, A. 2018. *Geminiviridae*. https://talk.ictvonline.org/ictv-reports/ictv_online_report/ssdna-viruses/w/geminiviridae

Fuchs, M. 2020. Grapevine viruses: A multitude of diverse species with simple but poorly adopted management solutions in the vineyard. Journal of Plant Pathology, 102:643-653.

Gasperin-Bulbarela J., Licea-Navarro AF, Pino-Villar, C., Hernández-Martínez, R. and Carillo-Tripp, J. 2019. First report of grapevine red blotch virus in Mexico. Plant Disease 103:381.

Goodin, M.M., Zaitlin, D., Naidu, R.A and Lommel, S.A. 2008. *Nicotiana benthamiana*: Its history and future as a model for plant-pathogen interactions. Molecular Plant-Microbe Interactions 21:1015-1026.

Guo, T.W., Vimalesvaran, D., Thompson, J.R., Perry, K.L. and Krenz, B. 2015. Subcellular localization of grapevine red blotch-associated virus ORFs V2 and V3. Virus Genes 51:156-158.

Gray, S., Cilia, M. and Ghanim, M. 2014. Circulative, nonpropagative virus transmission: An orchestra of virus-, insect- and plant-derived instruments. Advances in Virus Research 89:141-199.

He, Y-Z., Wang, Y-M., Yin T-Y., Fiallo-Olivé, E., Liu, Y-Q., Hanley-Bowdoin, L., Wang X-W. 2020. A plant DNA virus replicates in the salivary glands of its insect vector via recruitment of host DNA synthesis machinery. Proceedings of the National Academy of Sciences of the United States of America www.pnas.org/cgi/doi/10.1073/pnas.1820132117

Heck, M. 2018. Insect transmission of plant pathogens: s systems biology perspective. mSystems 3:e00168-17. https://doi.org/10.1128/mSystems.00168-17.

Herrbach, E., Alliaume, A., Prator, C.A., Daane, K.M., Cooper, M.L. and Almeida R.P.P. 2017. Vector transmission of grapevine leafroll-associated viruses. In: Grapevine Viruses: Molecular Biology, Diagnostics and Management. Meng, B., Martelli, G.P., Golino, D.A. and Fuchs, M.F (eds). Springer Verlag, pp. 483-504.

Hoffmann, M., Talton, W., Nita, M., Jones, T., Al Rwahnih, M., Sudarshana, M.R., and Almeyda, C. 2020. First report of grapevine red blotch virus, the causal agent of grapevine red blotch diseases in *Vitis vinifera* in North Carolina. Plant Disease https://doi.org/10.1094/PDIS-07-19-1539-PDN

Kliot, A., Kontsedalov, S., Lebedev, G., Brumin, M., Cathrin, P.B., Marubayashi, J.M., Skaljac, M., Belausiv, E., Czosneck, H. and Ghanim, M. 2014. Fluorescence *in situ* hybridization (FISH) for the localization of viruses and endosymbiotic bacteria in plant and insect tissues. Journal of Visualized Experiments 84:e51030.

Krenz, B., Thompson, J., McLane, H., Fuchs, M. and Perry, K.L. 2014. Grapevine red blotch-associated virus is widespread in the United States. Phytopathology 102:1232-1240.

Krenz, B., Thompson, J., Fuchs, M. and Perry, P. 2012. Complete genome sequence of a new circular DNA virus from grapevine. Journal of Virology 86:7715.

Kron, C.R. and Sisterson, M.S. 2020. Identification of nonhost cover crops of the three-cornered alfalfa hopper (*Spissistilus festinus*). Amercian Journal of Enology and Viticulture 7:175-180.

Kunugi, Y., Asari, S., Terai, Y. and Shinkai, A. 2000. Studies on the Grapevine berry inner necrosis virus disease. 2. Transmission of Grapevine berry inner necrosis virus by the grape erineum mite *Colomerus vitis* in Yamanashi. Bull. Yamanashi Fruit Tree Experiment Station 10:57-63.

Kurtural, K., Martínez-Lüscher, J., Brillante, L., Yu, R., Plank, C., Smith R.J., Cooper, M. and Oberholster, A. 2019. Grapevine red blotch virus may reduce carbon translocation leading to impaired grape berry ripening. Journal of Agriculture and Food Chemistry 67:2437-2448.

Lim, S. Igori, D., Zhao, F. and Moon, J.S. 2016. First report of Grapevine red blotch-associated virus on grapevine in Korea. Plant Disease 100:1957.

Linak, J.A., Jacobson, A.L., Sit, T.L. and Kennedy, G.G. 2020. Relationships of virus titers and transmission rates among sympatric and allopatric virus isolates and thrips vectors support local adaptation. Scientific Reports 10:7649, https://doi.org/10/1038/s41598-020-64507-1.

Luna, F., Debat, H., Moyano, S., Zavallo, D., Asurmendi, S. and Gomes-Talquenca, S. 2019. First report of grapevine red blotch virus infecting grapevine in Argentina. Journal of Plant Pathology 101:1239.

Malagnini, V., de Lillo, E., Saldarelli, P., Beber, R., Duso, C., Raiola, A., Zanotelli, L., Valenzano, D., Giampetruzzi, A., Morelli, M., Ratti, C., Causin, R. and Gualandri, V. 2016. Transmission of grapevine Pinot gris virus by *Colomerus vitis* (Acari: Eriophyidae) to grapevine. Archives of Virology 161:2595-2599.

Marwal, A., Kumar, R., Paul Khurana, S.M. and Gaur, R.K. 2019. Complete nucleotide sequence of a new geminivirus isolated from *Vitis vinifera* in India: a symptomless host of grapevine red blotch virus. Virus Disease 30:106-111.

Meisch, M.V. and Randolph N.M. 1965. Life-history studies and rearing techniques for the three-cornered alfalfa hopper. Journal of Economical Entomology 58:1057-1059.

Nault, L.R. 1997. Arthropod transmission of plant viruses: a new synthesis. Annals of the Entomological Society of America 90:521-541.

Paplomatas, E.L., Patel, V.P., Hou Y-M., Noueiry, A.O. and Gilbertson R.L. 1994. Molecular characterization of a new sap-transmissible bipartite genome geminivirus infecting tomatoes in Mexico. Phytopathology 84:1215-1224.

Perry, K.L., McLane, H., Hyder, M.Z., Dangl, G.S., Thompson, J.R. and Fuchs, M.F. 2016. Grapevine red blotch-associated virus is present in free-living *Vitis* sp. proximal to cultivated grapevines. Phytopathology 106:663-670.

Pinheiro, P.V., Ghanim, M., Alexander, M.M., Rebelo, A.R., Santos, R.S., Orsburn, B.C., Gray, S. and Cilia, M. 2016. Host plants indirectly influence plant virus transmission by altering gut cysteine protease activity of aphid vectors. Molecular and cellular Proteomics https://doi.org/10.1074/mcp.M116.063495

Poojari, S., Alabi, O.J., Fofanov, V. and Naidu, R.A. 2013. A leafhopper-transmissible DNA virus with evolutionary lineage in the family *Geminiviridae* implicated in grapevine redleaf disease by next-generation. PLOS One 6:e64194.

Poojari, S., Lowery, D.T., Rott, M., Schmidt A.M. and Úrbez-Torres, J.R. 2017. Incidence, distribution and genetic diversity of grapevine red blotch virus in British Columbia. Canadian Journal of Plant Pathology 39:201-211.

Preto, C.R., Bahder, B.W., Bick, E.N., Sudarshana, M.R. and Zalom, F.G. 2019. Seasonal dynamics of *Spissistilus festinus* (Hemiptera: Membracidae) in a Californian vineyard. Journal of Economical Entomology 112:1138-1144.

Preto, C.R., Sudarshana, M.R., Bollinger, M.L. and Zalom, F.G. 2018a. *Vitis vinifera* (Vitales: Vitaceae) as a reproductive host of *Spissistilus festinus* (Hemiptera: Membracidae). Journal of Insect Science 18:1-7.

Preto, C.R., Sudarshana, M.R. and Zalom, F.G. 2018b. Feeding and reproductive hosts of *Spissistilus festinus* (Say) (Hemiptera: Membracidae) in a Californian vineyard. Journal of Economical Entomology 111:2531-2535.

Qin, F., Liu W., Wu, N., Zhang, Z., Zhou X., Wang, X. 2018. Invasion of midgut epithelial cells by a persistently transmitted virus is mediated by sugar transporter 6 in its insect vector. PLoS Pathogens 14(7):e1007201. https://doi.org/10.1371/journal.ppat.1007201

Rajabu, C.A., Kennedy, G.G., Ndunguru, J., Ateka, E.M., Tairo, F., Hanley-Bowdoin, L., Ascencio-Ibáñez, J.T. 2018. Lanai: A small, fast growing tpomato variety is an excellent model system for studying geminiviruses. Journal of Virological Methods 256:89-99.

Reynard, J.S., Brodard, J, Dubuis, N., Zufferey, V., Schumpp, O., Schaerer, S. and Gugerli, P. 2018. Grapevine red blotch virus: Absence in Swiss vineyards and analysis of potential detrimental effect on viticultural performance. Plant Disease 102:651-655.

Ricketts, K.D., Gomez, M.I., Fuchs, M.F., Martinson, T.E., Smith, R.J., Cooper, M.L. and Wise, A., 2017. Mitigating the economic impact of Grapevine Red Blotch: Optimizing disease management strategies in U.S. vineyards. American Journal of Enology and Viticulture 68:127-135.

Rojas, M.R., Macedo, M.A., Maliano, M.R., Soto-Aguilar, M., Souza, J.O., Briddon, R.W., Kenyon, L., Rivera-Bustamante, R.F. Zerbini, F.M., Adkins, S., Legg, J.P., Kvarnheden, A., Wintermantel W.M., Sudarshana, M.R., Peterschmitt, M., Lapidot, M., Martin, D.P., Moriones, E., Inoue-Nagata, A.K. and Gilbertson, R.L. 2018. World management of geminiviruses. Annual Review of Phytopathology 56:637-677.

Ryckebusch, F., Sauvion, N., Granier, M., Roumagnac, P. and Peterschmitt, M. 2020. Alfalfa leaf curl virus is transmitted by *Aphis craccivora* in a highly specific circulative manner. Virology 546:98-108.

Schoelz, J., Volenberg, D., Adhab, M., Fang, Z., Klassen, V., Spinka, C. and Al Rwahnih, M. 2020. A survey of viruses found in grapevine cultivars grown in Missouri, American Journal of Enology and Viticulture, doi: 10.5344/ajev.2020.20043

Setiono, F.J., Chatterjee, D., Fuchs, M., Perry, K.L. and Thompson, J.R. 2018. The distribution and ability to detect grapevine red blotch virus in its host depends on time of sampling and tissue type. Plant Disease 102:2187-2193.

Simons J.H., and Coe, D.M. 1958. Transmission of pseudo-curly top virus in Florida by a treehopper. Virology 6:43-487.

Soltani, N., Hu, R., Lockwood, D., Perry, K. and Hajimorad, M. 2020. A survey of nine major viruses of grapevines in Tennessee vineyards. Plant Heath Progress https://doi.org/10.1094/PHP-03-20-0018-RS

Soto, M.J. and Gilbertson, R.L. 2003. Distribution and rate of movement of the curtovirus *Beet mild curly top virus* (family *Geminiviridae*) in the beet leafhopper. Phytopathology 93:478-484.

Sudarshana, M.R., Perry, K.L. and Fuchs, M.F. 2015. Grapevine red blotch-associated virus, an emerging threat to the grapevine industry. Phytopathology 105:1026-1032.

Sun, S., Hu, Y., Jiang, G., Tian, Y., Ding, M., Yu, C., Zhou, X. and Qian, Y. 2020. Molecular characterization and genomic function of grapevine geminivirus A. Frontiers in Microbiology https://doi.org/10.3389/fmicb.2020.555194

Vargas-Asencio, J., Liou, H., Perry, K.L. and Thompson, J.R. 2019. Evidence for the splicing of grablovirus transcripts revelas a putative novel open reading frame. Journal of General Virology 100:709-720.

Varsani, A., Roumagnac, P., Fuchs, M., Navas-Castillo, J., Moriones, E., Idris, I., Briddon, R.W. Rivera-Bustamante, R., Murilo Zerbini, F. and Martin, D.P. 2017. *Capulavirus* and *Grablovirus*: Two new genera in the family *Geminiviridae.* Archives of Virology 162:1819-1831.

Wilson, H., Yazdani, A. and Daane, K. 2020. Influence of riparian habitat and ground covers on threecornered alfalfa hopper (Hemiptera: Membracidae) populations in vineyards. Journal of Economic Entomology https://doi.org/10.1093/jee/toaa151

Whitfield, A.E., Falk, B.W. and Rothenberg, D. 2015. Insect vector-mediated transmission of plant viruses. Virology 479-480:278-289.

Xiao, H., Kim, W.S. and Meng, B. 2015. Comparison and improvement of methodologies for isolation of quality RNA from diverse woody plant species and utilization in detection of viral pathogens. Virology Journal 12:171.

Yang, X., Thannhauser, T.W., Burrows, M., Cox-Foster, D., Gildow, F.E. and Gray, S.M. 2008. Coupling genetics and proteomics to identify aphid proteins associated with vector-specific transmission of polerovirus (*Luteoviridae*). Journal of Virology 82:291-299.

APPENDIX IV

LACK OF VERTICAL TRANSMISSION OF GRAPEVINE RED BLOTCH VIRUS BY SPISSISTILUS FESTINUS AND DIFFERENTIAL SEX-ASSOCIATED HORIZONTAL TRANSMISSION*

ABSTRACT

Grapevine red blotch is an emerging disease that threatens vineyard productions in North America. Grapevine red blotch virus (GRBV, species *Grablovirus vitis*, genus *Grablovirus*, family *Geminiviridae*), the causal agent of red blotch disease, is transmitted by *Spissistilus festinus* (Hemiptera: Membracidae) in a circulative, nonpropagative mode. To gain new insight into GRBV-*S. festinus* interactions, we delved into vertical transmission and documented a lack of transovarial transmission. In addition, we investigated *S. festinus* sex differences in horizontal transmission of GRBV by creating small arenas with 30 detached trifoliates of common bean, an experimental host of GRBV and a preferred feeding host of *S. festinus*. Tracking the movement of viruliferous males, females, or a combination of the two sexes over two weeks in replicated experiments demonstrated that male *S. festinus* dispersed more than females with specimens of both sexes predominantly spatially grouping together on trifoliates surrounding the trifoliate onto which they were released upon. These behaviors resulted in a greater rate of GRBV transmission by *S. festinus* males (17%, 20 of 120) than females (4%, 5 of 120) or mixed-sex cohorts (9%, 17 of 180). In arenas with aviruliferous *S. festinus* and a single or four (hotspot) GRBV-infected out of 30 trifoliates, a higher GRBV transmission rate by males was confirmed in both single

infection (50%, 30 of 60) and hotspot infection (83%, 50 of 60) arenas than by females in single infection (35%, 21 of 60) and hotspot infection (67%, 40 of 60) arenas. These findings highlighted sex-associated differences in the transmission of GRBV by *S. festinus* and a positive correlation between the initial virus incidence and the rate of transmission. Finally, secondary spread of GRBV resulted primarily from *S. festinus* dispersal by walking or jumping. Together, these unique GRBV transmission features support the need to characterize dispersal behaviors of *S. festinus* in vineyard ecosystems.

---

*This appendix has been published: Hoyle, V., Schultz, M., McGinnity Schneider, E., Roy, B., and Fuchs, M. (2024). Lack of vertical transmission of grapevine red blotch virus by *Spissistilus festinus* and differential sex-associated horizontal transmission. Submitted.

INTRODUCTION

Vineyards in North America have been devastated by the emergence of grapevine red blotch disease in the early 2010's (Krenz et al. 2023). Grapevine red blotch virus (GRBV, species *Grablovirus vitis,* genus *Grablovirus*, family *Geminiviridae*), the causal agent of the disease (Yepes et al. 2018), delays fruit ripening, reduces fruit quality, and alters wine composition and sensory attributes (Cieniewicz et al. 2017; Rumbaugh et al. 2021). The resulting impacts can vary annually but can affect vineyard profitability with up to $68,548 losses per hectare over the 25-year lifespan of a vineyard (Ricketts et al. 2017). Isolates of GRBV belong to two phylogenetic clades for which the genetic diversity can differ by up to 9.1% (Krenz et al. 2014).

GRBV is transmitted by the three-cornered alfalfa hopper, *Spissistilus festinus* [Say, 1830] (Hemiptera: Membracidae) (Flasco et al. 2021; Hoyle et al. 2022). GRBV isolates of phylogenetic clades 1 and 2 are transmissible by *S. festinus* (Flasco et al. 2021). Transmission of GRBV by this treehopper species is circulative, non-propagative, meaning that GRBV must transit through the body of *S. festinus* and reach the salivary glands before it can be transmitted upon feeding through the salivary glands within the stylets (Flasco et al. 2021). It is unknown whether GRBV can transverse other barriers beyond the gut and salivary glands within the bodies of *S. festinus* such as the reproductive organs.

Spissistilus festinus is a dimorphic insect, with distinct male and female forms and five instar development stages (Jordan 1952). Within vineyard ecosystems, more males than females have been observed among *S. festinus* populations (Jordan 1952, Hoyle et al. 2024), but it is not known how a differential sex-related abundance of

specimens may impact the spread of GRBV. In addition, males have been demonstrated to have a greater flight capacity in comparison with females under laboratory conditions (Antolínez et al. 2023). It is not known if such a differential dispersal behavior of *S. festinus* males and females affects the spread of GRBV.

The aim of our study was to assess the vertical transmission of GRBV by *S. festinus* and characterize sex-associated differences in horizontal transmission using dispersal and behavioral assays combined with transmission assays with either aviruliferous or viruliferous *S. festinus* specimens. By analogy with other geminiviruses (Czosnek et al. 2017; Fiallo-Olivé et al. 2018; Rojas et al. 2018), we hypothesized a lack of transovarial GRBV transmission. We also hypothesized that *S. festinus* male dispersal results in a greater rate of GRBV transmission, particularly from a disease focus. Here, we present the results of replicated transmission assays and discuss our findings with regard to red blotch disease management strategies.

MATERIALS AND METHODS

Plant materials

Healthy *Phaseolus vulgaris* 'Hystyle' and *Medicago sativa* were used as a rearing host of *S. festinus*. Alfalfa plants were also used as gut clearing material and snap bean plants were used as recipient plant material in transmission assays. Snap bean and alfalfa plants were set and maintained in greenhouses and later moved to controlled environmental chambers with the following growing conditions: 25°C, 16 h:8 h light:dark photoperiod, and 80% relative humidity.

Snap bean inoculations with GRBV

Snap bean trifoliates were used as GRBV donor material in transmission assays. Trifoliates were derived from two to three-week old *P. vulgaris* 'Hystyle' plants that were pinprick-inoculated in 2-cm intervals along the stems and petioles and three to four inches from the soil line. Inoculations were performed using sterile dissecting needles swabbed with recombinant *Agrobacterium tumefaciens* harboring an infectious clone of GRBV isolate NY175 (phylogenetic clade 1) or isolate NY358 (phylogenetic clade 2), as described by Flasco et al. (2021) and Hoyle et al. (2023).

Spissistilus festinus

S. festinus specimens were derived from a colony population collected in Yolo, San Joaquin, and Fresno Counties in California. They were maintained in a controlled environmental chamber at Cornell AgriTech in Geneva, NY with rearing conditions set at 26°C, 14:10 light/dark photoperiod, and 70-80% relative humidity (Meisch & Randolph 1965). Individual insects were sexed upon molt into adulthood and separated into males and females before use in experimentation.

Transovarial transmission assays

Cohorts of either newly emerged adult *S. festinus* males, females, or a combination of the two were exposed to GRBV-inoculated bean plants for 1-2 weeks. *P. vulgaris* stems not inoculated with GRBV were wrapped with cheese cloth to encourage feeding by *S. festinus* on GRBV-inoculated areas (Hoyle et al. 2024). Next, cohorts were moved to alfalfa and joined by cohorts of the opposite sex, not previously

exposed to GRBV-inoculated plants for 2 weeks to reproduce and lay eggs. After two weeks, adults were removed, and alfalfa plants were monitored for the emergence of progeny. First instars through newly emerged adult *S. festinus* were moved in cohorts of 5-7 onto uninoculated bean trifoliates enclosed in a clear polypropylene 950-ml container (cat. no. PK32T, Fabri-Kal, Kalamazoo, MI) sealed with a polypropylene donut lid carrying a nylon screen (BugDorm 5002, MegaView Science, Taichung, Taiwan) for possible GRBV transmission. After each molt, nymphs were moved to new healthy detached trifoliates. All *S. festinus* were collected after their final molt and tested for GRBV by multiplex PCR and qPCR. Similarly, bean trifoliates were collected for each treatment and tested for GRBV by multiplex PCR and qPCR (**Figure A4-1**).

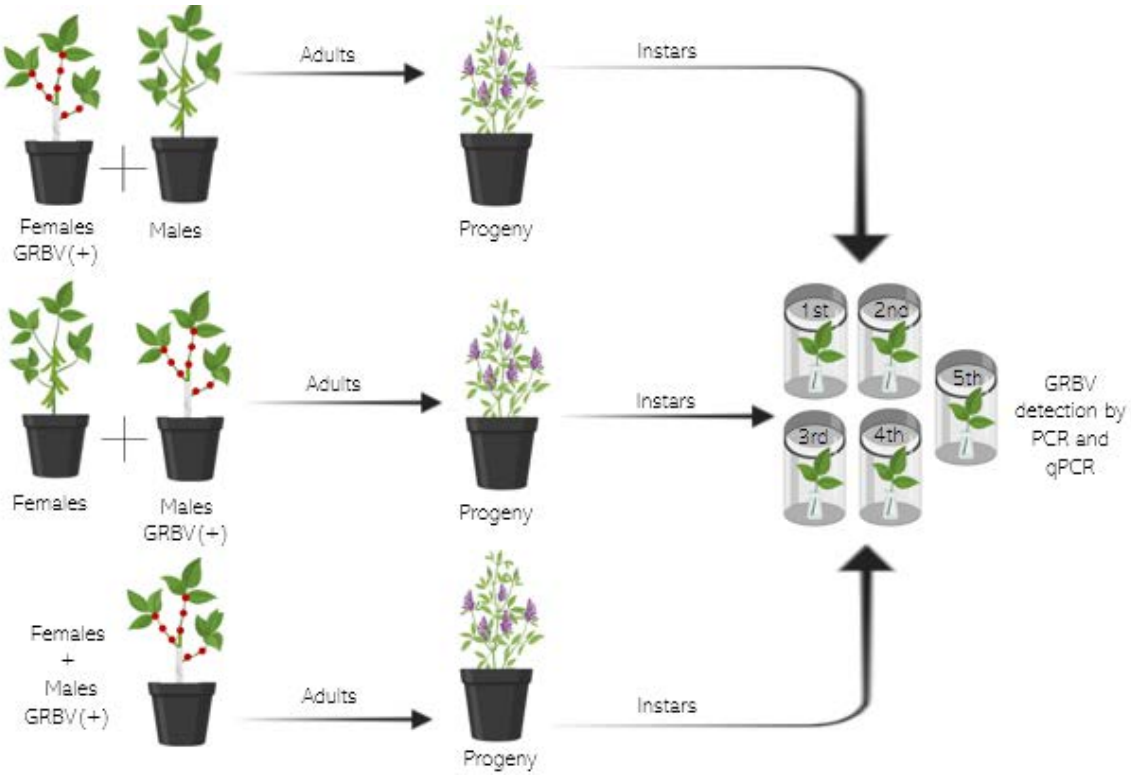

Figure A4-1 Schematic representation of the transovarial transmission assays performed in this study. Assays used GRBV-inoculated or uninoculated *Phaseolus vulgaris* as donor material and healthy, detached trifoliates from *P. vulgaris* as recipient material. Healthy, excised trifoliates were placed in parafilm-covered 2-mL collection vials filled with sterile water that were inserted into sealed polypropylene containers for exposure to nymphal progeny from all instar stages of *Spissistilus festinus*. Recipient tissues were collected for GRBV testing and replaced at every molt. The artwork was produced using the program BioRender (Toronto, ON, Canada).

Dispersal assays of viruliferous *S. festinus* and impact on GRBV transmission

Cohorts of either newly emerged adult *S. festinus* males, females, or a combination of the two were exposed to GRBV-inoculated bean plants. *P. vulgaris* stems not inoculated with GRBV were wrapped with cheese cloth to encourage feeding by *S. festinus* on GRBV-inoculated areas. *S. festinus* fed on inoculated *P. vulgaris* tissue in cages (BugDorm 6E610 Insect Rearing Cage, MegaView Science, Taichung, Taiwan) separated by treatment type for 7-10 days. Arenas were set up containing 30 healthy excised bean trifoliates in parafilmed water vials spaced out in 2–3-inch intervals, with 10 trifoliates per row (**Figure A4-2**). Ten GRBV-exposed *S. festinus* pertaining to each treatment type (all males, all females, or 50/50 mix) were moved on alfalfa enclosed in a clear polypropylene 950-ml container (cat. no. PK32T, Fabri-Kal, Kalamazoo, MI) sealed with a polypropylene donut lid carrying a nylon screen (BugDorm 5002, MegaView Science, Taichung, Taiwan) for 48-hours for a gut clearing period before being released on the first trifoliate of the second row in their arenas (**Figure A4-2**). To test for GRBV acquisition, subsets of 3-5 *S. festinus* per treatment were collected following the 48-hours on alfalfa and dissected for heads with salivary glands and guts to be tested for GRBV by multiplex PCR. Experiments were replicated 2-3 times.

Following a 48-hour gut clearing on alfalfa, *S. festinus* from their respective treatments were released into arenas (BugDorm-4S4590DH Specimen Handling Cage, MegaView Science, Taichung, Taiwan) containing 30 healthy bean trifoliates in water, spaced 2-3 inches apart. Dispersal behavior of *S. festinus* was recorded twice daily, in the morning and afternoon, for two weeks, noting the presence and absence of *S.*

festinus on each trifoliate and on the cage, accounting for all ten *S. festinus* in each cage at each time point. Following a two-week period of behavioral movement tracking, *S. festinus* and plant tissues were collected and tested for GRBV using multiplex PCR and qPCR (**Figure A4-2**). Plant tissues were processed into the petiole, leaf-petiole junction, and leaf midrib prior to nucleic acid extraction to account for differential hopper feeding behavior. Experiments were replicated 3-4 times. A trifoliate was considered positive if one or more tissue types, i.e., petiole, leaf-petiole junction, and/or midrib, tested positive for GRBV by multiplex PCR.

Dispersal assays of aviruliferous *S. festinus* and impact on secondary spread of GRBV

Snap bean plants were agroinoculated using the aforementioned approach (Flasco et al. 2021; Hoyle et al. 2024). After at least one week, trifoliates were detached from GRBV-inoculated plants and placed into water vials into an arena (BugDorm-4S4590DH Specimen Handling Cage, MegaView Science, Taichung, Taiwan) containing either a single GRBV-inoculated leaf at the first location of the second row (single infection point) or at three first positions plus the second position of the second row (hotspot) (**Figure A4-3**). All remaining excised leaves in each arena were healthy, uninoculated trifoliates. Ten colony reared, non-viruliferous male or female *S. festinus* were released on the first trifoliate of the second row in their arenas (**Figure A4-3**) and allowed to move around freely feeding for two weeks. Following a two-week period, *S. festinus* and plant tissues were collected and tested for GRBV using multiplex PCR (**Figure 4-3**). Snap bean tissue from the petiole, leaf-petiole junction, and midrib were processed separately. Experiments were replicated 3-4 times.

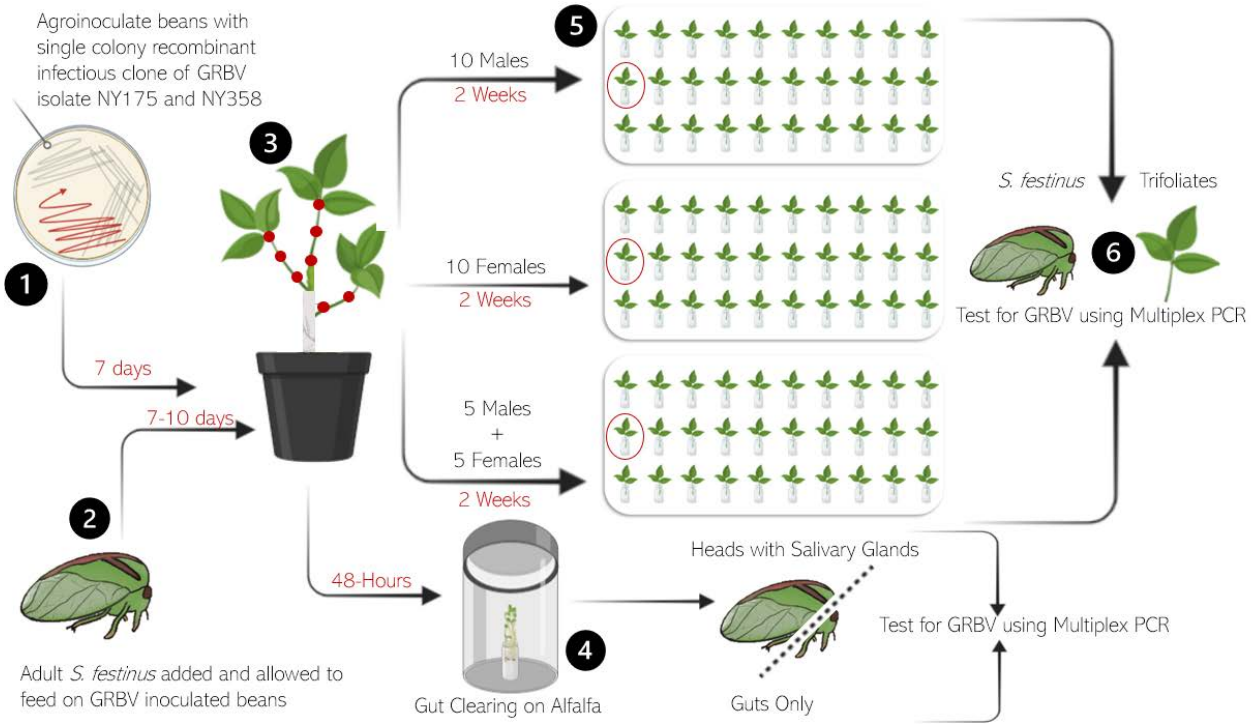

Figure A4-2 Schematic representation of the *Spissistilus festinus* dispersal experiments on detached snap bean trifoliates with (1) GRBV inoculation of snap bean plants, (2) *S. festinus* from the colony being exposed to GRBV inoculated beans, (3) the acquisition access period, (4) the gut clearing of *S. festinus* on alfalfa plantlets to test for acquisition, (5) behavior and movement tracking in separate arenas, and (6) testing of plants and insects for GRBV using multiplex PCR. The artwork was produced using the program BioRender (Toronto, ON, Canada).

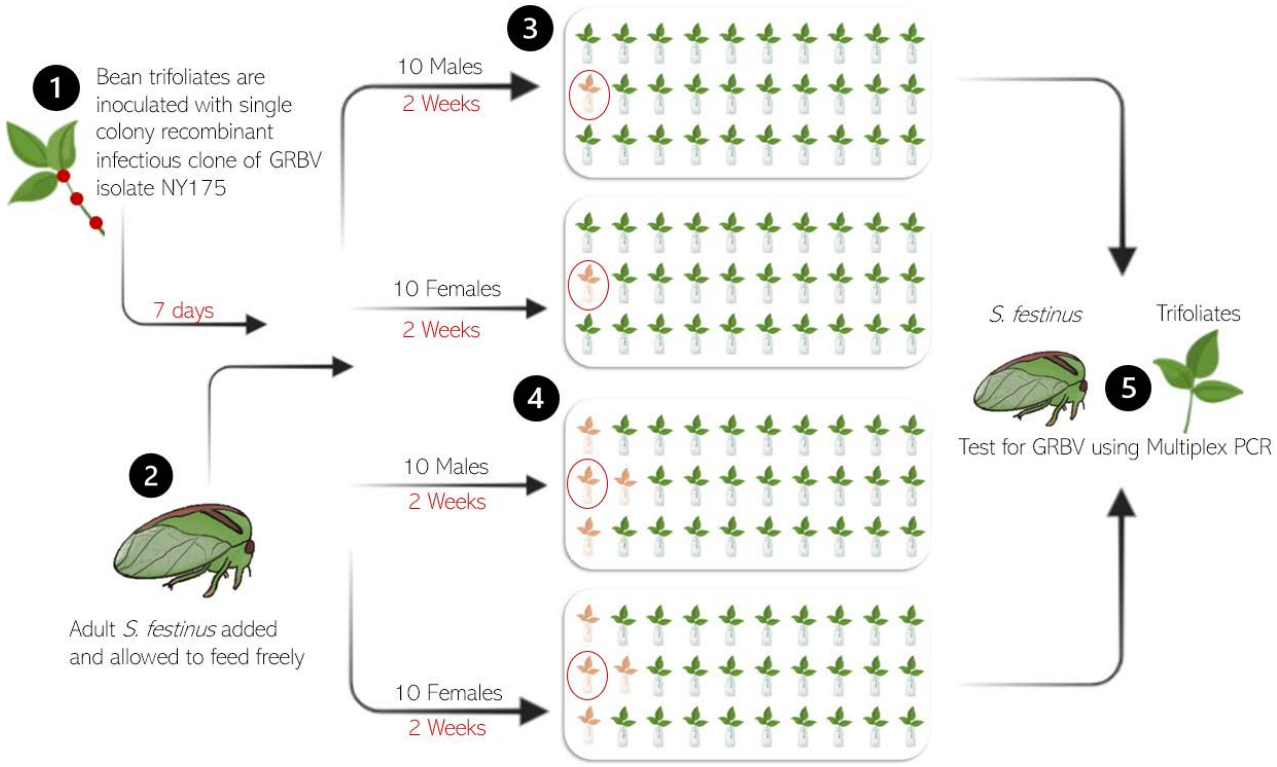

Figure A4-3 Schematic representation of transmission assays with GRBV-infected bean trifoliates and aviruliferous male and female *S. festinus* with (1) GRBV inoculation of snap bean trifoliates, (2) *S. festinus* from the colony released in each arena, (3) arenas where *S. festinus* placed on a single (red circle) or (4) four red trifoliate (hot spot), and (5) testing of plants and insects for GRBV using multiplex PCR. The artwork was produced using the program BioRender (Toronto, ON, Canada).

Feeding and dispersal behaviors of *Spissistilus festinus*

The feeding and movement behaviors of *S. festinus* were observed on bean trifoliates. Feeding behaviors were classified into two categories: probing (gentle feeding of trifoliate tissue with minimal signs of injury to the plant) and girdling (destructive, circular feeding of the trifoliate tissue, often cutting off its vasculature). Dispersal behaviors were classified into three categories: walking (movement long or across bean trifoliates, up and down, or side to side), jumping (bounding motion to move multiple trifoliates away without flight), and flying (movement requiring the extension and fluttering of winds, general upward until coming in contact with the cage).

Nucleic acid isolation, diagnostic GRBV multiplex PCR, and quantification of GRBV Nucleic acid isolation, diagnostic GRBV multiplex PCR, and quantification of GRBV by qPCR

Genomic DNA was isolated from either plant tissue using the MagMAX™-96 A1/ND Isolation Kit (ThermoFisher Scientific, Waltham, MA, USA) or from *S. festinus* using the MagMAX™ DNA Multi-Sample Ultra Kit (ThermoFisher Scientific, Waltham, MA, USA) on a KingFisher™ instrument. To test for GRBV in plant tissue and *S. festinus* by PCR, primer pairs designed in the open reading frame (ORF) coding for the predicted coat protein (CP) gene and replication-associated proteins (RepA) were utilized to amplify the isolated genomic DNA (Flasco et al. 2021). DNA amplicons were visualized by agarose gel electrophoresis and UV illumination following GelRed® staining (Biotium, Fremont, CA, USA).

For the quantification of GRBV in plant samples and *S. festinus* specimens by qPCR, each reaction was conducted in triplicate (three technical replicates) on a Biorad C1000 Touch thermocycler and utilized SYBR® Green reagents (iTaq Bio-Rad Universal SYBR® Green Supermix, Hercules, CA, USA). Testing plant tissue for GRBV by qPCR required primers pREP3v and pREP4v (Setiono et al. 2018) and a primer pair designed in the bean housekeeping gene T197 coding a guanine nucleotide-binding protein beta subunit-like protein (Pereira et al. 2017; Hoyle et al. 2022). Negative controls included sterile water and nucleic acids isolated from healthy excised bean trifoliates. Testing *S. festinus* for GRBV by qPCR required primers pREP3v and pREP4v (Setiono et al. 2018) and *S. festinus* primers Sf18SFor and Sf18SRev (Flasco et al. 2023). Negative controls included sterile water and nucleic acids isolated from *S. festinus* from the colony maintained on *P. vulgaris*.

Statistical Analysis

Statistical analyses were performed on the GRBV titers in plant tissue and insect specimens, according to qPCR Ct values with ANOVA in R Studio. Fold differences in GRBV titer were based on ΔΔCt values. Statistically significant differences between ΔΔCt expression fold change values ($2^{(-\Delta\Delta Ct)}$) in excised leaves and adult *S. festinus* were determined using Tukey's Honestly Significant Difference (HSD) test. To assess dispersal behavior and the pattern of influence for transmission, we utilized ANOVA and linear modeling. The significance level was set at $\alpha = 0.05$ for all statistical analyses performed in this study.

RESULTS

Transovarial transmission of GRBV by *Spissistilus festinus*

The possibility of vertical transmission of GRBV by adult female *S. festinus* to their progeny was assessed by rearing a generation of *S. festinus* nymphs derived from parents exposed to GRBV-infected *P. vulgaris* plants and mated prior to being released on alfalfa, a non-host of GRBV (Flasco et al. 2021), where oviposition occurred (**Figure A4-1**). First through fifth instar *S. festinus* were moved to healthy detached trifoliates to develop to adulthood, with trifoliates collected and replaced between each molt. No adult progeny derived from any of the three treatment types (males, females and 50/50 mix) (0%, 0/195) tested positive for GRBV in PCR or qPCR (**Table A4-1**). As expected, none of the bean trifoliates (0%, 0/324), to which the different instars or treehopper adults were exposed tested positive for GRBV in PCR or qPCR (**Table A4-2**). These results revealed a lack of transovarial GRBV transmission by *S. festinus*.

Table A4-1. Lack of transovarial transmission of GRBV by *Spissistilus festinus*. The number of *S. festinus* progenies from females and males that were exposed to GRBV-infected plants and tested negative for GRBV by multiple PCR or qPCR following transfer to healthy detached bean trifoliates at all developmental stages to live through adulthood is indicated.

Progeny	1st instars	2nd instars	3rd instars	4th instars	5th instars	Adults
Females	0/4	0/5	0/4	0/13	0/17	0/20
Males	0/1	0/5	0/9	0/14	0/19	0/13
50/50 Mix	0/3	0/5	0/13	0/14	0/17	0/19
Total GRBV Positive Progeny	0/8 (0%)	0/15 (0%)	0/26 (0%)	0/41 (0%)	0/53 (0%)	0/52 (0%)

Table A4-2. No detectable GRBV in *Phaseolus vulgaris* trifoliates following feeding by the nymphal progeny of *Spissistilus festinus* females and males that were exposed to GRBV-infected plants across all developmental stages and through adulthood, as shown by multiplex PCR or qPCR with Ct values greater than 35.

		Treatment Origin of Progeny																								
		Males							Females							50/50 Mix										
Age of release			1st	2nd	3rd	4th	5th	Adult		1st	2nd	3rd	4th	5th	Adult		1st	2nd	3rd	4th	5th	Adult				
Total positive *P. vulgaris* trifoliates by developmental stage	1st	0 of 6							1st	0 of 6						1st	0 of 6									
	2nd	0 of 6	0 of 6						2nd	0 of 6	0 of 6					2nd	0 of 6	0 of 6								
	3rd	0 of 6	0 of 6	0 of 6					3rd	0 of 6	0 of 6	0 of 6				3rd	0 of 6	0 of 6	0 of 6							
	4th	0 of 6	0 of 6	0 of 6	0 of 6				4th	0 of 6	0 of 6	0 of 6	0 of 6			4th	0 of 6	0 of 6	0 of 6	0 of 6						
	5th	0 of 6	0 of 6	0 of 6	0 of 6	0 of 6	0 of 6		5th	0 of 6	0 of 6	0 of 6	0 of 6	0 of 6		5th	0 of 6	0 of 6	0 of 6	0 of 6	0 of 6					
	Adult	0 of 3	0 of 3	0 of 3	0 of 3	0 of 3	0 of 3	0 of 3	Adult	0 of 3	0 of 3	0 of 3	0 of 3	0 of 3	0 of 3	Adult	0 of 3	0 of 3	0 of 3	0 of 3	0 of 3	0 of 3				

Dispersal of viruliferous male and female *Spissistilus festinus* males and females and impact on GRBV transmission

Dispersal assays were performed in bean trifoliate arenas with viruliferous *S. festinus* males and females that were exposed to *P. vulgaris* plants infected with a GRBV isolate of phylogenetic clade 1 or 2. After two weeks of release in the arenas, all *S. festinus* specimens and the 30 trifoliates were removed from each arena and tested for GRBV. In inoculated plants that served as virus donor, a slightly lower GRBV titer was observed in clade 1- (Ct values of 23-27) than in clade 2-inoculated (Ct values of 20-23) plants. However, regardless of the GRBV isolate, a greater rate of GRBV transmission was observed in male only cages (17%, 20/120) in comparison with female only cages (4%, 5/120) or mixed cages (9%, 17/180) (**Table A4-3**).

Analyzing the distribution of GRBV-infected bean trifoliates in each arena indicated that most of them were near the single release trifoliate, suggesting a clustering behavior of the viruliferous *S. festinus*, though sometimes infected trifoliates were away from the single release trifoliate (**Figure A4-4**). In arenas with viruliferous *S. festinus* males only, a within row distribution patterns was apparent (**Figure A4-4**).

To determine if clustering behavior of viruliferous *S. festinus* males and females influence horizontal transmission of GRBV, a logistic regression model was conducted to determine if the count of total *S. festinus* present on a trifoliate influenced the likelihood of a trifoliate to test positive for GRBV, across the different treatments. Though the log-odds of infection increased with additional *S. festinus* presence on trifoliates, there was no significant increase in GRBV infection across treatments (p=0.160). However, the inclusion of females did reduce the likelihood of transmission

(p=0.00143). These results demonstrated a difference in transmission among the two sexes of *S. festinus* and warrant further analysis to draw conclusion on whether this influence is behavioral or biological.

Table A4-3. Transmission of GRBV isolates NY358 (phylogenetic clade 2) and NY175 (phylogenetic clade 1) by male and female *Spissistilus festinus*. The total number of *P. vulgaris* trifoliates that tested positive for GRBV by PCR or qPCR following a 10-day AAP and a 2-week IAP on bean trifoliates in arenas of males, females, and a mix of males and females is indicated.

	Males	**Females**	**50/50 Mix**
Clade 2	11/60	2/60	0/60
Clade 1	9/60	3/60	18/120
Total	20/120 (17%)	5/120 (4%)	18/180 (10%)

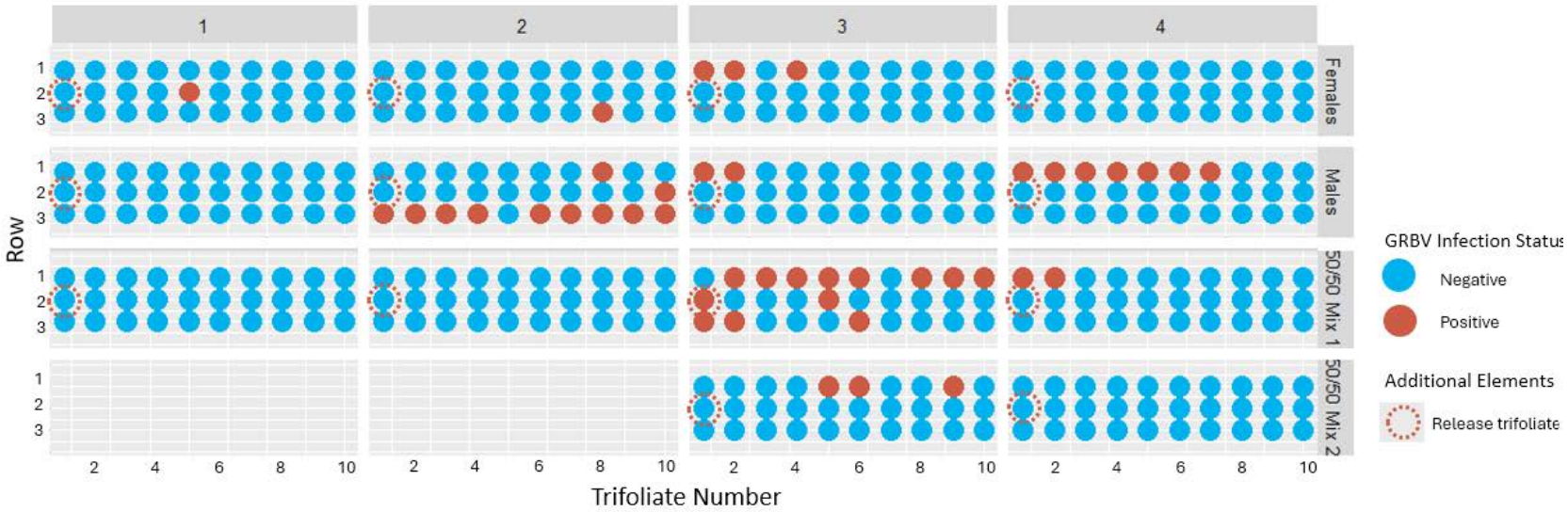

Figure A4-4. Transmission of grapevine red blotch virus (GRBV) from bean trifoliate to bean trifoliate by viruliferous male (n=10), female (n=10), or a mix of male (n=5) and female (n=5) *Spissistilus festinus*, over two-weeks. *S. festinus* were deposited on a single trifoliate (dotted circle) located at one edge of each arena. Data show GRBV-infected trifoliates (red dot) and noninfected trifoliates (blue dots), as determined by PCR.

The dispersal behavior of male and female *Spissistilus festinus*

Dispersal behaviors of *S. festinus* were observed in arenas with either 10 males, 10 females, or a mix of both sexes (n=5+5) in the mornings and afternoons, for two weeks, in four replicated experiments. Male *S. festinus* dispersed more than females, spending more time in the afternoons off trifoliates and on the cages, as illustrated by overall small size dots for males compared with females (**Figure A4-5**). However, even though there was a reduction effect on total male *S. festinus* on trifoliates, this result was not statistically significant (p=0.178). Moreso, specimens of both sexes predominantly grouped together over time on trifoliates surrounding the trifoliate onto which they were released in the arenas, suggesting prevalent spatiotemporal clustering (**Figure A4-6**).

Observations on the behaviors of *S. festinus* over time indicated three distinct types of movement within arenas: walking, jumping and flying (**Figure A4-5, A4-6**). Similarly, two distinct feeding behaviors of *S. festinus* were noticed: probing and girdling (**Table A4-5**). Distinct feeding behaviors were only observed in arenas with mixed males and females with *S. festinus* males girdling the petiole leaf junction (**Figure A4-7A, B**) and *S. festinus* females girdling the petiole above the oviposition site (**Figure A4-7C, D**).

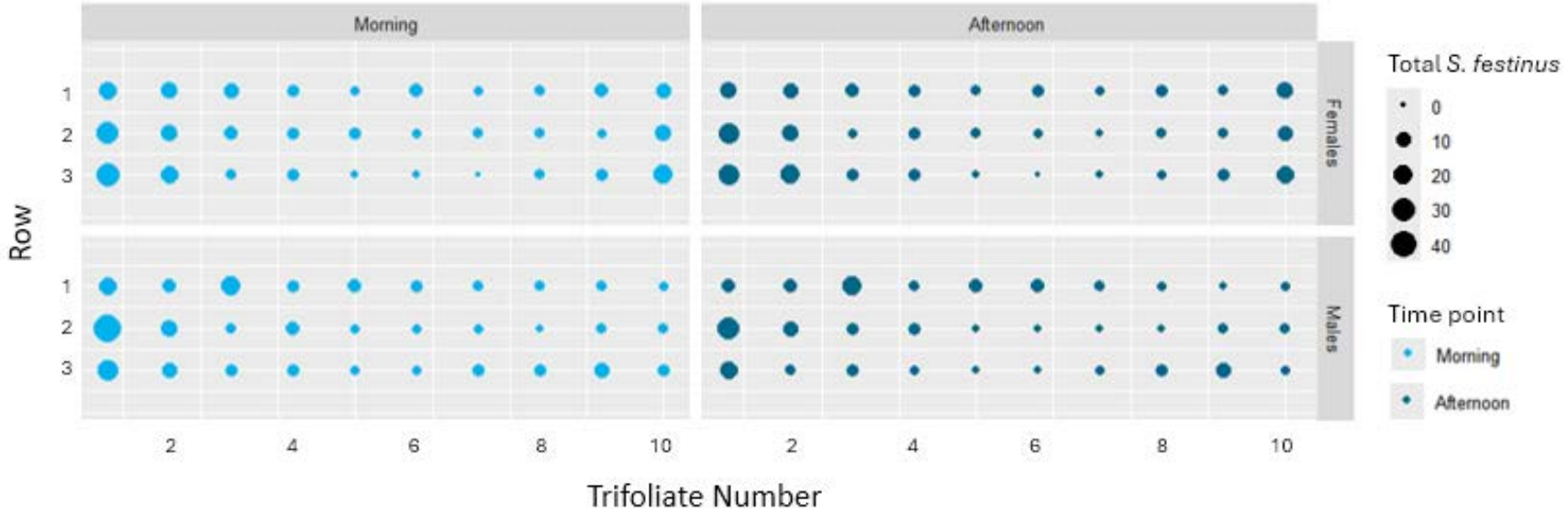

Figure A4-5. The cumulative distribution of *Spissistilus festinus* across 30 *Phaseolus vulgaris* trifoliates in arenas with 10 males, 10 females in the morning or afternoon, over two weeks, from four experimental replicates. The counts of *S. festinus* per trifoliate were derived from the total counts across all four replicates per time point.

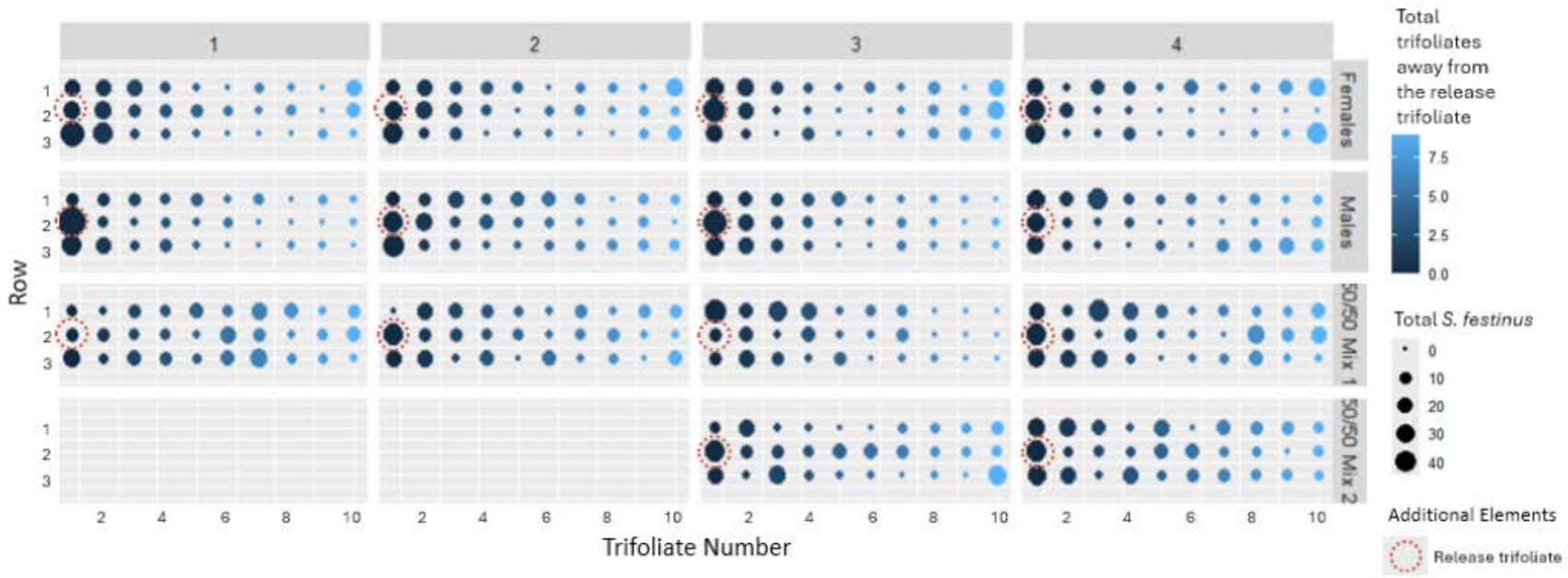

Figure A4-6. The cumulative distribution of *Spissistilus festinus* across 30 *Phaseolus vulgaris* trifoliates in arenas with 10 males, 10 females or mixed males (n=5) and females (n=5) over two weeks, from four experimental replicates (1-4). The darker the circle, the closer the column distance to the release point, and the larger the circle, the greater the total number of *S. festinus* present on that trifoliate over time. The counts of *S. festinus* per trifoliate were derived from a cumulative average of the morning and afternoon counts.

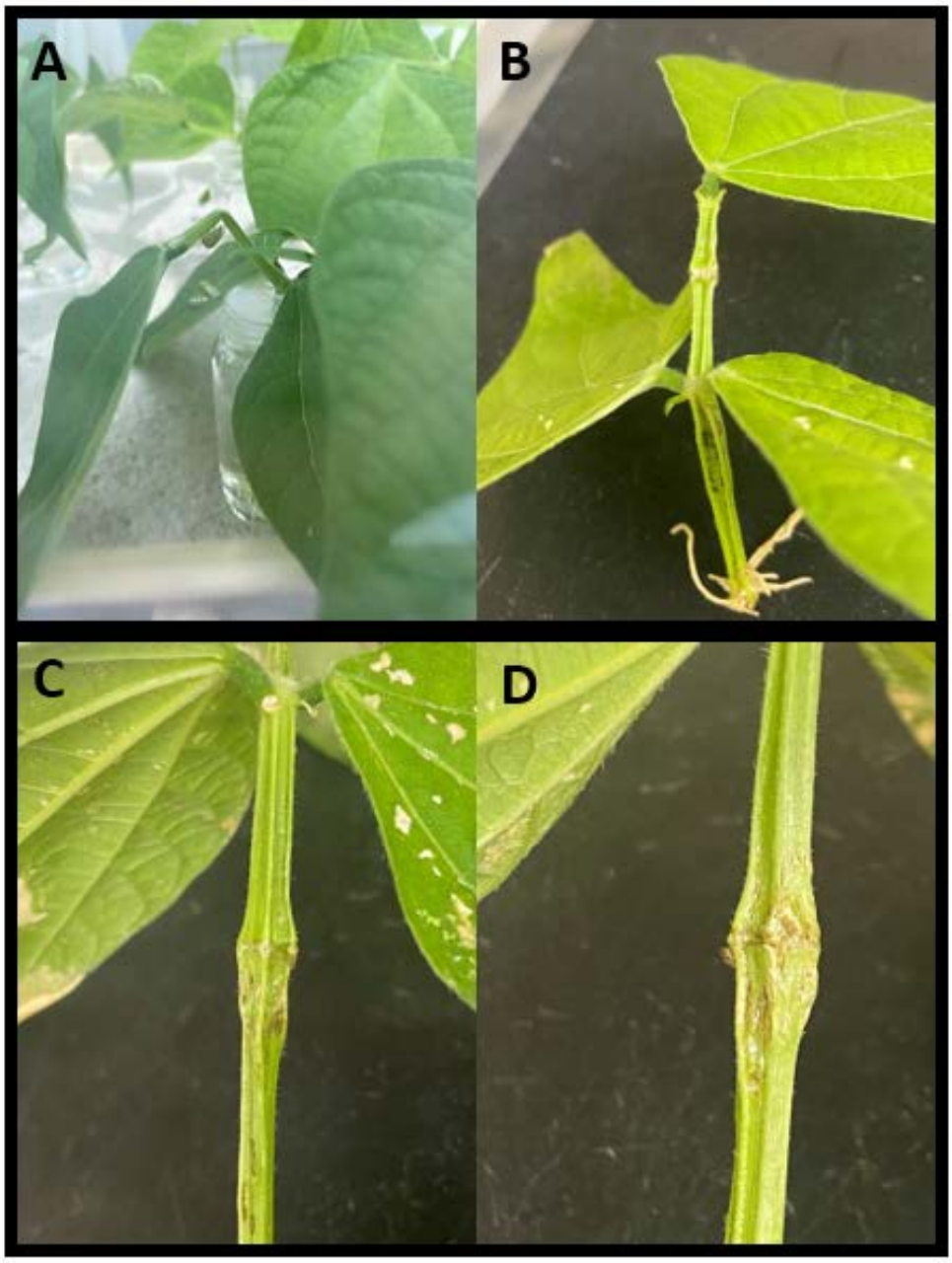

Figure A4-7. The different locations of girdling behaviors observed by male and female *Spissistilus festinus* in arenas with both sexes present. Male girdling behaviors were often observed around the time of mating (Figure A4-7A) and would result in vascular cut off along the petiole leaf junction (Figure A4-7B). Female girdling behaviors were often observed around the time of oviposition and were right above the oviposition sites (Figure A4-7C, D). This behavior is characteristic of mothering and could be done to encourage proper feeding of nymphs upon emergence (Figure A4-7D).

Dispersal of aviruliferous *Spissistilus festinus* males and females and impact on secondary GRBV spread in arenas with single and multiple initial infections

In experiments with aviruliferous *S. festinus* and a single or four (hotspot) GRBV-infected *P. vulgaris* trifoliates at one edge of each arena (**Figure A4-3**), GRBV transmission occurred at a higher rate with males in both single (50%, 30/60) and hotspot (80%, 32/40) arenas than with females in single (35%, 21/60) and hotspot (67%, 40/60) arenas (p=0.00334) (**Table A4-4**).

Testing of *S. festinus* at the completion of the dispersal experiments revealed a similar acquisition rate of GRBV by males (88%, 35/40) and females (78%, 28/36), with no statistically significant differences in GRBV titer in a randomly selected subset of these specimens, as shown by qPCR (p=0.360) (**Figure A4-8**). These findings highlighted sex-associated behavioral differences in the transmission of GRBV by *S. festinus* and a positive correlation between the initial virus incidence and the rate of transmission.

Analyzing the distribution of newly infected GRBV-infected trifoliates in single infection arenas revealed a clustering near the virus donor trifoliate upon which *S. festinus* specimens were released and a predominant within-row spread (**Figure A4-9**). These results may result from a walking and jumping movement of *S. festinus* that acquired GRBV by feeding on the single infected trifoliate. In hotspot arenas, the distribution of newly infected GRBV-infected trifoliates confirmed a predominant walking and jumping movement behavior of *S. festinus* (**Figure A4-9**). These results revealed secondary spread of GRBV primarily in relation to a walking and jumping movement behavior of *S. festinus*.

Table A4-4. Rate of grapevine red blotch virus transmission by *Spissistilus festinus* males and females in arenas with single or hotspot infections.

	Males	**Females**
Single Infection Arena	30/60 (50%)	21/60 (35%)
Hotspot Infection Arena	50/60 (83%)	40/60 (67%)
Total GRBV-Infected Trifoliates	80/120 (67%)	61/120 (51%)

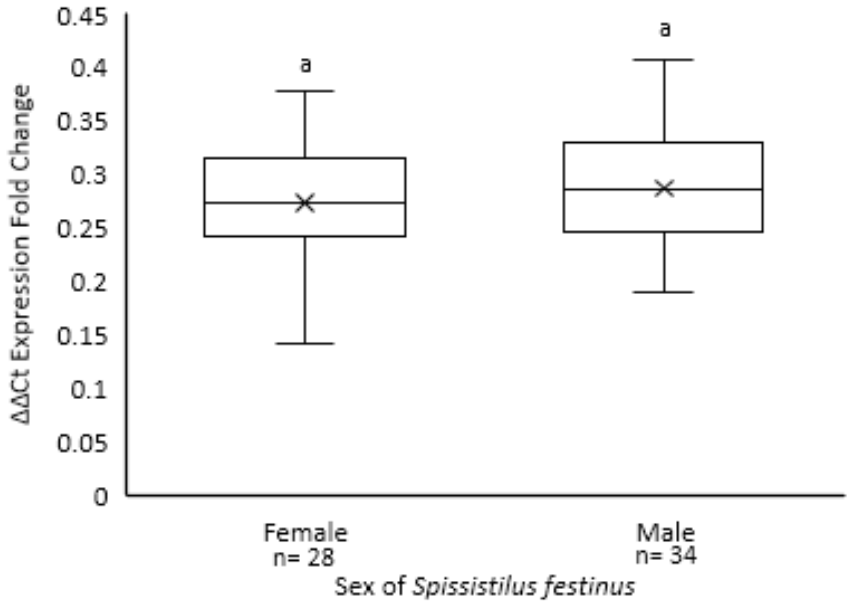

Figure A4-8 Quantification of grapevine red blotch virus in female and male *S. festinus* used in single and hot spot infection assays by qPCR. Data show the ΔΔCt expression fold change values (2(−ΔΔCt)). The (x) represents the mean expression fold change. Error bars indicate standard error of the mean. Lowercase lettering indicating insignificant differences between 2(−ΔΔCt) values, as determined by Tukey's honestly significant difference test ($p < 0.05$), are shown above standard error bars.

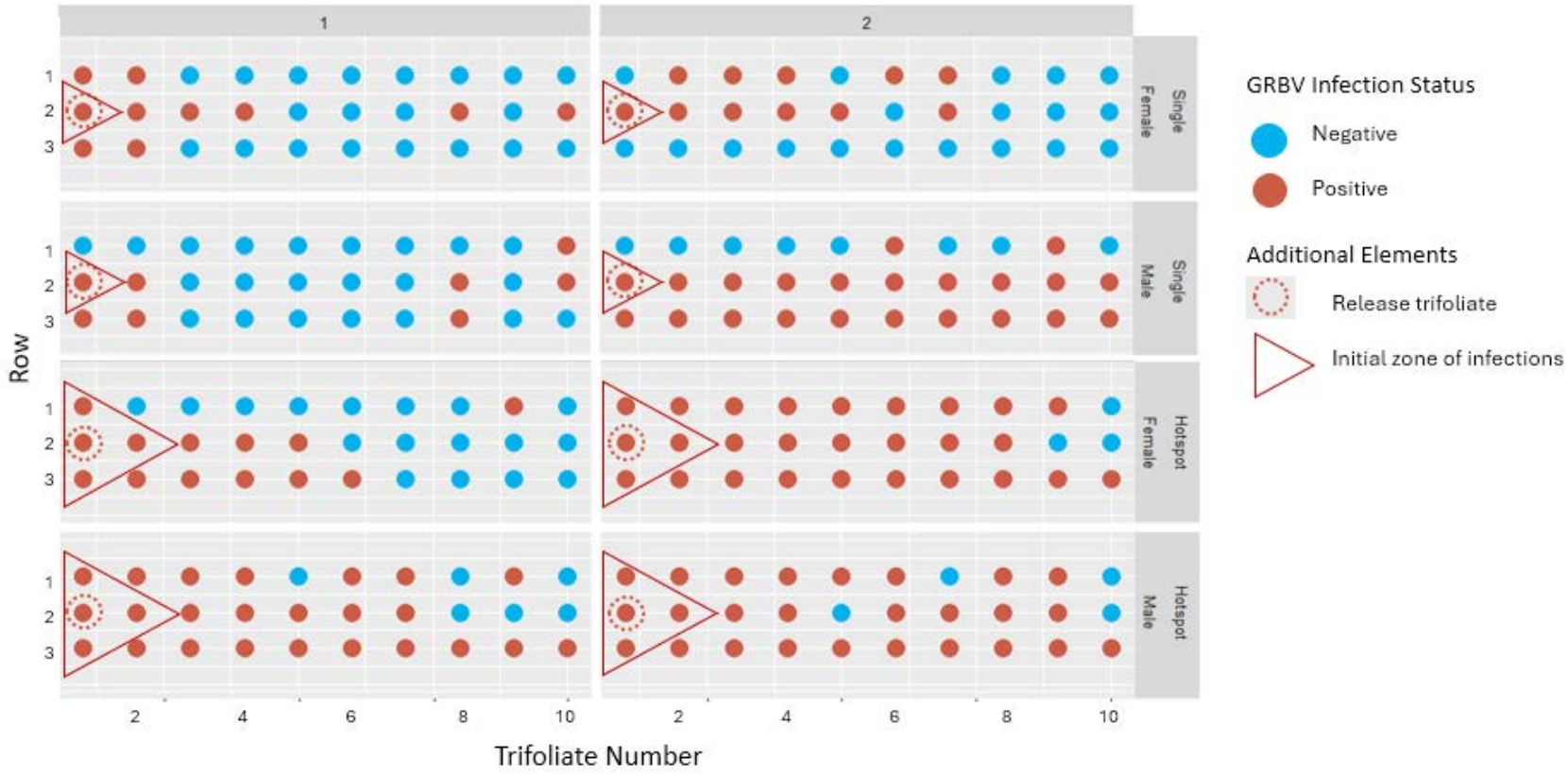

Figure A4-9. Transmission of grapevine red blotch virus (GRBV) from bean trifoliate to bean trifoliate by aviruliferous male (second and fourth row arenas) or female (first and third row arenas) *Spissistilus festinus*, over two-weeks, in arenas with single (first and second row arenas) or four (hotspot) (third and fourth row arenas) GRBV-infected *P. vulgaris* trifoliates (red triangle). Insects were deposited on a single trifoliates (dotted circle) located at one edge of each arena. Data show GRBV-infected trifoliates (red dot) and noninfected trifoliates (blue dots), as determined by PCR.

DISCUSSION

In this study, we documented a lack of vertical transmission of GRBV by *S. festinus* using transmission assays with *P. vulgaris*, a rearing host of *S. festinus* and a pseudo systemic host of GRBV (Flasco et al. 2021). These results are consistent with similar reports on viruses in the family *Geminiviridae* (Czosnek et al. 2017; Fiallo-Olivé et al. 2018; Rojas et al. 2018). Therefore, the absence of transovarial transmission of GRBV by the progeny of viruliferous *S. festinus* is validating our hypothesis.

We further investigated the dispersal of *S. festinus* males and females in small arenas with *P. vulgaris* trifoliates. Following the release of cohorts of 10 specimens on a single trifoliate, both sexes were shown to preferentially aggregate near the trifoliate of release, though males were more likely to disperse in the afternoons, returning overtime to near their trifoliate of release. This differential behavioral dispersal of *S. festinus* resulted in a greater rate of transmission of GRBV by males in comparison to females, and a clustering of newly infected trifoliates near the single trifoliate upon which insects were released. Similarly, males contributed to more efficient secondary spread of GRBV than females, though both sexes had similar rates of virus acquisition. In addition, a positive correlation was found between initial virus incidence and transmission rate and movement behaviors of *S. festinus* based on walking and jumping explained secondary spread. It will be interesting to monitor the behavior and dispersal of *S. festinus* males and females in vineyard ecosystems. Such studies should help better understand the unique epidemiological attributes of red blotch disease previously reported (Cieniewicz et al. 2017; Cieniewicz et al. 2019; Dalton et al. 2019; Flasco et al. 2023; KC et al. 2022).

Male *S. festinus* have a greater flight capacity in comparison with females (on average 570.22 m vs. 239.57) (Antolínez et al. 2023). It is not known if this sex-based difference may affect secondary spread of GRBV in vineyard ecosystems. However, based on our findings, it is reasonable to anticipate that *S. festinus* males are major contributors to the spread of GRBV in vineyards. Furthermore, more males than females are caught on sticky cards in vineyards (Hoyle et al. 2024) and alfalfa fields (Johnson and Mueller 1990), although a balanced sex-ratio was observed with the use of sweep netting in alfalfa fields (Johnson and Mueller 1990). This is suggesting differences in male and female dispersal behaviors. In this study, we observed a large proportion of afternoon flights by males, coupled with a greater rate of GRBV transmission, suggesting that sex-associated differences in transmission are influenced by behavior.

An overabundance of *S. festinus* and feeding was previously found to negatively impact the transmission success of GRBV, likely due to girdling of grapevine tissue (Flasco et al. 2023). It is possible that feeding behaviors and larger aggregations of *S. festinus* females could result in lower rates of transmission due to extensive feeding damages. In contrast, *S. festinus* male dispersal and potential probing rather than girdling behaviors during this time could promote the spread of GRBV. This should be monitored further to better understand *S. festinus* feeding and/or reproduction behaviors by, for instance, using electrical penetration graph technologies.

In this study, transmission of GRBV by *S. festinus* was low (10%, 42/420) with viruliferous specimens when combining data obtained with males, females and a 50/50 mix across replicated experiments. Nonetheless, this transmission rate is consistent with those previously observed in transmission assays in the greenhouse (4-42%) on

cultivated grape (Flasco et al. 2021; Hoyle et al. 2022) and vineyards (3-28%) (Cieniewicz et al. 2017; Cieniewicz et al. 2019; Dalton et al. 2019; Flasco et al. 2023; KC et al. 2022). In contrast, a high rate of transmission of GRBV (56%, 123/220) was observed by both *S. festinus* sexes when aviruliferous specimens had to acquire the virus first on infected trifoliates and transmit it to healthy trifoliates in the arenas. This high rate of transmission suggests that *S. festinus* were almost immediately feeding on infected trifoliates upon release, considering that a 6-day acquisition access period is needed for bean-to-bean transmission (Flasco et al. 2021) and our experiments lasted 14 days. This marked difference in GRBV transmission by viruliferous and aviruliferous *S. festinus* could be related to the age of the insects, as discussed below.

In experiments using viruliferous insects, very few *S. festinus* tested positive for GRBV (15%, 9/60), whereas in experiments using aviruliferous hoppers from arenas with single (70%, 28/40) or hotspot infections (97%, 35/36) *S. festinus* tested positive for GRBV at the completion of the transmission assays. These differences in virus acquisition could be due to the age of the S. *festinus* specimens when they were released into the arenas. Experiments with viruliferous *S. festinus* relied on specimens that were approximately 2 weeks older than those used in experiments with aviruliferous specimens. This is around the time when female *S. festinus* lay their first eggs if they had an opportunity to mate. It is likely that this important step within the life cycle of adult *S. festinus* alters movement and feeding behaviors, thus reducing the rate of virus acquisition and transmission. In addition, more *S. festinus* specimens, primarily males, died due to old age, during the experiments with viruliferous insects, impacting the rate of virus transmission.

Epidemiological studies have documented an edge effect in the spatiotemporal distribution of GRBV-infected vines in vineyards at an early stage of a red blotch disease epidemic (Cieniewicz et al. 2017; Dalton et al. 2019). Diseased vines clustering at the edge of a vineyard could serve as a transmission hotspot to facilitate secondary spread of GRBV. Based on our dispersal assays, there was an increase in GRBV-positive *S. festinus* as the size of the inoculum increased. Similarly, there was a positive association between the initial virus incidence and the rate of GRBV spread.

In vineyard ecosystems, *S. festinus* interact with free-living vines, using them as a feeding and possible overwintering host (Hoyle et al. 2024). If the behavior of *S. festinus* in vineyards is similar to the behavior observed in this study, *S. festinus* visiting vineyards, including disease vineyards, could return to their preferred feeding and reproductive hosts in natural habitats, potentially resulting in a buildup of virus inoculum in riparian areas, as previously suggested (Cieniewicz et al. 2018). More work is needed to confirm this potential.

The primary source of GRBV in vineyards is planting material. Newly established grapevines that are infected by GRBV form a source of inoculum for secondary spread, which can be extensive if virus incidence is high (Cieniewicz et al. 2019; Flasco et al. 2023; this study) although *S. festinus* is an inefficient vector of GRBV and transmission rates are not as high otherwise (Flasco et al. 2021; Hoyle et al. 2022; this study). Based on the polyphagous nature of *S. festinus* and their preferred feeding and reproductive hosts in natural and riparian habitats rather than in vineyards, we cannot stress enough the importance of planting certified, clean planting stocks that have been extensively tested for the absence of GRBV, and the roguing of diseased vines or

removal of entire vineyards if disease incidence is below or above 30%, respectively (Ricketts et al. 2017). To refine these disease management responses, more work is needed to characterize the sex ratio of male and female *S. festinus* in vineyards, and their dispersal in relation to disease epidemiology.

REFERENCES

Antolínez, C.A., Chandler, M., Hoyle, V., Fuchs, M., & Rivera, M.J. 2023. Differential flight capacity of *Spissistilus festinus* (Hemiptera: Membracidae) males and females. J. Insect Behav. 36:347–357.

Cieniewicz, E.J., Perry, K.L. and Fuchs, M. 2017. Grapevine red blotch virus: Molecular biology of the virus and management of the disease. In: Grapevine Viruses: Molecular Biology, Diagnostics and Management. Meng, B., Martelli, G.P., Golino, D.A. and Fuchs, M.F (eds). Springer Verlag, pp. 303-314.

Cieniewicz, E., Thompson, J.R., McLane, H., Perry, K.L., Dangl, G.S., Corbett, Q., Martinson, T., Wise, A., Wallis, A., O'Connell, J., Dunst, R., Cox, K. and Fuchs, M. 2018. Prevalence and diversity of grabloviruses in free-living *Vitis* spp. Plant Disease 102:2308-2316.

Cieniewicz, E., Flasco, M., Brunelli, M., Onwumelu, A., Wise, A. and Fuchs, M. 2019. Differential spread of grapevine red blotch virus in California and New York vineyards. Phytobiomes Journal 3:203-211.

Dalton, D. T., Hilton, R. J., Kaiser, C., Daane, K. M., Sudarshana, M. R., Vo, J., Zalom, F. G., Buser, J. Z., & Walton, V. M. 2019. Spatial associations of vines infected with grapevine red blotch virus in Oregon vineyards. Plant Dis. 103:1507–1514.

Fiallo-Olivé, E., Zerbini, F.M., Briddon, R.W., Martin, D.P., Navas-Castillo, J., Roumagnac, P. and Varsani, A. 2018. *Geminiviridae*. https://talk.ictvonline.org/ictv-reports/ictv_online_report/ssdna-viruses/w/geminiviridae

Flasco, M., Hoyle, V., Cieniewicz, E., Roy, B., McLane, H., Perry, K.L., Loeb, G., Nault, B., Heck, M., Fuchs, M. 2021. Grapevine red blotch virus is transmitted by the three-cornered alfalfa hopper in a circulative, nonpropagative mode with unique attributes. Phytopathol. 111:1851-1861.

Flasco, M., Hoyle, V., Cieniewicz, E.J., McLane, H.L., Perry, K.L., and Fuchs, M. 2023. The three-cornered alfalfa hopper, *Spissistilus festinus*, is a vector of grapevine red blotch virus in the vineyard. Viruses 15:927.

Flasco, M., Hoyle, V., Powell, G., Seiter, J., Wise, A., Cieniewicz, E.J., and Fuchs, M. 2023. Seasonal variation in grapevine red blotch virus titer in relation to disease symptom expression in vineyards. Phytobiomes Journal 8:192-200.

Hoyle, V., Flasco, M.T., Choi, J., Cieniewicz, E.J., McLane, H., Perry, K., Dangl, G., Al Rwahnih, M., Heck, M., Loeb, G., Fuchs, M.F. 2022. Transmission of grapevine red blotch virus by *Spissistilus festinus* [Say, 1830] (Hemiptera: Membracidae) between free-living vines and *Vitis vinifera* 'Cabernet franc'. Viruses 14:1156.

Hoyle, V., Flasco, M., and Fuchs, M. 2024. Transmission of Grabloviruses by Insect Vectors. In: Methods Molecular Biology – Geminiviruses (eds. E. Fiallo Olivé, F. Murilo Zerbini, J. Navas-Castillo), Springer Nature. in Press.

Hoyle, V., Headrick, H., Cooper, W.R., Fendell-Hummel, H.G., Cooper, M.L., Flasco, M., Cieniewicz, E., Heck, M., Fuchs, M. 2024. Connectivity of plant

communities for viral disease dynamics informed by the dietary profiles of a treehopper. Submitted.

Johnson, M. P. and Mueller, A. J. 1990. Flight and diel activity of the threecornered alfalfa hopper (Homoptera: Membracidae), Enviro. Entom. 19:677–683.

Jordan, C. R. 1952. The biology and control of the three-cornered alfalfa hopper *Spissistilus festinus* (Say). Ph. D. dissertation Texas A&M University, College Station.

Krenz, B., Thompson, J.R., McLane, H.L., Fuchs, M., Perry, K.L. 2014. Grapevine red blotch-associated virus is widespread in the United States. Phytopathol. 104:1232–40.

Krenz, B., Fuchs, M., Thompson, J.R. 2023. Grapevine red blotch disease: A Comprehensive Q&A Guide. PLOS Path. 19(10): e1011671, doi.org/10.1371/journal.ppat.1011671.

Meisch, M.V. and Randolph N.M. 1965. Life-history studies and rearing techniques for the three-cornered alfalfa hopper. Journal of Economical Entomology 58:1057-1059.

Pereira, W.J.; Bassinello, P.Z.; Brondani, C.; Vianello, R.P. 2017. An improved method for RNA extraction from common bean seeds and validation of reference genes for qPCR. Crop Breed. App. Biotechnol. 17:150–158.

Perry, K.L., McLane, H., Hyder, M.Z., Dangl, G.S., Thompson, J.R. and Fuchs, M.F. 2016. Grapevine red blotch-associated virus is present in free-living *Vitis* sp. proximal to cultivated grapevines. Phytopathology 106:663-670.

Ricketts, K.D., Gomez, M.I., Fuchs, M.F., Martinson, T.E., Smith, R.J., Cooper, M.L. and Wise, A., 2017. Mitigating the economic impact of Grapevine Red Blotch: Optimizing disease management strategies in U.S. vineyards. American Journal of Enology and Viticulture 68:127-135.

Rojas, M.R., Macedo, M.A., Maliano, M.R., Soto-Aguilar, M., Souza, J.O., Briddon, R.W., Kenyon, L., Rivera-Bustamante, R.F. Zerbini, F.M., Adkins, S., Legg, J.P., Kvarnheden, A., Wintermantel W.M., Sudarshana, M.R., Peterschmitt, M., Lapidot, M., Martin, D.P., Moriones, E., Inoue-Nagata, A.K. and Gilbertson, R.L. 2018. World management of geminiviruses. Annual Review of Phytopathology 56:637-677.

Rumbaugh, A.C., Sudarshana, M.R., Oberholster, A. 2021. Grapevine red blotch disease etiology and its impact on grapevine physiology and berry and wine composition. Horticulturae 7:552.

Setiono, F.J., Chatterjee, D., Fuchs, M., Perry, K.L. and Thompson, J.R. 2018. The distribution and ability to detect grapevine red blotch virus in its host depends on time of sampling and tissue type. Plant Disease 102:2187-2193.

Yepes, L.M. Cieniewicz, E., Krenz, B., McLane, H., Thompson, J.R., Perry, K.L. and Fuchs, M. 2018. Causative role of grapevine red blotch virus in red blotch disease. Phytopathology 108:902-909